Modelling γ'' ($D0_{22}$) Precipitate Nucleation, Growth and Coarsening in the Nickel-base Superalloy 625

Ian James Moore

Thesis submitted for the degree of Doctor of Philosophy

Department of Materials Science and Engineering

15 May 2017

University of Sheffield

To my family, thank you for your love and support.

Acknowledgements

This research project would not have been possible without the support of a few significant people. The author wishes to express his principle gratitude to his two supervisors, Professor Eric Palmiere and Professor Grace Burke, who have been incredibly helpful and offered invaluable assistance, encouragement and guidance. In addition, thanks are also made to the technical staff at the University of Sheffield and University of Manchester for their help and patience. Finally, deepest appreciation is extended to the Engineering and Physical Sciences Research Council who provided funding for the work through the Nuclear FiRST doctoral training centre based at The University of Sheffield and The University of Manchester (Grant EP/G037140/1).

Abstract

Although typically thought of as a solid solution strengthened material, Alloy 625 is susceptible to significant precipitation hardening through the formation of γ'' ($D0_{22}$) precipitates. These particles can form both during manufacture and in high temperature service and, consequently, the accurate prediction of their behaviour is crucial. To this end, a model is developed in this work which describes γ'' precipitation in Alloy 625, encompassing the concurrent homogeneous nucleation, growth and coarsening of different particles and allowing for them to be shape changing. Based on the Svoboda-Fischer-Fratzl-Kozeschnik (SFFK) framework, the model is calibrated with respect to experimental measurements of aspect ratio evolution at 650°C where the statistics were acquired through a novel analysis methodology. The outputs generated by the model for interfacial energy, particle size distribution and number density are in excellent agreement with experimental data for a simulation of 1000 hours of ageing at 650°C; however, beyond this point a divergence is introduced by the phenomenon of precipitate "encounter" (described by Davis *et al.* [1]). Following suitable changes for descriptions including precipitation driving force and material elastic constants, application of the model to the evolution of γ'' precipitates in Alloy 718 at 700°C measured by Han *et al.* [2] reveals reasonable agreement. Whilst the results presented in this paper are predicated on a homogeneous microstructure and the formation of exclusively γ'' precipitates, the underlying frame work outlined is flexible enough for inhomogeneous and competitive precipitation to be included at a later date. Furthermore, through the application of an additional class management mechanism, the model is likely applicable to a large range of ageing temperatures and durations.

Publications

I.J. Moore, M.G. Burke and E.J. Palmiere, Modelling the nucleation, growth and coarsening kinetics of γ'' ($D0_{22}$) precipitates in the Ni-base Alloy 625, *Acta Materialia*, 119:157-166, 2016.

I.J. Moore, J.I. Taylor, M.W. Tracy, M.G. Burke and E.J. Palmiere, Grain coarsening behaviour of solution annealed Alloy 625 between 600-800°C, *Materials Science and Engineering A*, 682:402-409, 2017.

I.J. Moore, M.G. Burke, N.T. Nuhfer and E.J. Palmiere, Evaluation of classical precipitation descriptions for γ'' (Ni_3Nb-$D0_{22}$) in Ni-base superalloys, *Journal of Materials Science*, 52(14):8665-8680, 2017.

(Planned)

I. J. Moore, M. G. Burke and E. J. Palmiere, Application of an SFFK model for the nucleation, growth and coarsening kinetics of γ'' ($D0_{22}$) precipitates in Ni-base superalloys.

Contents

List of Tables

List of Figures

List of Symbols

α	Precipitate aspect ratio
α_k	Aspect ratio of precipitate k defined as $L_{\mathrm{m}}/L_{\mathrm{M}}$
β	Generic precipitate phase
β^*	Precipitate atomic absorption rate
γ	FCC system matrix phase
γ^*	Supersaturated matrix phase
γ''	Ordered $\mathrm{D0}_{22}$ precipitate phase with composition $\mathrm{Ni}_3\mathrm{Nb(Al,Ti)}$
γ'	Ordered $\mathrm{L1}_2$ (FCC) precipitate phase with the formula $\mathrm{(Ni,Co)}_3\mathrm{(Al,Ti)}$
δ	$\mathrm{D0}_a$ orthorhombic precipitate phase with composition $\mathrm{Ni}_3\mathrm{Nb}$
$\Delta\varepsilon$	Additional precipitate-matrix misfit eigenstrain along the precipitate's axis of rotation
ϵ	Strain tensor
ε	Isotropic precipitate-matrix misfit eigenstrain
ζ	Interfacial energy per unit area
ζ_k^E	Interfacial energy per unit area on ends of cylindrical precipitate k
ζ_k^M	Interfacial energy per unit area on mantle of cylindrical precipitate k
η	$\mathrm{D0}_{24}$ precipitate phase with composition $\mathrm{Ni}_3\mathrm{Ti}$
θ	Angle between the two boundaries of a lens precipitate nucleated on an isotropic planar boundary.
ϑ	Angle between the opposite faces of a Vickers Hardness indenter
ι	Dimensionless parameter describing the normalised “catalytic effect of a dislocation on precipitate nucleation
κ	Constant associated with the length scale of atomic diffusion

λ	Precipitate-matrix misfit strain
λ_k	Precipitate-matrix misfit strain energy for precipitate k
μ	TCP precipitate phase with ideal stoichiometry $\mathrm{A_6B_7}$
ν	Poisson's ratio
ξ_k	Dimensional ratio of precipitate k
π	The ratio of the circumference of a circle to its diameter
$\bar{\rho}$	Mean value of ρ distribution
ρ	Precipitate equivalent spherical radius
ρ^*	Critical equivalent spherical radius for a stable nucleating precipitate
ρ_k	Equivalent spherical radius of precipitate k
ϱ	Number of system vacancies per atom
ϱ^*	Number of system vacancies per atom required to form a stress free precipitate
σ	TCP precipitate phase with ideal stoichiometry $\mathrm{A_2B}$
σ_r	Standard deviation of r_{M} distribution
$\sigma_r^\dagger$	Log-Normal standard deviation of r_{M} distribution
φ	Radius of interface curvature
χ	Factor associated with the grain boundary energy
ψ	Vertical displacement between the growth ledges of a precipitate
ω	Factor which describes the vibration frequency of atoms
τ	Precipitate nucleation incubation period
Φ	Partial molar free energy / Chemical potential
Ψ_0	Accelerating potential
Ω	System molar volume
Υ	Accommodation factor *i.e.* Probability of a solute atom being accommodated in the precipitating phase
Λ_k	Contribution to ζ_k^E from the reduction in misfit strain
a	Precipitate shape factor
$a_{\gamma''}$	γ'' phase a lattice parameter
a_γ	γ matrix lattice parameter

b	Burgers vector of a dislocation
$c^e(n)$	Equilibrium concentration of microclusters with size n
c_γ^0	Initial concentration of solute atoms in the system matrix
c_γ^{e}	Equilibrium concentration of solute atoms in the system matrix
$c_{\gamma i}$	Concentration of element i in the system matrix
$c_{\gamma i}^{\mathrm{eq}}$	Concentration of element i in the system matrix at equilibrium
$c_{\gamma''}$	γ'' phase c lattice parameter
c_{ki}	Concentration of element i in precipitate k
$\bar{d}$	Mean of the two square diagonals of a Vickers Hardness indentation
dd	Mathematical distribution density
Δe	Energy difference between two electron states
e_λ	Electron de Broglie wavelength
e_{C}	Electron charge, 1.6022×10^{-19} C
e_{m}	Electron rest mass, 9.1094×10^{-31} kg
f	Wave frequency
f_{LN}	Log-Normal distribution probability density
f_{LSW}	Lifshitz-Slyozov-Wagner distribution probability density
f_{Norm}	Normal distribution probability density
g	Elastic shear modulus
h	Planck's constant $6.6261 \times 10^{-34} Js$
i	Elemental component index
j	Atomic flux
$_k$	Subscript indicating both an individual precipitate and precipitate class
k_B	Boltzmann constant, 1.3806×10^{-23} J/K
m	Total number of model precipitate classes
n	Number of elements/components in a system
n^*	Critical number of precipitate atoms to form a precipitate
n_i	Number of atoms inside a precipitate

p_{e}	Electron momentum
$\dot{q}$	Time derivatives of the set of system defining independent state parameters
q_l	Set of system defining independent state parameters
r	Spherical precipitate radius
$\bar{r}(t)$	Average particle radius at time t
$\bar{r}_0$	Average initial particle radius
$\bar{r}_{\mathrm{M}}^{\dagger}$	Log-Normal mean value of r_{M} distribution
$\vec{r}$	Multidimensional vector defining the state of an individual microcluster
$\vec{r}'$	Multidimensional vector defining the state of an individual microcluster
r^*	Critical radius for a stable nucleating spherical precipitate
r_{M}	Oblate spheroidal precipitate major radius
s	Concentration of microclusters defined by $\vec{r}$
t	Time in seconds
u_{c}	Speed of light
u_{e}	Electron velocity
v	Precipitate growth rate
w	Transition frequency of a microcluster between $\vec{r}$ and $\vec{r}'$
x	Displacement
A	Precipitate surface area
A_{r}	Arrhenius equation prefactor
A_k	Ellipsoidal major axis of precipitate k
A_ζ	Second degree polynomial coefficient describing ζ_k^E
B_k	Equivalent cylinder diameter of precipitate k
B_ζ	First degree polynomial coefficient describing ζ_k^E
B_Z	Zero degree polynomial coefficient describing Z_k^E
C	Relative elastic contrast C between the precipitate and matrix
ΔC	Absolute elastic contrast C between the precipitate and matrix
C_ζ	Zero degree polynomial coefficient describing ζ_k^E

D	Diffusion coefficient
D_0	Atomic diffusion constant
$D_{\gamma i}$	Bulk diffusion coefficient of component i in the matrix
E	Young's modulus
E_γ	Young's modulus of the matrix phase γ
E_a	Reaction activation energy
E_e	Electron energy
F_0	Factor accounting for the distribution of strain in a spheroidal particle with a degree of 0 in the polynomial component of the equation describing λ_k
F_1	Factor accounting for the distribution of strain in a spheroidal particle with a degree of 1 in the polynomial component of the equation describing λ_k
F_2	Factor accounting for the distribution of strain in a spheroidal particle with a degree of 2 in the polynomial component of the equation describing λ_k
G	System Gibbs free energy
ΔG	Total system free energy change associated with precipitate formation
ΔG^*_het	Critical change in free energy/work of formation for a heterogeneously nucleated stable precipitate
ΔG^*_hom	Critical change in free energy/work of formation for a homogeneously nucleated stable precipitate
ΔG_D	Activation energy for atomic migration
ΔG_d	Nucleation site energy reduction associated with a defect
ΔG_eff	Effective driving force for precipitation
ΔG_s	Misfit strain energy per unit volume
ΔG_v	Difference in free energy per unit volume of the matrix and precipitate
$\Delta G_{D\mathrm{eff}}$	Effective activation energy for atomic migration
ΔG^*	Critical change in free energy/work of formation for a stable precipitate
G_ASTM	G ASTM grain size number
GB_C	Fraction of grain boundary length covered in precipitates
ΔH	Enthalpy of precipitate formation
I	Width of the curve of $\Delta G(n)$ approximately k_BT below ΔG^*

J	Joule
K	Degrees Kelvin
$\bar{L}$	Average grain size
L_{M}	Precipitate major axis length
L_{m}	Precipitate minor axis length
M	Precipitate-matrix interface mobility
M	Metallic cation
$\dot{N}$	Precipitate nucleation rate
$\dot{N}(n)$	Rate of precipitates changing in size from n to n+1
$\dot{N}_{\mathrm{het}}$	Heterogeneous precipitate nucleation rate
$\dot{N}_{\mathrm{hom}}$	Homogeneous precipitate nucleation rate
N_0	Total number of remaining precipitate nucleation sites
N_c	Total number of nucleating precipitates
N_i	Moles of element i
$N_{0,\mathrm{het}}$	Total number of remaining heterogeneous precipitate nucleation sites
O_k^1	Factor derived from the dissipation of the Gibbs energy to account for a cylindrical precipitate shape
O_k^1	Factor to account for cylindrical shape assumed for precipitate k
O_k^3	Factor derived from the dissipation of the Gibbs energy to account for a cylindrical precipitate shape
O_k^3	Factor to account for cylindrical shape assumed for precipitate k
P_1	Single current precipitate atomic absorption probability/rate
P_2	Single current precipitate atomic desorption probability/rate
Q	Rate of free energy dissipation
R	Ideal gas constant, 8.3145 J K^{-1} mol^{-1}
R_{a}	Average surface roughness
$\mathrm{R_c}$	Mean height of profile irregularities
T	Absolute temperature (K)

ΔT	Undercooling temperature/temperature difference to that at which all precipitates are solutionised
HV*p*	Vickers hardness number where *p* is replaced by the load in kilograms used
U	U factor
V	Precipitate volume
V_{a}	Phase atomic volume
V_{M}	Phase molar volume
V_{OS}	Oblate spheroid volume
ΔX	Instantaneous difference to equilibrium elemental mole fraction
X^{e}	Element mole fraction at equilibrium
X_0	Initial element mole fraction in matrix
X_{φ}	Element mole fraction in matrix at Gibbs-Thomson modified equilibrium
X_i	Element mole fraction at precipitate-matrix interface
Z	Zeldovich factor
Z_k^E	ζ_k^E with misfit strain contribution removed
APB	Anti-phase-boundary
BCT	Body-Centred-Tetragonal (crystal structure)
BF	Bright-field electron image
DF	Dark-field electron image
ESR	Electro-Slag Re-melting
FCC	Face-Centred-Cubic (crystal structure)
HCP	Hexagonal-Close-Packed (crystal structure)
INVH	Isothermally Normalised Vickers Hardness
JMAK	Johnson-Mehl-Avrami-Kolmogorov modelling method
KWN	Kampmann and Wagner numerical modelling method
MC	Monte-Carlo modelling method
NA	Numerical Aperture
PSD	Precipitate/Particle Size Distribution
SEM	Scanning Electron Microscope/Microscopy

SFFK	Svoboda-Fischer-Fratzl-Kozeschnik modelling method
TCP	Topologically-Close-Packed (crystal structure)
TEM	Transmission Electron Microscope/Microscopy
VAR	Vacuum Arc Re-melting
VIM	Vacuum Induction Melting

Introduction

At a high concept level, the driving force behind materials science and engineering research can be best understood as the ability to design and control the structure and properties of materials. Such research has defined mankind's development, with the majority of human history segmented (even in the common vernacular) not in terms of art, language or culture, but the materials (Stone, Bronze and Iron) used to make tools owing to the accompanying huge leaps in the ability of societies to grow and prosper. Today, even with the plethora of new materials developed over recent decades, humanity remains very much in the iron age with metals undoubtedly contributing most to the development of modern society *viz.* almost all modern buildings, transportation methods, technologies and agriculture still rely on metals in some crucial way.

At the heart of the utilisation of (transition) metals such as iron lies their unique and useful properties which can be induced from combinations of alloying, heat treatment and mechanical working. Although known for millennia in many instances (*e.g.* the creation of bronze and brass to improve the properties of copper), however, the scientific basis for these characteristics only became properly understood during the nineteenth and twentieth centuries with the advent of rigorous experimentation/testing and microscopy. Such developments led to both the dramatic/rapid improvement of existing products such as steels and the creation of new ones such as aluminium-base and nickel-base alloys which are now ubiquitous.

Despite its evidenced maturity, progress in material science even with respect to metals remains considerable owing to ever increasing characteristic demands from corrosion resistance to strength, very often all in the same alloy. A perfect illustration of this development is that of nickel-base super alloys, with, for example, jet engine manufacturer's demanding alloys which will retain their strength at higher and higher temperatures to improve efficiency and power. Similarly, nuclear power companies require ever more resilience to radiation damage whilst retaining corrosion properties and structural integrity. Achieving such stringent demands is possible only through the individual tailoring of alloys (chemistry, thermomechanical processing and design) predicated not only on the results of direct experimentation but increasingly computational modelling.

The use of computation has been embraced by materials scientists and engineers (much like colleagues in other fields such as biology and physics) thanks to its combined flexibility and relative speed compared to physical measurements. Crucially, however, models remain far from perfect in many instances due to problems which can be attributed generally to their ability to describe a system (owing to its immense complexity) and to generate results with applicable outcomes. In this circumstance, any model created to describe a metallic system must still currently be validated against at least some appropriate experimentally acquired data to ensure applicability. Consequently, the vast majority of modern day metallurgical research comprises synergistic experimental and computational studies.

Although comparatively narrow in scale, it is in the above context that the research outlined in this thesis was conducted into thermally induced evolution of the nickel based superalloy 625. Specifically, the work was formulated and conducted with a view to producing components with properties corresponding to those required for specific practical applications and to evaluate any changes which may happen to products in high temperature service.

Chapter 1

Background and Literature review

In order to both shape and guide their endeavours (as well as avoid needless repetition), before embarking on a new piece of research scientists and engineers necessarily review all previously documented studies. To this end, the relevant work identified in the literature for the investigation of precipitation in Alloy 625 in this work is utilised both for the purposes of providing background and also the determination of areas in which the current understanding is limited.

§ 1.1 Fundamentals of Superalloys

With a metallic alloy ubiquitously understood (in its fundamental sense) as a mixture of a metallic element with at least one other element, a "superalloy" is defined as a metallic alloy which possesses multiple superior/high performance properties [48]. The principle driving force for the invention and evolution of superalloys was, and continues to be today, the development of gas turbine engines for powered flight *viz.* the thirst for higher efficiencies and power outputs is insatiable and has resulted in modern engines consisting of the most expensive and high tech alloys ever developed. Despite this, however, the excellent high temperature strength and corrosion resistance properties of superalloys has meant that their development and use has not remained solely the preserve of the jet engine manufacturer, but rather has become extensive in many industries including petrochemicals, shipping and power.

Since their inception, three distinct superalloy classes/types have been developed, defined by their majority constituent, with each possessing their own distinct characteristics and, resultantly, applications: Cobalt-base superalloys are typically looked upon as the first true superalloys to have been developed, with their utilisation in aero engines turbochargers starting in the 1930s [49, 50, 51]. Their metallurgy is such that they typically comprise an austenitic matrix phase (providing excellent ductility and toughness [52]), stabilised by the additions of face-centred-cubic (FCC) elements such as nickel, and are strengthened either by the addition of solid solution strengtheners, most usually tungsten and molybdenum, or via the precipitation of carbide phases. Additional solid solution strengthening is supplied to these alloys by chromium but its principal function is the provision of oxidation resistance [53]. Notwithstanding their any excellent properties, the use of cobalt-base superalloys has become somewhat marginalised over recent decades thanks to the development of better and/or cheaper nickel-base alternatives; however, they do still find application in a number specialist components [49].

Developed shortly after the second world war, nickel-base superalloys constitute the majority of high-temperature superalloy products in use today [54, 55]. Similar to the aforementioned cobalt-base ones, all alloys of this type comprise an austenitic (in this case nickel) solid solution matrix phase for superior mechanical properties as well as large quantities of chromium and/or molybdenum for the purposes of corrosion resistance as well as solid solution strengthening [54, 53, 55, 56]. Beyond this primary make-up, however, their metallurgy splits into two principal categories: Precipitation strengthened Ni-base alloys most commonly contain significant quantities of aluminium and titanium (or niobium) to induce the formation of secondary phases during pre-service applied heat treatments. Solution annealed components on the other hand, have low Al and Ti contents but may still include niobium as a solid solution strengthener. Other common constituents of both types of nickel superalloys include iron (acts to stabilise the austenitic matrix), and carbon which, through the precipitation of carbide phases, increases creep strength (in polycrystalline alloys) [53, 55, 56].

The final class of superalloys in use today are those based on an iron majority matrix. These alloys share many features of their nickel counterparts both in terms of chemistry and their performance with major alloying additions comprising chromium and molybdenum for corrosion resistance and solid solution strengthening and aluminium and titanium (and/or niobium) for precipitation hardening. Moreover, nickel is also often added in significant quantities to iron-base superalloys primarily to stabilise the austenitic matrix at low temperatures, but also to encourage precipitation hardening and increase corrosion resistance [53, 56, 55]. Despite possessing poorer high temperature properties than those based on nickel [54, 53, 56], the quantity of applications where this is not a factor combined their significantly lower price, has resulted in iron-base superalloys becoming the most widely utilised (overall) superalloy class.

In light of the above discussion, it is clear that the unique combination of high temperature application and complex chemistry means that, of all the three superalloy flavours, nickel-base superalloys possess the most complex challenges in terms of microstructural design and prediction. The high alloying content of these alloys, particularly, means that precipitation and/or evolution of secondary phases is almost certain to occur in all alloys (whether it is desired to or not), and this has significant implications for mechanical properties.

§ 1.2 Precipitation in Nickel-base Superalloys

Fundamentally, solid state[1] precipitation in nickel-base superalloys occurs due to a super saturation of the majority austenitic matrix phase (known commonly as γ) with respect to one or more elements. That is to say, the fast cooling of these alloys from casting (after solidification) or working results in a greater quantity of alloying elements being present within the matrix (at lower temperatures) than would be thermodynamically allowed at equilibrium. As a result, there is a thermodynamic driving force for alloying elements to exit the majority matrix and form secondary phases. Before precipitation can take place, however, the energy costs associated with the formation of secondary phases, such as increased interfacial energy (discussed in Section 1.3.1), must be overcome by the provision of an additional amount of energy. Most often this energy comes from heat but other sources such as radiation can also be more than sufficient. Rather than an incidental phenomenon, the precipitation behaviour of nickel-base alloys is particularly significant due to the plethora of possible secondary phases and their resultant impact on the material/component properties. Consequently, given that the exact conditions required for the precipitation of secondary phases in a particular superalloy, and the behaviour of such phases over time, are unique to both the system and the type of precipitate, the goal of much nickel-base superalloy metallurgy is the effective prediction and control of precipitation/precipitate phases to obtain desirable mechanical properties which are stable over the lifetime of a component. The most widely observed secondary phases in nickel-base superalloys and their properties are discussed below.

1.2.1 GAMMA PRIME (γ')

Gamma prime is an ordered $L1_2$[2] (FCC) precipitate with the formula A_3B [53]. It has a cube-cube orientation relationship with the matrix and is found insuperalloys containing significant quantities of aluminium and titanium where it exists as $(NiCo)_3(AlTi)$; aluminium/titanium atoms occupy the corners of the cubic structure, and nickel (or cobalt) the faces [54, 56]. Its name derives from the fact that it bears a close similarity, in terms structure and of lattice parameters, to that of the disordered austenitic matrix phase γ.

Most commonly γ' precipitates nucleate and grow interspersed within grains, although heat treatments may be applied so that they form on grain boundaries. Within grains the specific morphology of γ' as it exists at a particular temperature in a given superalloy is dependent on a number of parameters, chief among which is the lattice misfit (strain) between γ' and γ [5]. That is, at the start of nucleation γ' particles display a small misfit and high coherency with γ (precipitate-matrix coherency is discussed further in Section 1.3), resulting in a spherical morphology because of the elastic modulus isotropy of the matrix. As ageing progresses and the particles grow and coarsen, however, the increasing strains imposed by the coherency condition with the austenitic

---

[1] The term solid state is used here to differentiate from processes which may occur as a molten/liquid state superalloy mixture cools.

[2] Crystal structure classification in the partly systematic Strukturbericht method [57].

matrix lead to the γ' shape altering from spheres to cuboids to cuboidal arrays and finally to solid state dendrites. Owing to the temperature dependence of the magnitude of the precipitate-lattice misfit [58, 59], the precipitate size at which the shape transition from spherical to cuboidal occurs varies noticeably with temperature *viz.* a smaller misfit necessitates a larger γ' particle size before the coherency strain energy forces a change in shape and *vice versa* [5]. For context, examples of the various shapes presented by γ' precipitates are displayed in Figure 1.1 with a) containing (approximately) spherical, b) cuboidal and c) dendritic shaped precipitates.

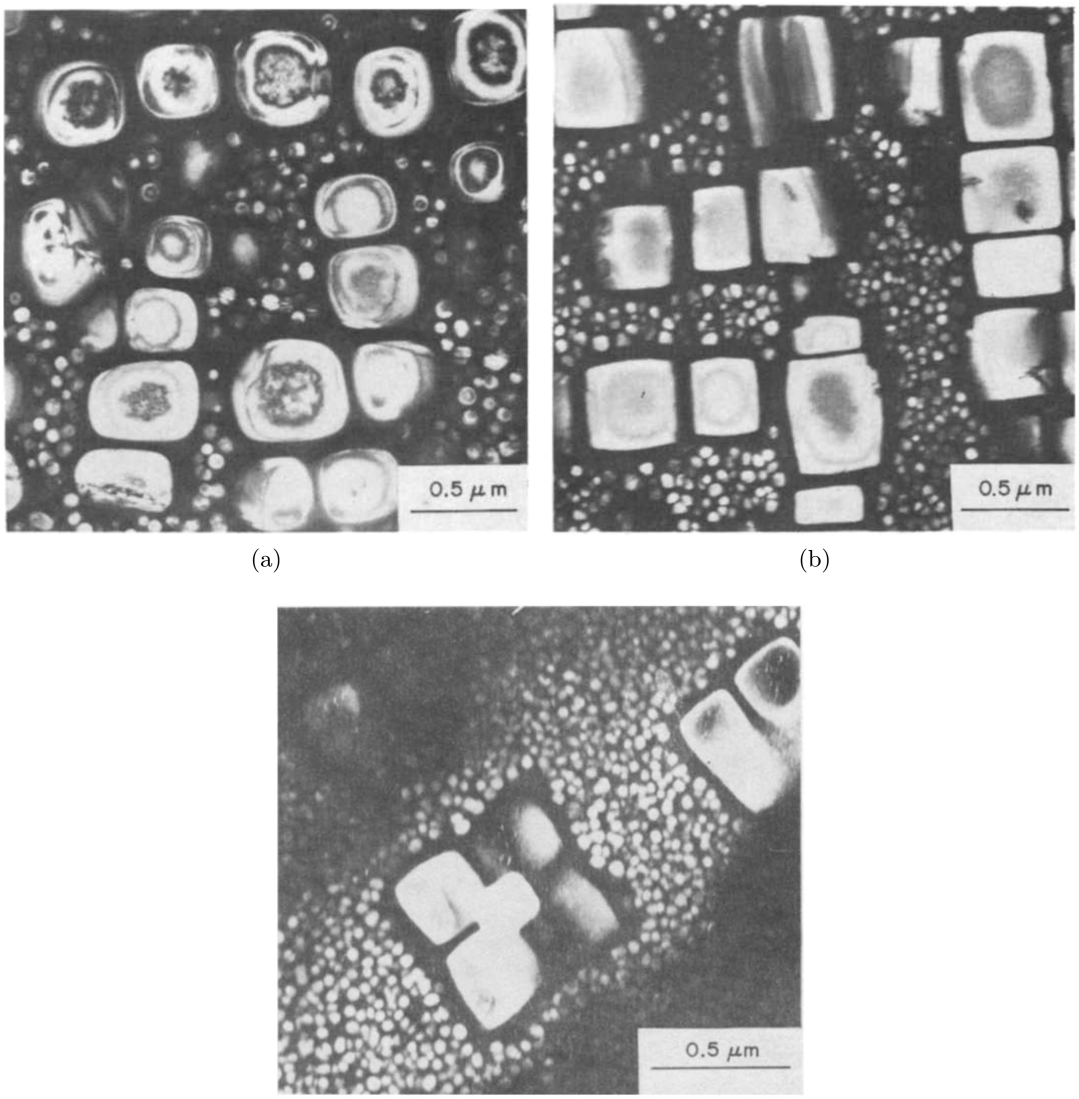

(a)

(b)

(c)

Figure 1.1: a) Udimet 720 aged for 4 hours at 1443K, 4 hours at 1353K, 24 hours at 1116K and finally 16 hours at 1033K. b) Nimonic 115 aged for 1.5 hours at 1463K then 6 hours at 1373K. c) Nimonic 115 aged for 24 hours at 1418K. Small spherical γ' precipitates are observed as a result of homogeneous nucleation during quenching. Images adapted from [5].

In addition to misfit strain, as evidenced by Figure 1.1, another fundamental factor governing the morphology of γ' is the precipitate density. If sufficiently high that the diffusion fields of neighbouring precipitates overlap, soft impingement occurs, preventing particle growth and thereby slowing morphological evolution (see Section 1.3.3). Coarsening will still take place but at reduced rate owing to the smaller size differential between particles (see Section 1.3.4) [5]. These effects are shown by the contrasting microstructures of Nimonic 115 in Figures 1.1b and 1.1c where the lower precipitate density in the alloy treated at 1418K has enabled the evolution of a cuboidal dendrite.

Of the precipitates which can possibly form in nickel-base superalloys, γ' is the most widely understood and utilised due to the high temperature creep resistance and tensile strength it imparts in a number of different alloy systems through a process known as anti-phase-boundary (APB) hardening [60, 61, 62]. That is, dislocations travelling through the γ matrix cannot enter a γ' precipitate without the formation of an APB, presenting a significant energy barrier and therefore impeding dislocation motion. Moreover, the restriction on dislocation movement is further enhanced by the fact that the antiphase boundary created for γ' is sufficiently high energy that dislocations necessarily travel in pairs such that the following dislocation reduces the system energy by eliminating the APB created by the first. Finally, owing to the high coherency of the γ-γ' interface, additional contributions to the strengthening effect of γ' are predominately limited to Orowan strengthening[3] (coherency strains may contribute as particle size increases during growth and coarsening) [53].

In order to fully harness their strengthening effects, γ' precipitates are generated, principally, in components through the application of heat treatments (either during or after manufacture) carefully designed so that the homogeneous γ' precipitate population possesses a particle size where the coupling between a pair cutting of dislocations lies at the transition from the weak to strong [62, 6] regimes presented in Figure 1.2. This morphology imparts maximum hardening owing to the fact that in the weak coupling regime, the critical shear stress required to cut through a precipitate of radius r has a dependence that goes as $\mathrm{r}^{\frac{1}{2}}$, whereas in the strongly coupled regime the dependence changes to $\mathrm{r}^{-\frac{1}{2}}$ [63, 64]. Equating the governing functions describing these regimes, the precipitate size which provides maximum resistance to dislocation shearing is determined as $r \approx 2T/\gamma_{APB}$ where T is the absolute temperature and γ_{APB} is the anti-phase-boundary energy.

Whilst the strengthening imparted by γ' occurs because of the aforementioned mechanisms, arguably the most significant factor for its application in the strengthening of superalloys is its high thermal stability: The structure of $\mathrm{Ni_3Al}$ has been extrapolated to remain ordered up to $\approx 1375^\circ$C [65] *i.e.* until melting; however, additional studies have found a decrease in lattice reflections before melting implying some ordering is lost [66]. As a result, (ignoring the effects of growth and coarsening) γ' is able to retain a coherent interface with the γ matrix, and therefore impart order strengthening, at significant fractions of the alloy melting temperature. Similarly, for components which

---

[3] Orowan strengthening describes the increase in the resistance to deformation caused by dislocations being forced to bow/loop around rather than cut precipitates owing to their distribution and/or size/coherency.

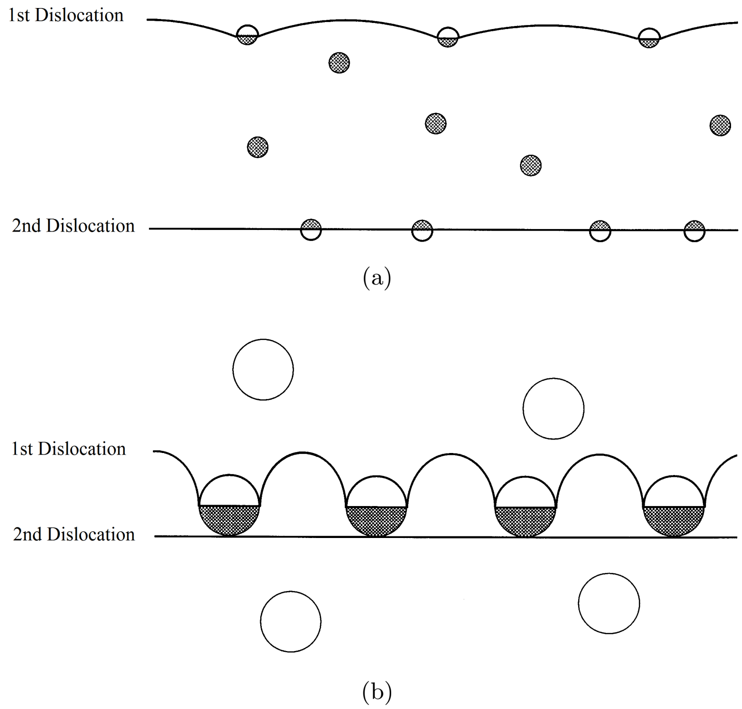

Figure 1.2: Movement of dislocation pairs in a) Weak coupling regime (distance between dislocations is large compared to precipitate diameter) b) Strong coupling regime (distance between dislocations is comparable to or less than precipitate diameter). Images adapted from [6].

are designed for long service lives at high operating temperatures, the high possible thermodynamic stability of γ' is also of significance: In terms of chemistry, the stability of γ' at a given temperature is found to depend on the quantity of the alloying elements aluminium, titanium, niobium and tantalum such that when Al is present in sufficient quantity Ni_3(Al,Ti) is stable; however, when Ti, Nb and Ta exceed a specific quantity ($\approx$ Al/Ti $= 1/2$) other phases such as η (hexagonal-close packed Ni_3Ti) are favoured thermodynamically at high temperatures [53]. These phases (discussed below) impart much poorer mechanical properties and thereby limit the service criterion of some alloys. An example of metastable γ' transforming to η is found in the alloy Inconel 740, which has a nominal composition of 1.8wt% Ti, 2.0wt%Nb and 0.9wt%Al [67, 68].

1.2.2 Gamma Double Prime (γ'')

In nickel-base superalloys containing the specific levels of niobium and iron, an alternative intermetallic strengthening phase to γ', possessing an ordered body-centre-tetragonal (BCT) $D0_{22}$ structure and composition Ni_3Nb(Al,Ti) is thermodynamically favoured in many instances. The unit cell of this phase, as shown in Figure 1.3, bears a striking resemblance to that of γ', with a c_0 parameter approximately double that of a_0 in γ', resulting in it receiving the designation γ'' [69].

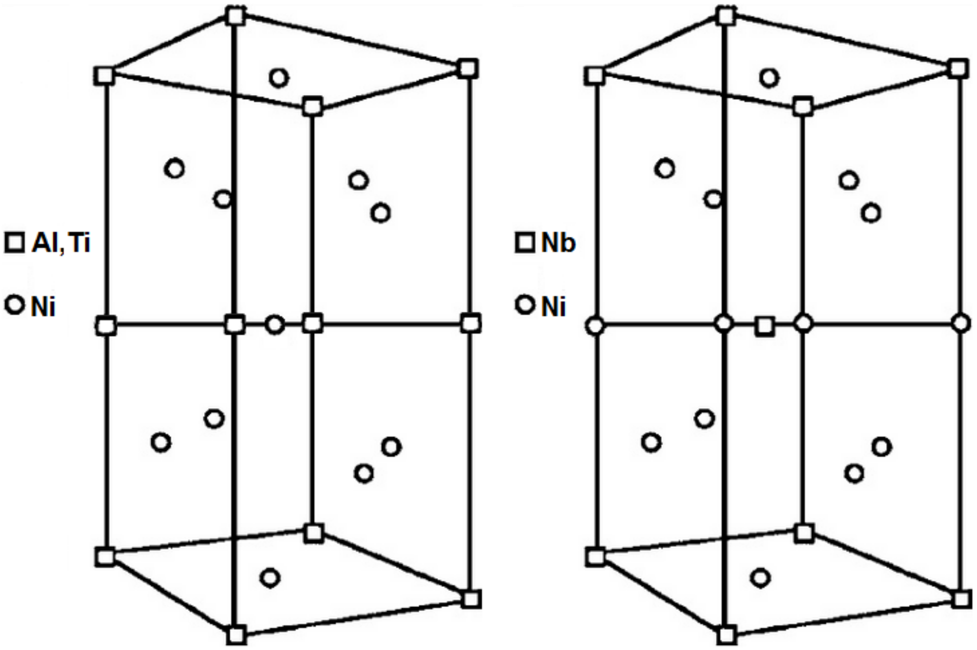

(a) (b)

Figure 1.3: a) FCC L1_2 unit cell of γ' b) BCT D0_{22} unit cell of γ'' ($c_0^{\gamma''} \approx 2a_0^{\gamma'}$). Adapted from [7].

Unlike γ' discussed previously, the strengthening imparted by γ'' chiefly derives from coherency hardening [40] *viz.* the tetragonal distortion of γ'' and its high coherency with the matrix leads to significant coherency strains, impeding the motion of dislocations. However, like γ', γ'' also strengthens by APB generation/hardening with this second mechanism actually enhanced in γ'' by the fact that only three possible slip directions are available in the BCT structure. Order is restored along one by the motion of two dislocations (as for γ'), and along the other two by the motion of four dislocations [70, 7]. Consequently, even though shearing by $^{a}/_{2}$ $<110>$ dislocation quadruplets is calculated as lower energy, the fact that observations indicate that shear by $^{a}/_{2}$ $<110>$ pairs is dominant due interaction between the moving dislocations and the high coherency strain fields surrounding the precipitates [40], means that dislocation movement is severely restricted to just one direction.

The morphology presented by γ'' precipitates, as shown in Figure 1.4, is typically that of small ellipsoids. Similarly, (as also depicted) most commonly such particles are found dispersed homogeneously throughout a given grain, observing a $(100)_{\gamma''} \parallel \{100\}_{\gamma}$; $[001]_{\gamma''} \parallel <100>_{\gamma}$ orientation relationship with the matrix [69]. With respect to optimal strengthening, owing to the aforementioned enhanced resistance to dislocation cutting provided by the higher coherency (primarily) and APB barriers, the hardening effect imparted by γ'' is not only greater than that of γ' but also occurs at a smaller precipitate size *i.e.* the size dependence exceeds $r^{\frac{1}{2}}$) [71]. Accordingly, given these evidenced characteristics it is clear that, much like for γ', the selection of the heat treatment parameters for components desired to harness the strengthening effect of γ'' is a critical task. In this instance, however, it must be pointed out that this is made all the more difficult and, therefore, crucial by the fact that the dislocation sheering mechanism is observed to switch to deformation twinning along the $\{100\}$ precipitate planes once particles exceed approximately 10nm [72, 73]. This phenomenon greatly reduces the strengthening effect of γ'' precipitates below that imparted by Orowan looping and, consequently, changes the precipitate size and distribution at which peak hardening is obtained.

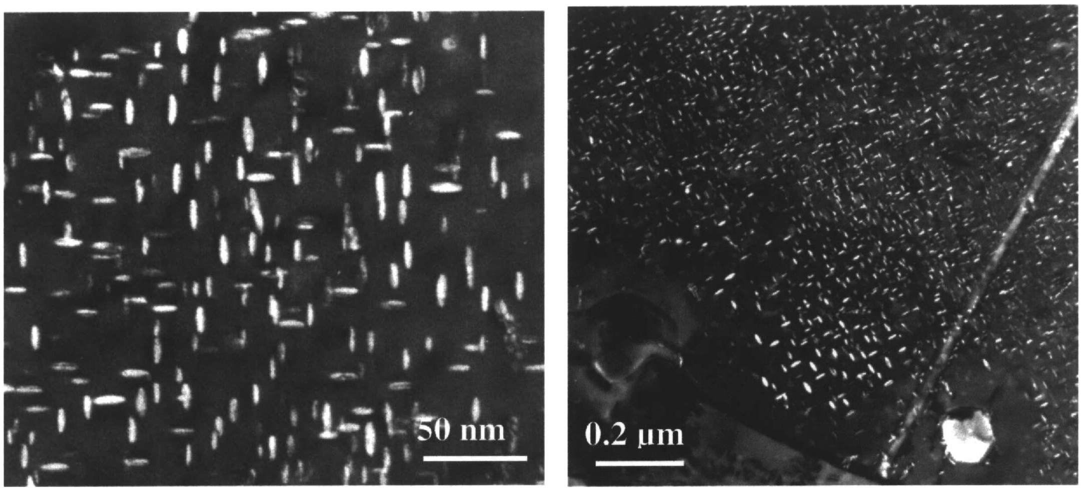

(a)

(b)

Figure 1.4: γ'' precipitates observed in direct aged Alloy 625 (2 variants/orientations). Images adapted from [8].

In view of the critical dependence on precipitate size just outlined it is perhaps surprising that the most significant factor which must be considered for alloys strengthened by γ'' is that of microstructural stability. This reality, however, is nevertheless true owing to the fact that γ'' is strictly always metastable [53, 74] *viz.* the phase cannot be stabilised through composition changes meaning ageing or service conditions may lead to the conversion of γ'' to thermodynamically stable δ-phase which (as discussed in Section 1.2.3) possesses much poorer strengthening properties. Consequently, in addition to considerations of precipitate size evolution, the design of heat treatments and applications for components designed to be hardened by γ'' must also take account of the phase's metastability; it is for this reason that components are generally limited to operating temperatures below 650°C [75].

1.2.3 Delta Phase (δ)

Existing as the stable counterpart to γ'', δ-phase (also with composition Ni_3Nb) inevitably also occurs in superalloys containing significant levels of iron and niobium. The structure of the phase is $D0_a$ orthorhombic, observing a $(010)_\delta \parallel \{111\}_\gamma$; $[100]_\delta \parallel <110>_\gamma$ orientation relationship with the γ matrix; however, misorientation can occur when the phase is located on grain boundaries [53, 74, 76]. Normally, δ presents in the form of sharp intergranular needles, nucleated either on grain or twin boundaries or on stacking faults in MC carbides (*q.v.* Section 1.2.6) [53] or γ'' precipitates although it has also been observed with a cellular morphology in some alloys [70, 74, 77, 78]. An example of two highly developed δ-phase precipitate populations conforming to the common nucleation and shape behaviour in Alloy 718 and Alloy 625 is given in Figure 1.5

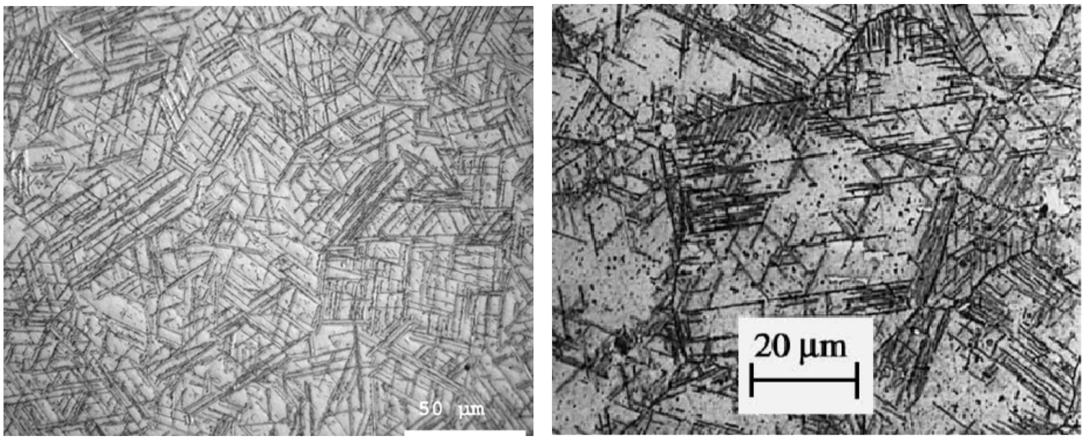

(a) (b)

Figure 1.5: δ-phase precipitation observed in a) A718 [9] b) A625 [10].

The formation and resultant morphology of δ within an appropriate (*i.e.* Fe and Nb containing) alloy is dependent, most significantly, on the thermal profile the material is exposed to. In general, below 700°C δ-phase forms very slowly (100's-1000's of hours) on grain boundaries/carbide particles whereas between 700-885°C nucleation and growth occurs more rapidly, accompanied by fast coarsening of γ''. Above 885° formation is observed to no longer be preceded by that of γ'', with δ-phase rapidly precipitating directly from the supersaturated matrix [53, 74]. From this temperature dependence, therefore, it is evident that prolonged or high temperature ageing will result in a Widmanstätten type morphology[4], whereas lower temperature shorter duration treatments are likely to result in the phase being absent all together. Depending on the chemical composition of the alloy, δ-phase can remain stable up to 950-1150°C.

Contrasting with both γ' or γ'', δ-phase is not utilised for precipitation hardening due to the poor mechanical properties it imparts *viz.* δ is much less coherent with the γ matrix and, therefore (consistent with the discussion in previous sections), does not significantly strengthen (impede dislocation movement/cutting) by either coherency strains or APB generation [53, 80]. It is for this reason (alluded to in the previous section) that the precipitation of δ during ageing, service or manufacture is typically discouraged in alloys strengthened by γ''; not only does δ inhibit the formation of γ'' by competing for the same elements but it also results in a degradation in properties

---

[4] The term "Widmanstätten pattern" (or alternatively "Thomson structure") defines the specific octahedral arrangement of nickel-iron crystals first observed in iron meteorites [79].

such as strength and fracture toughness [53, 56, 81].

In spite of the aforementioned detrimental properties, it should nevertheless be noted that one key caveat applies with respect to the aim of avoiding δ production during manufacture, specifically its purposeful creation for the function of grain refinement when processing polycrystalline superalloys [82, 83, 84, 85]: The achievement of small grain micro-structures (desirable for increased strength and toughness as described by the Hall-Petch effect [86, 87]) is facilitated, in alloys susceptible to δ-phase formation, by forging (large reduction) just below the δ solvus temperature resulting in the rapid formation of an extensive network of acicular/needle shaped intragranular precipitates which act to inhibit the motion of grains boundaries during subsequent, deformation induced, recrystallisation [53, 83, 84]. Unsurprisingly, given its detrimental mechanical effects, the forging temperatures selected for δ-phase precipitation are tightly controlled as not only will high volume fractions be difficult to remove but γ'' precipitation will also be impeded thanks to the decrease in the concentration of niobium in the matrix [88, 89]. Similarly, any post recrystallisation solutionising treatments are also restricted because of the increase in the driving force for δ-phase coarsening. Ultimately, however, the retention of some grain boundary δ-phase with the right morphology (spaced out globular particles), can actually lead to an improvement of certain mechanical properties such as notch stress rupture ductility and creep resistance by the retardation of intergranular cracking and grain boundary sliding respectively [53, 90]. Application of δ processing has been demonstrated to result in the production of extremely fine grained superalloy products (ASTM 7), with concurrent excellent toughness, strength and fatigue properties [85].

1.2.4 Eta Phase (η)

The formation of η phase (Ni_3Ti), as discussed briefly in Section 1.2.1, occurs after prolonged and/or high temperature ageing (the exact, time and temperature conditions are dependent on the alloy chemistry) inside alloys which contain a sufficient quantity of titanium to stabilise the phase over γ' and accompanies, analogous to δ in γ'' strengthened alloys, a transition to much much poorer mechanical properties. As a result, undesirable η phase production poses significant implications for heat treatments, component performance, operating conditions and lifetimes. Despite this, however, (identical to δ-phase again) the phase is still utilised during the thermomechnical processing of many alloys for the purpose of grain refinement: Forging just below its solvus temperature (900°C) and ageing results in an optimal (small) amount of finely dispersed η particles [53].

In terms of morphology, η exhibits a hexagonal-close-packed (HCP) $D0_{24}$ structure and exists in either a cellular or plate-like distribution, with platelets observing a $<011>_\gamma \parallel <2110>_\eta$; $\{111\}_\gamma \parallel \{0001\}_\eta$ orientation relationship with the γ matrix [91, 92]. The deleterious mechanical properties associated with η phase formation, including decreases in strength and ductility, derive particularly from the reduction in γ' and solid solution (matrix) strengthening elements. η phase precipitation does not lead to significant strengthening itself due to the fact that it has a much lower coherency with

γ [93].

1.2.5 TOPOLOGICALLY CLOSE PACKED PHASES (σ, μ, LAVES)

Topologically-close-packed (TCP) phases occur in nickel-base superalloys due to the local concentration of solution strengthening elements (*e.g.* chromium, molybdenum, tungsten, cobalt and rhenium) that results either from solidification or poorly controlled superalloy chemistry [53, 54]. They comprise of high density complex crystal structures, with layers of atoms forming "basket weave" nets aligned along the octahedral planes of γ. The composition of TCP phases is of the type A_xB_y where A and B lie either side of group 8 within the transition metal block of the periodic table of elements shown in Figure 1.6 [11].

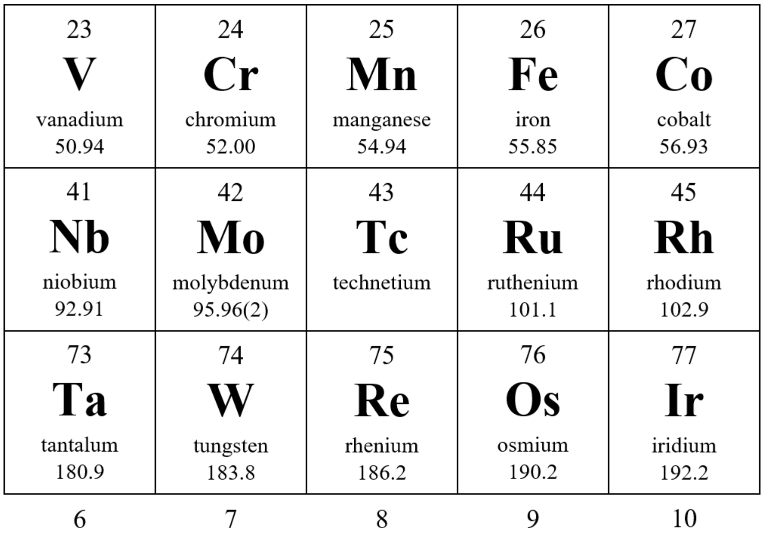

23 **V** vanadium 50.94	24 **Cr** chromium 52.00	25 **Mn** manganese 54.94	26 **Fe** iron 55.85	27 **Co** cobalt 56.93
41 **Nb** niobium 92.91	42 **Mo** molybdenum 95.96(2)	43 **Tc** technetium	44 **Ru** ruthenium 101.1	45 **Rh** rhodium 102.9
73 **Ta** tantalum 180.9	74 **W** tungsten 183.8	75 **Re** rhenium 186.2	76 **Os** osmium 190.2	77 **Ir** iridium 192.2
6	7	8	9	10

Figure 1.6: Section of the periodic table of elements. Those metals which lie either side of group 8 (Mn, Tc, Re) constitute the A and B of A_xB_y TCP phases found in nickel-base superalloys [11]. Table from [12].

Depending on the size ratio of the constituent atoms, generally three different simple TCP phases are found to exist in superalloys (though more are possible) known as σ, μ and Laves phase [53, 54]. σ phase is based upon the composition $A_{1-7}B_{1-7}$ (ideal stoichiometry A_2B) with A and B composing of elements of approximately equal size, *e.g.* $Cr_{61}Co_{39}$. μ phase occurs with similar composition range but is based on the ideal stoichiometry A_6B_7 and comprises constituents of larger size disparity such as molybdenum and cobalt (Mo_6Co_7). Laves phases exist with formula A_2B and constitute size factor compounds *i.e* specific differences in the sizes of the elements (20-30%) allow for the formation of a structure in which the average coordination number is higher than that achieved by packing atoms of equal size [94]. The morphology of these phases is almost always plate-like, with nucleation tacking place at grain boundaries and/or on carbide particles; however, blocky TCP phases have also been observed some systems.

The result of excessive TCP phase precipitation in nickel-base superalloys has been routinely measured as a severe degradation in mechanical properties including ductility, fatigue resistance and stress rupture life [95, 96, 97] (small amounts often have little impact [98]), with the effects themselves deriving principally from two key factors. Firstly, the elemental composition of TCP phases is such that they are rich in solid solution strengthening elements and, therefore, the depletion which occurs as a result of their formation has a weakening effect on the matrix. Secondly, the hardness and plate like morphology of these phases means TCP precipitates can become sites for the formation of voids (through vacancy condensation), as shown in Figures 1.7a and b, which act not only as fracture initiation sites [13, 99] but also create a low energy path for fracture propagation [95] (Figure 1.7c). In addition to these two effects, TCP phases have also been observed to diminish fracture resistance by delaminating in the final fracture zone [98].

1.2.6 CARBIDES

Present in addition to the intermetalic phases outlined previously, carbide phases exert a significant influence on the mechanical properties of superalloys and, consequently, control of the formation and evolution of carbides is of particular importance to superalloy product manufacturers and end users. Depending on the alloy chemistry, melting conditions and thermomechanical processing history, a large number of different carbide phases are possible. The most common carbides nickel-base superalloys are MC, M_6C and $M_{23}C_6$ where M signifies a metal cation (normally Cr, Nb, Ta, Ti or Mo) [53, 54, 56].

Owing to their high thermodynamic stability, MC carbides such as TiC and NbC (M is usually refractory) form in superalloys almost immediately on cooling from the melt [100]. In Alloy 718 containing 0.03 at% carbon for example, MC precipitation starts at 40°C below the equilibrium liquidus temperature [101]. As a result, these phases are typically found as discrete particles heterogeneously distributed throughout a given alloy (*e.g.* in interdendritic regions) and have little or no orientation relationship with the matrix [53, 54]. The appearance of MC carbides during solidification, rather than ageing as with other carbides (discussed below) leads to their common designation as "Primary Carbides". In terms of morphology, MC carbides are highly variable with, in René N5 and N6 for example, blocky, nodular and script TaC precipitates all being observed [102]. Furthermore, the phase itself possesses an FCC structure and has been demonstrated to significantly improve creep rupture properties by retarding both grain boundary sliding, when located on grain boundaries, and dislocation motion, particularly when dispersed intragranularly [103, 104]. In alloys containing nitrogen, primary carbide precipitation is enhanced through nucleation on nitride particles such as TiN; however, this effect is depressed in most superalloys due to the implementation of Vacuum Induction Melting (VIM), Vacuum Arc Re-melting (VAR) and Electro-Slag Re-melting (ESR) to lower the nitrogen content because of the severe degradation of mechanical properties it causes [105, 55]. An example of intragranular MC carbides (specifically NbC) in a 0.05C-16Cr-8W-5Al-1.2Nb-69.75Ni alloy is given in Figure 1.8a.

.

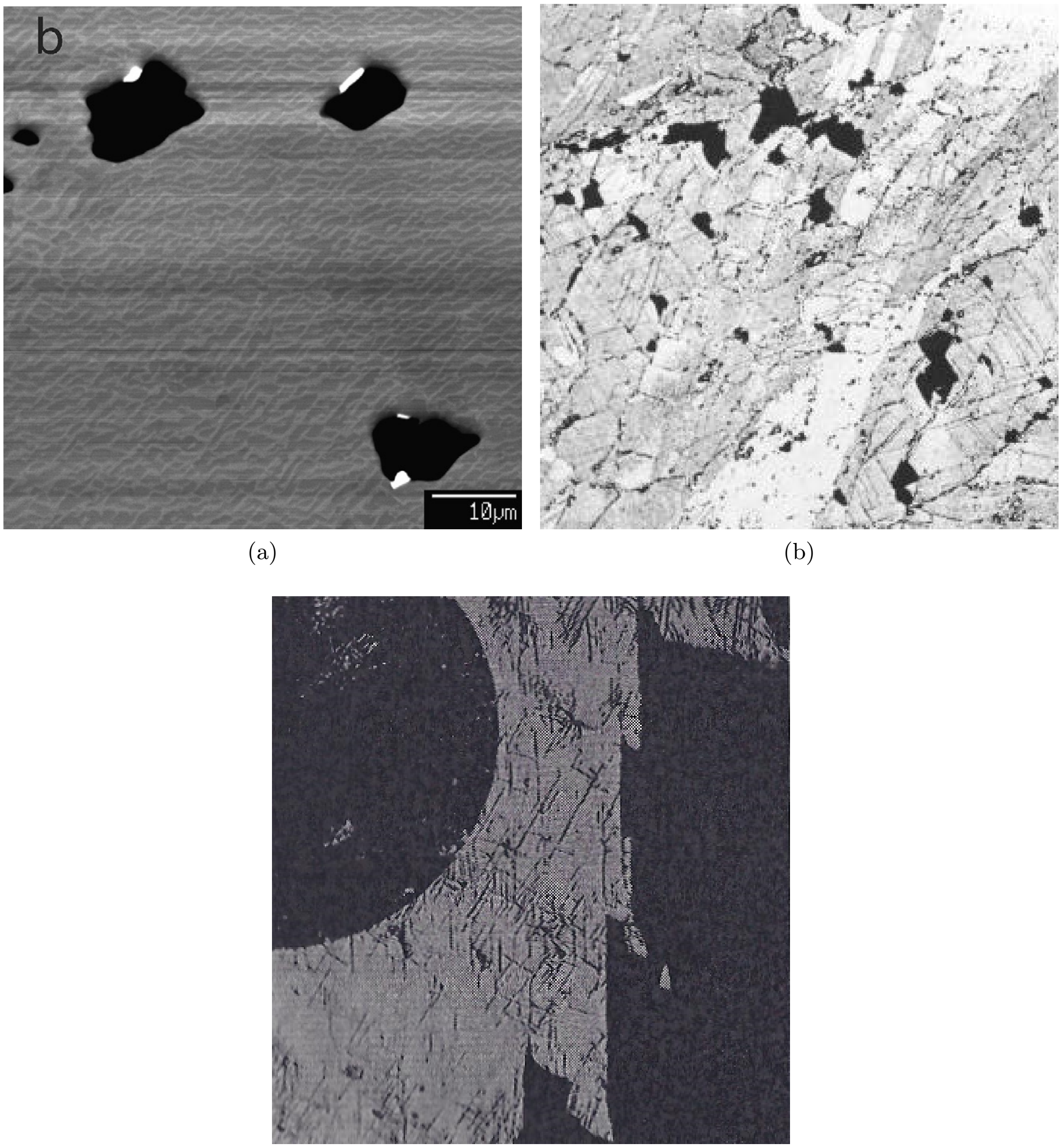

(a) (b)

(c)

Figure 1.7: Micrographs of voids forming around a) μ phase (bright regions) in CMSX-4 [13], and b) plate-like σ phase in Udimet 700 [14]. c) Shows "intersigmatic fracture" arising from fracture zigzagging between voids formed alongside sigma phase plates.

Following primary carbide formation the development of different/additional carbides in superalloys occurs as a result of both the presence of residual carbon in the matrix and the decomposition of primary carbides. Owing to their high thermodynamic stability, at first glance the solid-state mechanism for this latter phenomenon is not obvious; however, experimental investigations reveal it to be fundamentally a result of the substitution of additional refractory elements such as molybdenum and tungsten into the (Ti,Nb)C matrix [53, 106, 107]. That is to say, these substitutional elements act to destabilise the phase and, ultimately, result in its slow decomposition [53, 54] through sequential processes such as those presented for M_6C and $M_{23}C_6$ in Equations 1.1, 1.2 and 1.3 [106, 107][5]. Moreover, these substitution reactions do not cease with the destruction of primary carbides but continue up until equilibrium such that quantities of secondary carbides, as illustrated for M_6C and $M_{23}C_6$ in Equation 1.4 (where M' and M'' denote different metals), are in constant flux.

$$\mathrm{MC} + \gamma \longrightarrow \mathrm{M_{23}C_6} + \gamma' \tag{1.1}$$

$$\mathrm{MC} + \gamma \longrightarrow \mathrm{M_6C} + \eta \tag{1.2}$$

$$\mathrm{MC} + \gamma \longrightarrow \mathrm{M_6C} + \mathrm{M_{23}C_6} + \eta \tag{1.3}$$

$$\mathrm{M_6C} + \mathrm{M'} \rightleftharpoons \mathrm{M_{23}C_6} + \mathrm{M''} \tag{1.4}$$

The thermodynamic stability of $M_{23}C_6$ and its kinetics of formation mean it is usually found to develop most readily within a given alloy after exposure (ageing or service) in the range 760-982°C [53, 55, 108]. However, depending upon the alloy chemistry this range can be expanded significantly, for example in an Ni-Cr-W superalloy precipitation of $M_{23}C_6$ has been noted after ageing for 100 hours across the range 650-1000°C [109]. Composition wise, whilst a number of possible cations can form the carbide, owing to its combination of greater electropositivity and large abundance, the most common cation in $M_{23}C_6$ phase formed in nickel-base superalloy alloys is chromium but non-negligible amounts of nickel ($(\mathrm{Cr,Ni})_{23}\mathrm{C}_6$) and even iron (in those alloys witch contain it as a significant alloying addition) substitution ($(\mathrm{Cr,Ni,Fe})_{23}\mathrm{C}_6$), are also frequently observed. Furthermore, the bounding and structure of the phase (discussed subsequently) means the substitution of other group 6 (refractory) elements such as W or Mo to substitute into the phase (forming $\mathrm{Cr}_{21}(\mathrm{Mo,W})_2\mathrm{C}_6$) is not uncommon [53].

In terms of structure, despite the fact that $M_{23}C_6$ is coherent with the γ matrix, observing a cube-cube orientation relationship, the phase actually possesses a complex cubic structure similar (when the carbon atoms are removed), to that of σ phase (Section 1.2.5). Accordingly, it is this high coherency of the two phases results in the observed nucleation σ precipitates on $M_{23}C_6$ particles [110]. Morphologically, $M_{23}C_6$ is found predominantly on grain boundaries (although location on twins and stacking faults is also possible) where it exists as either irregular/rounded/blocky discontinuous particles (Figure 1.8b) or as intergranular plates. This nucleation behaviour signifies that these carbides can act to inhibit grain boundary sliding and thereby improve creep rupture properties, with highest creep resistance (and therefore stress rupture life)

---

[5] In accordance with the discussion in Section 1.2.4 the occurrence of η phase rather than γ' in stages 2 and 3 is attributed to the high local concentration of the carbide forming elements Ti, Nb that arises in the vicinity of the carbide particles (due to their low relative diffusivity) which acts to stabilise η over γ'

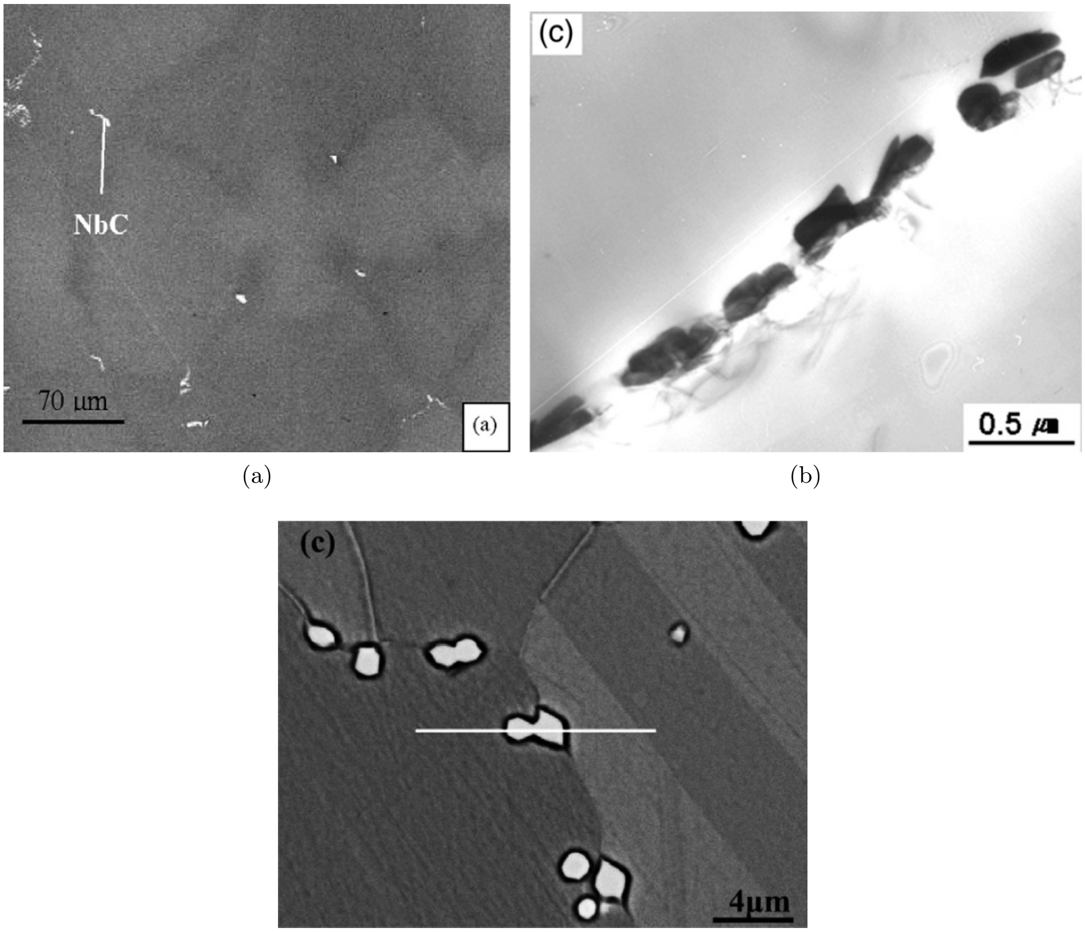

(a) (b)

(c)

Figure 1.8: a) NbC particles in a 0.05C-16Cr-8W-5Al-1.2Nb-69.75Ni alloy [15], b) Discontinuous particles of $M_{23}C_6$ in Alloy 690 [16], c) Intergranular M_6C carbides in a Hastelloy N type alloy [17]

achieved by small, closely spaced discretised blocky particles [111, 112, 113][6]. In most cases, however, although the coherency of discrete $M_{23}C_6$ particles and γ theoretically facilitates the carbide to also impart significant coherency as well as and precipitate strengthening effects, the typical grain boundary location of these carbides means that the beneficial effects of $M_{23}C_6$ precipitates can only be harnessed at low temperatures *viz.* their rapid coarsening at high temperatures and the resultant development of continuous carbide films [114, 104, 103] (let alone the fact that even cellular $M_{23}C_6$ has been demonstrated to initiate rupture [53, 115]) is always detrimental.

M_6C carbides habitually form at higher temperatures than $M_{23}C_6$ (815-1038°C) leading to them occurring as primary carbides in some systems [116, 117]. They form predominantly in alloys/regions with high molybdenum and/or tungsten contents (6-

---

[6] Even with an optimum morphology it should be noted that rupture failure still occurs during creep either as a consequence of carbide particle fracture or decohesion of the $M_{23}C_6/\gamma$ interface [111]

8 at%) with formulas $(Ni,Co)_3Mo_3C$ and $(Ni,Co)_3W_4C$, although a wider range of compositions (*e.g.* $(Ni,Co)_3Nb_3C$, $(Ni,Co)_3Ta_3C$) and formulas/structures such as M_3C and $M_{13}C$ have also been observed in some systems [118, 119]. Similarly to $M_{23}C_6$, the location of M_6C is most commonly on the grain boundary (Figure 1.8c) and consequently, in addition to inhibiting grain boundary sliding (*i.e.* improving creep resistance) its high formation temperature means it can be utilised for the purpose of grain refinement in thermochemical processing [55, 120]. The formation of an intergranullar Widmanstätten morphology, resulting from poorly controlled processing or service conditions, is also possible for this phase and leads to a severe reduction in ductility and rupture life [55]. In terms of structure, M_6C is complex cubic and, analogous to $M_{23}C_6$ and σ phase discussed previously, is actually closely related to that of μ phase [53, 121].

Uniquely amongst the precipitate phases considered for superalloys, owing to their specific effects on the alloy chemistry, an additional factor to the control of mechanical properties which must be considered when designing heat treatments to manipulate carbide formation is that of corrosion resistance. Specifically, by creating a large concentrated (*e.g.* at grain boundaries) $M_{23}C_6$ population a phenomenon known as to the sensitisation (discussed in Section 1.4.1) can occur due to the localised depletion of chromium (principally) and molybdenum [122, 103]. Unfortunately, once induced, the removal of this effect within a given alloy (particularly important for application in the most aggressive environments) is only possible through the implementation of techniques such as solutionising heat treatments (effecting other precipitate phase morphologies); however, its occurrence can be minimised at the alloy design stage through the utilising of a sufficiently low carbon and high chromium alloy chemistry [53].

§ 1.3 Nucleation, Growth and Coarsening

Nucleation, growth and coarsening are words used to described the often relatively indistinct stages of secondary phase formation and evolution. In the simplest interpretation, it is presumed that a sequential process is followed whereby nucleation occurs, followed by growth and finally coarsening, with the secondary phase particles described as precipitates if the transformation occurs in the solid state [123]. It turns out that the elemental composition of nickel-base superalloys is such that precipitation reactions typically transpire via the long range diffusion of elements and are expressed by Equation 1.5, where * signifies the solid solution is supersaturated (and therefore metastable) and β represents the precipitated, secondary phase [19]. Consequently, it is in this regard, that the thermodynamic descriptions of the processes of nucleation, growth and coarsening are outlined below.

$$\gamma^* \longrightarrow \gamma + \beta \tag{1.5}$$

1.3.1 Homogeneous Nucleation

The nucleation of precipitates within a particular solid solution matrix can generally be categorised into two regimes: homogeneous and heterogeneous. Fundamentally, homogeneous nucleation can be understood as the random agglomeration of solute atoms within a majority matrix, through bulk diffusion, to form a volume with the elemental composition and (through rearrangement) the crystal structure of a secondary phase. The driving force for this mechanism is given by the overall free energy change ΔG associated with forming a volume V of precipitates and is calculated according to Equation 1.6, where ΔG_{v} and ΔG_{s} are, respectively, the difference in free energy per unit volume of the matrix and precipitate and the misfit strain energy per unit volume and ζ is the interfacial energy per unit area (A) [19].

$$\Delta G = -V\Delta G_{\mathrm{v}} + \sum_{k} A_k \zeta_k + V\Delta G_{\mathrm{s}} \tag{1.6}$$

Breaking down the individual terms in Equation 1.6 these can be understood such that:

$-V\Delta G_{\mathbf{v}}$ corresponds to the reduction in free energy associated with formation of a volume V of precipitate.

$\sum_k A_k \zeta_k$ represents the increase in free energy derived from forming particles of surface area A_k with interfacial energy ζ_k. The summation in this term arises due to the fact that ζ is not constant but rather varies substantially depending on the coherency of the precipitate matrix interface, as illustrated in Figure 1.9.

$V\Delta G_{\mathbf{s}}$ denotes the increase increase in free energy caused by the misfit strain between the precipitate phase and the majority matrix. The strain corresponding to the coherency of spherical precipitates in the matrix is also shown in Figure 1.9.

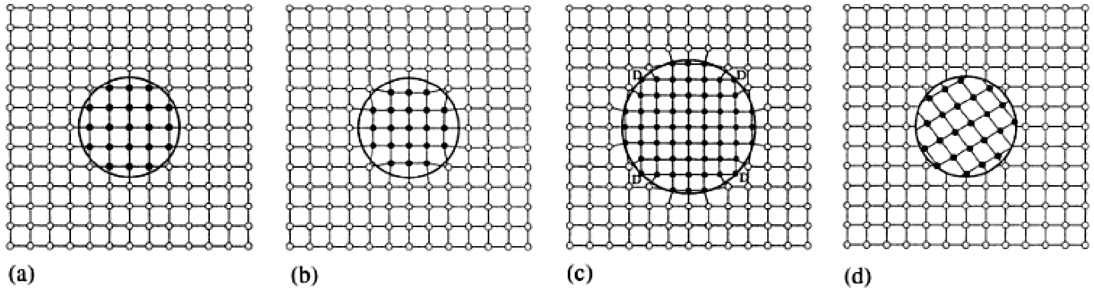

Figure 1.9: Types of coherency between a precipitate and the matrix and the resultant effect on the magnitude (increase moderately $\uparrow$ or significantly $\Uparrow$, and vice-versa) of the values of ΔG_{s} and ζ in Equation 1.6. a) Strain free (perfect) coherency $\longrightarrow \Downarrow \zeta$, $\Downarrow \Delta G_{\mathrm{s}}$. b) Coherent interface with strained bonds $\longrightarrow \Downarrow \zeta$, $\Uparrow \Delta G_{\mathrm{s}}$. c) Semi-coherent interface (strain relieved by dislocations) $\longrightarrow \uparrow \zeta$, $\downarrow \Delta G_{\mathrm{s}}$. d) Incoherent interface $\longrightarrow \Uparrow \zeta$, $\Downarrow \Delta G_{\mathrm{s}}$. Adapted from [18].

Owing to their relative signs and dependence on the precipitate size (surface area and volume), the contribution of each of the terms in Equation 1.6 to the value of ΔG for a given spherical precipitate radius can be illustrated according to Figure 1.10. Moreover, assuming no change in coherency/interfacial orientation between precipitates, one is able to derive from Equation 1.6 (by evaluating ${}^{d\Delta G}/_{dr} = 0$) the critical number of precipitate atoms n^* (Equation 1.7, where a is a factor which depends on the shape of the precipitate nucleus and V_a is the atomic volume) and the critical change in free energy or work of formation ΔG^* (Equation 1.8) required for the establishment of a stable precipitate in a given system [20].

$$n^* = \left(\frac{2a\zeta}{3V_a(\Delta G_{\mathrm{v}} - \Delta G_{\mathrm{s}})} \right)^3 \tag{1.7}$$

$$\Delta G^* = \frac{1}{3}\zeta n^{*\frac{2}{3}} \tag{1.8}$$

Following on from the aforementioned descriptions, if spherical precipitates are assumed *i.e.* $4\pi r^2 = an^{\frac{2}{3}}$, the critical radius r^* and energy of formation ΔG^* are defined according to Equations 1.9 and 1.10 respectively [19, 123]. Irrespective of the particular set of equations utilised, however, the significant implication is that it is the interfacial energy which is the dominant factor in minimising both n^*/r^* and ΔG for the nucleation of a precipitate. That is to say, for homogeneous nucleation to occur, precipitates must form with a low ζ value (*i.e.* they must possess a large degree of coherency with the matrix) as the magnitude of this term means the concurrent increase in misfit strain energy (ΔG_{s}) is more than compensated for.

$$r^* = \frac{2\zeta}{\Delta G_{\mathrm{v}} - \Delta G_{\mathrm{s}}} \tag{1.9}$$

$$\Delta G^* = \frac{16\pi\zeta^3}{3(\Delta G_{\mathrm{v}} - \Delta G_{\mathrm{s}})^2} \tag{1.10}$$

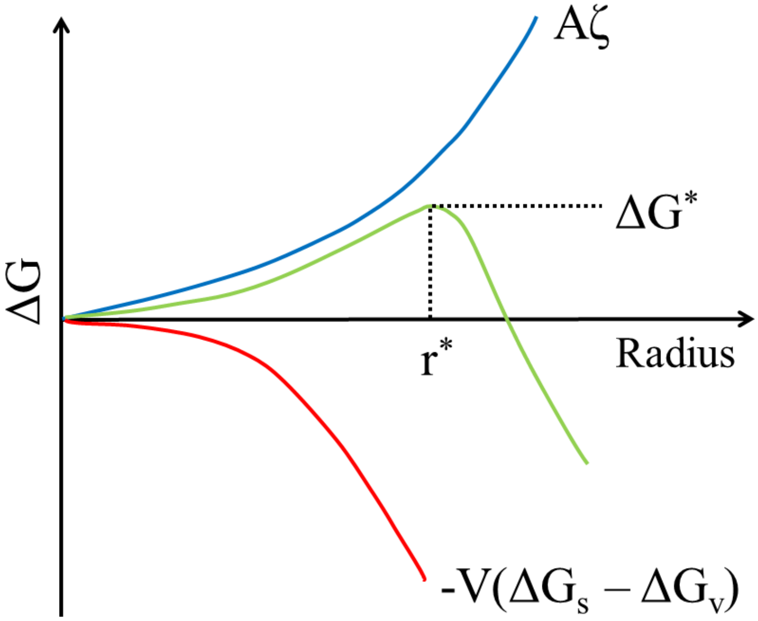

Figure 1.10: Dependency of the Gibbs free energy change associated with the homogeneous formation of a precipitate within a given solid solution matrix (Equation 1.6) and the contribution of each of the individual terms. The critical radius and Gibbs free energy change corresponding to Equations 1.9 and 1.10, respectively, are also indicated.

With their formation fundamentally operating as a chemical reaction, assuming they are in equilibrium with the matrix, it can be reasonably assumed that precipitate nuclei of critical size have a concentration within the matrix derived from Boltzmann statistics *viz.* a concentration described by the Arrhenus law in Equation 1.11, where N_0 and N_c are the total number of atoms and critical nuclei per unit volume respectively, k_B is the Boltzmann constant and T is the absolute temperature.

$$N_c = N_0 \exp\left(\frac{-\Delta G^*}{k_B T}\right) \tag{1.11}$$

As a result of this description, by approximating Fick's First law of diffusional growth in a supersaturated matrix according to Equation 1.12 (where j is the atomic flux, c_γ^0 and c_γ^{e} are the initial and equilibrium concentration, respectively, of the solute in the γ matrix and D is the diffusion coefficient) and utilising another Arrhenius law for D (Equation 1.13, where ΔG_D is the activation energy for atomic migration and D_0 is the atomic diffusion constant) one is able to write an expression for the homogeneous nucleation rate $\dot{N}$ of precipitates in a given matrix based on the rate at which critical nuclei are made supercritical: Equation 1.14 where ω is a prefactor which describes the vibration frequency of the atoms [123, 19].

$$j \approx D\frac{c_\gamma^0 - c_\gamma^{\mathrm{e}}}{r^*} \tag{1.12}$$

$$D = D_0 \exp\left(\frac{-\Delta G_D}{k_B T}\right) \tag{1.13}$$

$$\frac{\mathrm{d}N}{\mathrm{d}t} = \dot{N} = N_c 4\pi r^{*2} j = \omega N_0 \exp\left(\frac{-\Delta G_D}{k_B T}\right) \exp\left(\frac{-\Delta G^*}{k_B T}\right) \tag{1.14}$$

The dependency of the nucleation rate on undercooling ($\Delta T = T_{\text{solutionised}} - T$) can be understood from the behaviour of the two exponent terms in Equation 1.14 as illustrated in Figure 1.11a. Assuming the prefactor ω and activation energy $-\Delta G_D$ are constant with respect to temperature, one is able to infer that the first term in Equation 1.14 will decrease rapidly with temperature (high magnitude ΔT), corresponding to a significant reduction in diffusion with large undercoolings. At small undercoolings, however, the activation energy for precipitation ΔG^* is significantly increased according to Equation 1.15, when the enthalpy of formation ΔH is assumed to be constant with temperature, leading the second term to decrease substantially. Consequently, the competition of these two effects, as illustrated in Figure 1.11b, means that the nucleation rate will be at a maximum at intermediate undercoolings [20, 19].

$$\Delta G^* = \frac{16\pi\zeta^3}{3}\left(\frac{T}{\Delta H \Delta T}\right)^2 \tag{1.15}$$

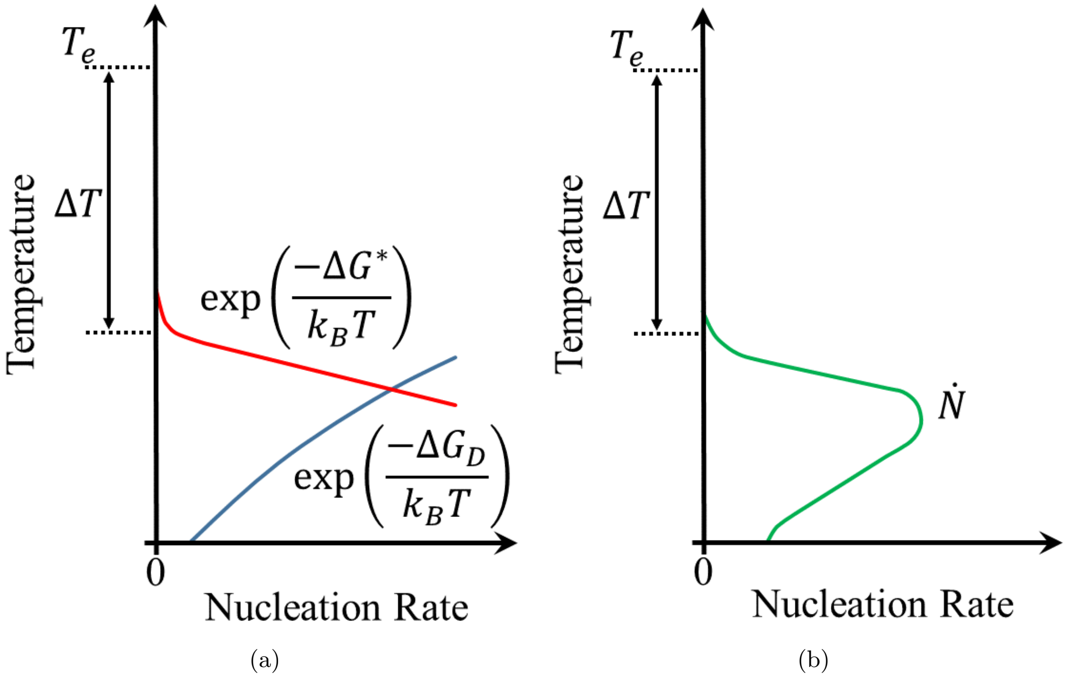

(a) (b)

Figure 1.11: Homogenous nucleation rate. a) Separate effects of exponent terms in Equation 1.14. b) Overall trend. Adapted from [19].

As, by its very existence, precipitate nucleation removes solute atoms from a matrix, it is axiomatic that it will also lead to a decrease in supersaturation. Furthermore, it is also clear that this phenomenon will be exacerbated by the subsequent growth of the nucleated particles. Accordingly, as nucleation and growth proceeds, the value of ΔG_{v} and, therefore, the effective driving force $\Delta G_{\mathrm{eff}} = (\Delta G_{\mathrm{v}} - \Delta G_{\mathrm{s}})$ will decrease, resulting in a reduction in the nucleation rate. To be more rigours, however, this outcome is best illustrated through the use of Equation 1.16 which describes the evolution of ΔG_{eff} in the small supersaturation limit of element B dissolved in a matrix γ of element A. Here x_B is the atomic fraction of element B and the superscripts $^{\infty}$ and ^{e} signify the mole fractions far away from the interface in the supersaturated matrix and at equilibrium in the given phase (*i.e.* when γ and β have planar interfaces) respectively [123].

$$\Delta G^{*}_{\mathrm{eff}} = \frac{\partial^2 G^{*}_{\mathrm{eff}}}{\partial x_B^2}(x_B^{\infty} - x_B^{\gamma,e})(x_B^{\beta,e} - x_B^{\gamma,e}) \tag{1.16}$$

Substituting Equation 1.16 into Equations 1.9 and 1.10 one is able to see that as nucleation (and subsequently growth and coarsening) proceeds *i.e.* $x_B^{\infty} \longrightarrow x_B^{\gamma,e}$ (Supersaturation $\longrightarrow 0$), $-\Delta G^{*} \longrightarrow -\infty$ and $r^{*} \longrightarrow \infty$ and hence by Equation 1.14 $\dot{N} \longrightarrow 0$.

The occurrence of purely homogeneous nucleation within an alloy system is very rare due to the necessity for a small lattice mismatch between the matrix and solute species in order to obtain a sufficiently low value of ζ. However, despite this reality, such nucleation has been observed in some copper cobalt alloys [124] and for metastable Guinier-Preston (GP) zones in some other alloys [19, 18]. Similarly, in relation to nickel-base superalloys, as discussed in Sections 1.2.1 and 1.2.2, homogeneous morphologies of γ' and γ'' are also evidenced in susceptible alloys (allowing for the conference of maximum high temperature strengthening effects) because of the small lattice mismatch and magnitude of ζ between γ'/γ'' and γ.

1.3.2 Heterogeneous Nucleation

Although most straightforwardly defined as the opposite regime to homogeneous nucleation, heterogeneous nucleation is more appropriately described as the phenomenon by which precipitates preferentially nucleate on inhomogeneities within a material matrix such as vacancies, interstitials, dislocations, inclusions, stacking faults and grain boundaries. These defects act to increase the local free energy of the system via the introduction of interfaces and matrix strains, and, consequently, their removal via the formation of a new precipitate phase releases energy (ΔG_{d}), decreasing the activation energy required for nucleation (following Equation 1.6) according to Equation 1.17 [19].

$$\Delta G_{\mathrm{het}} = -V\Delta G_{\mathrm{v}} + \sum_i A_i \zeta_i + V\Delta G_{\mathrm{s}} - \Delta G_{\mathrm{d}} \tag{1.17}$$

Comparing Equations 1.6 and 1.17 the principal difference between the mathematical descriptions of the homogeneous and heterogeneous regimes is revealed simply as the size of the driving force and type of nucleation site. As a result of this fact, it is easily deduced that the nucleation rate for heterogeneous precipitates in a particular system will be the same as that described in Equation 1.14 but with modified values for the nucleation site density $N_{0,\text{het}}$ and activation energy ΔG^*_{het} as detailed in Equation 1.18 [20, 19].

$$\dot{N}_{\text{het}} = \omega N_{0,\text{het}} \exp\left(\frac{-\Delta G_D}{k_B T}\right) \exp\left(\frac{-\Delta G^*_{\text{het}}}{k_B T}\right) \tag{1.18}$$

Taking into consideration the above descriptions of both homogeneous and heterogeneous nucleation (and the behaviour of the phases discussed in Section 1.2) it is self -evident that no physical restriction exists whereby a system is always limited exclusively to either one nucleation type or the other. In this regard, the competitive balance between homogeneous and heterogeneous nucleation in a susceptible system can be inferred from the magnitudes of their different rates. Specifically, taking the ratio of Equations 1.18 and 1.14, and assuming ω and ΔG_D are invariant between the two regimes, yields Equation 1.19 from which it can inferred that for a given heterogeneous nucleation site (*i.e.* ΔG^*_{het}), heterogeneous nucleation will exceed that of homogeneous nucleation in cases where: 1) The driving force ΔG_{v} is low leading to a large homogeneous activation energy in accordance with Equation 1.10 and/or 2) The number of heterogeneous nucleation sites is not sufficiently small for the ratio N_{het}/N_0 to dominate. Correspondingly, from comparison of Equations 1.15, 1.17 and 1.19 it is evident that as cooling/heating proceeds within a system, the degree of heterogeneous and homogeneous precipitation will depend on the potency of the heterogeneous nucleation site(s) and the degree of undercooling. In other words, if ΔG_{d} is too low, or the undercooling (ΔT) is large (creating a large driving force ΔG_{v}), homogeneous nucleation will dominate, an effect which is exploited in thermomechanical processing of many alloys to increase the quantity of homogeneous precipitates over heterogeneous precipitates (and therefore achieve enhanced mechanical properties).

$$\frac{\dot{N}_{\text{het}}}{\dot{N}_{\text{hom}}} = \frac{N_{0,\text{het}}}{N_0} \exp\left(\frac{\Delta G^*_{\text{hom}} - \Delta G^*_{\text{het}}}{k_B T}\right) \tag{1.19}$$

Planar defects

As alluded to previously, the (heterogeneous) nucleation of secondary phases on planar defects such grain or phase boundaries/edges/corners, stacking faults or twins is widely observed in a number of alloy systems; the magnitude of ΔG^*_{het} for planar defects is commonly the smallest of any heterogeneous nucleation site. For these sites, assuming a completely incoherent ($\Delta G_{\text{s}} = 0$) β precipitate nucleating on an isotropic boundary between two regions (*e.g.* grains) of phase γ, illustrated in Figure 1.12, the original free energy change equation (1.17) is modified to Equation 1.20 where $A_{\gamma\beta}$ and

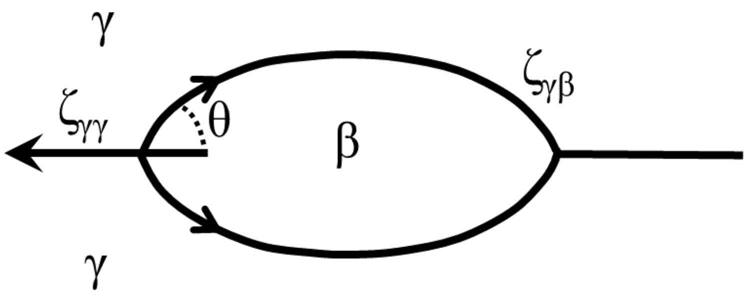

Figure 1.12: Nucleation of doubly spherical lens β phase precipitate on an isotropic $\gamma\gamma$ boundary. Adapted from [20].

$A_{\gamma\gamma}$ are, respectively, the areas of the $\gamma\beta$ and $\gamma\gamma$ interface with associated interfacial energies $\zeta_{\gamma\beta}$ and $\zeta_{\gamma\gamma}$.

$$\Delta G_{\text{het}} = -V\Delta G_{\text{v}} + A_{\gamma\beta}\zeta_{\gamma\beta} - A_{\gamma\gamma}\zeta_{\gamma\gamma} \tag{1.20}$$

Evaluation of the coefficients in Equation 1.20 using the just outlined "isotropic lens" configuration is made following the descriptions in Equation 1.21 where the angle θ (as labelled in Figure 1.12) is itself determined from the balance of the interfacial tensions in the plane of the $\gamma\gamma$ interface according to Equation 1.22.

$$\begin{gathered} A_{\gamma\beta} = 4\pi r^2(1-\cos\theta) \\ A_{\gamma\gamma} = \pi r^2 \sin^2 2\theta \\ V = \frac{2\pi r^3(2+\cos\theta)(1-\cos\theta)^2}{3} \end{gathered} \tag{1.21}$$

$$\cos\theta = \frac{\zeta_{\gamma\gamma}}{2\zeta_{\gamma\beta}} \tag{1.22}$$

Given the added complication of the so called "wetting" angle θ, a straightforward comparison of the magnitude of ΔG^*_{het} with ΔG^*_{hom} is not obvious. Nevertheless, through harnessing Equations 1.10 and 1.9 (and making the assumption $\Delta G_{\text{s}} = 0$ in Equation 1.6) the relative ratio of the activation energy ΔG^*_{het} for planar precipitates to ΔG^*_{hom} can be derived according to Equation 1.23 [19, 20]. An additional benefit of this transformation is the enabling of a direct comparison of the absolute behaviour of the relative critical energies as a function of the precipitate size as shown diagrammatically in Figure 1.13: As $\theta < 90^\circ$ the absolute value of the energy barrier for heterogeneous nucleation on planar defects is always lower than that for homogeneous nucleation although the critical radius r^* remains constant across both regimes.

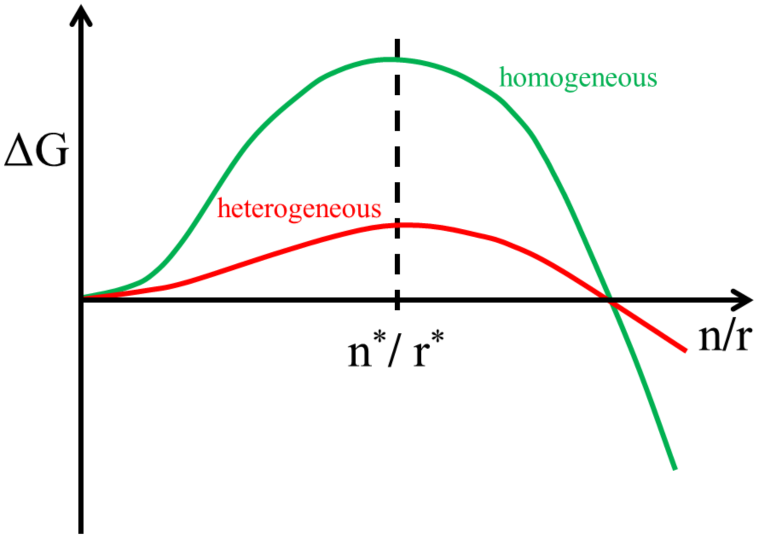

Figure 1.13: Homogeneous and heterogeneous nucleation barrier as a function of precipitate size r or number of atoms n.

$$\begin{gathered}\Delta G^*_{\text{het}} = \left(\frac{1}{2}(2+\cos\theta)(1-\cos\theta)^2\right)\cdot\left[\frac{-4\pi r^3}{3\Delta G_{\text{v}}} + 4\pi r^2 \zeta_{\gamma\beta}\right] \\ \frac{\Delta G^*_{\text{het}}}{\Delta G^*_{\text{hom}}} = \frac{1}{2}(2+\cos\theta)(1-\cos\theta)^2\end{gathered} \tag{1.23}$$

Across the various types of planar defects the nucleation rate is observed to follow, in accordance with the above discussion, the order of interfacial energy. Higher interfacial energy sites will lead to faster nucleation resulting, generally, in the $\dot{N}_{\text{het}}$ order: Phase Boundaries → Grain Boundaries → Incoherent Twins → Coherent Twins → Stacking Faults [125, 126]. The nucleation of grain boundary precipitates in nickel-base superalloys and stainless steels, particularly M_{23}C_6, has been demonstrated to be encouraged by high-angle grain boundaries and those with coincidence site lattice (CSL) values $> \Sigma 9$ due to their high interfacial energies [116, 125] (resulting in a high value of ΔG_{d}). However, the coherency of these grain boundary carbides also has an effect on their formation and morphology, with coherent precipitates having a lower activation energy and growing into the adjacent matrix rather than along grain boundaries [116, 125, 127].

Fundamentally, it is the reduction in activation energy offered by planar defects which leads to the heterogeneous nucleation behaviour discussed for many of the phases in Section 1.2 *e.g.* the preferential nucleation M_{23}C_6, δ, η and TCP phases on grain boundaries rather than twins and stacking faults and the nucleation of δ-phase on stacking faults within γ''. In general, however, it should be pointed out that, in addition to these nucleation site energy effects, another significant factor in this nucleation process is the typically faster diffusion rate along planar defects *viz.* by reducing the value of ΔG_D (becoming $\Delta G_{D\text{eff}}$) the value of $\dot{N}_{\text{het}}$ (calculated by Equation 1.18

through the evaluation of Equation 1.13) is amplified in all instances.

Point Defects and Dislocations

Excess vacancies and interstitials exist within supersaturated solid solutions principally as a result of a quench from high temperature; the massive and rapid temperature reduction does not allow atoms to return to their equilibrium lattice sites. Fundamentally, their effect on precipitate nucleation is twofold: Firstly, much like planar defects, dislocations act to increase the nucleation rate by enabling the faster transport of solutes through the matrix via the provision of a rapid diffusion path (decreasing ΔG_D). Second, they relive the misfit strain energy associated with secondary phase formation, decreasing ΔG_{s} and, therefore, lowering the activation energy ΔG^* [19, 20, 128]. The magnitude of this latter phenomenon is illustrated by considering the number of vacancies per atom required to form a stress free precipitate according to Equation 1.24 where V_{a}^{β} and V_{a}^{γ} are the atomic volumes of the precipitate and matrix respectively. Specifically, in the presence of vacancies ΔG_{d} in Equation 1.17 is defined by Equation 1.25 where ΔG_{n} is the free energy change associated with vacancy formation.

$$\varrho^* = \frac{V_{\text{a}}^{\beta} + V_{\text{a}}^{\gamma}}{V_{\text{a}}^{\gamma}} \tag{1.24}$$

$$\Delta G_{\text{d}} = \Delta G_{\text{s}} \frac{\varrho}{\varrho^*} - \Delta G_{\text{n}} \tag{1.25}$$

Owing to the complexities and variation associated with dislocations, a specific quantification of their impact on the nucleation of a specific precipitate is highly non-trivial. The dominance of the interfacial energy ζ in Equation 1.10 combined with the need to relieve the stress of the dislocation, for example, creates a severe complication as it is only specifically oriented semi-coherent precipitates which are likely to achieve a sufficiently lowest value of ΔG^* in the majority of systems. Despite these facts, however, given the distribution of strains possessed by such particles (Figure 1.14) and their diminishing with precipitate growth, a useful evaluation can be achieved using the assumption of full incoherence. In this regard for incoherent spherical particles the so called "catalytic effect" of dislocations is described by the trend in Figure 1.15 where the dimensionless parameter ι is defined in Equation 1.26 (g represents the elastic shear modulus and b the Burgers vector of the dislocation).

$$\iota = \frac{\Delta G_{\text{hom}} b^2 g}{2\pi\zeta^2} \tag{1.26}$$

In addition to the aforementioned mechanisms for semi-coherent particles, it should be noted that (through the removal/suppression of dilatational strains in the surrounding matrix) dislocations can actually also indirectly bring about the local precipitation of

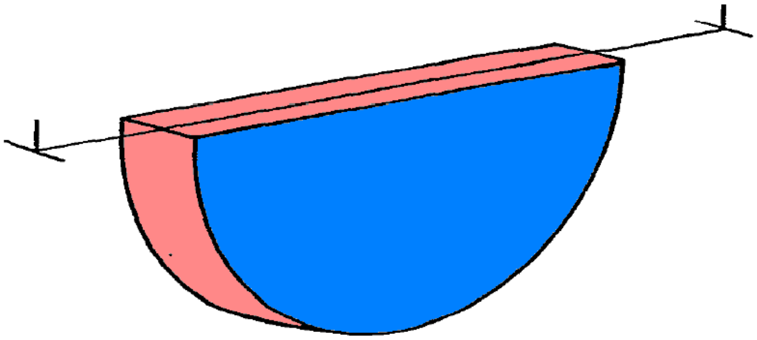

Figure 1.14: Semi-coherent precipitate nucleated on an edge dislocation. The broad (blue) faces are coherent with the matrix and the narrow (red) faces are incoherent. Adapted from [21].

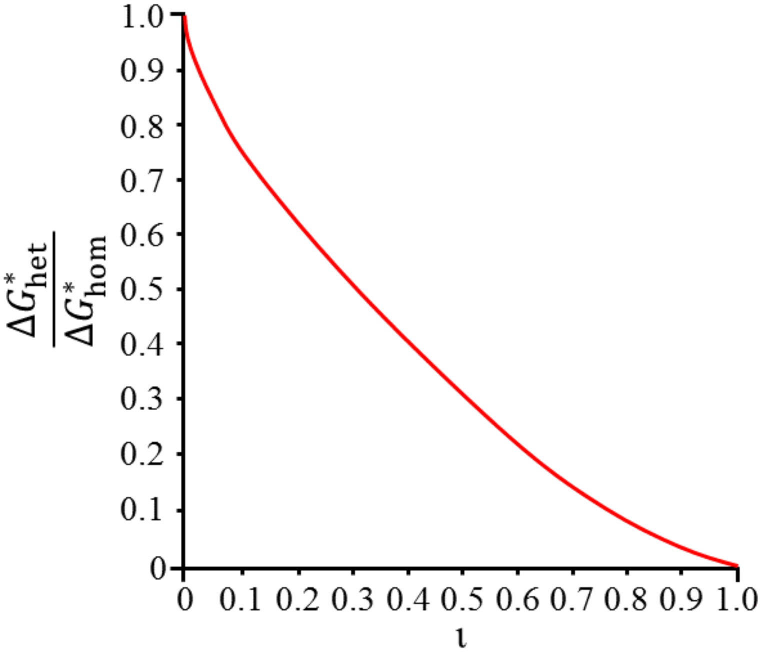

Figure 1.15: Activation barrier for incoherent nucleation as a function of the parameter ι. Values are normalised to that for homogeneous nucleation. Adapted from Cahn [22].

highly coherent precipitates in the adjacent matrix. In the case of a small(large) particles for instance, these will preferentially nucleate in the compressive(tensile) region above(below) a dislocation due to the reduction the energy/magnitude of the strains associated with the formation of a precipitate (ΔG_{s}), compared to the bulk. Similarly, soft (low shear modulus) rather than hard precipitates will form preferentially near to dislocations as they also act to reduce the strain energy of the matrix and thereby decrease ΔG_{s} [129, 130]. Notwithstanding such formation mechanisms, however, each of these locally nucleated precipitates are most appropriately considered as matrix nucleated as their growth is dictated according to the diffusion of solutes in the bulk rather than along the dislocation [21].

1.3.3 Growth

Following nucleation, precipitates above the critical size r^* will begin to grow/increase in volume due to the thermodynamic driving force emanating from the remaining supersaturation. This growth manifests as a migration of the interfaces of the precipitate into the surrounding matrix, with the movement of a specific interface defined as either interface controlled, diffusion controlled or under mixed control according to the limiting process. An outline of these three different regimes can be made most readily by considering a system of secondary phase β precipitating from a supersaturated solid solution of B atoms in a matrix (γ) of A atoms as illustrated in Figure 1.17a.

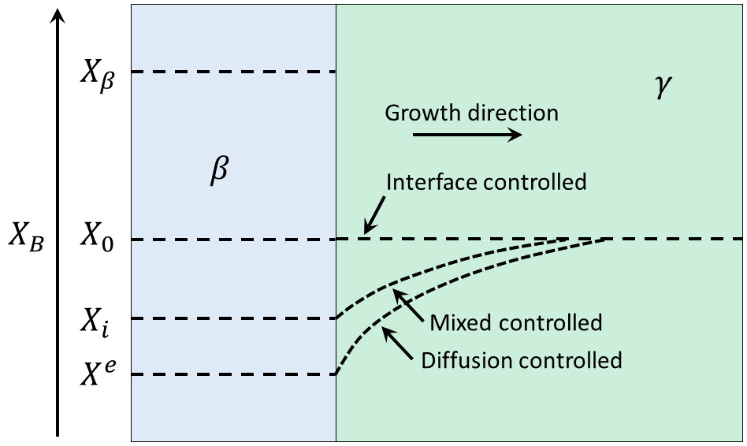

Figure 1.16: Schematic for a precipitate β rich in B atoms growing into a matrix γ rich in A atoms. Molar concentrations for B atoms are indicated with X_β the mole fraction of element B in the precipitate phase β, X_{i} the mole fraction of element B at precipitate-matrix interface for a mixed controlled regime, and X_0 and X^e the initial ($X(t=0)$) and equilibrium mole fractions of element B in the γ matrix. The direction of precipitate growth and profiles for the pure interface and diffusion controlled regimes are indicated. Adapted from [19].

In the aforementioned system, the driving force for B atom transport from γ across the interface is given by the difference in the partial molar free energy (chemical potential) Φ of B atoms in A and at the interface *i.e.* $\Delta\Phi_{\mathrm{B}}^{i}$ as calculated in Figure 1.17. Consequently, given a specific interface mobility M (velocity per unit a given driving force) the molar flux of B atoms (j) across the interface from γ to β is j_{B}^{i} is defined in Equation 1.27 (V_{M} is the molar volume of phase β). Separately, the flux of B atoms in γ towards the interface generated by the concentration gradient according to Fick's First Law j_{B}^{γ} is given by Equation 1.28 where c_{B} is the molar concentration of B in γ [19].

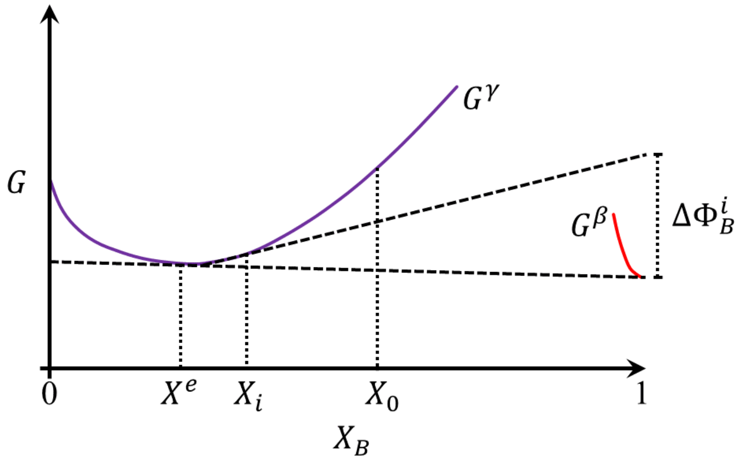

Figure 1.17: Indicative representation of the molar Gibbs free energy G diagram defining the origin of the driving force $\Delta\Phi_{\mathrm{B}}^{i}$ for β precipitate growth into the matrix γ in Figure .

$$j_{\mathrm{B}}^{i} = \frac{-M\Delta\Phi_{\mathrm{B}}^{i}}{{V_{\mathrm{M}}}^{2}} \tag{1.27}$$

$$j_{\mathrm{B}}^{\gamma} = -D\left(\frac{\partial c_{\mathrm{B}}}{\partial x}\right)_{\text{interface}} \tag{1.28}$$

Considering the separate operation of the two fluxes j_{B}^{i} and j_{B}^{γ}, a steady state can only (from mass conservation) be achieved with their balance. Taking into account this condition, therefore, one is able to define a diffusion controlled regime (*i.e.* where most of the energy is dissipated during the diffusion process and growth effectively takes place as fast as diffusion allows) as one in which M is high and $X_{\mathrm{i}} \approx X^{e}$ leading (in accordance with Figure 1.17) to a low $\Delta\Phi_{\mathrm{B}}^{i}$ and the condition of local equilibrium [131]. Correspondingly, if the interface velocity is very low, $X_{\mathrm{i}} \approx X_{0}$ leading to the effective elimination of the solute depleted region around the interface (*i.e.* diffusion is fast enough to make ${}^{\partial c_{\mathrm{B}}}/_{\partial x} \approx 0$) and a high value of $\Delta\Phi_{\mathrm{B}}^{i}$ (meaning most of the energy is dissipated transporting atoms across the interface) the growth is termed as interface controlled. Finally, for the remaining case where the energy released during growth is split such that it is spent more evenly over both interface and bulk diffusion, the system is said to be under mixed control [132] *viz.* customarily in mixed controlled systems the value of X_i results in a balance of the two fluxes j^i_{B} and j^γ_{B} but the interface mobility is lower than that for the diffusion controlled regime leading to a higher value of $\Delta\Phi^i_{\mathrm{B}}$ and a departure from local equilibrium at the interface [131].

Assuming the same rate of solute diffusion, the velocity of a given interface boundary can be inferred form Equation 1.27 to depend principally on the precipitate-matrix interface mobility M. Furthermore, in the absence of strain energy, it is the variation that can occur in M around a precipitate surface, due to possible changes in crystal structures between the two phases and their coherency, which dictates the precipitate shape/morphology [19]. Rather than a combination of equal factors, however, it turns out that the most important variable contributing to the behaviour of M in this instance is a variable known as the accommodation factor Υ (defined as the probability of the solute atom being accommodated in the precipitating phase) with increasing values accompanying a shift from interface to diffusional controlled growth. As a result of this fact, therefore, in such a strain-free regime it is more appropriate to rewrite Equation 1.27 in terms of Υ as per Equation 1.29 where n^{B} and ω^{B} are the number and vibrational frequency, respestively, of solute atoms able to cross the interface from γ to β and $\Delta\Phi^a$ is the activation energy required for the solute to leave the matrix γ.

$$j^i_{\mathrm{B}} = \frac{\Upsilon_\beta n^{\mathrm{B}}_\gamma \omega^{\mathrm{B}}}{RT} \exp\left(\frac{-\Delta\Phi^a}{RT}\right) \Delta\Phi^i_{\mathrm{B}} \tag{1.29}$$

In light of the above revelation, considering now the effect of coherency and crystal structure on Υ and,therefore, growth: In the case of a coherent interface between a matrix and precipitate of the same crystal structure Υ is high, meaning that not only is the method of interface growth purely that of vacancy controlled diffusion of atoms into the precipitate, but the rate of growth is dictated by the mobilities of the constituent atoms. Similarly, for semi-coherent interfaces who's misfit dislocations can climb by vacancy creation/annihilation Υ is also high. In contrast, for coherent and semi-coherent interfaces between phases of different crystal structures the value of Υ for precipitate growth normal to the surface is small leading to a low growth rate. Nonetheless, in this circumstance, however, the growth rate can be enhanced by a so called "ledge" mechanism whereby diffusion controlled growth occurs normal to the faces of facet ledges *i.e.* stepwise, parallel to the precipitate matrix interface. As a result, the overall rate of precipitate growth in the latter system is dedicated by both the speed of the diffusion of elements to the smaller ledge interface and the rate of nucleation of new ledges; the interface can be said to be under mixed control. Finally for fully incoherent boundaries, the value of Υ is again high meaning that growth in this case is a solely diffusion controlled process.

In the case of planar and curved incoherent interfaces, assuming growth occurs purely by volume diffusion, the initial rates of growth v (assuming $V_{\mathrm{M}} = \mathrm{const}$) ultimately determined (using mass balance) from Equation 1.28 are defined, separately, by Equations 1.30 and 1.31 where the different X variables correspond (as per Figure 1.17) to the mole fraction of B in β (X_β), in the matrix at time t $(X(t))$, at equilibrium (X^e) and at Gibbs-Thomson modified equilibrium $(X^\varphi)^7$, κ is a constant associated with the length scale of the atomic diffusion taking place, φ is the radius of curvature (r for a sphere) t is the time and $\Delta X = X(t) - X_e$ [19, 132]. Accordingly, following Equation 1.13, it can bee seen in both cases that the fastest growth will occur for intermediate undercoolings. Furthermore, at later stages/higher degree of cooling, as the overlap of the diffusion fields of neighbouring precipitates leads to a decrease in ${}^{\partial c_\mathrm{B}}/_{\partial x}$ (under this diffusion controlled regime) a decrease in the growth rate will also occur.

$$v = \frac{\Delta X}{2(X_\beta - X(t))^{\frac{1}{2}}(X_\beta - X^e)^{\frac{1}{2}}}\sqrt{\frac{D}{t}} \tag{1.30}$$

$$v = \frac{D\Delta X}{\kappa\varphi(X_\beta - X(t))^{\frac{1}{2}}(X_\beta - X^\varphi)^{\frac{1}{2}}}\left(1 - \frac{\varphi^*}{\varphi}\right) \tag{1.31}$$

For coherent/semi-coherent interfaces growing via the "ledge" mechanism discussed previously in this section, assuming the ledges are separated by a constant a displacement ψ, the initial growth rate via volume diffusion (*i.e.* before ${}^{\partial c_\mathrm{B}}/_{\partial x}$ begins to decrease) is described by Equation 1.32. This expression, however, is only applicable for the case of already nucleated ledges *viz.* for real systems (as discussed previously) it is the nucleation rate of new facets/ledges which is the dominating factor in the growth of these secondary phase boundaries. In addition, the assumption of ψ being constant for all ledges is only valid in the case of spiral growth. Other mechanisms such as nucleation on the surface or at precipitate intersections produce facets/ledges with variable ψ and, therefore, are much less uniform in terms of their growth rate.

$$v = \frac{D\Delta X}{\lambda\kappa(X_\beta - X^e)} \tag{1.32}$$

The fact that different growth rates are observed for each of the aforementioned interface types means that, for a given precipitate matrix system in which both have different crystal structures, the growth of incoherent and coherent/semi-coherent interfaces will occur at different rates. Ultimately, therefore, one can infer that precipitates which happen to contain both such faces will grow into long needles or plates and, in fact, it is this mechanism which is commonly believed to be responsible the formation of the Widmanstätten pattern observed for secondary phases in a number of different alloys [133, 134].

Finally, whilst the mechanism of intergranular volume diffusion moderated precipitate growth outlined above is valid in the case of interstitial solutions (owing to the high

---

[7] The "Gibbs-Thomson effect" describes the increase in the Gibbs free energy that occurs because of the effective increased pressure exerted by particle curvature/interfacial energy

volume diffusion rate), it must be pointed out that for substitutional systems, the rate of precipitate growth is modified/enhanced due to the presence of fast diffusion paths for solutes created by dislocation and vacancy networks. In these systems (as discussed with respect to nucleation in Section 1.3.2) the diffusion constant is modified to D_{eff} which is greater in magnitude and therefore, in accordance with Equation 1.28, leads to faster growth in diffusion controlled systems. Likewise, in the case of grain boundary precipitates, the rate of growth is also enhanced by the faster diffusion of elements; volume diffusion of solutes to the grain boundary and then the fast transport along grain boundaries (and the precipitate matrix interface) acts to increase the value of D.

1.3.4 Coarsening

During the processes of precipitate nucleation and growth, both the number and volume density of precipitates within a given system is constantly increasing. Once the supersaturation has been sufficiently depleted by these processes that the soft impingement of neighbouring precipitate diffusion fields occurs, however, the balance of the terms in Equation 1.6 changes such that there is a driving force for a reduction in the number of particles. That is, at this point the driving force for nucleation and growth ΔG_{v} declines to a level where the overall change in free energy ΔG begins to be dominated by the interfacial energy term $\sum_k A_k \zeta_k$; decreasing the number of particles causes a concomitant drop in the overall interfacial energy of the system. The most significant reduction is achieved for the case of large particles growing at the expense of small ones and in such a regime there is said to be a morphological coarsening of the grain size towards larger magnitudes [123, 19, 20, 132].

In a quantitative manner, for the case of spherical particles in diffusion controlled and, separately, interface controlled regimes the phenomenon of precipitate coarsening (also known as Ostwald ripening) is described mathematically according to Equations 1.33 and 1.34 (where $\bar{r}$ is the average particle radius initially (0) and at time t, X^e is the equilibrium solute concentration in the matrix, κ is a constant which includes in the interface mobility, R is the ideal gas constant and the other symbols have their usual meanings), respectively [135, 136]. Alternatively, for the case of grain boundary precipitates where χ is a factor associated with the grain boundary energy and GB_C is the fraction of the grain boundary covered in precipitates [137] coarsening of the precipitate population is instead defined by Equation 1.35.

$$\bar{r}(t)^3 - \bar{r}_0^3 = \frac{8 D \zeta V_{\mathrm{M}} X_\gamma^{\mathrm{e}} t}{9 R T} \tag{1.33}$$

$$\bar{r}(t)^2 - \bar{r}_0^2 = \frac{64 \kappa V_{\mathrm{M}} X_\gamma^{\mathrm{e}} t}{81 R T} \tag{1.34}$$

$$\bar{r}(t)^4 - \bar{r}_0^4 = \frac{9 \zeta X_e^\gamma V_{\mathrm{M}} D_{\mathrm{eff}} t}{16 \chi R T \ln(\frac{1}{f})} \tag{1.35}$$

Although derived under the dilute solution limit ($X_e^{\beta} \approx 0$ $X_e^{\gamma} << 1$, volume fraction of $\beta << 1$ and the activity coefficient is constant), from both of the above descriptions one is able to conclude the rate of coarsening in diffusion controlled systems will increase strongly with temperature (the values of D and X^e, as discussed previously, increase strongly with temperature) [138]. Additionally, much as in the case for of nucleation and growth, the rate of coarsening is also enhanced in these cases by the increased diffusion rate provided for by vacancy and dislocation networks [123, 20].

Specifically in the case of nickel-base superalloys, looking at terms in the Equations 1.33 and 1.35 it is clear that population of the strengthening phases γ' and γ'' should experience only slow rates of coarsening thanks to their high coherency with the matrix (low ζ). This is an important factor for the utilisation of these alloys at high temperatures as (as discussed in Sections 1.2.1 and 1.2.2) these precipitates only exert their maximum strengthening within a narrow precipitate size and distribution range any significant evolution would prove fatal in terms of maintaining peak mechanical properties. In addition, (following the same rational) it is also evident that the formation of incoherent precipitates such as δ and η phase (as well as grain boundary carbides) has the potential to drastically effect properties because of their high potential for both growth and coarsening; however, it is exactly this property which enables their utilisation for grain refinement.

§ 1.4 Superalloy 625

The nickel-base superalloy with designation 625 (UNS N06625/W.Nr. 2.4856) was first developed in the late 1950s and early 1960s by Inco Alloys International Incorporated, with the patent actually granted on the material on 8 December 1964 (Pat no. 3160500). The original driving force for the production of the alloy centred on the desire for high strength main steam-line piping (utilised in supercritical steam power plants) with improved performance over components made from 316 stainless steel [105]. To this end, the key criteria for the properties of the alloy, laid out before its inception, were excellent corrosion resistance, good weldability, high creep resistance, that it be fabricable into tubing and that it not be susceptible to age-hardening (*i.e.* stable microstructure). Along the way to its creation, however, the trial and error methods employed by alloy developers at the time led to a significant digression which ultimately resulted in the development of Alloy 718 (Patented 24 July 1962, no. 3046108). This deviation, whilst highly lucrative and successful, was of sufficient length for the original market and, therefore, the design basis for Alloy 625 to have disappeared. Consequently, in order to establish the alloy as an alternative for those already on the market (*e.g.* Waspalloy, Alloy 600, Alloy X-750), the decision was taken to modify the design parameters such that the fabricability requirement was removed and a desire for high tensile strength at both ambient and high temperatures was added. It was on this design basis, therefore, that the patented alloy was created.

1.4.1 CHEMISTRY

Since its inception the design composition of Alloy 625 has not remained constant but rather has been progressively been tweaked/modified over the years, by a number of different manufacturers, in order to hone its properties for specific applications. The composition range for Alloy 625 defined by the Special Metals Corporation (who acquired Inco Alloys International in 1998) today is given in Table 1.1. Accounting for solubility limits within the nickel matrix, the quantity of each of the alloying elements present in Alloy 625 is set according to the properties imparted and those which are required in the final product. A summary of how the elemental composition is used to achieve the properties stipulated by the design criteria outlined above is given in Table 1.2.

Table 1.1: Composition range for Alloy 625. The indexes ^{a} and * signify minimum and maximum content respectively [3].

Element	Ni	Cr	Fe	Mo	Nb(+Ta)	C	Mn	Si	P	S	Al	Ti	Co
Weight%	58^a	20–23	5^*	8–10	3.15–4.15	0.1^*	0.5^*	0.5^*	0.015^*	0.015^*	0.4^*	0.4^*	1^*

Whilst not included within the elemental composition defined by the Special Metals Corporation, given their natural abundance and the affinity of metallic elements such as titanium, chromium and molybdenum for them, it should also be assumed that all Alloy 625 products contain at least some quantity of oxygen and nitrogen. This

Table 1.2: Elemental control used to achieve design basis properties.

Design Basis Property	Elements	Details
Strength	Cr, Mo, Nb(+Ta), Al, Ti, Mn, Co	These elements are solid solution strengtheners and are therefore added in significant overall quantities to achieve high tensile strength. Niobium only imparts measurable strengthening when present above 2wt% [105].
Corrosion Resistance	Cr, Mo	Chromium gives excellent oxidation resistance through the provision of a protective oxide scale. Additionally, the high quantity of chromium with respect to carbon vastly reduces susceptibility to sensitisation. Molybdenum provides resistance to corrosion in reducing environments such as hydrochloric acid. Both elements act to greatly improve resistance to pitting and stress corrosion cracking [139].
Age Hardening /Stability	Ti, Al	Titanium and aluminium, as discussed in Section 1.2.1, act to age harden nickel-base superalloys through the formation of γ' precipitates and, consequently, are kept to low levels to avoid such a response in Alloy 625.
Weldability	Ti, Al, Si, Mn, P, S	The strong propensity for titanium and aluminium to form γ' precipitates means they are kept to a low level to avoid strain-age cracking [140]. Tramp elements such as sulphur and phosphorous are removed from the melt as much as possible due to the fact that they have a tendency to result in hot/liquation cracking (a.k.a microfissuring) [55]. Although also classified as a tramp element, silicon is not eliminated to the extent of phosphorus or sulphur owing to its action in reducing the negative effects of sulphur by removing oxygen (oxygen lowers the formation energy of detrimental sulphates) [141, 142]. Manganese is added for the same role but titanium and aluminium also work to remove oxygen.
Creep Resistance	Cr, Mo, Nb(+Ta), Ti, Al, C	The solid solution strengthening of molybdenum, chromium and niobium contribute significantly to the creep resistance of the alloy. Retaining at least 0.2wt% of both titanium and aluminium is also beneficial to creep resistance because of solid solution strengthening [105]. Precipitation of blocky carbides, typically (Nb,Ti)C and $Cr_{23}C_6$, along grain boundaries during cooling from the melt acts to inhibit grain boundary sliding (see Section 1.2.6).

eventuality, whilst potentially important as both of these elements severely degrade the mechanical and welding properties of Alloy 625 (reduce cracking resistance), can largely be ignored, however, due to their concentrations being kept to an almost insignificant level through careful selection of raw materials and the (as discussed Section 1.2.6) employment of high-tech Vacuum Induction Melting (VIM), Vacuum Arc Remelting (VAR) and Electroslag Remelting (ESR) refining processes. Coincidentally, it is these same techniques that also keep the levels of sulphur, phosphorus and unwanted silicon at a minimum.

1.4.2 Applications

The option of Alloy 625 as a candidate material has become possible in many industries thanks to the number of different properties it possesses, each of which have been (and continue to be) assessed through exhaustive experimentation. (Aside from situations where better alternative materials are available) with much cheaper (even if poorer performing) alloys such as Alloy 718 on the market, however, the main prohibiter to the application of Alloy 625 is cost. Consequently, it is only in the most specialised of applications, where the capital investment becomes economically viable (or the safety case necessitates it), that the alloy is ultimately employed. A number of such applications, and the commercial sectors in which they reside, are discussed below.

Chemical Processing

> Because of the exposure to (and even push towards) ever more corrosive feed stocks and products, the excellent corrosion resistance of Alloy 625 to a number of different forms of attack and its ease of fabrication means it has found application in a number of chemical processing plants. In refining sour (high sulphur) crude oil for instance, the excellent corrosion/stress-corrosion-cracking (SCC) resistance of Alloy 625 products have resulted in their employment in areas contacting naphthenic acid (such as the distillation and thermal cracking units), polythionic acid (such as the flare stack tip) and chlorides (typically overhead condensers) [118, 143]. Analogously, in the field of heavy water production (by the ammonia-hydrogen exchange process) Alloy 625 has also been utilised for ammonia cracker tubes because of its high strength at both ambient and elevated temperatures, good oxidation and corrosion resistance, good resistance to creep deformation and hydrogen attack, and low hydrogen permeability [10, 144].

Transportation

> Alloy 625 is utilised in automotive exhaust systems primarily due to its ability to be manufactured in thin section and resistance to oxidation, hot-salt corrosion, pitting and stress-corrosion cracking. Separately, in the gas turbine engines utilised on aircraft, Alloy 625 is commonly used for tailpipes, hush kits, vector nozzles and bellows on account of its excellent resistance to sensitization, high strength and toughness and excellent thermodynamic stability [145, 146, 147].

Marine

> As a consequence of its resistance to local attack (*i.e.* pitting and crevice corrosion), its high corrosion-fatigue resistance and tensile strength as well as its

resistance to chloride-ion stress-corrosion cracking, Alloy 625 has been widely utilised in a diverse array of marine/sea-water applications including mooring cables, propeller blades, submarine propeller sleeves, submarine snorkel tubes, exhaust ducts for boats and sheathing for undersea communication cables [148]. It is also applied in off-shore oil rigs [149, 150].

Power

In the power sector Alloy 625 has been applied in across a number of different generation technologies. For example, the high concentration of halogens in municipal waste has resulted in Alloy 625 being used either independently or as cladding/overlay for boiler tubes in waste-to-energy incinerator plants owing to its excellent resistance to halogen attack at high temperatures [151, 152]. Similarly, the high temperature strength and excellent corrosion resistance of the alloy has also led to its being the material of choice for molten salt (KNO_3, $NaNO_3$) containing tubing within concentrated solar power plants [153, 154].

The employment of Alloy 625 in water moderated nuclear power reactors has resulted not only from its high elevated temperature strength and excellent corrosion/pitting resistance in the high temperature coolant water, but also its resistance to irradiation assisted SCC (IASCC) [155]. Several current and planned generation III/III+ reactors, based the pressurised water design, utilise the material including the Westinghouse (Combustion Engineering) PWR reactor and the KEPCO APR-1400 reactor where it is used in control element assemblies (CEAs) Full strength CEAs contain boron carbide (or a combination of silver-indium-cadmium and boron carbide) with Alloy 625 cladding, part strength CEAs are solid Alloy 625 slugs with Alloy 625 cladding [156, 157, 158, 159]. Westinghouse have also utilised the material for the bottom grid in fuel assemblies and, in the new AP-1000, for the construction of the vessel used to seal the flywheel assembly in the coolant pump from the primary coolant water [160, 161]. Aside from Westinghouse, additional manufacturers in the nuclear sector are also researching the alloy for use in high strength applications such as bolts, tie rods and springs in new Gen III+ reactors [162]. Looking to the more distant future, Alloy 625 is a candidate material for components in some generation IV reactors including fuel cladding and fasteners in the Super-Critical Water Reactor (SCWR) and control rod chains in the Pebble Bed Modular Reactor (PBMR) [163, 164, 165]. Finally, the alloy is also under consideration for application in nuclear fusion reactors, specifically blanket loop components in molten salt, self-cooled tritium breeder designs [166].

1.4.3 Precipitation

Although originally conceived as a thermodynamically stable solid solution strengthened alloy (low aluminium and titanium contents), Alloy 625 was quickly shown to be susceptible to both carbide precipitation and (through intermetallic secondary phase formation) age hardening after prolonged exposure at elevated temperatures during service/ageing [105]. An estimate of the time-temperature-transformation (TTT) diagram for the most common precipitates in Alloy 625 is given Figure 1.18. Unfortunately, as stated by Floreen *et al.* [23], no definitive TTT diagram can be said to exist because of both the variable composition of the alloy (Table 1.1), which is known to have a marked impact on precipitation kinetics, and the analysis technique[8] used in its derivation.

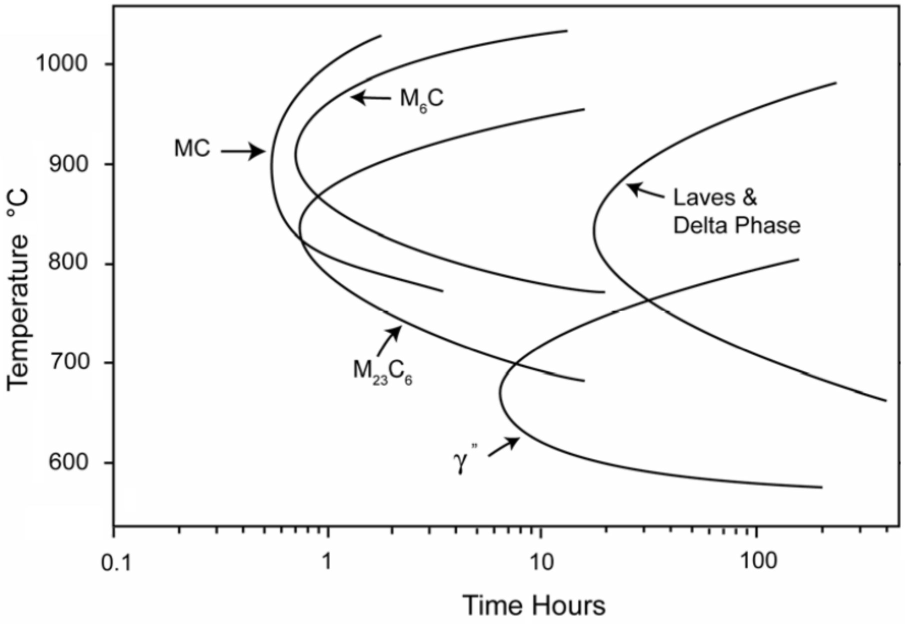

Figure 1.18: Time-Temperature-Transformation diagram for Alloy 625. Adapted from [23].

Intermetallic phases

Thanks to its high niobium and low aluminium and titanium contents, in short term (100's of hours) ageing the predominant intermetallic phase formed within Alloy 625 is that of γ'' [3], inducing marked increase in hardness, yield strength and tensile strength, along with concomitant reductions toughness, ductility [167, 168, 10, 169] and even corrosion resistance [170]. Nevertheless, however, direct precipitation and even coarsening of δ-phase in Alloy 625 between 700-900°C has also been commonly observed by a number of researchers after such ageing durations, with the incubation period for precipitation decreasing with increasing temperature [10, 41, 169]. In addition to both of these phases, Mittra *et al.* [169] have also found a Ni_2(Cr,Mo) metastable precipitate phase with an orthorhombic Pt_2Mo structure and a seeming snow-flake morphology after ageing for 1200 hours at 540°C which produced a simultaneous marked strengthening of material and drop in ductility through its high coherency with the matrix. Similarly, Shaikh *et al.* [171] have also detected γ' with its occurrence attributed to compositional variations.

---

[8] Direct detection methods are subject to threshold limits whereas indirect methods (*e.g.* measurement of changes in hardness) are subjective owing to the identification of the point at which initial precipitate influence is perceived.

In terms of size, the behaviour of γ'' has arguably been most thoroughly examined by Suave *et al.* [41] at ageing temperatures between 550-900 °C and durations up to 2000 hours through the use of high resolution scanning electron microscopy. Consistent with the observations in other nickel alloys, the shape of the γ'' precipitates was found by the authors to change as growth and coarsening proceeded, evolving from a spherical to an oblate spheroidal shape such that the aspect ratio (the ratio of the minor radius to the major radius) of the spheroids continually decreased with time [47, 172]. However, whilst reasonable agreement with the data at 650 °C was realised, fitting of the major radius size evolution of these particles according to the classical diffusion-governed coarsening equation (Equation 1.33) identified that other temperatures did not show a tight correlation *viz.* a large scatter from the proposed linear trend was observed which the authors attributed in part to heterogeneous nucleation. Support for this detrimental influence of heterogeneous nucleation is provided by absence of such an effect in the data of both Devaux *et al.* and Han *et al.* for γ'' in Alloy 718 [47, 2]. The work of Devaux *et al.* is particularly significant as, uniquely, it also features a plot for the change in precipitate aspect ratio as a function of the major diameter according to particles measured in their own work and by others in the literature. The interpretation this trend measurement was made by the authors such that two behavioural regions, corresponding to coherent (oblate spheroidal precipitate major radius $r_{\mathrm{M}} <$30nm) and incoherent particles ($r_{\mathrm{M}} >$30nm), were identified: The aspect ratio change for coherent precipitates was marked whereas for incoherent particles it was only slight, highlighting that coherency strain had a significant influence on the shape of γ'' precipitates. Extended ageing of Alloy 625 to 2000 hours at 650 °C and 1000 hours at 700 °C by Suave *et al.* [41] indicated a marked coalescence of identically orientated γ'' precipitates, claimed by the authors to be a transformation to δ-phase[9].

Van der voort *et al.* [173] performed an analogous but simpler study to that of Suave *et al.*, measuring the major radius of γ'' precipitates in samples of Custom Age 625 PLUS (higher Ti and Al levels that Alloy 625) aged for 20-1800 minutes (0.33-30 hours) at temperatures of 1350, 1425 and 1475 °F (732, 774 and 802 °C) through transmission electron microscopy (TEM). In this instance, transformation of the original data to achieve comparison with Equation 1.33 reveals apparently equivalent levels of agreement to that observed by Devaux *et al.* and Han *et al.* in Alloy 718. As a result of this outcome, therefore, owing to heterogeneous nucleation being commonly observed in standard Alloy 625 at these temperatures [171, 174, 175], the increased quantities of aluminium and titanium can be concluded as the underlying cause for their absence in Custom Age 625 PLUS.

In the longest published lab based ageing study, Radavich *et al.* observed that ageing for 16,000 hours at 1200 °F (648.9 °C) led to a dense matrix precipitation of γ'' accompanied by some δ-phase at the grain boundaries [176]. The precipitation and growth of αCr, typically associated with both the residual strain being present in the superalloy and the microsegregation of chromium in the matrix that results from δ-phase formation [177], was also noted at this temperature along grain boundaries. Further ageing of the same samples at this temperature up to 46,000 hours resulted in the substantial

---

[9] Owing to the necessary crystallographic rearrangement that would be necessitated by such a transformation, this claim is likely false

formation and growth of δ-phase, principally nucleated on grain boundaries. The presence of γ'' was still extensive at this time but had reduced from its peak because of its progressive transformation to thermodynamically stable δ. After 16,000 and 46,000 hours at 1400°F (760°C), the same authors found extensive δ-phase precipitation in Alloy 625 but γ'' was not detected. Finally at 1600°F (871.1°C) the microstucture was observed to be mostly free from intermetallic precipitates after 16,000 and 46,000 hours, with only a few residual coarsened δ plates remaining; this temperature is therefore inferred to be near to or above the δ solvus [176]. The effect of extensive γ'' precipitation in each of these long term studies was found, universality, to be a considerable increase in strength accompanied by a reduction in toughness and ductility.

Despite the extreme duration of the work of Radavich *et al.* even longer term precipitation behaviour of intermetallic phases in solution annealed Alloy 625 has been analysed in the literature through the characterisation of products which have endured extensive service times: After 50,000 hours at 500°C Thomas *et al.* detected the extensive precipitation of very fine intergranular γ'' in Alloy 625 taken from a feedstock superheater, accompanied by a concomitant substantial increase hardening and reduction in toughness [178]. No significant growth or coarsening of the particles, or transformation to δ-phase was detected. Similarly, at temperatures quoted as "close to but less than 600°C", Sundararaman *et al.* have observed significant intergranular γ'' precipitation in separate samples taken from ammonia cracker plants after 28,000 hours and 70,000 hours of service [179, 180]; however, they also found the presence of the phase Ni_2(Cr,Mo). The same precipitates were also found by Shankar *et al.* in Alloy 625 taken from the same plant after 60,000 hours of service at 600°C [10]. The only detection of δ-phase at this temperature was found by Chakravartty *et al.* who noticed it on grain boundaries, along with γ'' and Ni_2(Cr,Mo), in a one of the plant's cracker tubes after 100,000 hours of service [144] a found it to be accompanied by a dramatic loss in the ductility and toughness of the material. Ni_2(Cr,Mo) formation was linked to age hardening.

Perhaps surprisingly given the transformation of γ'' to δ-phase, intermediate ageing studies for Alloy 625 are seemingly absent in the literature; however, under the guise of a corrosion test Garcia-Fresnillo *et al.* found extensive bulk (*i.e.* away from the surface where the effects of corrosion are not present) precipitation of δ-phase in samples held for between 1000 and 10000 hours in steam at temperatures in the range of 700-800°C.

Carbides

The existence/precipitation of a number of different carbides in Alloy 625 has been noted by a numerous researchers after both long and short ageing at elevated temperatures, with behaviour consistent with that described in Section 1.2.6: Primary MC ((Nb,Ti)C) carbides have been found typically to exist in a blocky morphology at grain boundaries due to their role in the crystallisation of the alloy on cooling from the melt *viz.* the high energy of the carbide-γ interface means the particles are not incorporated easily in to the matrix and consequently act to pin grain boundaries as the melt crystallises [10, 181]. Additional carbides such as $M_{23}C_6$ and M_6C have been observed to begin to nucleate at, and grow along grain boundaries after ageing for as little as 4 hours at temperatures between 600-900° C, with significant growth occurring during subsequent ageing [168, 181, 182, 41, 8]. The distribution between the carbide types, concluded as resulting from their relative stabilities, is such that the fraction of M_6C increases with temperature. Extended ageing is at 900° C above 1000 hours was observed by Suave *et al.* to lead to the complete dissolution of grain boundary carbide particles. In terms of mechanical properties, the formation of grain boundary carbides during these ageing times in Alloy 625, as with most superalloy systems (*q.v.* Section 1.2.6), has been found by both Köhler *et al.* and Vernot-Loier *et al.* to impact on both the ductility and toughness of the material such that a reduction in both parameters is observed [167, 183]. The competition for elements and the relative stability of the carbide and intermetallic phases means that carbides are typically found in aged Alloy 625 material to be surrounded by a intermetallic precipitate (particularly γ'') free zone.

Similarly to the above discussion on intermetallic precipitates, the behaviour of carbides has also been examined after long ageing times with, for example, Thomas *et al.* finding the quantity of grain boundary carbides after 50,000 hours at 500° C to be almost identical to that in solution annealed material, indicating a very slow growth of these phases [178]. Furthermore, over extended service periods (16,000 - 100,000 hours) between 600-650° C, the behaviour of carbides on the grain boundary has been observed by numerous researchers to be uniform *viz.* the growth and coarsening of the same phases ($M_{23}C_6$ and M_6C) takes place [10, 144, 180, 176]. After 16000 and 46,000 hours at 1400° F (760° C) and 1600° F (871.1° C) Radavich *et al.* could only confirm the presence of M_6C at the grain boundaries, with two different structures of the carbide present at the higher temperature. The effect of these grain boundary carbides on the mechanical properties of the materials has been found to be primarily a reduction in ductility and toughness as well as a increase in creep resistance.

§ 1.5 Research Project Justification

Despite its original design being predicated on it being a solid solution strengthened material, the precipitation of secondary phases in Alloy 625, particularly γ'' (as discussed in Section 1.4.3), has been discovered, and ultimately utilised, by many researchers/companies to increase both the high temperature strength and creep resistance of products made from it [10, 184, 185]. The effects of these precipitates (as discussed in Sections 1.2.1 and 1.2.2) is optimal only for a narrow size range and distribution and, consequently, to achieve peak properties it is necessary to apply strict thermomechanical processing and ageing treatments [186].

In the early days of the thermomechanical processing of metals, the key factor in deciding what treatment should be applied to a given material, age hardened or not, was experience. Trial and error experimentation, much like that utilised in the original development of Alloy 625 (Section 1.4), as well as lengthy ageing and material characterisation studies were employed until materials achieved the desired mechanical properties whilst also maintaining the critical attributes such as corrosion resistance. In more recent history, however, the design of such heat treatments has become much more refined, with mathematical models being developed to quickly and accurately predict the both the behaviour of grains (*i.e.* recrystallisation) and precipitates.

For recrystallisation, the mechanisms involved (*e.g.* relieving the strain energy imparted through deformation) have resulted in models of its behaviour, including that in Alloy 625, focusing primarily on the Finite Element (FE) methodology [187] owing to its remarkable successful many systems. Moreover, its constant development and adaptation by researchers has enabled the design and production of evermore efficient processing techniques and desirable microstructures. Regardless of this achievement, however, the primacy of the grain structure in determining mechanical properties of metals means its modelling still retains much more focus amongst researchers than precipitation and, therefore, the prediction of secondary phase formation and behaviour is much less developed. Nevertheless, the models which have been constructed for precipitation have proven crucial for the development of many systems, most notably in aluminium alloys and high-strength low-alloyed (HSLA) steels [188, 189, 190, 191, 192, 193, 194, 195].

In the case of superalloys, their complicated chemistries and relatively small market (*cf.* aluminium and steel) has led to relatively few tailored models of secondary phase formation and behaviour being developed, even with their significance in determining/providing the desirable high temperature mechanical properties of the alloys. Consequently, owing to its primacy in imparting strengthening, if the design of optimal ageing treatments is to be achieved for a given Alloy 625 component it is clear that the development of a model which describes the behaviour of γ'' nucleation, growth and coarsening at appropriate temperatures (based on the TTT diagram shown in Figure 1.18) is necessary. To the author's knowledge no model for γ'' precipitation in Alloy 625 exists in the literature and, therefore, it is the novel aim of this research to create such a model.

By enabling the accurate prediction of the formation and evolution of γ'', the model created in this research will be highly useful to companies or individuals concerned with Alloy 625 performance and/or manufacture. That is, by utilising this model peak material performance should be more easily obtainable in products manufactured for use in any one of the applications detailed in Section 1.4.2. In addition to this, persons tasked with the maintenance of Alloy 625 products would also find the model beneficial due to the fact that it could be employed to predict when sufficient precipitate evolution has taken place that the material properties no longer satisfy the design requirements. In other words, variations in characteristics such as strength and toughness, and therefore component lifetime, should be predicable from their relationship to microstructure which changes because of the evolution (nucleation, growth and coarsening) of γ''. Other more specialist applications will include the prediction of precipitate number, size and density prior to service in nuclear environments to allow for the easier prediction of mechanical property changes due to radiation flux acting up on precipitates *viz.* if radiation fluxes are known to have a certain effect on precipitates with a given size/distribution then knowledge of the initial distribution (assuming no more evolution which reasonable at the low temperatures employed in current water cooled reactors) will allow for a more accurate prediction of the changes in material characteristics (such as ductility) over time. Finally, by allowing for the prediction of precipitate behaviour, it likely that the model will enable the refinement of the alloy composition (Table 1.1) to encourage/discourage the desired precipitate morphology in a given component. Ultimately, the key outcome of the implementation of this model, in whatever circumstance it is applied, should be that of increased economical and mechanical performance as well as improved assessment of Alloy 625 for applications in which it is a candidate material.

Chapter 2

γ'' Nucleation, Growth and Coarsening in Alloy 625 Model

In order to successfully predict the ageing behaviour of γ'' in Alloy 625, one is able to define 3 key characteristics a numerical model must possess:

1) ***It must be able to describe precipitation in complex multi-component system.***

   Alloy 625, contains at least 13 alloying elements (Table 1.1) and, therefore, the model must be able to take account of this complex chemistry.

2) ***It must include information on precipitate size, shape and number density.***

   As discussed with reference to γ'' in Section 1.2.2, the strengthening effect of matrix precipitates depends significantly on their size (related to their changing shape) and number density [6, 71, 186]. Consequently, both of these parameters must be outputted by the model in order to correctly allow for the prediction and achievement of peak hardness properties.

3) ***It must be valid over a large range of temperatures and time scales.***

   For the model to be applicable to individuals manufacturing and maintaining Alloy 625, it will be necessary for it to be calibrated and checked against both short and long term ageing data.

In addition to these criteria it is clear that, for it to be of most benefit to those seeking to implement it, the model must also comprise an additional attribute:

4) ***It must be reasonable practicable in terms of its application.***

Utilising over complicated descriptions (*e.g.* requiring excessive inputs) and necessitating very long computing times and/or high computing power will only act to inhibit the application of the model. In contrast, making it streamlined and fast will result in its being most useful, especially in evaluation of multiple ageing regimes.

Before a model which fulfils each of these requirements can be created, it is first necessary to evaluate each of the appropriate techniques previously designed and developed by other researchers for application to both superalloy and non-superalloy systems. Such an evaluation will allow for the correct selection of the numerical basis for the model in this research and, consequently, is given below. At this point, however, it is first necessary to outline and justify two initial assumptions on which the numerical model to be created in this research is to be based in order to provide additional context for the subsequent evaluation and technique selection.

I) ***The initial microstructure of the alloy is solution annealed (i.e. no pre-existing precipitates) and comprises a homogeneous (ideal) mixing of alloying elements.***

Short term precipitation hardening ageing treatments employed by product manufacturers are preceded by a solution anneal to ensure uniform and controllable behaviour of precipitates. Additionally, as the original design basis for Alloy 625 was predicated solely on solid solution strengthening and grain structure (*q.v.* Section 1.4) providing the desired mechanical properties, many of the Alloy 625 products employed in high temperature applications are installed with a solution annealed microstructure.

II) ***The precipitation of γ'' is assumed to occur with equal probability at any point in the matrix.***

The aforementioned solution anneal is assumed to have removed defects such as dislocations from the microstructure and, as a result, there are no preferential sites for intragranular γ'' nucleation (regime is described according to Section 1.3.1 rather than 1.3.2). As discussed in Section 1.2.2, a homogeneous distribution of γ'' is the most commonly observed (and widely utilised/employed) owing to the high coherency of the precipitates with the matrix [8, 10, 23].

§ 2.1 Technique Selection

The complexity of precipitation in even systems as low as ternary, and the shear computational power available, has led to a plethora of techniques being developed, adapted and applied over the years in order to model it. In general these models of secondary state formation and evolution can be divided into three distinct groups:

- Atomic Scale
- Mesoscopic Scale
- Macroscopic Scale

As the names suggest, the principal difference between these categories is the length scale over which they are valid/based and therefore, concomitantly, the degree of resolution they provide. To this end, a brief description of the techniques (lying across each technique group) which have been most commonly (and successfully) applied to the problem of precipitate modelling as well their associated advantages and limitations is given in Table 2.1.

Table 2.1: Modelling techniques employed for secondary phase precipitation in metals. Colours indicate class of method *viz.* Atomic, Mesoscopic or Macroscopic.

Technique	Description	Advantages	Limitations
Monte-Carlo (MC)	After descriptions for both the diffusion mechanism (vacancy jumps, interstitial jumps *etc.*) and the frequency of atom jumps (analogous to Equation 1.13) have been created, MC algorithms (such as residence-time algorithms) are utilised to describe the evolution of an initial predetermined state [196, 197, 198, 199]. In such a set-up, during each time step t_{MC} a transition occurs for each diffusing element with a probability proportional to the corresponding jump frequency. This process is repeated over a given simulation time with the incremental time step defined according to $t_{\mathrm{MC}} = {}^{1}\!/\sum_{y}(\Gamma_y)$ where Γ_y equates to the frequency of an atomic jump y.	Fundamental *ab initio* modelling. A full description of the kinetics is given. Suited to tackling complex systems/conditions such as precipitation induced by radiation and, separately, in alloys with high concentrations of solutes [196, 200].	High computing power/time required. Short modelling times. Difficult to describe: multi-component systems greater than ternary, phases of complicated crystallography, heterogeneous precipitation or elastic effects [196, 200].
Cluster Dynamics	Values for the precipitate-matrix interface free energies and solute diffusion coefficients, determined by experiment or atomistic simulation, are entered into the model. Precipitate nucleation, growth and coarsening processes are calculated in terms of a cluster size distribution through the use of kinetic/rate equations describing the absorption and evaporation of solutes from clusters [201, 202, 203, 204, 205, 206].	Lower computational power and time than atomistic models. Allows for longer modelling times and larger systems [196, 203, 204, 206].	Descriptions of multi-component/phase systems is difficult. Spatial information is lost [203, 204, 206].
Phase-Field	Centred on a diffuse-interface description of phase formation (field variables, *e.g.* structural order, are continuous across interfacial regions), where the microstructural evolution is defined according to the Cahn-Hilliard non-linear diffusion equation and time-dependent Ginzburg-Landau (also knowns as the Allen-Cahn) equation. Models are constructed such that they reproduce an intended sharp interface description. [207, 208, 209, 210, 211, 212, 213, 214].	Versatile in terms of the parameters which can be included and applicable to large complex, multi-component systems [211, 212].	Challenging/intricate set-up and calculation. Requires high computing power and time. This is exacerbated in multi-component systems [210].
Svoboda Fischer Fratzl Kozeschnik (SFFK)	Onsager thermodynamic extremum principle applied within a mean field approach *i.e.* no concentration gradients. The evolution of the system is described by a set of linear equations: $\frac{\partial G}{\partial q_l} = -\frac{1}{2}\frac{\partial G}{\partial \dot{q}_l}$ $(l = 1, 2, ..., K)$ where G and Q are, respectively, the Gibbs free energy and rate of Gibbs energy dissipation, and q_i are the parameters of the system. Constructed as a class computation with the nucleation rate calculated using a classical time dependent kinetic nucleation method. [215, 216, 217]	Able to handle large systems by using a higher level of abstraction. Produces information on many key variables including those of interest in this research [215, 216, 217].	Approximate solution by definition. Low volume of literature on its successful utilisation. Requires multiple experimental inputs. No spatial information.
Kampmann & Wagner Numerical (KWN) Method	Often referred to as a classical nucleation and growth type. Expands on the theories of Langer and Schwartz. Particle size distribution split into size classes and its evolution modelled numerically under the condition of a continuity equation: Nucleation rate calculated using a classical time dependent kinetic nucleation method. Growth modelled using the Zenner growth Equation 1.30 and coarsening through the use of the non-linearised Gibbs-Thomson Equation [218, 219, 220, 221, 222].	Theoretically applicable to large complex systems. Describes the evolution of desired parameters. Large quantity of associated literature. [104, 192, 223, 224, 225, 226, 227, 189, 228, 229, 230, 188, 231, 232]	Does not provide spacial information. Significant number of parameters which must be acquired from fitting to experimental data [200, 206, 210].
Johnson Mehl Avrami Kolmogorov (JMAK) Kinetics	Describe the fraction of microstructure transformed to a secondary phase based on the assumption that the system is homogeneous and isotropic and that the rate of growth is always constant. The transformed fraction (Y) is given by $Y(t) = 1 - exp(-kt^n)$, where k contains kinetic information including the nucleation and growth rate and n is the "JMAK exponent". The values for these parameters are obtained from experiment or atomistic/mesoscale modelling [233, 234, 235, 236]	Large and complex systems can be handled. Simple to implement. Simulations of long/extended time scales are possible [42, 237, 238, 236]	All specific microstructural information (*e.g.* precipitate size, number density) is lost [236].

Comparison of the requirements (outlined above) of the model to be created in this research with the techniques listed in Table 2.1 immediately allows both the atomistic and macroscopic techniques to be ruled out: Atomistic techniques, whilst providing a high degree of resolution and outputting data on a large number of variables are not compatible (at the current time) with a system which comprises as many elements as Alloy 625 and additionally would require too much computing power/simulation times. Macroscopic (JMAK) modelling, on the other hand would not yield the required information on γ'' precipitate size and density. Consequently, it is clear that the technique to be harnessed in this research must be based on one of those in the mescoscopic classification.

Considering each of the mescoscopic approaches individually, models centred on Phase-Field descriptions are able to be eliminated from contention due to their requirement of high computing power, whereas those based on Cluster Dynamics are also excluded because of the difficulty associated with describing multi-component systems. Of the two remaining techniques both can be seen to fulfil each of the requirements laid out previously of the model to be created in this research and, consequently, either would constitute a valid numerical basis. However, the higher level of abstraction in the SFFK model, specifically the lack of concentration profiles means that it can be much more easily applied to many component systems saving significant computation time. That is to say, although the KWN method can theoretically be applied to complex systems, substantial numerical difficulties are incurred (particularly associated with coupling conditions across the precipitate matrix interface) when modelling systems with component numbers equivalent to those of Alloy 625. By using a mean field approach the SFFK model avoids this problem [239]. As a result of these factors it is the SFFK technique that it is selected to be the basis of the model in this research.

§ 2.2 Svoboda-Fischer-Fratzl-Kozeschnik (SFFK) Model

As alluded to in Table 2.1, fundamentally the SFFK model is most appropriately considered as a re-imagining of the classical precipitation problem based on the utilisation of old theory from chemical engineering (Onsager's thermodynamic extremum principle [240, 241]) which states that (based on experimental measurement and physical reasoning rather than derivation as an absolute law of nature) systems not at equilibrium will evolve along a path towards equilibrium that produces the maximum entropy change. First designed for spherical particles[215, 216], its original framework has been applied[1] successfully and subjected to many adaptations over the years to suit more and more systems. The key developments of the SFFK formalism and their results are detailed in Table 2.2.

---

[1] Commonly SFFK is employed under the auspices of the program MatCalc developed by the same institution(s)/research group(s) as J. Svoboda, F.D. Fischer, P. Fratzl and E. Kozeschnik [242]

Table 2.2: Papers in which the SFFK model has been used to predict precipitation.

Paper (Year)	Model Adaptations	Results
Svoboda *et al.* (2004) [215] Kozeschnik *et al.* (2004) [216]	-	Comparison of (spherical) cementite (Fe_3C) precipitate size evolution with that predicted by a classical diffusion controlled description in a binary Fe-C system shows excellent agreement. Examples of cementite precipitate growth in the ternary Fe-Mn-C system are also given with the results obeying self consistent trends. No comparison to experimental data is made in this latter case. Subsequently, simulation of the Fe-Mn-C ternary system containing cementite is made with the inclusion of nucleation in the description. Results for particle size distribution in the coarsening regime are in accordance with the LSW theory and other simulation (experimentally validated) studies. Finally, the precipitation of multiple carbide phases in a seven component Fe based alloy is modelled with self consistent results (including the effects of metastable phases) being obtained.
Kozeschnik *et al.* (2006) [243]	Variable precipitate shape introduced. Disc and needle like precipitates approximated by cylinders.	Parameters introduced from modification are such that (in an isotropic strain field) the growth rate of small precipitates is highest when the cylinder dimensions are approximately equal as this shape provides the minimum surface to volume ratio (lowest interfacial energy). For large precipitates, the chemical driving force dominates precipitate evolution and the growth rate decreases for needle precipitates and increases for disc shaped ones. Such a phenomenon results from the larger surface area of the disc which maximises to collection of diffusing elements.
Svoboda *et al.* (2008) [244]	Precipitates can change shape as they evolve. Separate interfacial energies allowed for cylinder mantle and ends.	Constant misfit eigen strain maintained (*i.e.* constant lattice parameters); however, overall strain evolves with aspect ratio. Shape change necessitates the introduction of shape factors which account for the changing distribution of the elastic misfit strain energy. Examples do show good agreement with experimental databut only after reasoned extensive modification of the misfit strain and through setting the driving force as a free parameter so that the growth rate always matches the experimentally observed value.
Kozeschnik *et al.* (2010) [245] Radis *et al.* (2010) [246]	Accelerated diffusion along grain boundaries introduced to model grain boundary precipitate evolution.	Only growth and coarsening considered. The impacts of grain size on the bulk diffusion of elements included through consideration of the solute depleted zone around grain boundaries. Predictions made by modified equations for AlN precipitating in a system of Fe microalloyed with Al and N show excellent agreement with experimental observations.

With respect to Ni-base alloys, a review of the literature reveals that precipitation applications of the SFFK model have almost solely concentrated (to the commencement of this work) on the phase γ', yielding reasonable success for the prediction nucleation, growth and coarsening through the treatment of the cuboidal precipitates as (*q.v.* Section 1.2.1) spheres [247, 248, 249]. As alluded to in Section 1.5, however, the shape changing behaviour of γ'' precipitates means that such an approach cannot be adopted if the goals outlined for this study are to be met *viz.* it is clear that the problem of γ'' precipitation in Alloy 625 constitutes a unique implementation of the SFFK model for Ni-base alloys. As a result, harnessing the developments presented in Table 2.2, a new/necessarily modified SFFK framework is developed in this study as detailed below.

2.2.1 Geometry and Free Energy Balance

As discussed in Sections 1.2.2 and 1.4.3 γ'' precipitates exist as oblate spheroids in the matrix, with their eccentricity about the major axis becoming more pronounced as they grow. This shape behaviour ultimately results from non-uniform strain being exerted on the faces of the precipitate and consequences in variations in the coherency and, ultimately, interfacial energy between the precipitate and matrix. The actual strain field created by the precipitate, as well as its interfacing energy distribution, is not only complex but ever changing and, as a result, would incur massive computational cost if one tried to fully describe it in a precipitation model. Furthermore, given the abstractness of the SFFK model, maintaining this level of detail would be unreasonable and, in the long run, pointless. As as a result of this fact, it is the much simpler, biaxial geometry of a cylinder developed by Kozeschnik *et al.* [243] and Svoboda *et al.* [244] which is utilised in the computation instead.

The dimensions of the real oblate spheroidal precipitate are related to that of the model cylinder such that they both have the same volume and aspect ratio (α_k). This is described mathematically by Equation 2.1 where A_k is the major axis of the real ellipsoid (shown in Figure 2.1a) and B_k is the diameter of the cylinder (shown in Figure 2.1b) [244]. Similarly, the relation between the cylinder diameter B_k and the particle equivalent (volume) spherical radius ρ used in the evolution equations in this model, concurrently defining the dimensional ratio ξ_k, is given in Equation 2.2. For clarity, it should be noted here that subscript k is utilised interchangiably throughout this section to correspond to both individual model precipitates and precipitate classes. The utilisation of a equivalent spherical radius in the expressions, corresponding to a radius of a sphere with the same volume as that of the model precipitate, is made in the model simply for ease of computation.

$$B_k = \sqrt{\frac{4}{3}} A_k \tag{2.1}$$

$$B_k = \xi_k \rho_k, \tag{2.2}$$

$$\xi_k = \left(\frac{16}{3\alpha_k}\right)^{\left(\frac{1}{3}\right)} ; \tag{2.3}$$

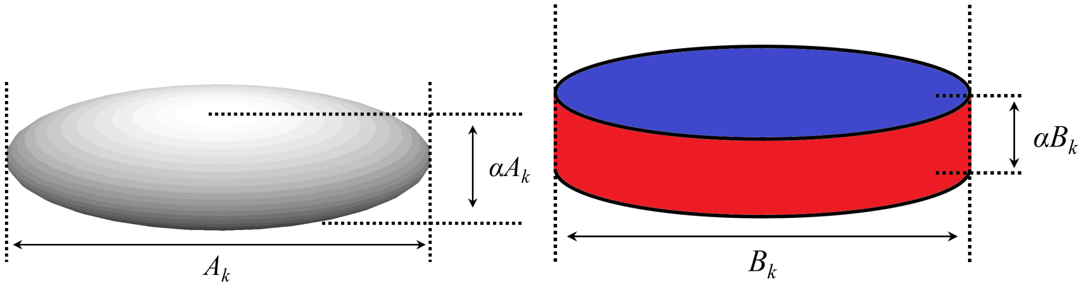

(a) (b)

Figure 2.1: a) Oblate spheroidal precipitate geometry displayed by γ'' precipitates in Alloy 625. Edge on view. b) Cylindrical precipitate geometry used in the model in this research where the red surface is defined as the precipitate mantle and the blue surface is one of the two precipitate ends.

Utilising this biaxial precipitate shape approximation, Svoboda *et al.* [244] showed that the change in the Gibbs free energy of the system ΔG associated with homogeneous precipitation (detailed classically in Equation 1.6) can be defined according to Equation 2.4 where the symbol λ_k corresponds to the precipitate-matrix misfit strain energy, ζ_k^E and ζ_k^M are the interfacial energies on the precipitate ends and mantle (indicated in Figure 2.1) respectively, m is the total number of precipitates and all the other symbols have their previously defined meanings.

$$\Delta G = \sum_{k=1}^{m} \frac{4\pi\rho_k^3}{3}\left(\lambda_k(\alpha_k) - \Delta G_{\mathrm{v}}\right) + \sum_{k=1}^{m} 4\pi\rho_k^2 \frac{\xi_k^2}{8}\left(\zeta_k^E(\alpha_k) + 2\alpha_k\zeta_k^M(\alpha_k)\right) \tag{2.4}$$

Following the methodology outlined in Section 1.3.1 when producing the relation shown in Equation 1.9, one is able to define the critical stable radius ρ^* for the biaxial precipitates modelled in SFFK as the root of the maxima of the function defining the differential of Equation 2.4 with respect to the particle equivalent spherical radius ρ. As indicated from Equation 2.4, however, in contrast to the classical regime, this calculation is far from trivial and is made uniquely more complex in this work by allowing for a full dependence on the precipitate aspect ratio and, by extension, the misfit strain between the matrix and precipitate and also their elastic contrast.

2.2.2 GROWTH AND COARSENING

The governing set of linear equations used to calculate system evolution in the SFFK model, derived from Onsager's thermodynamic extremum principle for a closed system under constant temperature and external pressure (making assumptions on system geometry etc.) are defined by the expression in Equation 2.5. Here q_l $(l = 1, 2, ..., K)$ is a set of independent state parameters such as particle radius, aspect ratio and solute concentration, $\dot{q}_l$ are their time derivatives and the Gibbs energy of the system G and rate of dissipation Q can be expressed as $G = G(q_1, q_2, ..., q_K)$ and $Q = Q(q_1, q_2, ..., q_K, \dot{q}_1, \dot{q}_2, ..., \dot{q}_K)$ respectively [250].

$$\frac{\partial G}{\partial q_l} = -\frac{1}{2}\frac{\partial Q}{\partial \dot{q}_l} \tag{2.5}$$

There are three mechanisms of Gibbs energy dissipation incorporated into the term Q: Dissipation by interface movement, dissipation by diffusion in the precipitate and diffusion outside the precipitate [250]. Consequently, by collecting relevant terms from the derivatives of the functions defining each of these three processes and the Gibbs free energy with respect to state parameters, Svoboda *et al.* showed that one is able produce a matrix of equations which describe how parameters such as precipitate size will evolve with respect to time [215, 250]. In the case of this research, using the assumption that inter-facial mobility is unrestricted (*i.e.* operating in the diffusion controlled regime outlined in Section 1.3.3) and including the desired full dependency on the variables of misfit strain and aspect ratio made in this research, the original expressions taken from the matrix defined by Svoboda *et al.* [244] for describing equivalent radius and aspect ratio evolution become those shown in Equations 2.6 and 2.7 respectively. The terms O_k^1 and O_k^3 are necessarily developed (through finite element modelling) corrections by Svoboda *et al.* to the original SFFK formalism to account for the effect of the shape of a cylindrical precipitate on the external diffusive flux elements versus spherical precipitate[2], R is the ideal gas constant, c_{zi} is the concentration of component i in either the precipitate $(z = k)$ or $(z = \gamma)$ the matrix, n is the number of elements/components in the system and $D_{\gamma i}$ is the bulk diffusion coefficient of component i in the matrix.

$$\dot{\rho_k} = -\left(\frac{\xi_k^2}{4\rho_k}\left(\zeta_k^E + 2\alpha_k\zeta_k^M\right) + \lambda_k(\alpha_k) - \Delta G_{\mathrm{v}} + \frac{\rho_k}{3}\frac{d\lambda}{d\rho} + \frac{\xi_k^2}{8}\left(\frac{d\zeta_k^E}{d\rho} + \frac{d\zeta_k^M}{d\rho}\right) - \frac{\xi_k^2}{12\alpha_k}\frac{d\alpha}{d\rho}\left(\zeta_k^E - \alpha_k\zeta_k^M\right)\right) \cdot \left[\rho_k RTO_k^1 \sum_{i=1}^{n}\frac{(c_{ki} - c_{\gamma i})^2}{c_{\gamma i}D_{\gamma i}}\right]^{-1} \tag{2.6}$$

$$\dot{\alpha_k} = -\left(\frac{\rho}{3}\frac{d\lambda}{d\alpha} - \frac{\xi_k^2}{12\alpha_k}\left(\zeta_k^E - \alpha_k\zeta_k^M\right) + \frac{\xi_k^2}{8}\left(\frac{d\zeta_k^E}{d\alpha} + \frac{d\zeta_k^M}{d\alpha}\right)\right)\left[\rho_k^3 RTO_k^3 \sum_{i=1}^{n}\frac{(c_{ki} - c_{\gamma i})^2}{c_{\gamma i}D_{\gamma i}\alpha_k^2}\right]^{-1} \tag{2.7}$$

---

[2] The equation including O_k^2 derived by Svoboda *et al.* is omitted here due to the condition imposed in this research of no diffusion taking place inside the precipitate

In addition to the growth of individual precipitates, Equations 2.6 and 2.7 also facilitate the simulation simultaneous and competitive phenomena such as coarsening. The concentration elements in the matrix which determine the relative evolution of the parameters of each precipitate in these processes are calculated from the continuity equation shown in Equation 2.8 where N_i corresponds to the total quantity/moles of element i in the system, Ω is the system molar volume (in the derivation of SFFK the molar volume is assumed to be the same in both the matrix and precipitate phases for simplicity) and the rest of the symbols have their usual meaning. In the case of a multicomponent alloy ΔG_{v} is calculated in SFFK according to Equation 2.9, where c_i^{eq} signifies the concentration of a component at equilibrium and the remaining symbols again have their predefined meanings [239].

$$c_{\gamma i} = \left(N_i - \sum_{k=1}^{m} \frac{4\pi\rho_{ki}^3 c_{ki}}{3} \right) \left[\Omega \sum_{i=1}^{n} \left(N_i - \sum_{k=1}^{m} \frac{4\pi\rho_{ki}^3 c_{ki}}{3} \right) \right]^{-1} \tag{2.8}$$

$$\Delta G_{\mathrm{v}} = -\frac{RT}{\Omega} \sum_{k=1}^{m} \sum_{i=1}^{n} c_{ki} \ln \left(\frac{c_{\gamma i}^{\mathrm{eq}}}{c_{\gamma i}} \right) \tag{2.9}$$

Allowing for variation of the precipitate and matrix lattice parameters (and *ipso facto* the eigenstrain ε of precipitates) with aspect ratio, the original expression derived by Svoboda *et al.* [244] for calculation of the misfit strain of precipitates λ_k is modified in this research to the form shown in Equation 2.10. The variables F_0, F_1 and F_2 are complex factors evaluated based on work carried out by Fisher *et al.* on the Eshelby scheme which account for the distribution of strain in a spheroidal particle based on its aspect ratio and the contrast in the Young's modulus E between the precipitate and matrix phases [251, 252, 253]. When evaluated using a Poisson's ratio (ν, negative ratio of transverse to axial strain) of 0.3 the trends for the natural logarithm of each of the factors F_0, F_1 and F_2 against the natural logarithm of the aspect ratio for different elastic contrasts have been shown by Svoboda *et al.* to be well approximated by third order polynomials. The symbols ε and $\Delta\varepsilon$ in Equation 2.10 correspond to the isotropic and additional misfit eigenstrain (arising from the precipitate shape/lattice parameters being unequal).

$$\lambda_k = \frac{E_\gamma \varepsilon^2}{1-\nu} \left[F_0 + F_1 \frac{\Delta\varepsilon}{\varepsilon} + F_2 \left(\frac{\Delta\varepsilon}{\varepsilon} \right)^2 \right] \tag{2.10}$$

For clarity/simplicity, comparison between the growth description outlined in Equation 2.6 and the classical Zenner growth equation (1.31) is most easily made when the later is formulated under the conditions of the depletion zone being much larger than the precipitate ($X(0) - X^e << X_\beta - X^e$) [254] and the matrix and precipitate atomic volumes being equal as shown in Equation 2.11 (all symbols have the meanings defined in Section 1.3.3). Inspection of these two expressions shows them seemingly to be very different in terms of their arrangement; however, both contain the same physical quantities including elemental diffusivity and supersaturation. Consequently, one is able to deduce that, whilst the derivation of the governing equations of the SFFK model utilising Onsager's thermodynamic extremum principle has resulted in a different description of precipitation, it still captures all of the same variables as more physically strict/theoretically accurate classical descriptions.

$$v = \frac{\mathrm{d}R}{\mathrm{d}t} = \frac{D_{\mathrm{B}}}{\kappa r}\frac{X(t) - X^r}{X_\beta - X^r}, \qquad X^r = X^e \mathrm{exp}\left(\frac{2\zeta V_{\mathrm{at}}^{\beta}}{r k_B T}\right) \tag{2.11}$$

2.2.3 Time Dependent Kinetic Nucleation

Despite being an significantly different approach to precipitation modelling, the expression used to describe the nucleation rate of secondary phase particles in SFFK is ultimately the time dependent version of the classical equation detailed in Equation 1.14. More specifically, however, for ease of computation in the calculation, the exact form of the equation used in the SFFK model is the well known expression derived by Russell [255] from the concepts outlined by Volmer and Becker-Döring *viz.* that precipitation is analogous to an atom polymerisation process [256, 257]. In this circumstance the evolution of all the microclusters[3] in a system conforms to Equation 2.12, where $\vec{r}$ and $\vec{r'}$ are multidimensional vectors whose components are the variables used to describe/define individual microclusters (*e.g.* n_1, n_2, n_3, ...), $w(\vec{r},\vec{w}')(\omega(\vec{r'},\vec{r}))$ is the transition frequency of a microcluster from(to) $\vec{r}$ to(from) $\vec{r'}$ and $s(\vec{r},t)$ is the concentration of microclusters at $\vec{r}$ [21, 258].

$$\frac{\partial f(\vec{r},t)}{\partial t} = \sum_{\vec{r}} \big(w(\vec{r},\vec{r'})s(\vec{r'},t) - w(\vec{r'},\vec{r})s(\vec{r},t)\big) \tag{2.12}$$

In the simplest case of only the number of atoms n changing (*i.e.* a single current process) where the distinction between classes is single atoms ($\vec{r'} = n \pm 1$), the rate of microcluster exchange (current) $\dot{N}(n)$ from size/class n to $n+1$ is defined by Equation 2.13 [123] where $P_1(n)$ and $P_2(n{+}1)$ are the atomic absorption and desorption probabilities/rates respectively.

$$\dot{N}(n) = P_1(n)f(n,t) - P_2(n+1)s(n+1,t) \tag{2.13}$$

---

[3] Microclusters may contain only a few atoms or molecules, and if smaller than the critical nucleus will usually decay away on an atom by atom basis.

Assuming detailed balancing takes place[4] between the two probabilities and that $P_2(n+1)$ is unchanged away from equilibrium conditions (reasonable as $1/P_2(n)$ is large compared to time taken for a microcluster to internally relax between atomic additions, and the concentrations of microclusters is low), the relation $P_2(n+1) = P_1(n)c^e(n)/c^e(n+1)$ (where $c^e(n)$ is the equilibrium concentration of microclusters with size n) can be defined [259]. Inserting this expression into Equations 2.12 and 2.13 yields the nucleation Equations 2.14 and 2.15 respectively [21, 260].

$$\frac{\partial s(n,t)}{\partial t} = \frac{\partial}{\partial n}\left(P_1(n)c^e(n)\frac{\partial s(n,t)/c^e(n)}{\partial n}\right) \tag{2.14}$$

$$\dot{N}(n) = P_1(n)c^e(n) - \left(\frac{s(n+1,t)}{c^e(n+1)} - \frac{s(n,t)}{c^e(n)}\right) \approx -P_1(n)c^e(n)\frac{\partial s(n,t)/c^e(n)}{\partial n} \tag{2.15}$$

Finally, replacing $c^e(n)$ in Equation 2.15 with Equation 1.11 and integrating yields the steady state nucleation rate shown in Equation 2.16 [123, 21]. The limits of the integrands are defined according to the boundary conditions imposed by the nucleation barrier (shown in Figure 1.13); microclusters smaller than n^* will become equilibrated with monomer clusters therefore $\frac{s(n)}{C(n)} \rightarrow 1$ as $n \rightarrow 1$ and as $n \rightarrow \infty$, $\frac{s(n)}{c^e(n)} \rightarrow 0$ ($c^e(n) >> s(n)$). The integrand on the right hand side (RHS) is evaluated by first making the equivalence $b(n^*) = \beta^*$ and then using a Taylor expansion around n^* for $\Delta G(n)$, both of which are valid given the shape of the distribution in Figure 1.13 (the majority of the integrand total lies at this point) [261].

$$\frac{1}{\dot{N}} = \int_{1}^{\infty} \frac{\mathrm{d}n}{P_2(n)N_0\exp\left(\frac{-\Delta G(n)}{k_BT}\right)} \tag{2.16}$$

Explicitly in the SFFK model used in this research, *i.e.* substituting in Equation 2.4, the nucleation rate becomes Equation 2.17 where the symbol Z is the Zeldovich factor (calculated according to Equation 2.18) which corresponds to inverse of the width I of the curve of $\Delta G(n)$ approximately k_BT below ΔG^* [260] and accounts for the fact that ${}^{f(n^*)}/_{c^e(n^*)} = {}^1/_2$ and the majority of particles nucleating with size $n > n^*$ will actually dissolve [261, 262]. Further, by assuming that the nucleation of precipitates in multi-component systems is controlled by the same combination of diffusive processes derived from Onsager's thermodynamic extremum principle for growth and coarsening, the atomic absorption rate is defined by Equation 2.19.

$$\dot{N} = N_0 Z \beta^* \exp\left(\frac{-\Delta G^*}{k_BT}\right) \tag{2.17}$$

---

[4] Detailed balancing describes a regime in which each process and its inverse takes place at the same rate at equilibrium.

$$Z = -\sqrt{\frac{1}{2\pi k_B T}\left(\frac{\partial^2 \Delta G(n)}{\partial n^2}\right)_{n^*}} = \frac{\Omega}{2\pi\rho^{*2}}\sqrt{\frac{\frac{\xi^2}{8}(\zeta_k^E + 2\alpha\zeta_k^M)}{k_B T}} \tag{2.18}$$

$$\beta^* = \frac{4\pi\rho^{*2}}{a^4\Omega}\left(\sum_{i=1}^{n}\frac{c_{\gamma i}D_{\gamma i}}{(c_{ki} - c_{\gamma i})^2}\right) \tag{2.19}$$

In the case of time dependent nucleation, the steady state description given in Equation 2.17 is appended with an exponential term which includes an incubation period τ and describes the time lag between the start of ageing and the nucleation of the first precipitates as shown in Equation 2.20.

$$\dot{N} = N_0 Z \beta^* \exp\left(\frac{-\Delta G^*}{k_B T}\right)\exp\left(\frac{-\tau}{t}\right) \tag{2.20}$$

The equation for calculation of the incubation period in the SFFK model is the well know expression derived by Feder *et al.* [261] from diffusion theory (Equation 2.21) under the assumption that the time taken for a critical microcluster to reach a size $n^* + {}^{I}\!/_{2}$ comprises two components: 1) The time for a microcluster to drift from monomer ($n = 1$) to size $n^* - {}^{I}\!/_{2}$ and 2) the time to get from size $n^* - {}^{I}\!/_{2}$ to $n^* + {}^{\mathrm{I}}\!/_{2}$ by random walk, the latter of which dominates the incubation [261, 263, 264, 262].

$$\tau = \frac{1}{2Z^2\beta^*} \tag{2.21}$$

Chapter 3

Model Implementation

The model created in this research, based on the SFFK formalism, is executed as a so called class computation. That is, rather than corresponding to specific precipitates, the suffix k in the equations detailed in Section 2.2 instead represents a group of identical (*i.e.* same radius, aspect ratio) precipitates. Such a methodology is chosen in this research due to the ability to calculate the whole precipitate particle size distribution (PSD) with the highest computational efficiency *viz.* alternative applications would lose advantageous detail (from a material design perspective) or incur undesirable computational penalties. The inspiration for this approach is taken from the classically based Kampmann and Wagner numerical (KWN) method discussed in Table 2.1 [219, 265]. A discussion of the application of classical precipitation equations through a number of different class based approaches is given by Perez *et al.* [221, 222].

§ 3.1 Calculation Inputs

Prior to any computation being carried out for γ'' precipitates in Alloy 625, it is clear from the from the governing equations described in Section 2.2 that a number of different inputs are required. Fortunately many of these variables can be sourced or extrapolated from analysis of studies detailed in the literature; however, the determination requires of the rest requires the development/utilisation of more novel approaches.

3.1.1 Thermodynamic Driving Force

The values for the concentrations of elements in the matrix at equilibrium ($c_{\gamma i}^{\mathrm{eq}}$), used to calculate the thermodynamic driving force for precipitation via Equation 2.9, are calculated over the temperature range of interest in this research from the molar phase diagram for Alloy 625 and, separately, elemental composition diagram for γ'' (both calculated via the Calphad method) presented in Figures 3.1 and 3.2, respectively. Specifically, using the quantity of γ'' (Figure 3.1) and its composition (Figure 3.2) a mass balance calculation is performed to determine the amount of each type of element which is present at equilibrium in the matrix at a specific temperature. A similar methodology is also employed for the calculation $c^{\mathrm{eq}}_{\gamma i}$ harnessing the fact that (as is discussed later in Section 3.2) in the model created in this research the concentration of elements in the γ'' precipitates is chosen to be invariant with time at a given temperature *viz.* the mass balance calculation to determine $c_{\gamma i}$ is made with respect to the instantaneous phase fraction.

Given its relatively minor usage in this research as a purely user interface driven program, a detailed discussion of the software known as Thermo-Calc used to produce the diagrams shown in Figures 3.1 and 3.2 is justifiably avoided here. Nevertheless, for completeness a simple discussion of the software and the Calphad method on which it is ultimately based is presented in Appendix A.

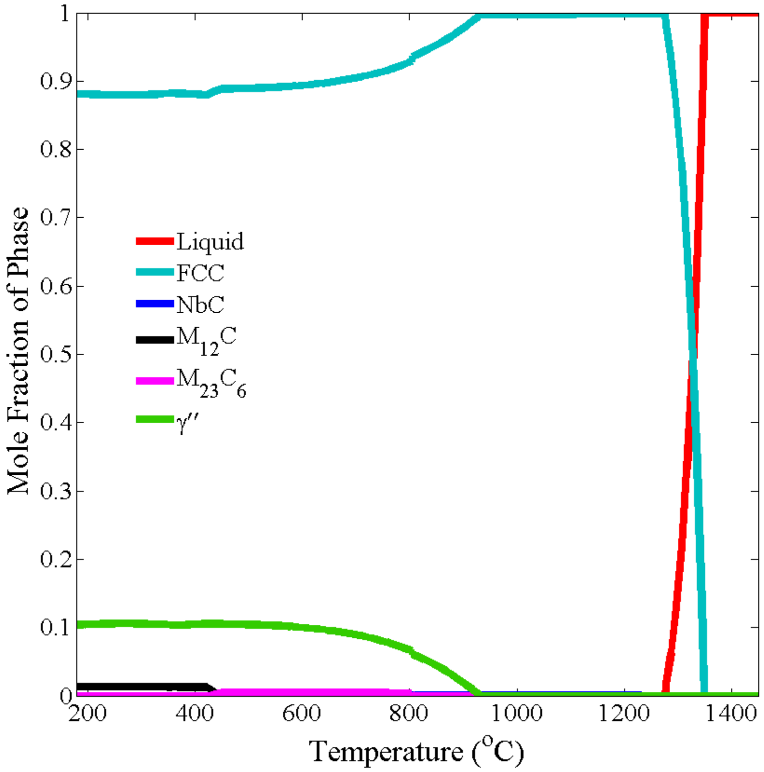

Figure 3.1: Molar phase composition of Alloy 625 as a function of temperature. Results calculated using the software Thermo-Calc (via the Calphad technique) operating with data from the Thermo-Calc Software TCNI7 Ni-based Superalloys database version 7 [24, 25, 26].

3.1.2 Diffusion Constants

Based on the elemental composition of γ'' precipitates indicated in Figure 3.2, the model created in this research only focuses on five elements (Ni, Nb, Ti, Cr, Mo). As a result, it is only the diffusion of these species which are of interest; however, unfortunately, likely owing to the speciality of Alloy 625 and the difficulties/complex analytical techniques associated with precisely determining inter-diffusion coefficients [266], no experimentally measured values for the diffusion constants of Ni, Nb, Ti, Cr

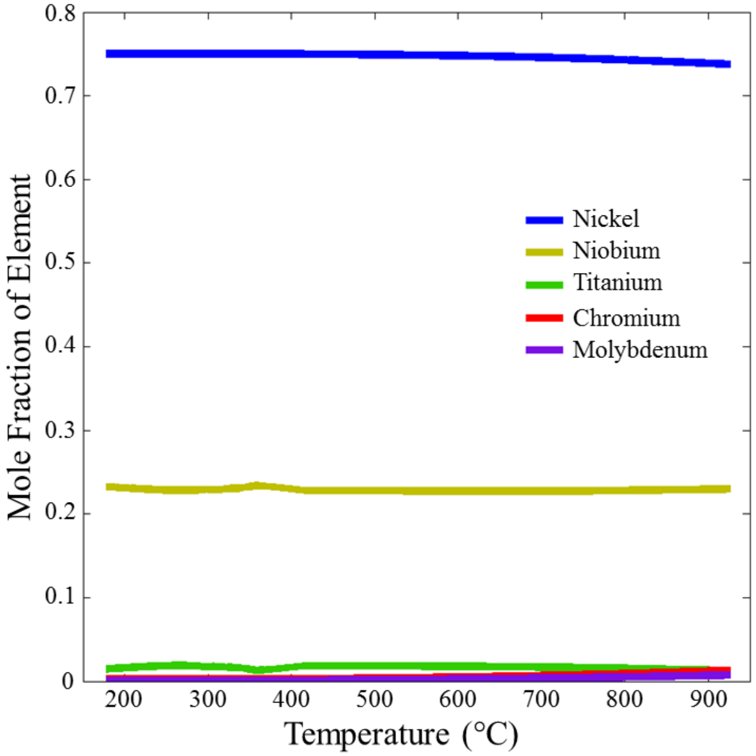

Figure 3.2: Elemental composition of γ'' precipitates in Alloy 625 as a function of temperature. Results calculated using the software Thermo-Calc (via the Calphad technique) operating with data from the Thermo-Calc Software TCNI7 Ni-based Superalloys database version 7 [24, 26].

and Mo in Alloy 625 are available in the literature. Accordingly, given that the alloy possesses a primarily nickel matrix, the values for D_{Nb}, D_{Ti}, D_{Cr} and D_{Mo} selected for use in the model created in this research are those determined from $\mathrm{Ni}-\mathrm{X}$ diffusion couples. D_{Ni} is equivalent to the self diffusion value.

A summary of the specific selected experimental magnitudes for the coefficients in the Arrhenus equation for the diffusion coefficient D (Equation 1.13, but where the Boltzmann constant k_B is replaced by the ideal gas constant R for convenience) are given in Table 3.1. It should be noted that whilst values calculated from simulations are available in the literature, experimental values were chosen so that the model in this research would not be impacted/subject to any assumptions made in the calculations of the theoretical values. Also, the simulated values for diffusion constants which are available currently in the literature are only validated against the same experimental data chosen here thereby making the selection of simulated rather than experimental data nonsensical [267, 268, 269].

Table 3.1: Experimentally measured diffusion constants for the elements determined from equilibrium thermodynamic calculations to be contained within γ'' precipitates in Alloy 625.

Element	D_0 ($\mathrm{m^2s^{-1}}$)	ΔG_D ($\mathrm{Jmol^{-1}}$)	Reference
Nickel	0.00019	66800	Wazzan [270]
Niobium	0.000088	257000	Karunaratne *et al.* [271]
Titanium	0.00086	283813	Karunaratne *et al.* [272]
Chromium	0.001187	299638	Karunaratne *et al.* [272]
Molybdenum	0.00012	281300	Karunaratne *et al.* [271]

3.1.3 ELASTIC CONSTANTS

Calculation of the coefficients F_0, F_1 and F_2 in the misfit strain equation (Equation 2.10) used in the SFFK model requires precise knowledge of the elastic constants of both the matrix and precipitate phase. Fortunately, for Alloy 625 the behaviour of the macroscopic constants for solution annealed material over a wide range of temperatures have been determined by the Special Metals Corporation (the main vendor of the material) and are readability available to anyone[1]. Conversely, the values for the elastic constants of $\mathrm{NbNi_3}$ with a BCT $D0_{22}$ structure (*i.e.* the γ'' phase) as a function of temperature cannot be found anywhere. Due to this fact, the magnitudes of these parameters for this intermetallic phase must be obtained by more innovative means.

Trends for the elastic constants of pure nickel over a wide range of temperatures have been calculated from molecular dynamics simulations by Luo *et al.* [28] with the results validated where possible against experimental data. Additionally, Connétable *et al.* have found through their own first principle calculations, again validated against experimental data where available, that the relative magnitude of the individual elastic constants of BCT $\mathrm{NbNi_3}$ at 0K are consistent with those of pure nickel [27]. Therefore, from these two pieces of research, a first approximation of the trend in the elastic constants of the γ'' phase can be made by mapping of the behaviour of nickel onto the single value determined for BCT $\mathrm{NbNi_3}$ determined by Connétable *et al.* [27] (similar values have also been calculated by Dai *et al.* [273] and, more recently, by Lin *et al.* [274]). The values for the elastic constants produced from this mathematical operation, together with those for Alloy 625 are shown in Figure 3.3.

---

[1] The elastic properties of Alloy 625 are listed on the data sheet published online by Special Metals Corporation for the benefit of customers interested in purchasing the material [3]

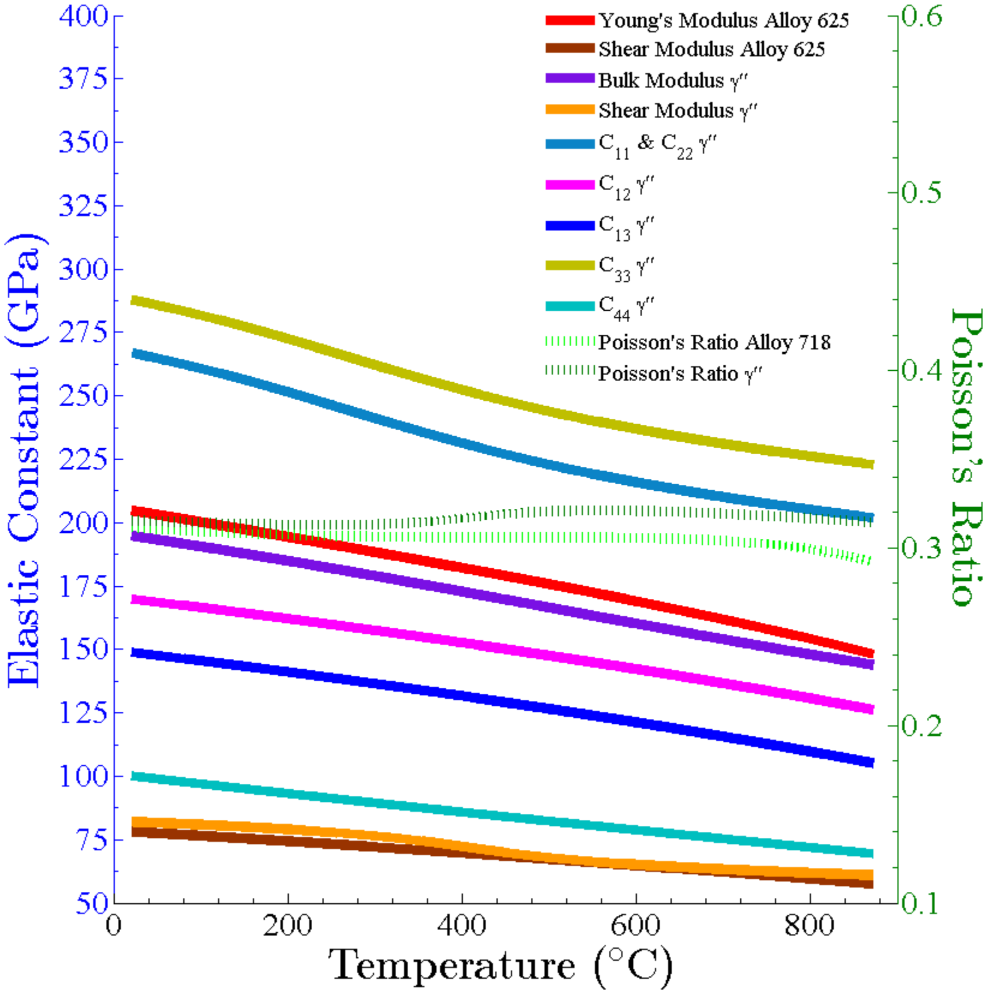

Figure 3.3: Elastic constant behaviour for the Alloy 625 matrix and γ'' precipitates interpreted in this research. Alloy 625 data taken from the material data sheet issued by the Special Metals Corporation [3]. γ'' data calculated from the extrapolating the results of Connétable *et al.* [27] using the trends calculated for nickel by Luo *et al.* [28]

3.1.4 Lattice Parameters

The magnitudes of ε and $\Delta\varepsilon$ in Equation 2.10 are evaluated for γ'' in Alloy 625 by inserting the relevant strain tensor components $\epsilon_{i,j}$ into Equation 3.1. In accordance with the work of Devaux *et al.* [47], the strain tensor components are themselves calculated from the lattice parameters of both phases (a_γ, $a_{\gamma''}$ and $c_{\gamma''}$) according to Equation 3.2.

$$\varepsilon = \epsilon_{1,1}, \epsilon_{2,2} \qquad \Delta\varepsilon = \epsilon_{3,3} - \epsilon_{1,1} \tag{3.1}$$

$$\epsilon_{i,j} = \begin{pmatrix} \frac{a_{\gamma''} - a_\gamma}{a_\gamma} & 0 & 0 \\ 0 & \frac{a_{\gamma''} - a_\gamma}{a_\gamma} & 0 \\ 0 & 0 & \frac{\frac{c_{\gamma''}}{2} - a_\gamma}{a_\gamma} \end{pmatrix} \tag{3.2}$$

Despite being measured in a number of studies and in a range of different superalloys over the years [275, 276, 277, 278, 40, 279, 280, 4, 281, 172], the selection of the lattice parameters for both the alloy matrix and the γ'' precipitate phase is not trivial. The reason for this two fold: First, as illustrated most clearly by Collier *et al.* in their study of Alloy 718 [276], the magnitude of the lattice parameters for γ'' seems to be significantly influenced by changes in alloy composition. Secondly, whilst other models/studies have employed constant values for the lattice parameters of both the matrix and precipitate phases when performing similar misfit calculations (including the original work of Svoboda *et al.* [244] and others using different modelling techniques such as Rettig *et al.* [210]), this is not appropriate for the case of γ'' precipitates. Evidence for this latter conclusion comes from experimental data produced by material aged isothermally for different time periods: Whilst not yielding the same absolute values for the lattice parameters the studies of Mukherji *et al.* [277] (Alloy 706), Sarkar *et al.* [280] (Alloy 625) and Slama *et al.* [4] (Alloy 718) separately each show the lattice parameters of both the matrix and precipitate phase to vary significantly with time. Given the concomitant changes in precipitate morphology also indicated by these authors, it is axiomatic to link the change in lattice parameters to precipitate evolution and, consequently, conclude that for the precipitation model created in this research to be as accurate as possible, the variation in lattice parameter values must be taken into account.

In face of the problems just highlighted, when selecting literature parameter values for this model it is clearly necessary to impose the criteria that they constitute a single data set *viz.* measurements from a single alloy composition aged at different temperatures and durations. Unfortunately for the purposes of this research, however, only a few such data sets exist and each are subject to separate key limitations: The results of Mukherji *et al.* [277] are not only taken from material which differs significantly from the composition of Alloy 625 (Alloy 706) but are also the result of X-ray diffraction scans of bulk samples - the use of bulk specimens (*i.e.* simply sectioned material) for X-ray diffraction measurement means that the peaks in the scans obtained cannot be properly correlated to the phases of interest owing to influences of crystallographic orientation. In addition, the measurement is also subject to a significant error because of the overlapping of the matrix and precipitate phase peaks. The consequence of these aforementioned factors is the generation of a dataset which, under the assumption of the peak locations being correct leads to values being calculated for the misfit strains which would be energetically insurmountable (from a precipitate formation standpoint) if borne out in reality. Unsurprisingly, being performed by the same research group, the results of Sarkar *et al.* [280], whilst taking place on a sample Alloy 625 and thereby minimising any effect of composition, are produced using the same methodology as that discussed for the study of Alloy 706 by Mukherji *et al.* meaning they are subject to the same significant error. Unlike the previous two studies, the results of Slama *et al.* [4] are produced for precipitates which have been extracted from the alloy matrix meaning they do not incur the aforementioned difficulties in X-ray analysis and, therefore, the calculated parameters should correspond to those actually possessed by the precipitates. Nevertheless, even in this instance, the fact that these results are obtained for precipitates formed in Alloy 718 suggests that some discrepancy with the values which occur for precipitates in Alloy 625 will be present.

The implication of the above discussion is that, from an uncompromising standpoint, it can be argued that the data which currently exists in the literature for the lattice parameters of γ'' and the matrix phase in nickel superalloys is not suitable for the model created in this research. Fortunately, however, the flexible framework of the SFFK model means that, so long as the data obtained by Slama *et al.* [4] is comparable with that which would be obtained for Alloy 625 with regard to both the absolute values and their behaviour with time, the data of Slama *et al.* [4] is acceptable. Consequently it is this data, displayed graphically for ease of reference in Figure 3.4, which is selected for use in the model created in this research. Notwithstanding this fortuitous eventuality, it should be mentioned here that Slama *et al.* published a subsequent study (using the same methodology) but found an undulating rather than consistently increasing trend for the value of $a_{\gamma''}$ [281]. Immediately, this result would seem to question the appropriateness of the selection of the first data set for use in the simulation; however, the second study of Slama *et al.* (contrary to the first) also found a similar undulating behaviour for the precipitate aspect ratio which is not in agreement with other published data [172, 47]. As a result of this discrepancy, the second data set produced by Slama *et al.* is concluded here to be flawed due to the influence of some significant error, thereby negating any possible implications it may have.

Another qualifier which must be placed on the adoption of the available literature data by the present authors is the infeasibility of conducting appropriate measurements like those of Slama *et al.* on Alloy 625 in this research due to a lack of material *viz.* the only

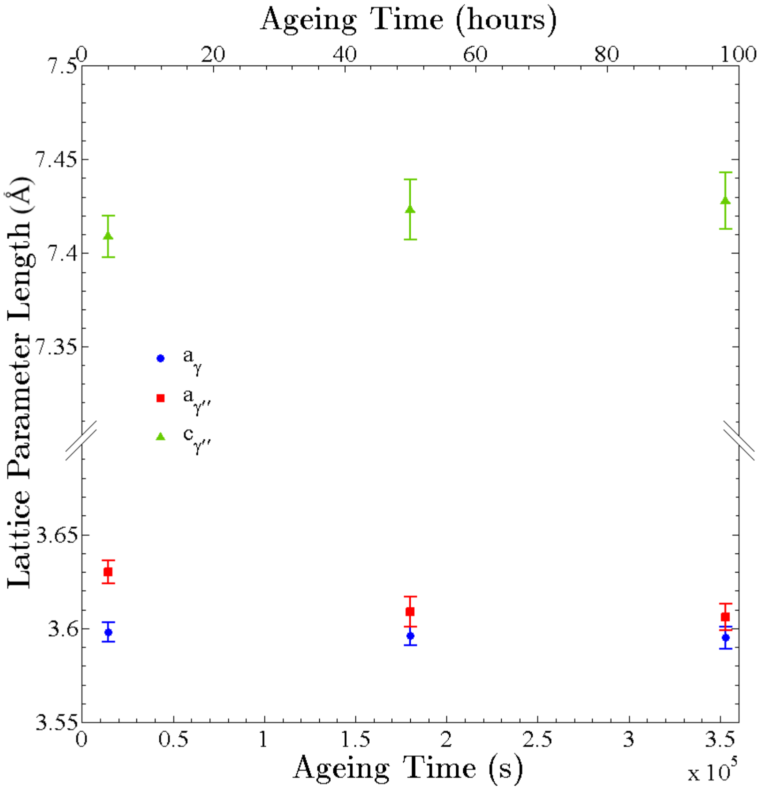

Figure 3.4: Lattice parameters measured for the matrix (a_γ) and γ'' precipitates ($a_{\gamma''}$, $c_{\gamma''}$) by Slama *et al.* in Alloy 718 when ageing at 680^{o}C [4].

macroscopic experimental option available was the fundamentally unsuitable technique performed by Sarkar *et al.* [280] and Mukherji *et al.* [277]. Whilst obviously no longer relevant given the non-use of the experimental data produced by this technique, for the benefit of clarity, a more rigorous outline of the problems associated with it and why alternative techniques such as precipitate extraction could not be used in this research is given in Appendix B. Additionally, it should also be noted that although alternative microscopic techniques (requiring only small amount of material) such as TEM (*q.v.* Section 4.2.8) could be employed for the determination of lattice parameters, the macroscopic nature of the model produced in this research means such a methodology is unsuitable as a macroscopic value is required. That is, the value produced by X-ray diffraction corresponds to the average values for many thousands of precipitates and the statistically driven nature of the SFFK model means it is such a value which is necessitated. Obtaining an analogous quantity from TEM, whilst theoretically allowing for more detailed measurement (*e.g.* lattice parameter distributions rather than ones corresponding to average precipitates), would be unworkable because of the time taken to produce the data set.

3.1.5 Interfacial Energy

A procedure for determining the interfacial energy of γ'' precipitates derived from the application of the theories outline by Eshelby [251, 282], was reported in a well known paper by Cozar *et al.* [172] published in 1973. The calculation principally utilises experimental data regarding the lattice parameters in the system (for the calculation of precipitate/matrix misfit strain) and the relationship between precipitate shape (α) and L_{M}, together with a series of derived relationships, to define a single interfacial energy value (under the specified conditions) over the whole surface of a precipitate with a given size. In this research, however, the mathematical technique derived by Cozar *et al.* cannot be implemented owing to fact that not only (as discussed in Section 2.2.1) does the computation relate to cylindrical precipitates with non-uniform interfacial energy, but it also requires that this value can change. Put another way, the symmetry arguments associated with precipitate shape and strain distribution relied upon by Cozar *et al.*, the isotropic interfacial energy values produced and the assumption of constant lattice parameters (and *ipso facto* misfit strain) are all not valid.

In the absence of such a direct method for calculating the desired interfacial energy values, it instead becomes necessary to infer them from experimentally observed precipitate behaviour. Specifically through rearrangement of Equation 2.7 (accounting for transformation between ellipsoidal and cylindrical geometries) one is able to calculate the interfacial energy of any given precipitate from the measured rate of change of its aspect ratio if the behaviour of the variables such a misfit strain (Equation 2.10) have already been established through the use of literature data. Consequently, it was this calibration methodology which is adopted for the calculation of ζ_k^E and ζ_k^M in this research. Once this calibration has been performed, calculation of the interfacial energy is possible from the magnitudes of the precipitate size and aspect ratio.

3.1.6 Aspect Ratio vs. Precipitate Size

The last input parameter required for the model, specifically in Equation 2.6, is the relationship between precipitate aspect ratio and size. A continuous single mathematical function based on fitting to precisely measured experimental data is desired for the easiest implementation within the model, however, multiple functions maybe required.

§ 3.2 Calculation Parameters and Flow-Chart

Fundamentally, the SFFK based precipitation model created in this research is an iterative calculation that is encapsulated by the flow chart given in Figure 3.5. A summary of the processes carried out at each stage of the flow chart, and their specific implementation with respect to γ'' precipitates in Alloy 625 (*i.e.* detailing the exact parameters used), is given in the subsequent sub-sections. Each section corresponds to the identically labelled stage.

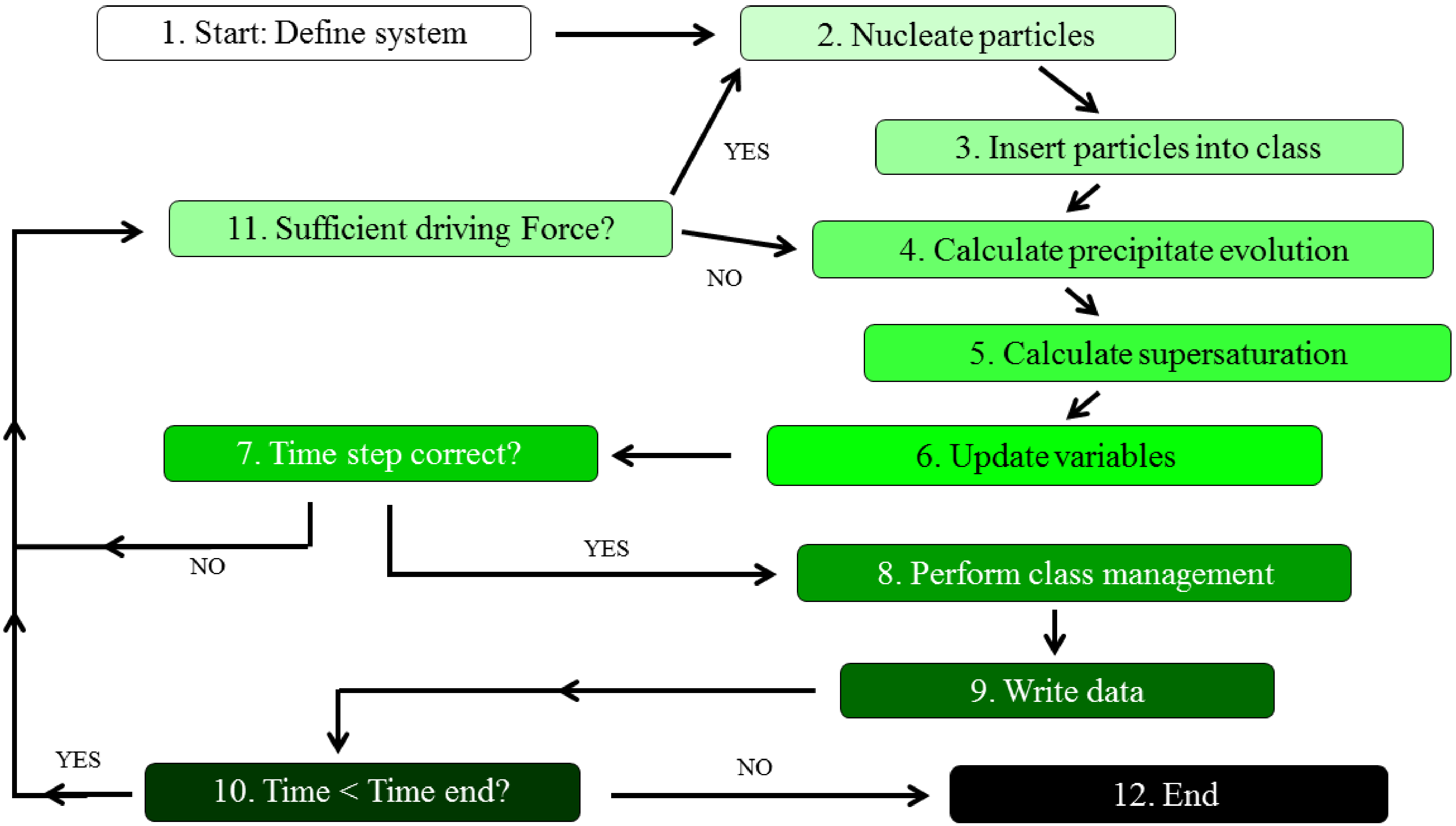

Figure 3.5: Flow chart of the numerical model created in this research indicating.

3.2.1 Start: Define conditions

Before the calculation can commence it is first necessary to define the conditions under which it is to be carried out. Principally, if a isothermal calculation is to be performed, the user defined variables are those of system molar size, temperature and ageing duration[2]. From the value of the temperature entered, the first function of the model is to calculate the physical constants for the simulation detailed in Section 3.1 (*e.g.* equilibrium elemental concentrations, elastic constants). Subsequently, the so called "independent variables" of the simulation time step are initialised and the independent constants which are used in the equations listed in Section 2.2 such at the Boltzmann Constant are called. Although largely arbitrary, it should be stated that the system sized used in this research was that of one mole (6.02×10^{23}) of atoms.

With all of the fixed variables defined, the first calculation actually performed by the model is associated with the initial critical stable precipitate radius. As alluded to in Section 2.2.1, an expression for the value of the critical radius can be defined through minimisation of Equation 2.4 with respect to ρ. Unfortunately, however, the value of the critical stable radius cannot be calculated strictly through such a formula in this model because of a mathematical impasse: The introduction of variable interfacial energies in the calculation necessitates that the value of ρ^* (and α) be known in order to calculate their magnitude but, conversely, ρ^* (and α) can only be computed if the interfacial energies are quantified. In other words, the values cannot be calculated independently. To avoid this vicious cycle, the approach taken in this research is to impose a critical stable radius of 1nm at the start of precipitation (*i.e.* during the first iteration) through selection of the value of the system molar volume Ω, thereby allowing a value for the interfacial energies to also be calculated. Moreover, owing to the fact that critically sized particles have finite chance of crossing back over the nucleation barrier curve (Figure 1.13) and dissolving, the magnitude of the critical radius actually used in the computation is increased by 1% (*i.e.* the value becomes 1.01 nm) in order to enhance the stability of nucleated particles. The value of the initial aspect ratio is that which is determined from the input experimentally derived relation between particle aspect ratio and size (*q.v.* Section 3.1.6).

Although not previously remarked upon, a contributing factor to the above defined mathematical impasse is the calculation of the derivative of the misfit strain λ_k (Equation 2.10) with respect to ρ_k. However, once the value of the aspect ratio is imposed from the critical radius, the initial values the coefficients F_0, F_1 and F_2 and their derivatives can also be calculated through harnessing the magnitude of the elastic constants for each phase defined. Specifically, given the high complexity involved in the evaluation the Eshelby scheme performed by Svoboda *et al.* [244], and the values of the Poisson's ratio for both the Alloy 625 matrix and the γ'' phase (*cf.* Figure 3.3), to avoid the introduction of errors the coefficients are evaluated based on the trends calculated by Svoboda *et al.* for material with a Poisson's ratio of 0.3. In this regard, during the initialisation of the calculation, the model obtains the values of F_0, F_1 and F_2 from the

---

[2] Selection between compositions can be made but this requires all the information about the new system (such as thermodynamic driving force) to be input to the model before hand *viz.* only fixed compositions can be analysed within the current framework.

appropriate point on the surfaces shown in Figures 3.6a, b and c respectively. Similarly, the derivatives for each function are calculated from the contour corresponding to the relevant change in the elastic contrast value ΔC[3]. As alluded to in Section 3.1.4, the initial eigen-strains ε and $\Delta\varepsilon$ are also calculated from this aspect ratio value according to the modified descriptions for the precipitate lattice parameters detailed in Section 6.1.1.

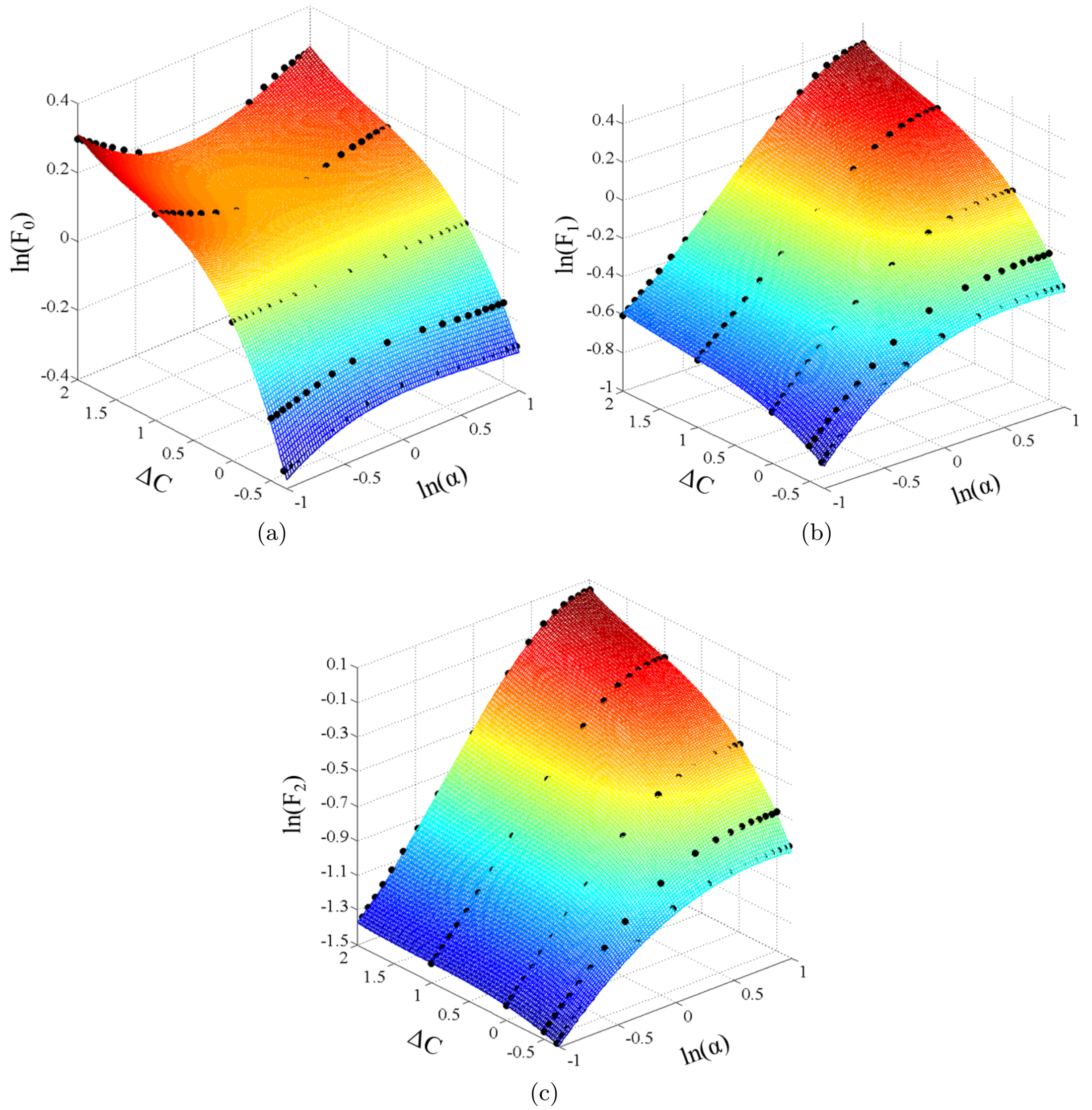

(a) (b)

(c)

Figure 3.6: Surface fits made to the data calculated by Svoboda *et al.* (indicated by spherical points) for the values of a) F_0, b) F_1 and c) F_2 in Equation 2.10.

---

[3] The relative elastic contrast C corresponds to the ratio of the Youngs modulus in the precipitate phase versus that in the matrix. ΔC is further defined as the absolute elastic contrast *i.e.* $\Delta C = C - 1$.

3.2.2 Nucleate particles

The nucleation rate of precipitates is calculated in the simulation according to Equation 2.20. All of the relevant parameters such as the Zeldovich factor, β^* and the incubation time τ evaluated from their corresponding expressions in Section 2.2.3; in the first iteration the value used for the incubation period τ is that calculated in Section 3.2.1. Similarly, the critical Gibbs energy ΔG^* is found from substitution of the initial critical radius value into the single particle (*i.e.* $m = 1$) version of Equation 2.4. After the initial iteration, each subsequent time step requires a new value for ΔG^* to be evaluated via the same method but using an updated value of ρ^*. The calculation of ρ^* is made at the end of the previous iteration during step 6 (*q.v* Section 3.2.6).

As discussed in Sections 1.3.1 and 1.3.2, the number of available nucleation sites (N_0) in Equation 2.20 is determined by the nucleation regime. Accordingly, the underlying assumption of homogeneous precipitation of γ'' in Alloy 625 (outlined at the start of Section 2 when selecting the SFFK modelling frame work) dictates that the value of N_0 correspond to the instantaneous number of atoms available to form precipitates. This quantity is calculated at the start of each iteration from a simple elemental/mass balance equation whereby, first the total volume of existing precipitates is found before, second, the number of each of the relevant atoms sequestered inside the precipitates is determined from division by the molar volume Ω. The value of N_0 then follows from subtraction of the number of locked up atoms from the total number of precipitate forming atoms (namely, Ni, Nb, Cr, Mo, Ti) and in the system.

Owing to the fact that the nucleation equation is not conditioned to produce integer values for the number of precipitates, correspondence to real systems is ensured through rounding down the number of particles entering a class to the nearest whole value. Similarly, because of to the imposition of a threshold on the minimum radius required by a precipitate/class for it not to be removed (discussed in Section 3.2.4), the balance of equations in the model may mean that, at late time steps, a spike in the supersaturation caused by the removal of a class causes the nucleation of a new class to be predicted. This phenomenon is clearly not representative of the behaviour of real systems and, as a result, it is suppressed in the model by mandating a maximum gap be adhered to between the creation of successive classes.

3.2.3 Insert particles into class

After the number of particles nucleating within a given time increment is known, a new class for the precipitates is created. This size class, illustrated graphically with respect to aspect ratio and radius in Figures 3.7a and b respectively, is constructed in the model as an array of data containing information on the number of particles (calculated in Section 3.2.2), particle size (corresponding to the enhanced critical stable radius), aspect ratio, interfacial energies, aspect ratio change rate and precipitate radius growth rate.

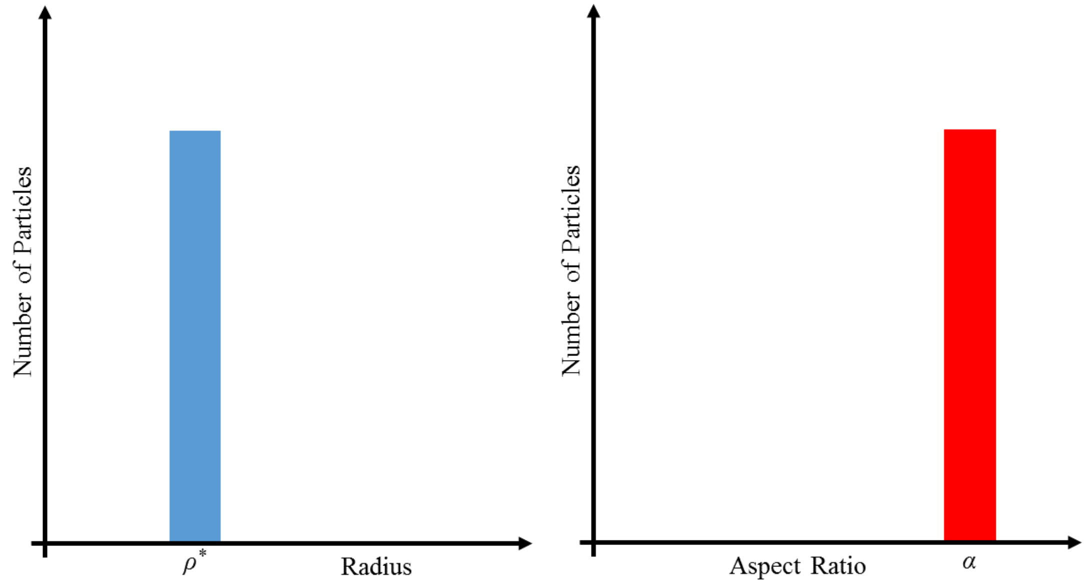

(a) (b)

Figure 3.7: a) Particle size distribution indicating position of a new, nucleated size class and b) aspect ratio distribution also indicating position of a new, nucleated size class.

3.2.4 Calculate precipitate evolution

Using the data contained in the arrays corresponding to a new size class and any already existing in the simulation, the respective evolutions of precipitate radius and aspect ratio are determined from Equations 2.7 and 2.6. These computations are performed independently such that only the system state in the prior time iteration effects the evolution of either variable. As calculations are completed, the corresponding, informative variables for each class such as the interfacial energy, major radius and aspect ratio change rates are recorded in the array also.

By definition, particles in a newly nucleated class will grow during their first iteration (and therefore reduce with respect to aspect ratio). Contrastingly, as coarsening proceeds the fortunes of some existing classes will be opposite, with larger ones growing at the expense of smaller ones. These phenomena are shown graphically in Figure 3.8.

Straightforwardly, one would expect shrinking classes to be removed only once their radius reduces to a value less than or equal to zero. However, owing to the reduced rate of radius decrease at smaller radius values, using this condition in the computation can lead to much greater simulation times being incurred because of the prevalence of a large amount of small radius classes. What is more, the requirement for the radius to reach zero can also be considered unphysical as in real systems a precipitate would necessarily possess a minimum size equivalent to that of one molecule. Consequently, in order to both expedite the calculation and make it more representative of real systems, a threshold molecular size limit is imposed in the calculation with classes falling below the limit being removed.

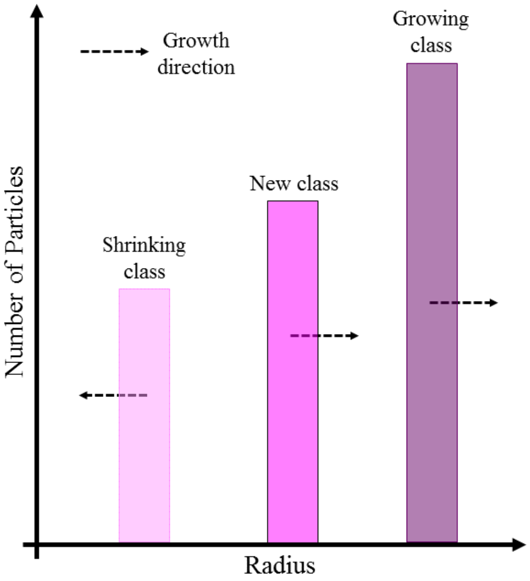

Figure 3.8: Graphical illustration of the evolution of a newly formed precipitate class and two example existing precipitate classes.

3.2.5 CALCULATE SUPERSATURATION

On completion of the class evolution calculations, the particle size distribution is fixed for the remainder of the iteration effectively marking the end of the dynamic calculations. The computations which follow on from that point instead consist of checks imposed to maintain detail and stop unphysical results and, separately, preparatory work for the next iteration. As alluded to in Sections 2.2.1 the first of these calculations entails the determination of the remaining elemental composition of the alloy and, therefore, supersaturation through implementation of the continuity equation (Equation 2.8). With respect to γ'' precipitation in Alloy 625 only five elements are processed in this calculation (Ni, Nb, Cr, Mo, Ti), the quantities of the rest assumed to remain the same in the matrix.

3.2.6 UPDATE VARIABLES

With the concentrations in the model updated it immediately becomes possible to calculate the new thermodynamic driving force for precipitation according to Equation 2.9. Correspondingly, the next stage in the computation is to use this value to calculate the new magnitude of ρ^* via the same method as that employed at the simulation start (*i.e.* Section 3.2.1) but with the modification that ρ^* is treated as a free variable. The initial aspect ratio and interfacial energies are maintained at their original (first iteration) values.

3.2.7 Time step correct?

The use of a constant time step in the simulation is undesirable owing to the fact that consistently big time steps are likely to result in aberrations such as negative concentrations and large oscillations in growth rates, whereas consistently small steps incur severe computational cost because of both the resultant increased number of iterations and the greater quantity classes. As a result, the approach taken in the model designed in this research is the use of an incrementally increasing (1%) time step that is subject to an upper limit of 3600s (to prevent the aforementioned oscillations associated with very large tome steps) and checks that can lead to its reduction.

The checks placed on the time step consist primarily of five flags placed throughout the computation that will result in the time step being halved and the iteration re-run. These flags in the simulation fall into three categories and can be summarised:

Saturation check

> It is evident from Equation 2.6 that, given the evolution of each class is calculated in isolation (using the values either at the start or from the previous iteration), a sufficiently large time step could make the radii and *ipso facto* total volume precipitates such that they comprise more than 100% of the thermodynamically available solutes. This result is also possible from equation and 2.20 through the nucleation of too greater an amount of precipitates. Clearly this eventuality is unphysical and, therefore, a saturation check is placed at the end of steps 2 (*q.v.* Section 3.2.2) and 4 (*q.v.* Section 3.2.4) to detect and raise a flag on its occurrence.

Aspect ratio check I

> Another scientifically impossible result which may arise because of a very large time step is that of a zero or negative valued aspect ratio being output from Equation 2.7. Accordingly, in addition to the saturation check previously mentioned, an aspect ratio check is also placed in Section 3.2.4 to flag for this result.

Aspect ratio check II

> Unlike the previous two checks, the final check category is not concerned with maintaining correspondence with real systems but instead maintaining calculation detail. Precise knowledge of the PSD evolution is essential throughout the simulation and this is ensured through mandating that the change in aspect ratio of any class between two iterations does not exceed an imposed limit. If this limit is exceeded it will be flagged by yet another check routine at the end of the precipitate evolution *i.e.* step 4 detailed in Section 3.2.4.

The upshot of a flag being raised by any of the aforementioned checks is that the iteration is recomputed with a time-step reduced in magnitude by 50%.

3.2.8 Perform class management

Given the desirable qualities of short simulation times and model detail, at this point of the simulation two class management operations are performed on the PSD once the number of classes has exceeded four (a limit imposed by their mathematical construction): In order to further expedite a simulation made by the model, both an absolute and relative conditionalities are placed on the number of particles a class must contain, with classes failing below the threshold being flagged for removal. Rather than simply deleting such classes from the particle size distribution, however, so as to counteract the possible incurrence of missing particles in the simulation (especially at the beginning of a run), the limit is implemented such that classes with too few precipitates are instead amalgamated into the upper adjacent (major radius not equivalent radius) class.

The mathematical method employed to carry out the amalgamation of classes in the model created in this research is derived from the procedure of class insertion outlined by Perez *et al.* [42] which centres on maintaining the value of the distribution density, rather than the distribution, owing to the arbitrary location of classes within a descretised distribution. An example of this technique is best illustrated through consideration of the merger of two of the three classes in Figure 3.9, the process for which outlined stepwise below. In such a regime the distribution density dd of each class can be calculated through the relationships in Equation 3.3.

$$dd_p = \frac{N_p}{\rho_f - \rho_p}, \qquad dd_f = \frac{N_p}{\rho_k - \rho_f}, \qquad dd_{\mathrm{New}} = \frac{N_{\mathrm{New}}}{\rho_k - \rho_p} \tag{3.3}$$

1 The particle size distribution is sorted in to an order corresponding to major radius rather than equivalent radius so that the true adjacent classes to the one lying below the threshold can be found.

2 The values of each of the variables except the particle number/density, such as the aspect ratio and interfacial energy, for the new class correspond to those of the class exceeding the threshold.

3 The number of particles in the new class is calculated through the addition of the number in the original two classes. Such a methodology accounts for the correct proportionate contribution of the individual number densities of the existing two classes to the number density of the new class when dd for each class is calculated via Equation 3.3.

4 Once the above calculations have been made the two old classes are removed from the PSD and the new one is inserted.

5 As highlighted by Perez *et al.* this approach changes the precipitate volume fraction thereby leading to a violation of mass conservation. Resolution of this problem is achieved through rescaling of the new particle size distribution so that it matches the old one via Equation 3.4 where N' represents the rescaled

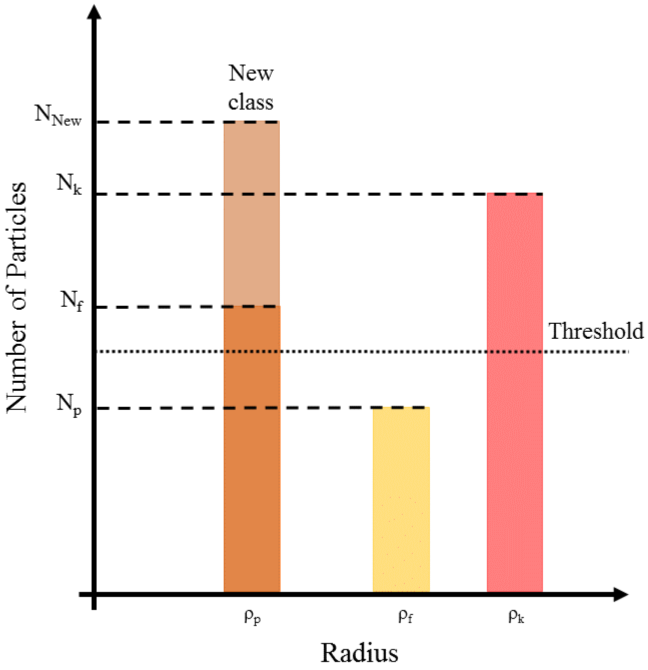

Figure 3.9: Merger of two classes in the particle size distribution corresponding to the threshold implementation procedure.

value, the index k corresponds to each precipitate class, m is the total number of classes and the other symbols have their predefined meanings. The aspect ratio is included here as, in this case, the value of ρ represents the particle major radius.

$$N'_k = N_{\text{New},k}\left(\frac{\sum_{k=1}^{m_{\text{New}}} \rho^3_{\text{Old},k} N_{\text{Old}}}{\sum_{k=1}^{m_{\text{New}}} \rho^3_{\text{New},k} N_{\text{New}}, k}\right) \tag{3.4}$$

3.2.9 WRITE DATA

The requirement of the model to be able to repeat iterations where needed means that two copies of the PSD are retained throughout the calculation. The first of these (PSD_{Old}) corresponds to the distribution as it was on completion of the last successful iteration whereas the second (PSD_{New}) represents the PSD as it exists during the current iteration. Should any of the flags in step 7 (Section 3.2.7) be triggered, the value of PSD_{New} is reset to that of PSD_{Old} and the iteration is run again with the new time step. If all of the checks are successfully negotiated, however, on completion of the class management stage the value of PSD_{Old} is over written using the PSD_{New} in preparation of the next iteration. In addition, when the simulation reaches predefined time intervals a copy of the PSD is saved separately for output (each iteration is not saved owing to the copious amounts of data storage this would require).

3.2.10 Time<Time end?

The main function of this stage is simply check if the simulation time is below the end time value set at the start. If this is indeed found to be case, another iteration is initialised with the time step for the next iteration calculated such that it is 1% bigger than that used for the previous one up to a limit of 3600s (1 hour) per step. If the time exceeds the desired end time, a flag is raised and then the simulations stops.

3.2.11 Sufficient driving force?

Although indicated to be a separate stage, this point of the flow sheet is introduced to show the break in the simulation which occurs when the driving force is not sufficient enough to nucleate a number of precipitates in excess of unity. As indicated in Figure 3.5, if such a eventuality is realised, the simulation simply skips to the class evolution stage (Section 3.2.4) so that only the change in the existing classes is computed.

3.2.12 End

Once the simulation run has completed the final values contained in the PSD are saved and the real time taken for the simulation to complete is outputted. Accordingly, the total outputs of the simulation can be summarised as: Spread sheets listing the data within each of the class arrays written at the “Write data” stage when a desired output time was reached, the final PSD and, separately, the actual time each of the PSDs correspond to. This latter detail is required as the variable time step used in the calculations means that the specific time desired will, in almost all cases, not correspond exactly to any of the iterations.

§ 3.3 Model Calibration and Validation

It is immediately obvious that anyone wishing to use the model created in this research must be confident in its precision and accuracy. Such reassurance can only be gained through the reliable prediction of results consistent with those which have been measured experimentally. Consequently, for the purpose of validation it becomes necessary to evaluate appropriate data published in the literature and identify where additional experimentation must be undertaken. As mentioned in Sections 3.1.5 and 3.1.6, experimentally derived statistics are also needed for the determination/calibration of interfacial energy and the relationship between particle size and aspect ratio.

3.3.1 AVAILABLE LITERATURE DATA

The most pertinent literature studies with respect to γ'' precipitation in Alloy 625 were discussed at length in Section 1.4.3. However, as illustrated in the discussion in that section, the overwhelming majority of these publications are qualitative with respect to the precipitate evolution *viz.* no specific statistical information on particles size, shape and number density change is given. Furthermore, aside from the recent work of Suave *et al.*, unfortunately all of the most relevant quantitative studies into γ'' evolution have been conducted using Alloy 718 or Custom Age 625 Plus. Consequently, in the absence of other Alloy 625 based data sets, the results found by these Alloy 718 studies and by Suave *et al.* are discussed and related to the requirements for validation and calibration in this research in Table 3.2.

Table 3.2: Appropriate published γ'' evolution studies. Samples correspond to Alloy 718 unless otherwise stated.

Paper (Year)	Temperatures (°C)	Ageing times (hours)	Analysis technique	Comments
Han *et al.* (1982) [2]	700	50, 100, 200, 300	TEM performed on thinned foils	Statistics for both precipitate axes gathered at each condition. Particle size (major axis) distribution created with respect to normalised r_{M} values. Co-precipitation of γ' suggested to impact γ'' size distribution.
	725	25, 50, 100, 200, 300		
	750	15, 30, 50, 100		
Sundararaman *et al.* (1992) [39]	650	10, 24, 75	TEM performed on thinned foils	Average precipitate size and aspect ratio measured at three different temperatures. Detailed analysis at 750°C of particle size distribution with respect to both major axis and minor axis across all the times analysed. Similar measurements for γ' made, with the effect of co-precipitation observed. Quantitative analysis made for other conditions.
	700	20, 168		
	750	2, 20, 100, 192		
	800	24		
	900	20		
Dong *et al.* (1993) [283]	700	48, 92, 144	TEM performed on thinned foils	Trend for average diameter indicated. No quantification of precipitate shape or density evolution.
	730	48, 92, 144		
Van der Voort *et al.* (1994) [173]	732	1, 4, 16	TEM performed on thinned foils	Experiments performed using Custom Age 625 Plus. Major axis (L_{M}) measured at non-uniform time periods. Precipitate shape and number density evolution not measured.
	774	0.33, 0.5, 20		
	802	0.33, 0.66, 30		
Slama *et al.* (1997) [4]	550	50	TEM performed on thinned foils	Average values for particle major axis and aspect ratio values found for each of the samples aged at 680°C and 750°C through measurement of 20 precipitates per specimen. No quantification made for number density or size distribution.
	600	24		
	680	4, 50, 98		
	750	4, 50, 98		
Devaux *et al.* (2008) [47]	670	8, 16, 32	TEM performed on thinned foils	Major diameter (L_{M}) values and aspect ratios (α) measured for each condition. Average values for each foil calculated from statistics of 300 precipitates. Trend of aspect ratio and major radius inferred. Number density and size distribution of measured precipitates not given.
	700	8, 16, 32		
	730	8, 16, 32		
Suave *et al.* (2014) [41]	550	1527	Scanning electron microscopy on polished samples	Experiments performed using Alloy 625. Some quantitative analysis made using data from a good range of times and temperatures. No specific information on number densities or γ'' shape evolution. Radius values could allow for comparison; however, no calibration for interfacial energy change is achievable
	650	50, 500, 1002, 2012		
	700	113, 502, 1000, 1506		
	750	10, 100, 502, 1000		
	800	∼100, ∼1000		
Fisk *et al.* (2014) [284]	760	0.07, 0.13, 0.27, 0.53, 2, 4, 8	Small-Angle X-ray Scattering (SAXS) on solid specimens	Particle size distribution and size evolution obtained with respect to radius of gyration. Conversion to major and minor axes values calculated using the relationships produced by Devaux *et al.*. Could constitute a source of validation data if the correct relationship between major and minor axis length is known.

Individual examination of the studies detailed in Table 3.2 at this point yields many possible data sources for validation of the model created in this research but none constitute a truly holistic data set comprising each of the relevant statistics. The detailed information provided when ageing at 750 °C, 725 and, 700 means that studies of Han *et al.* [2] and Sundararaman *et al.* [39] will likely prove the most useful Alloy 718 study from a validation perspective; however, a key caveat must be highlighted with respect to the data all of the Alloy 718 studies. Namely, the behaviour of γ'' precipitates is subject to additional influences (such as competitive γ' precipitation which can act to change the PSD of γ'' precipitates [283, 171]) that are not present in Alloy 625. Disappointingly, a solution to this problem is not offered by the alternative use of the results of Suave *et al.* [41] because of gaps in the data set.

Notwithstanding the aforementioned applicability problems, it should also be stated that the use of amalgamated alloy 718 datasets from the papers listed in Table 3.2 (such as that constructed for particle aspect ratio versus particle size by Devaux *et al.* [47]) is precluded owing to the need for consistency between the data used for calibration. That is to say, the statistics gathered for precipitate aspect ratio evolution with time (used for the calculation of interfacial energies) and with particle size must be based on the same particles to avoid possibly significant disparities in the behaviours indicated by the two data sets resulting from random errors associated with material behaviour or measurement accuracy.

3.3.2 Experimentation required

In view of the problems associated with information contained in published studies, it is clear that a true validation would only be achieved for the model created in this research through comparison with a new, holistic Alloy 625 based data set. Similarly, the correct calibration of the interfacial energy, aspect ratio and size values necessitates the gathering of precise information on γ'' nucleation growth and coarsening in Alloy 625. Owing to both of these factors, therefore, experimental characterisation of γ'' precipitation in Alloy 625 is undertaken in this research.

The widely excepted TTT diagram for Alloy 625 shown previously in Figure 1.18 indicates that the largest range of temperatures in which γ'' is likely to be observed is 550-800 °C. Ageing below of this temperature range will result in exceeding low precipitating kinetics, whereas temperatures above will yield the alternative delterious phenomenon of direct precipitation of stable δ-phase. Additionally, it is also evident that ageing studies should follow a logarithmic type relationship with time *viz.* the use of a constant time interval will lead to either substantial material cost and a prohibitively large number of samples requiring analysis if it is too low, or the loss of a substantial amount of experimental information if it is too large. Finally, to ensure consistency between isothermal data sets, samples should be aged for the same times in each.

On first consideration, the creation of samples containing γ'' precipitates through isothermal annealing seems trivial *i.e* samples require ageing to a condition which lies within the TTT curve of the phase. However, as mentioned in Section 1.4.3 the accepted

TTT diagram is subject to influences both with respect to alloy composition and the experimental technique used in its creation. Consequently, whilst the accepted TTT diagram can be used as a guide, the presence of precipitates (especially at short ageing times) should be separately inferred from macroscopic analysis such as hardness testing before any more lengthy analysis techniques (such as microscopy) are undertaken.

It was with consideration of the above factors that the experimental programme detailed in Section 4 was made.

Chapter 4

Experimental Programme

§ 4.1 Aims and Objectives

The experimental part of this study is designed to fulfil the requirements for the calculation of i) the interfacial energy, ii) the relationship between precipitate aspect ratio and size and iii) the validation of the model. Succinctly, therefore, the singular aim can be summarised:

To gain statistics on the nucleation, growth and coarsening behaviour of the intermetallic precipitate phase γ'' within the nickel-base superalloy 625, over a wide range of temperatures and ageing durations.

Successful achievement of this goal requires specific, sequenced objectives to be defined, for which appropriate experimental techniques can be selected. Accordingly, in this context, the objectives of the experimental part of this research (in their progressive order), are detailed below. For the benefit of clarity, additional information for each stage is also provided where appropriate.

1 *Determine the exact chemistry of the Alloy 625 samples*

As detailed in Section 1.4, although the general precipitation behaviour of Alloy 625 has been defined in the literature, the precise response of a specimen is unique to its chemistry. Consequently, it is vital that the exact composition of any alloy subject to experimental analysis is known beforehand.

2 *Age samples of solution annealed material at various temperatures between 600-800° C.*

The nose of the γ'' precipitation curve in the TTT diagram for Alloy 625 lies within this temperature interval (Figure 1.18) meaning any age hardening treatments can only realistically utilise a temperature in this range. Studies of behaviour at temperatures lower than 600 °C would lead to the requirement of excessively long ageing times, whereas temperatures above 800 °C would likely result in the heavy co-precipitation (or even the exclusive formation) of δ-phase.

3 *Identify samples likely to contain γ'' precipitates.*

Owing to the fact that the TTT diagram for Alloy 625 is not definitive (as discussed in Section 1.4.3) and that even minor compositional changes having been shown to result in a marked change in γ'' precipitation kinetics [23], it would be unwise to base the procedure for the selection of samples which should be subjected to lengthy experimental investigation on purely comparisons of their ageing conditions to the TTT curve. Potentially considerable efficiency gains can be made by instead utilising independent analysis to highlight the possible presence of precipitates in samples.

4 *Determine the size, shape and number density of γ'' precipitates in a range of samples.*

With reference to the previous objective, the nature of the experimental conditions to be utilised are such that not all samples are likely to contain γ'' precipitates. Regardless of this implication, however, it is key to ensure that the selection of ageing times and temperatures is made such that data can be collected from a number of different temperatures at consistent ageing times.

§ 4.2 Experimental Flow Chart, Details and Methods

A schematic of the experimental flow sheet in this research is given in Figure 4.1; the techniques to be used in each of the individual stages sheet are discussed in the subsequent sub-sections with each section corresponding to the identically labelled stage.

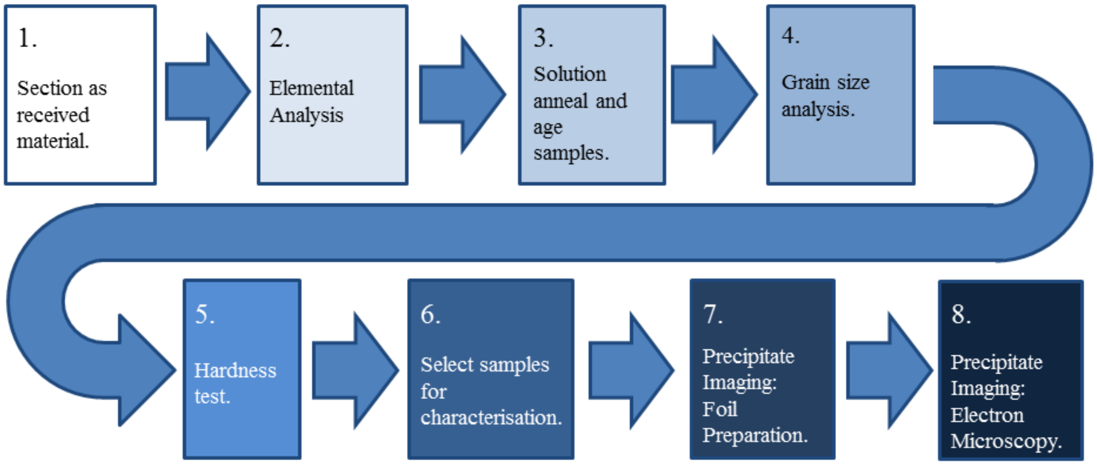

Figure 4.1: Experimental flow sheet created following the objectives outlined in Section 4.1.

4.2.1 Section as received material

The Alloy 625 material on which the experimental investigation was carried out constituted a piece of bar procured from the engineering consultancy and project management firm Amec (now Amec Foster Wheeler) [285]. An image of the sample as it existed in the bar and as it was received from Amec is given in Figures 4.2a and b respectively. Unfortunately, no detail of the processing conditions the material had been subjected to was provided by Amec; the summary which accompanied the material is reproduced in Appendix C.

To obtain a maximum number of workable samples, it was decided to section the single piece of Alloy 625 into pieces measuring approximately 2cm × 2cm × 2cm including any cut-outs and shape variation. Each of these samples would be subject to a unique ageing condition to make up the experimental matrix. Utilising such relatively small pieces it is important that deformation induced by cutting is minimised to maintain a consistent microstructure not only across a sample itself but also between samples. To achieve this, initial sectioning was gently made using a liquid cooled Buehler AbrasiMet abrasive saw equipped with a 250mm aluminium oxide based cut-off wheel. The resultant slices were then further cut down to the final size, prior to heat treatment, by use of a liquid cooled Buehler Isomet 5000 linear precision saw equipped with a narrow 180mm aluminium oxide based precision cut-off wheel and implementing a slow cut rate. Liquid cooling and slow cutting are essential for the minimisation of induced deformation that could disrupt the ageing response between samples.

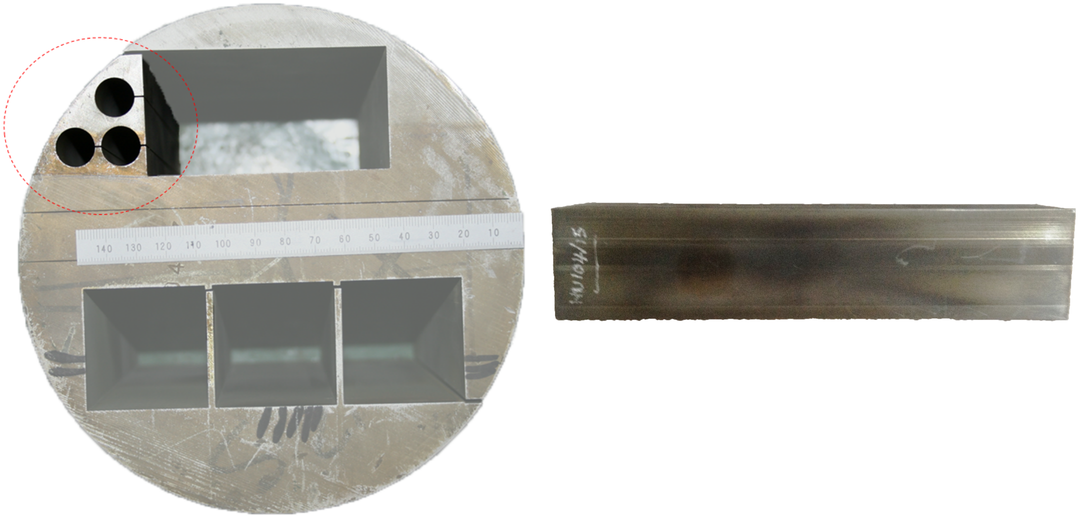

(a) (b)

Figure 4.2: Alloy 625 sample procured from Amec. a) Indicating its original location in the bar and b) as it was ultimately received. Approximate dimensions: $\frac{1}{4}$ of a cylinder with radius 40mm and length 185mm. As displayed, the sample contained 3 holes, each with a diameter of approximately 10mm, which ran along its entire length. These holes resulted from Electrical Discharge Machining (EDM), the process of which also caused the observed discolouration/staining of the surface.

4.2.2 Elemental Analysis

Although a chemical composition was provided with the alloy sample (see Appendix C) it was decided to perform additional analysis to verify the exact elemental make-up of the material to be investigated. The method harnessed to achieve this analysis was that of inductively coupled plasma optical emission spectroscopy (ICP-OES)[1]. This technique offers a large dynamic range, relatively precise detection limits and the ability to detect multiple elemental species simultaneously; a combination of features which is clearly crucial for the successful analysis of materials like Alloy 625. The use of even more exact but also more expensive techniques such as ICP mass spectrometry (ICP-MS) would not yield additional benefit in this research due to the desired levels of precision *viz.* the model created in this research will likely be unresponsive to changes in concentration of less than 1ppm (part per million) or 1×10^{-4} at%. For clarity, an outline of the principle function of ICP-OES device is given below.

Inductively coupled plasma optical emission spectroscopy (ICP-OES)

Fundamentally, optical emission spectroscopy is a technique which utilises the unique atomic structure of all elements, specifically their electron shells, for their identification. When atoms gain energy it is possible for electrons surrounding the nucleus to transition to a higher energy state [286]. In accordance with the first two (and implied

---

[1] Also known as inductively coupled plasma atomic emission spectroscopy (ICP-AES)

by the third) laws of thermodynamics, however, this "excitation" is only temporary and, consequently, after a while the electron will return to its lower energy state. In order to conserve energy, as the electron falls to the lower state it releases a photon, the frequency (f) of which can be calculated in accordance with the Planck-Einstein relation (via Bohr's frequency condition) as outlined in Equation 4.1 where Δe corresponds to the energy difference between the two electron states and h is Planck's constant [286]. Depending on the circumstance, the emitted photon either escapes or is absorbed by another electron in the atom. As the specific differences in the energies of the electron shells depends both on the magnitude and distribution of charges within the atom, the frequency of the photon emitted by a given element is unique and can ultimately, therefore, be used for its detection. The number of specific photons emitted by the sample gives the quantity of the element it contains.

$$f = \frac{\Delta e}{h} \tag{4.1}$$

A generalised layout of a modern ICP-OES device is given in Figure 4.3.

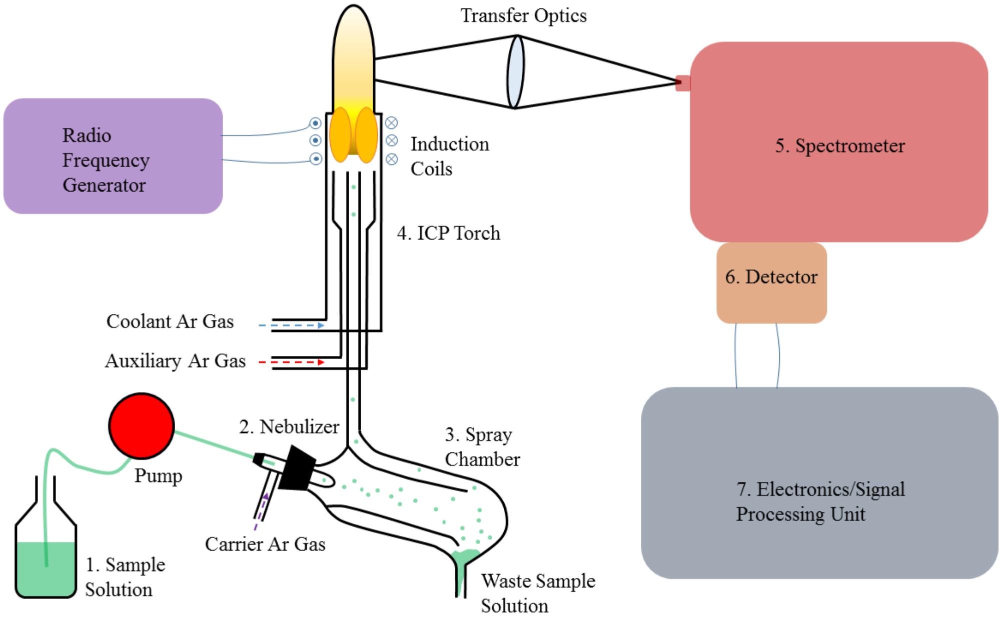

Figure 4.3: Layout of the key stages of an argon supported ICP-OES instrument. Adapted from Wang [29].

The principle features/functions of each of the stages displayed in the figure can be described sequentially as the following [29]:

1. ***Sample Solution.*** The operation of the ICP-OES requires that all samples be in a liquid form. For solid, metallic materials such as Alloy 625 this is achieved typically through dissolution in acid. Clearly, the quantities and types of elements added to the material to achieve the dissolution must be precisely known and controlled for an accurate result to be achieved.

2. ***Nebulizer.*** The liquid sample is converted into an aerosol in the nebulizer through mixing with argon.

3. ***Spray Chamber.*** This device is used to remove larger droplets and any remaining liquid as these cannot be successfully injected into the plasma.

4. ***ICP Torch.*** The function of the ICP torch is to excite all of the atoms in the sample being analysed such that they produce the desired/characteristic emission lines. This is achieved through use of inductive coupling *viz.* via the ohmic heating effect the torch is able to achieve very high plasma temperatures (up to 10000K) and thereby excite almost all elements.

5. ***Spectrometer.*** Light emitted by the elements in the plasma is focused into the spectrometer which splits split according to component monochromatic beams using a diffraction grating. Undesired wavelengths are subsequently filtered out using mono or polychromators.

6. ***Detector.*** The detector comprises a semiconductor-based charge-coupled device (CCD) in which the incoming photons create an increase in conductivity through the formation of electron-hole pairs. A separate detection/intensity measurement is made for each of the monochromatic beams.

7. ***Electronics/Signal Processing.*** The signal from the CCD measurements of each beam is digitised and converted into a measurement. Using software the elements contained with the sample, and their relative abundance, are identified.

4.2.3 Solution Anneal and Age Samples

In order to ensure correct measurement of precipitation kinetics it is necessary to either quantify the existing precipitate distribution within a sample or, more simply, to eliminate it via solution annealing. Similarly, the demand for statistics pertaining to homogeneous distributions necessitates the suppression/elimination of preferential nucleation sites such as dislocations. Shankar *et al.* have shown both that 1) a widely established precipitate microstructure in Alloy 625 developed over 60,000 hours at 600°C can be successfully eliminated by annealing at 1150°C for 30 minutes, and 2) a homogeneous distribution γ'' precipitates is produced in the same alloy during subsequent ageing [10]. Consequently, given that others have also found a similar result for a treatment of 1 hour at 1100°C [74, 174, 175], the simplest strategy of homogenising each of the samples was adopted in this research, specifically though the implementation of an identical anneal to that of Shankar *et al.*. At the end of the heat treatment the samples were subject to rapid cooling, implemented through quenching in water, to avoid the formation of new precipitates.

Owing to the amount of samples available and the time-scale of the work, objective 2 in Section 4.1 was fulfilled by creating five different isothermal data sets: Samples were aged for durations of 1, 10, 50, 100, 200, 1000 and 3000 hours at temperatures of 600, 650, 700, 750 and 800°C. Again, upon reaching the allotted time at temperature each sample was quenched into water to prevent any further precipitate evolution. A graphical illustration of the all the heat treatments for which samples were created in this research is given in Figure 4.4.

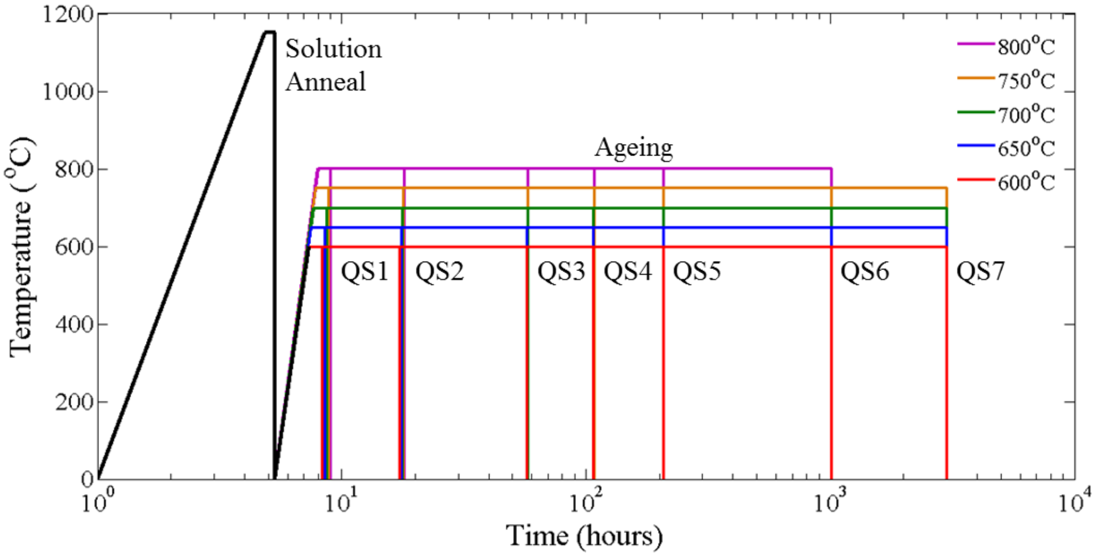

Figure 4.4: Heat treatment regime for different temperature sets. Solution anneal and ageing sections of the treatment are indicated along with the quench sample (QS) positions. Samples were aged in an electric furnace surrounded by an air atmosphere. Increases in temperature occurred at at a rate of 5 ° C min $^{-1}$ as indicated.

4.2.4 Hardness Test

As a result of the widely noted strengthening effect of γ'' precipitates (*q.v.* Section 1.2.2), it is self-evident that hardness testing offers a potential detection mechanism for the formation and evolution of the phase in Alloy 625. In fact, such analysis was performed by Crum *et al.* [37] when creating their TTT curve for γ'' in Alloy 625. For this reason, it was decided that hardness testing would be used in this research for the purpose of identifying precipitate containing specimens.

Because of its complex nature, unlike properties such as yield strength or fracture toughness, hardness is not a universal quantity *i.e.* independent of the apparatus used to measure it. Instead, measurements of hardness are taken as being unique to the type of test performed and the conditions used[2]. As a result of this fact, therefore, only relative comparisons of hardness can be made reliably between materials subjected to the same test [30, 287, 288]. Of all of the available methods, the Vickers technique developed by Smith and Sandland in 1925 [289] has proven to be the most popular due to its single scale and ability to test even very hard materials. Accordingly, it is this technique which was selected in this research for the testing of every specimen, maintaining the same conditions throughout.

---

[2] Tables allowing for the conversion of measurements from the units of one type of test to another have been derived but there are considerable doubts about their validity.

DESIGN AND OPERATION OF A VICKERS HARDNESS TESTER

Hardness in materials science is defined as the resistance of a material to plastic deformation. Correspondingly, Vickers hardness (HV) testing constitutes a static indentation test whereby a diamond is pressed, under a specific load and for a specific duration (dwell time), into a sample in a direction normal to the sample surface and the resultant deformation is measured [30, 287, 288]. In such a set-up, by cutting the diamond surfaces such that they constitute a pyramid with an angle of 136° between faces, a seemingly square (2D projection) impression is created in the sample with a footprint approximately 7 times greater than its depth as shown in Figure 4.5.

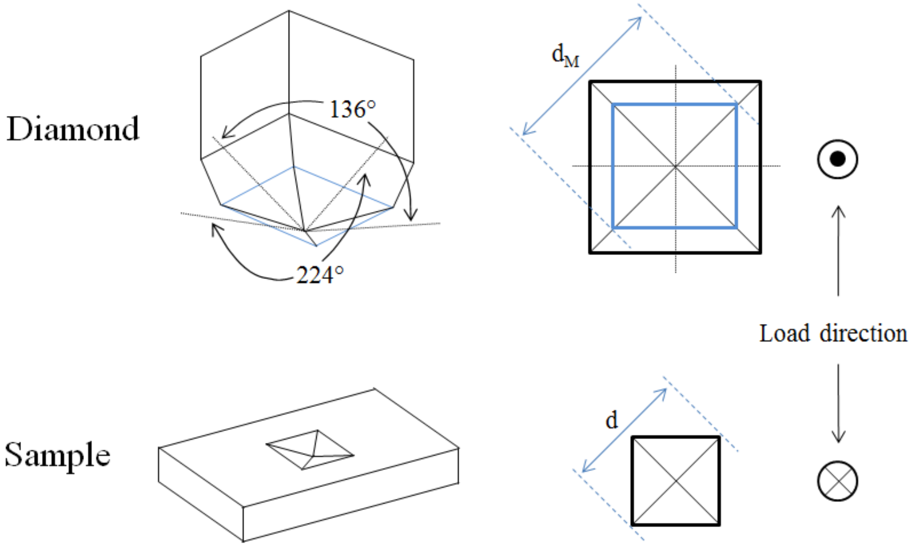

Figure 4.5: Schematic of the diamond used in Vickers hardness testing and the indentation it creates in a sample. 2D projections indicating the diagonals (d) of both the diamond and indentation are also displayed. Adapted from [30].

Once an impression of the diamond has been created in a sample, a measurement of the hardness is made via Equation 4.2 where HV*p* is the Vickers hardness number which has units of $\mathrm{kg \cdot mm^{-2}}$ (*p* signifies that this symbol is replaced by the load used, *e.g.* for a load of 1kg the hardness number would be HV1), $\bar{d}$ is the mean of two square diagonals of the indentation and ϑ is the angle between the opposite faces of the indenter (136°) [30, 287]. For the end user, calculating hardness directly from Equation 4.2 is rarely necessary, rather this is either given automatically by the device or obtained through a table look-up technique; precalculated tables of hardness values to loads applied and the diagonals they create are provided by the instrument manufacturer corresponding.

$$\mathrm{HV^*p^*} = \frac{2\mathrm{p}}{\mathrm{d}^2}\sin\left(\frac{\vartheta}{2}\right) = \frac{1.8544\mathrm{p}}{\bar{d}^2} \tag{4.2}$$

From Equation 4.2 one is able to infer that, because of the way the diamond is cut in HV testing, the value of hardness measured for a given material should be independent of the load applied[3]. However, despite this, the selection of the load used to test a sample, and the duration which it is applied, is not trivial due to the effects of ridging and sinking which occur as a result of the mechanical properties of the sample being tested [30, 287, 288].

In metals with a comparatively low strength and high degree of elasticity (*e.g.* solution annealed) the weakness of the lattice means that material is pushed down and outwards by the indenter. When the indenter is then removed, elastic recovery leads to a pinching in of the sides of the indent resulting, ultimately, in a pincushion shaped impression remaining as shown in Figure 4.6a. Conversely, in metals with high strength/low elasticities (*e.g.* work or precipitation hardened) a bulging effect occurs along the faces of the indenter as material is pushed up and outwards and does not spring back (Figure 4.6b). These distortion phenomena can, respectively, easily lead to the underestimation or overestimation of hardness values by a magnitude of up to 10% and, therefore, must be minimised if accurate results are to be obtained [287]. If indents appear as pincushions, higher loads and longer dwell times are required so that the majority of the elastic recovery occurs during loading, thereby shaping the specimen around the indenter (loads should not be increased to a point where cracking occurs). Conversely if indents appear to be bulging, lower loads and shorter dwell times are required to minimise the amount of material pushed out.

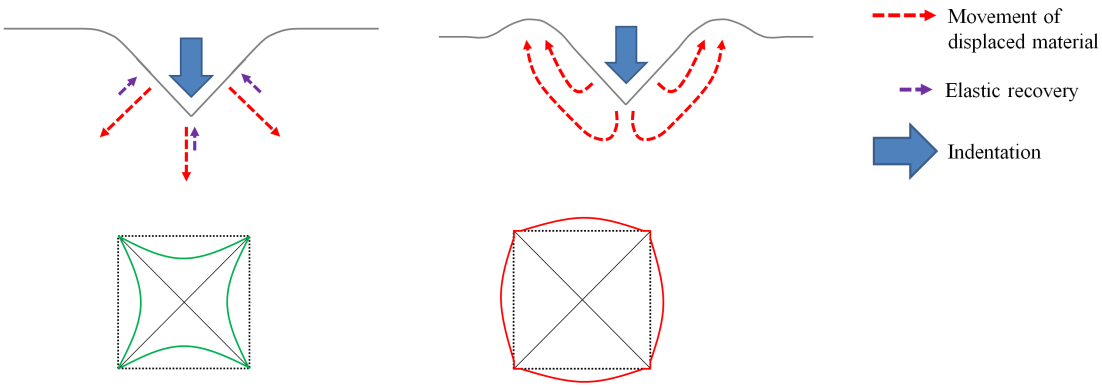

(a) (b)

Figure 4.6: Movement of material, subsequent elastic recovery and final shape of a indent created in Vickers hardness test. a) Low strength/high elasticity material results in a pincushion shaped indent. b) High strength/low elasticity material results in the indent looking bulged.

Precise measurement of indent dimensions is predicated on a flat sample surface. Consequently, prior to any hardness testing conducted in this research samples were subjected to the grinding and polishing regime detailed in Appendix D. The machine used to conduct the testing was a Struers DuraScan-80, taking measurements and producing results automatically from indents generated by a load of 1kg ($HV^*p^* = HV1$) applied

---

[3] Loads applied must be such that the value of d for the indentation lies in the range $d_m < d < d_M$ where, d_m is the smallest measurable diagonal size and d_M is the diagonal of the diamond pyramid as indicated in Figure 4.5.

for a duration of 60 seconds. Five measurements were taken from each sample in total (one from each of the 4 corners of the square sections and one from the centre) in order to minimise uncertainty and eliminate anomalous results.

4.2.5 Grain Size Analysis

The marked influence of grain size on the material hardness (described by the Hall-Petch relationship [86, 87]), means that detailed knowledge of the grain evolution of the alloy is required for the accurate interpretation of the aforementioned hardness data for each sample. That is to say, potential effects of phenomena such as recrystallisation on the data must be identified from grain size measurements.

Grinding, polishing and etching

The revealing of metallic grain structure is principally predicated on the careful preparation of a specimen surface. To this end, the methodology of achieving a scratch free finish for a variety of metallic alloys, specifically through grinding and polishing with abrasive materials, has been the subject of intense research and development by both companies and academic institutions for a number of years, yielding many recommended products and schemes. In the case of the Alloy 625 specimens examined in this research, their composition and the equipment available (Buehler EcoMet 250 Grinder-Polisher) meant the technique developed/recommended by the American company ITW Buehler Ltd (a wholly owned subsidiary of Illinois Tool Works) for Ni-base alloys detailed in Appendix D once again constituted an appropriate choice. Any surface effects induced by the heat treatment were avoided by sectioning the material again with the liquid cooled Buehler Isomet 5000 linear precision saw (maintaining the same conditions detailed in Section 4.2.1) to obtain a new sample face.

After grinding and polishing, etching (*i.e.* actively corroding) an alloy typically acts to reveal the grain boundaries it comprises because of the enhancement that the elimination of the higher free energy of these regions (discussed in Section 1.3.2) makes to the driving force. In the case of Alloy 625, its high corrosion resistance means the grain boundaries are able to withstand significant corrosive attack and, consequently, (for approaches based solely on submerging the specimen in the corrosive etchant) most resources recommend an aggressive mixed HCl-HNO_3-CH_3COOH based solution [290, 291, 292]. In this research, however, it was found that etchants of this type were ineffective, with too little grain boundary attack and substantial amounts of pitting (*i.e.* localised corrosion in the bulk) being observed. Successful etching was achieved instead by submersion in a 50:50 HCl-H_2O_2 solution (suggested in the book by DuPont *et al.* [291]) for a few seconds once the solution had begun to vigorously effervesce.

Grain Measurement: Heyn Intercept Method

The American (although also widely accepted internationally) standards for grain size measurement are outlined by ASTM (previously the American Society for Testing and

Materials) International in their document indexed E112-13 (ASTM E112-13) [293]. The principle techniques comprise the Jeffries planimetric method, the triple-point count method and the modified Heyn intercept method, but the fact that the same accuracy can be obtained for a simpler implementation means that it is the latter which has found most favour [294].

The process of the modified Heyn intercept method as outlined in the ASTM standard and by Van der Voort [294] can be best understood with reference to Figure 4.7: Lines of known length are drawn on to a grain structure image and (for a single phase grain structure) the number of grains or grain boundaries intercepted are counted. Grains which are not completely bridged by the line (*i.e.* at the line ends) are counted as half values. Once either of these values are known, the average grain size ($\bar{L}$) is simply computed from division of the line length by the number of counts and conversion to the ASTM grain size number G (if desired) is achieved via Equation 4.3

$$G_{\mathrm{ASTM}} = -6.6439\ln(L) - 3.288 \tag{4.3}$$

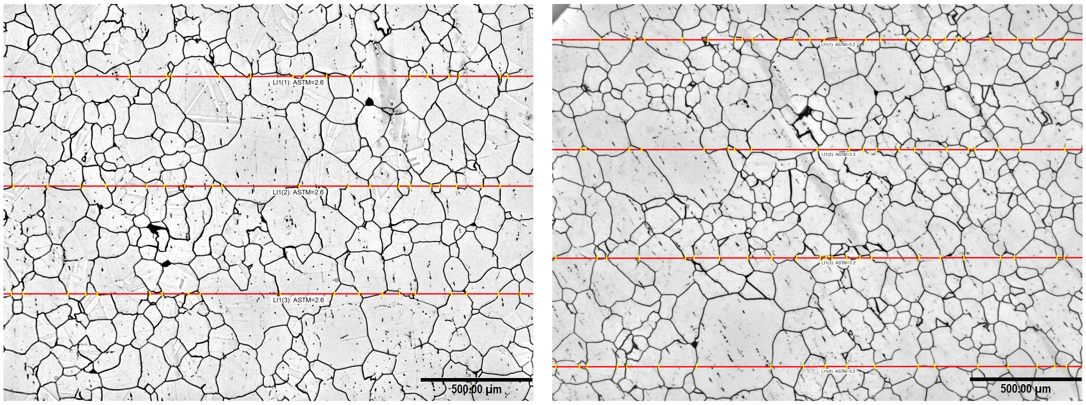

Figure 4.7: Illustration of the modified Heyn Intercept method for measuring grain size in Alloy 625. In this instance the number of grain boundaries crossed by three separate parallel lines are counted by the image analysis software OmniMet (developed by ITW Buehler Ltd) from corresponding marks placed by the user. The software automatically outputs the average grain size calculated for each line both in μm and ASTM G units. Images captured using a Nikon Eclipse LV150 light microscope.

An accurate measure of grain size was realised in this research through the use of five lines on five different (non-overlapping) images for each successfully etched specimen.

4.2.6 Select samples for characterisation

From the standpoint of the creation of a truly holistic data set on γ'' precipitation in Alloy 625 it follows that all of the samples created in this research should be subject to detailed characterisation with respect to precipitate size and number density. However, a fundamental problem arises with this approach owing to the nature of the study carried out here, namely the full examination of thirty-four different ageing conditions is not logical nor, based on time scale necessitated, feasible. In other words, as the principle aim of this research desires statistics only on γ'' precipitates, analysis of samples unlikely to contain such particles would (for the purposes of this study) constitute a lengthy and pointless endeavour. As a result, at this stage of the experimental work the data gathered from both grain size and hardness measurements was collated and those samples which are most likely to contain γ'' precipitates are identified.

4.2.7 PRECIPITATE IMAGING: FOIL PREPARATION

Using established stereological[4] principles, the desired statistics on particle shape, size and number density can each be gathered theoretically through the successful imaging of precipitates in the microstructure [295]. In spite of this, the discussion of the limit imposed by angular resolution in Appendix E highlights that the resolution of γ'' precipitates in Alloy 625 can only be achieved using radiation with extremely short wavelengths (high frequencies) owing to their sub-micron size. Fortunately, thanks to their wave-particle duality, rather than having to resort to instruments harnessing dangerous X-ray and γ-ray radiation, it turns out that electrons accelerated through a high voltage constitute an alternate suitable probe meaning it is the long established technique of electron microscopy which was selected as the method by which γ'' precipitates were imaged[5]. The de Broglie wavelength (e_λ) of an electron accelerated through 50kV as calculated via the relations in Equation 4.4 (where h is the Plank constant, u_c is the speed of light, p_e is the momentum of the electron, e_C is the charge of an electron, Ψ_0 is the accelerating potential, E_e is the energy of the electron, e_m is the electrons rest mass and u_e is the electron velocity) is approximately 5.5 pm [296].

$$e_\lambda = \frac{h}{p_\mathrm{e}} \qquad \text{where} \qquad E_\mathrm{e}^2 = (p_\mathrm{e} v_c)^2 + (m_\mathrm{e} v_c^2)^2 \approx (e_\mathrm{C}\Psi_0 + m_\mathrm{e} v_c^2)^2 \qquad p_\mathrm{e} = \left(1 - \frac{v_\mathrm{e}^2}{v_c^2}\right)^{-\frac{1}{2}} m_\mathrm{e} v_\mathrm{e} \tag{4.4}$$

Although both Scanning (SEM) and Transmission (TEM) electron microscopy techniques have been used in previous studies to image γ'' precipitates [176, 8] it is the latter technique which was selected here. Specifically, TEM was harnessed principally because of the ability to capture Dark-field (negative) images which are known to allow for the much easier resolution of the particles in the matrix phase [55, 140].

---

[4] Stereology (literally translated as the knowledge of space) describes the area of science where practical and mathematical methods are used to interpret three-dimensional (3D) structures from two-dimensional (2D) planer or projected images

[5] The greyscale images produced through electron microscopy constitute electron intensity maps.

Sample Preparation

Owing to the methodology of TEM analysis (detailed in Section 4.2.8), it is necessitated that a electron transparent[6] samples be created. In this research, the procedure used for the production of such samples was that of so called "thin foil" preparation as outlined below:

1 0.7-1.0mm slices taken from the aged Alloy 625 sample using a Buehler Isomet 5000 linear precision saw equipped with an 180mm aluminium oxide precision cut-off wheel.

2 Sample ground down to a width of 75-100μm (monitored using a Starret 0-25mm micrometer) by progressively using P320/P600/P800/P1200 Buehler grinding papers and taking an even amount from both sides to remove any material in which changes have been induced by the process of cutting.

3 3mm (by convention) discs punched from thinned sample foils.

4 Samples Twin-jet electropolished using an electrolyte of 20% Perchloric acid ($HClO_4$) 80% Ethanol (C_2H_5OH) at a temperature of -35°C to obtain a central sample region thin enough to be electron transparent. The electropolisher used in this investigation was a digitally controlled automatic Struers Tenupol 5.

Twin-jet Electropolishing

Twin-jet electro-polishing (TJEP) is an established, efficient method for obtaining electron transparent foils from metals/alloys. The first method of twin-jet electropolishing was invented by Schoone and Fischione in 1966 and since then apparatus for the task have been designed and developed by many manufacturer's [297, 298]. In its simplest interpretation, the process can be best understood as the controlled corrosion of a metallic sample to obtain a region of sufficient thinness that a TEM electron beam can penetrate through to produce an image of the features of interest within it.

A schematic of the typical set-up within a twin-jet electropolisher is given in Figure 4.8: The ground disc of metallic sample is placed within a sample holder such that its edge is in contact with an electrical contact and its centre is exposed on both sides. A corrosive electrolyte, (in the case of this research a 20% perchloric acid 80% ethanol mix) is then sprayed onto both sides of the sample (normal to the face) through jets with a bore of 1mm. Spraying the electrolyte in this way means that the corrosion is most intense at the centre of the disc and decreases with radius, leading to the sample thickness becoming a function of the radius (two jets are used on either side of the foil to reduce deformation). The jets of liquid are pumped until a hole forms at the centre of the sample of a sufficient size to let though a predetermined quantity of (infrared) light from a source incident onto the corroded area. Because of the dependency of the

---

[6] Electron transparent is defined here to mean that electrons can traverse through the material without being completely scattered or absorbed

severity of the corrosion on the sample radius, the electron transparent region forms at the edge of the central hole as shown in Figure 4.9.

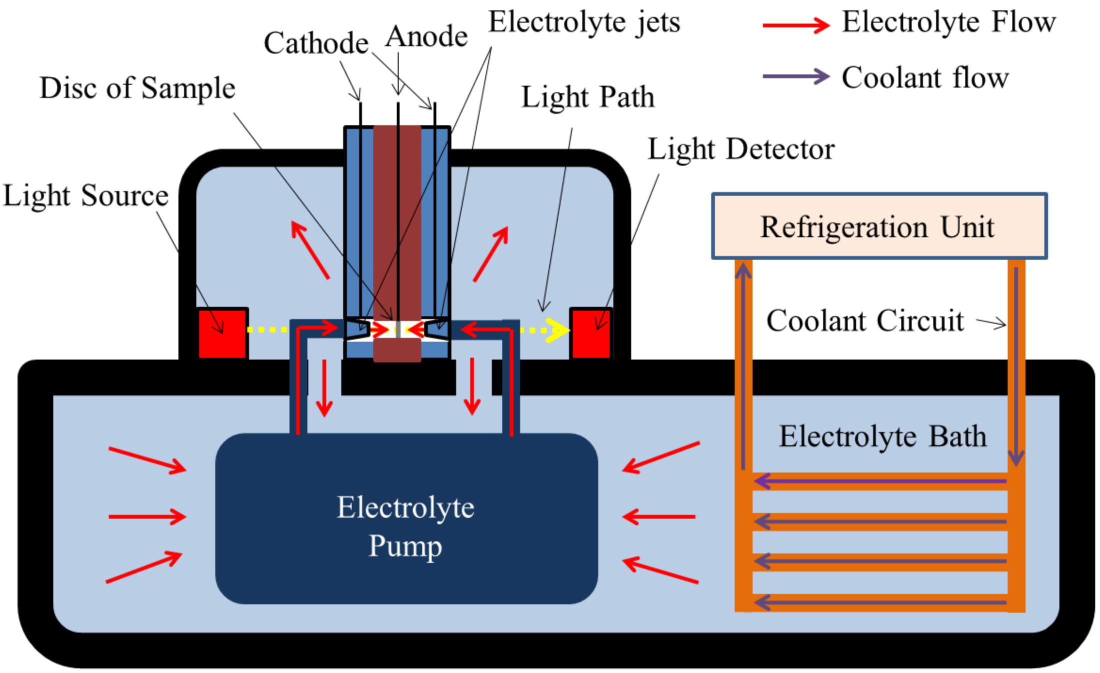

Figure 4.8: Schematic of a twin-jet electropolishing machine indicating all of the critical components as well as the coolant and electrolyte flows and the attached refrigeration unit.

In order to obtain the best TEM images is it desirable to have an electron transparent region which is as big as possible; such a region allows for more of the material to be analysed and finer features to be resolved. Nonetheless, it is also important that the region not be so large as to make handling the disc difficult and so thin as to eliminate the features of interest. Simply spraying the electrolyte on to the sample, whilst possibly creating an electron transparent region, would not result in such an optimal sample shape or one with uniform thickness due to the severity of corrosion being too great and the surface being uneven (weak electrolytes are not used as they would act slowly and thin too large of a region). Consequently, in TJEP it is necessary to utilise an aggressive electrolyte but control its severity and action through managing both its temperature and an applied potential difference, with the total balance of parameters defined according to their combined specific and relative effects:

Potential

Considering the preparation steps involved in creating TEM foils (*i.e.* sectioning and grinding) and the method of electropolishing, it is obvious, even to the laymen, that one of the biggest barriers to obtaining a large electron transparent region within a disc is non-uniform material thickness. The surface roughness resulting from grinding with P800 and P1200 silicon carbide papers on steel is

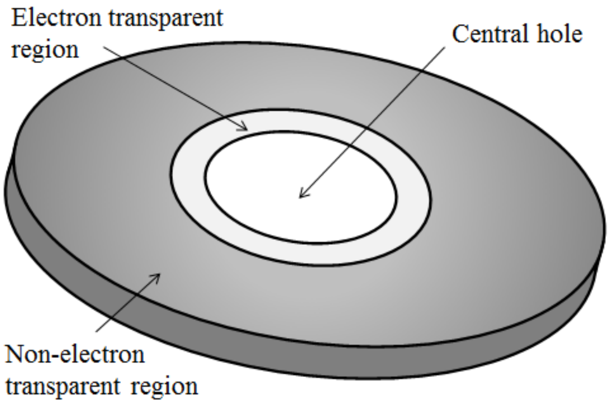

Figure 4.9: Illustration of a twin jet electropolished TEM foil indicating the central hole and surrounding electron transparent region.

quoted by PACE technologies as 120 and 110 $\mathrm{R_a}nm$[7] ($\mathrm{R_c}$[8] = 30) [301]. As a result, assuming a similar outcome is obtained for the polished Alloy 625 specimens analysed in this investigation, one is able to infer a maximum potential disparity in thickness between adjacent regions (accounting for both faces) of between 440-480nm. Considering the size of the precipitates of interest in this research are on the orders of a few nm requiring an electron transparent region just a few 10s of nm in thickness in order to be resolved, it is immediately obvious that simply spray etching a sample of such surface roughness would produce a less than optimal electron transparent region to say the very least.

Taking into account the extremely small length scales involved, overcoming the problem of surface roughness cannot be achieved neither easily, consistently or well via finer surface grinding/polishing. Contrastingly, however, it can be resolved through the application of a potential difference to the sample whilst it is sprayed with the electrolyte as shown in Figure 4.9: The positive terminal of a DC power supply is attached to the foil (via the, corrosion resistant, electrical contacts mentioned earlier) meaning it becomes an anode. The negative terminal is attached to nearby cathode coils in the jet assemblies. When spraying commences a stream of electrolyte forms between the two electrodes and current passes from the anode, where metal on the surface is oxidized and dissolved in the electrolyte, to the cathode, where a reduction reaction occurs producing hydrogen. A consequence of this process is so called anodic levelling/macrosmoothing or anodic brightening/microsmoothing (shown in Figure 4.10) whereby the protruding parts of a surface profile dissolve faster than the recesses owing to there being increased current density on corners and burrs versus recessed areas such as troughs and valleys [302]. It is this mechanism which allows electron transparent regions of uniform thickness to be created from textured samples through TJEP.

---

[7] $\mathrm{R_a}$ is the average surface roughness calculated according to $R_a = \frac{1}{n}\sum_{i=0}^{n}|y_i|$ where $|y_i|$ is the magnitude of the vertical distance from the mean line to the i^{th} data point [299].

[8] $\mathrm{R_c}$ is the mean height of profile irregularities [300].

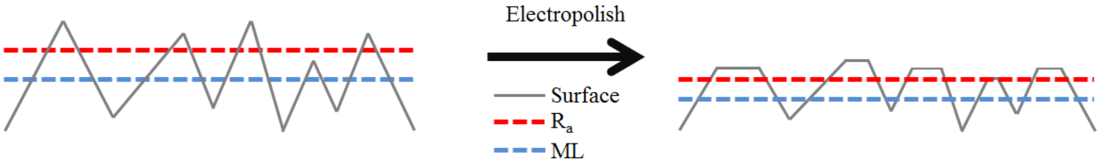

Figure 4.10: 2D illustration of the anodic levelling of a surface as a result of electopolishing. The initial and post values of $\mathrm{R_a}$ and ML (mean line or mean height) are indicated.

Given the aforementioned facts, it is axiomatic that the magnitude of the potential difference applied to the sample in TJEP is necessarily set such that the correct polishing condition is achieved: Principally, the voltage is dependent on the thickness of the anodic film[9] on the surface. At too low voltages (as shown in Figure 4.11) etching rather than polishing due their being only a small anodic film, producing an uneven surface as a result of the variation in etching rates between certain grains, phases and or dissimilar elements. Applying a potential difference which is too high, however, can lead to pitting of the surface due to bubbles (produced by the electrolysis) locally masking the surface and disrupting the film. Optimal electropolishing (both macro and microthinning) is achieved at a point in the central region due to the optimal size of the anodic layer; the layer is set so that the limiting current density is reached *i.e.* potential no longer effects the current distribution and dissolution within the anodic layer becomes transport controlled [303, 304]. Not all of the plateau region is optimal, however, due to oscillations within it and, therefore, care must be taken when selecting the actual potential used [305, 306].

Flow Rate:

The electrolyte flow rate is balanced such that it is both sufficient enough to carry away the oxidised material and stop gas bubbles forming on the surface (deposition of this material on the sample surface could lead to contamination and, together with the formation of gas bubbles, uneven etching) but not great enough to prevent formation of an anodic film, resulting in the specimen being etched rather than polished, and/or distorting the fragile electron transparent region [307].

Temperature:

Existing as a simple chemical reaction (Equation 4.5 where M signifies the metallic cation and y indicates its oxidation state after reaction with the acid), the effect of temperature on the severity/rate of the electropolishing follows an Arrhenius equation as out lined in Equation 4.6 (where [ ] signify reactant concentrations, L and W are the reaction orders, E_a is the reaction activation energy,

---

[9] The term anodic film describes the thick viscous diffusion layer which surrounds the surface of the sample and controls the dissolution of contours above $1\,\mu$m *i.e.* macrosmoothing. The dissolution of smaller contours (microthinning) is controlled by a thin solid salt film at the surface which governs the kinetics of anion removal due to cation vacancies and prevents preferential attack of high energy sites [303, 304].

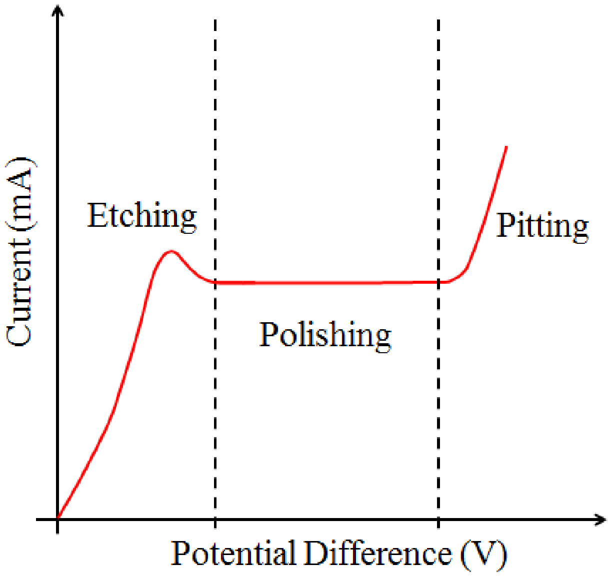

Figure 4.11: Correlation curve between the current and potential difference used for electropolishing. Plot is also referred to as a current density curve. The regions which result in etching, pitting and polishing (the ideal) are indicated. Inspired by [31]

A_r is the prefactor and other symbols have their predefined meanings) [308]. Accordingly, so as to obtain a slower reaction rate and, therefore, a larger thinned region, the aggressive electrolyte in TJEP is often cooled to a temperature 10's of degrees Celsius below 0° C[10] through the use of a refrigeration unit as shown in Figure 4.8. This low temperature also prevents the volatilisation of the electrolyte due to the heat released from the reaction, thereby further also inhibiting bubble formation and its associated pitting.

$$2\mathrm{M}_{(\mathrm{s})} + 2y\mathrm{HClO}_{4\,(\mathrm{aq})} = 2\mathrm{M}(\mathrm{ClO}_4)_{y(\mathrm{aq})} + y\mathrm{H}_{2\,(\mathrm{g})} \tag{4.5}$$

$$\mathrm{Rate} = \mathrm{k}(T)[\mathrm{HClO}_4]^{\mathrm{L}}[\mathrm{M}]^{\mathrm{W}} \qquad \mathrm{k}(T) = \mathrm{A}\exp^{\frac{-E_a}{k_B T}} \tag{4.6}$$

Light Sensor:

The setting on the light sensor is adjusted so that a hole with a maximally sized electron transparent region is obtained.

Bearing in mind the above discussion it should be pointed out that the determination of the exact potential difference to use for electropolishing was actually made in this research via an automatic function on the Struers TenuPol-5. This function operates

---

[10] The electrolyte remains liquid at this temperature thanks its significant alcohol content

by scanning over pre-defined voltage range to measure the current density curve (*cf.* Figure 4.11) from which the user can then select the correct voltage for the thinning process [309]. Noisy curves can be smoothed through the used of filter functions. An example of such a curve for mild steel is given in Figure 4.12.

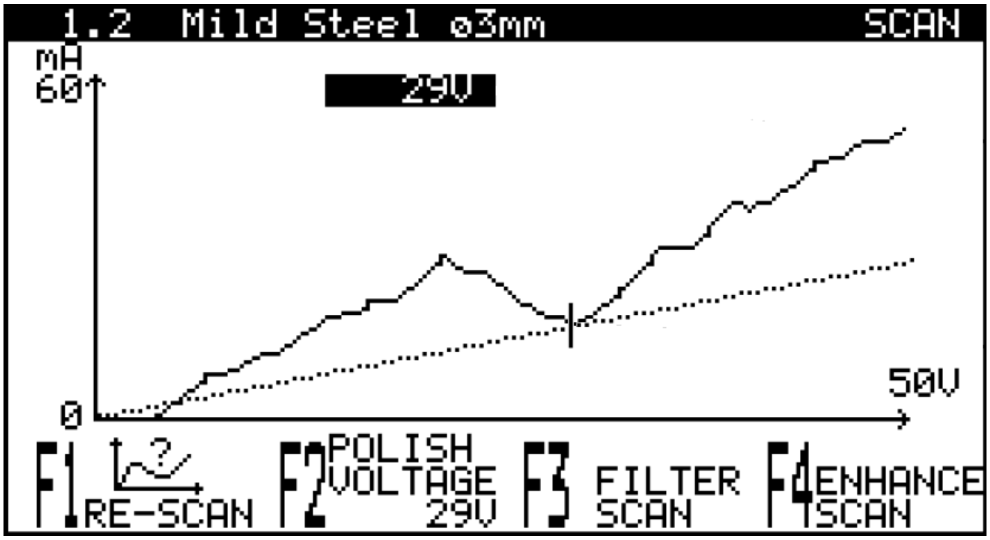

Figure 4.12: Screen shot of a example current density curve produced by Struers for a mild steel sample using the automatic scanning function on a Struers TenuPol-5. Diagonal line indicates offset.

4.2.8 Precipitate imaging: Electron Microscopy

TEM analysis was carried out in this research principally though the use of a FEI Tecnai 20 Analytical Electron Microscope. The microscope was equipped with a Lanthanum hexaboride (LaB_6) element and possessed a maximum accelerating voltage of 200kV. The use of such a high voltage is advantageous due to increased sample penetration (meaning thicker regions become electron transparent) and the decreased magnitude of electron scattering which provides for greater image resolution.

As the gathering of accurate statistics on the shape and size distribution of γ'' precipitates is dependent on the measurement of the maximum number of particles, the orientation relationship of the phase with the matrix (*q.v.* Section 1.2.2) meant images were only captured from grains with an [001] crystallographic orientation parallel to the electron beam. Such images have been shown to allow for simultaneous imaging of all three possible orientation variants [8], however, because of the low probability of a grain so happening to the correct orientation with the beam if the sample disc (prepared as per Section 4.2.7) is mounted normally to it, their capture requires the use of a double tilt (α and β) specimen holder. That is to say, the orientation of the sample has to be varied until the crystal lattice of a grain achieved the desired alignment. The use of tilting necessitates samples be mounted at the so called eucentric point whereby the specimen plane is coincident with the rotation axes of the sample holder or, in other words, the vertical position of the sample in the TEM column is such that the image produced does not move laterally as the tilt angle is varied.

Design and operation of a Transmission Electron Microscope

Since their first commercial production in 1936, the principle layout of TEM microscopes have changed very little. A cross-section of a generic, modern day TEM microscope, along with a more simple schematic of the major apparatus, is displayed in Figure 4.13. The fundamental stages of a thermionic emission (rather than field emission based on quantum mechanical effects) TEM, in the order in which the electrons pass through them (*i.e.* from top to bottom), and the basic function of the equipment which they comprise can be understood as the following:

(1) **Electron generation and acceleration.**

  (i) *Electrons are initially produced in a TEM by a filament consisting of either tungsten metal or lanthanum-hexaboride (LaB_6).*

  A tungsten filament acts as an electron source via thermionic emission[11] and is selected based on its high melting point, low vapour pressure and low reactivity. Lanthanum hexaboride (LaB_6) filaments also work by thermionic

---

[11] Thermionic emission describes the phenomenon whereby a metal is heated (typically through the application of a current *viz.* ohmic heating) to a sufficient temperature that the electrostatic force (the work function) holding electrons in the sample is exceeded by the kinetic motion induced by heat. At this point electrons begin to escape the sample.

emission but at a much lower temperature than tungsten making them more durable; however, they are also more expensive and chemically unstable (particularly with respect to oxygen) [34, 310].

(ii) *After production the electrons are accelerated using a high voltage Wehnelt cylinder cathode and a round metal anode.*

As shown in Figure 4.13b, a Wehnelt cylinder is a metal electrode which sits in the central axis of the microscope around the filament. By using a bias resistor (resistance = R_b) it is made to have a potential which is more negative than the filament, allowing control over the electron emission. That is to say, electrons can only be emitted at the tip of the filament (over which there is a small hole in the Wehnelt cylinder) as at any other point the electric field is too negative for them to escape. This configuration allows for the emission current (I_e) to be easily controlled by varying R_b, for I_e to be stable thanks to autobias[12] and for the cylinder to accelerate the electrons once they have passed through it. The centrally located metal anode (also containing small central hole) accelerates the electrons exiting the Wehnelt cylinder up to relativistic speeds thanks to its highly positive potential. The attraction is so strong, however, that only 1% of the electrons leaving the cathode pass though the hole at the anode's centre [34]. The potential difference applied to across the anode and cathode in modern day microscopes is typically on the order of 100s of kV although microscopes which operate with voltages in the MV range have also been constructed to achieve smaller wavelengths (*cf.* Equation 4.4) [34, 35, 36].

---

[12] If I_e spontaneously increases due to say thermal fluctuations, the Wehnelt cylinder will automatically become more negative to compensate due to the $I_e R_b$ potential difference relationship between the filament and the cylinder.

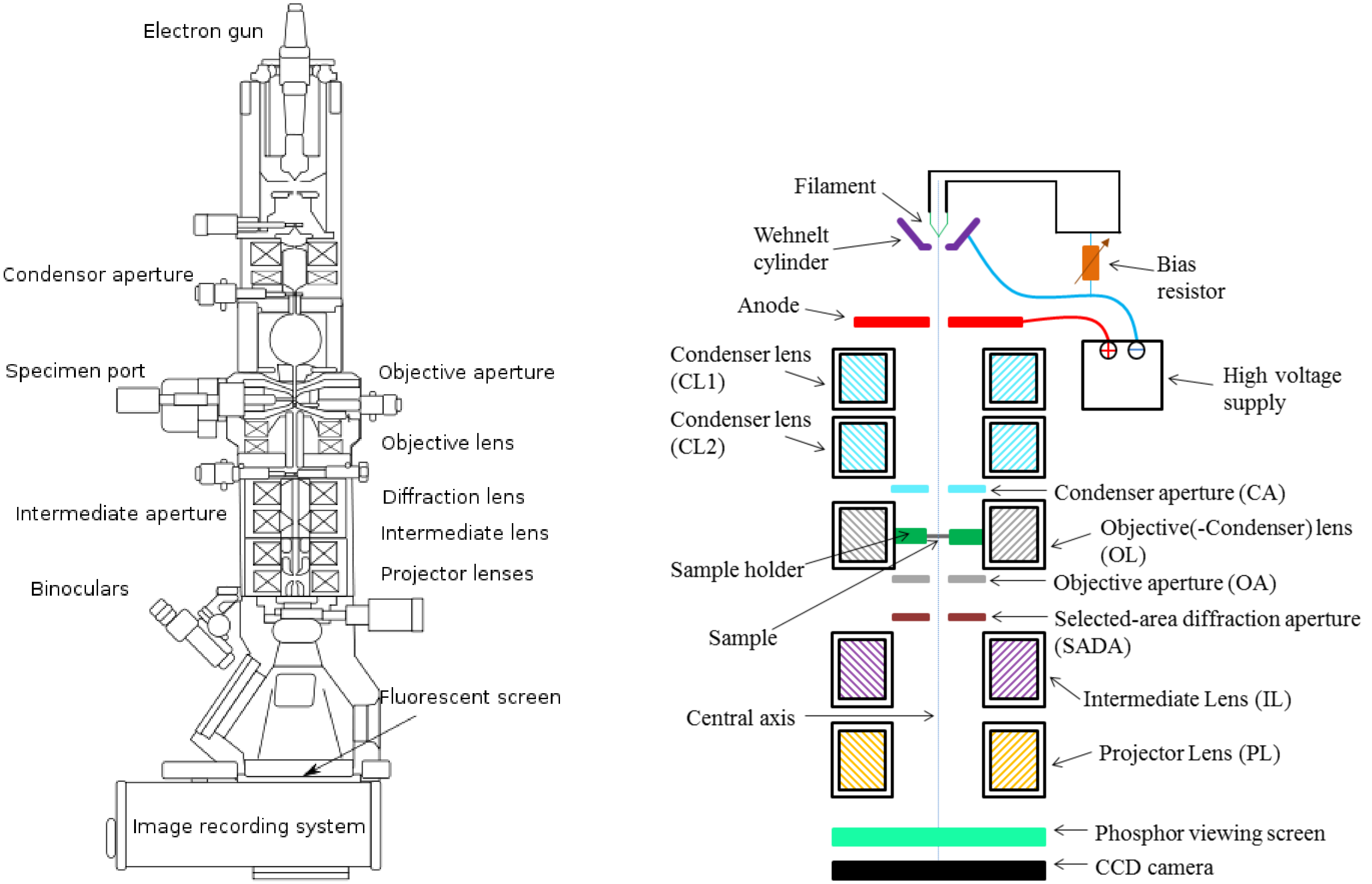

(a) (b)

Figure 4.13: a) Cross-section of a generic modern day TEM taken from [32]. b) Simplified schematic showing all the major stages of a TEM. The internals of the TEM are at very low pressure (approaching vacuum).

(2) **Focusing electrons onto sample.**

(i) *The accelerated electrons have a spread too large for high magnifications to be achieved. This problem is exacerbated by the electric fields of the cathode and anode which cause the beam of electrons to diverge. The electrons are, therefore, focused using a strong magnetic condenser lens.*

The magnitude of the magnification possible within a TEM depends strongly on the ratio of the viewing area to the area of sample illuminated. For a maximally sized (*i.e.* 15-20cm) image on the fluorescent viewing screen (shown in Figure 4.13) a magnification (M) of 10^5 requires the electrons to illuminate exclusively an area 1.5-2μm in diameter.

On leaving the anode the electron beam has relatively wide and divergent path (10s of μm) owing to both the size of the holes in the electrodes (holes have to be large enough to allow for a sufficient flux of electrons to get though to form a bright image but not so large as to cause significant aberrations) and the curvature of the equipotential electric field lines over them. As shown in Figure 4.14, this curvature at the cathode acts as a convex lens, first focusing and then spreading the beam as electrons crossover beyond the focal point [311]. Contrariwise at the anode the curvature acts as a convex lens, spreading the beam in such a manner it appears to come from a isotropically radiating virtual source $\approx 40\mu m$ in diameter [34, 35, 311].

To concentrate the diverging beam, a strong magnetic condenser lens like that shown in Figure 4.15a is utilised. Its principle design is such that windings of insulated copper wire are placed inside a soft (ferromagnetic) cylindrical iron casing; the casing contains a central bore, in the wall of which there is a gap filled with a non-magnetic material. When a current is passed through the copper windings an orthogonal magnetic field is produced proportional to the current and number of windings via the Biot-Savart Law [33]. The high magnetic permeability of iron means that most of the magnetic field lines lie within it, however, at the gap in the iron case the field lines stretch out into the central bore region. The density of the field lines produced is proportional to the narrowness of the gap meaning a high magnitude field can be created by making the gap as small as possible. In this configuration, by applying the current through the windings so that the magnetic field lines point downwards in the microscope/along the electron beam (Figure 4.15b), electrons passing through the lens will be focused by the strong magnetic field (typically ≈ 2 Tesla) via the Lorentz force law[13] [36, 33]. The focal point of the lens can be

---

[13] The curvature of the magnetic field acts to introduce a azimuthal (spiralling) component to the

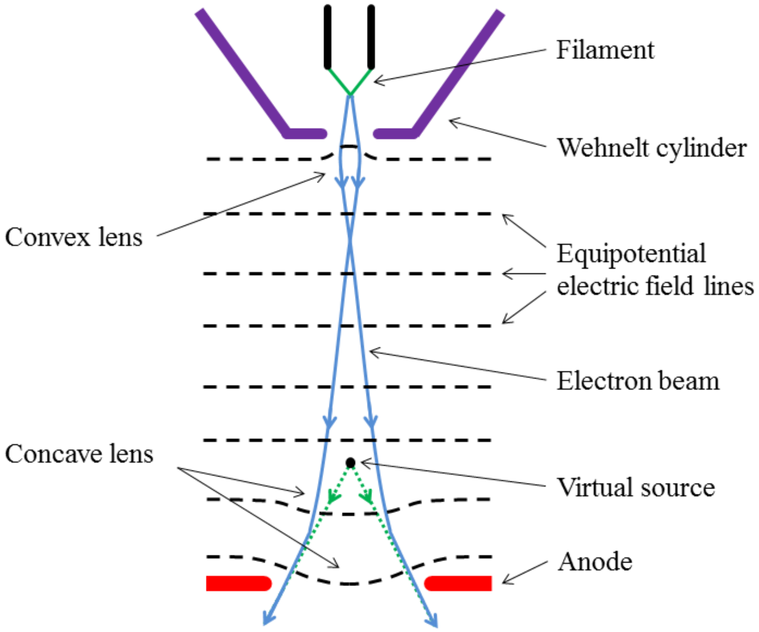

(a)

Figure 4.14: Effect of the electric field produced by the filament, Wehnelt cylinder and anode on the electron beam path in a TEM. The "convex lens" and "concave lens" arise from the gradient in negative potential and positive potential in the holes in the Wehnelt cylinder and the anode, respectively (*cf.* Coulomb's Law [33]).

varied by altering the current in the windings, and, consequently, the strength of the magnetic field produced. By employing a set-up in such a way that the object distance (the distance between the virtual source and the lens) is far greater than the focal length (the distance between the lens and focal point), at its highest strength the lens is able to reduce the spread in the beam at the focal point by a factor of over 100.

(ii) *Electrons leaving the first condenser lens (CL1) are incident into a second condenser lens (CL2) and, subsequently, a condenser aperture (CA). These devices allow for the size of the illumination spot on the sample to be varied and, therefore, the selection of the area to be examined. Ultimately, the size of the illumination spot harnessed by the user depends on the features of interest and the desired magnification.*

The CL2 the TEM is constructed in the same way as the CL1 (discussed previously) but is operated with a far smaller current thereby reducing its magnetic field and increasing its focal point. As the electrons pass through this lens they are incident onto an aperture consisting of a circular diaphragm

---

electron velocity which, in turn, decreases the radial component thereby focusing the beam. The azimuthal component is removed as the radial velocity reverses at the centre of the magnet, allowing the electrons to focus at the focal point and subsequently diverge.

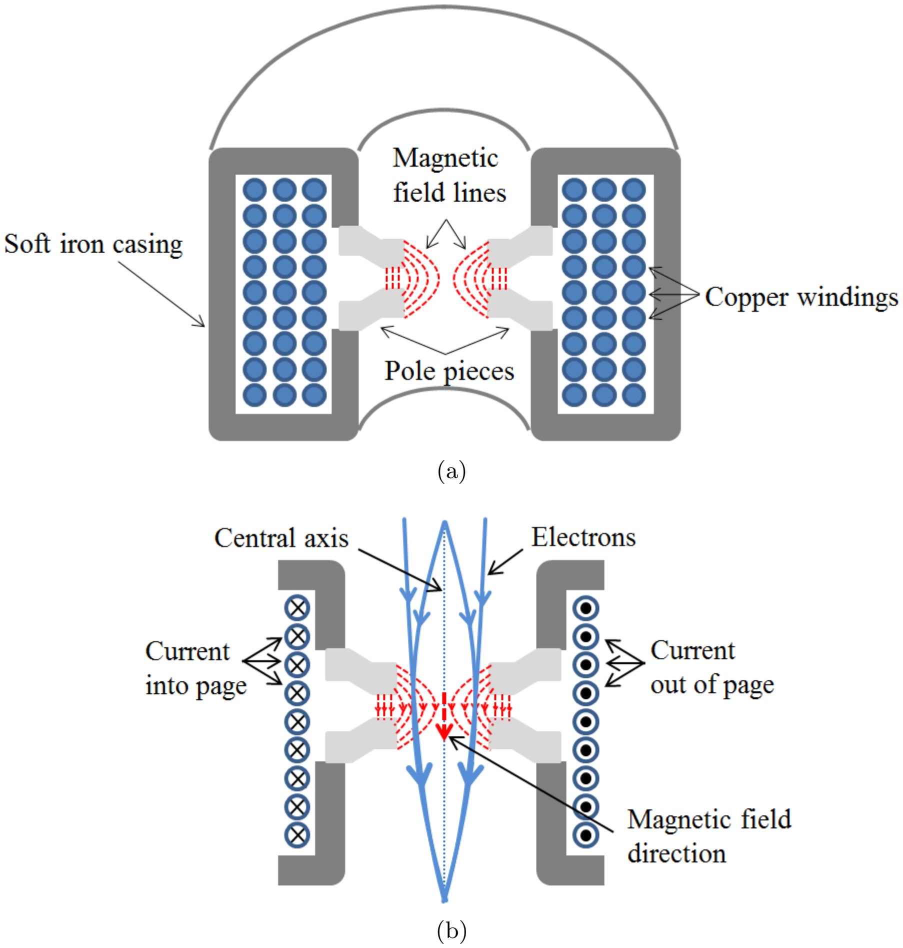

(a)

(b)

Figure 4.15: a) Principle layout of a magnetic lens used in a TEM. The magnetic field is enhanced in this design by using pole pieces constructed of a ferromagnetic material. These pieces decrease the gap in the casing (therefore increasing the magnetic field strength experienced by the electrons in the beam) and allow for a more homogenous field because of their precise construction [34, 35, 36]. b) Focusing effect of the magnet field produced by the copper windings on incoming electrons. The direction of both the current and magnetic field lines are indicated [34, 35, 36].

placed in close proximity. These two devices are operated in a complimentary fashion to manipulate the size of the electron beam as it hits the specimen [34, 35, 36].

Highest magnification is achieved in the microscope when the CL2 lens is operated in a manner whereby its focal point lies in the plane (same vertical position in the column) of the specimen (fully-focussed) and the condenser aperture is fully open. In this condition the spot size is as small as possible and the specimen illuminated at maximum brightness (electron flux). Underfocusing the beam (moving the focal point to below the specimen), whilst keeping the aperture fully open, increases the size of the illumination spot but also acts to decrease the convergence semi-angle of the beam (the angle over which electrons are accepted/can incident the sample). This set-up thus decreases magnification but also creates a beam of more parallel electrons which are useful for forming diffraction patterns to identify phases of interest [34, 310, 312]. A similar result to this is also observed in the over-focused condition (focal point lies above the specimen) but with the notable difference that the beam/image of the electron source is now flipped when it reaches the sample. By altering the focal points of both the CL1 and CL2 lenses it is possible to achieve the same incident brightness over all spot sizes. The restriction imposed by the condenser aperture is such that as it closes both the convergence semi-angle of the beam and its intensity/brightness are reduced thereby reducing resolution (by Equation A.6) but improving diffraction patterns.

(3) **Image Creation**

(i) *As electrons get close to the sample they are further focused via the top of another magnetic lens, referred to as the objective lens (OL), in which the specimen is positioned. The bottom half of the OL focuses scattered/diffracted electrons as they emerge from the back of the sample. If an image of the object rather than the diffraction pattern is required, an objective aperture (OA) located in the back focal plane (BFP) of the lens is used to block out the light from all but one of the diffraction spots.*

Using electrons directly focused onto the specimen from the CL2 lens can lead to a loss in resolution because of its comparatively long focal length ($\mathrm{CL2_f}$); aberrations in the image, which lead to blurring, scale with the focal length. In addition, the spot size produced by this lens is not sufficiently small to allow for the resolution of the finest microstructral features. To overcome this, modern TEMs employ an immersion lens set-up whereby the specimen is placed at the centre of the OL (creating a condenser-objective lens) rather than above it. In such a configuration, shown in Figure 4.16a, a parallel electron beam (resulting from an under-focused CL2) is focused by the upper half of the OL magnetic field onto an area on the sample as small as 1-10nm allowing for analysis of very small features. Conversely, a converging electron beam as shown in Figure 4.16b (resulting from a slightly over-focused CL2) is split by the OL such that it the electrons enter normal to the sample surface. Once the electrons have passed through the sample, the magnetic field inside the lower half of the OL restores the diffracted beams to being either parallel or focused with a focal length $\mathrm{OL_f} \leq 0.2\ \mathrm{CL2_f}$ (significantly reducing aberrations) [34, 35, 36, 313].

The diffraction of electrons takes place as they pass through a sample owing to their interaction with the crystallographic planes *viz.* the planes acts like a

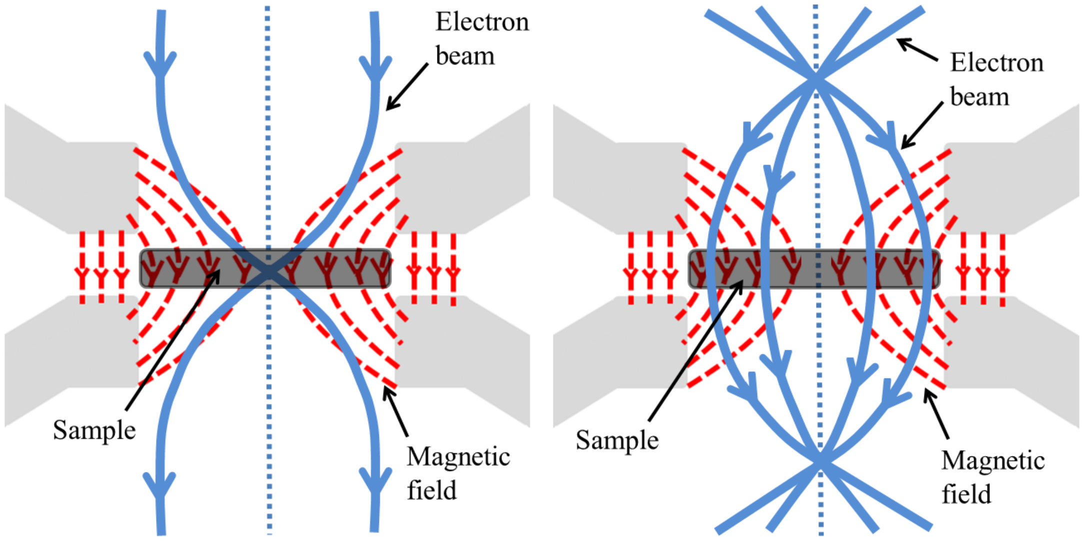

(a) (b)

Figure 4.16: Immersion lens configuration in a TEM. a) Parallel beam focused by pre-field and split by post-field. b) Focused beam made parallel by pre-field and re-focused by post-filed.

diffraction grating (*q.v.* Appendix B). Accordingly, therefore, in the slightly over-focused regime (Figure 4.16b), by setting it at the correct magnification, a fully focused interference pattern can be produced in the OL BFP as shown in Figure 4.17a. These diffracted electrons (through the use of further lenses) can then be projected on to the viewing screen if desired; however, utilising all of the electrons results in significant aberrations being present in the images [34, 35, 36, 313]. As shown in Figure 4.17b, inserting an aperture into the BFP of the OL reduces this problem by only allowing electrons which have been scattered through a certain range of angles to be projected onto the image plane. In addition to improving resolution, the aperture also increases contrast as regions which scatter electrons to paths outside of the acceptance angle will appear darker [312]. This is the mechanism behind bright-field (aperture set as in Figure 4.17b *viz.* such that mostly un-deflected electrons are accepted, producing images where scattering features like precipitates appear as dark spots on a white matrix/background) and dark-field (aperture set such that mostly deflected electrons are accepted producing images where the specific scattering source(s) appear as white spots on a dark matrix/background) imaging [313, 314, 310].

(ii) *Alternatively to the OA, an aperture known as a selected-area-diffraction (SADA) aperture located in the image plane of the OL can be used to select light emerging from a specific area of the sample. This allows for the diffraction pattern from small areas to be projected and, consequently, for their structure to be identified. Light emerging from the OL, and if in use either the OA or SADA, passes through an Intermediate lens (IL) which is used to both increase mag-*

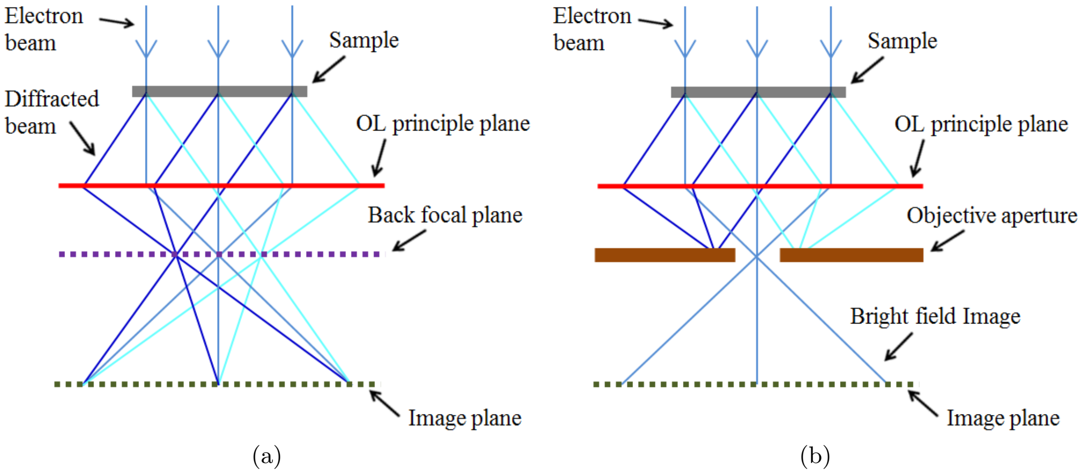

Figure 4.17: a) Formation of a diffraction pattern in the back focal plane of the objective lens. In this simplified set-up, bending of the electrons is assumed to take place singularly at the OL principle plane rather than gradually through the curved OL magnetic field. b) Selection of one diffraction spot using an aperture located in the back focal plane.

nification and focus either the image or diffraction pattern for viewing.

The selected area diffraction aperture (SADA) operates in the same way as the OA discussed previously, but is located in the image plane of the OL rather than the BFP (Figure 4.18). As a result, rather than selecting a specific diffraction spot as with the OA, the SADA is used to select light emanating from a particular area of the image. The size of the specimen area selected scales with the size of the SADA aperture. Restrictions imposed by contrast and resolution (resulting from diffraction and aberrations) limits the size of the aperture meaning it that the smallest specimen area that it can select is on the μm scale [34, 35, 36, 315].

The intermediate lens (IL) in a TEM is the first of the magnetic projector lenses whose function is to magnify the electron pattern/image stemming from the sample for viewing by the operator; its design is identical to that of the other magnetic lenses describes previously. In addition, however, the IL also acts as a mode selector, transmitting either the sample image (image mode) or diffraction pattern (diffraction mode), with or without the OA or SADA being utilised, depending on which is desired. As displayed in Figure 4.18, this mode selection is achieved through manipulating the focus of the IL (changing the current supplied to it) in a manner whereby the object plane lies in either in the BPF (for diffraction) or image plane (for imaging) of the OL [35, 315].

(iii) *The image produced by the IL is further magnified using an additional projection lens (PL). This image is projected onto a phosphor covered viewing*

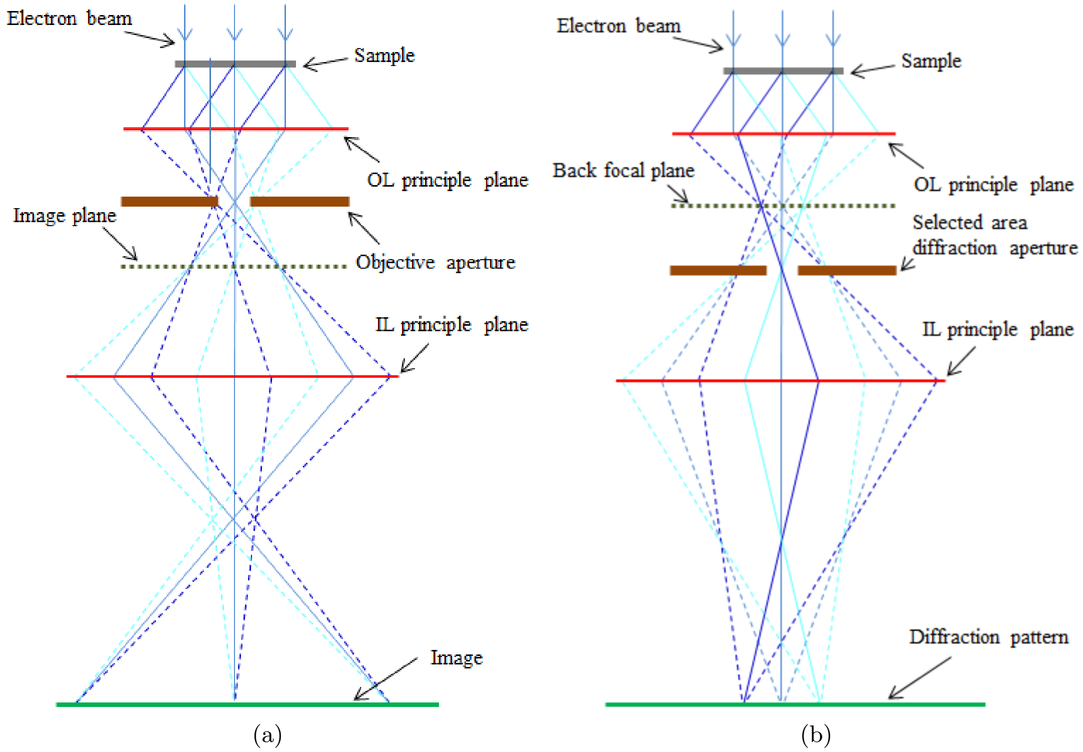

Figure 4.18: Basic modes in a TEM: a) Imaging where the OA selects a diffraction spot and the IL magnifies the image produced in the OL image plane. b) Diffraction where the SADA selects a part of the specimen and the IL magnifies the diffraction pattern emanating from that area. Dashed lines correspond to the electrons blocked out by the apertures.

> *screen, which luminescences under electron bombardment. Images are captured using a CCD camera or photographic film.*

After leaving the IL the electrons emanating from the specimen pass through a final magnetic lens known as the projection lens (PL), to enhance magnification. This lens also acts to balance out aberrations caused by the IL [35]. To remain in focus the IL and PL are operated/varied together under the condition that the final image produced has a size equal to that of a viewing screen located below. Owing to the fact that electrons are invisible to the human eye, the viewing screen in a TEM is covered in a phosphor such as ZnS as this luminescences under electron bombardment. It is based on the image on this screen that all of the apparatus discussed previously (lenses, apertures *etc.*) are adjusted. Permanent images are captured from a TEM using a CCD camera located below the viewing plate.

§ 4.3 Precipitate statistics measurement and calculation

Owing to the fact that they are projected images, the production of the desired precipitate statistics from the gathered TEM micrographs requires the use of stereology. Nevertheless, although a number stereological techniques have been established for the purpose of producing precipitate statistics from both planar (*i.e.* from light microscopy and/or SEM) and projected (*i.e.* from TEM) images over the years, their specificity means careful examination of the detail of the methods is required in order to establish their validity and subsequent selection for application in this research.

4.3.1 Established Stereological Techniques for Ellipsoids

The necessity for an appraisal of the applicability of the stereologlical techniques already established in the literature for γ'' precipitates in Alloy 625 arises strictly as a consequence their oblate spheroidal (or more simply regular but non-spherical) shape. That is to say, the simplified geometry means that the selection of a technique for successfully estimating particle size distributions and number densities for spherical precipitates such as carbides is trivial owing to them being long established for both planar [316, 317] and projected [318, 319] images. The principle complexities introduced by an ellipsoidal particle shape as compared to a spherical one can be best explained with regard to Figure 4.19: When analysing a distribution of spherical particles, the equiaxed particle dimensions mean that the principle factor in determining the projected or section shape is the original particle size *viz.* the sectioning direction is arbitrary. Conversely for ellipsoidal particles, particle orientation and shape introduce significant anisotropy.

In the case of randomly oriented ellipsoidal particles, the method derived by Cruz-Orive [316, 317] can be used to construct distributions for both particle shape and size as well as number density if the probe used is a true plain of section. However, application of this general technique to projected images as is desired in this research is considered to be impossible because of insurmountable analytical problems which arise as a consequence of the discrepancy between the projected image of a sectioned particle and the shape of its sectioned surface [295]. A partial solution to this problem, utilising a different mathematical construction, has been published by Andersen *et al.* [320]; however, their assumption of constant particle shape (aspect ratio) for all particle sizes means that this approach would not be valid for γ'' precipitates (*cf.* Section 1.4.3).

Whilst it is clear that the use of TEM images complicates the analysis of ellipsoidal particles, it should be noted that even with the use of a true plane of section or under the assumption of constant particle shape, the aforementioned techniques of Cruz-Orive [316, 317] and Andersen *et al.* [320] would not be suitable for γ'' precipitates owing to the assumptions made on random particle orientation. As discussed in Section 1.2.2 the γ'' phase obeys a strict orientational relationship with the matrix meaning that (by symmetry) only three possible alignments of particles are possible. To the author's knowledge, the only study published in the literature for the analysis of such a system is that of Jensen [321] who adapted the planar expressions of Saltykov [322]

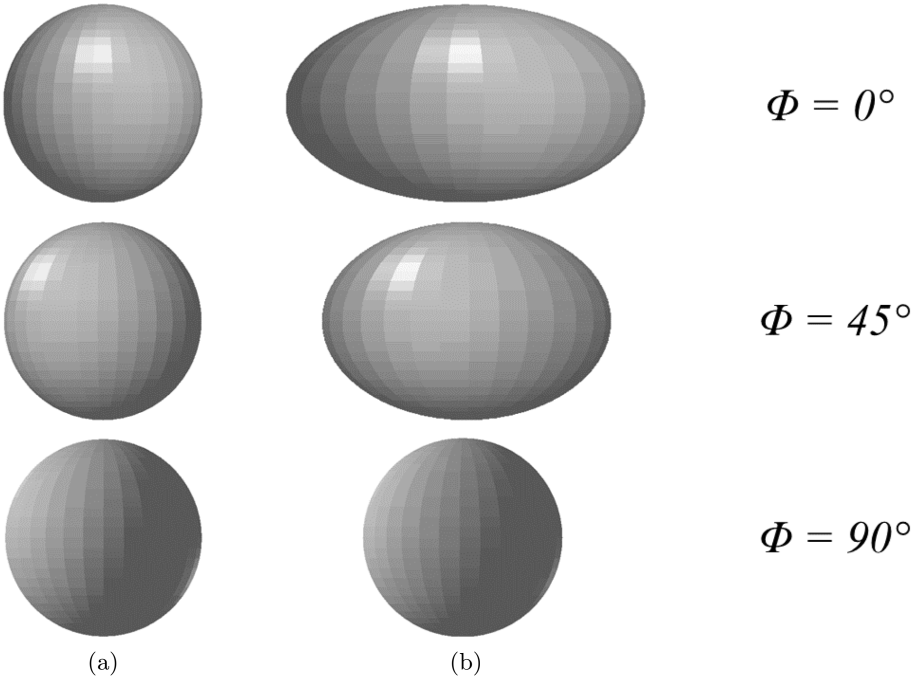

(a) (b)

Figure 4.19: Projected shape of a) spherical and b) ellipsoidal particles at different azimuthal angles.

with descriptions developed by Hilliard [318] and De Hoff *et al.*[323] for the analysis of [001] aligned oblate spheroidal precipitates in a $CeO_2-MgO-ZrO_2$ ceramic. Like the approach of Saltykov this technique requires that all of the measured particles be placed in classes according to size, however, additionally in this case it is also necessary that all particles within each class are defined as possessing the same aspect ratio. This latter imposition poses a key problem in this research de to the fact that, not only is such a phenomenon very unlikely to be strictly observed amongst complete particles, but sectioned particles will act to randomly distort the classes into which they are placed; the aspect ratio of an ellipsoid is independent of the slicing position allowing for precipitates of the same size (major axis length) but with very different aspect ratios. Accordingly, with the lack of validation and the significance of the requirement for consistent and accurate precipitate statistics here, this technique developed by Jessen could not be considered as applicable in this research.

4.3.2 New Method For Analysis Of Ellipsoids

In the absence of an appropriate published mechanism for gaining accurate γ'' precipitate statistics from TEM images a new technique was developed here. Specifically, given the complexities incurred by derived mathematical expressions discussed previously a new methodology was instead designed based on a numerical approach whereby the foil is effectively reconstructed in three-dimensional space, harnessing established assumptions on precipitate distribution and from stereology. The sequential stages of the technique, along with details of these assumptions where implemented and a discussion of their justification are given below. As implementation of the technique was carried out in this research using the forth generation high level programming software MATLAB [324], all functions utilised specific to the software are also identified/detailed.

1) Measure Size and Shape of Precipitates

The first process in the new technique is the precise and accurate measurement of the projected precipitate sizes and shapes. Although all three variants of the γ'' precipitates should be visible when imaged along an [001] crystallographic orientation, face on (major axis normal to the line of sight) precipitates present with a very low contrast and poorly defined edges, as shown in Figure 4.20a, owing to their being extremely thin along the microscope's line of sight (*cf.* the aspect ratios of edge-on/major axis parallel to line of sight precipitates). Consequently, it is evident that measurement of such precipitates is likely to be subject to significant error and, therefore, quantification of only edge on precipitates can be considered reasonable. To this end, measurement of precipitate number, size and aspect ratio was performed in this investigation by placing elliptical fits around the edge on particles[14] though the use of the MATLAB function `regionprops` to determine each of their centroids and maximum and minimum axis lengths. An example of the result of this fitting procedure is given in Figure 4.20b. Particles intersecting the foil edges in the experimental image are excluded from the precipitate statistics owing to the uncertainty of their true size and shape (reflected in the comparatively poor quality of their fit).

2) Calculate Foil Dimensions and Introduce Face-On Precipitates

Before the foil can be reconstructed it is first necessary to define its dimensions. Clearly for two of the dimensions (comprising the surface area) this is trivial but for the sample thickness the value is not obvious. As a result of the necessity of this value in almost all quantitative TEM stereological techniques, a number of different methods have been developed over the years in order to acquire it. Unfortunately, however, as detailed in the review by Scott *et al.*, most are associated with significant limitations, are difficult and time consuming to implement and often require expensive equipment [325].

Of all of the methods which have been developed, the most popular (where it can be implemented *i.e.* with an available spectrometer) is that which utilises the plasmon[15] loss peaks in an Electron Energy Loss (EELS) spectrum. The maximum accuracy achieved by this method is generally concluded at around 8-10% and, unlike the more precise but also more lengthy and intricate methods which harness convergent beam electron diffraction (CBED) (2-5% accuracy [326], it does not require crystalline samples [327]. Nevertheless, it must be highlighted

---

[14] The bright shapes imaged in the TEM are assumed here to correspond exactly to the outline of γ'' precipitates *i.e.* any small contribution/distortion from stain effects is not possible to quantify and it therefore ignored.

[15] Plasmons are the name given to the free electron oscillations within a conductor

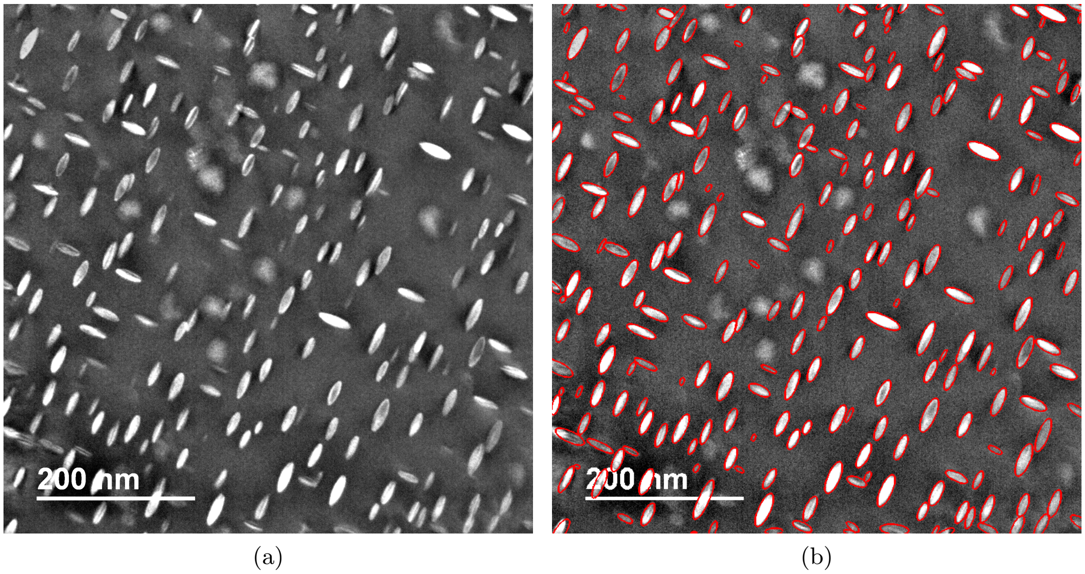

(a) (b)

Figure 4.20: [001]-orientated Dark-field TEM images of the three orientational variants of γ'' precipitates in Alloy 625 after ageing at 650 °C for 200 hours. a) Enhanced image, removing non-uniform illumination and increasing contrast. b) Image with elliptical fits made to edge-on precipitates.

that this limit on the accuracy of the measurement produced by EELS can only be adhered to if the value of mean free path for inelastic scattering of electrons by plasmon production is precisely known, and its determination involves lengthy investigation (*q.v.* the study of Bardal *et al.* for three Aluminium alloys [328]). Such a study was not feasible within this research for reasons of both equipment availability and time meaning that the use of EELS (with an estimated value for the mean free path) would likely have introduced significant, unquantifiable uncertainty. Similarly, whilst the samples examined in this research were obviously crystalline, signifying that the aforementioned techniques implementing CBED would theoretically have been possible, the associated complexities, time scales and/or extensive calibrations required [326] meant that such methods were also not considered viable.

The aforementioned key considerations with respect to the implementation time for thickness measurement techniques were made principally a consequence of the number of samples that were required to be analysed *viz.* whilst examination of material corresponding to all thirty-four ageing conditions was never likely, the necessity for multiple images and, therefore, foils for each of the conditions to gain accurate precipitate statistics meant any significant increase in analysis time would have been automatically compounded. In this light, although other techniques described by Scott *et al.* [325] did offer a more rapid assessment without the need for expensive equipment (most notably the contamination deposit method as latterly improved by Pan [329]), the propensity for errors with these techniques meant separate validation by more complicated methods would likely have been required for some samples anyway. Ultimately as a result of these facts, therefore, it was decided at an early stage of this research that an alternative, mathematical estimation of the foil thickness would be made instead.

In his work titled "The counting and sizing of particles in transmission microscopy" [318] Hilliard showed that for foils containing particles with an average diameter $\bar{D}$ the overlap of particles in an image was considered to be negligible if the thickness of the foil was less than twice the average diameter ($2\,\bar{D}$). This conclusion was also stated by Crompton *et al.* in their corrective paper to Hilliard's published four years later [319]. In accordance with this mathematical eventuality, therefore, it is evident that for images of γ'' precipitates where no overlapping of edge on precipitates is observed, the value of $2\,\bar{L_{\mathrm{M}}}$ constitutes a reasonable approximation (in actuality an upper limit) on the foil thickness. Consequently, given the possible rapidity for the calculation of this variable and the desirability for fast analysis, it was decided in this work to appropriate this value for the true foil thickness in the new reconstruction technique.

Once the foil dimensions have been determined, the final task which must be completed before reconstruction of the foil can occur is the introduction of face-on particles to account for those not included in the original measurement. This is achieved in the new method by logical extension of the presumed non-preferential orientation relationship of particles *viz.* particles form along each of the [001] axes with equal probability: Assuming the area observed in the TEM image is sufficiently large, it can be reasonably concluded from this probability distribution that the particles measured constitute only $^2/_3$ of the population present meaning that the face on precipitates can be reintroduced by adding 50% more particles to the experimentally measured distribution. Given the uniformity of these precipitates, their statistics (size and shape) are calculated such that they correspond to the distribution measured from the edge on particles.

3) Construct Foil and Calculate Number Density

As alluded to previously, the process of the reconstruction undertaken in the method is effectively that of a random numerical population of a volume equal to that calculated for the foil *i.e* the x-y and z positions of each individual precipitate is calculated through random number generation subject to two spatial/physical conditions. Explicitly, the mechanism proceeds such that a random position for the centroid of a given (sequentially added) particle is located within the foil volume and this position is retained if the particle does not either overlap (in the x-y plane) any other particles already located or intersect the foil edges in the x-y plane as per the measurement condition outlined (following Hillard) previously. A graphical illustration of the result of the reconstruction of a foil is given in Figure 4.21. The size of each particle corresponds exactly to the physical dimensions measured from the experimental image and statistics are computed from the fraction of each particle within the foil by integrating over the relevant volume. Once calculations have been made for all the particles, a PSD is produced.

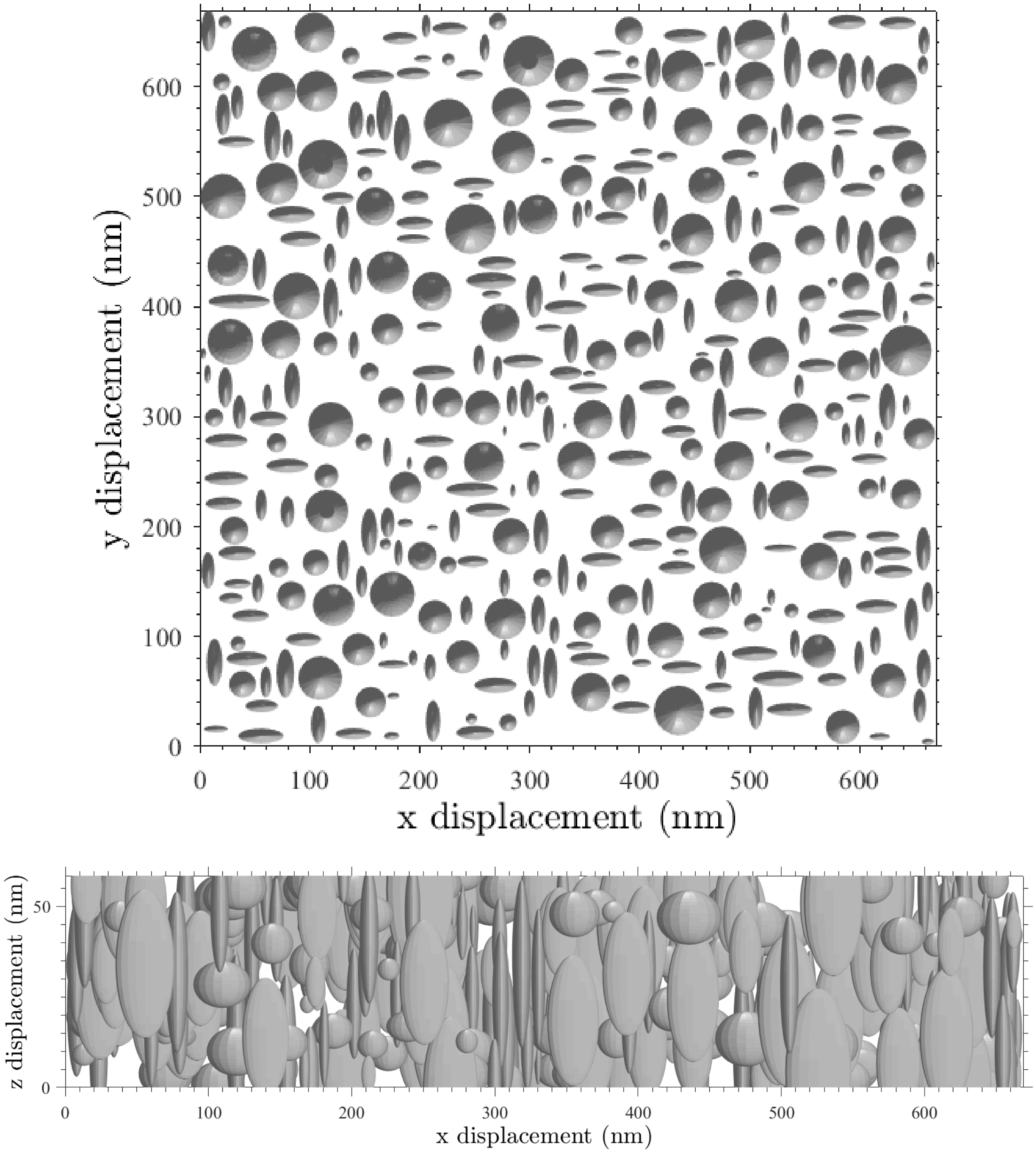

(a)

Figure 4.21: 3D reconstruction of the foil which produced the TEM image displayed in Figure 4.20. a) Top down view (along z-axis). b) Side on view (along y-axis).

The rationale of the adoption of the random location approach in this system is principally based on the underlying physical assumption that the γ'' precipitates have no preferential nucleation sites in the material and, therefore, the locations of the precipitates in the experimentally imaged foil are arbitrary. As a result, whilst the lack of precipitate location information allows for the rapid construction of such a foil, it is evident that only images free of such sites (*e.g.* dislocations) can be reconstructed. Another implication of this approach, however, is that because of the randomness of the precipitate location in the z direction, a true (in line with the other assumptions made here) representation of the fraction of each particle contained within foil will only result through the averaging of the statistics gleaned from many reconstructions. Accordingly, a rigorous average value for the volume located within the foil of each precipitate is determined from values calculated over all possible z positions.

Taking into consideration the above methodology, it should be pointed out that the restriction on centroid location in the z direction in the method is imposed so that same size and shape statistics are achieved when viewed normal to the x-y plane. That is, put succinctly, although the particle may be cut by the foil, the radius observed in the reconstructed foil corresponds exactly to imaged radius of the experimentally analysed precipitate. This result has two significant consequences for the results ultimately produced: The first, and most significant, of these is that a skew towards lower particle sizes will likely be incurred; many of the mathematical formalisms developed for planar images are concerned with correcting the increase in smaller sized particles apparently witnessed in planar images which result from the sectioning of larger ones [295]. The second consequence pertains to the method of the number density calculation *viz.* taken together with the restriction on the foil thickness it is clear that the implication of the condition of particles lying at least 50% inside the foil is to make value produced for the number density an upper limit.

4) Combine Image Statistics and Classify

Although, it is evident from Figure 4.20 that a significant number of particles can be captured and subsequently analysed from a single image, improved and more representative statistics are obviously gleaned through combining the data acquired from multiple micrographs. Accordingly, before the PSD for a given condition is produced the new technique includes a forth step which allows for the combination of statistics from multiple, non-overlapping images. Simply stated, during this stage the data pertaining to each individual precipitate from each image is inserted into a single array upon which the subsequent classification procedure can be carried out. Through combining raw particle data, the additional distortion of the PSD which would result from combining the classified statistics of individual images is avoided.

Like most classification procedures, the process implemented in the model created in this research to form a continuous PSD from the gathered precipitate statistics can be described best as a statistical data "binning" process whereby the ultimate result is a histogram of particle classes each with the same width in terms of precipitate size. Specifically, an iterative calculation is carried out in which the number and width of all the classes are reduced and increased, respectively, until the condition is fulfilled that each of the classes contains at least one precipitate *i.e.* producing a continuous PSD. By convention, once classified, the value for the size for each particle within a given class becomes equal to that of the lowest possible size as indicated by its lower boundary, leading to an inevitable distortion in the PSD. Nevertheless, the impact of such a consequence on the calculation of values such as the average particle size is negated in this method through the use of the original, raw data and a distribution density (*q.v.* Section 3.2.8). The harnessing of the distribution density also largely annuls any effect introduced by the arbitrary nature of specific class locations in the PSD.

Whilst the above arguments have been made with respect to particle "size" classification, it is obvious from the dimensions of the spheroidal precipitates that this is not an easily describable variable. For example, calculation of particle volume (V_{OS}) as per Equation 4.7 (where r_{M} is the oblate spheroidal precipitate major radius) and all other symbols have their predefined meanings) indicates that particles with very different dimensions (*i.e.* r_{M} and α) can posses the same volume and can therefore be considered as having the same size. Similarly, the consequence of using any single classifying variable is an inevitable significant loss of detail as particles with markedly disparate physical dimensions are homogenised. As a resolution of this problem, the technique created here performs two separate and independent classifications: one according to a physical dimension, chosen as the precipitate major radius, and the other according to the particle shape *i.e.* the aspect ratio which is referred to as an aspect ratio distribution (ARD).

$$V_{\mathrm{OS}} = \frac{4}{3}\pi\alpha_k r_{\mathrm{M}}^3 \tag{4.7}$$

4.3.3 New Technique Validation

Despite the physically based arguments and justifications made in its derivation, adoption of the new technique for ellipsoid analysis (within the constraints of particle alignment outlined previously) can only be argued as reasonable if it is validated. Unfortunately, the availability of appropriate experimentally generated images with prior known distributions is non-existent within the literature (*cf.* details already provided about the lack of quantitative investigation of such systems) necessitating an alternative approach be taken. To this end, validation of the technique was carried out using images of computationally generated distributions of ellipsoidal particles allowing for prior knowledge of all the true particle statistics (*i.e.* PSD, ARD, $\bar{\rho}/\bar{r}_{\mathrm{M}}$ etc.).

Owing to the unknown shape of the PSD and ARD for γ'' precipitates, and in light of the number of different distributions observed experimentally for various precipitates in a range of systems [330, 331], the validation of the new technique was made against images generated from three significantly different distributions; the results obtained for ellipsoidal particle populations corresponding to a normal, LSW and log-normal distribution are given below. An outline of the mechanism used to generate the synthetic images, highlighting the constraints such as that placed on precipitate overlap, is given in Appendix F. It should be noted, that the condition of no overlap between edge on particles is imposed on the synthetic images to allow for a thickness value complying both with that of Hilliard's mathematical limit [318, 319] (strictly that the foil corresponds exactly to $2\bar{L}_{\mathrm{M}}$) and the assumptions made in the reconstruction method. As a result, whilst a significant increase from this thickness value would inexorably lead to a substantial disparity in the particle number density values of the generated and reconstructed foil, such cases are ignored owing to their non compliance with Hilliard's limit. Similarly, by choosing a high number density and thereby creating packed foils, thinner thickness values are also ignored because of their low statistical probability.

A) Normal/Gaussian Distribution

Although not commonly observed in relation to precipitate sizes, the first test of the new procedure is made with regard to a normal/Gaussian distribution of particle radii. Such a distribution is considered as a base-line test owing to its simplicity and ubiquitous presence (to some degree) in almost all statistical data sets. The probability density of the normal distribution (f_{Norm}) is given in Equation 4.8 where $\bar{r}_{\text{M}}$ is the mean[16] or expectation value of the distribution and σ_r is its standard deviation; the value σ_r^2 indicates the distribution variance or width. From this equation, it is obvious that the position and width of the normal distribution is dependent only on the values of the distribution mean and standard deviation respectively. Consequently, the synthetically generated foils for testing the new image analysis technique were created so as to correspond to distributions with two different values for each of these parameters. The resultant four separate distributions, together with the magnitudes of $\bar{r}_{\text{M}}$ and σ_r used in their generation, are given in Figure 4.22; the corresponding aspect ratio distributions are also presented. Values for the mean particle major radius were chosen to be similar to those observed for γ'' precipitates in the literature [47, 41, 284].

$$f_{\text{Norm}}(x) = \frac{1}{\sigma_r \sqrt{2\pi}} \exp\left(\frac{-\left(x - \bar{r}_{\text{M}}\right)^2}{2\sigma_r^2} \right) \tag{4.8}$$

The reconstructed (output) distributions together with the input distributions (computed from re-classifying the particles defining the distributions in Figure 4.22a and b) are shown in Figures 4.23 and 4.24 respectively. Looking at the plots presented it is immediately apparent that whilst the classification of individual particles according to size recreates a relatively smooth distribution, this is not the case when classifying in terms of aspect ratio. Such a phenomenon is a direct consequence of the consistent class size used in the classification procedure, which, owing to the relationship imposed between precipitate radius and aspect ratio (*q.v* Appendix F), leads to some classes comprising significantly more particles than their adjacent neighbours. In accordance with this fact, therefore, the input and output shapes of these latter distributions are considered useful for illustrative purposes only.

Considering the shape of the input and output particle size distributions in Figures 4.23 and 4.24 it is clear that the reconstruction technique is able to reproduce a very similar distribution to that used to create the foil both in terms of shape and magnitude. Two principle differences between the input and output distributions are, plainly

---

[16] For a normal/Gaussian distribution the value of the mean also corresponds to that of the median and mode

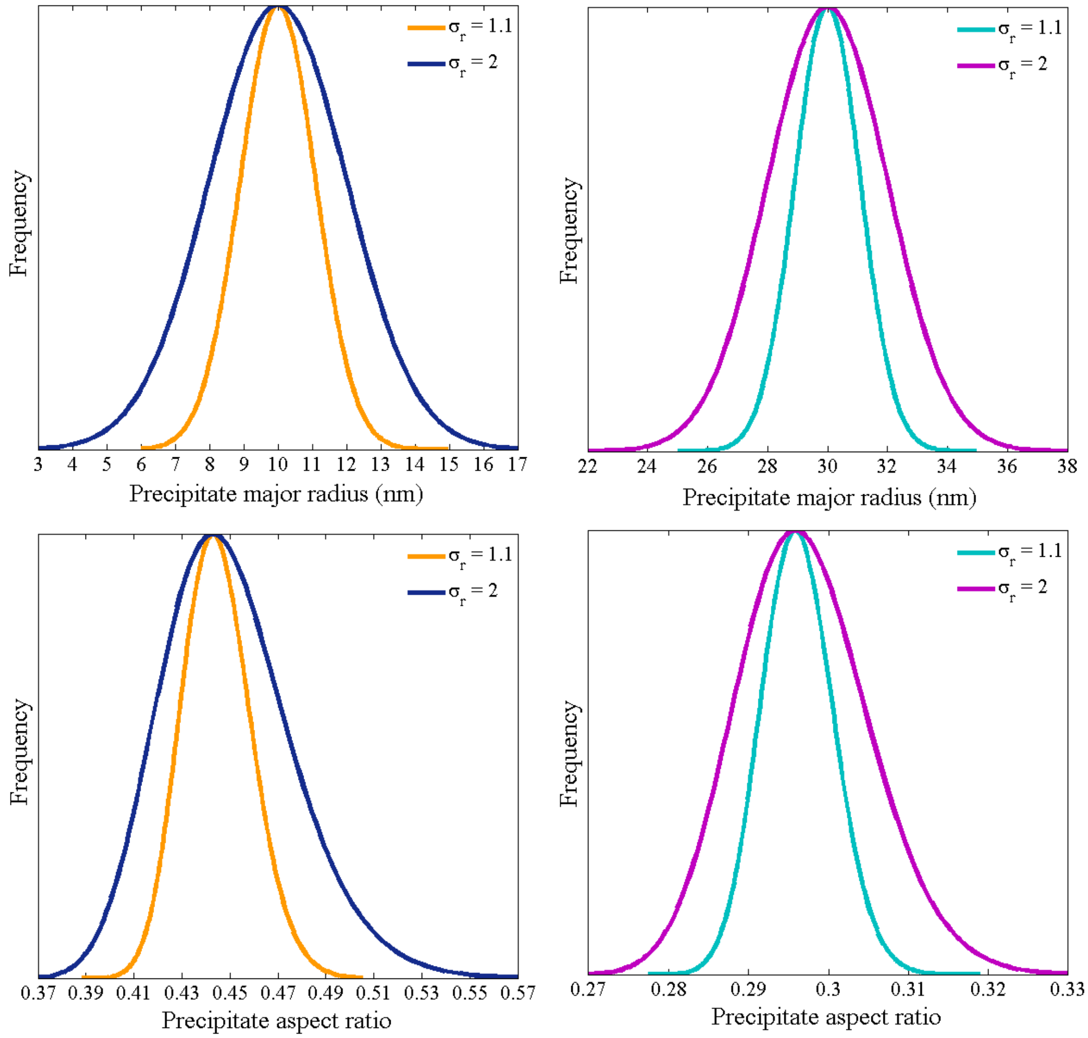

(a) (b)

Figure 4.22: Normal probability distribution functions for precipitate radius corresponding to $\bar{r}_{\mathrm{M}}$ values of: a) 10 and b) 30nm with two different σ_r values (1.1 and 2). Corresponding aspect ratio distributions are also presented.

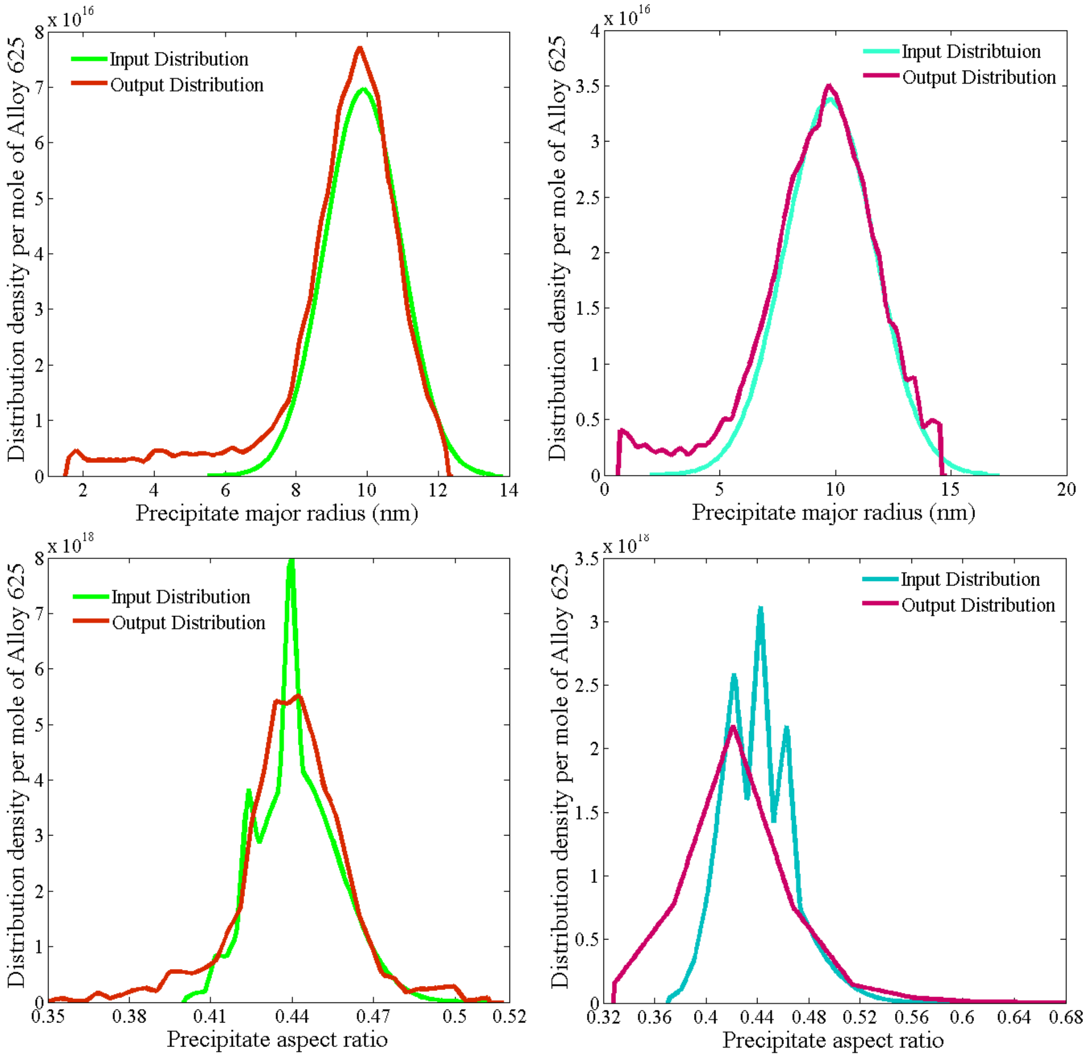

(a) (b)

Figure 4.23: Input and output classified distributions corresponding precipitates contained within a synthetic foil. a) Original normal mathematical distribution $\bar{r}_{\mathrm{M}} = 10$nm, $\sigma_r = 1.1$, b) Original normal mathematical distribution $\bar{r}_{\mathrm{M}} = 10$nm, $\sigma_r = 2$.

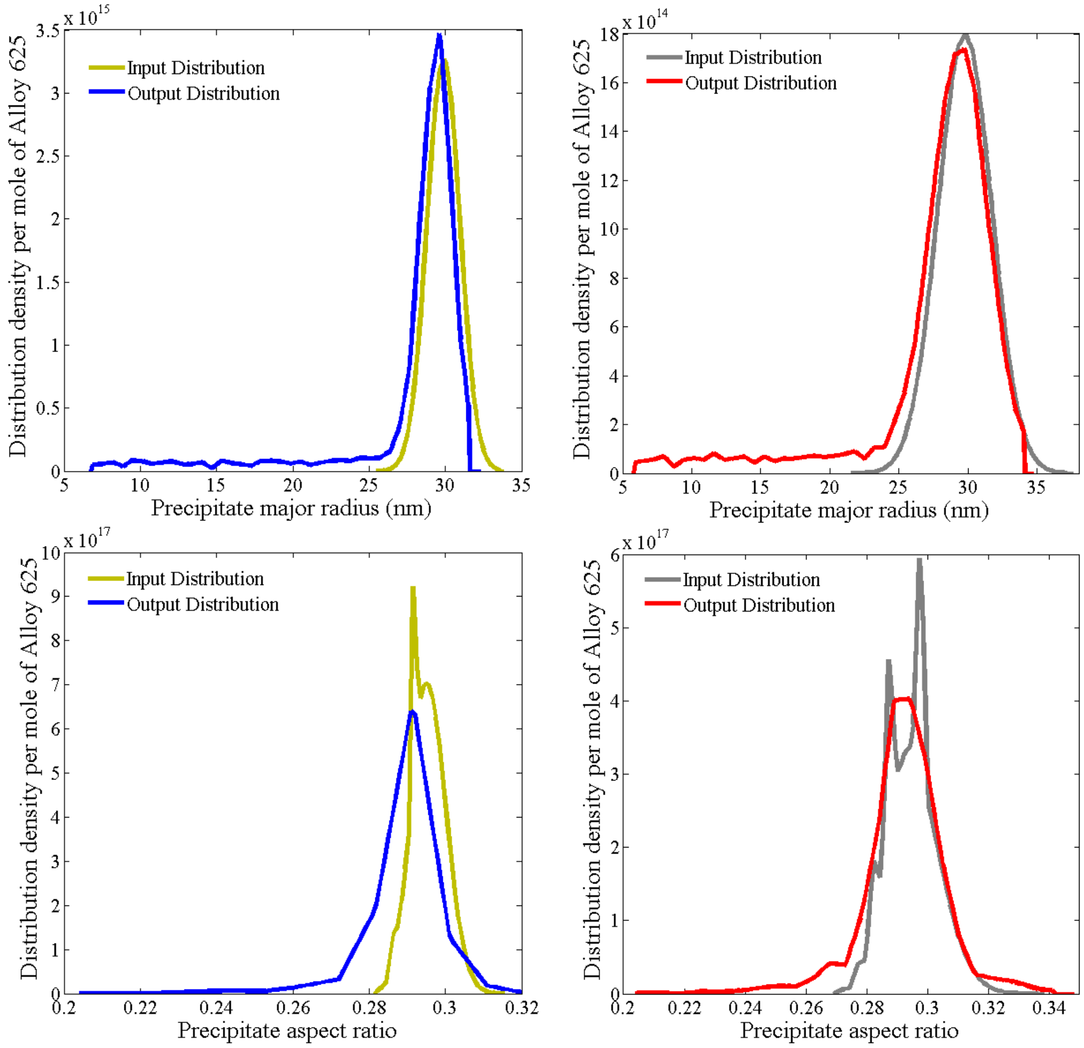

(a) (b)

Figure 4.24: Input and output classified distributions corresponding precipitates contained within a sythtic foil. a) Original normal mathematical distribution $\bar{r}_{\mathrm{M}} = 30$, $\sigma_r = 1.1$, b) Original normal mathematical distribution $\bar{r}_{\mathrm{M}} = 30$nm, $\sigma_r = 2$.

evident, however, namely an elongated distribution tale down to small particle radii and an accompanying overall shift in the distribution towards lower particle sizes. Both of these effects are an direct result of the classification of sectioned precipitates which concomitantly acts to increase the number of smaller particles counted whilst reducing the magnitude of larger particles below the "as batched" quantity. Quantitative comparison between the values of $\bar{r}_{\mathrm{M}}$ input into the foil and that calculated using the reconstruction technique as presented in Table 4.1 indicates the magnitude of the shift in each of the four distributions to be around 6%. With respect to the particle aspect ratios, whilst the illustrative distributions seemingly show a greater disparity in some instances (*e.g.* Figure 4.23b) this phenomenon can again be more appropriately attributed to the classification procedure *viz.* raw data calculated averages (Table 4.1) show an excellent agreement ($< 1\%$ disparity) between the input and output precipitate data.

Table 4.1: Parameters for original normal/Gaussian mathematical distributions and the resultant average particle statistics calculated from the data used in creating the corresponding foil (after descretisation) and output from the reconstruction of the same foil.

Distribution parameters		Constructed foil $\bar{r}_{\mathrm{M}}$			Constructed foil $\bar{\alpha}$		
$\bar{r}_{\mathrm{M}}$	σ_r	Input	Output	Difference	Input	Output	Difference
10	1.1	10.00	9.36	6.40%	0.444	0.442	0.46%
	2.0	10.00	9.43	5.70%	0.445	0.446	0.22%
30	1.1	30.00	28.11	6.30%	0.296	0.294	0.68%
	2.0	30.00	28.10	6.33%	0.296	0.295	0.34%

B) Lifshitz-Slyozov-Wagner (LSW) Distribution

Under the condition of diffusion-controlled growth and coarsening, the classical equation for Ostwald ripening (Equation 1.33) discussed in Section 1.3.4 was shown by Lifshitz *et al.* [136] to predict a particle size (ρ) distribution following Equation 4.9 where $\bar{\rho}$ is the mean particle size. This distribution f_{LSW}, termed an LSW (Lifshitz-Slyozov-Wagner) distribution[17], has been found experimentally to correctly describe some precipitate populations such as $\mathrm{Al_3Sc}$ in binary Al−Sc alloys [330]. Moreover, (and more relevantly here) the fundamental kinetic equations on which it is based (modified to account for particle shape) have been demonstrated by Han *et al.* [2], Devaux *et al.* [47] and Suave *et al.* [41] (*q.v.* Section 1.4.3) to be an apparently good description for γ'' precipitation kinetics in Alloy 718. As a result of these facts, therefore, it is clear that the LSW distribution constitutes a good candidate for validation of the new image analysis technique.

---

[17] The duplicate derivation possible from the equations of Wager [135] led Kahlweit [332] to give each author credit in the name of the overall theory describing Ostwald ripening

$$f_{\mathrm{LSW}} = \frac{4}{9}\rho^{*2}\left(\frac{3}{3+\rho^*}\right)^{\frac{7}{3}}\left(\frac{1.5}{1.5-\rho^*}\right)^{\frac{11}{3}}\exp\left(-\frac{1.5}{1.5-\rho^*}\right) \qquad \rho^* = \frac{\rho}{\bar{\rho}} \qquad \rho^* < 1.5 \tag{4.9}$$

Unlike the normal distribution, inspection of Equation 4.9 shows the LSW distribution to be only dependent on a single variable, namely the average particle radius. Accordingly, only two different LSW distributions, shown in Figure 4.25, corresponding to two different values of $\bar{r}_{\mathrm{M}}$ were used for the construction of synthetic foils.

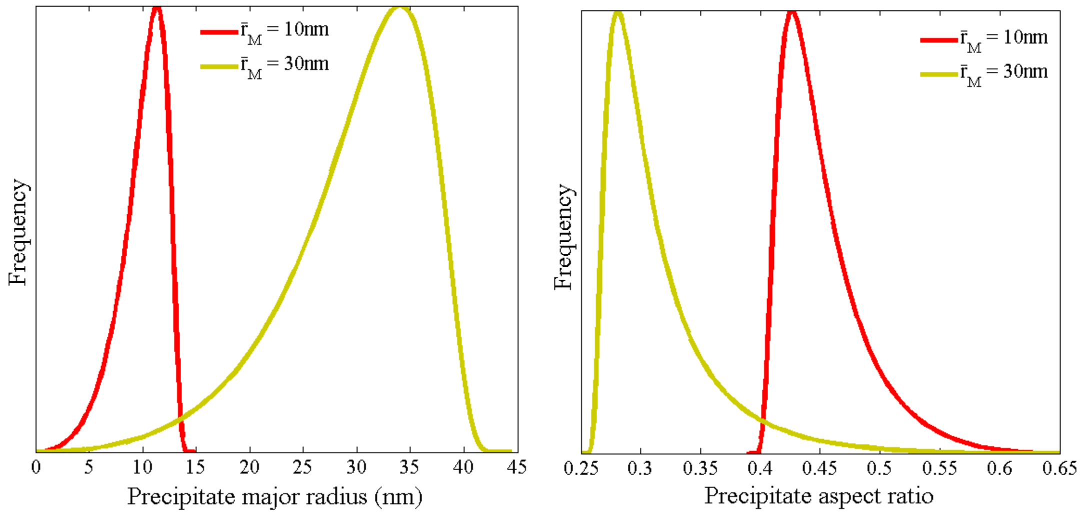

(a) (b)

Figure 4.25: LSW distributions corresponding to particle populations with mean radius values of : a) $\bar{r}_{\mathrm{M}} = 10$, b) $\bar{r}_{\mathrm{M}} = 30$.

Inspection of the classified input and output LSW type distributions corresponding to both of the two input radius values (Figure 4.26) reveals the reconstruction technique to be very successful in replicating the original distribution in both instances. Despite this outcome, however, it is immediately noticeable that there also exists an increase in the frequency of smaller particles, with the phenomenon attributable to the classification of sectioned precipitates in an identical manor to that discussed previously for the normal precipitate distribution. The illustrative aspect ratio distributions show good agreement.

Comparison of the average precipitate major radius of the input and output distributions (listed in Table 4.2) shows the overall effect of the assumptions made in the reconstruction technique to be almost identical to those listed for the normal distributions (Table 4.1) *viz.* a reduction of around 5-6% is calculated in both instances. Contrastingly, with respect to the aspect ratio statistics, the 2.67% increase in $\bar{\alpha}$ obtained for the $\bar{r}_{\mathrm{M}} = 30\,\mathrm{nm}$ LSW distribution is markedly higher. Given its heavily skewed shape, the reason for this latter increase in the disparity of the aspect ratio for the LSW participle distribution is straightforwardly attributable to the presence

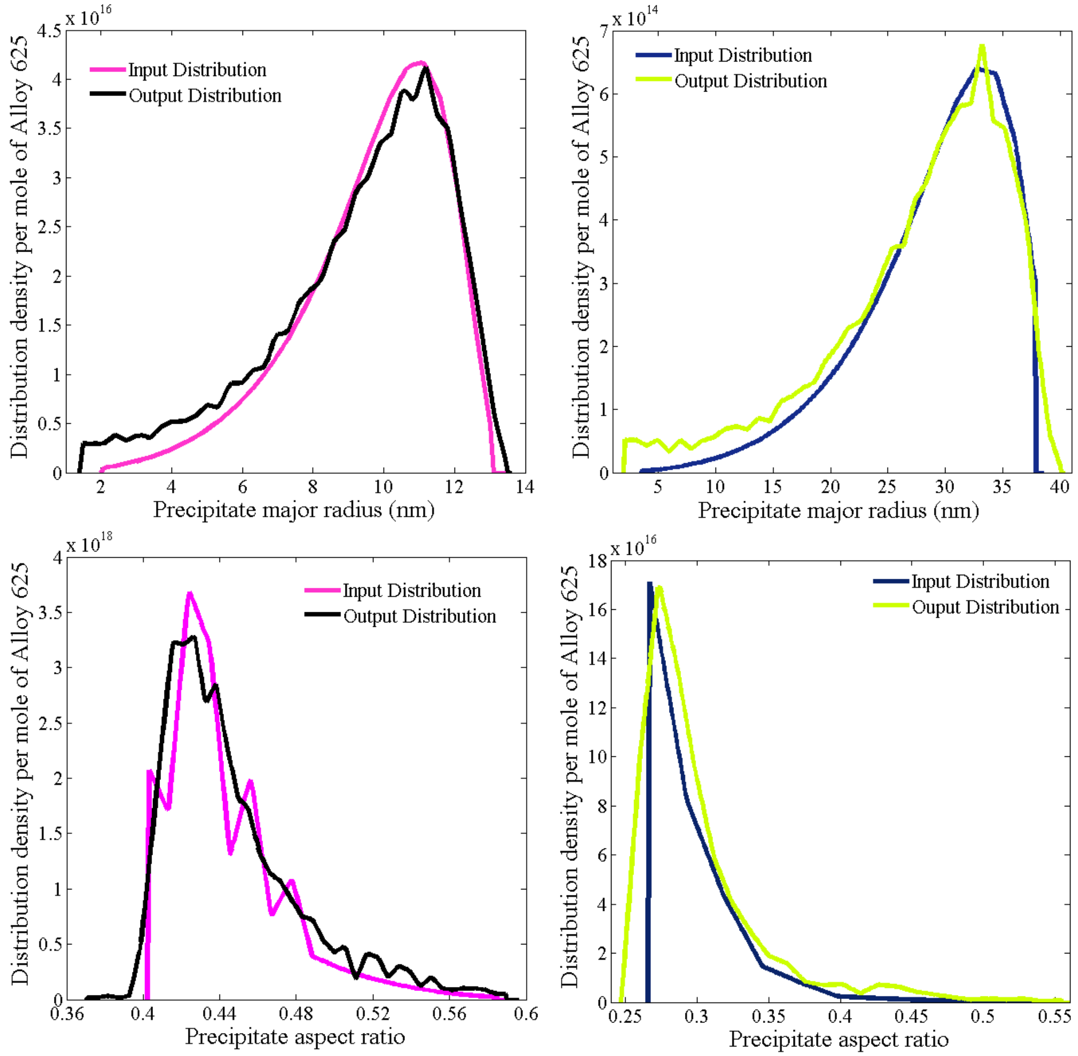

(a) (b)

Figure 4.26: Input and output classified distributions corresponding precipitates contained within a synthetic foil. a) Original LSW mathematical distribution $\bar{r}_{\mathrm{M}} = 10$, b) Original LSW mathematical distribution $\bar{r}_{\mathrm{M}} = 30$.

of high quantities of large particles. That is, the statistical averaging of particle positions along the z axis in the reconstruction method (*q.v.* Section 4.3.2) whilst retaining at least 50% of the particle volume within the foil implicitly leads to larger particles having a lower frequency because of their higher probability of being sectioned. This phenomenon leads to an inevitable skew, irrespective of the input distribution but owing to the significant number of large particles in the LSW distribution it is markedly enhanced in this case. It is this same mechanism which ultimately also leads the observed increased disparity between the input and output particle radius distributions with greater input $\bar{r}_{\mathrm{M}}$ values.

Table 4.2: Parameters for original LSW mathematical distributions and the resultant average particle statistics calculated from the data used in creating the corresponding foil (after descretisation) and output from the reconstruction of the same foil.

Distribution $\bar{r}_{\mathrm{M}}$	Constructed foil $\bar{r}_{\mathrm{M}}$			Constructed foil $\bar{\alpha}$		
	Input	Output	Difference	Input	Output	Difference
10	10.01	9.49	5.00%	0.445	0.449	1.12%
30	30.01	28.18	6.07%	0.300	0.308	2.67%

C) Log-Normal Distribution

The log-normal distribution (*viz.* probability distribution whose natural logarithm values are normally distributed) has been found experimentally to well describe the PSD of precipitates such as vanadium and niobium carbides in low alloyed steels [331]. Furthermore, and specifically with regard to this study, the measurements of the size distribution of γ'' precipitates in Alloy 718 through small angle X-ray scattering carried out by Fisk *et al.* [284] and through thin foil TEM examination by Han *et al.* [2] both indicate a log-normal type distribution to be followed[18]. In light of these facts therefore, although according to classical mathematical nucleation, growth and coarsening descriptions an LSW type distribution is expected for these systems, it is apparent that the evaluation of the results produced by the image analysis technique for a log-normal precipitate distribution constitutes a necessary exercise.

The equation for the log-normal distribution f_{LN} (Equation 4.10) is a modified version of that given for the normal distribution (Equation 4.8) but with the modifications that the variable x is replaced by its logarithm in the exponent and (by the change of variable rule for probability density functions) that an x term is added to the function denominator. The values of $\bar{r}_{\mathrm{M}}$ and σ_r are replaced by those of the normal distribution produced by taking the natural logarithm of the function *i.e.* $\bar{r}_{\mathrm{M}}^{\dagger} = \ln(\bar{r}_{\mathrm{M}})$ and $\sigma_r^{\dagger} = \ln(\sigma_r)$.

$$f_{\mathrm{LN}}(x) = \frac{1}{x\sigma_r^{\dagger}\sqrt{2\pi}}\exp\left(\frac{-\left(\ln(x) - \bar{r}_{\mathrm{M}}^{\dagger}\right)^2}{2\sigma_r^{\dagger 2}}\right), \tag{4.10}$$

The specific log-normal distributions used for the construction of the foils here are given in Figure 4.27. Again in this instance, the two variables of $\bar{r}_{\mathrm{M}}$ and σr were chosen such that four distributions were created *viz.* combinations of two different values of $\bar{r}_{\mathrm{M}}$ and σr were harnessed.

---

[18] Han *et al.* [2] suggested their observance of a log-normal rather than LSW distribution was likely a result of the so called “encounter” phenomenon outlined by Davis *et al.* [1] whereby the coalescence of adjacent particles causes an increased symmetry and broadening of the PSD as compared to the LSW distribution.

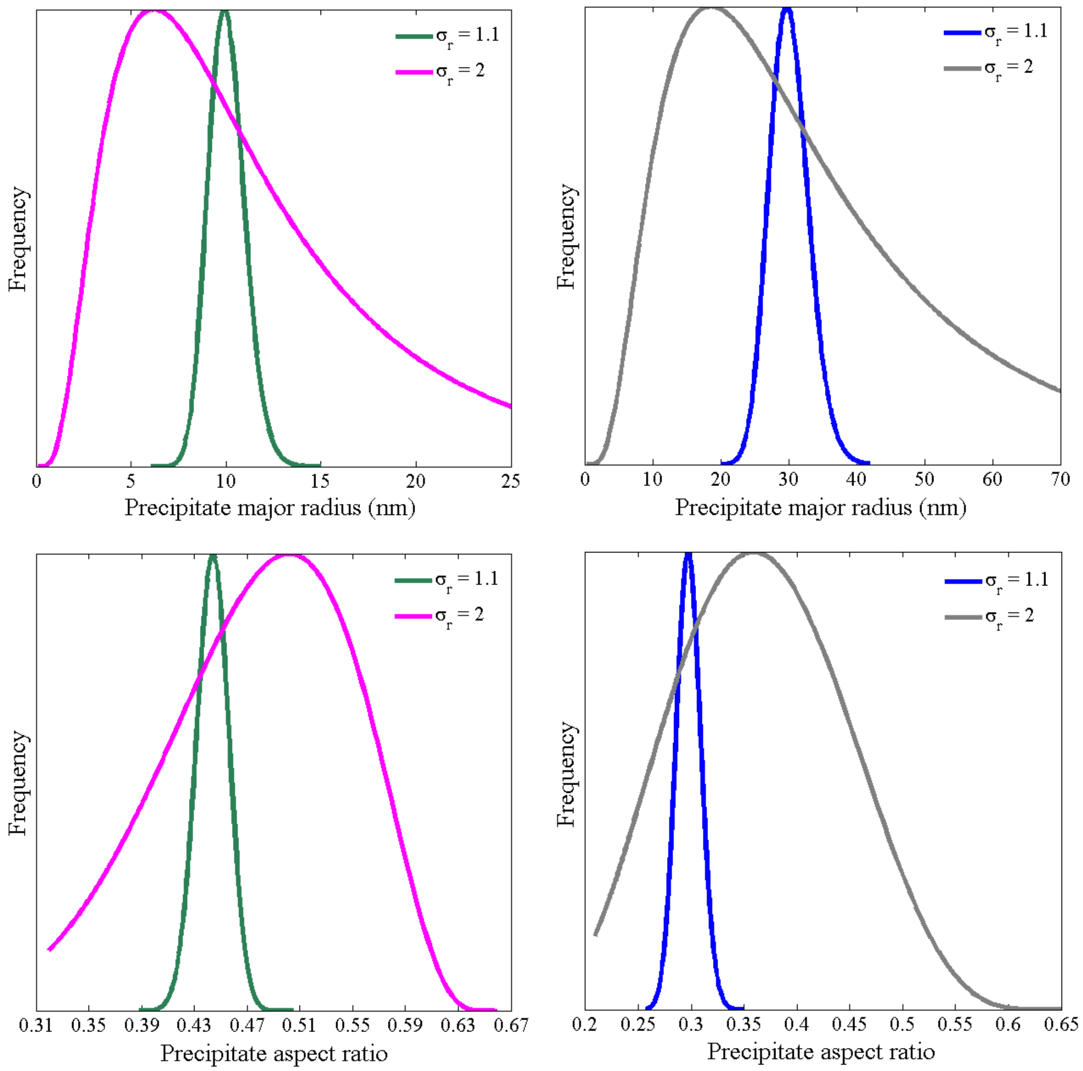

(a) (b)

Figure 4.27: Log-normal probability distribution functions drawn with $\bar{r}_{\mathrm{M}}$ values of: a) 10 and b) 30. Shapes corresponding to two different σ_r values (1 and 2) are indicated.

Once again, the distributions produced from the reconstruction technique can be observed from Figures 4.28 and 4.29 to both comprise the shift towards lower particle radius values and the reciprocal change in the frequency of larger and smaller size particles, discussed for the Normal and LSW distributions previously. Contrastingly in this instance, however, the the classification procedure also produces large peaks in the reconstructed size distribution as shown in Figure 4.29b. The underlying cause for the presence of latter phenomenon in this instance is undoubtedly the wide range of particle sizes present; constraints on the number density of the constructed foil leads to a significant proportion of sectioned precipitates which enhance adjacent classes and, unlike in other distributions, this effect is not “smoothed out” by the classification due to the large distribution width. The only way of limiting this particular effect when using a constant class width is through the use of a smaller number of classes. Nevertheless, in spite of this result is evident from the number density magnitudes and distribution widths that the shape of the distributions produced by the reconstruction technique show a good correlation with those used to produce the foil.

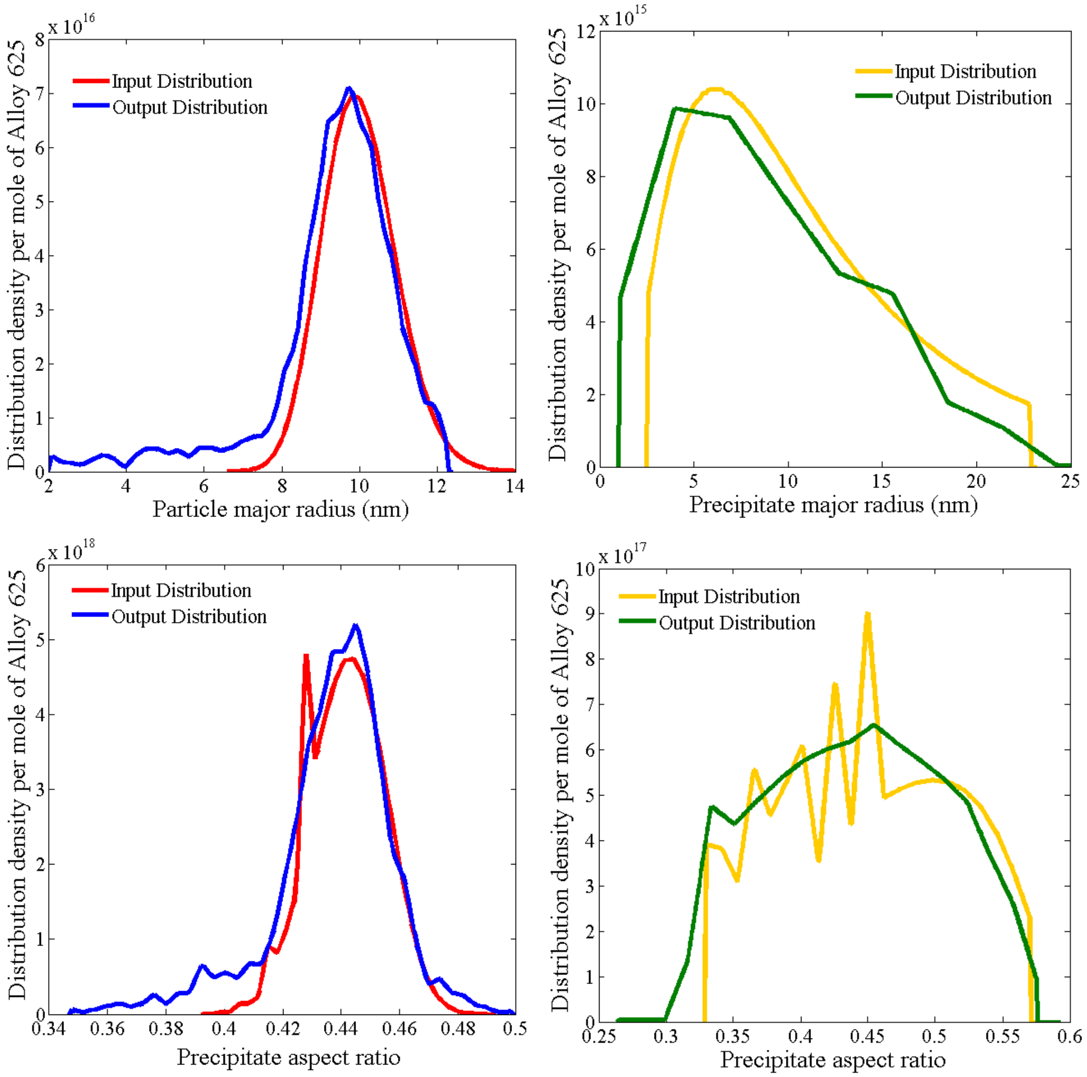

(a) (b)

Figure 4.28: Input and output classified distributions corresponding precipitates contained within a synthetic foil. a) Original log-normal mathematical distribution $\bar{r}_{\mathrm{M}} = 10$nm, $\sigma_r = 1.1$, b) Original log-normal mathematical distribution $\bar{r}_{\mathrm{M}} = 10$nm, $\sigma_r = 2$.

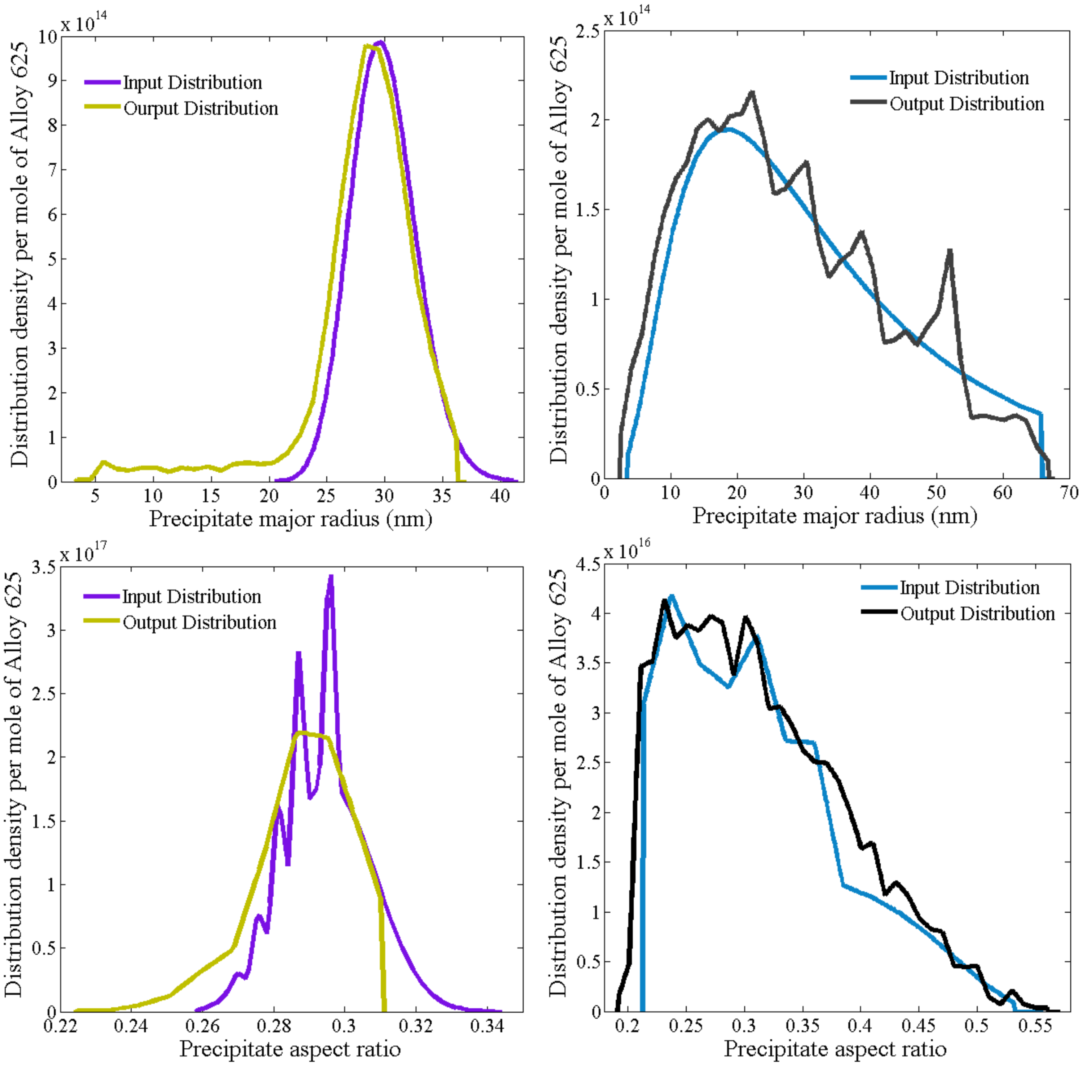

(a) (b)

Figure 4.29: Input and output classified distributions corresponding precipitates contained within a synthetic foil. a) Original log-normal mathematical distribution $\bar{r}_{\mathrm{M}} = 30\mathrm{nm}$, $\sigma_r = 1.1$, b) Original log-normal mathematical distribution $\bar{r}_{\mathrm{M}} = 30\mathrm{nm}$, $\sigma_r = 2$.

As shown in Table 4.3, the average particle statistics calculated from the input and reconstructed particle data indicate that (*cf.* Table 4.2 and Table 4.1) the reconstruction method developed in this research is most successful in replicating the parameters defining a log-normal precipitate population *viz.* the average deviation from the input distribution is lowest in this case. Furthermore, it is also evident that, in direct contrast to the result for the LSW distribution, the discrepancy between the input and output values of $\bar{r}_{\mathrm{M}}$ drops as the overall width of the distribution increases. Such behaviour is observed in this case because of the opposing skew of the log-normal distribution which acts to suppress the effect of the statistical averaging of particle z positions (discussed previously) thanks to the lower relative proportion of the distribution comprised by large precipitates.

Table 4.3: Parameters for original Log-Normal mathematical distributions and the resultant average particle statistics calculated from the data used in creating the corresponding foil (after descretisation) and output from the reconstruction of the same foil.

Distribution parameters		Constructed foil $\bar{r}_{\mathrm{M}}$			Constructed foil $\bar{\alpha}$		
$\bar{r}_{\mathrm{M}}$	σ_r	Input	Output	Difference	Input	Output	Difference
10	1.1	10.05	9.49	5.57%	0.443	0.439	0.90%
	2.0	10.52	10.04	4.56%	0.450	0.449	0.22%
30	1.1	30.13	28.70	4.75%	0.296	0.296	0.00%
	2.0	30.13	28.82	4.35%	0.318	0.319	0.31%

DISCUSSION

Considered in their entirety and with respect to the objectives of this research, the results outlined for each of the mathematical input distributions can be used to prove the validity of the reconstruction method described in this work based on consideration of three key parameters:

Major radius

> Although the classification procedure resulted in the creation of some undulations in the particle size distributions, it is clear that the shape of each of the reconstructed foil distributions closely resembles that used to create the synthetic foils, albeit with an overall shift towards lower precipitate sizes and a concomitant reduction/increase in smaller/larger particles resulting from sectioned particles. Furthermore, the 4-6% difference between the average input and output values for the particle radius constitutes a reasonable error considering the (mandated) rapidity of the technique and its ignorance to sectioned particles.

Aspect ratio

> Comparison between the shapes of input and output aspect ratio distributions was unfortunately inhibited by the undulations introduced by the constant class width classification procedure. Nevertheless, in each instance the overall envelope of both distributions could easily be identified as being similar. Utilising the raw input data and that produced by the reconstruction yields excellent agreement between the average aspect ratios of the two data sets; disparities of $\lessapprox 1\%$ were calculated for all but one LSW data set. The increased success with regard to the reproduction of aspect ratio values versus those of precipitate major radius is likely linked to the much smaller deviation expected in this value as particles are sectioned [321]. Considering the log-normal distributions observed for γ'' precipitates in Alloy 718, the results indicated that any deviation introduced for the aspect ratio will be suppressed.

Number density

> A key variable in the gathering of precise precipitate data is the number density of particles. In this regard, the reconstruction technique is evidenced to be successful from the close matching of the output precipitate distribution density values to those of the input distribution.

Owing to the points outlined it is clear that in regard to the data used the reconstruction method can be considered valid for use in this research; however, results are likely to contain an unavoidable error associated with the underestimation of the precipitate major radius. Moreover, although the magnitude of this error as measured in this research is relatively constant at around 5-6% such a value is subject to change as a result of imperfect and incomplete distribution datasets which are likely to be acquired experimentally. Accordingly, whilst present, no precise error in the magnitude of this value can be produced by the method.

In spite of the previously presented results it must be remembered that the validation performed here is associated with a key caveat with respect to the thickness imposed for the synthetic foil. Specifically, if it is found that Hilliard's mathematical limit [318] does not hold, then the estimations of number density particularly will likely deviate markedly from the true values in the real system.

Chapter 5

Experimental Results

Utilising the experimental techniques described in the previous chapter, data was acquired sequentially according to the flow sheet in Figure 4.1.

§ 5.1 Elemental Analysis

The elemental composition of the material used in this research, measured by ICP-OES, was found to correspond to the values in Table 5.1[1]

Table 5.1: Elemental composition of Alloy 625 measured by ICP-OES.

Element	Ni	Cr	Fe	Mo	Nb	C	Mn	Si	P	S	Al	Ti
wt%	bal.	21.74	2.87	8.58	3.80	0.021	0.20	0.23	< 0.01	0.003	0.12	0.16

§ 5.2 Vickers Hardness

Consistent with strengthening behaviour of the intermetallic precipitate phases γ'' and δ detailed in Sections 1.2.2 and 1.2.3, respectively, the Vickers hardness plots measured from the aged samples (shown in Figure 5.1) allowed one to infer their likely evolution during heat treatment[2]. Explicitly, the dramatic increase in hardness observed at 650°C likely signifies a significant homogeneous precipitation and growth of γ'' precipitates taking place up to at least 1000 hours. Beyond this point, however, a dip in

---

[1] For completeness, the actual certificate produced by Element Materials Technology who supplied the results is presented in Appendix G (results correspond to Sample A).

[2] It should be noted that although the relative trend of the plots is unaffected, the size of error bars in Figure 5.1 was undoubtedly enhanced by the high elasticity of the aged Alloy 625 specimens *viz.* even harnessing a 1kg load and dwell time of 60 seconds, pincushion indents were still observed at these conditions.

the hardness value indicates that the precipitate size distribution had coarsened significantly and/or a transformation to δ-phase had initiated. The amplified nucleation and slower growth rate expected at 600° C (as per the discussion in Section 1.3) for γ'' is inferred to ultimately lead to a hardening in excess of that at 650° C. An accordant but opposite behaviour displayed at higher temperatures is likely also partially a result of the same mechanism, although these latter sets were probably also influenced by a greater δ-phase precipitation.

In addition to the aforementioned features, perhaps the most surprising inference from Figure 5.1 is that in almost all instances, apparently contrary to the relative kinetics which should be experienced, the material aged at 750° C possessed a higher hardness than corresponding samples aged at 700° C. Given the identical pre and post ageing procedures applied to all of the sample sets, the origin of this phenomenon is unclear but it may be that the elevated temperature resulted in the activation of alternative precipitate nucleation (*e.g.* heterogeneous [174, 175]) and growth regimes for γ'' which acted to speed up the hardening rate of the material. On the other hand, an upsurge in the population of δ-phase, whilst detrimental to hardening with respect to γ'', could have sufficiently strengthened the material such that the hardness at shorter ageing times at 750° C was in excess of that at 700° C. Support for this second mechanism is provided by the work of Suave *et al.* [333] who found a similar crossover in their isothermal hardness measurements of samples definitely containing δ-phase precipitates. Finally, although cut from the same bar (depicted in 4.2) it is possible that the grain size of the material used to generate both data sets was markedly different owing to the processing it had received and/or recrystallization during heat treatment. Clearly, as discussed in Section 4.2.5 the potential influence of this latter phenomenon should be identifiable from the detailed analysis of the grain size evolution (Section 5.2.1); however, the two other potential causes necessitate direct investigation measurement of the respective precipitate populations (Section 5.3).

As a corollary to its individual analysis, comparison of Figure 5.1b to the TTT diagram for Alloy 625 can also allude to the type of precipitate phase responsible. Unfortunately, as highlighted in Section 1.4.3, the commonly referenced TTT diagram of Floreen *et al.* (Figure 1.18) is only indicative and highly susceptible to change based on material chemistry meaning evaluation with respect to other diagrams such as those shown in Figure 5.2 is required for validity. To this end Figure 5.3 was generated via overlaying the relevant TTT curves from all three sources on to the Figure 5.1 b.

Comparison of the change in hardness values with all three TTT curve sets in Figure 5.3 enables the conclusion that it is intermetallic precipitates which produce the detected hardening. More specifically, whilst the overlap of the curves means the conditions dominated by γ'' and δ-phase cannot be resolved exactly, the curves provide a strong indication of: 1) γ'' having had an overwhelming impact on the hardness properties and 2) that δ-phase likely existed in many of the samples aged at higher temperatures. Furthermore, as only the γ'' curve envelope produced by Floreen *et al.* corresponds well with the hardening response measured in this research over the full temperature range, the use of Figure 1.18 as common reference for the likely response of an Alloy 625 specimen is suggested to be appropriate from the results gathered here.

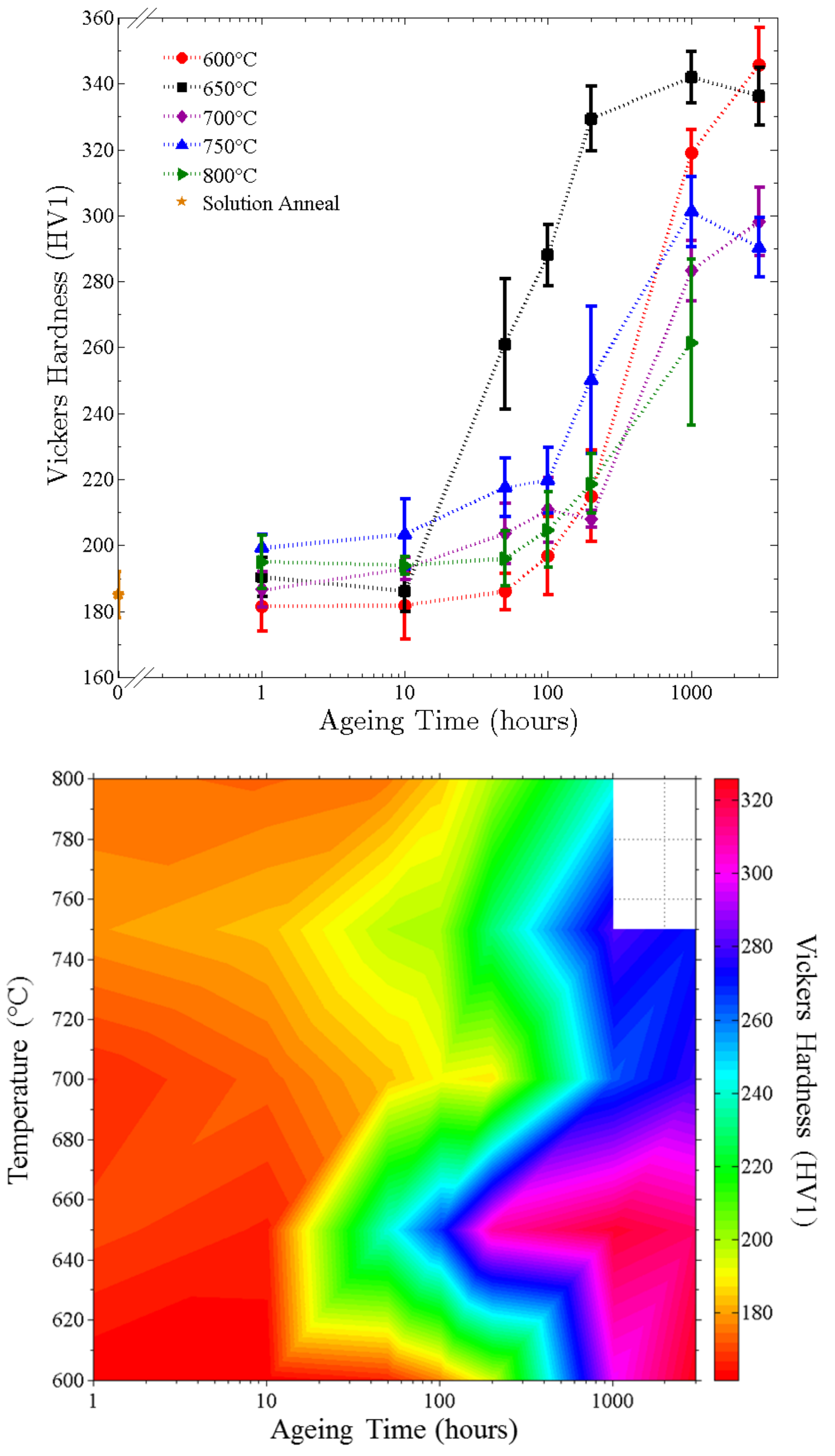

(a)

Figure 5.1: a) Vickers hardness plot and b) Vickers hardness surface generated from measurements made on aged Alloy 625 specimens using a load of 1kg and dwell time of 60 seconds. Error-bars correspond to 1 standard deviation about mean value.

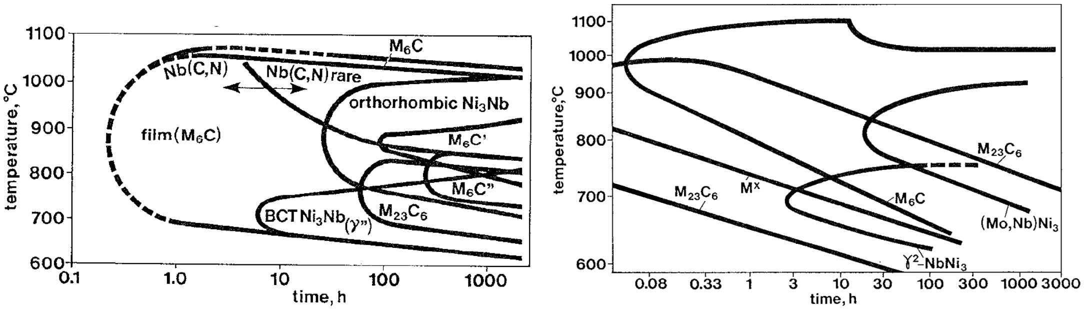

(a) (b)

Figure 5.2: Time-temperature-transformation (TTT) diagrams for Alloy 625 produced by a) Crum *et al.* [37] and b) Schnabel *et al.* [38].

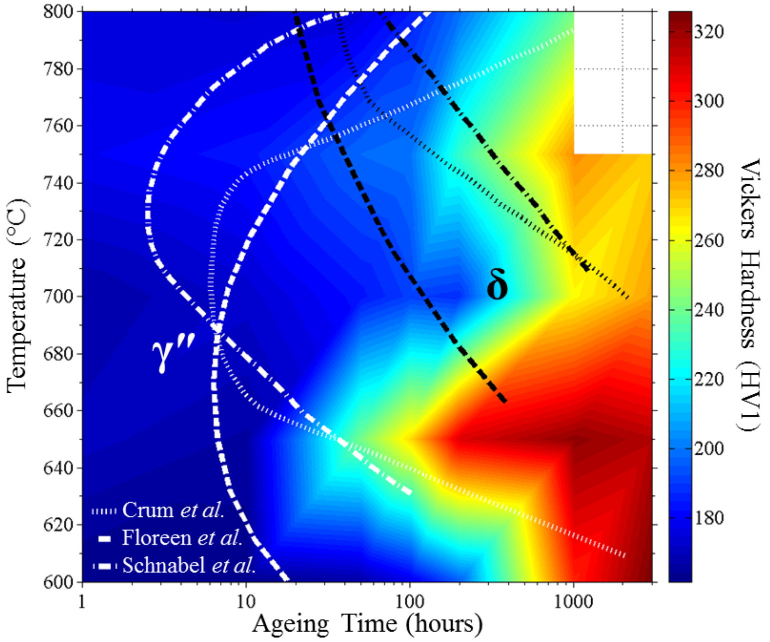

Figure 5.3: Vickers hardness surface generated from measurements made on aged Alloy 625 specimens overlayed with the γ'' and δ-phase TTT curves produced by Floreen *et al.* [23] (Figure 1.18) Crum *et al.* [37] and Schnabel *et al.* [38]. Line colours indicate the precipitate phase type and line dashes the literature source.

5.2.1 Grain Growth

Examples of the methodology outlined in Section 4.2.5 being successful in revealing the grain structure of Alloy 625 samples are presented in Figure 5.4. The different shading and the level of other microstructural features (*e.g.* crystalographic twin boundaries) evident in each image is related to the degree of corrosion experienced by the surface. Accordingly, whilst not specifically determined, the level of darkening most likely derived from the thickness of the oxide layer on the sample surface created by reaction with the highly oxidising etchant *viz.* nickel, for example, can form a number of different dark oxide and hydroxide compounds [334].

All of the statistics gathered from images of successfully etched samples are displayed in Figure 5.5. Missing data points signify an inability of the etch to reveal the grain structure in a particular sample.

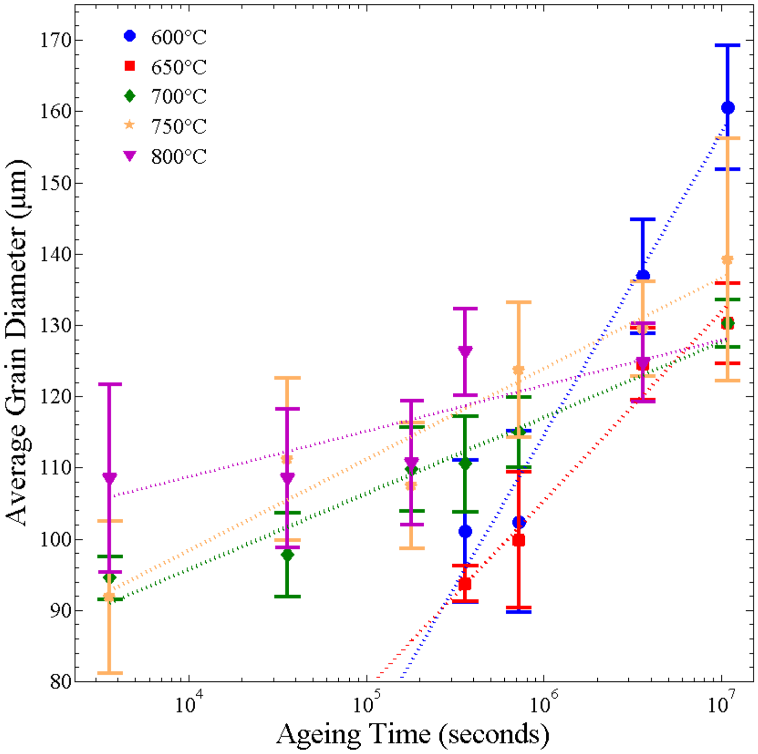

Figure 5.5: Grain diameters measured from aged Alloy 625 specimens. Error-bars correspond to 1 standard deviation about the mean value. Lines of best fit derived from first order polynomial fitting represent the trends interpreted for the grain evolution behaviour.

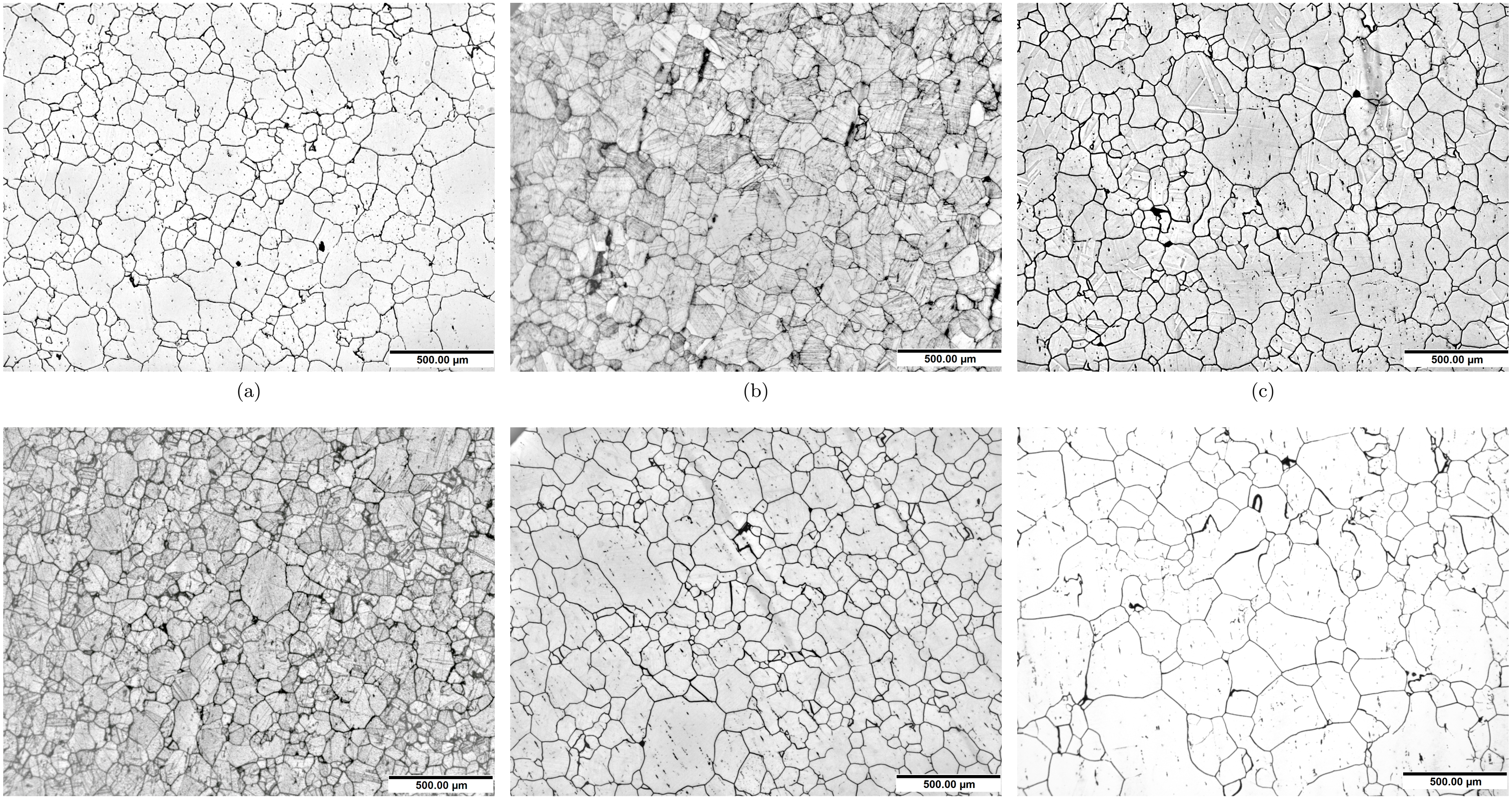

(a) (b) (c)

(d) (e) (f)

Figure 5.4: Images of grains revealed in Alloy 625 samples aged for the following durations and temperatures: a) 10 Hours at 700°C, b) 50 Hours at 700°C, c) 100 Hours at 700°C, d) 200 Hours at 650°C, e) 200 Hours at 700°C, f) 200 Hours at 750°C.

Initial inspection of the isothermal datasets indicates the grain evolution follows a logarithmic growth relationship in each case; all but one of the data points intersect respective linearised fits to the log of the ageing time. If a marked recrystallisation had occurred in any of the samples one would expect a significant downward undulation in one of the grain size trends, the fact that no such trend is present[3], therefore, means it can be reasonably concluded that no recrystallisation event had taken place. Similarly, comparison of the grain sizes of the material aged at 700 °C and 750 °C reveals the latter to possess an almost consistently larger grain size meaning the increased hardness of this data set cannot (from the Hall-Petch relationship [86, 87]) be attributed to a difference in grain size and, consequently, must be precipitate related.

For the sake of completeness it should be pointed out at this point that (whilst the number of data points means their omission is not significantly deleterious to the above conclusion) the little to no preferential attack experience by grain boundaries, compared to the matrix, at the shortest times ($<$ 100 hours) and lowest temperatures ($<$ 700° C) is fundamentally a consequence of sensitisation. That is to say, in accordance with the discussion in Section 1.2.6, samples which had more extensive carbide, specifically $M_{23}C_6$, precipitation (deduced from the TTT curve (Figure 1.18 as those aged at higher temperatures and for longer times) would have comprised boundaries that etch much more readily than those samples which do not. As a result of this observation, it is evident that the HCl-H_2O_2 submersion etch implemented to reveal grain boundaries in this research should be limited in future for use on sensitised samples only. A different, more complicated approach such as electrolytic etching is necessary for samples approaching the solution annealed state.

In addition to the aforementioned point it is further worth stating that the apparently inhomogeneous grain structure across all samples imaged in Figure 5.4 is attributed to the location, displayed in Figure 4.2a, of the material in the original forging. Specifically, numerous researchers have identified the deformation temperature to have a critical influence on the recrystallization behaviour of Alloy 625 [335, 336, 337, 338], leading to potential significant disparities in the recrystallisation fraction throughout the thickness of products because of thermal gradients [187]. It is, therefore, likely that the lower temperature experienced by the surface adjacent region of the Alloy 625 forging ultimately analysed in this work fell below (owing to convective/radiative cooling, conduction with the forging press and lower adiabatic heating) that which would have been sufficient (depending on the strain rate) to ensure a uniform recrystallisation.

Whilst the above discussion represents a sufficient level of analysis of grain growth kinetics for this research, the lack of literature studies regarding the isothermal grain growth behaviour of Alloy 625, particularly in the temperature range considered here, means additional analysis does constitute a worthwhile scientific exercise. In this regard, therefore, a more detailed analysis of the grain growth behaviour measured for alloy Alloy 625 is presented in a recent publication [339].

---

[3] The good agreement in the evolution behaviour between the shortest and longest aged material at 800 °C indicates the data point at 100 hours is most appropriately considered as an outlier resulting from a slightly different initial grain size.

5.2.2 Sample Selection

Utilising the conclusion that change in the hardness of the Alloy 625 material analysed in this research was almost entirely attributable to the evolution of either γ'' or δ-phase, it is clear that one should have been able make the necessary (*q.v.* Section 4.2.6) truncation of the sample matrix to those only likely to contain precipitates through analysis of the hardness magnitude of each sample relative to that measured for solution annealed material. However, owing to the strengthening behaviour of the precipitate phases, the implementation of such an approach was deemed as valid only if the hardness of samples was found during nucleation and growth to consistently increase; inspection of Figure 5.1a (taking uncertainties into account) highlights this not to be true. Furthermore, the seemingly self (rather than universally) consistent behaviour of the isothermal hardness value trends, as indicated by the similar absolute change between all points at 1-10 hours despite their having different magnitudes, meant the application of an absolute threshold for sample selection was considered specious.

In light of the aforementioned dilemma, the most feasible methodology for sample selection is that of a relative comparison between the values of each isothermal measurement whereby samples are chosen based on an evident increase in hardness over the shortest aged material. Accordingly, the samples selected to be examined by electron microscopy in this research were identified based on Figure 5.6 which shows the normalised/proportional value of the lower bound of the data points in Figure 5.1a to the upper bound of the 1 hour aged sample in the same isothermal temperature set. Samples with a normalised value greater than unity in Figure 5.6 were selected for examination thus forming the matrix displayed in Table 5.2.

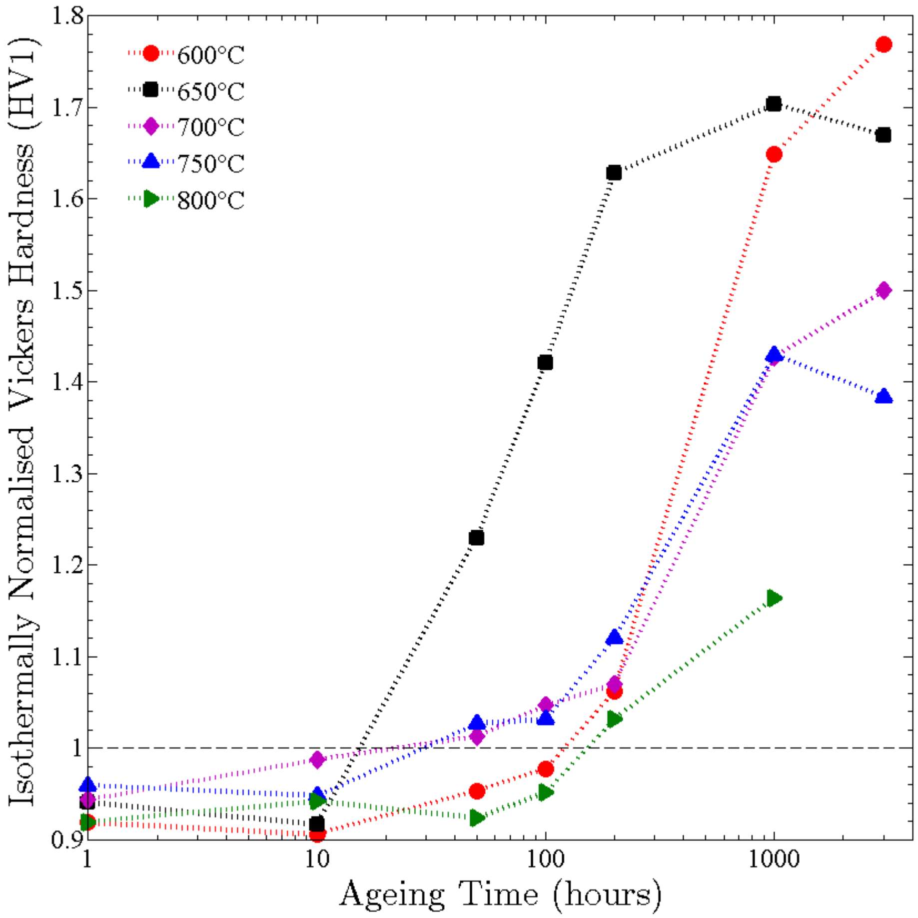

Figure 5.6: Lower bound of the Vickers hardness data presented in Figure 5.1a normalised to upper bound of the value at 1 hour in the same isothermal set.

Table 5.2: Matrix of the Alloy 625 aged specimens selected for electron microscopy based on Figure 5.6.

		Ageing Time (hours)						
		1	10	50	100	200	1000	3000
Temperature (°C)	600	-	-	-	-	✓	✓	✓
	650	-	-	✓	✓	✓	✓	✓
	700	-	-	✓	✓	✓	✓	✓
	750	-	-	✓	✓	✓	✓	✓
	800	-	-	-	-	✓	✓	N/A

Whilst strictly the procedure just outlined should have stood for the purposes of this research, given the discrepancy in the grain size of the sample aged at 800°C for 100 hours (discussed in the previous section) and the influence this may have had on the hardness results, to avoid the potential loss of useful data it was decided to append the sample selection matrix to include this sample as well (Table 5.3).

Table 5.3: Appended (red) matrix of the Alloy 625 aged specimens selected for electron microscopy.

		Ageing Time (hours)						
		1	10	50	100	200	1000	3000
Temperature (°C)	600	-	-	-	-	✓	✓	✓
	650	-	-	✓	✓	✓	✓	✓
	700	-	-	✓	✓	✓	✓	✓
	750	-	-	✓	✓	✓	✓	✓
	800	-	-	-	✓	✓	✓	N/A

§ 5.3 Electron Microscopy

The number and type of images acquired from each sample subjected to electron microscopy (*q.v.* Table 5.3) was decided based on the joint requirements of identifying accurately the exact microstructural evolution occurring within each sample, and gaining sufficient statistics on any homogeneous γ'' precipitates which were present. Accordingly, so as to ensure statistical validity, rather than a set number of images, a simple minimum requirement of the imaging of 100 precipitates was imposed founded on the conditions: 1) That the image set covered as larger sample area as possible (restricted by crystallographic orientation) and 2) As many precipitates as possible were captured in an individual image whilst maintaining resolution (restricted by optics, principally magnification). Finally, owing to the limited range of phases possible, diffraction patterns were only to be taken in instances where it was feasible to directly confirm the phases present (*i.e.* where the grain containing the phase could be orientated in the correct way) but at least one pattern was required for each image in which γ'' was detected in each isochronal set.

Supplementary to the aforementioned examination of aged samples, images and diffraction patterns were also produced from solution annealed material to act as a check on the success of the heat treatment in obtaining the desired homogeneous (*i.e.* precipitate and defect free) microstructure discussed in Section 4.2.3. Furthermore, it should be pointed out that the images ultimately presented in this research and harnessed for the model were subject to some processing, specifically the alteration of the lighting curve in order enhance contrast and suppress non-uniform illumination resulting from factors such as foil thickness/bend, objective aperture position and sample tilt.

5.3.1 MICROGRAPHS AND γ'' DISTRIBUTIONS

Though a number of images were captured from each sample, to prevent an unnecessarily verbose analysis, only representative images and diffraction patterns taken from the each of the material samples and, more broadly, isothermal data sets investigated in this research are presented and discussed below. That is, owing to their importance to the precipitation model at the centre of this research, attention is primarily focused on the precipitate size and aspect ratio distributions which comprise statistics produced from all the relevant images obtained at each condition (calculated using the techniques outlined in Section 4.3.2).

SOLUTION ANNEAL

Micrographs and diffraction patterns captured from material subjected to the anneal treatment of 30 minutes at 1150°C implemented in this research are displayed in Figure 5.7. The clean (precipitate free) matrix and grain boundaries captured in both the dark-field (DF) and bright-field (BF) images indicate the treatment to be successful in terms of removing any prior precipitate microstructure, a result which is supported by the lack of secondary phase reflections in the corresponding electron diffraction pattern[4]. Contrastingly, it is also evident from each of the images that the solution annealed microstructure retains a number of dislocations either from prior treatment or induced by quenching from the annealing temperature.

Comparing the acquired measurements to the assumptions made in the model derivation (detailed at the start of Chapter 2) and thereby the creation of the experimental program in this research (Section 3.3.2), it is obvious that whilst the first assumption of a solution annealed, homogeneously mixed starting condition for the alloy is strictly valid the second regarding the complete elimination of intragranular nucleation sites is not. *Prima facie* such a lack of compliance for the nucleation site distribution with the model assumptions apparently constitutes a fatal flaw; however, considering the work of Shankar *et al.* [10] and Sundararaman *et al.* [39] this transpires not to be the case: Specifically, both sets of researchers observed homogeneous precipitation of γ'' when ageing (at 650°C) solution annealed Alloy 625 and Alloy 718 material, respectively, which happened to contain an almost identical dislocation microstructure. Similarly, whilst the existence of pre-exiting primary carbides is likely in the alloy given analogous literature investigations (despite their not being directly detected in this research), their presence is not considered significant as they have been shown not to be detrimental to homogeneous γ'' nucleation and growth [10, 39, 175] in either Alloy 625 or Alloy 718.

---

[4] Owing to the orientation relationships of the expected precipitate phases in Alloy 625 with the matrix discussed in Section 1.4.3 each would produce distinguishable (*i.e.* non-overlapping) diffraction spots in an pattern captured along an [001] matrix axis.

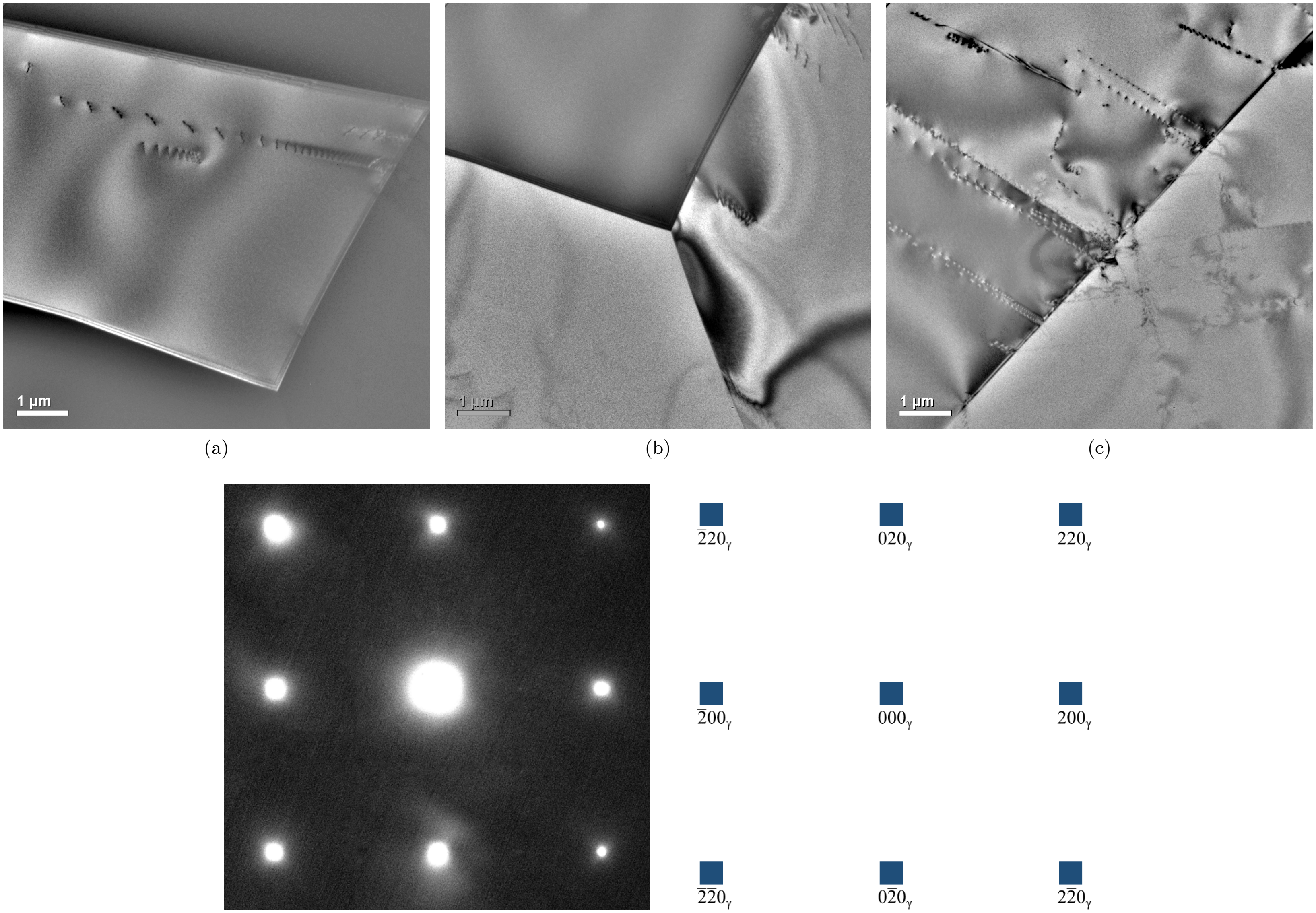

(a) (b) (c)

(d) (e)

Figure 5.7: a) Dark-field and b-c) Bright-field images of [001] orientated grains of Alloy 625 annealed at 1150 °C for 30 minutes, adjacent to grain boundaries. d) [001] oriented crystallographic diffraction pattern produced by the Alloy 625 matrix. e) Key adapted from Sundararaman *et al.* [39] identifying the diffraction spots as corresponding to the Alloy 625 matrix.

600° C

Analysis of the micrographs captured from samples aged for different durations at 600° C (examples of which are shown in Figure 5.8) produces the conclusion of an extensive, purely homogeneous and intragranular precipitation of γ'' (identified from diffraction pattern in Figure 5.8d) having taken place. In addition, collectively the images reveal a considerable growth and coarsening of the precipitate population with time, as well as the presence of no competitive phases such as δ, both of which are results consistent with the continuous hardening evidenced for the same samples in Section 5.2.

Considering the conditions individually, owing to the agreement of the images captured from material aged at 600° C for 1000 and 3000 hours with the criteria for the analysis method outlined in Section 4.3.2 (*i.e.* their containing a high number of non-overlapping, homogeneously distributed precipitates) the particle size (PSD) and aspect ratio (ARD) distributions for γ'' precipitates at both conditions were calculated as shown in Figure 5.9. In contrast, precipitates imaged in material aged for 200 hours were precluded from such analysis owing to their small size/thickness (Figure 5.8a) and the resultant inability to accurately distinguish the size and shape of a representative number of particles.

Inspection of the γ'' PSDs and ARDs in Figures 5.9a and b yields the conclusion that, ignoring the undulations created from the classification procedure, each follows a log-normal behaviour (*q.v.* Section 4.3.3) in agreement with the separate measurements of Han *et al.* [2], Sundararaman *et al.* [39] and Fisk *et al.* [284] of γ'' precipitates in Alloy 718. As a result of this fact, therefore, in harmony with the discussions of Fisk *et al.* and Han *et al.* [2], both of the distributions were interpreted as evidencing the "encounter" mechanism defined by Davies *et al.* [1] between precipitates within the material. That is to say, the inevitable overlap of adjacent precipitate diffusion fields caused by the large volume fraction of precipitate particles within the samples, resulted not only in the phenomenon of precipitate coarsening (*q.v.* Section 1.3.4) taking place during ageing, but also in particle coalescence. As described by Davies *et al.* [1], this second mechanism of particle growth/coarsening is much more rapid and, consequently, leads to a broader, more symmetrical PSD compared to that predicted by classical (LSW) growth and coarsening theories.

In addition to the log-normal type skewing of the PSD, direct evidence for the "encounter" mechanism from precipitate micrographs was presented by Han *et al.* [2] through the identification of particles in casual contact, specifically those γ'' precipitates seemingly conjoined along the major radius forming a "neck". Accordingly, although such particles were separated in the image analysis here (meaning they would have little impact on the shape of distribution), the presence of "necked" γ'' precipitates in Alloy 625 (as indicated in Figure 5.8c) provides further support of the mechanism occurring in this system. The effect of "encounter" (skew) remained within the gathered experimental data/PSD as precipitates existing after a complete merger cannot be distinguished, by the image analysis developed in this research, from those resulting purely from diffusional growth .

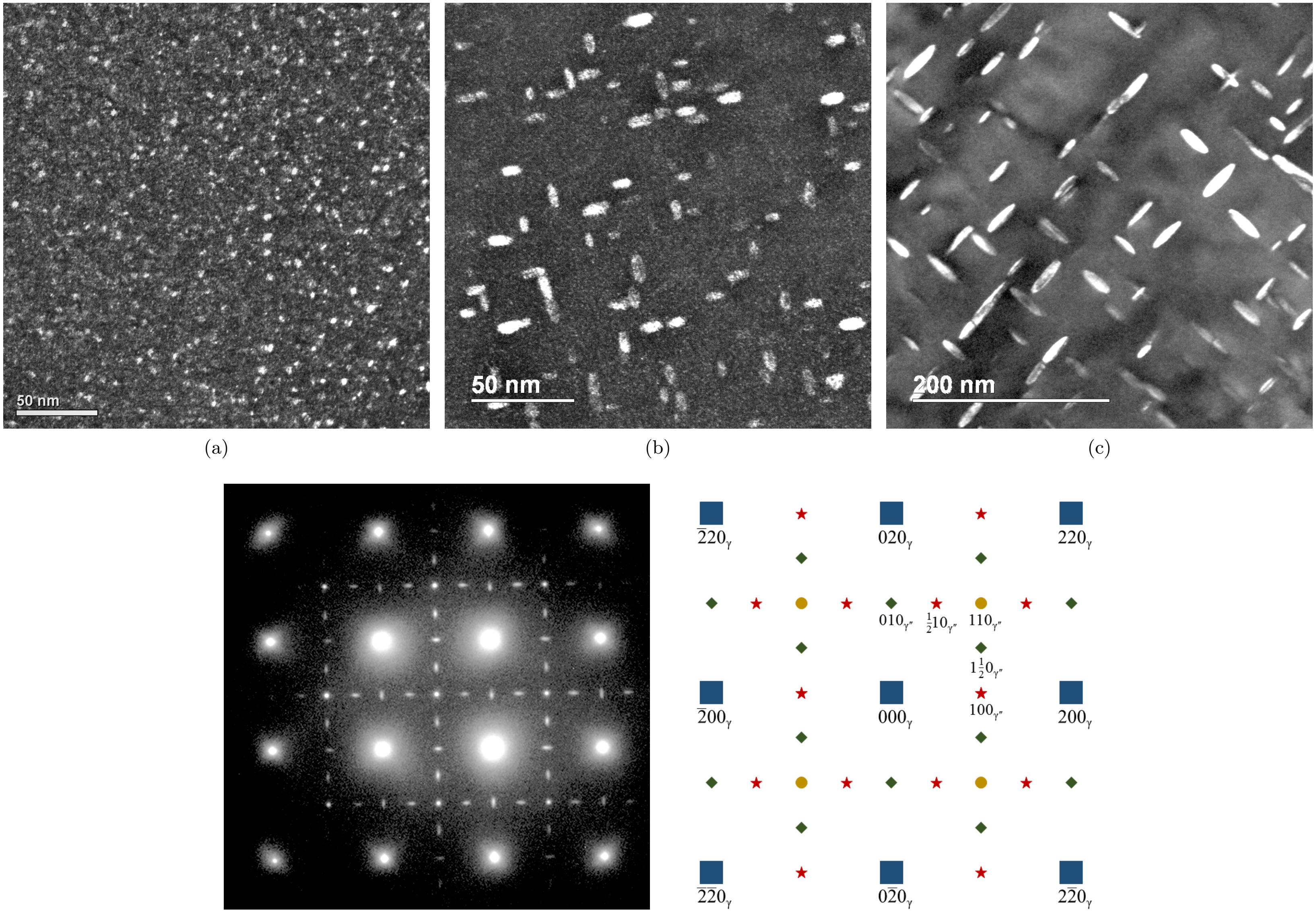

(a) (b) (c)

(d) (e)

Figure 5.8: γ'' precipitates imaged (dark-field) along an [001] crystallographic orientation in samples of Alloy 625 aged at 600 °C for a) 200 hours, b) 1000 hours and c) 3000 hours. d-e) Diffraction pattern and key adapted from Sundararaman *et al.* [39] identifying the phase as γ''; the streaked spots correspond to the two edge-on variants [40].

In view of the apparent confirmation of the "encounter" mechanism operating with respect to γ'' precipitates in Alloy 625 by the results presented in Figures 5.8 and 5.9, as an interesting aside it is curious to note the apparent successful use by Suave *et al.* [41] Devaux *et al.* [47] and Han *et al.* [2] of the modified (*cf.* Equation 1.33) classical growth equation (Equation 5.1 where all symbols have their predefined meanings) in predicting statistics such as the average precipitate size discussed in Sections 1.4.3 and 4.3.3: The formalism harnessed in each instance was that derived by Boyd *et al.* [340] who found the same parameters for plate like θ'' and θ' precipitates in Al-Cu alloys were well matched to that of a classical LSW distribution. However, direct comparison with the experimentally measured distribution analysed by Boyd *et al.* [340] showed a large discrepancy, specifically with the latter exhibiting key characteristics of a system where the "encounter" mechanism is operating. As a result of this outcome, it is clear that, although the ability[5] to analyse the results obtained by all three researchers with respect to purely classical mathematical descriptions of growth and coarsening was claimed as evidence of agreement between the evolution of the respective precipitate systems and the LSW formalism, this conclusion is not credible. In this regard, a justifiable statement of correspondence of the distribution shape with LSW based calculations would only be possible in each instance through a modification which incorporates the effect of "encounter" (*i.e.* the influence of high precipitate volume fraction) such as that implemented in either the Lifshitz-Slyozov-Encounter-Modified (LSEM) formalism of Davies *et al.* [1] or the Modified-Lifshitz-Slyozov-Wagner (MLSW) formalism of Ardell *et al.* [341].

$$\bar{r}_{\mathrm{M}}^{3}(t) - \bar{r}_{\mathrm{M}}^{3}(0) = \frac{128 D \zeta V_{\mathrm{M}} X_{\gamma}^{\mathrm{e}} t}{9 \alpha \pi R T} \tag{5.1}$$

Finally with reference to the micrographs obtained from material aged at 600 °C, it is worth commenting that the method used to eliminate samples from examination thorough analysis of their relative Vickers hardness (*q.v.* Section 5.2.2) was accurate owing to the inability to analyse precipitates formed in material aged for 200 hours *viz.* precipitate kinetics dictates that any γ'' precipitation which may exist in the samples aged for shorter than this duration would be be too small to gain useful statistics. Moreover, consistent with Section 4.3.3, the observation of homogeneously nucleated particles comprising a log-normal type distribution means that: Firstly, the utilisation of the outlined analysis method forγ'' precipitates is valid and, secondly, that the uncertainty from the reconstruction cannot be reasonably or accurately quantified and is, therefore, justifiable to ignore.

---

[5] Fits are made to measurements of precipitate size evolution and correspondence can be claimed owing to uncertainties or low amplitude variations.

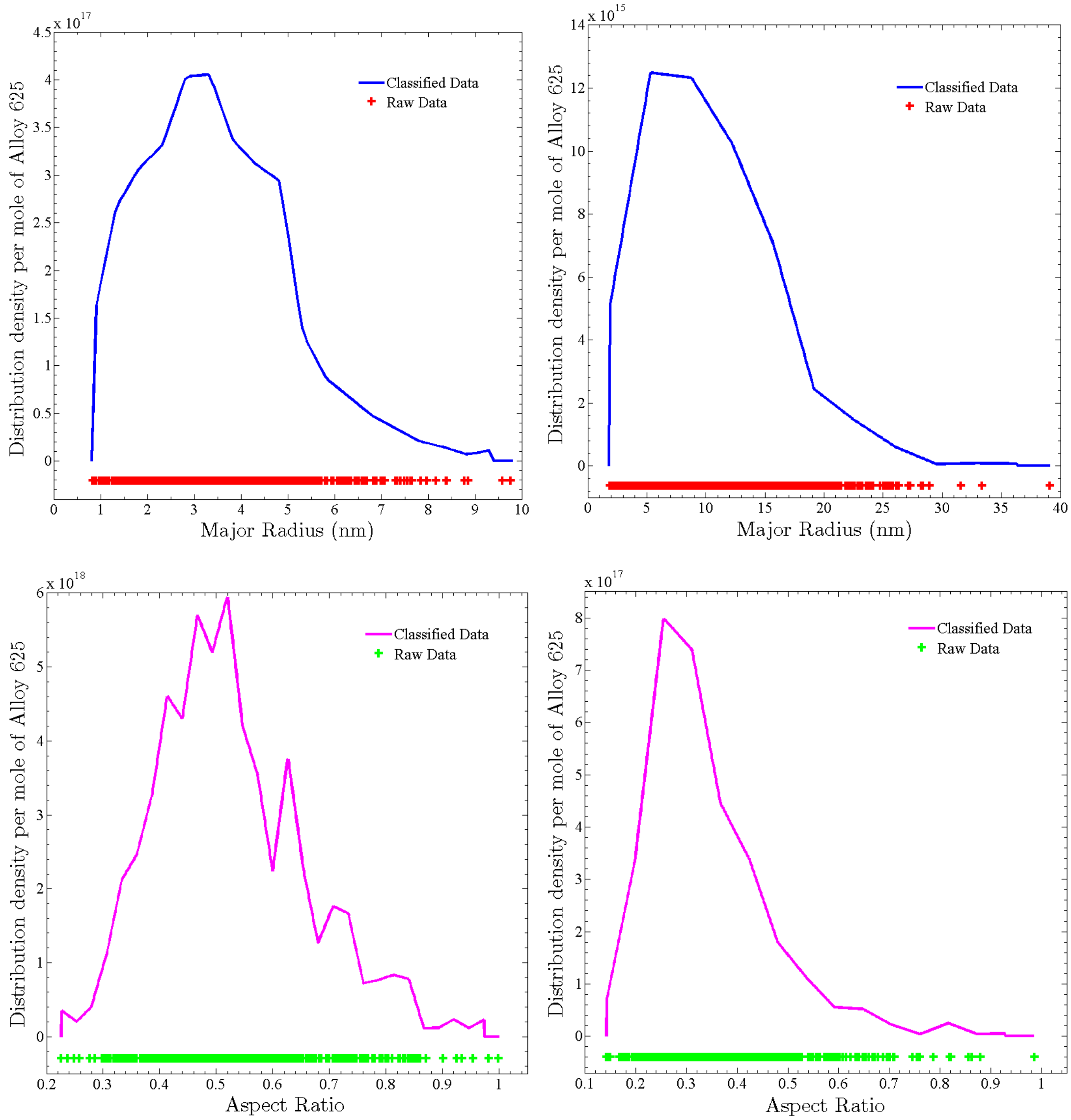

(a) (b)

Figure 5.9: Particle size and aspect ratio distributions created from measurements of precipitates in samples of Alloy 625 aged at 600 °C for a) 1000 hours and b) 3000 hours. Each "raw data" point corresponds to one precipitate.

650°C

Comparison of the images (Figure 5.10) and distributions (Figure 5.11) of γ'' precipitates produced in samples of solution annealed Alloy 625 aged at 650°C with those, discussed previously, in ageings at 600°C immediately allows one to deduce not only the presence of a similar, large homogeneous γ'' precipitate population at this temperature, but one which evolved (grew and coarsened) at much faster rate. Likewise, the log-normal shape of the envelope of almost all the population curves in Figure 5.11 simultaneously validates the use of the analysis method (by the same reasoning outlined with respect to the ageings at 600°C) and also enables the conclusion of "encounter" taking place in this population owing to the high precipitate volume fraction. In fact, seemingly visual examples of "encounter" are also readily discerned in Figures 5.10d and Figures 5.10e. Despite these outcomes, however, it is evident from Figure 5.11 that many of the distributions produced from the images of 650°C aged material contrast sharply with those in Figure 5.9, most particularly in regards to the presence of non-negligible undulations; the PSD for the precipitate population at 100 hours of ageing at 650°C (Figure 5.11b) has particularly large peaks and troughs.

Unfortunately, given that the precipitate population should plainly be smooth/continuous in all instances and, separately, the fact that each of the images complied with the requirements of the image analysis method, the reason for the PSD/ARD behaviour evidenced in Figure 5.11 is not obvious. Still, looking at the relative quantities of precipitates measured (indicated by the raw data plots) it is reasonable to presume this as the probable cause. In other words, even with the number of particles measured being over 150, the relative width of the distributions defining the γ'' populations at 100 hours and 1000 hours of ageing at 650°C means this wasn't sufficient to fully describe the PSD and/or ARD shape. Furthermore, as alluded to in Section 4.3.2, the requirement for a minimum of just one particle per class in the classification procedure facilitated the creation of spiky distributions (because of the narrow class widths) and, consequently, acted to compound any undulation introduced by particles "absent" in the experimental data set. In light of these facts, whilst striking, the outcome of the acquisition of such discontinuous distributions on parameters such as the average particle size and aspect ratio can be concluded as minimal as the omission of precipitates would have been purely random (normally distributed) over all sizes (as evidenced by the randomness of the undulations themselves). In other words, a statistically significant data set covering the entire distribution width would have led to the calculation of parameters with the same magnitude as the continuous distribution.

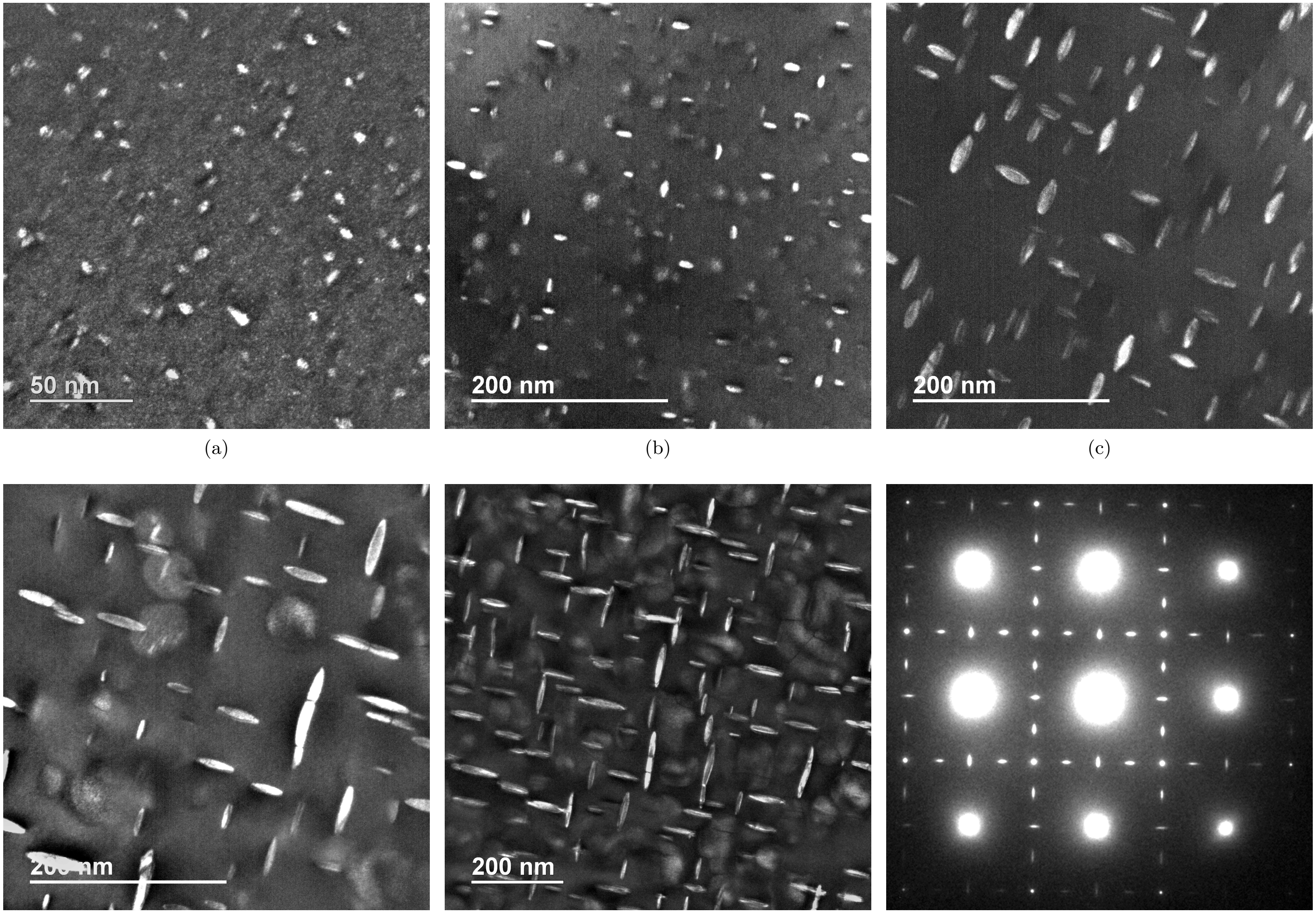

(a) (b) (c)

(d) (e) (f)

Figure 5.10: γ'' precipitates imaged along an [001] crystallographic orientation in samples of Alloy 625 aged at 650 °C for a) 50 hours, b) 100 hours, c) 200 hours, d) 1000 hours and e) 3000 hours. A diffraction pattern identifying the phase as γ'' is displayed in d); the streaked spots correspond to the two edge-on variants [40].

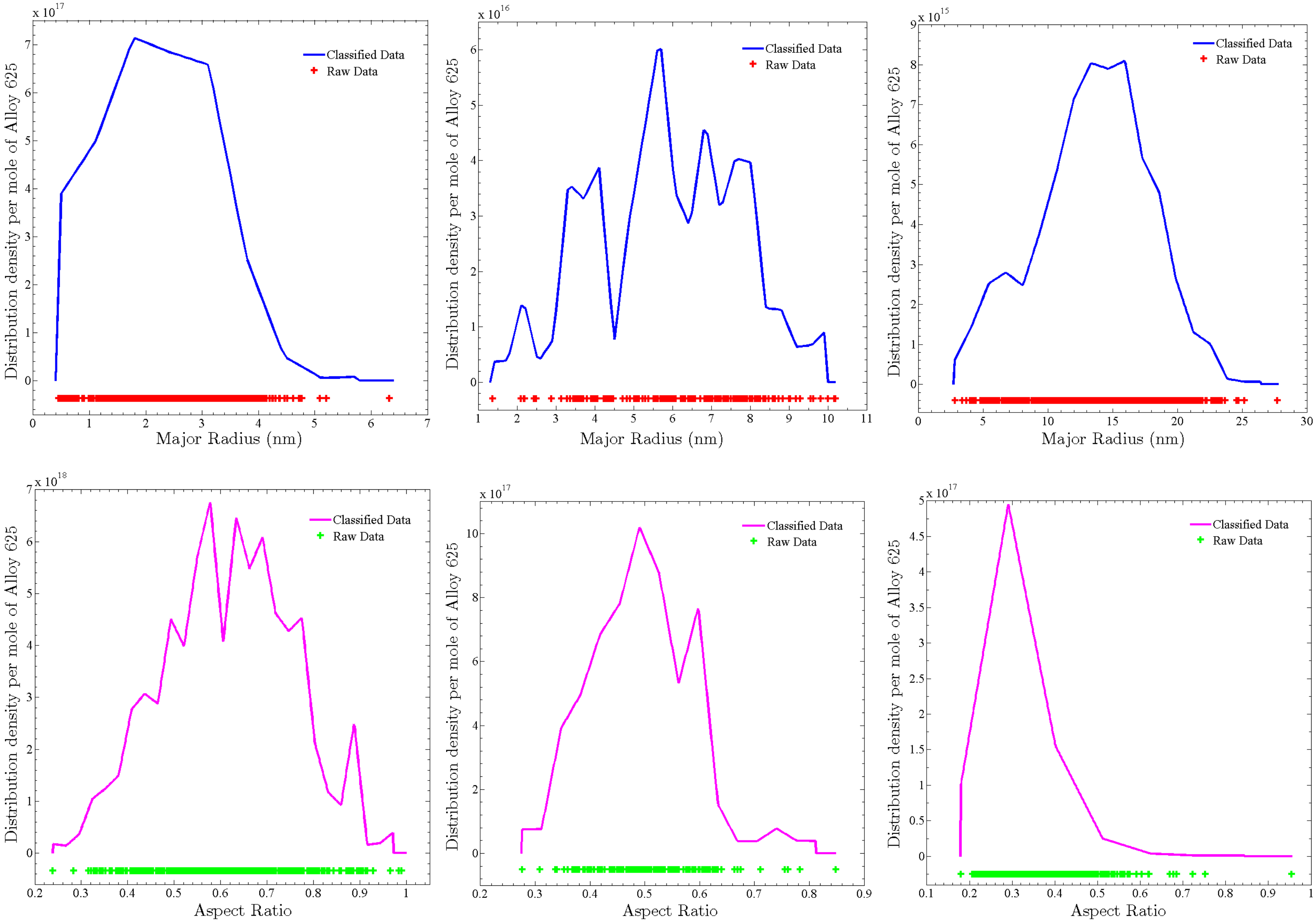

x 10^17
x 10^16
x 10^15
x 10^18
x 10^17
x 10^17
Distribution density per mole of Alloy 625
Classified Data
Raw Data
Major Radius (nm)
Aspect Ratio
0
1
2
3
4
5
6
7
8
9
10
11
15
20
25
30
0.2
0.3
0.4
0.5
0.6
0.7
0.8
0.9
1
0.1
0.5
1.5
2.5
3.5
4.5

(a) (b) (c)

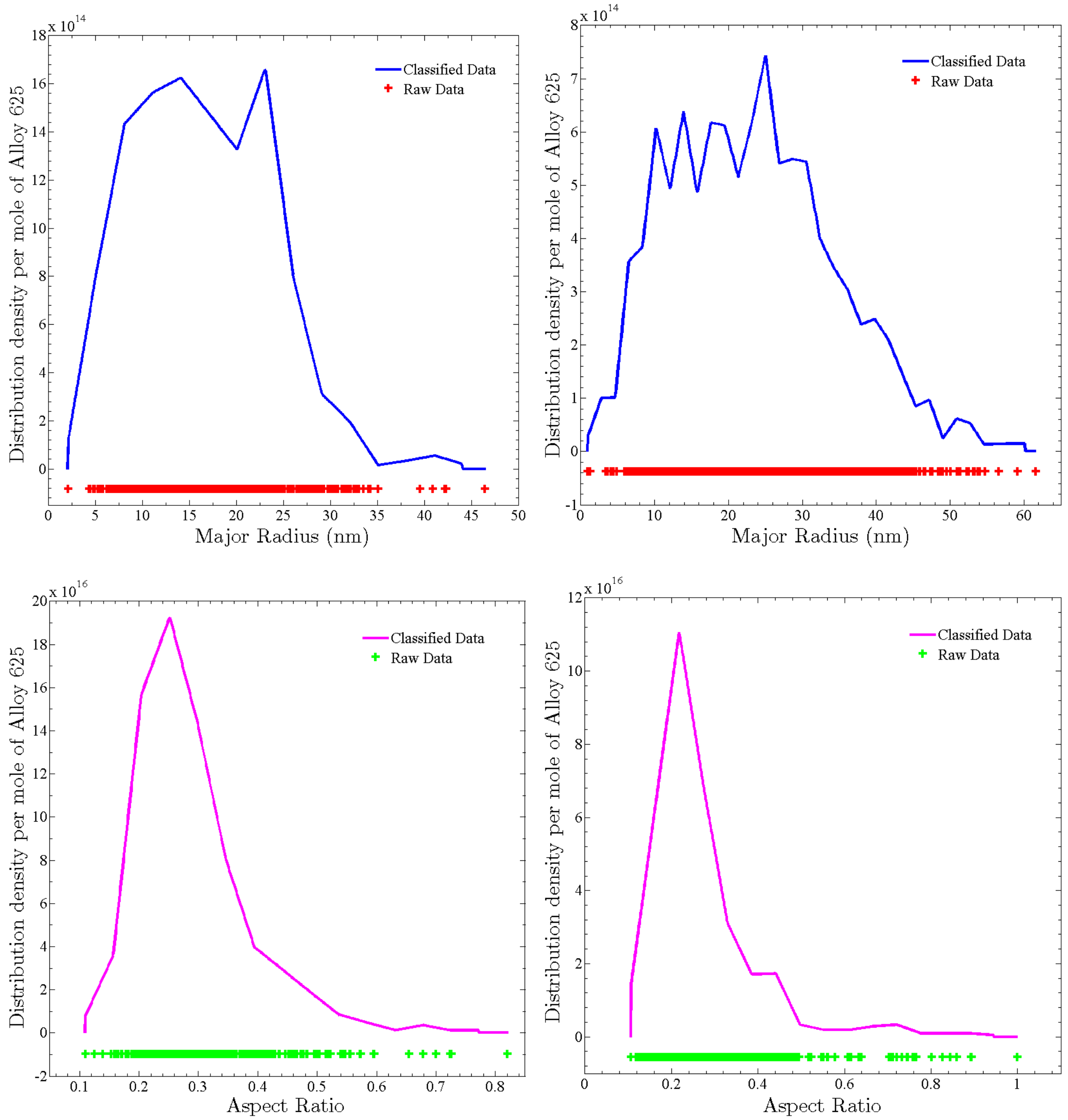

(d) (e)

Figure 5.11: Particle size and aspect ratio distributions created from measurements of precipitates in samples of Alloy 625 aged at 650 °C for a) 50 hours, b) 100 hours, c) 200 hours and d) 1000 and e) 3000 hours. Each "raw data" point corresponds to one precipitate.

Considering only the envelope of the various PSDs and ARDs in Figure 5.11, it should be pointed out that the contrasting relative spread/skew of those constructed from precipitates present after 50 hours is not consistent with what is expected during the growth and coarsening of the phase. Specifically, it is evident that the ARD of the 50 hours population is much wider than the more tightly clustered distribution (around higher α values consistent with γ'' precipitates at the start of growth as discussed in Section 1.4.3) expected from its PSD *cf.* the relative PSD and ARD distributions and their evolution with ageing time displayed in both Figures 5.11 and 5.9. Given the small size of the particles and their resolution/ill defined edges in Figure 5.10, it is almost certain that primary source for this disparity was the variation in particle thickness (normal to the image plane) along the major and minor axes which acted to diminish the magnitude of measured aspect ratios[6]. As a result, whilst the PSD produced by the analysis of the images of this specimen could be considered accurate because of its correspondence with later measurements, it is unlikely that the calculated ARD was a true reflection of the real precipitate population.

Support of the point just outlined with regard to the reliability of the PSD measurements made in this research can seemingly be provided the complete consistency of the data in Figure 5.11 with the Vickers hardness trend displayed in Figure 5.1 *viz.* the rapid increase and then plateau/fall measured when ageing 650 °C can be reasonably deduced as being principally the result of the impact of the changing measured particle size on the strengthening mechanisms of the phase (discussed in Sections 1.2.1, and 1.2.2). A singular key caveat, however, must be applied to this conclusion, namely that the drop in hardness between 1000 and 3000 hours of ageing may (at least partially) alternatively derive from the deleterious effect (*q.v.* Section 1.2.3) of a small evidenced precipitation of δ-phase, an example of which is shown in Figure 5.12.

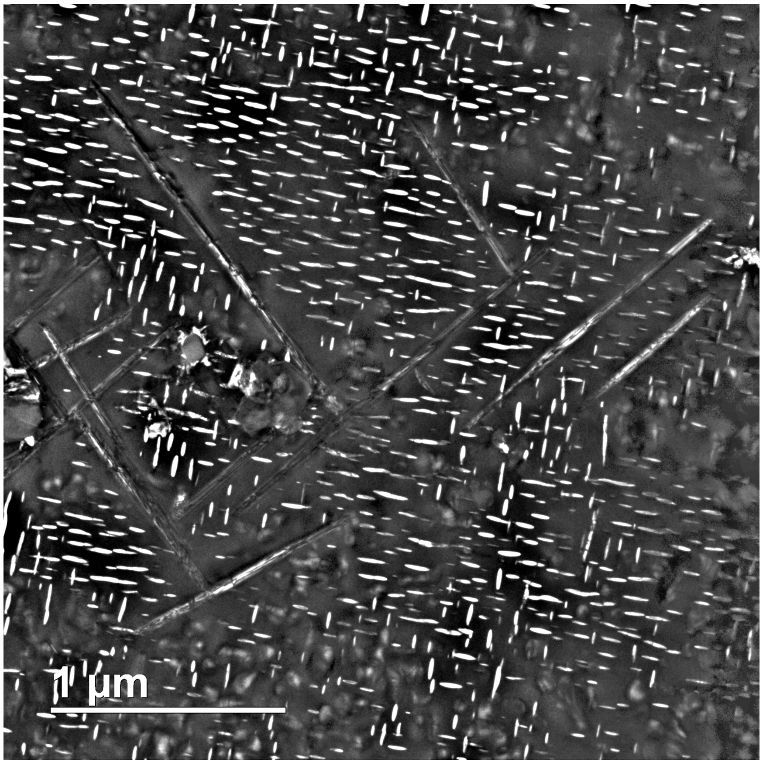

Figure 5.12: γ'' precipitates and δ-phase needles imaged in a sample of Alloy 625 aged at 650 °C for 3000 hours.

---

[6] Although alternative physical mechanisms such as "encounter" (indicated by the PSD) will skew the distribution directly, they will only compound the distortion of the ARD in this instance through increasing the differences in length and, therefore contrast between the two axes.

700° C

In stark contrast to the consistently homogeneous precipitation of γ'' observed previously in samples aged at 600° C and 650° C, at 700° C Figure 5.13 reveals the presence of a heterogeneous to homogeneous nucleation transition. Moreover, after 1000 hours the images captured also show both γ'' populations to be accompanied by a large volume fraction of intragranular δ needles.

Considering the γ'' nucleation mechanism first, because of the ageing response of solution annealed material at the lower temperatures investigated and the faster removal/annealing rate of remnant dislocations that should accompany higher temperature ageing [342], the sudden occurrence of a primarily dislocation nucleated precipitate population at 700° C is initially rather puzzling. Nevertheless, far from being an uncommon result, the literature reveals (as discussed in Section 1.4.3) that a similar phenomenon has been observed on numerous other occasions in Alloy 625, most notably[7] by Sundararaman *et al.* [174] and Pai *et al.* [175] who both argue (referencing the TTT diagrams of Schnabel *et al.* [38] (Figure 5.2b) and Floreen *et al.* [23] (Figure 1.18) respectively) the phenomenon to be an intrinsic result of the decrease in the magnitude of the undercooling (ΔT) in Equation 1.15: As discussed in Section 1.3.2, by increasing the barrier to homogeneous nucleation in a system containing sufficient heterogeneous sites, a reduction in ΔT will (according to classical theories) ultimately lead to a change in the dominant nucleation site for γ'' precipitation with increasing temperature. Furthermore, an observed reverse transition between two mechanisms when ageing at the same temperature/ΔT will result, via Equation 1.19, if the number of available heterogeneous nucleation sites ($N_{0,\mathrm{het}}$) is reduced through precipitation by a sufficient amount.

At first glance, the consistency with classical theories and the general trend of the observed behaviour in γ'' at 700° C, as well as the observed impact of composition in suppressing the effect in both Alloy 625 Plus [173] and Alloy 718 [2, 39, 283] through changing the under cooling magnitude at a given temperature, means the interpretation just outlined from both Sundararaman *et al.* [174] and Pai *et al.* [175] seems plausible. However, closer scrutiny reveals a fundamental flaw with respect to the re-emergence of a homogeneous population. Specifically, owing to the increased stability of heterogeneously nucleated precipitates, simply the appearance of a homogeneously nucleated population after prolonged ageing (due to heterogeneous nucleation site saturation) would not lead to the observed elimination of the former population, rather an enduring co-nucleated precipitate microstructure would be formed instead. In view of this result, therefore, it is clear that an additional mechanism must be in operation.

---

[7] Papers such as that of Shaikh *et al.* [171] and Suave *et al.* [41] provide no discussion of the mechanism behind the result.

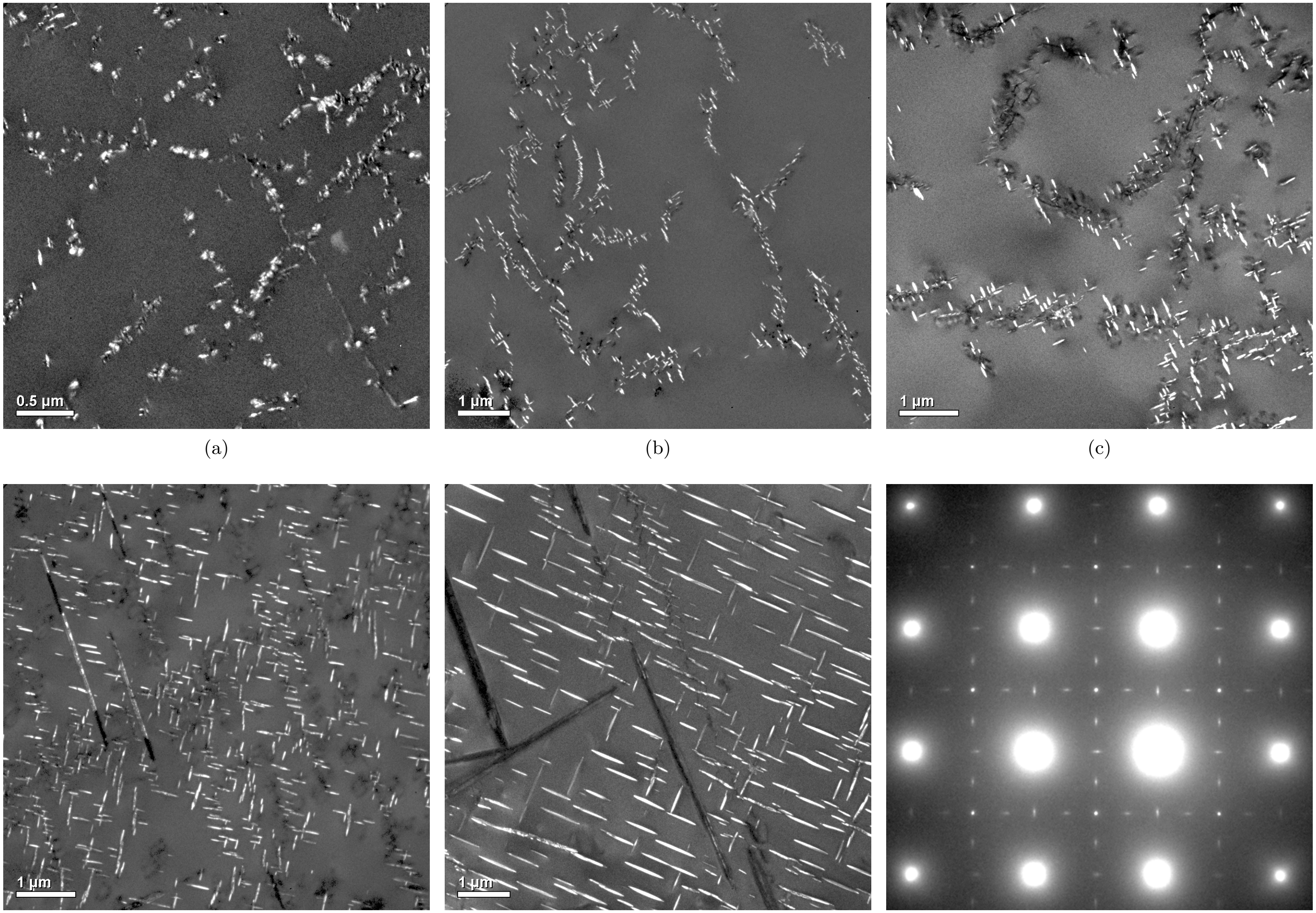

(a) (b) (c)

(d) (e) (f)

Figure 5.13: γ'' precipitates imaged along an [001] crystallographic orientation in samples of Alloy 625 aged at 700 °C for a) 50 hours, b) 100 hours, c) 200 hours, d) 1000 hours and e) 3000 hours. A diffraction pattern identifying the phase as γ'' is displayed in f); the streaked spots correspond to the two edge-on variants [40].

Considering the available information in this research, precise identification of the processes which led to the heterogeneous γ'' elimination is impossible; however, given the emergence of δ-phase which accompanies the phenomenon means it is reasonable to conclude that the second phase exerted some influence. For instance, in view of the fact that, firstly, intragranular δ has an apparent propensity to nucleate on γ'' precipitates (*q.v.* Section 1.2.3) and, secondly, the formation kinetics of δ-phase at 700° C are slow (as indicated by the TTT diagram in Figure 1.18) suggesting a high activation barrier, it may be that the δ-phase nucleated on the heterogeneous precipitates and caused their dissolution all whilst leaving the homogeneous γ'' population unaffected (thanks to diffusion occurring solely along the dislocation network). Such a mechanism is valid thermodynamically but it would require (at least) the direct identification of some γ'' nucleated δ-phase precipitates in the analysed samples for its confirmation *viz.* in the absence of such data the mechanism can only be ascribed to an "educated guess".

Given each of the aforementioned particularities in the discussion of the distribution of the precipitate population produced when ageing 700° C, it is axiomatic that the use of the data acquisition methodology outlined in Section 4.3.2 is not viable. What's more, it is also evident that this is a particularly unfortunate result as it is likely that the ageing of a truly defect/dislocation free microstructure (as was obviously intended to be created by solution annealing treatment), would have yielded an appropriate population (at least at the shortest ageing times). However, despite these facts, the collection of basic precipitate size data corresponding to the raw size distribution of the resolvable precipitates at each condition still constitutes a worthwhile endeavour for qualitative comparison with the behaviour at other conditions and the results produced by the model on which this experimental work is predicated. To this end, PSDs and ARDs calculated from the raw fits made to measurable/resolvable precipitates in images corresponding to all five ageing durations at 700° C are displayed in Figure 5.12.

Ignoring the unquantifiable impact of the likely non random[8] distortion on the two distribution types, following the discussion for 600° C and 650° C aged specimens previously it is immediately clear that each (unsurprisingly given their proximity when nucleating) display the distinctive log-normal shape associated with "encounter". Similarly, the 50° C increase in temperature is again noticed to have a marked influence on the speed of precipitate growth. Considered in isolation, this evolution in the γ'' population could be considered as consistent with the trend in Vickers hardness measurements; however, comparison with the effect of coarsening and δ-phase at 650° C indicates that, despite its diminished properties compared to γ'', δ actually acts to continue the hardening of the material in this instance.

---

[8] The proximity of smaller, dislocation nucleated particles and the division of larger particles through cutting by δ needles means the error in measurement is particularly pronounced for in the corresponding areas of the PSD.

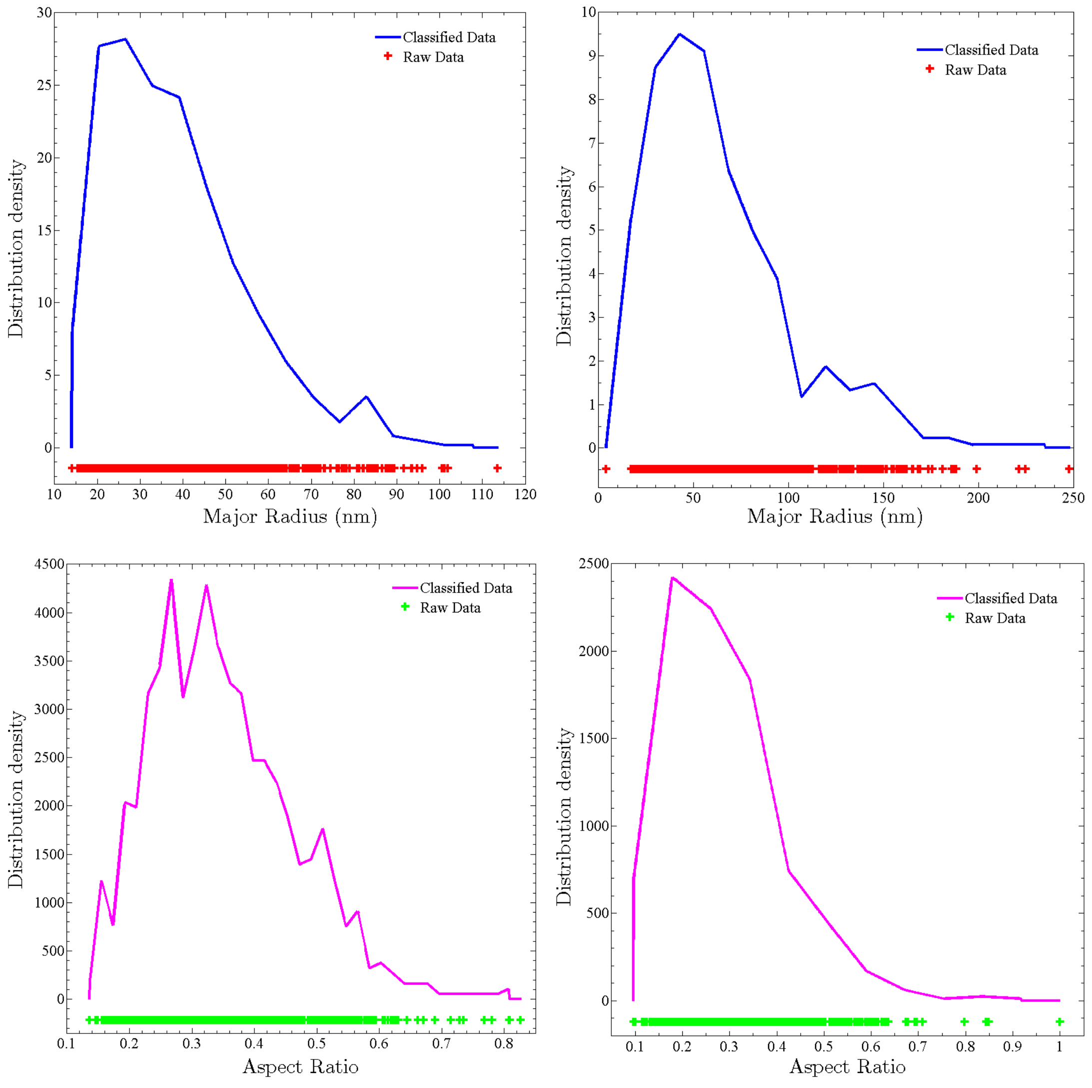
Distribution density
Major Radius (nm)
Classified Data
Raw Data
0
5
10
15
20
25
30
10
20
30
40
50
60
70
80
90
100
110
120
Distribution density
Major Radius (nm)
Classified Data
Raw Data
0
1
2
3
4
5
6
7
8
9
10
0
50
100
150
200
250
Distribution density
Aspect Ratio
Classified Data
Raw Data
0
500
1000
1500
2000
2500
3000
3500
4000
4500
0.1
0.2
0.3
0.4
0.5
0.6
0.7
0.8
Distribution density
Aspect Ratio
Classified Data
Raw Data
0
500
1000
1500
2000
2500
0.1
0.2
0.3
0.4
0.5
0.6
0.7
0.8
0.9
1

(c)

(d)

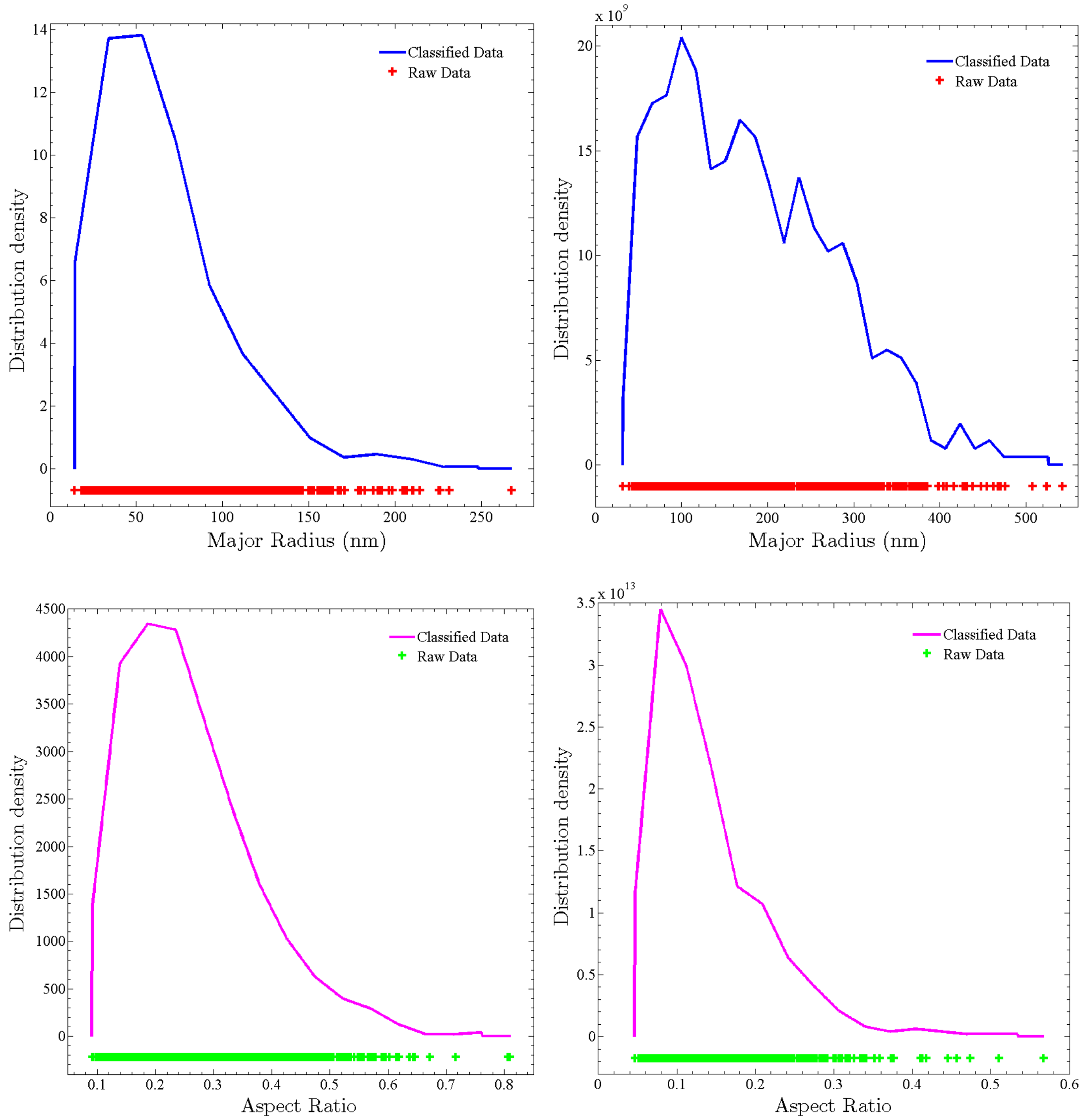

(d) (e)

Figure 5.12: Particle size and aspect ratio distributions created from measurements of precipitates in samples of Alloy 625 aged at 700 °C for a) 100 hours, b) 200 hours, c) 1000 hours and d) 3000 hours. Each "raw data" point corresponds to one precipitate.

750°C

From Figure 5.13 it is immediately seen that the precipitate populations produced while ageing at 750°C bare a striking resemblance to those produced after longer durations at 700°C *viz.* whilst γ'' is initially nucleated heterogeneously on defects/dislocations, after longer ageing periods a transformation to a homogeneous distribution is evidenced concurrent to the formation and growth δ-phase. Accordingly, utilising the same rational as that employed in the discussion of the samples aged at lower temperatures, one can directly infer the principal conclusions that:

1) The combination of the diminished driving force for precipitation (smaller ΔT) which exists at 750°C and the evidenced number of heterogeneous/low energy sites is sufficient to cause a change in the initial nucleation mechanism of γ'' from that at 600°C and 650°C.
2) Only basic PSD's and ARD's can be constructed for γ'' precipitates aged at 750°C.

In addition to these points, closer examination of the material exposed to extended ageing and comparison with the hardness data in Figure 5.6 enables the further interpretations:

3) The increased temperature at 750°C leads to the complete replacement of γ'' before 1000 hours of ageing.
4) The extensive formation of δ-phase initially continues to harden the material; however, softening ultimately results as the precipitate population coarsens.

Given the continuously emphasised diminishing of material properties which should accompany δ formation (*q.v.* Section 1.2.3), the observation of a continued, significant hardening again being imparted by the phase is again curious, especially in circumstance that, in this instance (unlike at 700°C), the γ'' phase is noted to be completely absent. Interestingly, however, analysis of the literature indicates that, rather than a direct result of the strengthening imparted by δ-phase, this increased level of hardness is likely instead associated with two mechanisms: The first is the so called composite or fibre strengthening observed by Detrois *et al.* [343], whereby the stiffer δ needles act to increase the overall resistance of alloy to deformation. The second is the formation of “punched out” dislocations induced by the nucleation and growth of δ-phase [74]. Figure 5.13d reveals this harder sample contains many dislocations adjacent to δ needles whereas Figure 5.13e shows a comparatively dislocation free matrix. This detection of the strengthening imparted by δ-phase at temperatures $\geq$ 750°C in Alloy 625 constitutes a validation of the measurement of the same phenomenon by Suave *et al.* [333] (alluded to in Section 5.2) and (inferred from) Shankar *et al.* [10].

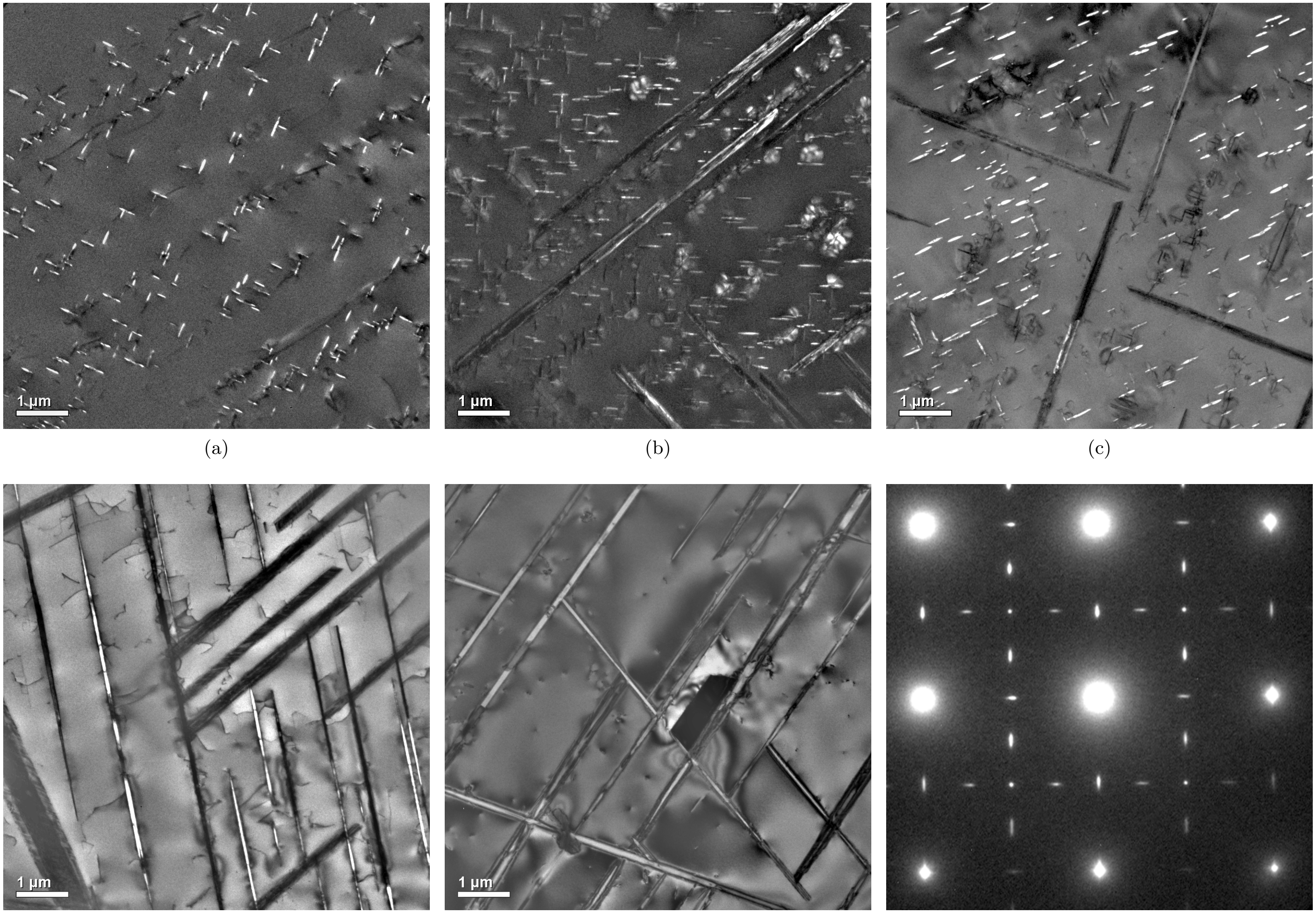

(a) (b) (c)

(d) (e) (f)

Figure 5.13: γ'' precipitates and δ-phase needles imaged along an [001] crystallographic orientation in samples of Alloy 625 aged at $750\,^{\circ}$C for a) 50 hours, b) 100 hours and c) 200 hours. δ-phase needles imaged in material aged at $750\,^{\circ}$C for d) 1000 hours and e) 3000 hours. A diffraction pattern identifying the phase as γ'' is displayed in f); the streaked spots correspond to the two edge-on variants [40].

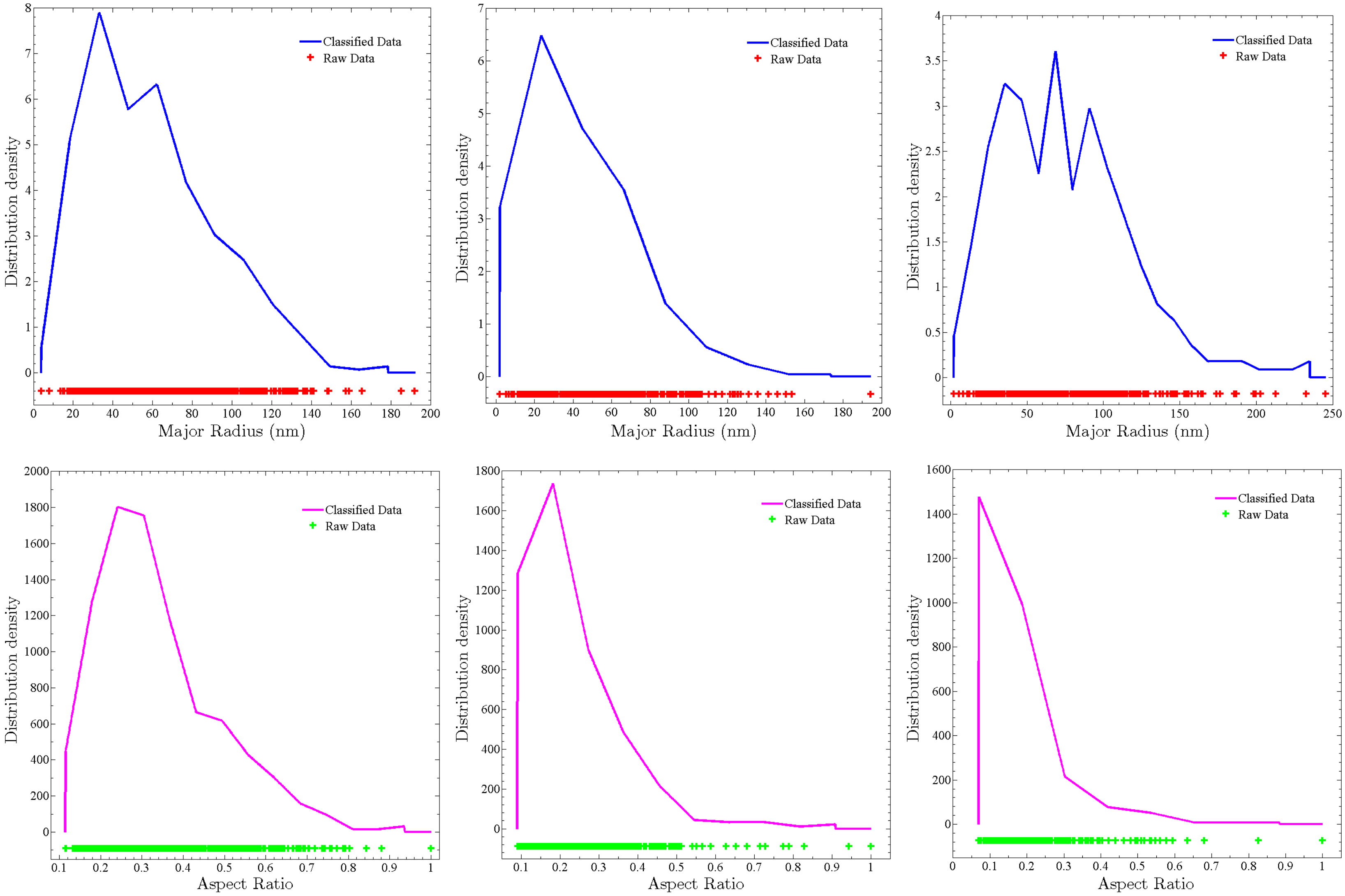

(a) (b) (c)

Figure 5.14: Particle size and aspect ratio distributions created from measurements of precipitates in samples of Alloy 625 aged at 750 °C for a) 50 hours, b) 100 hours and c) 200 hours. Each “raw data” point corresponds to one precipitate.

Consistent with the trends interpreted with temperature previously, quantitative comparison of the basic PSDs and ARDs corresponding to each of the ageing times at 750° C (Figure 5.14) yields the deduction of enhanced precipitate formation and growth kinetics compared to lower temperatures. Similarly, the distribution shapes are again indicative of the process of "encounter" taking place.

800° C

Examination of each of the samples corresponding to the ageing durations at 800° C shows an extensive precipitation of exclusively δ-phase in each instance marking a cross over to the thermodynamic region in which the phase nucleates (almost) directly from the matrix (described in Section 1.2.3). Clearly this outcome precludes the acquiring of any useful data regarding γ''; however, it is worth commenting that the observed seeming correspondence between the presence of dislocations in the matrix of each sample and the continued isothermal hardening measured in Figure 5.1 may be further evidence of this hardening mechanism operating within the alloy. Furthermore, the fact that the extensive array of dislocations observed at 700° C and 750° C are also absent in each image highlights the smaller pinning pressure exerted by δ-phase compared to γ'', consistent with the discussion in Section 1.2.3.

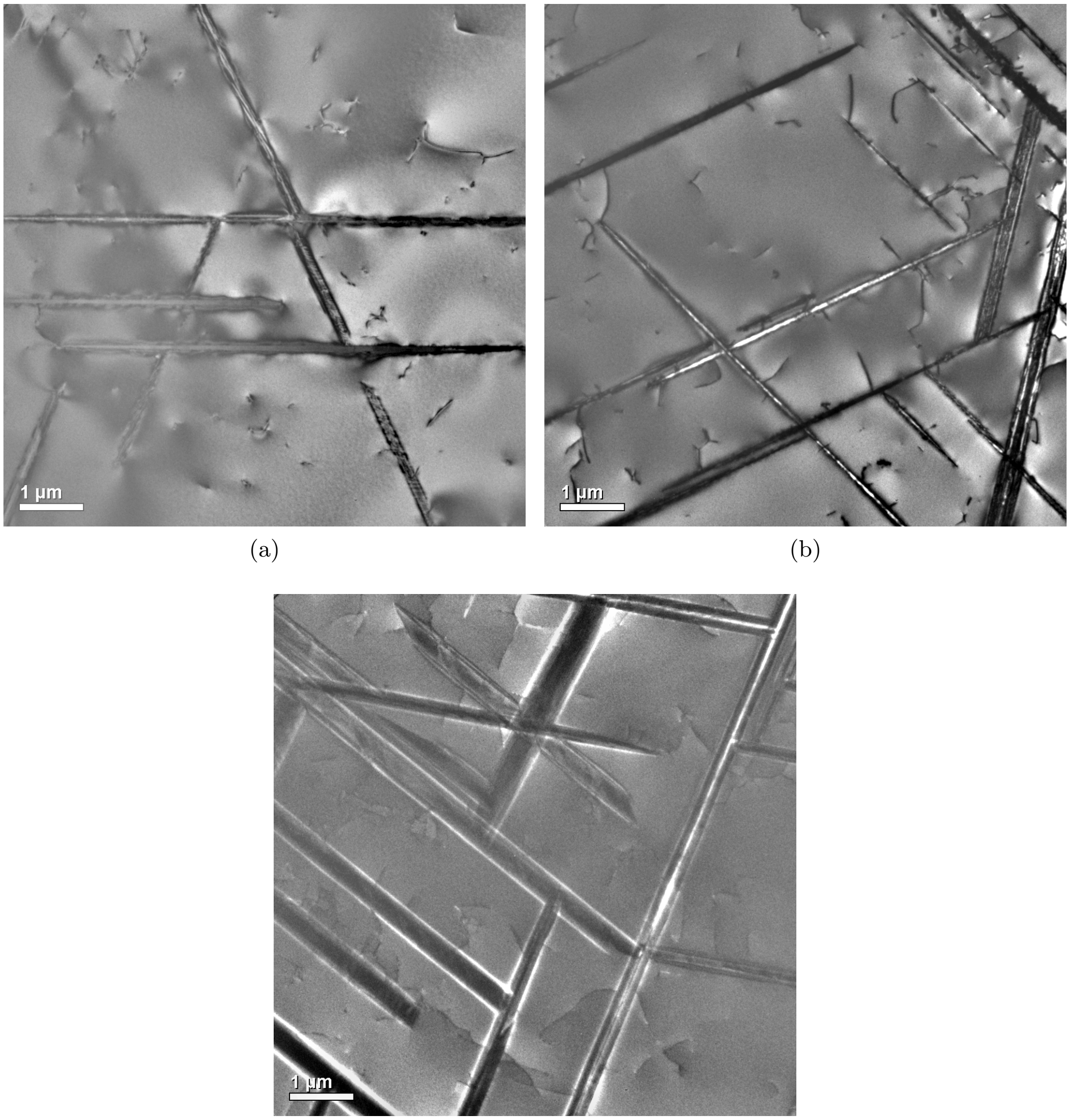

(a)

(b)

(c)

Figure 5.15: δ-phase needles imaged in a sample of Alloy 625 aged at 800°C for a) 100 hours, b) 200 hours and c) 1000 hours.

5.3.2 γ'' Evolution Trends

Utilising the data just presented, it is instantly possible for one to draw direct conclusions regarding the evolution behaviour of γ'' precipitates with respect to both time and shape as presented below. In addition, however, it should also be pointed out that, despite lacking lacking direct relevance in this research because of its fundamental flaws with respect to its description of the shape of the PSD of γ'' precipitates (*q.v.* Section 4.3.3), owing to the existence of similar comparative studies in the literature a worthwhile analysis of the data acquired could also be conducted with respect to the LSW theory (*q.v.* Section 1.3.4). As a result, a concurrent LSW study of γ'' size evolution in Alloy 625 using the same data as that presented here is detailed by the author in a recent article [344].

Aspect Ratio vs Major Radius

On account of its construction from raw precipitate statistics, and thus the existence of a uniform methodology across all the gathered data sets, the first evolution trend examined in this research was that of the change in aspect ratio with γ'' major radius *i.e.* $\alpha(r_\mathrm{M})$. In this regard, plots constructed from the raw size and shape statistics of every measured precipitate in the images of each of the separate isothermal γ'' populations are presented in Figure 5.16.

Most strikingly on initial inspection of the individual plots in Figure 5.16 one can immediately distinguish two separate γ'' populations at 750°C, with the precipitates measured after 50 hours of ageing displaying a markedly higher α than those which existed later. Comparison with the images and discussion made in the previous section straightforwardly enables the deduction that this behaviour is principally an effect of the heterogeneous to homogeneous nucleation transition. More specifically, however, the change in α can only be understood to have been brought about as a consequence of the relative strain environments of the two different populations: As discussed in Section 2.2.1 the shape changing behaviour of γ'' precipitates is ultimately a result of the change in misfit strain around the particle surface as they grow. Furthermore, as separately detailed in Section 1.3.2, precipitates nucleated on dislocations have a lower misfit strain with the matrix. In light of these two factors therefore, it is simple to identify the lower misfit strain of dislocation nucleated particles as the cause of their elevated α values. Similarly, the faster diffusion rate along dislocations (known as pipe diffusion) and resultant enhanced growth of dislocation nucleated particles yields the near identical r_M range of the heterogeneous and homogeneous populations despite the latter having had longer to evolve.

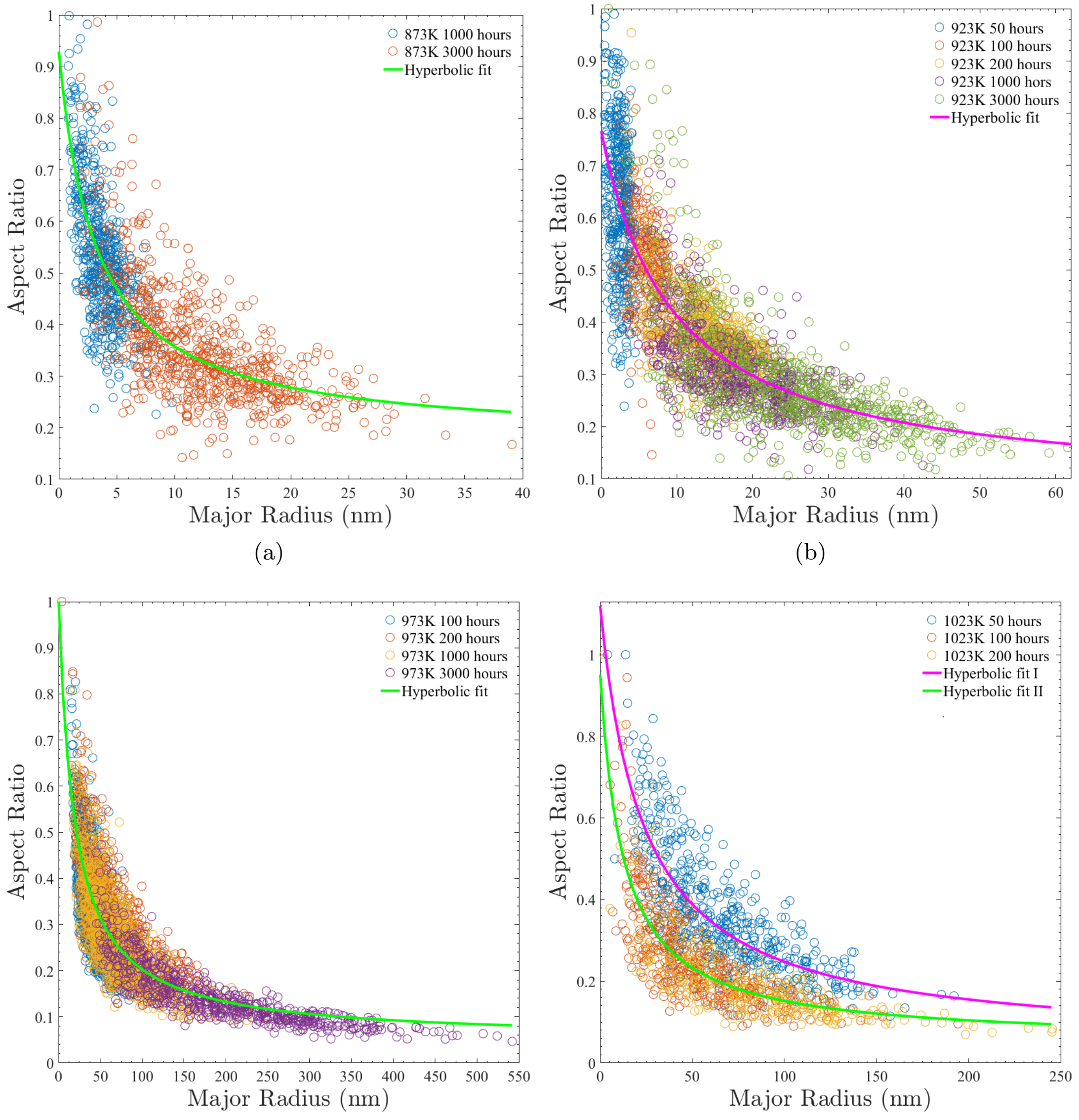

(a)

(b)

(c)

(d)

Figure 5.16: Aspect ratio and major radius of all precipitates measured from the micrographs of material aged at a) 600° C, b) 650° C c) 700° C and d) 750° C in Section 5.3.1. Hyperbolic fits to each population are also indicated.

Switching focus to the relative behaviour between the different plots in Figure 5.17, the effect of temperature can be most easily determined through the use of the indicated hyperbolic fits. Selected on the basis that hyperbolic decay tends towards a physical singular value in a finite time (eventually all coherency would be lost between the precipitate and matrix effectively eliminating the driving force for a reduction in aspect ratio) and their good correspondence with the general trend of the data, when plotted on the same axes (Figure 5.17) these interpretations can be first seen to reveal a general increase in α for $0 < r_{\mathrm{M}} < 25\,\mathrm{nm}$ before an apparent crossover occurs.

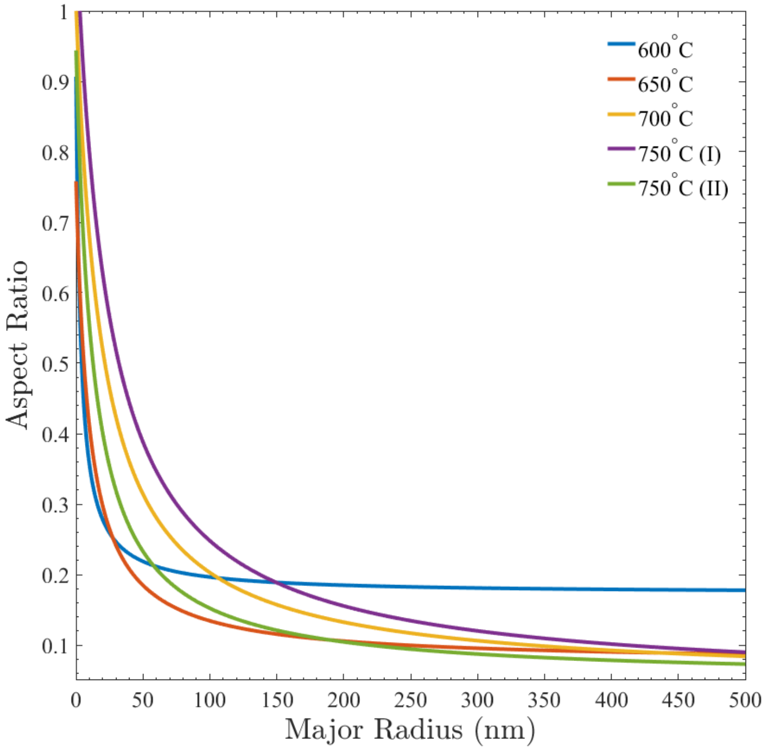

Figure 5.17: Fits made to the plots of Aspect ratio and major radius in Figure 5.16

Considering the physical processes involved, much like the previous discussed behaviour for the two populations at 750° C, the initial cross-over phenomenon with temperature (specifically between the 600° C and 650° C curves) can be attributed to principally the decrease in misfit strain; however, in this instance, the data range also has a significant effect: From Equation 2.10, the value of λ is suppressed with increasing temperatures via both the reduction in the values $\Delta\varepsilon$ and ε (measured to occur by Slama *et al.* as detailed in Table 5.4) and the Young's modulus (from Figure 3.3). Consequently, all things being equal, an increase in the misfit strain when decreasing temperature from $650 \leftarrow 600^{\circ}\mathrm{C}$ should always lead to an decrease in the value of r_{M} at a specific α. The only reason why this was limited in this particular instance to values where $r_{\mathrm{M}} \leq 25\mathrm{nm}$ was the narrower range of the data gathered at this temperature (*i.e.* a lack of data distorts the fit sufficiently that a cross over is seen).

Table 5.4: Average values of ε and $\frac{\Delta\varepsilon}{\varepsilon}$ for γ'' in Alloy 718 determined from the measurements of Slama *et al.* [4].

		Ageing Time (hours)					
		4		50		98	
		$\varepsilon(\times10^{-3})$	$\frac{\Delta\varepsilon}{\varepsilon}$	$\varepsilon(\times10^{-3})$	$\frac{\Delta\varepsilon}{\varepsilon}$	$\varepsilon(\times10^{-3})$	$\frac{\Delta\varepsilon}{\varepsilon}$
Temperature (°C)	680	8.06	2.76	4.17	6.73	3.34	10.29
	750	8.89	2.33	3.62	7.88	3.06	9.82

In light the aforementioned temperature-strain behaviour, another significant but separate implication which can also be inferred from Figure 5.17, particularly through comparison of the plots made to the populations at 700°C and 750°C, is the fact that the trend fitted to the γ'' precipitates at 700°C must primarily pertain to heterogeneously nucleated particles. That is to say, based on the two behaviours at 750°C and the relative change between the 600°C and 650°C curve, a purely homogeneous population at 700°C would be expected to have a fit in which the magnitude of $\alpha(r_{\mathrm{M}})$ is lower than that of 750°C (I). This result is important in this research as it provides a justification for the absence in Figure 5.16c of the two population behaviour seen in Figure 5.16d despite the clear indication of both populations Figure 5.13 (*i.e.* experimental error could be ruled out). Similarly, the observed deviation of the fit line from the data collected from homogeneously nucleated precipitates existing after 3000 hours at 700°C in Figure 5.16c can be understood as not relating to the suitability of the mathematical function but rather the weighting of the data points corresponding to earlier heterogeneously nucleated γ''.

Finally with reference to the behaviour of $\alpha(r_{\mathrm{M}})$, it is worth commenting on the contrast of the clearly continuous behaviour of γ'' evolution observed in this research in Alloy 625 with the step change behaviour deduced by both Cozar *et al.* [172] and Devaux *et al.* [47], and modelled recently by Ji *et al.* [345] in Alloy 718. In all three instances the threshold at which the step-change is supposed to occur is theorised as being attributable to a marked change in coherency between precipitate and matrix. However, considering the mathematical treatment by both sets of authors and the experimental results presented in Figure 5.16, these observations can now instead be straightforwardly identified as the change in physical characteristics of both the precipitate and matrix discussed previously. That is to say, as the mathematical description developed by Cozar *et al.* [172] assumes constant values for parameters such as the misfit strain despite this being (via Table 5.4) demonstrably not true, their concluded regions of coherence and full incoherence can be more appropriately interpreted as the separate regions where their assumption holds and where it breaks down. Likewise, the two stage strain behaviour produced by the more intricate approach of Ji *et al.* [345] is attributable to their use of two sets of strain values, one exclusively for full coherent particles and one exclusively for semi-incoherent precipitates (*i.e.* no transition).

AVERAGE PRECIPITATE ASPECT RATIO

The time evolution of the γ'' populations at each temperature with respect to aspect ratio (*i.e.* $\bar{\alpha}(t)$) can be inferred from the distributions in Section 5.3.1 according to Figure 5.18. Aside from the trivial linear case brought about by the existence of only two data points for the 600°C series, at each temperature it is observed that the decay in the magnitude of $\bar{\alpha}$ during ageing was (much like $\alpha(\rho)$) well described (at least partially) by a hyperbolic decay fit. This result is consistent with the eventual occurrence of complete precipitate matrix incoherency *viz.* the elimination of misfit strain and *ipso facto* the driving force for α change.

On account of the predisposition just outlined for γ'' precipitates to ultimately achieve an almost time invariant aspect ratio, the significant deviation from a hyperbolic trend of the PSD corresponding material aged for 3000 hours 700°C seems implausible. However, a simple explanation of this phenomenon can be provided by closer consideration of the mechanism of γ'' "encounter" (inferred from the PSD shapes and images in Section 5.3.1): As depicted most strikingly in the literature by Suave *et al.* [41] (image reproduced for ease of reference in Figure 5.19) as well as in this research, rather than being randomised, the agglomeration of γ'' precipitates is consistently observed as directional, specifically in that they seemingly only coalesce through conjunction along their major axis. The result of this particular mechanism for "directional encounter", therefore, was likely a reduction in the aspect ratio of large particles by a magnitude dramatically greater than that achievable by the misfit strain alone. Moreover, referring back to the discussion in Section 5.3, given the fact that, from Figure 4.27, particle shape changing during growth and coarsening should not result in a significant change in the relative shape of the ARD, the ever increasing distortion/log-normal skew of the distribution at extended ageing times (also evidenced in Figure 5.18 from comparison of the mean and quartile positions) can be primarily attributed to the enhancement of the magnitude of low α precipitate classes by "directional encounter".

In view of the prior discussion made with respect to $\alpha(r_{\mathrm{M}})$, it is clear that, as well as being associated the thermal influence on the pure kinetics of particle growth and coarsening (via Equations 1.13 and 2.7), the differing comparative behaviour of $\bar{\alpha}(t)$ at each temperature was also a result of the change in the influence of misfit strain. Furthermore, however, the influence of misfit strain can now also be deduced as another cause for the disparate behaviour of the samples aged at 700°C *viz.* unlike at 3000 hours, the values corresponding to ageing times between 100-1000 hours were heavily influenced by lower stain heterogeneously nucleated particles reducing their rate of evolution. This latter conclusion is particularly noteworthy as it provides further support to the previously made affirmation that the trend for precipitates aged at 700°C in Figure 5.16 primarily pertains to heterogeneous precipitates. That being stated, this outcome cannot be considered as definitive proof given the surprisingly continuous behaviour evidenced at 750°C despite the undoubted presence of analogous two population influences.

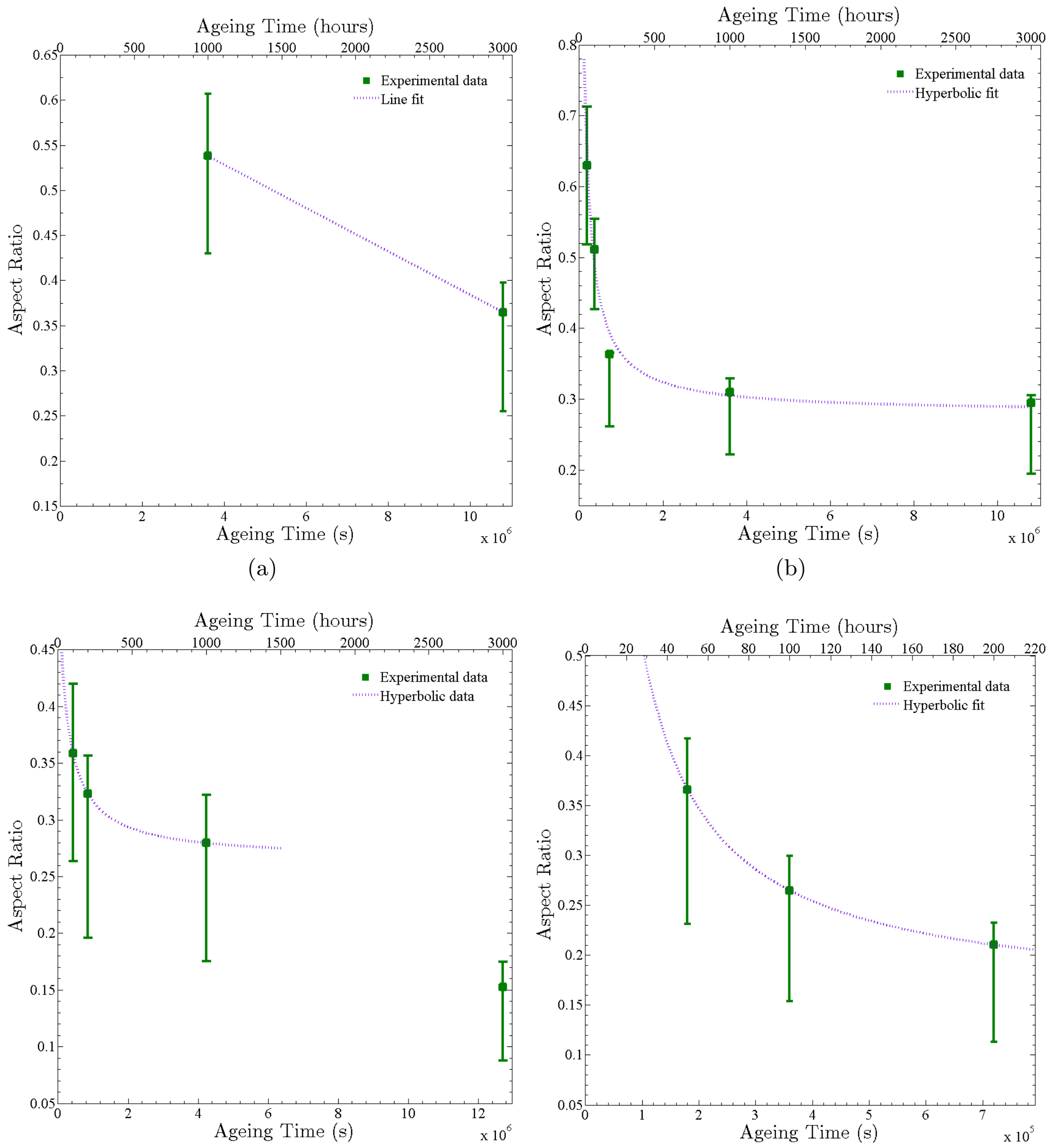

(a) (b)

(c) (d)

Figure 5.18: Time evolution of the aspect ratio distribution of γ'' precipitates in Alloy 625 aged at a) 600° C, b) 650° C c) 700° C and d) 750° C in Section 5.3.1. The data points correspond to mean values and the error bars indicate the first and forth quartiles of the distribution.

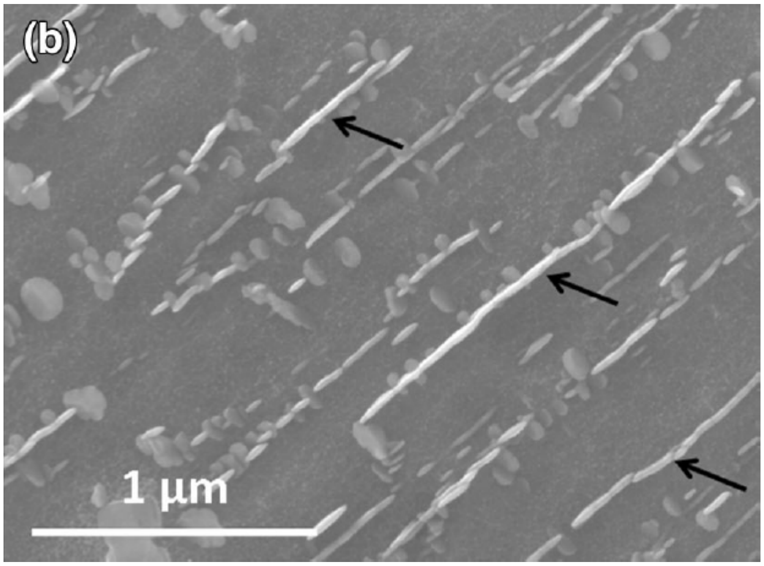

Figure 5.19: Extensive, large scale γ'' coalescence imaged via scanning electron microscopy (SEM) in a sample of Alloy 625 by Suave *et al.* [41].

Average Precipitate Major Radius

Inspection of the different isothermal behaviours of $\bar{r}_{\mathrm{M}}$ in Figures 5.20b and c (excluding the data for particles existing after 3000 hours at 700 °C) reveals both to be well described by hyperbolic growth equations suggesting, in line with the previous discussions, the existence of an upper limit for the size of γ'' precipitates. Rather than an obviously consistent result with the hyperbolic behaviour of the precipitate aspect ratio discussed previously, however, this phenomenon is surprising as (in line with the discussion in 1.3.4) the reduction in misfit strain should have led to a dominance of the coarsening process in the population evolution and therefore a consistently increasing $\bar{r}_{\mathrm{M}}$ until (at equilibrium) all of the solute is (theoretically) bound up into a single mass.

A rationalisation of the seemingly contradictory implications of the hyperbolic fits made to the major radius and aspect ratio of the γ'' precipitates measured in Alloy 625 in this research can be made through considering the outcome with respect to $\bar{r}_{\mathrm{M}}$ as a coincidence. In other words, following the arguments presented by Janssens *et al.* [239] with respect to spherical precipitates in the KWN model, it is just a happenstance that the behaviour of $\bar{r}_{\mathrm{M}}$ follows a hyperbolic growth curve over the ranges considered: As the growth and coarsening of the γ'' population proceeds not only does the degree of supersaturation drop but the stability of all of the remaining particles increases. Consequently, as time progresses the average rate of particle growth decreases. Eventually during coarsening a point is reached where the shrinking precipitates are sufficiently large in size for both their relative stability to be quite high and duration of their reduction to be extensive. This phenomenon results in the growth of the precipitates becoming almost a "zero-sum game"[9] with respect to the value of $\bar{r}_{\mathrm{M}}$ and, thus, creates

---

[9] As defined in game theory, a "zero-sum game" is one in which each competitors gain is derived

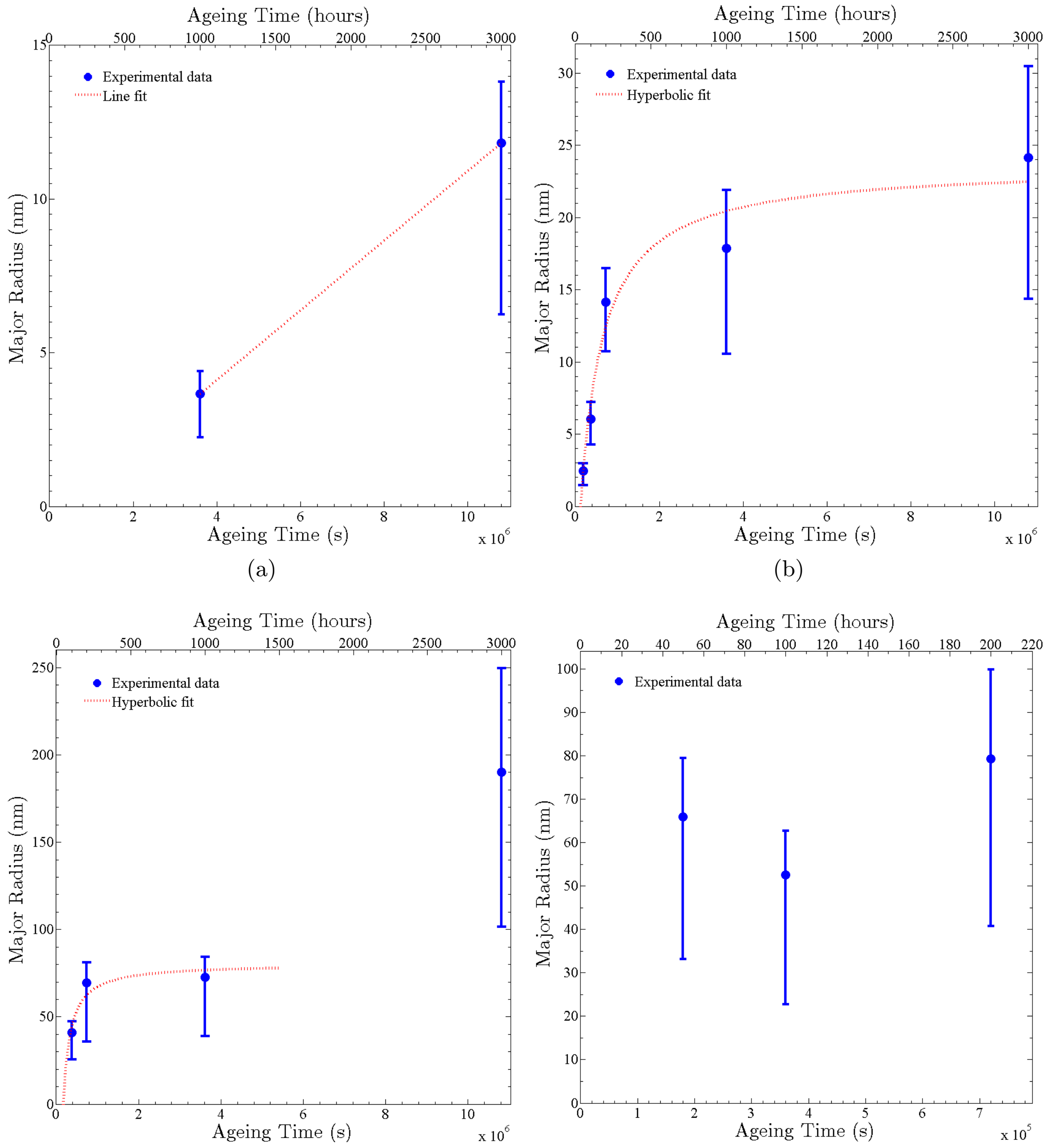

(a)

(b)

(c)

(d)

Figure 5.20: Time evolution of the particle size distribution of γ'' precipitates in Alloy 625 aged at a) 600° C, b) 650° C c) 700° C and d) 750° C in Section 5.3.1. The data points correspond to mean values and the error bars indicate the first and forth quartiles of the distribution.

the apparent plateau in particle average radius evidenced in Figures 5.20b and c. Utilising this rationale, therefore, had precipitate evolution been analysed for a sufficient period, the hyperbolic type behaviour would have changed to one of consistent growth as the ultimate disappearance of the smaller particles eliminates their contribution to the calculation of $\bar{r}_{\mathrm{M}}$.

As well as the plateau in precipitate sizes, through the population retaining the same average major radius and particle number, another consequence of the growth mechanism just outlined can be easily inferred as the transition in the shape of the distribution from one analogous to a log-normal plot to one closer to a normal distribution or even LSW plot. In the case of the figures displayed here, therefore, such a transition should have been indicated through the switching of the bound which lies closest to the average radius from the lower quartile to the upper quartile. As a result, the apparent occurrence of an opposite effect in the relative positions of the quartiles all of the isothermal sets featured in Section 5.3.1 can (in view of the discussions made with respect to both $\alpha(r_{\mathrm{M}})$ and $\bar{\alpha}(t)$) be attributed to the skewing (now towards the lower quartile) effect of "directional encounter". Similarly, owing to the conclusions made in the analysis of $\bar{\alpha}(t)$, instead of a possible transition away from the plateau behaviour, the significant enhancement of the value of $\bar{r}_{\mathrm{M}}$ calculated for 3000 hours at 700° C is likely more attributable to a combination of particle coalescence and the nucleation regime.

Next with respect to $\bar{r}_{\mathrm{M}}$, it is evident from Figure 5.20d that, in contrast to $\bar{\alpha}(t)$, the heterogeneous to homogeneous γ'' nucleation transition had a significant effect characterised by the presence of an apparently unphysical dip. Whilst this eventuality is unfortunate from an analysis standpoint, it does provide justification for the deductions made with respect to the effect of misfit strain on the evolution of the value of $\bar{\alpha}(t)$ for the γ'' populations at 700° C. Specifically, the existence of the seemingly inconsistent behaviour at 750° C can instead be interpreted as resulting from a coincidence in the magnitudes of the relative values at 50 and 100 hours and that which is compliant with a hyperbolic fit.

Finally it is worth pointing out that, likewise to previous discussions, the consistent increase in the overall magnitude of $\bar{r}_{\mathrm{M}}$ with temperature is a result not only of the faster diffusion kinetics (via Equations 1.13 and 2.6) but also the increased diffusion along dislocations (*cf.* Section 1.3.3) and the reduced stain barrier for heterogeneously nucleated particles (*cf.* Section 1.3.2)

---

solely from the loss of another competitor.

Average Precipitate Number Density

Before data on the precipitate number density can be presented, it is obvious that owing to the technique used to calculate the experimental data described in Section 4.3.2, specifically the exclusion of precipitates which are sectioned by the image edge (resulting in an automatic reduction in the number density measured for γ'' precipitates), a correction was required so that they more accurately represented the real system statistics. Fortunately, assuming that the excluded particles have no effect on the average precipitate size, the randomness of homogeneous precipitation means that the magnitude of the reduction in the number density ($N_{\downarrow}$) can be derived simply from the probability of an averaged sized particle intersecting with the image edge (first term) and the average amount of such a precipitate which would lie within the image area (second term). Consequently, utilising this methodology the values for the number density of the two obtained datasets in Figure 5.21 were corrected in this investigation by means of a uniform inflation of each of the precipitate frequency values implemented through a multiplication by the factor $(1 - N_{\downarrow})^{-1}$ during the image combination stage outlined 4.3.2. For the square images analysed in this research, the expression for $N_{\downarrow}$ is defined according to Equation 5.2, where $\bar{\rho}$ is the effective average spherical radius ($\bar{\rho} = \bar{r}_{\mathrm{M}}\bar{\alpha}^{\frac{1}{3}}$, $\bar{r}_{\mathrm{M}}$ and $\bar{\alpha}$ are the average precipitate major radius and aspect ratio respectively) and x is the length of one of the image sides.

$$N_{\downarrow} = \left(\frac{(x + 4\bar{\rho})^2 - x^2}{(x + 4\bar{\rho})^2} \right) \cdot \frac{1}{2} \tag{5.2}$$

Because of the lack of a detailed evolution path for the precipitates evolving at 600 °C, aside from a general comment regarding the consistency at both temperatures of the number density behaviour with coarsening precipitate coarsening (*cf.* Section 1.3.4) the analysis of the number density plots in Figure 5.21 necessarily focused on the data acquired from precipitates aged at 650 °C: Comparison of the number density evolution with precipitate major radius reveals it to be consistent with the mechanism outlined for the plateau in $\bar{r}_{\mathrm{M}}$ *viz.* the almost constant number density of γ'' between 200-3000 hours of ageing means their evolution will follow the "zero-sum game" with respect to $\bar{r}_{\mathrm{M}}$ previously alluded to. Furthermore, the observed decrease in experimental uncertainty with increasing ageing duration is attributable to the increased difficulty in obtaining good quality images of smaller particles and the accompanying effect higher magnifications have on the suitability of the random orientation assumptions made in the image analysis technique (*q.v.* Section 4.3.2). In other words, the fact that the number density measurement is predicated on individual image statistics, and that the probability of the assumption of equal numbers of γ'' precipitates following the three possible [001] orientations in any one area decreases with decreasing image/sample size, means the error bar trends in Figure 5.21 are correlated inextricably with precipitate size/image magnification.

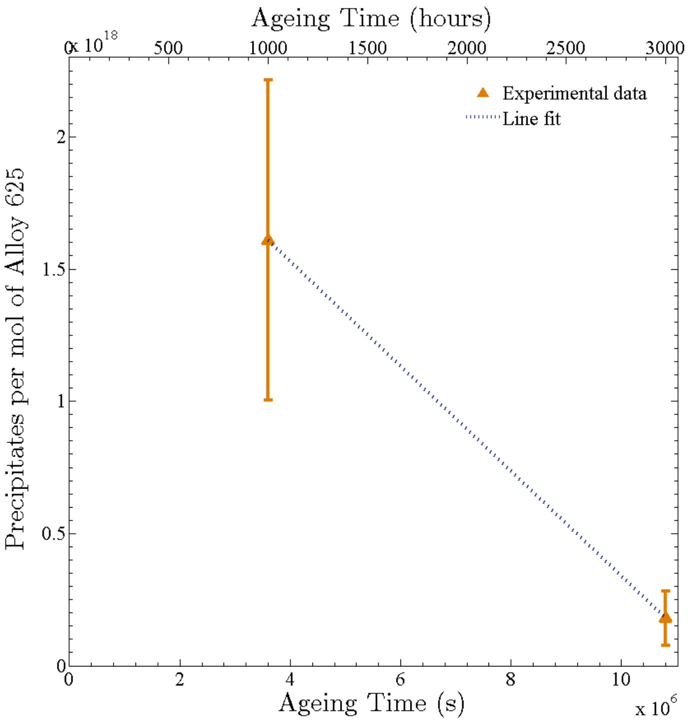

(a)

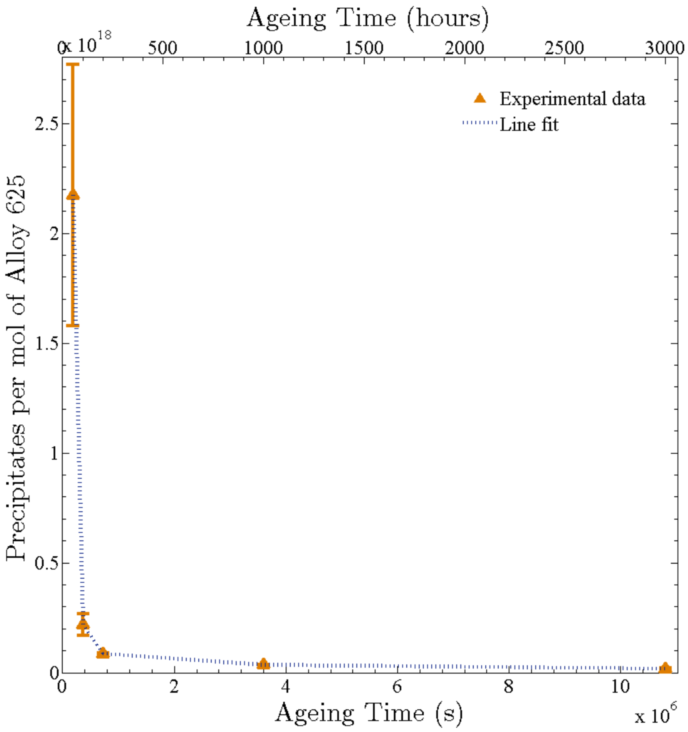

(b)

Figure 5.21: Time evolution of the molar density of γ'' precipitates in Alloy 625 aged at a) 600°C and b) 650°C imaged in Section 5.3.1. Error-bars correspond to 1 standard deviation about mean value.

Chapter 6

Precipitation Model

The iterative calculation constituting the model created in this research (as described in Section 3.2) was created/implemented using the forth generation high level programming software MATLAB [324]. The execution of the code was performed on a personal laptop.

§ 6.1 Calibration Methodology

The necessary calibration of the model with respect to the end(s) and mantle interfacial energies ζ_k^E and ζ_k^M of the modelled γ'' precipitates, as discussed in Section 3.1.5, principally requires the use of a single isothermal trend describing the evolution of precipitate aspect ratio with time. Taking into consideration the experimental results detailed in the previous section, however, for reasons of consistency it is also evident that a key stipulation is added, namely that the mathematical function $\alpha(t)$ pertains to a single γ'' population. To this end, given the axiomatic preclusion of the measurements made from material aged 700° C and 750° C on the basis of the latter criterion, the data acquired from material aged at 650° C is selected for the basis of the calibration for two principle reasons: 1) As shown by the Vickers hardness results in Section 5.2, the 650° C dataset contains five evaluations of the precipitate population thereby allowing for a more accurate description of precipitate evolution with time than can be obtained from the two datapoints in the 600° C set. 2) Similarly, as indicated in directly in Figure 5.18, the faster evolution kinetics present at 650° C mean the data points acquired necessarily cover a greater range of ageing durations and aspect ratios than those gathered at 600° C.

In accordance with utilisation of $\alpha_k(t)$ at 650° C, the required (as per Section 3.1.6) function of $\alpha_k(r_\mathrm{M})$ is also taken to be that fitted to precipitates evolving at the same temperature both to ensure consistency/eliminate sources of error and because of its much larger range compared to the data at 600° C. Nevertheless, it must be pointed out that the actual function used is not that displayed in Figure 5.16c for a key reason: Following the discussion in Section 5.3.1 it is immediately deducible that part of the isothermal data set ultimately used in the derivation of the $\alpha_k(t)$ curve in Figure 5.16c suffers from two key flaws. Firstly, the precipitate population measured in material aged for 50 hours is characterised (Figure 5.11) as having poorly defined aspect ratios. Second, the precipitate population after 3000 hours likely suffers from the influence of coprecipitating δ-phase (Figure 5.12). In line with these facts, therefore, and given the paramount need for accurate data to ensure the correct calibration of the SFFK model defined here, the mathematical description for $\alpha_k(r_{\mathrm{M}})$ harnessed instead is that defined in Equation 6.1 which is based purely on the hyperbolic fit to the precipitates measured after 100, 200 and 1000 hours of ageing (presented in Figure 6.1).

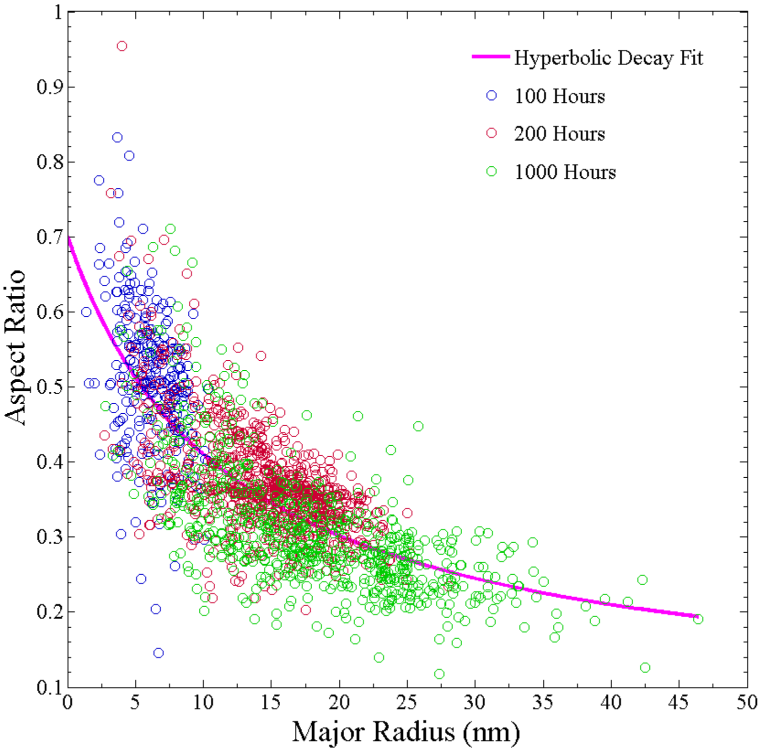

Figure 6.1: Aspect ratio and major radius for γ'' precipitates formed at 650 °C after the indicated ageing time. Hyperbolic decay fit made to data as a whole.

$$\alpha_k(r_{\mathrm{M}}) = 0.0625 + \frac{0.6368 \times 12.003 \times 10^{-9}}{12.003 \times 10^{-9} + r_{M,k}} \tag{6.1}$$

Accepting the aforementioned implication for $\alpha_k(r_{\mathrm{M}})$, it is axiomatic that, owing to its construction from the same data, the requirement for a minimisation of the influence of error on the mathematical relationship for $\alpha_k(t)$ necessitates that the relationship in Figure 5.18b is also precluded from use in the calibration. Unfortunately in this instance, however, it turns out that the three remaining data points are not sufficient on their own to allow for the creation of a sufficiently "good" hyperbolic fit[1] meaning another data point must be appended to the isothermal set. As a result of this

---

[1] The quality of the hyperbolic fit made to the data is determined by the fitting software thorough the use of a quantity known as the coefficient of determination (R-squared) *viz.* the software will only

eventuality, therefore, given the elimination of the remaining experimental data, the fit utilised for the calibration detailed in Equation 6.2 and illustrated graphically in Figure 6.2 is computed based not only on the data points at 100, 200 and 1000 hours of ageing in Figure 5.18c but also $\alpha_k(20\text{ hours}) = 0.7$. The latter value is defined according to $\alpha_k(0) = 0.7$ in Figure 6.1 and (by linear interpolation of the values at 50, 100 and 200 hours) INVH(20 hours) = 1 in Figure 5.6.

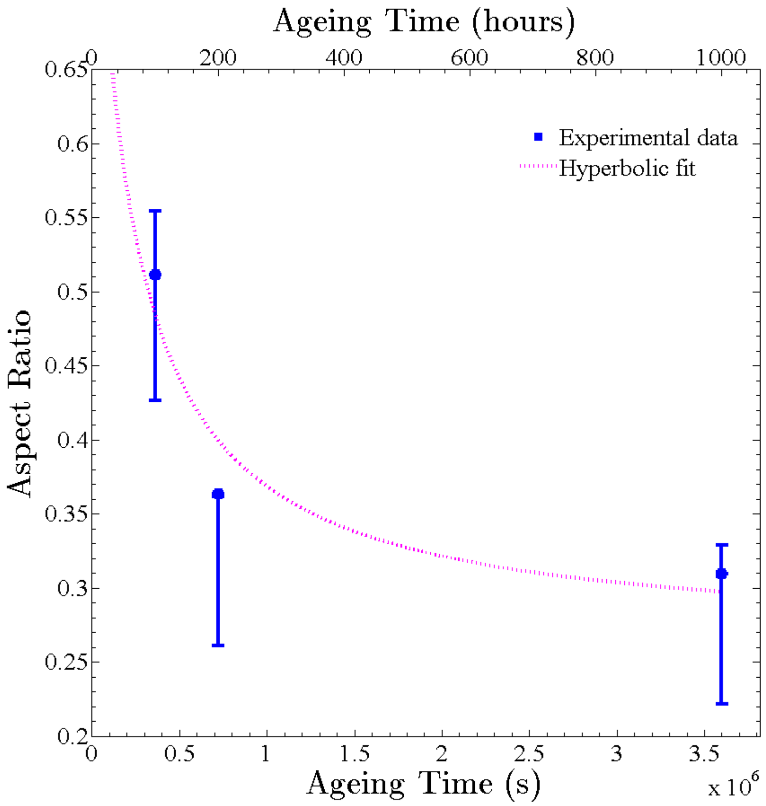

Figure 6.2: Aspect ratio and major radius for γ'' precipitates formed at 650 °C after the indicated ageing time. Hyperbolic decay fit made to data as a whole.

$$\alpha_k(t) = 0.2645 + \frac{0.5852 \times 0.01668}{0.01668 + t(s)} \tag{6.2}$$

6.1.1 Misfit Strain

Although the parameters required with reference to the misfit strain (λ) attributed to a particle were seemingly only those outlined in Sections 3.1.3 and 3.1.4, Equation 2.7 dictates that the specific relationship between the value of λ (and therefore ε and $\Delta\varepsilon$) and the aspect ratio also be defined. The functions $\varepsilon(\alpha)$ and $\Delta\varepsilon(\alpha)$ cannot, however, be calculated directly from the results of Slama *et al.* [4] selected for use

---

produce fit parameters if the value of (R-squared) exceeds a certain threshold defined by the software designers.

in this research because of both the lack of precipitate size data presented and the difference in temperature compared to calibration data used in this research (680° C vs. 650° C). Consequently, before any calculation can be performed it is required that both functions be evaluated using additional experimentally gathered data.

Considering the uncertainties associated with directly correlating the experimental data of Slama *et al.* to that acquired in this research for Alloy 625 (resulting from likely differences in their precipitate kinetics as evidenced by their TTT curves [23, 346, 347, 348]) it is reasonable to argue that the adoption of simple approximations are suitable *viz.* treatments which attempt more precise conversions will likely yield no additional benefit. In this regard, the following approach is undertaken: Firstly, utilising the fact that the time lag for the same precipitate statistics (size and aspect ratio) being attained between ageing at 750° C and 680° C is measured by Slama *et al.* as approximately 50 hours, the time difference between precipitates attaining the same lattice parameters at 650° C as those measured at 680° C in Alloy 718 is calculated from linear extrapolation as 21.4 hours. Next, the precipitation kinetics of the γ'' phase in Alloy 718 and Alloy 625 are assumed to be identical at 650° C with justification taken from the similar locations of the TTT curve for the phase in both alloys at this temperature [23, 346, 347, 348]. Finally, the aspect ratio values corresponding to the lattice parameters measured by Slama *et al.* are found by inserting the relevant time value calculated for ageing at 650° C (from the linear extrapolation) into the relation shown in Figure 6.2.

With the values for the lattice parameters evaluated, plots of the $\epsilon_{1,1}$ and $\epsilon_{3,3}$ components of the strain tensor against aspect ratio can be created using the expressions detailed in Equation 3.2 as shown in Figure 6.3. Similarly, the values of ε and $\Delta\varepsilon$ can in turn be computed from these data points according to Equation 3.1. As a result of this methodology, therefore, as the calculation designed in this research proceeds, the correct misfit strain of a particle is ultimately determined from its aspect ratio α through the use of a continuous mathematical relationship fitted to the data. Nevertheless, because of the relatively large error bars associated with each of the data points and the resultant large a number of different possible mathematical trends can be drawn with equal validity, before the model can be executed it is first necessary to calibrate this variable through the identification of the fit which corresponds to the true behaviour experienced in the real alloy system.

6.1.2 Interfacial Energy

Unfortunately for this research project, any attempted rearrangement of Equation 2.7 inevitably yields the result that the separate calculation of the values for ζ_k^E and ζ_k^M is impossible using this relation alone. Put simply, one is always left with an equation containing a scalar[2] and the two unknown variables. Accordingly, without an alternative solution, the only viable method for deriving a value for either of the interfacial energies involves the setting of the other as having a magnitude equal to zero. In a number of circumstances/systems the reasoning for the adoption of such an

---

[2] Once values for each of the variables have been inserted into Equation 2.7 a single value can be calculated but functions depending on the interfacial energies remain.

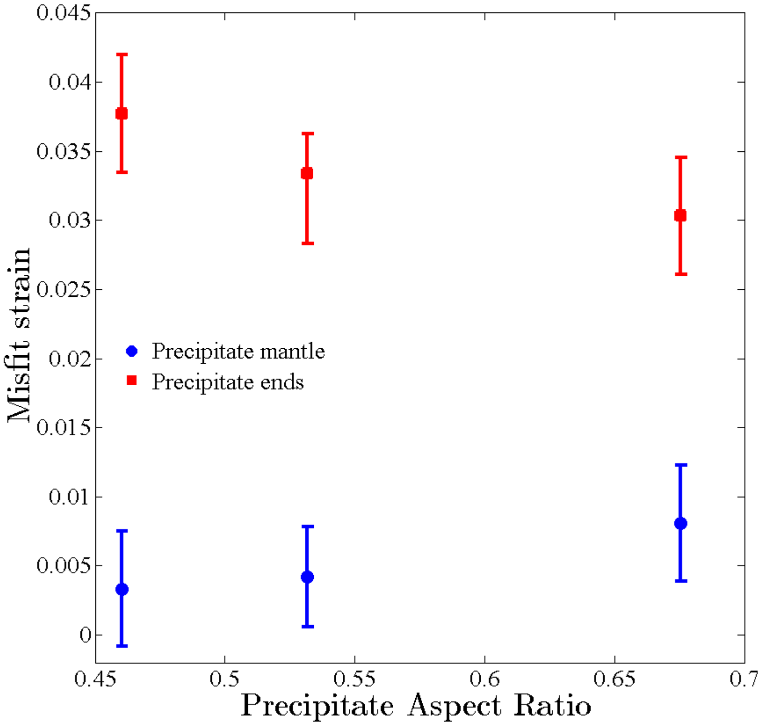

Figure 6.3: Eigenstrain values calculated for γ'' precipitates possessing different aspect ratios. Uncertainties calculated from combining uncertainties in the original measurements of precipitate lattice parameters made by Slama *et al.* [4].

approach would be spurious, however, the work of Hagel *et al.* [349] provides a sound basis for such a methodology with respect to the γ'' precipitates modelled here.

Analysis of γ' precipitates performed by Hagel *et al.* [349] led the authors to conclude that the interface between the matrix (γ) and the precipitate would only remain coherent if the volume strain ($\epsilon_{i,j}$) is below 1%. Inspection of the volume strains values calculated in Section 6.1.1 (Figure 6.3) highlights that this criterion is always obeyed for the strains experienced in an interface at the cylinder mantle ($i = j = 1, 2$) but not at the cylinder ends ($i = j = 3$) and, as a result, the former may be considered as remaining coherent throughout the a particle's evolution. Following the discussion in Section 1.3 that the interfacial energy of any two phases varies inversely to their coherence, therefore, the high coherence between the precipitate mantle and matrix means that one can reasonably make the approximation in the case of the particles described by the model in this research that $\zeta_k^M = 0$.

The result of the rearrangement of Equation 2.7 to create an expression for the calculation of ζ_k^E is presented in Equation 6.3. Evaluation of the differential expressions is achieved through the use of substitution whereby a "guess" is made as to the dependence of the interfacial energy on the aspect ratio: ζ_k^E is replaced with $\zeta_k^E(\alpha) = \zeta\alpha^{-1}$ where $\zeta \neq \zeta(\alpha)$. Justification of the relationship being of this type is taken from the behaviour of the accompanying variable of misfit strain at the precipitate ends ($\epsilon_{3,3}$) as illustrated in Figure 6.3.

$$\zeta_k^E = \frac{24\alpha}{5\xi_k^2}\left(\frac{\rho}{3}\frac{d\lambda}{d\alpha} + \dot{\alpha}_k\rho_k^3 RTO_k^3\sum_{i=1}^{n}\frac{(c_{ki}-c_{\gamma i})^2}{c_{\gamma i}D_{\gamma i}\alpha_k^2}\right) \tag{6.3}$$

As alluded to previously, it is clear from Equation 6.3 that calculation of the specific value of ζ_k^E for a precipitate of a particular r_{M} and α is only achievable with the use of the defined functions $\lambda(\alpha)$ and $\alpha(t)$. Accordingly, owing to the dependence of the misfit strain on $\alpha(t)$ also, the calibration of this variable is performed principally in this research using the mathematical relationship for $\alpha(t)$ at $650°C$ shown in Figure 6.2. Specifically for the length of the calibration calculation, the value of ζ_k^E is determined directly (via Equation 6.3) for each class during each iteration using the input values for $\lambda(\alpha)$ and $\alpha(t)$.

§ 6.2 Calibration Results

With calibration calculation designed, the final task necessitated before its execution was the setting of the value for each of the conditions/thresholds discussed in Section 3.2:

Time step and duration

As stated in Sections 3.2.7 and 3.2.10, the model created in this research is designed such that the time step is allowed to both increase and decrease in order to provide for both faster calculation times and the maintenance of detail. Unsurprisingly, therefore, a similar consideration is also made in the selection of the starting/initial value for the time step (Δt_0) as 0.1 seconds. This magnitude for Δt at the start of the calculation provides for not only the slow build up of the number of nucleating particles per iteration, but also the maintenance of small changes in the aspect ratio and radius of each of the precipitate classes between iterations, despite their relative change rates being at a maximum (as evidenced by the figures in Section 5.3.2). The outcome provided by a still smaller time step would not prove beneficial from a detail standpoint, but because of the incremental increase of 1% per iteration, would add an extra 232 iterations[3] for every factor of 10 decrease in the size of the initial time step.

Both the duration of the model and the intervals at which data is recorded are chosen based on the experimental data gathered in this research: For the calibration, the model duration was set at 1000 hours (3.6×10^6 seconds) with data recorded after 1, 10, 100, 200, 300, 400, 500, 600, 700, 800, 900 and 1000 hours. Smaller time intervals are used at the start of ageing due to the more rapid change in precipitate statistics expected to result from the higher driving force present.

---

[3] The number of iterations taken to achieve a ten fold increase in the time step is calculated from a simple logarithmic calculation: $\log_{1.01}10 \approx 232$

Precipitate size and aspect ratio

As discussed in Section 3.2.4, whilst particle classes shrinking in radius evolve, they are removed from the PSD before they reach a value of zero for reasons of physicality and calculation time. The limit of this threshold for the equivalent radius, corresponding to the size of one molecule of precipitate (or the matrix given their equivalence in the model), is calculated (consistent with Section 3.2.1) from the value of the molar volume Ω required to achieve a critical stable radius of 1.0100nm at the start of the calculation ($\Omega = 4.10637 \times 10^{-5}\,\text{mol m}^{-3}$) as 0.3nm;

Aspect ratio

The aspect ratio change limit selected as per the aspect ratio check mechanism detailed in Section 3.2.7 is that of 0.01 per time step for any one class. This limit was chosen based on the expected change in the magnitude of α for a typical precipitate depicted in Figure 6.1 and the time step previously discussed; whilst obviously relatively high, the implementation of a smaller limit was dismissed because of the small time step implemented at low ageing durations which ensured a small change in the aspect ratio at these conditions. Additionally, the comparatively negligible impact that a reduction of 50% in the time step would have on the overall magnitude of the aspect ratio change at short ageing times means that any limit set such that it was continuously breached at the start of ageing would, inescapably, result in a significant increase in the computational time required.

Precipitate number

The limit for the minimum number of particles required for a class to contain so that it is retained in the PSD, necessitated to expedite the calculation (Section 3.2.2), was determined based on a decision that no class would exceed any other in size by a factor ≥ 100000. From preliminary results the maximum number of particles found in any one class was always $< 10^{19}$ leading to the threshold for the minimum number of particles being set as 10^{14}.

6.2.1 Aspect ratio

Considering the importance of $\alpha(t)$ in the derivation of the calibrated values for both $\lambda(\alpha)$ and ζ_k^E (*q.v.* Sections 6.1.1 and 6.1.2 respectively), it is logical that it is this variable which should be examined first when analysing the results of the calibration calculation: As depicted in Figure 6.4, upon initial comparison between the experimental (input) and model generated results it is clear that, whilst the shape and magnitude of the two sets of data are in excellent agreement, a time (x-axis) shift exists between them. The source for this phenomenon can be identified as the set-up of the calculation detailed in Section 3.2.1, specifically the requirement that new, nucleating particles during the first iteration of the model possess a critical radius of 1.01nm. That is, owing to the use of input experimentally derived data, such a condition on the initial radius has the effect of skipping the point at which the model starts ($t_{\text{Model}} = 0$) to that at which the real system possess this same critical radius ($t_{\text{Real}} \neq 0$). The magnitude of this translation in the time values between the model and experimental data can be found by sequentially evaluating the value of $\alpha(\rho)$ when $\rho = 1.01$ nm according to Equation 6.1 and $t(\alpha)$ by rearrangement of Equation 6.2 (defining the trend shown in Figure 6.2), yielding a value of 32.73 hours.

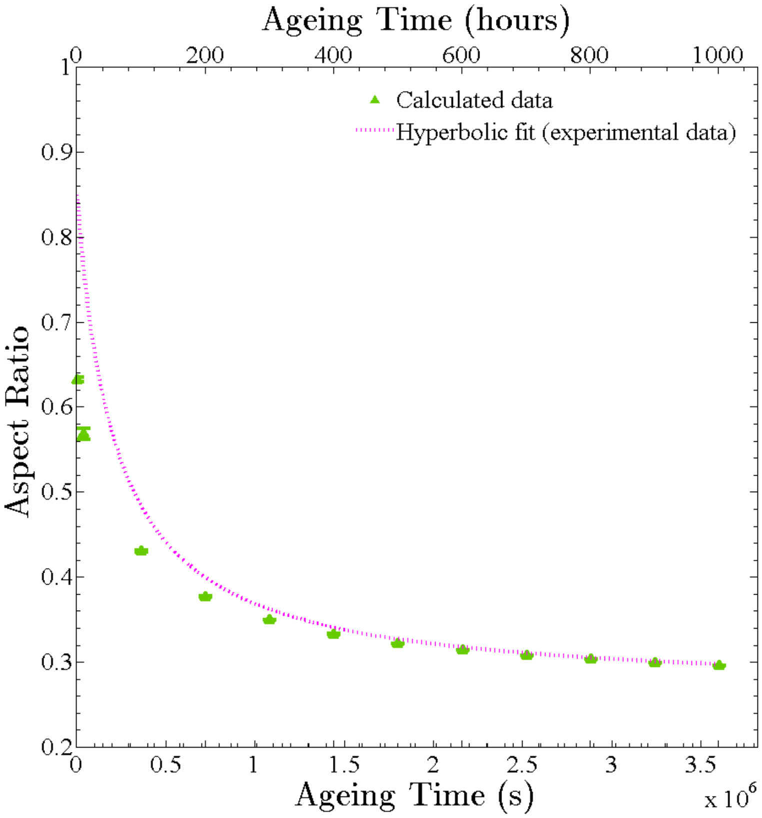

Figure 6.4: Calculated aspect ratio evolution for γ'' precipitates predicted by the SFFK based model created in this research. Data points correspond to average values and the error bars to the first and third quartiles of the aspect ratio distribution. Mathematical trend defined in Figure 6.2 shown for comparison.

An amended version of Figure 6.4 in which the time shift incurred from the computation has been applied is shown in Figure 6.5. In this case, the figure displays that agreement between the two data sets is now almost total, particularly at longer ageing times, indicating not only that the time discrepancy between the two trends has been successfully accounted for, but also that the model correctly reproduces the calibration data. Such a correlation between the input (for the calculation of both the misfit strain and the inter-facial energy model) and output average $\alpha(t)$ trends, whilst important, was necessarily expected for the calibration as any other outcome would have indicated some problem within the calculation script. A superfluous (from a calibration standpoint) but equally expected outcome also observed in Figure 6.5, however, is the very narrow limit the spread of generated distributions (indicated by the error bars) with respect to the aspect ratio. Predictability of this latter phenomenon derives from the fact that the mechanism for calculating the misfit strain and interfacial energy of all the classes utilises an average trend for $\alpha(t)$ thereby necessitating all particles principally follow this path. Clearly, the contrast between such a mathematically generated aspect ratio distribution and those which are measured experimentally has implications for the physicality, and ultimately the usefulness, of the results produced by the model created in this research using the calibration method employed but, owing to the problems previously outlined, no viable alternative exists. Furthermore, as average values constitute the key statistic in calculating the impact of a precipitate distribution on the properties of Alloy 625 material, and because the variables of precipitate size and number density are more important in this regard, the lack of correspondence in aspect ratio distribution spread is unlikely to constitute a significant problem in many applications of the model results.

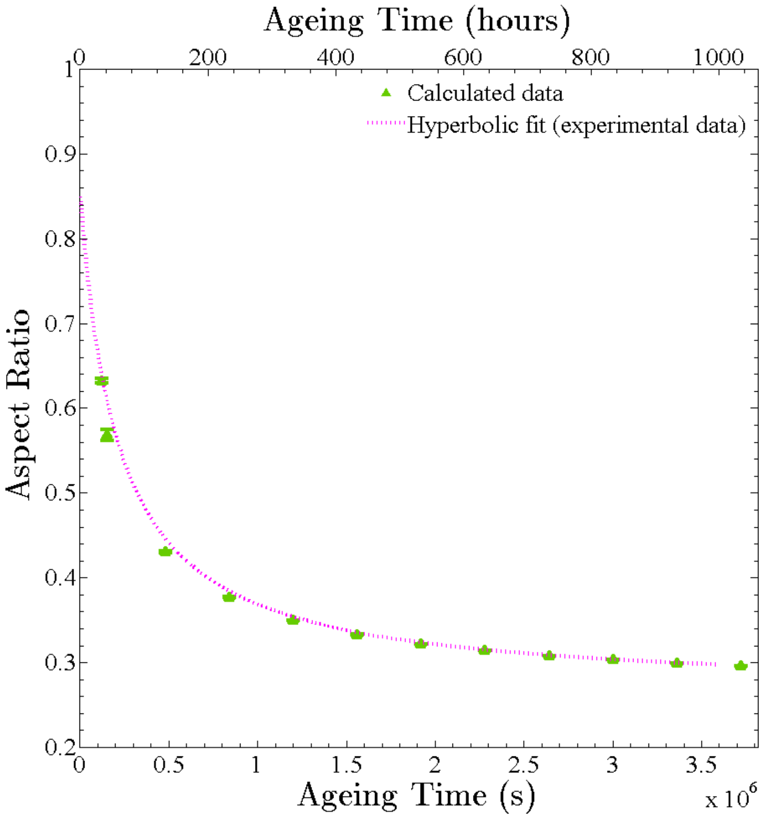

Figure 6.5: Calculated aspect ratio evolution for γ'' precipitates predicted by the SFFK based model created in this research with time-shift correction applied. Data points correspond to average values and the error bars to the first and third quartiles of the aspect ratio distribution. Mathematical trend defined in Figure 6.2 shown for comparison.

6.2.2 Misfit Strain

As alluded to in Section 6.1.1, the identification of the correct trends for the misfit strains between the precipitate and matrix ($\epsilon_{1,1}$, $\epsilon_{3,3}$) is complicated severely by the large error bars associated with each of the data points. Under such a condition, the only viable course of action was determined in this research to be the performance of exhaustive trial and error calculations; the correct trends were established based on the model producing results which correlated best to those observed experimentally in respect of r_{M}. The effect of changing the interpreted fit for both of the misfit strains on the outcome of the calculation, thereby indicating the sensitivity of the model to these parameters as encountered throughout the trial and error study, is outlined in Appendix H.

The resultant hyperbolic relationships[4] produced by the aforementioned trial and error study conducted in this research for both $\epsilon_{1,1}$ and $\epsilon_{3,3}$ are shown in Figure 6.6. Their corresponding mathematical descriptions are defined in Equations 6.4 and 6.5 respectively.

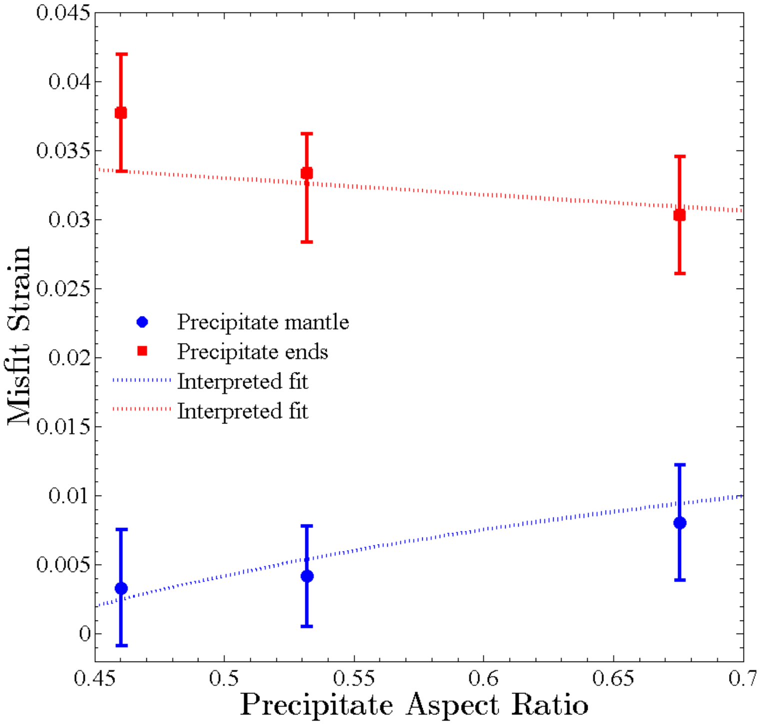

Figure 6.6: Hyperbolic fits to misfit strains $\epsilon_{1,1}$ and $\epsilon_{3,3}$ interpreted as corresponding to the true behaviour of these parameters for γ'' precipitates in an Alloy 625 matrix. Data points displayed separately in Figure 6.3 are also indicated.

---

[4] Interpretations for the data were limited to hyperbolic type fits because of their identification in Section 5.3.2 as the underlying trends for $\alpha(t)$ and $\alpha(r_{\mathrm{M}})$.

$$\epsilon_{1,1} = \frac{0.424\alpha}{0.0259 + \alpha} - 0.3989 \tag{6.4}$$

$$\epsilon_{3,3} = \frac{0.1065 \times 6.8057}{6.8057 + \alpha} - 0.0633 \tag{6.5}$$

Inspection of the fits (and *ipso facto* their governing equations) in Figure 6.6 highlights the paths followed by the two variables to be opposite, with the misfit strain on the precipitate mantle $\epsilon_{1,1}$ following the trend of hyperbolic growth and the misfit strain on the precipitate ends $\epsilon_{3,3}$ obeying a hyperbolic decay type relationship. In addition to this discrepancy in the direction of their behaviour, it is also observed that the value of $\epsilon_{1,1}$ undergoes a much more significant change than that of $\epsilon_{3,3}$ and possess a more pronounced curvature. Of course it should be remembered that both of these relationships are defined according to an increasing aspect ratio *viz.* the value of $\epsilon_{1,1}/\epsilon_{3,3}$ actually decreases/increases according to the defined relationships as particles grow and their aspect ratio reduces.

In Section 6.1.2 it was shown that the calculated value of $\epsilon_{1,1}$ implies the interface will retain coherency throughout the evolution of the precipitate over the defined range (0.68-0.46). Given the limitations placed on the fitting, therefore, it is unsurprising that the trend accepted predicts the same behaviour the same values; however, the interpreted fit also additionally shows the interface to seemingly improve in terms of misfit as a particle evolves, reaching a minimum value at around 0.41 before regressing. Bearing in mind this information, one is able to surmise that, owing to the fact that underlying calculation of the strain tensor components is associated with the lattice parameters, there appears to be a continuous reduction in the value of $a_{\gamma''}$ with respect to a_{γ}. Moreover, it can also be concluded that this reduction leads to a breakdown of the coherency of the interface when $\alpha \leq 0.28$ as $\epsilon \geq 1\%$. Performing similar analysis with respect to the equation accepted for the governance of the misfit at the precipitate ends ($\epsilon_{3,3}$), it can be concluded that the interface becomes more incoherent over time at a very gradually changing rate. Additionally, this $\epsilon_{3,3}$ behaviour can also be used to interpret the variation of the relevant precipitate lattice parameter $c_{\gamma''}$ yielding the conclusion of a constantly increasing value as precipitates grow in size and their aspect ratio reduces.

Direct calculation of all three of the relevant lattice parameters used in the strain tensor (Equation 3.2 from the two trends displayed in Figure 6.6 is impossible owing to there being too many unknown variables. In light of this fact, therefore, a different approach is taken whereby the evolution of the matrix lattice parameter (a_{γ}) is determined from those values which construct a hyperbolic type relationship and, concomitantly, result in hyperbolic trends for $a_{\gamma''}$ and $c_{\gamma''}$ that remain inside the regions parametrised by the experiential uncertainty. Fortunately, this approach proves to be far from arbitrary, with only a single possible fit for each parameter complying with the outlined criteria when parameters are defined (consistent with the Slama *et al.* [4]) according to 3 decimal places. The inferred a_{γ} behaviour, together with the resultant value trends produced for $a_{\gamma''}$ and $c_{\gamma''}$, are outlined mathematically in Equation 6.6 and shown graphically in Figure 6.7.

$$a_{\gamma} = 3.5607 + \frac{0.1455 \times 0.1703}{0.1703 + \alpha} \qquad a_{\gamma''} = 2.0257 + \frac{1.6527\alpha}{0.0233 + \alpha}$$
$$c_{\gamma''} = 7.1796 + \frac{0.4366 \times 0.6865}{0.6865 + \alpha} \tag{6.6}$$

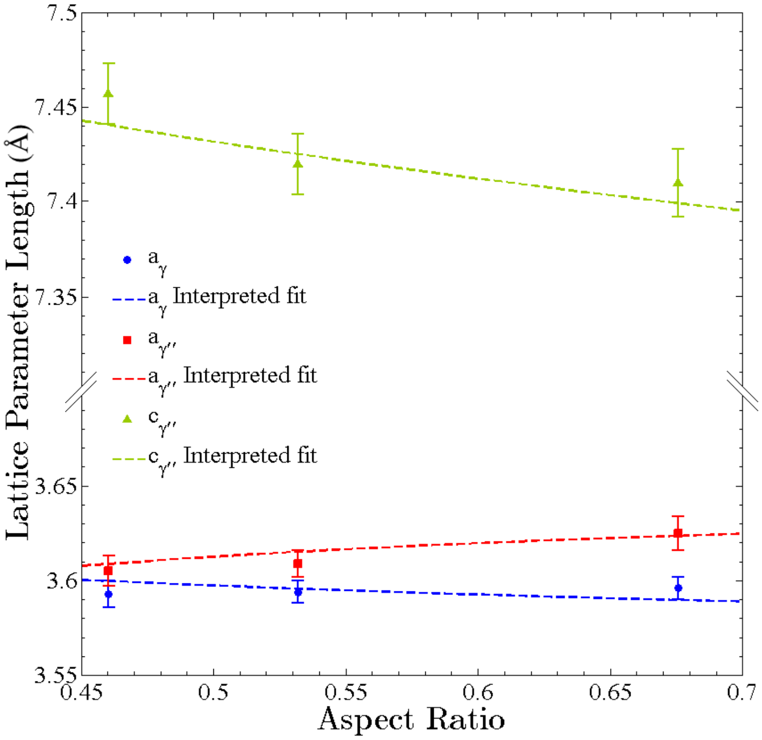

Figure 6.7: Trends calculated for the lattice parameters a_{γ}, $a_{\gamma''}$ and $c_{\gamma''}$ from the fits made to the misfit strains $\epsilon_{1,1}$ and $\epsilon_{3,3}$ shown in Figure 6.6. Data points calculated from the experimental measurements of Slama *et al.* [4] are also shown for comparison.

Rather than incidental result, the observation of a singular hyperbolic trend for the value of a_{γ} being valid for the calculation of both $\epsilon_{1,1}$ and $\epsilon_{3,3}$ (when the result produced by the model most closely matches the experimentally acquired data) is significant because of the way the calibration was performed: During the trial and error study undertaken to determine the appropriate interpretations for $\epsilon_{1,1}$ and $\epsilon_{3,3}$, each mathematical description was incrementally changed (independent of the other) to allow for a full exploration of the possible evolutions of both variables. Consequently, in many instances, as discussed in Appendix H), the value of a_{γ} implied by the fits was incompatible over some or all of the particle evolution *viz.* whilst the interpretations were still bounded by the error bars in Figure 6.3, the values of $\epsilon_{1,1}$ and $\epsilon_{3,3}$ at an instantaneous moment could not be calculated using the same value of a_{γ}. Had such a discrepancy between the fits presented Equations 6.4 and 6.5 and the extrapolated data points from Slama *et al.* [4] used in their derivation been present, significant questions about the appropriateness of the extrapolation procedure would have inevitably arisen. The fact that the fits actually found to produce a result most consistent with the experimental data used in the calibration were also discovered to comply with a common value of a_γ evolving in a hyperbolic manner, therefore, suggests that the procedure for producing Figure 6.3 (outlined in Section 6.1.1) is sound. Similarly, the observance that only a single hyperbolic type relationship can be used to define a valid path for a_γ suggests that the evolutions presented are representative of those which would occur in a real system, albeit with the relevant modifications according to the assumptions of the model.

6.2.3 MAJOR RADIUS

The γ'' major radius distribution evolution predicted by the model during ageing at 650° C using the previously defined mathematical descriptions $\epsilon(\alpha)$, $\alpha(t)$ and (by Equation 6.3) ζ_k^E is shown in Figure 6.8. Again, as detailed for the aspect ratio evolution, a time-shift correction of 32.73 hours is necessarily applied to each of the data points to account for the impact of the conditions applied in the set-up of the calculation.

Initial inspection of Figure 6.8 yields the conclusion that reasonable agreement between the modelled and experimental $\bar{r}_{\mathrm{M}}$ values is obtained over the entire ageing range. More detailed analysis, however, reveals that whilst particularly strong conformity between the calculated and interpreted data sets is obtained up to 232.73 hours, a consistent absolute magnitude underestimation of the experimental fit of approximately 1nm is seemingly introduced by the model thereafter. The principle reason for this slight discrepancy at long ageing times most likely derives from the hyperbolic fit made to the experimental data being an over estimate (greater correspondence is observed with the experimental data point). Nevertheless, the phenomenon of particle coalescence at this condition (*q.v.* Section 5.3.1) also almost certainly comprises a contributory factor owing to the fact that it will increase the average particle size in a manner not accounted for in the model. Quantitatively, the divergence between the average value trends of two data sets evidenced in Figure 6.8 has an average relative magnitude after 232.73 hours of around 5%, which, in the light of the assumptions made in the derivation of the model and the input calibration parameters, can be considered an acceptable discrepancy.

In contrast to the results obtained for the aspect ratio discussed in Section 6.2.1, due to the fact that r_{M} is not used as a calibration parameter, the major radius distribution is observed to possess a large spread akin to that expected in experimentally measured statistics. Furthermore, quantitative comparison of the relative first and third quartiles of both the experimental and the corresponding (albeit time shifted) model generated distributions shows their magnitudes to be remarkably similar beyond 100 hours indicating the shape of the calculated distributions to be in good agreement at these ageing times. Given this correspondence, the larger disparity between the two datasets at 100/133 hours is likely a result of the relatively rapid divergence in the particle distribution, which is evidenced to happen around these ageing times, causing significant evolution in the time-shift period.

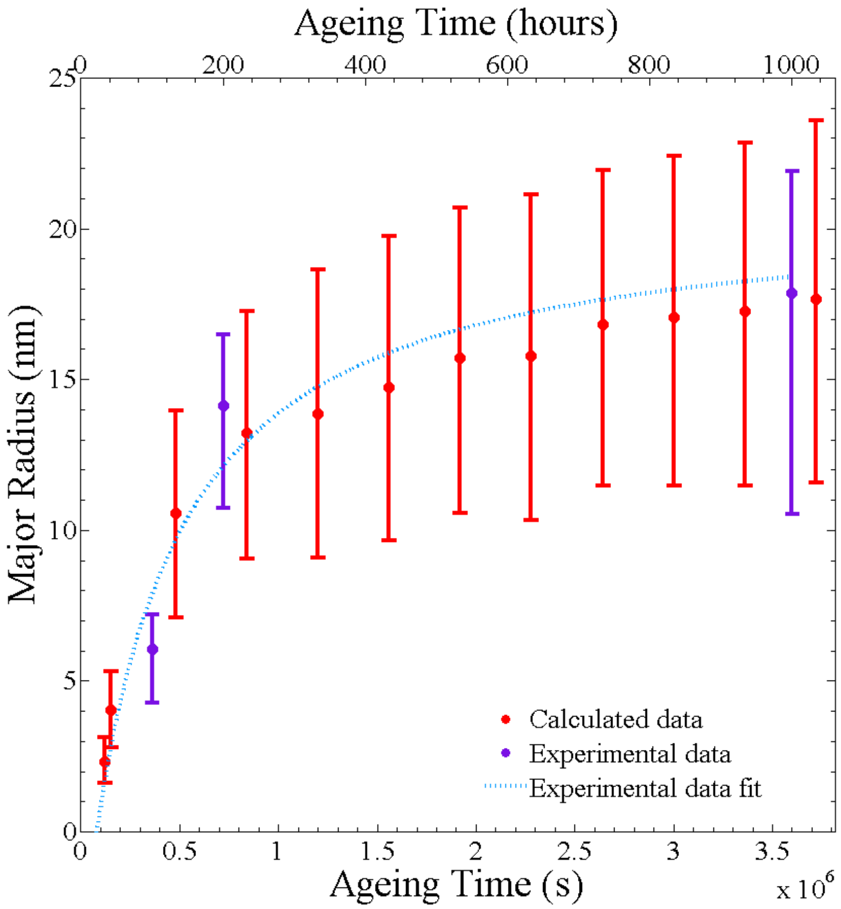

Figure 6.8: Calculated major radius (r_M) evolution for γ'' precipitates predicted by the SFFK based model created in this research with time-shift correction applied. Data points correspond to average values and the error bars to the first and third quartiles of the PSD. Experimental data points for populations existing after 100, 200 and 1000 hours of ageing along with an illustrative hyperbolic fit are shown for comparison.

Clearly a more direct and detailed comparison of the calculated distributions, just discussed, can be made with the corresponding experimentally measured ones through assessing their actual shapes rather than just their indicative variables. To this end a presentation of the particle size distributions recorded at a simulation time of 100, 200 and 1000 hours, corresponding to time shifted values 33 hours greater is made in Figure 6.9.

Considering, initially, the model distributions themselves, it is clear from Figure 6.9 that, whilst a smooth continuous distribution is observed over nearly all values, at the largest radii a huge spike in particle number is present in tiny number of classes. A first glance, the presence of such a spike would seem alarming; however, consideration of how the displayed distributions are produced identifies the phenomenon as not being a detrimental mathematical flaw but a reasonable outcome that arises from a single computational constraint. Explicitly, a grouping of classes in the model PSD around a small range of large radius values means that, as the separation between these classes

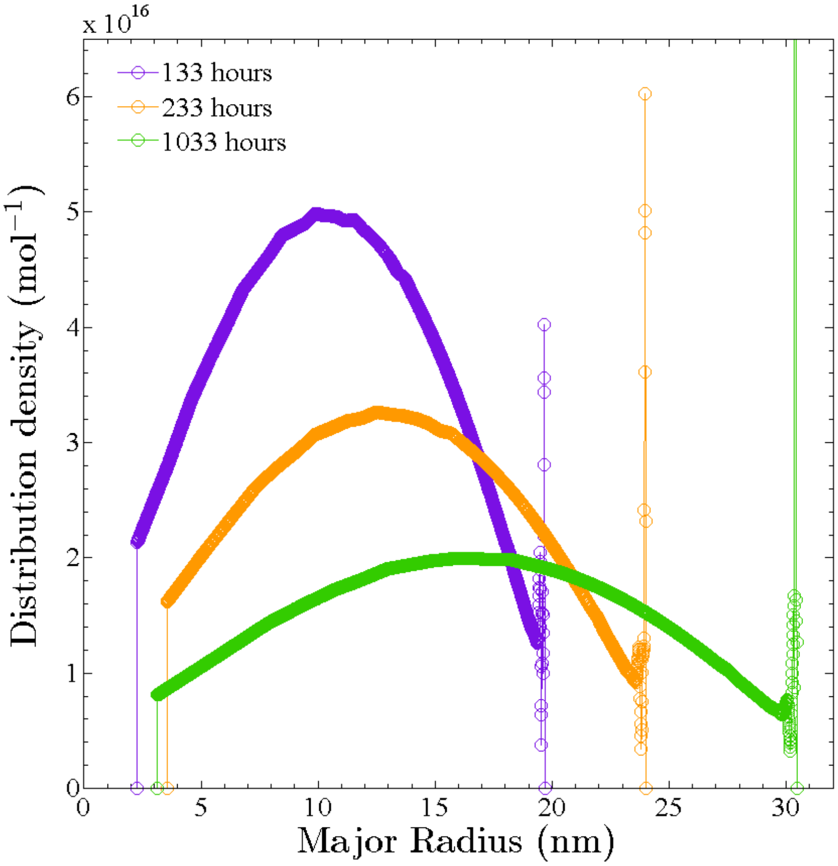

Figure 6.9: Calculated particle size distributions for γ'' precipitates when ageing for the specified times at $650°C$.

is unusually small, the process used to calculate the particle distribution density (*q.v.* Section 3.2.8) results in their possessing a value significantly higher than other classes in the distribution.

The specific origin of the grouping of large particle classes can be attributed to a resolution by the governing equations of a problem created by the iterative procedure used to calculate the evolution of the particle size distributions: Firstly, as outlined in Section 3.2.4, the independent calculation of the growth rate of each class from the supersaturation remaining from the previous time iteration inevitably leads to instantaneous growth rates larger than those which would be expected from the continuous (*i.e.* infinitesimally small time step) concurrent growth of all classes. Second, the large time gap between the successive nucleation of new particle classes at long ageing times (owing to the large time step present) allows for the enhanced evolution of existing classes between time steps because of there being too few particles to suppress the driving force. Ultimately, the combination of these two factors means that, near the end of the nucleation and growth stage, some classes possess an overly large radius which depresses the driving force for new nucleating classes sufficiently for them not to exceed the old classes and take their correct place in the PSD as indicated by their particle number. In other words these classes become stuck amongst the larger particle classes. A visual representation of this intermingling of the smaller and larger particle classes is given by the undulations in the spike in the PSDs in Figure 6.9. If the suppression phenomenon were not present, the smaller classes would have grown to considerably larger radius values and (through the dictation of the driving force equations) have contributed the same to the particle size distribution as the spike. That is to say, the presence of the same driving force for coarsening, operating under the same conditions detailed at the start of Section 6.2, would inevitably lead to the same volume of precipitate being present beyond this part of the PSD at the specified time interval.

Returning to the comparison of the shape of the most closely matched (*i.e.* 200/233 and 1000/1033 hour) experiential and modelled distributions (overlaid in Figure 6.10), considering the undulations in the data it is clear that a particularly good replication of the experimental PSD has been achieved by the model at 1000/1033 hours up to the data cut-off. At 200/233 hours the two distributions are less harmonious (the modelled distribution is much flatter), however, as indicated previously by comparison of the quartiles, good correspondence between the width of the two PSDs is still obtained. Moreover, considering that the flattening of the 233 hour PSD with respect to the 200 hour experimental PSD will be more heavily enhanced by the time-shift at this ageing duration, owing to the faster evolution of the PSD which takes place (evidenced in Figures 6.8 and 6.9), it is likely that the distribution at $t_{\mathrm{Model}} = 200$ hours would show much closer agreement.

Supplementary to the aforementioned observations, additional analysis of the PSDs in Figure 6.10 also yields further evidence for the cause of the spike in the experimental distributions at the largest radius values to be that of small particle classes not being able to grow as much as would be expected. Specifically, the extension of the experimental distributions to radius values markedly beyond those bound by the model distribution, despite the good agreement seen over all other values, highlights there to be a problem with the model replicating only this area of the PSD. What is more, the similar positions of the quartiles and averages of the two distributions (Figures 6.8) shows the contribution of large experimental particles to be almost exactly the same as that of the spike in the model PSD.

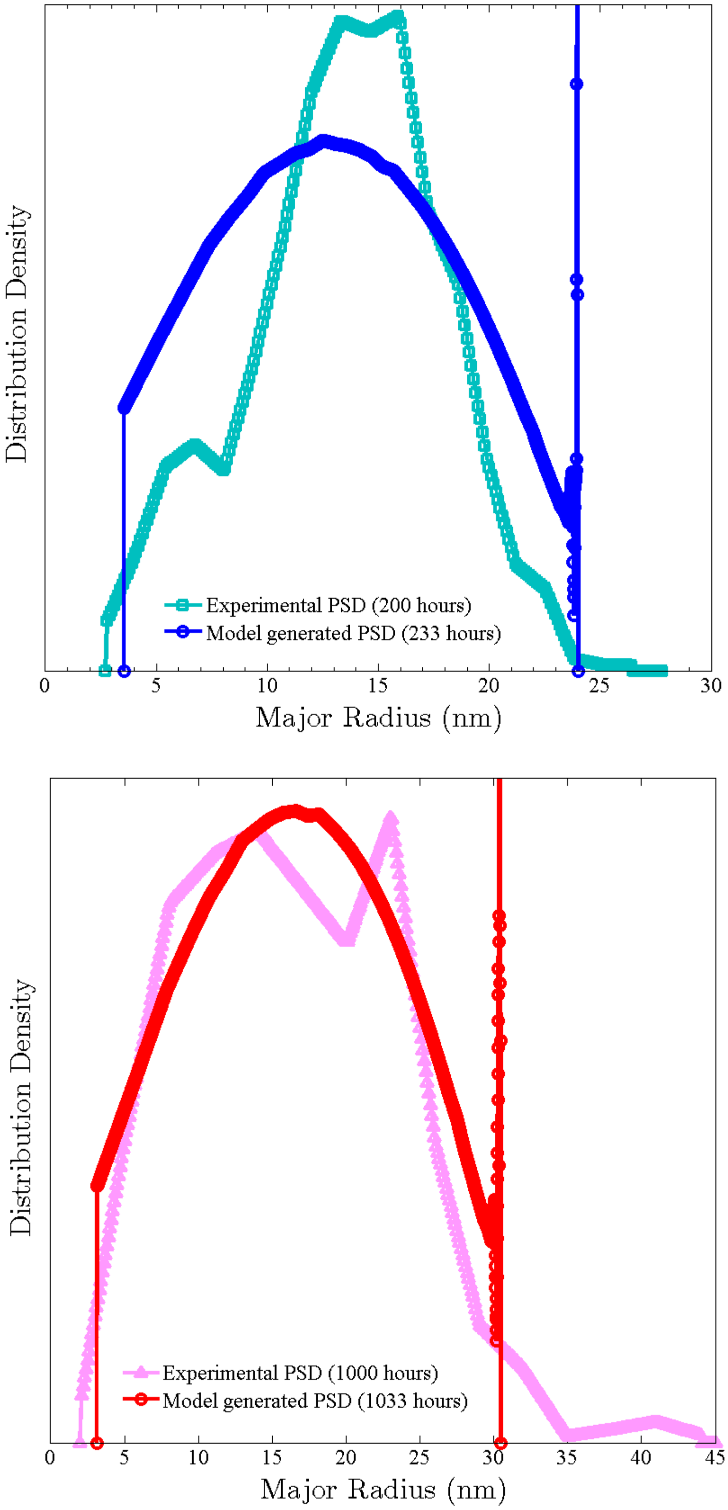

Figure 6.10: Model and experimental particle size distributions (PSDs) for γ'' precipitates created in Alloy 625 when ageing at 650° C for the indicated times. For ease of comparison the value of the distribution densities have been altered such that the same number of particles are contained within both distributions making their specific magnitudes arbitrary.

6.2.4 Number Density

To make an assessment of the accuracy of the predicted value for the number density of γ'' precipitates present within Alloy 625, the arbitrary nature of the specific location of classes defining a descretised distribution means it is again necessary to utilise the distribution density. To this end, the indicative number of particles ($N_{\mathrm{New},k}$) in classes located at small, regular intervals is calculated via Equation 6.7 (where the index k corresponds to each precipitate class, ρ_k is the equivalent spherical radius, and d_k is the value of the distribution density evaluated at ρ_k), before each of the values are rescaled ($N_{\mathrm{New},k} \rightarrow N''_k$) to maintain the same precipitate volume fraction as that of the original distribution ($N_{\mathrm{Old},k}$) via Equation 6.8 (N''_k represents the rescaled value, m is the total number of classes and the other symbols have their predefined meanings). It should be noted that in this instance the distribution density is calculated with respect to ρ rather than r_{M} (as before) owing to the complications introduced by attributing correct α values to any class taken from the major radius distribution density. The results of the aforementioned procedure on the model data produced during the calibration calculation is shown, together with the experimental data, in Figure 6.11.

$$N_k = d_k(\rho_{k+1} - \rho_k) \tag{6.7}$$

$$N''_k = N_{\mathrm{New},k} \left(\frac{\sum\limits_{k=1}^{m_{\mathrm{Old}}} \rho^3_{\mathrm{Old},k} N_{\mathrm{Old},k}}{\sum\limits_{k=1}^{m_{\mathrm{New}}} \rho^3_{\mathrm{New},k} N_{\mathrm{New},k}} \right) \tag{6.8}$$

Comparison of the two data point sets in Figure 6.11 reveals that, whilst relatively good agreement can be inferred both with respect to the magnitude of the number density of γ'' precipitates and their evolution behaviour, a distinct disparity is evident especially at short ageing times. Considering its marked impact on the size/quantity of precipitates to constitute a particular molar fraction, an obvious contributory factor to this disagreement can immediately be deduced as the different values for the molar volume associated with/used in the calculation of each dataset. That is to say, the changing magnitude for the molar volume of Alloy 625 and γ'' (evidenced by the changing lattice parameters in Figure 6.7) means that the, different, constant values used when calculating both the model precipitate statistics and those from the experimental micrographs (as performed in Section 5.3.1) result in both trends being somewhat erroneous and incompatible. A successful relative correction for this implication is achieved through two transformations, both applied to the modelled data, based on the key assumptions that: 1) The behaviour of the lattice parameters inferred from the misfit strain evolution (Figure 6.7) occurs in both the modelled and experimental system and 2) The molar volume fraction occupied by both phases remains constant.

The first of the transformations applied to the modelled data accounts for discrepancy between the molar volume of γ'' (calculated from the lattice parameters) and Ω and is

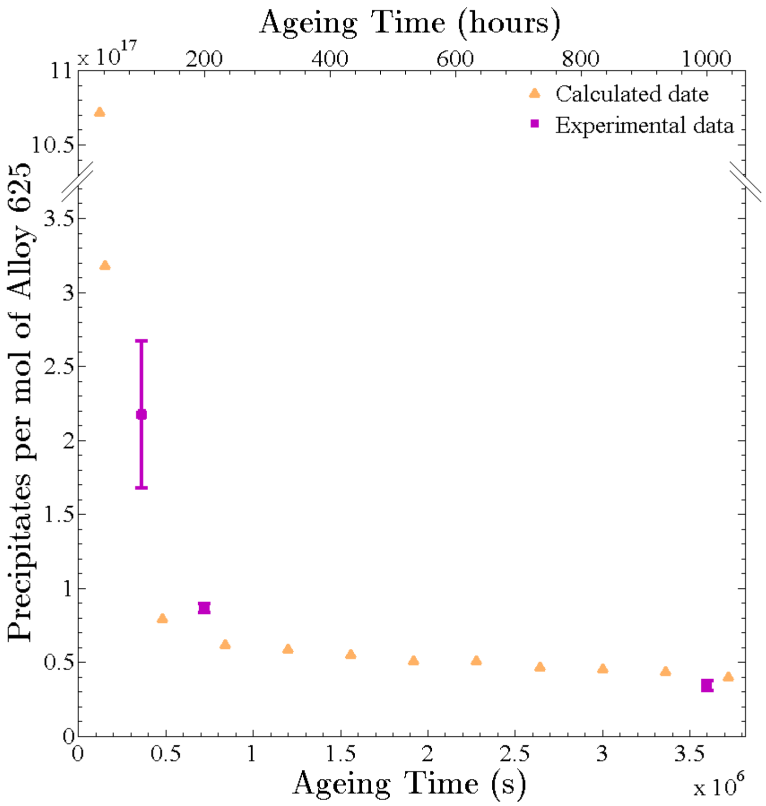

Figure 6.11: Calculated number density evolution for γ'' precipitates predicted by the SFFK based model created here. Experimental data points shown for comparison.

implemented through increasing the number of particles by the ratio of the two volumes at the relevant time *i.e.* at the relevant average aspect ratio. The second transformation accounts for the changing molar volume of Alloy 625 when evaluating the experimental number densities and constitutes a similar rescaling through calculation of the ratio of the actual average molar volume in Alloy 625 (calculated from the respective molar volumes and mole fractions of the precipitate and matrix phases) to the assumed molar volume. Manifestly, the second transformation should be applied to the experimental data points in Figure 6.11 but a lack of detailed information about the phase fractions in the system means that the correction was applied instead through the multiplication of the model values by the inverse ratio.

The values of the modelled data points after the application of the aforementioned mathematical operations are shown once again with the experimental data in Figure 6.12. Now the two datasets evidence a much tighter correlation, suggesting the previously outlined transformations to be successful in accounting for the problems discussed. However, despite this achievement, an increasing remnant divergence between the two trends persists owing to three compounding factors:

1) *The spikes in the particles size distribution depicted in Figure 6.9 act to significantly enhance the number of precipitates in the model by an ever increasing*

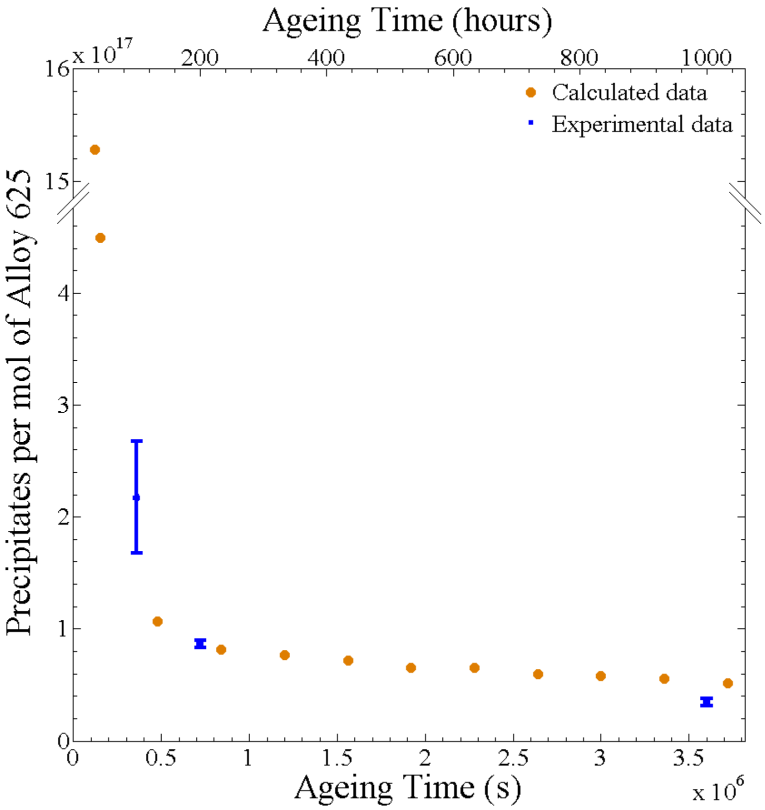

Figure 6.12: Calculated number density evolution for γ'' precipitates predicted by the SFFK based model created in this research adjusted to account for change in the molar volume of the system and the difference in the between the calculated, changing molar volume of the precipitate phase and the fixed value of Ω used in this research.

magnitude, reaching around 8% at 1033 hours.

In accordance with the discussion in Section 6.2.3, the mechanism behind this phenomenon derives from the fact that as the required contribution to the precipitate volume fraction from classes which have been restricted in their growth grows, so the number of particles contained within them must also increase (manifested as a reduction in the separation for the distribution classes). As a result, an ever growing disparity in the particle number calculated from the model and experimental distributions is incurred during growth and coarsening.

2) *The coalescence of γ'' precipitates reduces the number precipitates in the experimental system to a magnitude below that which would occur via a purely diffusion moderated coarsening regime.*

The phenomenon of γ'' coalescence is known to effect the coarsening behaviour of the precipitates observed in this research (*q.v.* Section 5.3.1). Moreover, the manner of this effect is such that its influence becomes amplified with increasing ageing duration. As a result, the absence of accounting for such a mechanism in the SFFK model inevitably leads to an increasing diversion with respect to the number density as ageing proceeds.

3) *The lack of competing precipitate phases in the model calculation.*

   Based on theoretical thermodynamic calculations (Figure 3.1), the generic TTT-curve published by [23] *et al.* (Figure 1.18) and the grain growth measurements performed in this research (Section 5.2.1) it is reasonable to conclude that an increasing quantity of carbide phases should also be present in Alloy 625 in addition to γ''[5] when ageing at 650° C. Furthermore, although only the niobium free $M_{23}C_6$ and $M_{12}C$ carbides are predicted at equilibrium at this temperature, the kinetics of both primary carbide dissolution (*q.v.* Section 1.2.6) and the enhanced nucleation and growth rate experienced by grain boundary nucleated precipitates (*q.v.* Section 1.3) means that a proportion of the carbides present during the evolution period in question will[6] be niobium containing M_6C type. As a result, in the real alloy system, a competition for niobium between the two precipitate phases is present, suppressing the driving force for γ'' precipitation below that calculated from the equilibrium (*i.e.* accounting for $M_{23}C_6$ and $M_{12}C$ carbides) phase fractions used by the model and, ultimately, reducing (owing to the increased stability of the carbide) the quantity of γ'' precipitates by an ever greater amount as the M_6C phase grows. Direct evidence for this competition occurring in the samples analysed in this research is given in Figure 6.13: A γ'' free region adjacent to the grain boundary is observed as a thanks to the growth of the carbide phase and its depletion of surrounding niobium.

   An accurate, quantitative estimate of the amount of niobium sequestered by M_6C carbides is impossible from purely thermodynamic calculations because of the competition for carbon with the $M_{23}C_6$ phase, especially given that the latter is calculated to account for over 99% of the carbon in the system at equilibrium. However, by making the simple assumptions that all of the carbon that ultimately ends up in $M_{23}C_6$ is bonded first with niobium to form M_3Nb_3C phase and that the concentration of niobium in the matrix remains the same, an upper limit for the reduction in the volume fraction of γ'' precipitates caused by carbide precipitation can be calculated as 13%[7].

Although relatively large, the maximum combined reduction in the modelled precipitate number density at 1033 hours that results from the three physical factors just discussed may still not be sufficient to fully account for the difference observed with the experimental data. Reflecting additionally on the remaining likely sources of error,

---

[5] Clearly at equilibrium a complete transformation of γ'' to δ-phase should have occurred as per the discussion in Section 1.2.3; however, this is irrelevant for the arguments being made here because of the lack of the latter phase in any of the relevant 650° C micrographs in Section 5.3.1

[6] Evidence of such particles produced at different ageing temperatures is presented by the author in a recent publication [339]

[7] According to Gibbs energy minimisation $M_{23}C_6$ carbides comprise 0.1032 Alloy 625 mole percent of carbon meaning 0.3095 Alloy 625 mole percent of Nb or 13% of the total forms a corresponding amount of M_3Nb_3C.

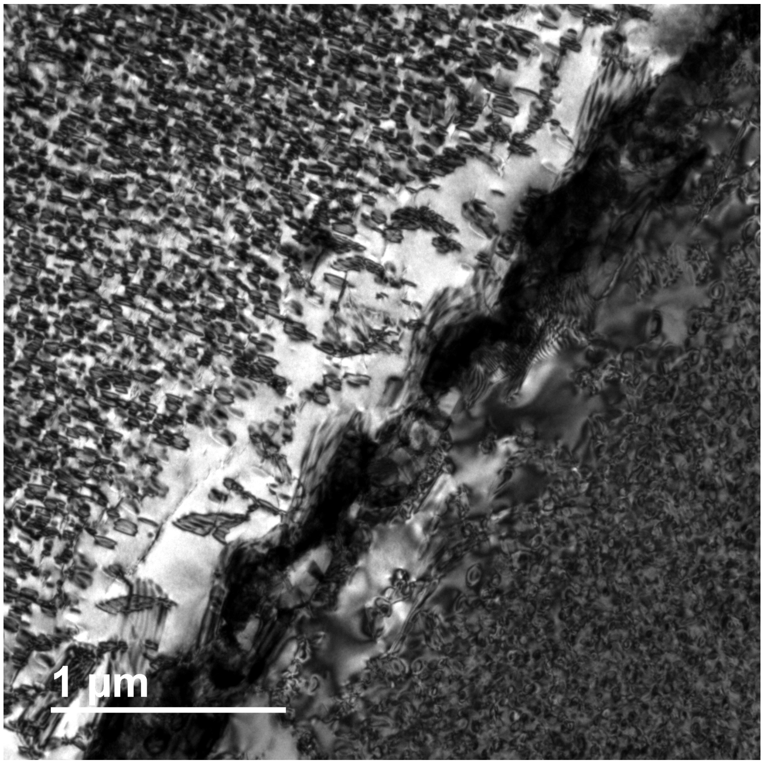

Figure 6.13: γ'' free zone adjacent to grain boundary in Alloy 625 material aged for 1000 hours at 650°C.

therefore, leads to the conclusion that the likely most significant are associated with both the under counting of particles in the experimental imaging (owing to the estimate of the foil thickness being slightly to large) and the increasing disparity between the actual molar volume and the misfit strain values used in the model. Notwithstanding all of these factors, however, the corrected data presented in Figure 6.12 can still be concluded to show the model is successful in reproducing the number density statistic. Specifically, this judgement can be made based on the grounds not only of the excellent correspondence at short ageing times but the relative magnitude of the discrepancy at 1000 hours when compared to the evolution of the total number density throughout the precipitate evolution. Furthermore, the impact of this discrepancy on any calculation of the material properties such as hardness is likely to be minor compared to the desired level of precision.

In addition to the above conclusions and in respect of the number density statistic particularly, it should be pointed out at this point that the evidenced agreement of the model with the experimental data itself constitutes a validation of the image analysis method detailed in Section 4.3.2, and significantly the use of Hilliard's mathematical limit in deriving the number density *viz* such an outcome is not mandated by the only fixed input experimentally derived aspect ratio evolution trend used in the calibration.

6.2.5 Interfacial Energy

Using the data contained within each of the recorded arrays (corresponding to a particle class), a plot of the evolution of the interfacial energy value ζ_k^E can be constructed as shown in Figure 6.14. As observed in the figure, rather startlingly the trend for ζ_k^E reveals that although the quantity starts out positive, the value of the interfacial energy on the precipitate ends quickly becomes negative, implying (from Equation 2.4) that the misfit strain actually becomes a driving force for particle growth rather than a restrictive one. Such a consequence is not only counter intuitive from an engineering nomenclature standpoint but is also unphysical and, therefore, *prima facie* could only be interpreted as highlighting a fundamental floor in the SFFK based description implemented in this research. Fortunately, however, this turns out not to be the case as the occurrence of this phenomenon can be instead be understood and accounted for by considering the physical mechanisms at work in the real system and the assumptions made in the derivation of the mathematics applied.

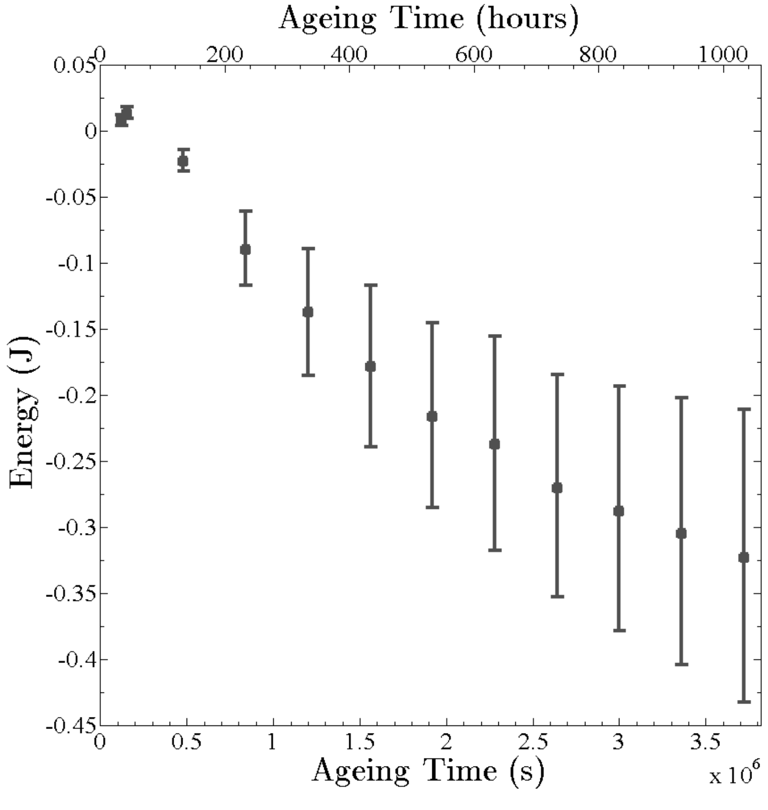

Figure 6.14: Calculated ζ_k^E evolution for γ'' precipitates predicted by the SFFK based model created in this research with time-shift correction applied. Data points correspond to average values and the error bars to the first and third quartiles of the major radius particle size distribution.

Conceptually, the value of ζ_k^E can be allowed to take a negative value if it is considered as being an effective interfacial energy which includes contributions from not only the physical interfacial energy but also from the reduction in the misfit strain which occurs as the particles evolve. The reasons why this latter phenomenon is not only introduced but also only effects ζ_k^E, rather than any other term, are two-fold: 1) The calculation of misfit strain as per Equation 2.10 is based principally on the lattices of precipitate and matrix always retaining full coherency but with an ever increasing strain between bonds (analogous to the situation shown in Figure 1.9b). Consequently the reduction in strain which accompanies the transition to a semi-coherent or fully incoherent interface (Figures 1.9c and d) in the real system cannot be accounted for. 2) During the calibration all of the other relationships in Equation 2.4 are defined, meaning that only the interfacial energy term can accommodate the change in misfit strain necessary to match the experimentally acquired trends. In accordance with these dependencies, therefore, the value of ζ_k^E in the free energy equation can be defined mathematically according to Equation 6.9, where Z_k^E corresponds to the actual/true interfacial energy which should be attributed to the ends of the cylindrical precipitates constructed in the model and Λ_k is the contribution from the reduction in misfit strain.

$$\zeta_k^E = Z_k^E + \frac{8\rho_k}{3\xi_k^2}\Lambda_k^E \tag{6.9}$$

A procedure for the separate calculation of the values of Z_k^E and Λ_k from is not obvious as both unknown variables are contained within a single expression. Nevertheless, deconvolution of their respective contributions to the value of ζ_k^E is possible from the contour/surface plot generated under the condition of a fixed U value (as defined in Equation 6.10) shown Figure 6.15a: At constant aspect ratio the behaviour of the value of ζ_k^E is well fitted by a second order polynomial as shown in Figure 6.15b. Accordingly, if it is then assumed that the form of $\zeta_k^E(\rho_{\alpha=\text{constant}})$ is that same as that of $Z_k^E(\rho_{\alpha=\text{constant}})$ (*i.e.* a second order polynomial), the relations shown in Equation 6.11 should hold. Finally, considering that, from these relations, the contribution of the misfit strain only effects first order coefficients, its magnitude at each point is calculable from comparison of the behaviour of the first order polynomial coefficients to that of both the second order coefficients and the intercepts.

$$U = \sum_{i=1}^{n} \frac{(c_{ki} - c_{\gamma i})^2}{c_{\gamma i} D_{\gamma i}} \tag{6.10}$$

$$\begin{gathered} A_\zeta \rho_k^2 + B_\zeta \rho_k + C_\zeta = A_Z \rho_k^2 + B_Z \rho_k + C_Z + \frac{8\rho_k}{3\xi_k^2}\Lambda_k^E \\ A_\zeta = A_Z \qquad B_\zeta = B_Z + \frac{8}{3\xi_k^2}\Lambda_k^E \qquad C_\zeta = C_Z \end{gathered} \tag{6.11}$$

Trends for the coefficients A_ζ and C_ζ calculated from fitting to constant α and U value plots of ζ_k^E are shown in Figures 6.16a and 6.16c respectively. Consistent with the reasoning outlined above, the behaviour for both these parameters are well characterised themselves by polynomials of the second order; however the behaviour of B_ζ

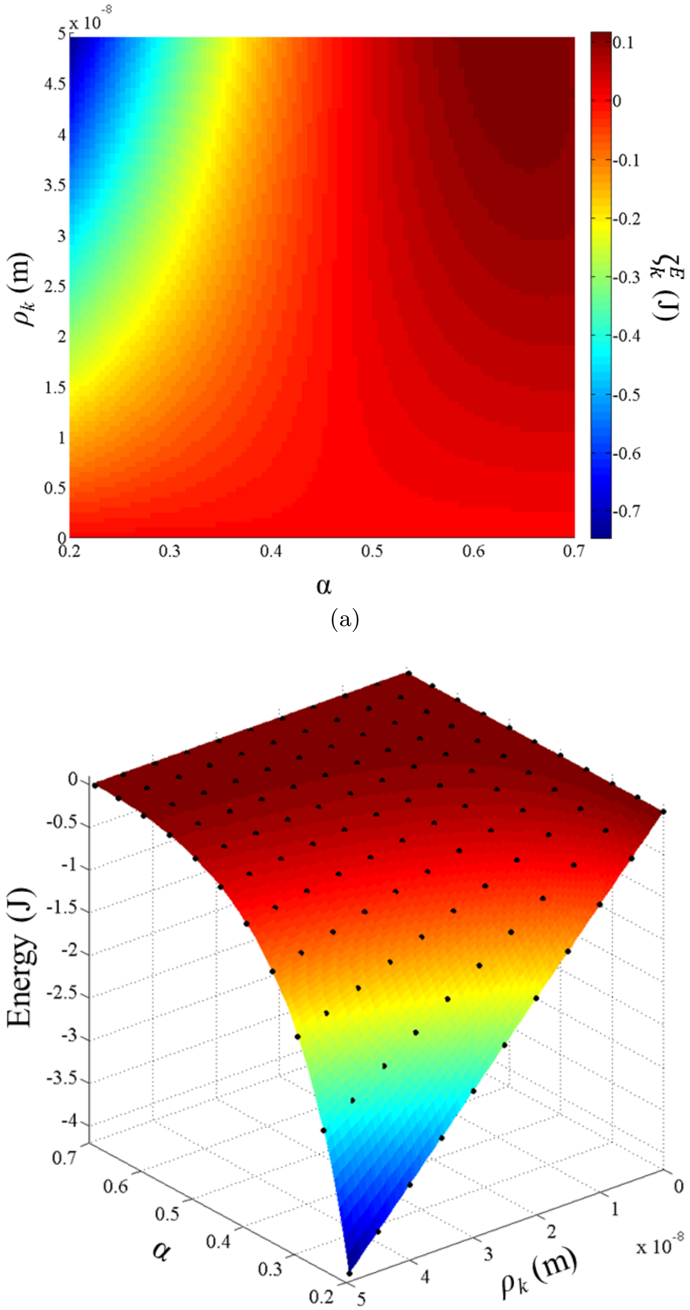

(a)

(b)

Figure 6.15: a) Surface corresponding to the effective interfacial energy ζ_k^E as a function of particle size and aspect ratio at $U(t = 0)$. b) Points generated from polynomial fits made to the data overlaid on the surface of ζ_k^E.

shown in Figure 6.16b is not. Assuming a second order polynomial type behaviour is followed also by B_Z, therefore, following the previously outlined rationale, its value is calculable through fitting such a function to data free of the influence of the misfit strain contribution *i.e.* at high aspect ratios which, from previous sections, are known to correlate to small nucleating particles. Applying this methodology to produce the deconvoluted trends presented Figure 6.16b, the separate surface plots corresponding to each of contributions in Equation 6.9 to ζ_k^E at $U(t=0)$ shown in 6.17 are generated.

Clearly the retention of a fixed value for U is not representative of the calculations actually carried out during a computation by the model created in this research; however, the introduction of this as a free parameter would preclude the initial deconvolution of the two contributions to ζ_k^E. Consequently, incorporation of the U value for the calculation of ζ_k^E and Z_k^E is instead achieved through an assessment of its impact on the polynomial coefficients $A_{\zeta/Z}$, B_ζ, B_Z and $C_{\zeta/Z}$ in Equation 6.11 *viz.* evaluating the trends for each coefficient with α at regular intervals between $U(t=0)$ and $U(t=\infty)$ generates the contour plots shown in Figure 6.18a-d.

Following the methodology used in the definition of the ρ_k/α surface, the most obvious method for the inclusion of U as a free value in the calculation of ζ_k^E and/or Z_k^E is through the creation of fits to the generated surface (*e.g.* $A_\zeta(U)$). However, the adoption of such a methodology would lead to the repeated use of α in the sequential steps in which the various polynomials are evaluated creating a conceptual complication. As an alternative, therefore, for the sake of relative simplicity, the approach taken in this research is to instead fit the evolution of the "sub coefficients" defining the polynomials $A_{\zeta/Z}$, B_ζ, B_Z and $C_{\zeta/Z}$ themselves in accordance with Equation 6.12. Consistent with the linear evolution of the parameters at constant α in Figures 6.18a-d, these "sub coefficients" are themselves defined by first order polynomials, which for A_Z, B_Z and C_Z (via Equation 6.12) correspond to Equations 6.13, 6.14 and 6.15 respectively.

$$\begin{gathered}
A_Z = A_Z^1\alpha_k^2 + A_Z^2\alpha_k + A_Z^3 \\
B_\zeta = B_\zeta^1\alpha_k^7 + B_\zeta^2\alpha_k^6 + B_\zeta^3\alpha_k^5 + B_\zeta^4\alpha_k^4 + B_\zeta^5\alpha_k^3 + B_\zeta^6\alpha_k^2 + B_\zeta^7\alpha_k + B_\zeta^8 \\
B_Z = B_Z^1\alpha_k^2 + B_Z^2\alpha_k + B_Z^3 \\
C_Z = C_Z^1\alpha_k^2 + C_Z^2\alpha_k + C_Z^3
\end{gathered} \tag{6.12}$$

$$\begin{gathered}
A_Z^1 = -5.10159 \times 10^{-10}U - 6.25309 \\
A_Z^2 = 2.69744 \times 10^{-10}U - 6.85270 \\
A_Z^3 = -3.56587 \times 10^{-11}U - 1.84166
\end{gathered} \tag{6.13}$$

$$\begin{gathered}
B_Z^1 = 6.23790 \times 10^{-18}U - 7.28126 \times 10^6 \\
B_Z^2 = 0 \\
B_Z^3 = -1.14943 \times 10^{-18}U + 8.57408 \times 10^6
\end{gathered} \tag{6.14}$$

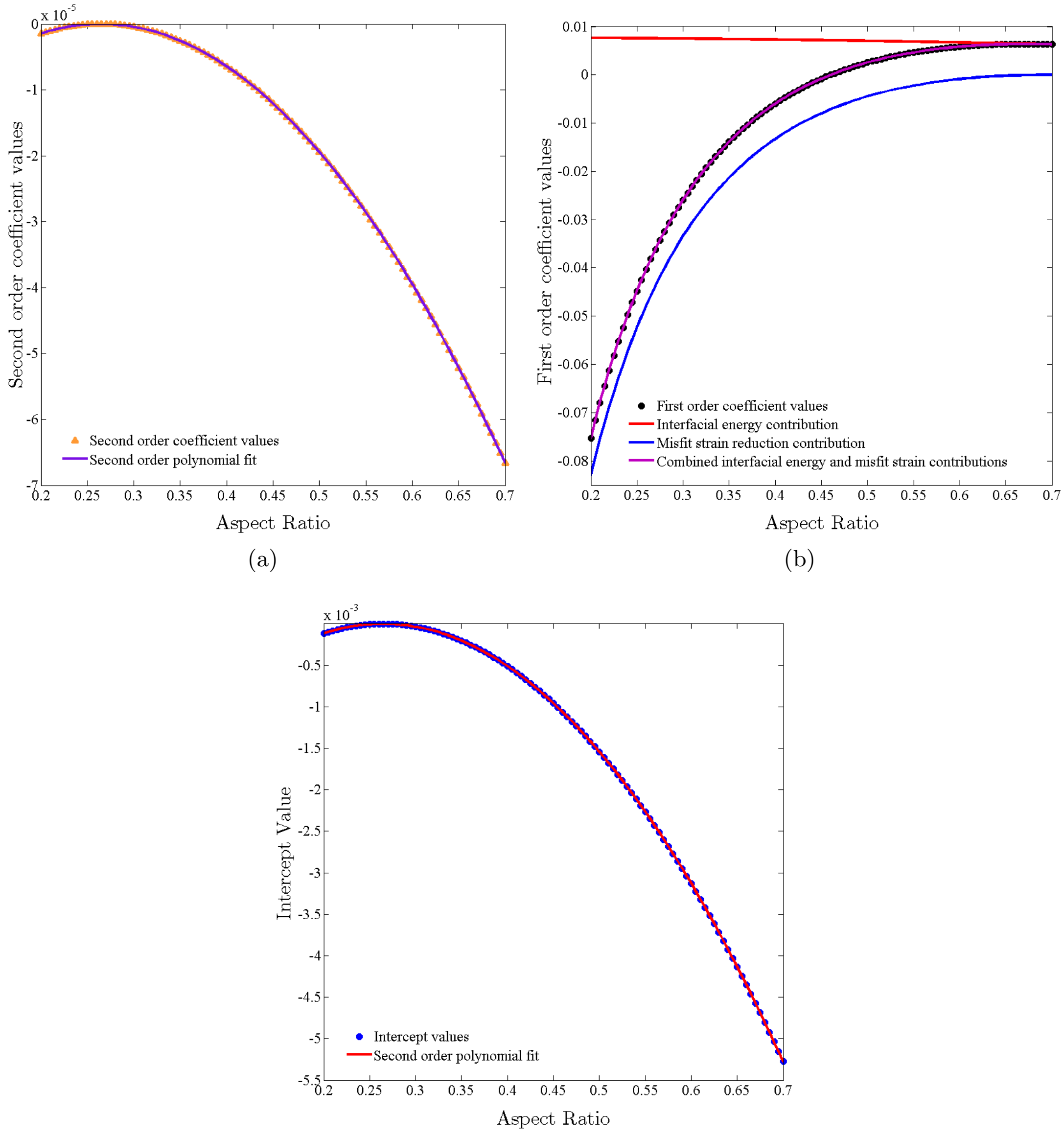

(a)

(b)

(c)

Figure 6.16: Trends calculated for the coefficients a) A_ζ, b) B_ζ and c) C_ζ in Equation 6.11 at $Q(t=0)$. Second order polynomial fits equated to A_Z and C_Z, along with a seventh order polynomial fit to B_ζ are also shown in each plot respectively

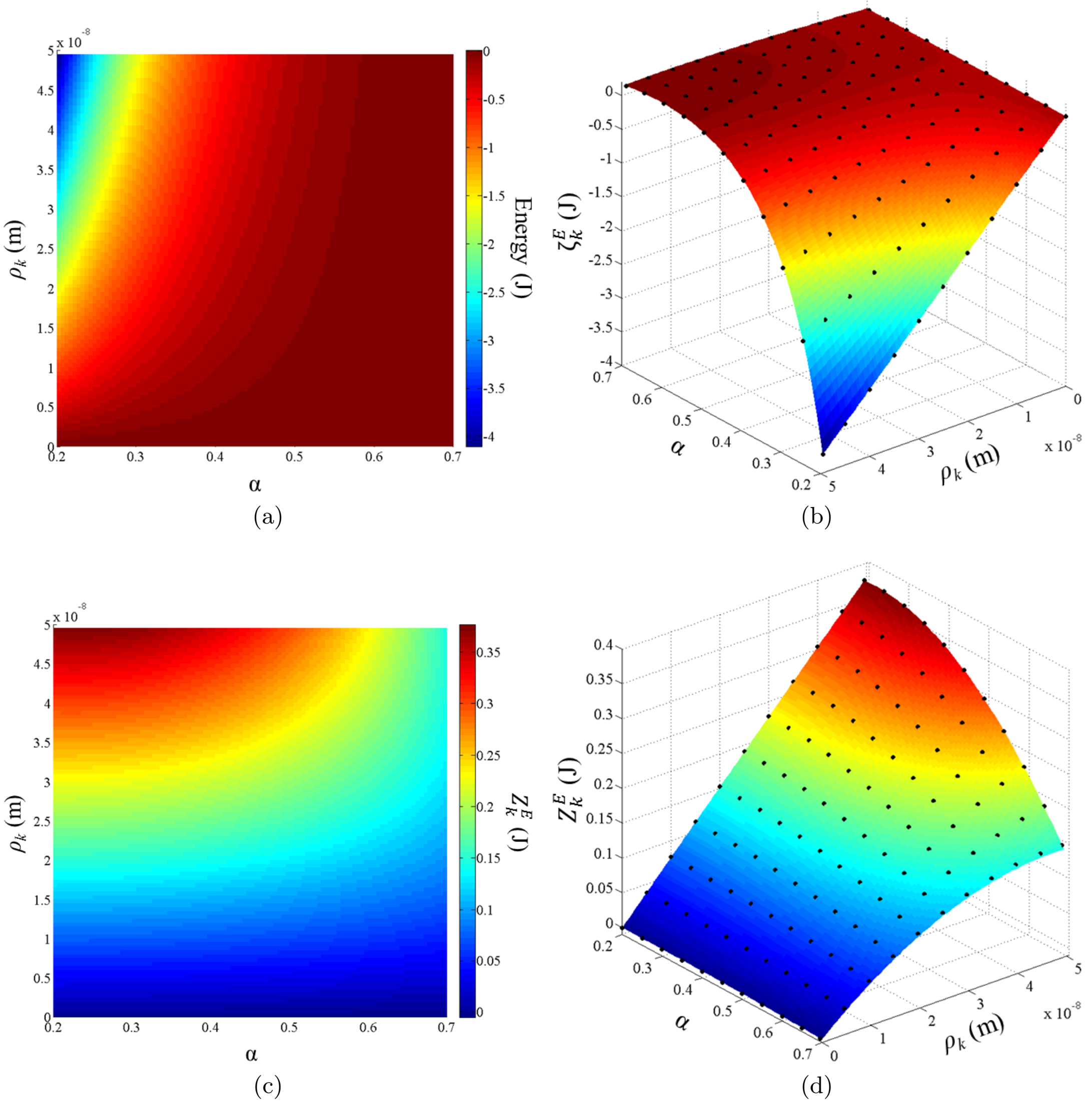

(a) (b)

(c) (d)

Figure 6.17: Contributions to the effective interfacial energy surface in Figure 6.15 from a-b)the reduction in misfit strain $(8\Lambda_k)(3\xi_k^2)^{-1}$ and c-d) the actual interfacial energy Z_k^E.

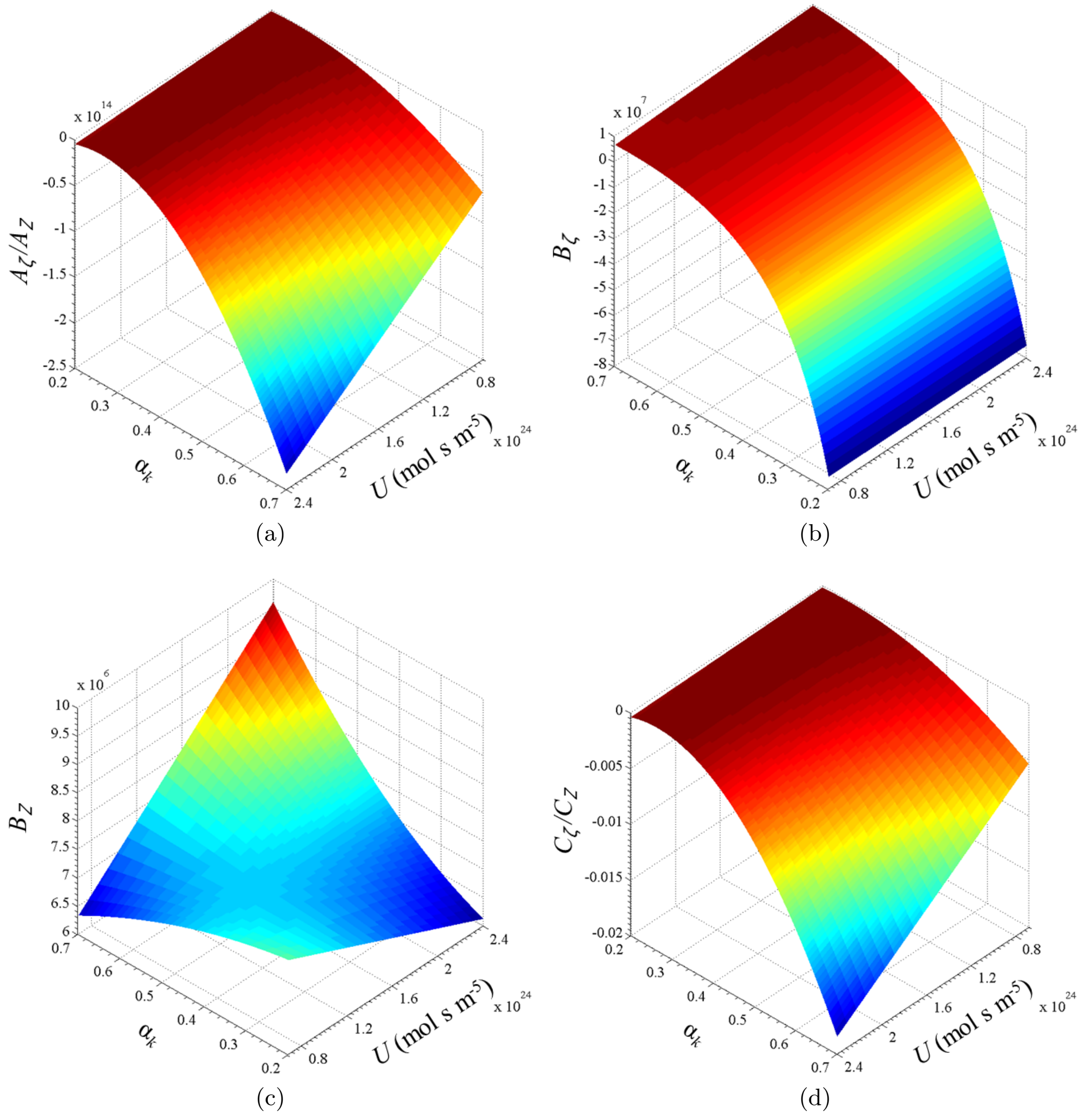

(a) (b) (c) (d)

Figure 6.18: Surfaces for a) A_ζ , b) B_ζ , c) B_Z and c) C_ζ .

$$
\begin{aligned}
C_Z^1 &= -4.04131 \times 10^{-26} U - 2.19919 \times 10^{-15} \\
C_Z^2 &= 2.13682 \times 10^{-26} U - 2.52491 \times 10^{-15} \\
C_Z^3 &= -2.82476 \times 10^{-27} U + 6.90369 \times 10^{-16}
\end{aligned}
\tag{6.15}
$$

Utilising the mathematical descriptions for both Z_k^E and the factor associated the reduction in the misfit strain, their separate/deconvoluted contributions to the ζ_k^E distribution values in Figure 6.14 can be calculated as shown in Figure 6.19. Now, not only is it seen that the interfacial energy of the precipitates does observe a physically viable evolution behaviour, but the misfit strain energy evolution predicted by the model is also consistent with precipitates becoming more incoherent with the matrix as they grow.

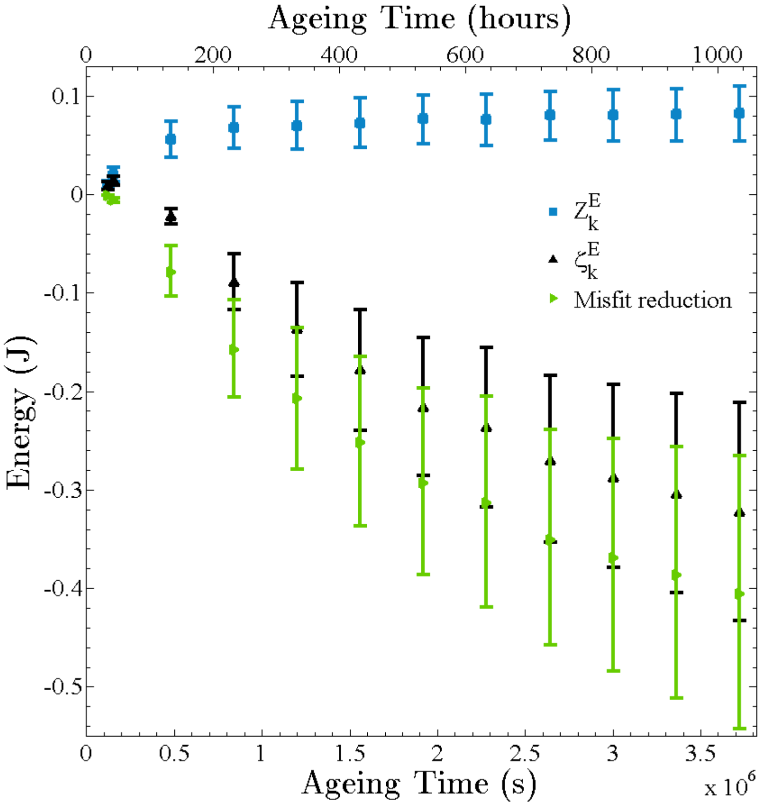

Figure 6.19: ζ_k^E evolution for γ'' precipitates from Figure 6.14 together with is deconvoluted contributions from Z_k^E and the reduction in misfit strain energy ($8\rho_k\Lambda_k^E[3\xi_k^2]^{-1}$). Data points correspond to average values and the error bars to the first and third quartiles of the major radius particle size distribution.

Owing to the technique used for the derivation of the interfacial energy, namely the imposition of the whole of the energy being associated with the precipitate ends (the mantle having an energy of zero), direct comparison with literature data cannot be made without first applying a correction. Specifically, rather than separate energies for the two interfaces (the evaluation of which was actually shown to be accompanied by impassible mathematical constraints in Section 6.1.2), the derivation of the literature data means that appropriate values actually correspond to the average interfacial energy over the entire precipitate. To this end, the values in Figure 6.19 are modified to those shown in Figure 6.20 (ζ_k, Z_k and $8\rho_k\Lambda_k[3\xi_k^2]^{-1}$) through a rescaling of the interfacial energy by a factor that equates to the fractional area accounted for by the precipitate ends ($[1+2\alpha_k]^{-1}$).

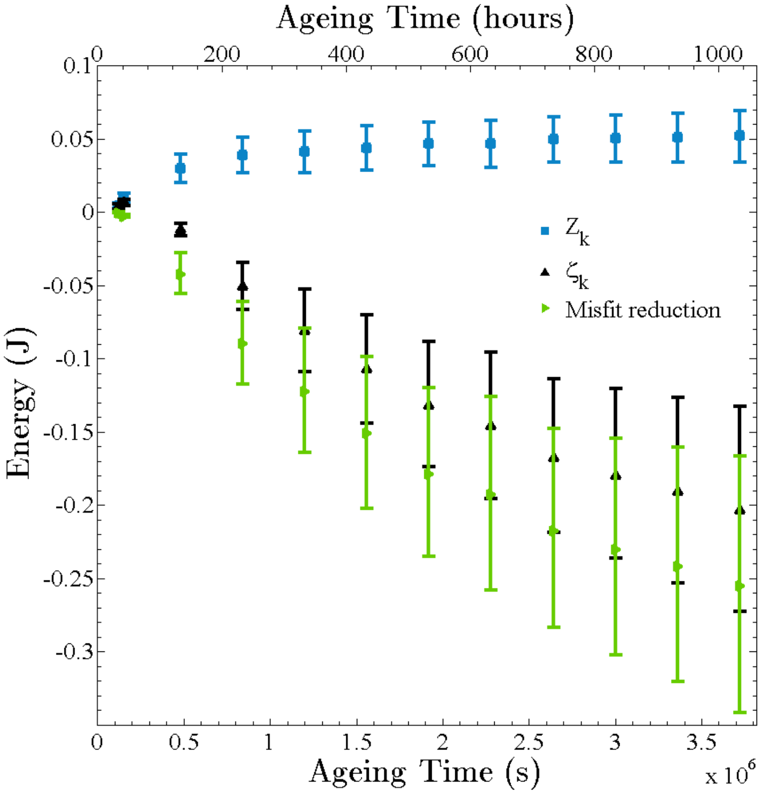

Figure 6.20: Trends for ζ_k, Z_k and the reduction in misfit strain energy calculated by averaging the trends shown in Figure 6.19 over the entire particle surface.

Despite the implementation of the rescaling operation, straightforward comparison with the most relevant literature values calculated by Cozar *et al.* [172] and Devaux *et al.* [47] is still complicated for the reason that, as laid out in Section 3.1.5, they pertain to a constant rather than evolving variable. Under this condition, the most appropriate comparison between the interfacial energy values can seemingly be made by utilising the values of the misfit strains ϵ_{11} and ϵ_{33} used in their derivation shown in Table 6.1 *viz.* identifying the value for Z_k outputted by the model for an average precipitate at the corresponding strain values. Unfortunately, however, such an approach is fundamentally flawed because of the large disparity (unaccounted for simply by temperature differences) in the relative magnitude of the two variables *cf.* Figure 6.6) *e.g.* when $\epsilon_{33} = 2.86 \times 10^{-2}$ Devaux *et al.* state $\epsilon_{11} = 6.67 \times 10^{-3}$ whereas the model predicts $\epsilon_{11} = 2.2 \times 10^{-3}$.

The cause for the significant disagreement of the results produced here with the misfit strains and, ultimately, the interfacial energies listed by both Cozar *et al.* [172] and

Table 6.1: Literature values for the interfacial energy and misfit strain between γ'' precipitates and the matrix of nickel based alloys.

	System	Interfacial Energy (mJ)	$\epsilon_{11}(\times 10^{-3})$	$\epsilon_{33}(\times 10^{-2})$
Cozar *et al.* [172]	Fe 30.8-Ni 9.1-Ta	145	9.4 ± 0.3	3.72 ± 0.06
		185	7.0	3.46
Devaux *et al.* [47]	Alloy 718	97 ± 17	6.67	2.86
Slama *et al.* [4] (750°C, 4h)	Alloy 718	–	8.9 ± 3.1	2.96 ± 0.30
This Study (Average Precipitate)	Alloy 625	$0 \rightarrow 51.84$	$8.69 \rightarrow -7.61$	$3.1 \rightarrow 3.56$

Devaux *et al.* is most likely attributable to the different systems each is associated with and the assumptions made in their derivation: With respect to the results of Cozar *et al.*, the author's note that the value for the interfacial energy is probably enhanced because of the loss in coherency between the γ'' precipitates in the majority iron matrix as opposed to a majority nickel one. However, it is far more likely that it is the incorporation of tantalum rather than niobium into the precipitate phase leading to much a longer $c_{\gamma''}$ lattice parameter (whilst leaving a_γ and $a_{\gamma''}$ relatively unchanged), which is responsible for incompatibility with the model Z_k and ϵ_{33} values. Contrastingly, although the values calculated by Devaux *et al.* [47] are apparently principally based on the values for the lattice parameters of niobium containing γ'' measured by Wagner *et al.* [279] at 750° C, comparison with those of Slama *et al.* [4] and (for ϵ_{11}) Cozar *et al.* [172] in Table 6.1 suggest they represent a severe under estimate owing to too large a value being utilised for a_γ. Assuming all other factors in the free energy balance equation (Equation 1.6) are approximately equivalent to those used in the model, therefore, the consequence of this underestimation would be a compensatory over estimation by Devaux *et al.* of the inter facial energy Z_k *cf.* for an average precipitate in the present model at 650° C when $\epsilon_{11} = 6.67 \times 10^{-3}$, $\alpha = 0.57$ and $Z_k = 9.22\,\text{mJ}$.

A more qualitative analysis of the results of the model can be achieved through the creation of a plot of the average value of ζ^E and its two contributions with the average aspect ratio (from Figure 6.5) as shown in 6.21. Inspection of the figure reveals the data to be consistent with the inclusion theory of Eshelby [251, 282]; a decrease in the aspect ratio is accompanied by both an increase in the interfacial energy and a drop in the elastic energy as evidenced by the trends in the values of Z_k^E and the misfit reduction $(8\rho_k\Lambda_k^E[3\xi_k^2]^{-1})$, respectively. Furthermore, detailed inspection of the values obtained indicates that the particles are predicted by the model to remain relatively coherent with the matrix as they initially nucleate and grow; however, the rate of decrease in the quality of the interface begins to increase rapidly after the particle reaches an α_k value of around 0.55. Owing to its origin, the asymptotic culmination of the misfit strain contribution can be inferred as representing the point of full incoherence between the two phases.

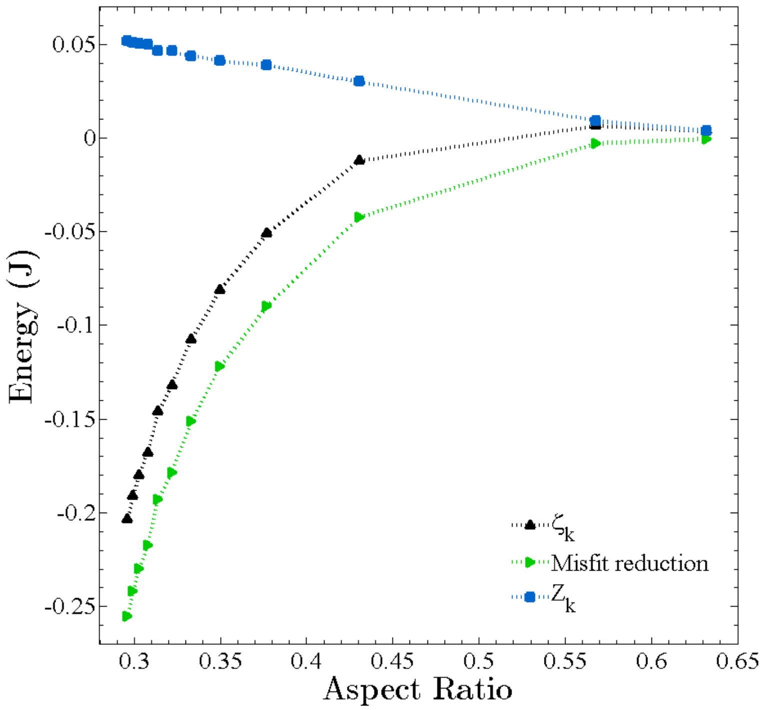

Figure 6.21: Evolution of the average values ζ_k, Z_k and $8\rho_k\Lambda_k[3\xi_k^2]^{-1}$ with average aspect ratio calculated from their relative distributions.

The observation of a size and shape at which γ'' precipitates are identified as having lost their coherency with the matrix has been made in Alloy 718 by a number of researchers [47, 172, 4]: An average major radius of around 50nm and aspect ratio of <0.2 are indicated in all cases. Although this aspect ratio is below that displayed, comparison of these literature values with the trend shown in Figure 6.21 (and the corresponding major radius value in Figure 6.8) indicates agreement would likely be achieved with sufficient ageing.

In the light of the problems discussed for the literature interfacial energy values calculated for γ'' precipitates, one can only make a conclusion that their conformity with respect to the order of magnitude evolution of the modelled data shows broad agreement is achieved. Similarly, the values calculated for γ' precipitates in the literature such as those found over many years in Ni-Ti and Ni-Al systems by Ardell [350, 351, 352] of *ca.* 10-100mJ can only comprise a successful order of magnitude check due to both their expected smaller magnitude (consistent with the discussion in Sections 1.2.1 and 1.2.1) and probable analogous problems with their applicability relating to their derivation[8]. Nevertheless, the fact that energies of the correct order of magnitude and with the right evolution behaviour are predicted by the model and the subsequent deconvolution procedure indicates both are successful and correctly calibrated.

---

[8] A verbose discussion of γ' interfacial energies is avoided here for reasons of applicability and relevance.

§ 6.3 Validation

The analysis presented with respect to the computation of the aspect ratio, major radius and number density evolution at 650 °C in the previous section signifies that the model has been apparently successfully calibrated such that self consistent (if not absolutely correct) values for previously unknown parameters such as ϵ, Ω, ζ_k and Z_k are calculated. In view of this outcome, therefore, it straightforwardly follows that it should be possible to use the model predict the evolution of γ'' precipitates when ageing at different temperatures and under the same system assumptions *i.e.* no competitive precipitation and/or transformation to δ-phase. That is to say, the definition of the calibrated parameters in terms of the precipitate dimensions rather than any directly temperature dependent quantities means that the only modification necessitated to the methodology of the calibration calculation is the use of Equation 6.16 (where all symbols have their usual meanings) rather than Equation 6.3 for the calculation of ζ_k^E.

$$\zeta_k^E = A_\zeta(\alpha_k)\rho_k^2 + B_\zeta(\alpha_k)\rho_k + C_\zeta(\alpha_k) \tag{6.16}$$

Under the aforementioned modifications, before any validation calculations were performed, a prior check was conducted to ascertain if the new calibrated model was able to accurately and precisely replicate the results of the calibration calculation. Disappointingly, the results of this computation were found to be in significant disagreement with those detailed in Section 6.2. Considering the apparent success of the calibration calculations, the failure of the calibrated model was surprising; however, upon investigation one principle source could be identified, namely the fits made with respect to α and U to define the values in Equation 6.11. Stated explicitly, although the fits made in defining all of the coefficients were associated with significant r^2 values, the minuscule remnant different between the calibration ζ surface and the fit points was sufficient to markedly change the behaviour of $\alpha(t)$ and by extension every other parameter.

The reason why even a tiny variations in the value of ζ could have such an impact on the computation can be most easily understood in terms of Equation 2.7. Fundamentally this relation for $\dot{\alpha_k}$ is a division operation whereby the numerator is a summation that depends both directly and indirectly on the value of ζ_k^E. As a result, because the factors in the summation are finely balanced, even a slight change in value of ζ_k^E is sufficient to significantly change both the magnitude and even the sign of $\dot{\alpha_k}$. Ultimately, considering the dependence of the magnitude of many other parameters in the SFFK model on α, it can be deduced that the minor deviation introduced by the fits “snow balls” to create a significant divergence and unphysical results.

Whilst extensive attempts were made to suppress or even eliminate the impact of the difference in ζ_k^E versus the calibration model (*e.g.* varying the range of fitted values, changing the type of fit *etc.* none were successful. As a result, therefore, in order to validate the SFFK model generated in this research an alternative approach was adopted, explicitly that detailed in Section 6.2. Clearly this modification has the prohibitive effect of requiring experimental data to be input always into the model; however, in the absence of alternative approaches this was taken to be an acceptable limitation.

6.3.1 EXPERIMENTAL DATA

In view of the discussion of the experimental results in Section 5.3.1 it is evident that conformity with the underlying assumptions of the model (*q.v.* Chapter 2), most crucially those of exclusively homogeneous nucleation and (as a corollary to a defect free matrix) bulk elemental diffusion, is not achieved for the data corresponding to ageing temperatures $\geq 700^\circ$C. Consequently, validation of the model with respect to the experimental data obtained in this research is principally restricted to the ageings performed at 600°C and 650°C.

650° C

The γ'' r_M distribution evolution computed by the model when ageing for up to 3000 hours at 650°C (and *ipso facto* using the same mathematical descriptions as the calibration calculation) is presented alongside all of the available experimentally acquired data in Figure 6.22. In this instance, although the agreement between the calculated and experimental is maintained for ageing durations $\leq 1000 hours$ (*i.e.* now including the experimental data for 50 hours of ageing) a significant disparity is observed for the data corresponding to the γ'' populations which exist after 3000 hours. Moreover, the modelled trend displays a marked undulation apparently indicating that after a certain degree of coarsening has taken place the average size of γ'' precipitates begins to first rapidly increase and then decrease before, finally, stabilising.

Considering the aforementioned phenomena individually, the fact that substantial disagreement ($\approx 42\%$) is obtained after 3000 hours of ageing is attributable primarily to the effect (not incorporated in the model) of “encounter” discussed at length in Section 5.3.1: As described by the author in a recent paper [344] the “encounter” phenomenon acts with greater frequency for larger γ'' precipitates owing to their lower ${}^{\epsilon_{1,1}}/_{\epsilon_{3,3}}$ ratio (in accordance with Figure 6.6). Accordingly, given the larger γ'' precipitates which exist after 3000 hours the effect of “encounter” is to yield both an accentuation of log-normal shape of the distribution in Figure 5.11d compared to the other (shorter) ageing times and the amplification of r_M to a magnitude above that predicted by the model. The separate, but ultimately similar, impact of co-precipitating δ-phase (*q.v.* Figure 5.12), through accelerating the shrinkage rate of small γ'' precipitates, can only be considered as a comparatively minor cause of the deviation between the experimental and modelled trends because of the small quantity of the thermodynamically stable phase that is present.

Turning to the observed undulation in the data, its origin can be identified as a computation effect associated with the methodology (outlined in 3.2.8) used to calculate the distribution density from the raw model PSD. Specifically, the fact that separation between two precipitate classes in the PSD is found to substantially decrease and then grow, ultimately has a marked effect on the distribution density. Considering that such a rapid set of changes in the γ'' precipitate population can be straightforwardly interpreted as unphysical, this result seemingly presents a significant problem for the model’s validity. However, it turns out that a simple change to the distribution calculation mechanism is sufficient for the effect to be overcome.

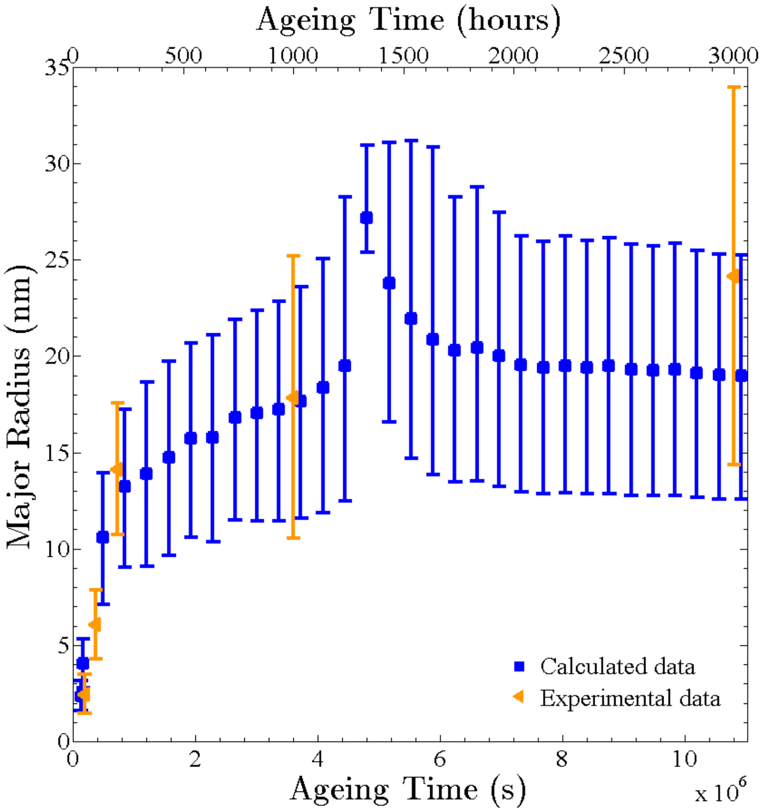

Figure 6.22: Major radius (r_{M}) evolution for γ'' precipitates predicted by the SFFK based model created in this research with time-shift correction applied. Data points correspond to average values and the error bars to the first and third quartiles of the PSD. Experimental data points for populations existing after 50, 100, 200, 1000 and 3000 hours of ageing are shown for comparison. Both sets of values are calculated from the distribution density according to the mechanism of Perez *et al.* [42].

An explanation of the new mechanism for calculating the distribution density is most easily made with the use of Figure 6.23: In the methodology of Perez *et al.* [42] the distribution density is calculated at a given point through dividing the frequency/number of precipitates in a class by the class width/separation (Equation 3.3). That is, in terms of Figure 6.23a the frequency a numbered class is divided by the width of the respective shaded area to produce the indicated distribution density trend. As a result of this approach, therefore, the distribution derived from a particular class is susceptible to rapid and large change if the separation from its higher r_{M} adjacent class becomes very small small. The new, alternative mechanism on the other hand suppresses the impact from any two classes by instead averaging over the widths of the areas illustrated in Figure 6.23b; if any two classes become very close whilst the others remain stationary, the widths over which the distribution density is calculated remains unchanged.

In addition to the desired effect of removing of undulations, the fact that the new mechanism effectively changes the values over which the classes are defined in the PSD is significant considering that all of the experimental data was calculated in Section 5.3.1 in accordance with the old mechanism of Perez. Explicitly, given the fixed class widths

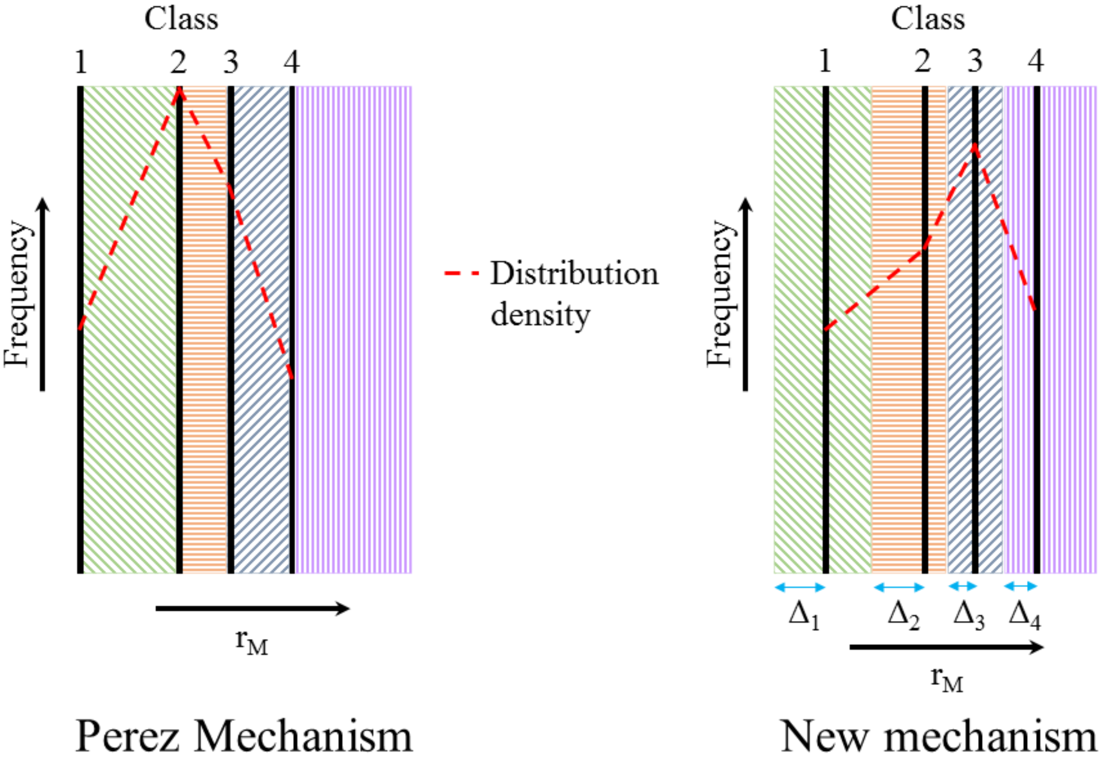

Figure 6.23: Comparison of the mechanism defined by Perez *et al.* [42] for calculating the precipitate distribution density from the classes in a PSD with a new, alternative mechanism that minimises abnormal results. In both instances all the classes contain the same number of precipitates and the absolute positions of classes 1, 2, 3 and 4 remain fixed. The different shaded areas define the position and r_{M} width over which the distribution density is calculated.

of the experimental PSDs, adoption of the new mechanism would inevitably result in the magnitudes/locations of the distribution averages and quartiles being shifted to lower r_{M} values by a magnitude equivalent to the half of the class width. Moreover, despite the apparent simplicity of applying such an operation, because all of the calibration calculations were made with respect to the Perez mechanism this would likely also lead to significant changes in variables such as fit parameters ($\alpha(r_{\mathrm{M}})$, $\alpha(t)$ *etc.*). As a result, an easier and (in fact) more valid (considering that the new mechanism would reduce experimental values to below their measured magnitudes) approach of shifting the r_{M} position of the statistics produced by the new mechanism so that they conform with the Perez methodology is adopted instead. Specifically, owing to the variable class width in the model PSD the statistics pertaining to each class are increased by their own relative amount *e.g.* in Figure 6.23b the position of distribution density values for Classes 1, 2, 3 and 4 are shifted with respect to r_{M} by a magnitude of Δ_1, Δ_2, Δ_3, and Δ_4 respectively.

The behaviour predicted by the model for γ'' major radius when ageing up to 3000 hours at 650°C calculated from the raw PSDs using the new mechanism is presented alongside the corresponding experimental data in Figure 6.24. From the new plot it is evident that, not only that the new mechanism is successful in removing the undulation in the data but that it also acts to increase the correspondence for $\bar{r}_{\mathrm{M}}$ with the experimental data for ageing durations $\leq$ 1000 hours. In contrast, although better agreement is observed between the widths of the experimental and model distributions for times $\leq$ 200 hours, at 1000 hours the model PSD (as indicated by the quantiles positions is notably narrower. Likewise, whilst a slight improvement between the relative magnitudes of $\bar{r}_{\mathrm{M}}$ is obtained at 3000 hours, the experimental value still remains markedly larger owing to "encounter".

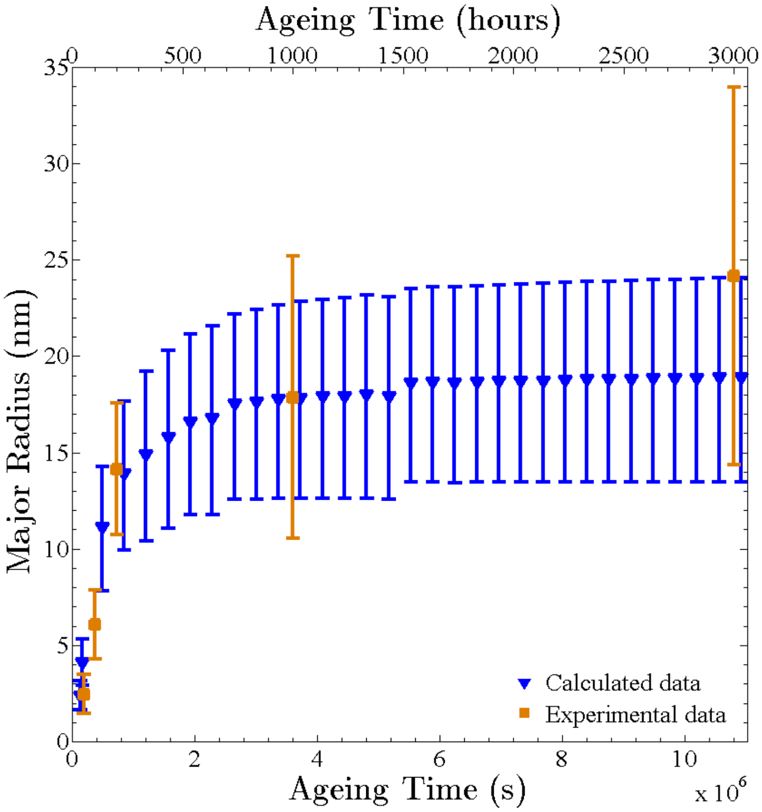

Figure 6.24: Major radius (r_{M}) evolution for γ'' precipitates predicted by the SFFK based model created in this research with time-shift correction applied. Data points correspond to average values and the error bars to the first and third quartiles of the PSD. Both sets of values are calculated from the distribution density according to the new mechanism displayed in Figure 6.23. Experimental data points for populations existing after 50, 100, 200, 1000 and 3000 hours of ageing are shown for comparison.

For completeness, direct comparison of the distributions obtained from the new mechanism and those analysed in the calibration calculation is presented in Figures 6.25a and b, revealing that (ironically) the new methodology actually acts to induce undulations. Clearly such an outcome is not desirable; however, considering that only part of the distribution is affected and that the overall envelope of the distributions maintains a similar level of agreement to that produced by the Perez mechanism, this result does not constitute a significant flaw. Separate analysis of the two PSDs in Figures 6.25c highlights that while good replication of the experimental data PSD shape is achieved by the model for small r_{M} γ'' precipitates, at large r_{M} values the agreement is poor; the contrasting shapes are entirely in agreement with "encounter" significantly affecting one PSD but not the other [344].

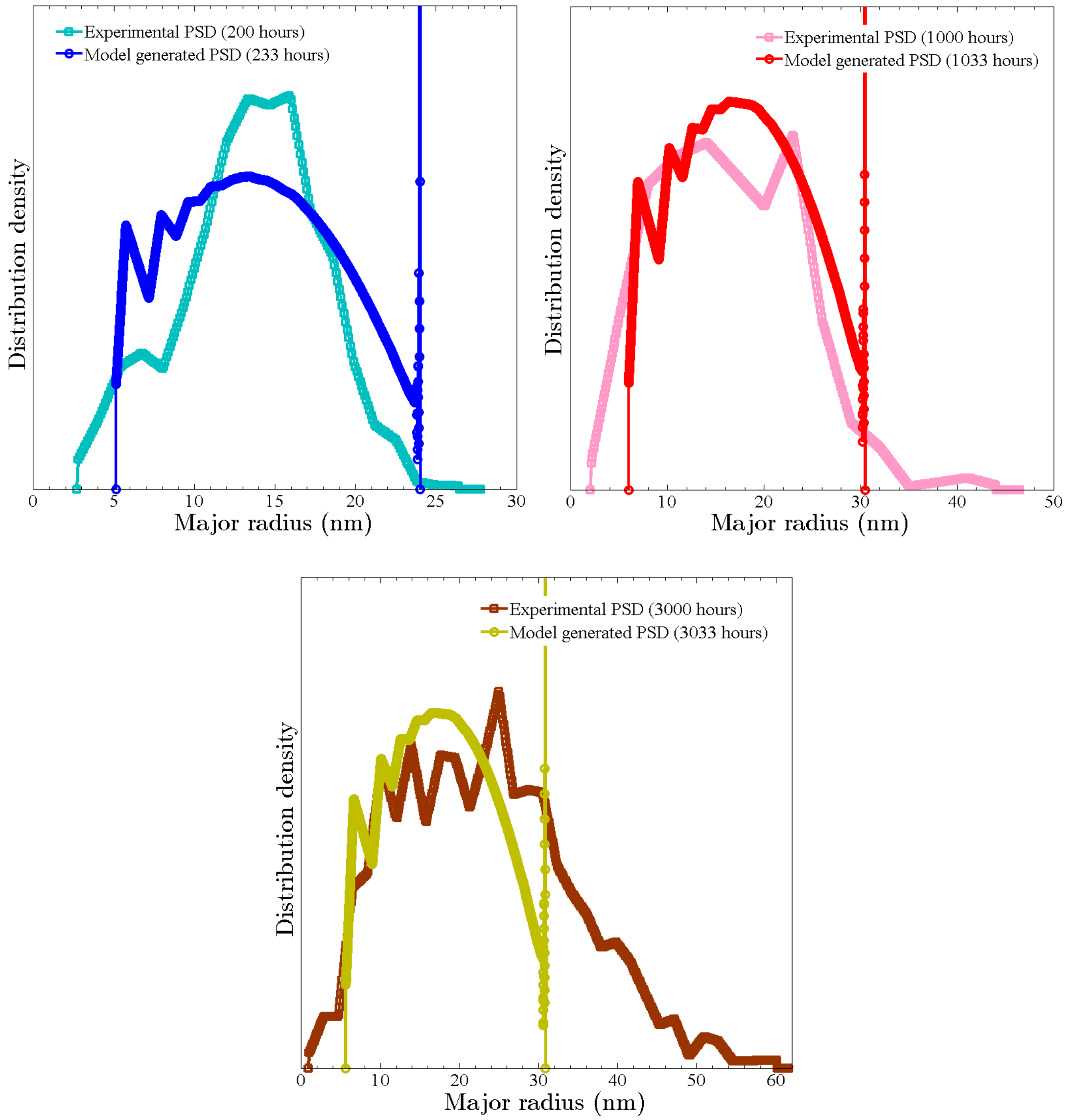

Figure 6.25: Model (new mechanism) and experimental (Perez mechanism) particle size distributions (PSDs) for γ'' precipitates created in Alloy 625 when ageing at $650^{\circ}C$ for the indicated times. For ease of comparison the value of the distribution densities have been altered such that the same number of particles are contained within both distributions making their specific magnitudes arbitrary.

The aspect ratio evolution calculated using the new mechanism obeys an expectedly tight correspondence with experimental values derived from material aged for durations between 100-1000 hours as shown in Figure 6.26. More importantly, however, similar agreement is also observed for both the material aged at 50 hours and 3000 hours. As a result, considering the model result for 50 hours aged material with respect to r_{M}, its congruence with $\bar{\alpha}$ also signifies (taken together with the other data points) the model to be entirely successful in predicting average physical behaviour of γ'' precipitates when ageing for durations of less than 1000 hours at 650°C. Contrastingly, the now good agreement obtained for $\bar{\alpha}$ at 3000 hours versus the large disparity for r_{M} in Figure 6.24 suggests that the effect of "encounter" is far more significant for r_{M}.

Owing to the experimental results obtained at 700°C (Figures 5.20c and 5.18c), the disparate impact of "encounter" indicated by the model on $\bar{\alpha}$ and $\bar{r}_{\mathrm{M}}$ for γ'' precipitates at 650°C is *prima facie* a surprising result *viz.* one would expect the phenomenon to result in a concomitant increase in $\bar{r}_{\mathrm{M}}$ and decrease in $\bar{\alpha}$ always. Nevertheless, the fact that this is an apparently physical result also (*i.e.* it is reflected in the experimental data through the result $\bar{r}_{\mathrm{M}}$ (3000 hours) $>>$ $\bar{r}_{\mathrm{M}}$ (1000 hours) whilst $\bar{\alpha}$ (3000 hours) $\approx$ $\bar{\alpha}$ (1000 hours)) indicates that this is not necessarily a flaw in the model. Succinctly stated, a relatively stable $\bar{\alpha}$ value could be maintained during earlier stages of "encounter" whilst $barr_{\mathrm{M}}$ increases owing to the rate and effect "encounter" has on the absolute magnitude of both variables. That is, for example, assuming each variable evolves inversely to the other, at long ageing times where the major particle radii are large and aspect ratios

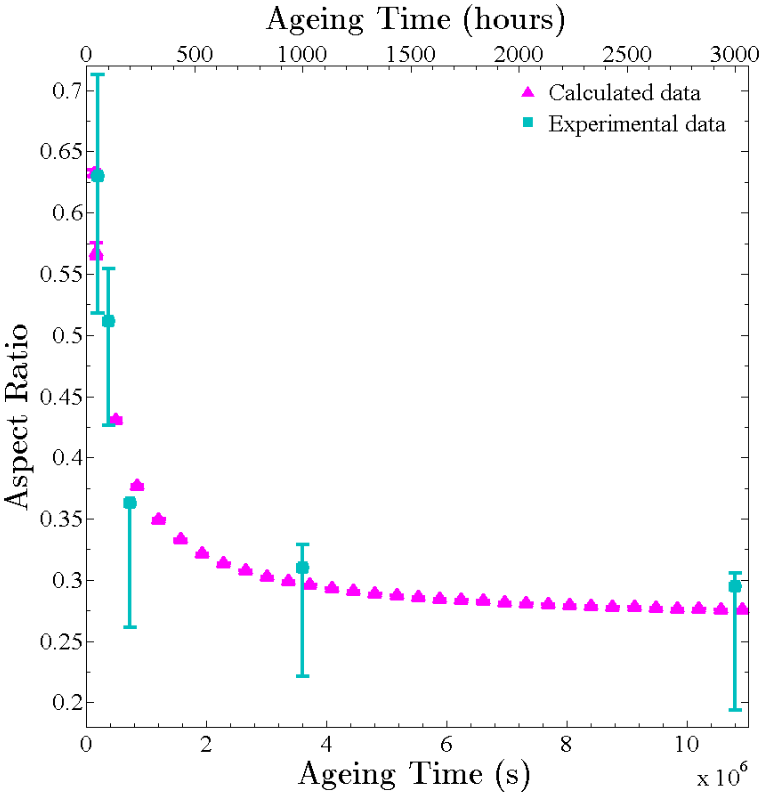

Figure 6.26: Calculated aspect ratio evolution for γ'' precipitates predicted by the SFFK based model created in this research (via the new distribution density calculation mechanism) with time-shift correction applied. Data points correspond to average values and the error bars to the first and third quartiles of the aspect ratio distribution. Experimental data points for populations existing after 50, 100, 200, 1000 and 3000 hours of ageing are shown for comparison.

smaller the coalescence of two precipitates would lead to a large absolute change in the major radius but only small absolute change in the aspect ratio. What is more, if sufficient "encounters" take place, the aspect ratio would still reduce significantly as observed 700 °C owing to the faster precipitation kinetics at this temperature (and ignoring the effect of the different nucleation sites).

Amongst the three principle variables, from Figure 6.27 it can be seen that arguably the worst reproduction of the experimental results by the model is achieved for the precipitate number density; neither of the points not used in the calibration intersects with the modelled trend. Regardless of this fact, however, reasonable agreement can nevertheless still be claimed owing to the nature of the evolution conducted by the parameter: Considering the incredibly large (negative) gradient of the number density trend at short ageing times, a value within the range parametrised by the experimental data point at 50 hours of ageing would likely be achieved through only a small (negative) lateral movement (<5 hours) along the modelled number density trend. Similarly, the apparent disparity between the experimental and modelled values at 3000 hours of ageing is easily inferable as a continuation of the effect of previously described phenomena (*q.v.* Section 6.2.4) such as spikes in the modelled PSD, carbide precipitation in the real system and "encounter". The significant implication of such continued conformity of the modelled and experimental number densities, in addition to validating the model at this temperature, is the validation of the use Hilliard's mathematical limit for the thickness of the experimentally examined TEM foils.

Finally with regards to the validation calculation at 650 °C, although (as detailed in Section 6.2.5) they cannot be appropriately assessed with respect to experimental data, the trends for Z_k^E and Z_k predicted by the model and calculated by the new distribution density mechanism are displayed in Figure 6.28. Just as was the case in the calibration calculation, a consistent increase in the interfacial energy is predicted as precipitates grow in size and the precipitate-matrix interface becomes more incoherent. Likewise, the magnitude misfit strain experienced by the precipitate exhibits a simultaneous decrease. Both results are harmonious with the theories outlined in Section 1.3.

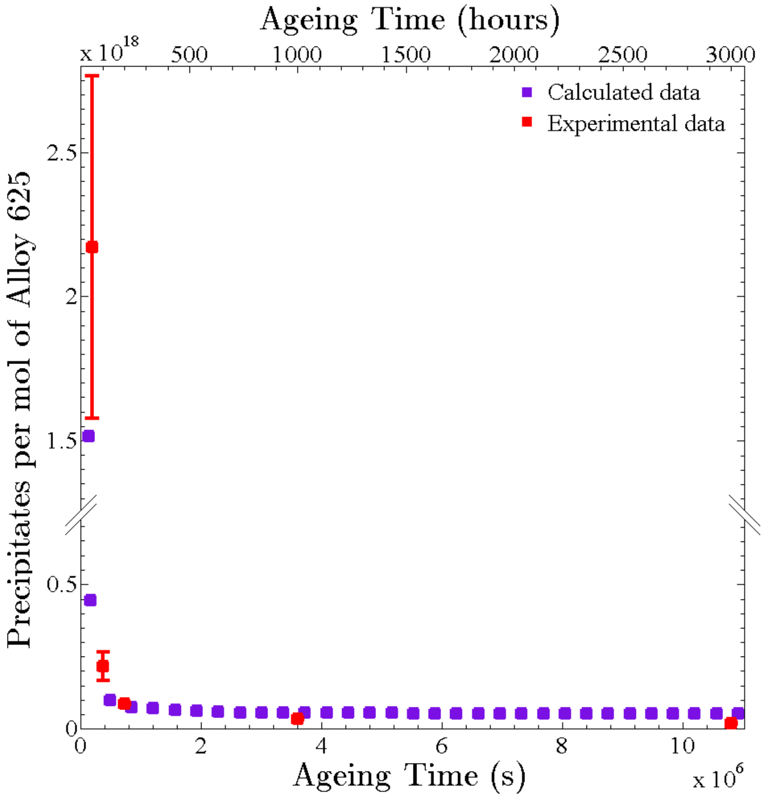

Figure 6.27: Calculated number density evolution for γ'' precipitates predicted by the SFFK based model created in this research, adjusted to account for change in the molar volume of the system and the difference between the calculated, changing molar volume of the precipitate phase (implied from the changing misfit strain) and the fixed value of Ω implemented in SFFK. Experimental data points for populations existing after 50, 100, 200, 1000 and 3000 hours of ageing are shown for comparison.

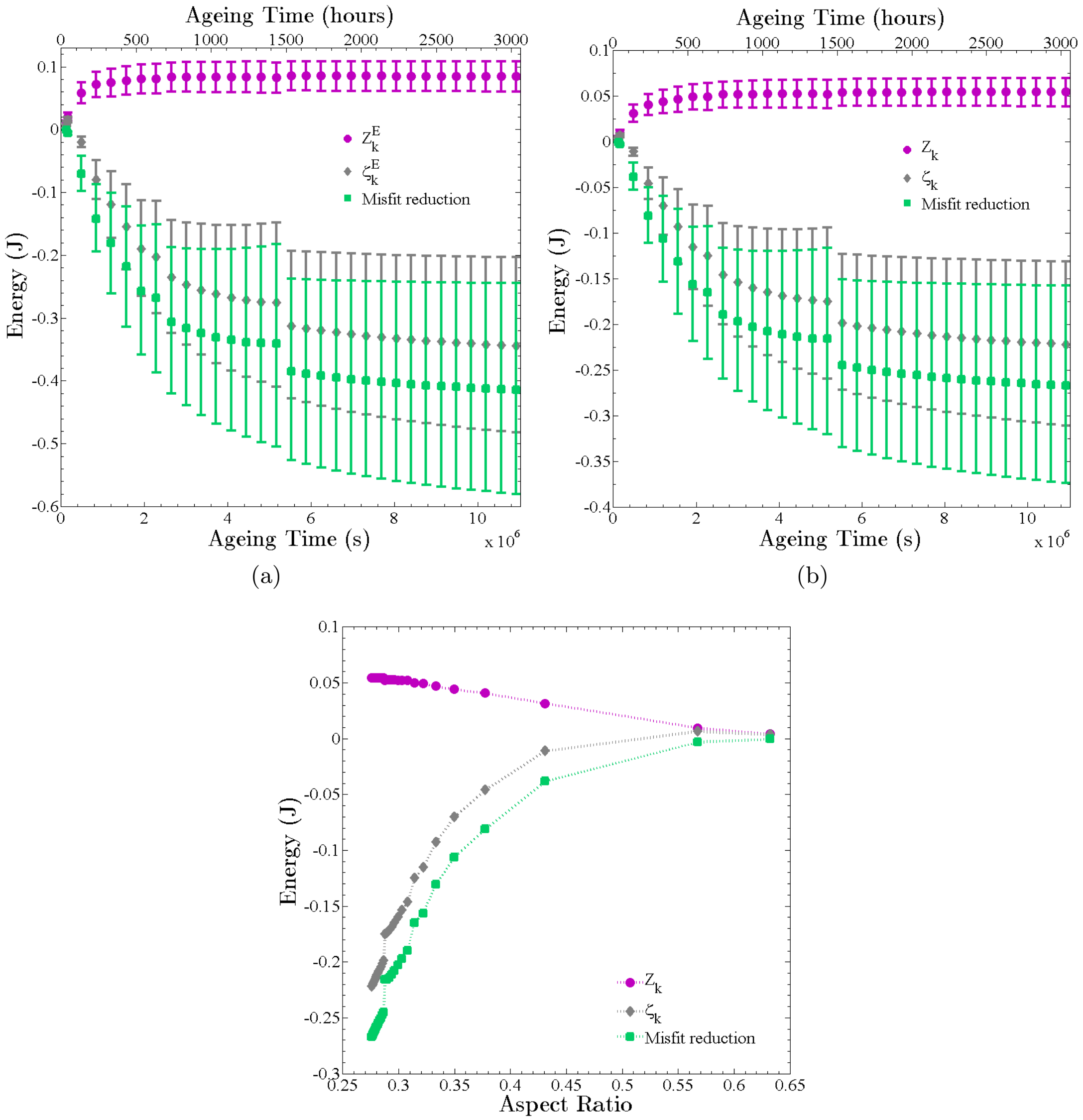

(a)

(b)

(c)

Figure 6.28: Time evolution of a) ζ_k^E, Z_k^E and $8\rho_k\Lambda_k^E[3\xi_k^2]^{-1}$ and b) ζ_k, Z_k and $8\rho_k\Lambda_k[3\xi_k^2]^{-1}$. Data points correspond to average values and the error bars to the first and third quartiles of the major radius particle size distribution. c) Evolution of the average values ζ_k, Z_k and $8\rho_k\Lambda_k[3\xi_k^2]^{-1}$ with average aspect ratio calculated from their relative distributions.

600°C

In view of the experimental data pertaining to γ'' precipitates in Section 5.3.2, the application of the methodology defined in Section 6.2 to perform the SFFK calculation for precipitates evolving at 600°C poses (in accordance with the discussion in Section 6.1) two distinct problems: Firstly, the requirement for the trend of $\alpha(t)$ to calculate ζ_k^E cannot be reasonably argued to be fulfilled by the linear relationship depicted in Figure 5.18a owing to its stark contrast to other experimental data gathered in this research and by others (*e.g.* Slama *et al.* [4]). Secondly (and similarly), the relationship of $\alpha(r_{\mathrm{M}})$ defined in Figure 5.16a cannot be reasonably harnessed because of both its marked difference to those defined at different temperatures (*q.v.* Figure5.17) and the fact that the behaviour which it describes is not consistent with expected physical behaviour.

Considering their origin, it is obvious that an independent solution to the aforementioned problems in setting up the SFFK based calculation for γ'' evolution at 600°C is impossible. Nonetheless, utilising the fact that the simulation was successful at 650°C, a reasonable approximation of the functions defining $\alpha(t)$ and $\alpha(r_{\mathrm{M}})$ at 600°C can be made through comparison with those defined in Equations 6.1 and 6.2: An evaluation of the times at which $\alpha(t)_{650} = \alpha(3.6 \times 10^6)_{600}$ and $\alpha(t)_{650} = \alpha(10.8 \times 10^6)_{600}$ yields average the result that $\alpha(t)_{600} = \alpha(12.48t)_{650}$. Similarly, the best correspondence with the behaviour of the raw values in Figure 5.16a yields $\alpha(r_{\mathrm{M}})_{600} = \alpha(0.8r_{\mathrm{M}})_{650}$. It was in accordance with these results, therefore, that the SFFK simulation at 600°C was undertaken using the functions defined in Equations 6.17 and 6.18 (depicted graphically in Figures 6.29a and b, respectively).

$$\alpha_k(r_{\mathrm{M}}) = 0.0625 + \frac{0.6368 \times 9.6024 \times 10^{-9}}{9.6024 \times 10^{-9} + r_{M,k}} \tag{6.17}$$

$$\alpha_k(t) = 0.2645 + \frac{0.5852 \times 0.20818}{0.20818 + t(s)} \tag{6.18}$$

Retaining the same conditions/thresholds described at the start of Section 6.2 (with exception that now $\Omega = 4.69953 \times 10^{-5}$), the aspect ratio evolution at 600°C computed by the model (and calculated using the new distribution density method) is displayed in Figure 6.30. Strikingly in this instance, in contrast to the results at 650°C, a significant disparity between the calculated and input hyperbolic trend to the calculation is observable at all but the shortest ageing duration. This phenomenon is observed, despite the application of the relevant time shift of 449.40 hours, signifying a marked problem with the calculation process at this temperature *viz.* if working correctly the model would necessarily reproduce this input parameter. In light of the conformity with the calculation at 650°C, a physical reason for the appearance of a discrepancy at 600°C is not clear (the behaviour or change in magnitude of temperature dependent input parameters such as the driving force for precipitation, elemental diffusivities and elastic constants should not yield a incompatibility with calculation following the input

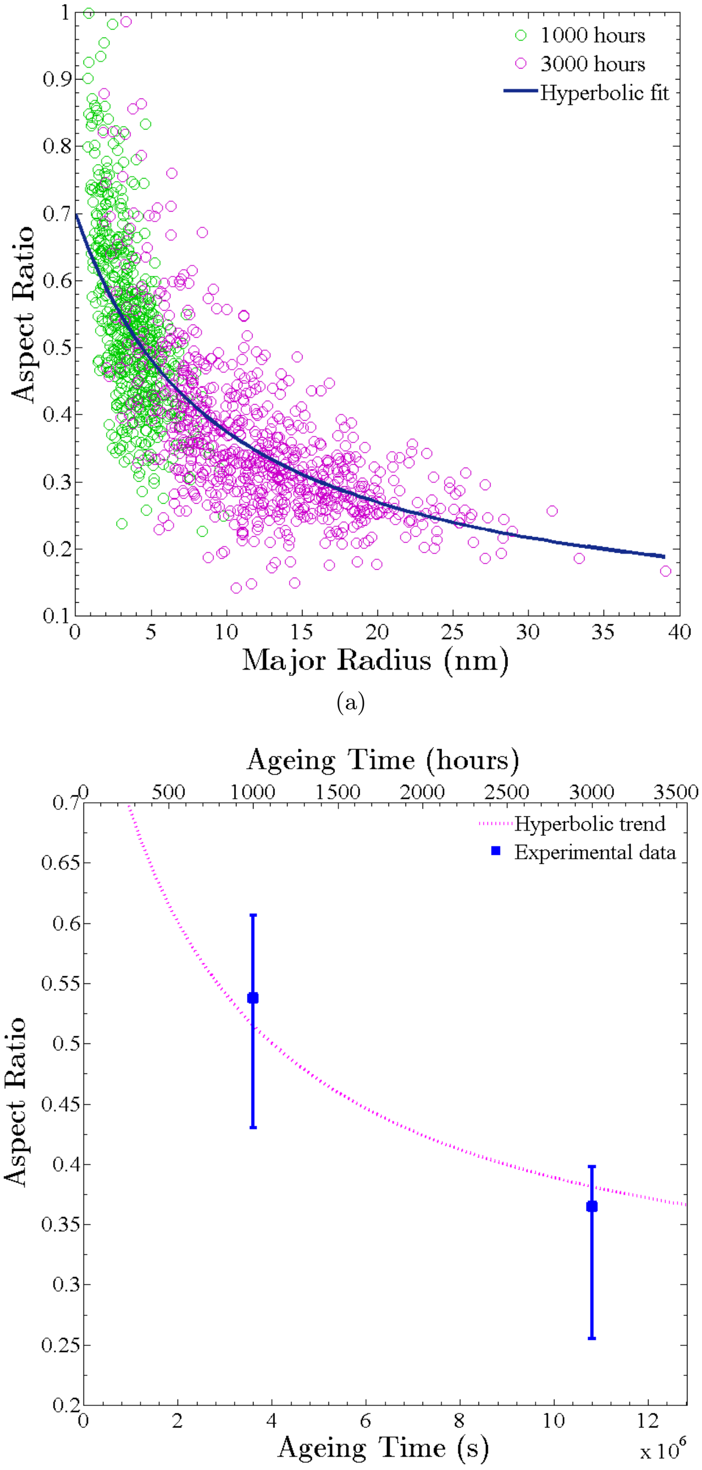

(a)

(b)

Figure 6.29: Data points generated from the measured statistics of γ'' precipitates in Alloy 625 material aged at 600°C and presented in Figures 5.16a and Figure 5.18a compared to a) the hyperbolic function defined in Equation 6.17 and b) the hyperbolic function defined in Equation 6.18, respectively.

aspect ratio behaviour), alternatively, however, considering the different evolution rates at each temperature it is obvious that the mechanisms for managing the time evolution comprise a likely source: Explicitly, if one or both of the functions defining the initial time step and its evolution are incompatible with the evolution rates at 600 °C, an uncorrectable deviation from the input behaviour is possible.

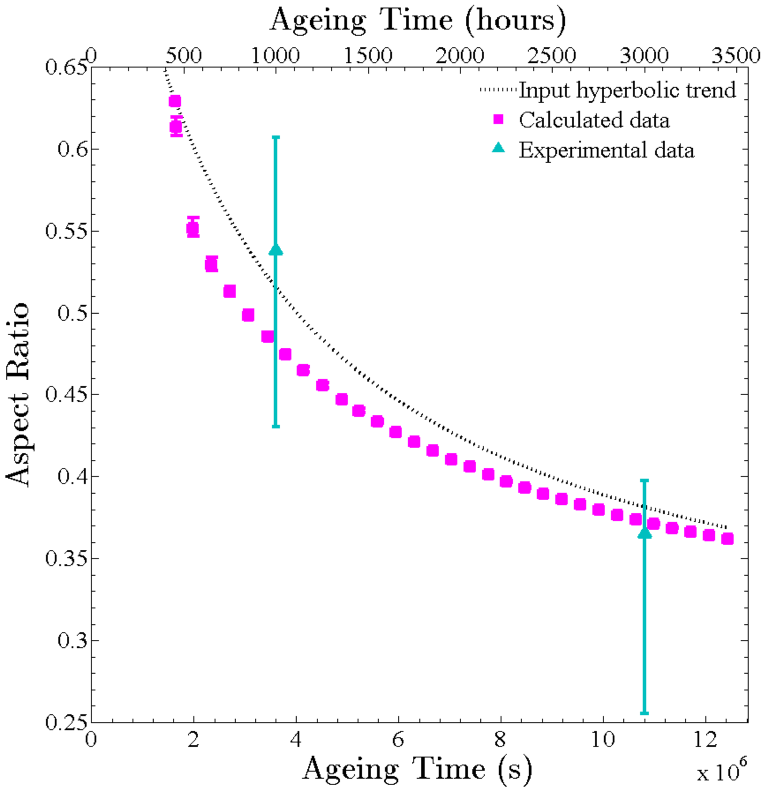

Figure 6.30: Calculated aspect ratio evolution for γ'' precipitates predicted by the SFFK based model created in this research (via the new distribution density calculation mechanism) with time-shift correction applied. Data points correspond to average values and the error bars to the first and third quartiles of the aspect ratio distribution. Experimental data points for populations existing after 1000 and 3000 hours of ageing are shown for comparison.

In view of the technical possibility for its existence, direct evidence for specific origin of the aforementioned time deviation phenomenon occurring when modelling γ'' evolution 600 °C can actually be deduced from the relative behaviour of the first few data points in Figure 6.30: Initially (*i.e.* when the time step is small), a good correspondence with the input distribution is observed signifying no underlying physical cause for any discrepancy with the input $\alpha(t)$ function. As the time step increases, however, a growing deviation from the input trend is observed for ageing durations up to 600 hours which then subsequently diminishes in magnitude. Coincidentally, examining the information contained in the raw output arrays/classes, it is found that nucleation of new classes in the PSD continues up to ≈ 36 modelled hours (≈ 576 hours in Figure 6.30), meaning that as each class initially evolves with respect to aspect ratio at approximately the same rate, under the implemented time step condition new classes are evolving for over 1000 seconds at rates which previous classes only evolved for a few 10s of seconds. Comparing the former observation with the latter process, therefore, it is evident that a causality is in effect.

With the origin for the inconsistency between the input and output aspect ratio behaviour identified as the time step, it is self-evident that its solution comprises a tailoring of the time step initial magnitude and/or progression to a calculation at 600°C. Moreover, it is also clear that the particular form of this tailoring is a substantial reduction in the magnitude of the time step at least until the nucleation of new precipitates in the model has ceased. Once again taking into account the behaviour/results for ageings at 650°C, an appropriate value for the reduction in the magnitude of Δt_0 and the increase in time step (previously 1%) can be inferred from the relative behaviours of $\alpha(t)$ at 600°C and 650°C as 12.48 *i.e.* $\Delta t \rightarrow 0.08\Delta t$, $1\% \rightarrow 0.08\%$. Given this conclusion, therefore, by retaining all other input parameters it is evident that, *prima facie*, a successful replication of the input $\alpha(t)$ should be achieved by a trivial alteration to the time step behaviour. Unfortunately, however, the execution of such a script is all but prohibited by the massive effect such a change would have on the duration of the computation.

As described at the start of Section 6.2, the magnitude of the time step and increase rate in the SFFK model created in this research was specifically designed in view of a trade-off between simulation detail and speed. Specifically, it was illustrated that for every factor 10 decrease in $\Delta(t)_0$ an extra 232 iterations were required in the simulation; however, it now must be stressed that this value is not directly proportional to the simulation duration. Furthermore, any change in the magnitude by which the time step increases is far more severe both in terms of the number of iterations and total computation times. As an illustrative example, considering that the duration of the calculation of the evolution of a particular class in a particular time step is invariant (meaning that the simulation duration correlates purely to the product of the number of iterations and classes), under the new time step scheme the simulation of 3000 hours of ageing would take 55 times longer even allowing for a maximum time step of 12.48 hours. Accordingly, considering that the original simulation took around 240,000 seconds, the nominal computation time for the new simulation would be over 13.13×10^6 seconds, or a prohibitive 152 days.

Taking into account the above discussion, it is evident that without considerable alteration of the model to facilitate faster computation (likely through a complex mechanism to facilitate class agglomeration/merger) the results produced for γ'' evolution at 600°C will undoubtedly be incorrect. Nevertheless, despite this outcome it is still worth examining the results produced for possible revelations regarding the input parameters and/or calculation procedure and/or interfacial energy deconvolution operation. To this end, the major radius, number density and interfacial energy evolution predicted by the SFFK model (under the current time step mechanism) are presented in Figures 6.31, 6.32 and 6.33 respectively: Initial inspection of the major radius evolution in Figure 6.31 reveals the model to substantially over estimate the precipitate sizes whereas Figure 6.32 displays a vast, consistent under estimation of the number density. Considering the fixed volume of solute available for precipitation, it is clear that these two behaviours are directly correlated, signifying the model to remain self consistent and once again likely omitting any physical cause for the disparity in the modelled and input aspect ratio distributions. Furthermore, taken individually it is evident that the major radius evolution bears a similar response to that of the aspect ratio. Specifically, if one compares the relative change in aspect ratio and major radius of the simulated precipitates between 1000-3000 hours (*i.e.* when the distorting influence of the time step on nucleating precipitate is absent) with the input distribution/experimental data points one finds a similar magnitude change. This latter result is particularly significant as potentially identifies that the model could be successful in replicating the experimental data if the aspect ratio behaviour is corrected.

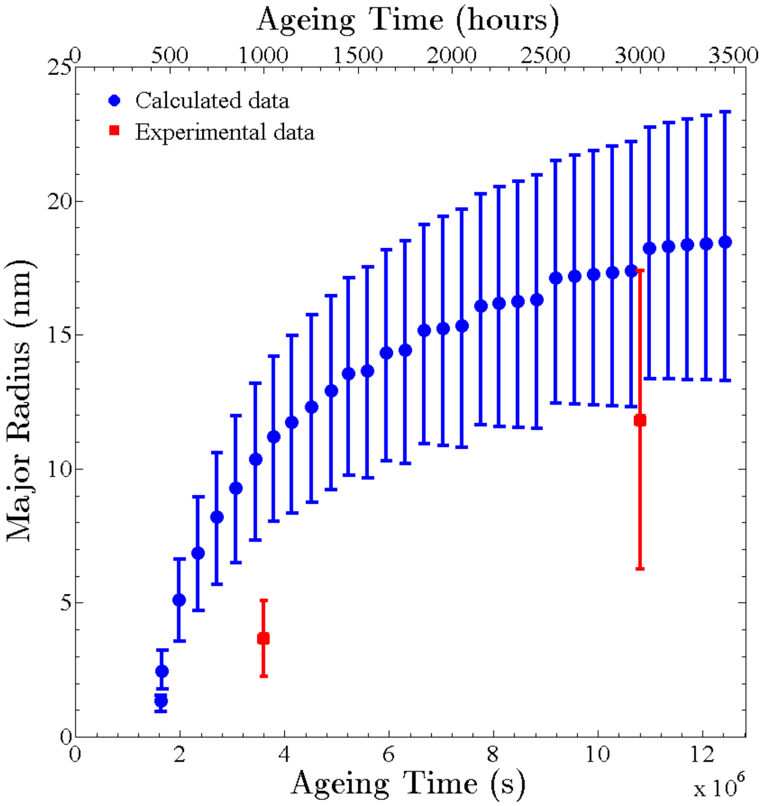

Figure 6.31: Major radius (r_{M}) evolution for γ'' precipitates predicted by the SFFK based model created in this research with time-shift correction applied. Data points correspond to average values and the error bars to the first and third quartiles of the PSD. Experimental data points for populations existing after 1000 and 3000 hours of ageing are shown for comparison.

The final important factor to be considered from the modelled results in Figure 6.31/6.32 is the reason why they comprise an overestimation/underestimation of the experimental statistics rather than the other way around. Discounting any residual discrepancy, an overestimation of the major radius is consistent with the aspect ratio behaviour for two principle reasons: Firstly, for a given equivalent spherical radius ρ in the simulation the corresponding value of r_{M} will increase as the aspect ratio reduces. Secondly, simultaneous to "over reducing" the aspect ratio, the initial large time step previously discussed would also "over inflate" the size of the precipitates in later nucleating classes

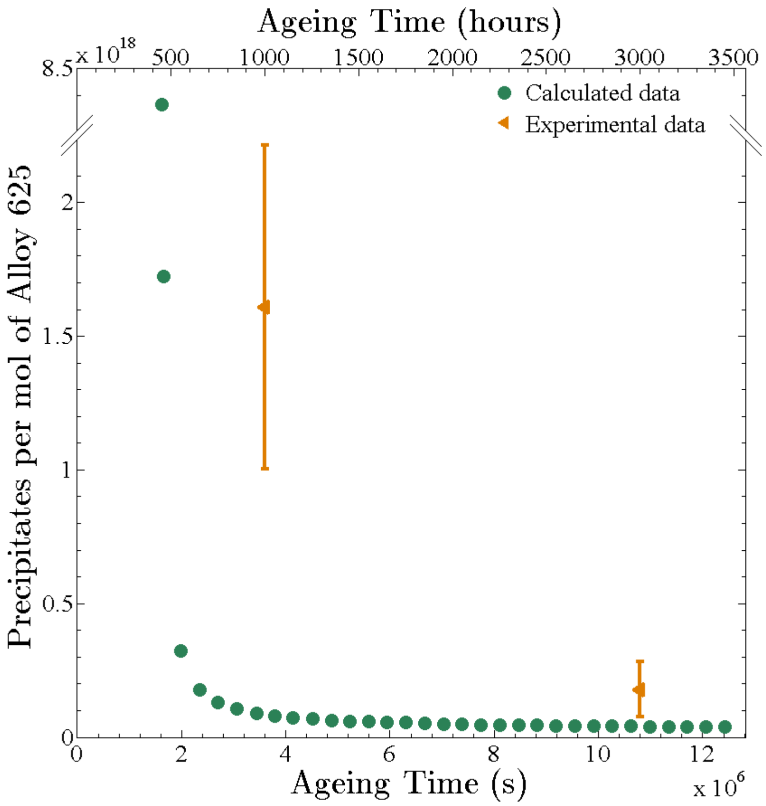

Figure 6.32: Calculated number density evolution for γ'' precipitates predicted by the SFFK based model created in this research, adjusted to account for change in the molar volume of the system and the difference between the calculated, changing molar volume of the precipitate phase (implied from the changing misfit strain) and the fixed value of Ω implemented in SFFK. Experimental data points for populations existing after 1000 and 3000 hours of ageing are shown for comparison.

owing to their initial rapid growth rate being computed over large simulation times. The tandem effect of this secondary phenomenon is to over sequestrate solute and thereby reduce the number of nucleating particles.

Despite their magnitudes clearly being erroneous, the interfacial energy results produced from the simulation at 600°C (Figure 6.33) are significant as they reveal the technique described in Section 6.2.5 to be successful in deconvoluting the effect of reducing misfit strain from increasing interfacial energy. Furthermore, they provide the final source of evidence for the aspect ratio behaviour described previously to be attributable primarily to the time step mechanism in the SFFK model.

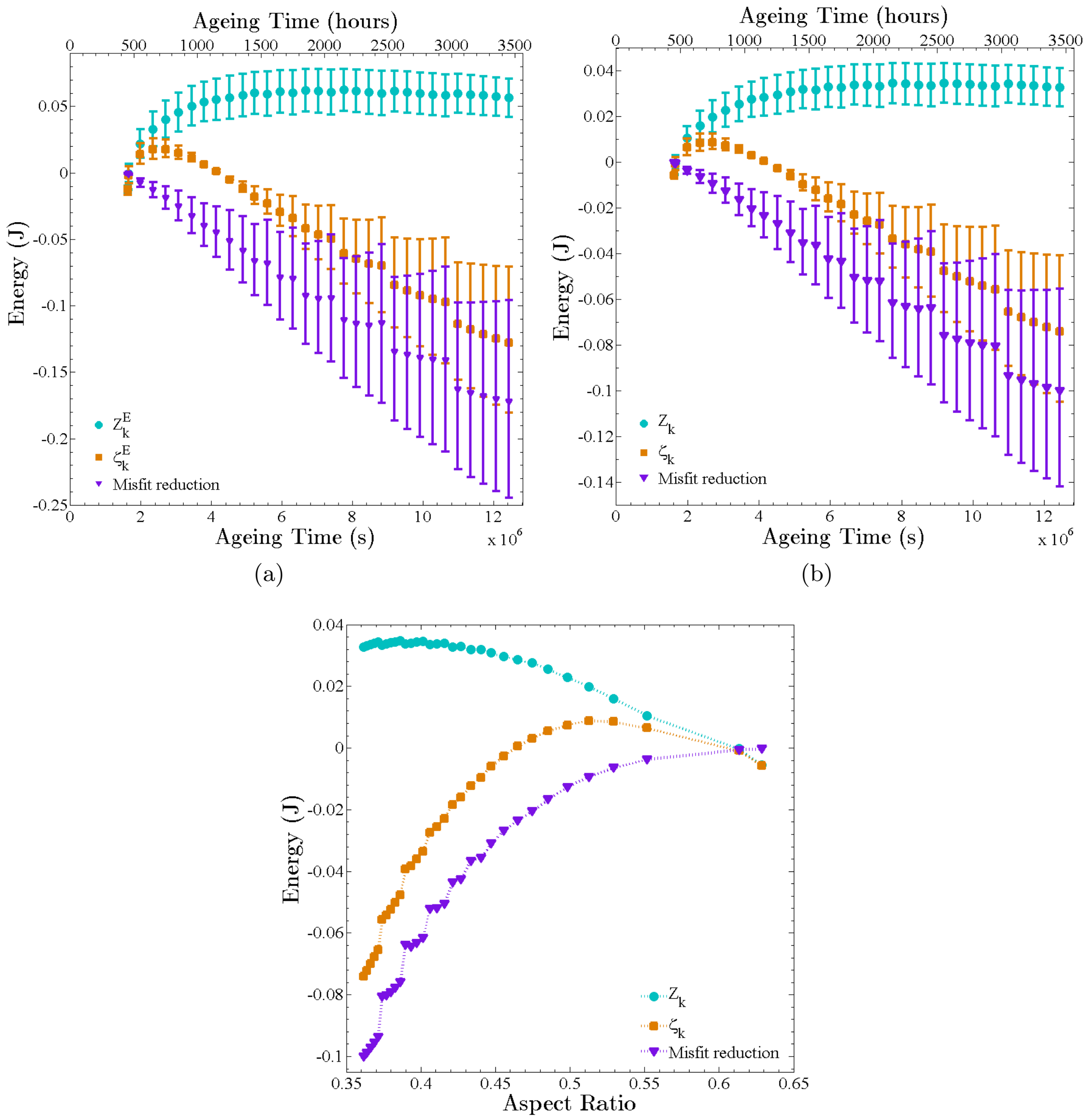

(a)

(b)

(c)

Figure 6.33: Time evolution of a) ζ_k^E, Z_k^E and $8\rho_k\Lambda_k^E[3\xi_k^2]^{-1}$ and b) ζ_k, Z_k and $8\rho_k\Lambda_k[3\xi_k^2]^{-1}$. Data points correspond to average values and the error bars to the first and third quartiles of the major radius particle size distribution. c) Evolution of the average values ζ_k, Z_k and $8\rho_k\Lambda_k[3\xi_k^2]^{-1}$ with average aspect ratio calculated from their relative distributions.

6.3.2 Literature Data

As alluded to in Section 3.3.1, the most relevant literature studies with respect to the SFFK model designed in this research are those of Han *et al.* [2] and Sundararaman *et al.* [39] owing to their both containing information on three of the most pertinent γ'' precipitate statistics, namely $\bar{L}_{\mathrm{M}}$, $\bar{\alpha}$ and the PSD. Consequently, the principal evaluation of the validity of the model against literature data was designed to comprise a comparison against the results of both of these studies; the provision of statistics on only $\bar{L}_{\mathrm{M}}$ and $\bar{\alpha}$ by Slama *et al.* [4] were also considered owing to their potentially facilitating a similar, but less rigorous and, therefore, weighty evaluation.

Reflecting on the different composition and resultant mechanical properties of Alloy 718 compared to Alloy 625, it is evident from Section 3.1 that before the Alloy 625 based model could be appropriately used to calculate γ'' precipitation behaviour it was first necessary to modify the relevant input parameters. To this end, assuming behaviours such as $\lambda(\alpha)$ are independent of the relatively minor compositional/structural differences between Alloy 625 and 718 and, similarly, the binary diffusion constants harnessed for Alloy 625 are just as valid for Alloy 718, the temperature dependence of the elastic constants of the matrix phase were evaluated based on the same methodology detailed in Section 3.1.3, producing Figure 6.34. Likewise, the binary diffusivities of those elements predicted to exist in greater quantity in γ'' precipitates in Alloy 718 owing to the alloy composition, thereby necessitating their inclusion in the Alloy 718 calculations, are detailed in Table 6.2. Finally, the driving forces for precipitation and elemental sequestration were evaluated according to the equilibrium phase fraction diagrams in Figures 6.35, 6.36 and 6.37.

Table 6.2: Experimentally measured diffusion constants for the elements determined from equilibrium thermodynamic calculations to be contained within γ'' precipitates in Alloy 718 in addition to those listed in Table 3.1.

Element	D_0 ($\mathrm{m^2s^{-1}}$)	ΔG_D ($\mathrm{Jmol^{-1}}$)	Reference
Iron	0.0537	326320	Ganesan *et al.* [353]
Aluminium	0.002798	293083	Karunaratne *et al.* [272]

Despite the publication in each of the aforementioned literature studies of some average precipitate aspect ratio and major radius statistics, the functions defining of $\alpha(r_{\mathrm{M}})$ and $\alpha(t)$ were calculated via linear extrapolation of the methodology applied for the simulation of precipitation in Alloy 625 at 600°C. That is to say, a change in the temperature was computed to result in a proportional change in the values of $\alpha(r_{\mathrm{M}})$ and $\alpha(t)$ such that for every 50°C increase in temperature $\alpha(r_{\mathrm{M}})_{\mathrm{T+50}} = \alpha(1.25r_{\mathrm{M}})_{\mathrm{T}}$ and $\alpha(t)_{\mathrm{T+50}} = \alpha(0.08t)_{\mathrm{T}}$. The principal reason for this approach was two fold: 1) The calibration of parameters such as $\lambda(\alpha)$ have been made with respect to specific limits on values such as the aspect ratio, therefore the insertion of markedly different aspect ratio behaviour is likely to require a full and lengthy reassessment of the function. 2) Some of the literature results are rather unphysical, with significant undulations and

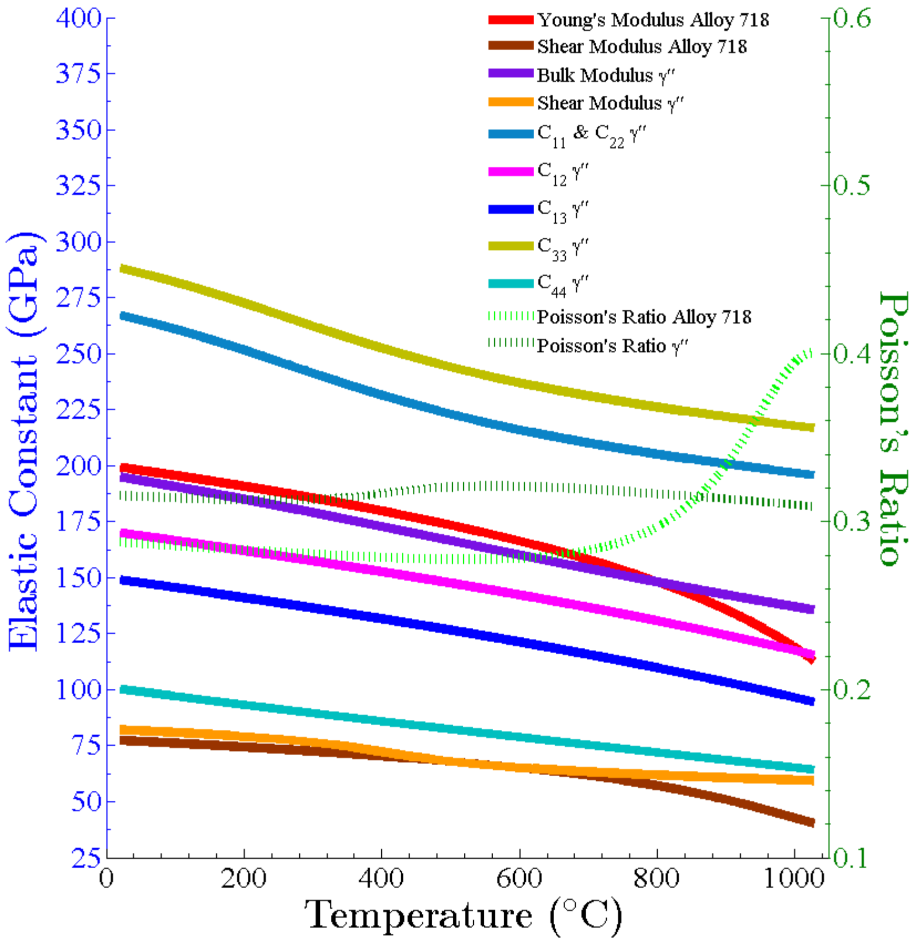

Figure 6.34: Elastic constant behaviour for the Alloy 718 matrix and γ'' precipitates interpreted in this research. Alloy 718 data taken from the material data sheet issued by the Special Metals Corporation [43]. γ'' data calculated from the extrapolating the results of Connétable *et al.* [27] using the trends calculated for nickel by Luo *et al.* [28]

even increases in aspect ratio indicated.

Considering the apparent availability of the required input descriptions, the computation of the nucleation growth and coarsening behaviour of Alloy 718 is straightforward. Nonetheless, it should be pointed out at this stage that irrespective of the results obtained, a fundamental key restriction applies with respect to the range of temperatures over which any Alloy 718 validation could appropriately be defined. Specifically, the fact that the value of the Poisson's ratio (ν) for Alloy 718 comprises a significant deviation away from the temperature invariant behaviour imposed in Section 2.2.2 (for the calculation of the coefficients F_0, F_1 and F_2 in Equation 2.10) at $\approx 800°C$ means that calculated results above this limit could not be considered an appropriate representation of the real system.

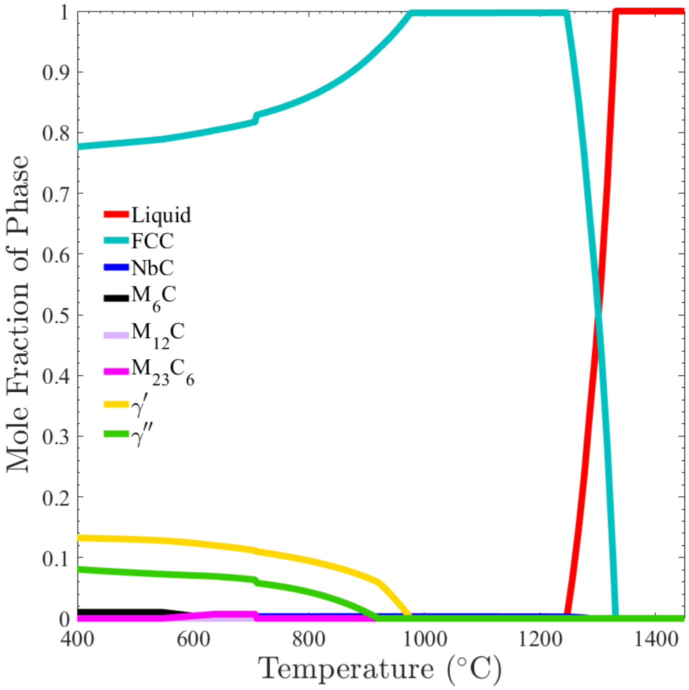

(a)

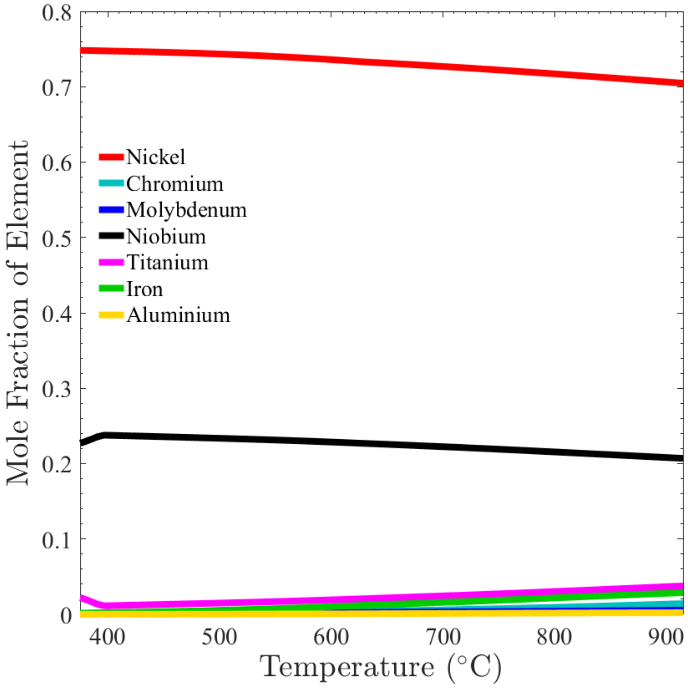

(b)

Figure 6.35: a) Molar phase composition of Alloy 718 (Han *et al.* [2]) and b) elemental composition of γ'' precipitates in Alloy 718 (Han *et al.* [2]), both as a function of temperature. Data calculated using the software Thermo-Calc via the Calphad technique with data from the Thermo-Calc Software TCNI8 Ni-based Superalloys database version 8 [24, 25, 44].

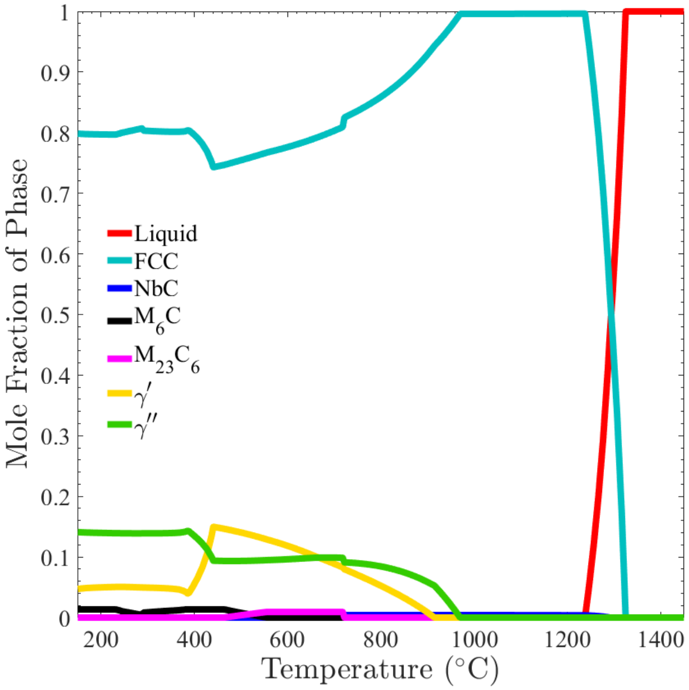

(a)

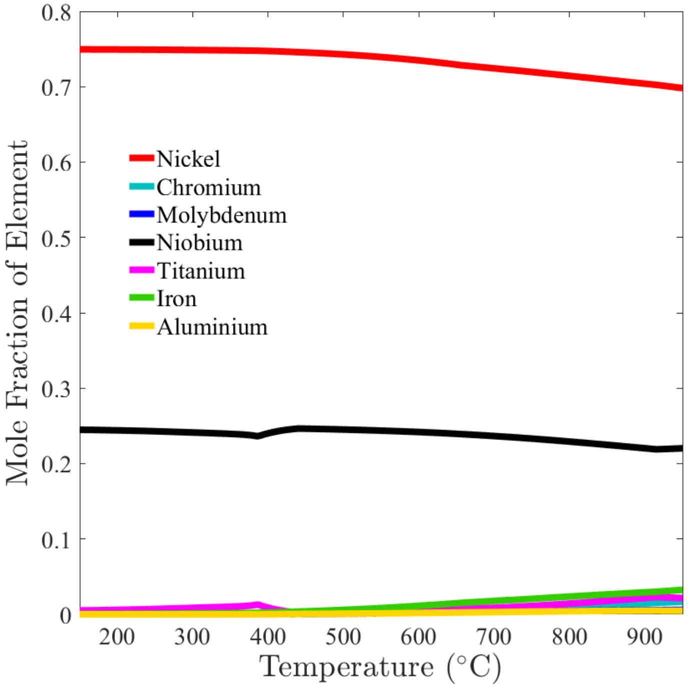

(b)

Figure 6.36: a) Molar phase composition of Alloy 718 (Sundararaman *et al.* [39]) and b) elemental composition of γ'' precipitates in Alloy 718 (Sundararaman *et al.* [39]), both as a function of temperature. Calculated using the software Thermo-Calc via the Calphad technique with data from the Thermo-Calc Software TCNI8 Ni-based Superalloys database version 8 [24, 25, 44].

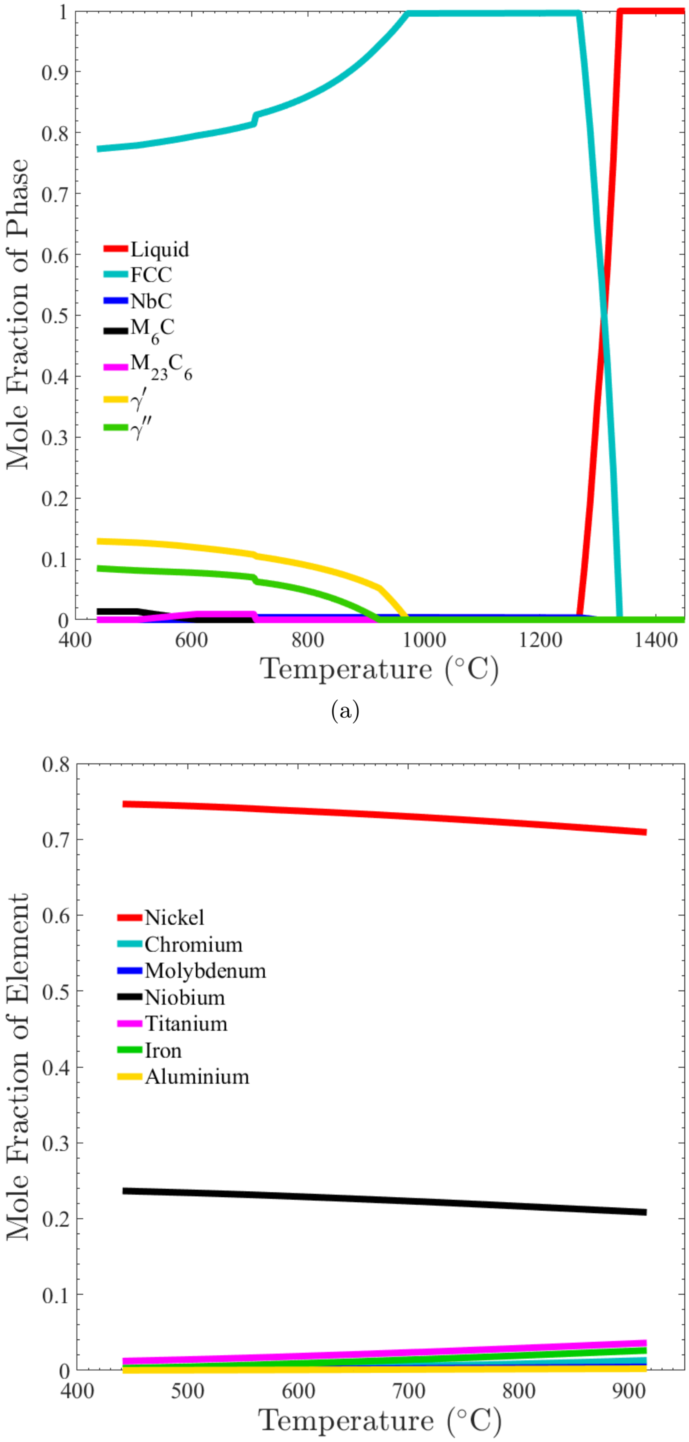

(a)

(b)

Figure 6.37: a) Molar phase composition of Alloy 718 (Slama *et al.* [4]) and b) elemental composition of γ'' precipitates in Alloy 718 (Slama *et al.* [4]), both as a function of temperature. Data calculated using the software Thermo-Calc via the Calphad technique with data from the Thermo-Calc Software TCNI8 Ni-based Superalloys database version 8 [24, 25, 26].

700° C

Of the available literature sources the lowest temperature experimental evaluation of γ'' evolution is that conducted by Han *et al.* [2] at 700° C. Accordingly, only the simulation of Han's alloy was undertaken at this temperature. The functions defining $\alpha_k(r_{\mathrm{M}})$ and $\alpha_k(t)$ are detailed in Equations 6.19 and 6.20, respectively.

$$\alpha_k(r_{\mathrm{M}}) = 0.0625 + \frac{0.6368 \times 15.004 \times 10^{-9}}{15.004 \times 10^{-9} + r_{M,k}} \tag{6.19}$$

$$\alpha_k(t) = 0.2645 + \frac{0.5852 \times 0.00134}{0.00134 + t(s)} \tag{6.20}$$

Analysis of the γ'' aspect ratio evolution in Alloy 718 at 700° C output by the SFFK model created in this research (Figure 6.38) reveals an excellent correspondence with the input function and also good agreement with the values measured by Han *et al.*. Considering the problems incurred in the previous section for the simulation at 600° C and the much more marked difference in physical parameters in the current simulation to that at 650° C in Alloy 625, this result is particularly significant as it provides further proof for the time step being the origin of the discrepancy at the previous condition. In addition, however, the correspondence with the genuinely independent experimental data apparently reveals the temperature transformation applied to $\alpha_k(t)$ to be remarkably accurate, and, therefore, that the trend in Figure 6.29 is also appropriate.

In contrast to the good replication of the aspect ratio evolution, analysis of major radius evolution in Figure 6.39 reveals the model to output values consistently and significantly below those reported by Han *et al.* [2]. Considered in isolation, this result clearly indicates the model to be apparently unsuited (in its current form) to the prediction of γ'' precipitates in Alloy 718; however, an interesting outcome that must also be considered is that of the precipitate number density: Analysis of the number density values reveals that, in contrast to Equation 1.11, the lower driving force for precipitation (*c.f.* Figure 3.1) and increased temperature resulted in the number of γ'' precipitates predicted to exist by the model per mole of Alloy 718 after 300 hours at 700° C ($\approx 6 \times 10^{17}$) being in excess of that after 300 hours at 650° C in Alloy 625 ($\approx 7 \times 10^{16}$) .

Considering the outline of the mathematical descriptions in Section 1.3, the aforementioned outcome with respect to the precipitate number density is plainly not physical and could, therefore, straightforwardly be interpreted as a flaw in the original model methodology. More specifically, however, given that the description for handling nucleation in the SFFK model is that described in Section 2.2.3 and was successful at 650° C, it is also evident that this problem is unlikely to be associated with the governing equations; in view of the possible contributory factors, the time step mechanism is again identified as the principle cause.

The fact that the time step mechanism also introduces a problem at higher temperatures could be considered surprising given the apparent conformity of the aspect ratio

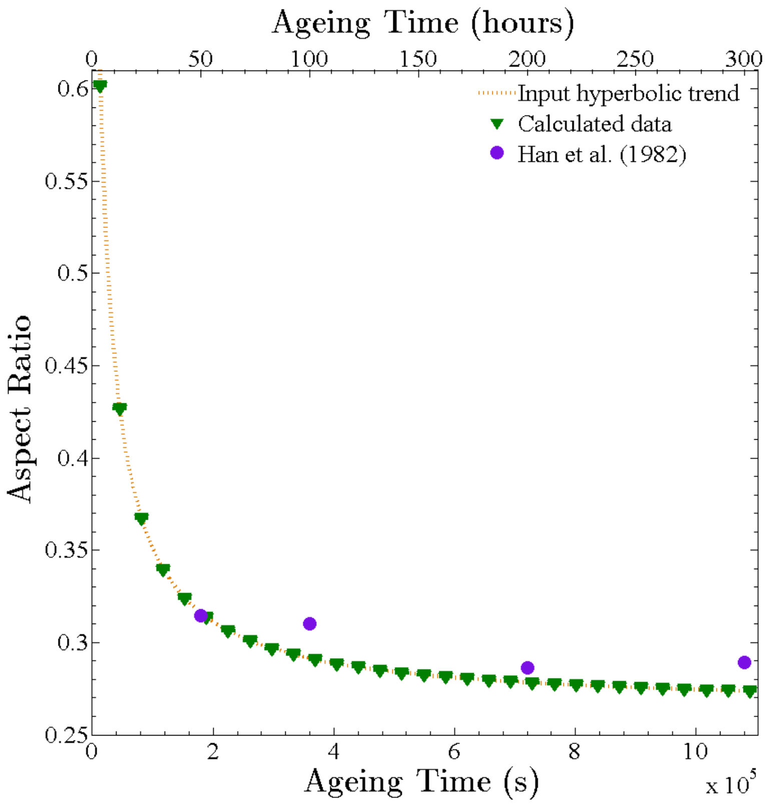

Figure 6.38: Aspect ratio evolution for γ'' precipitates predicted by the SFFK model created in this research (via the new distribution density calculation mechanism) with time-shift correction of 2.42 hours applied. Data points correspond to average values and the error bars to the first and third quartiles of the distribution. Comparative experimental data points measured by Han *et al.* [2] for populations existing after 50, 100, 200 and 300 hours of ageing are also indicated.

evolution predicted by the model with the input trend; however, when considered thoroughly, this outcome can be considered equally expected for the same reasons as the discrepancy at lower temperatures. Explicitly, if the time step mechanism in this instance was now such that the time step during a given iteration was too small compared to previous iterations, two main outcomes are likely: 1) The aspect ratio of new nucleating particles will not decrease sufficiently quickly to match their larger size meaning an outcome where smaller precipitates actually have a smaller aspect ratio than larger precipitates is possible. The impact of this result would be to effect the evolution kinetics of respective precipitate classes such that small/large precipitates reduce/increase too slowly and thereby suppress coarsening and ultimately producing a PSD with a smaller average precipitate size. 2) As smaller precipitate classes remain in the PSD, the number of precipitates increases to a larger value than it otherwise would. The outcome of this latter effect, therefore, would be to increase the precipitate number density and, furthermore, reduce precipitate growth by forcing the available solute to be shared amongst more particles. The conformity with the aspect ratio is merely a consequence of the faster nucleation rate *viz.* the time step at the maximum nucleation time is sufficiently small to prevent any significant deviation from the input function.

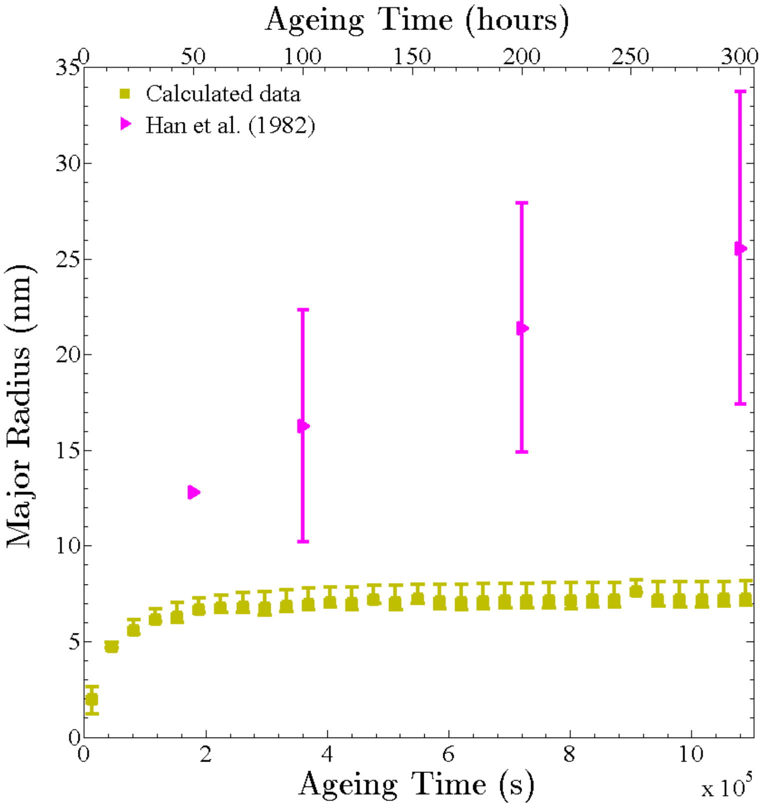

Figure 6.39: Major radius (r_{M}) evolution for γ'' precipitates predicted by the SFFK based model created in this research with time-shift correction of 2.42 hours applied. Data points correspond to average values and the error bars to the first and third quartiles of the PSD. Both sets of values are calculated from the distribution density according to the new mechanism displayed in Figure 6.23. Experimental data points measured by Han *et al.* [2] for populations existing after 50, 100, 200 and 300 hours of ageing are shown for comparison.

As a consequence of its identical origins, the solution to the error introduced by the time step mechanism in this instance is the same that discussed in the Section 6.3.2 with respect to the simulation of γ'' precipitates evolving at 600 °C in Alloy 625. Moreover, however, owing to the time step and compounding rate actually being increased by a factor of 12.48 in this instance (*i.e.* $\Delta(t)_0 = 0.1248$, rate $= 12.48\%$), the simulation time is actually reduced and could therefore be reasonably executed even with a maximum time step of $3600/12.48 = 288$s. The results produced for the aspect ratio, major radius and number density evolution subsequent to such a modification to the SFFK model are, therefore, displayed in Figures 6.40, 6.41 and 6.42 respectively.

Inspecting each of the aforementioned figures in turn: Figure 6.40 reveals the modified time step mechanism to still facilitate the accurate replication of the input aspect ratio distribution, thereby also suggesting that the time step is not sufficiently big to introduce a marked distortion. Separately, Figure 6.41 now indicates a much closer correspondence with the experimental data published by Han *et al.* [2] and Figure 6.42 reveals an expected drop in the number of precipitates from that predicted in Figure 6.27.

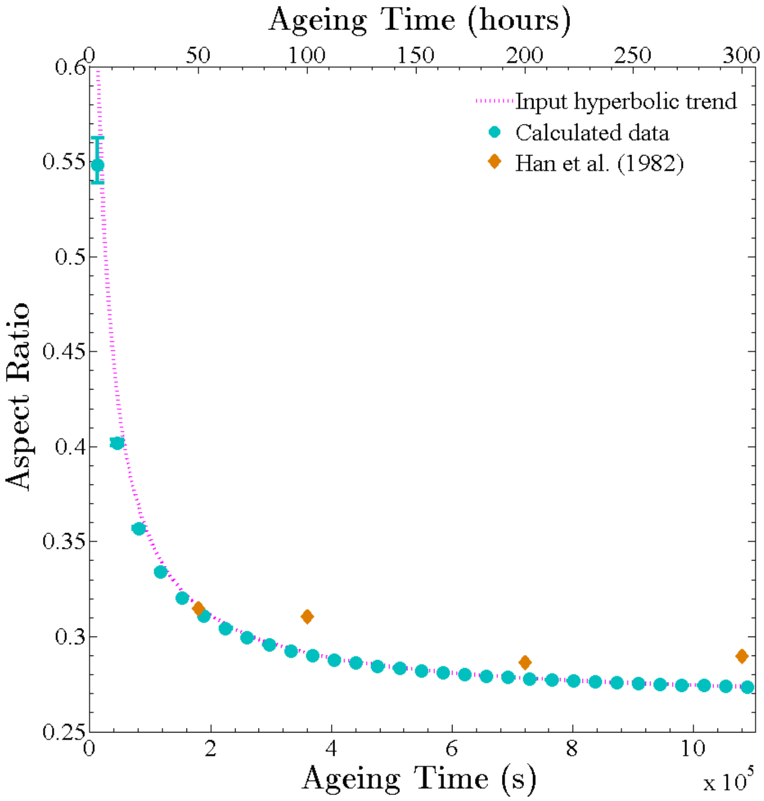

Figure 6.40: Calculated aspect ratio evolution for γ'' precipitates predicted by the SFFK based model created in this research (via the new distribution density calculation mechanism) with time-shift correction applied. Data points correspond to average values and the error bars to the first and third quartiles of the aspect ratio distribution. Experimental data points measured by Han *et al.* [2] for populations existing after 50, 100, 200 and 300 hours of ageing are shown for comparison.

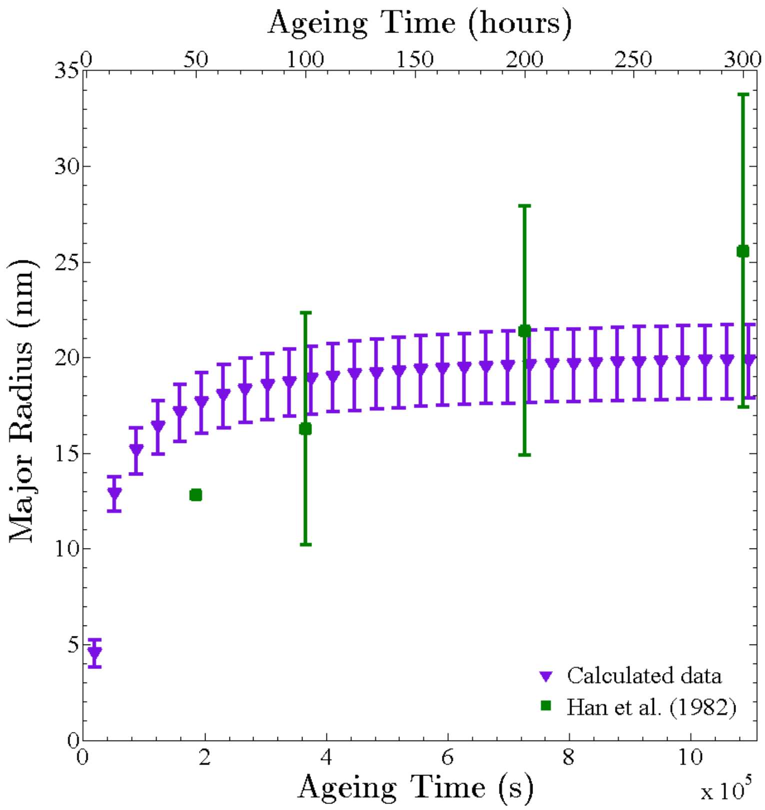

Figure 6.41: Major radius (r_{M}) evolution for γ'' precipitates predicted by the SFFK based model created in this research with time-shift correction applied. Data points correspond to average values and the error bars to the first and third quartiles of the PSD. Experimental data points measured by Han *et al.* [2] for populations existing after 50, 100, 200 and 300 hours of ageing are shown for comparison.

Even with the improvement in the replication of the major radius values measured by Han *et al.* [2] at 700° C, it is clear from Figure 6.41 that a noticeable disagreement remains particularly at the longest and shortest ageing periods. The fact that this result is in stark contrast to that of the aspect ratio is concerning; however, it also provides for a number of potential sources for its origin: In the first, as the evolution kinetics observed by Han *et al.* for the two parameters of major radius and aspect ratio are contrasting, in so far as the aspect ratio remains stable whilst the major radius changes, a potential problem in the measurements is indicated. For instance, because the aspect ratio is independent of the relative magnification used to capture γ'' precipitates but the major radius is not, this would provide for one value to change independently of the other. Particular evidence for the average major radius after 50 hours being under estimated is provided by a comparison to the similar value measured after 100 hours of ageing at 650° C (Figure 5.20b) despite the formation of the phase always being measured as more rapid in Alloy 718 at 700° C [23, 38, 37, 346, 347, 348]. A second reason for the disagreement with the modelled data is the effect of "encounter". Specifically, as the measurements were made by a different researcher their threshold for resolving impinging precipitates would likely be different to that used in this research.

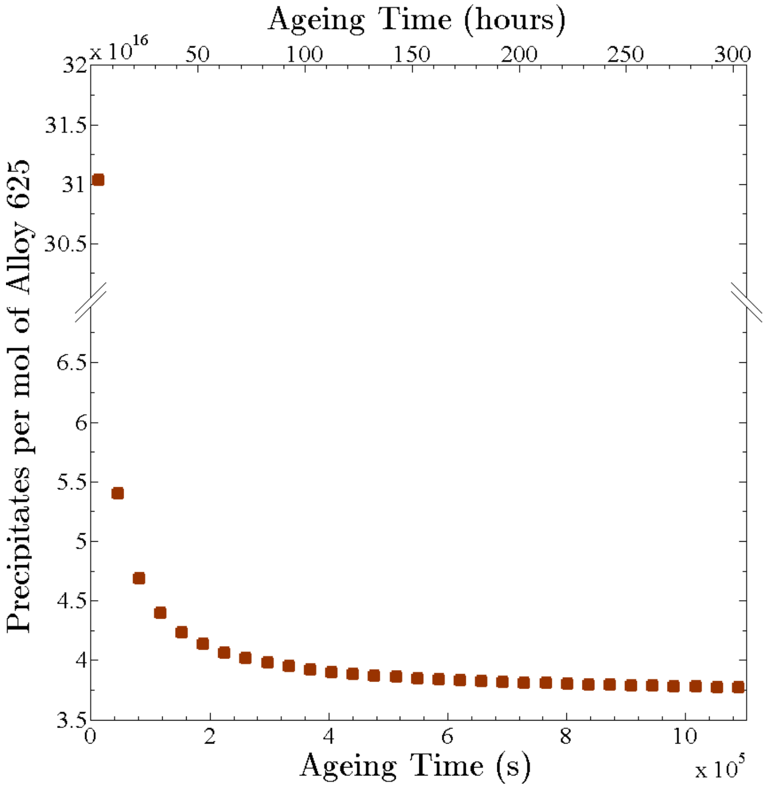

Figure 6.42: Calculated number density evolution for γ'' precipitates predicted by the SFFK based model created in this research, adjusted to account for change in the molar volume of the system and the difference between the calculated, changing molar volume of the precipitate phase (implied from the changing misfit strain) and the fixed value of Ω implemented in SFFK.

Moreover, as discussed with respect to Figure 6.24, the effect of “encounter” is much more pronounced for average major radius values at extended ageing compared to aspect ratio values, allowing for different levels of conformity with the model.

In addition to the aforementioned discrepancies for the modelled and reported precipitate major radius, it is also worth remarking upon the contrast in the spread/shape of the two populations. Simply stated, the narrow spread in the modelled distribution compared to those measured by Han *et al.* [2] derives primarily from the modification made to the time step mechanism. That is, the larger time step intervals resulted in fewer classes and therefore a necessarily poorer representation of the entire PSD. Once again, the broad methodology to rectification of this problem is obvious, namely the splitting of existing classes to cover a larger range of radius values; however, this process remains non-trivial due to the competing effects on the aspect ratio, interfacial energy and driving forces.

Taking into account the above explanation for the discrepancies with the data of Han *et al.* [2] it is concluded here that the model out represents a reasonable reproduction of the experimental behaviour and therefore that the examination of the interfacial energy behaviour constitutes a worthwhile exercise. Accordingly, utilising the deconvolution methodology defined in Section 6.2.5 to produce the diagrams in Figure 6.43 reveals the value of Z_k and the misfit reduction to follow trends consistent with theoretical expectations. Furthermore, the appropriate comparisons detailed in Table 6.3 highlight a conformity of the magnitude of the interfacial energy calculated for γ'' precipitates in Alloy 718 with those in Alloy 625. This result is again significant as it indicates the behaviour calculated by the model to be representative of the real system.

Table 6.3: Average values for the interfacial energy calculated between γ'' precipitates and the matrix of nickel based alloys.

	Aspect Ratio	Interfacial Energy (mJ)
Alloy 625 at 650°C (This Study)	0.29125	52.9
	0.27794	54.7
Alloy 718 at 700°C (Han *et al.* [2])	0.28995	57.6
	0.27787	61.7

725°C and 750°C

Following the methodology described for the production of the statistics at 700°C, calculations for the evolution of the alloy examined by Han *et al.* [2] at 725°C were performed using the relationships in Equation 6.21 and an initial time step (Δt_0) and increase rate of 0.44 seconds and 44%, respectively. Likewise, calculations for γ'' precipitates evolving at 750°C in the alloys of Han *et al.* [2], Slama *et al.* [4] and Sundararaman *et al.* [39] were performed using the functions in Equation 6.22 and an initial time step (Δt_0) of 1.56 seconds and an increase rate 156%. Unfortunately despite these modifications, the SFFK model created in this research was found to be unsuccessful is producing an appropriate calculation owing to a lack of multiple precipitate classes. As a result of this outcome, considering previous results at 600°C it is clear that without modification to allow for the correct splitting of precipitate classes, the model created in this research is limited realistically to temperatures between $\approx$ 650-700°C.

$$\alpha_k(r_{\mathrm{M}}) = 0.0625 + \frac{0.6368 \times 16.774 \times 10^{-9}}{16.774 \times 10^{-9} + r_{M,k}} \qquad \alpha_k(t) = 0.2645 + \frac{0.5852 \times 0.00038}{0.00038 + t(s)} \tag{6.21}$$

$$\alpha_k(r_{\mathrm{M}}) = 0.0625 + \frac{0.6368 \times 18.755 \times 10^{-9}}{18.755 \times 10^{-9} + r_{M,k}} \qquad \alpha_k(t) = 0.2645 + \frac{0.5852 \times 0.00011}{0.00011 + t(s)} \tag{6.22}$$

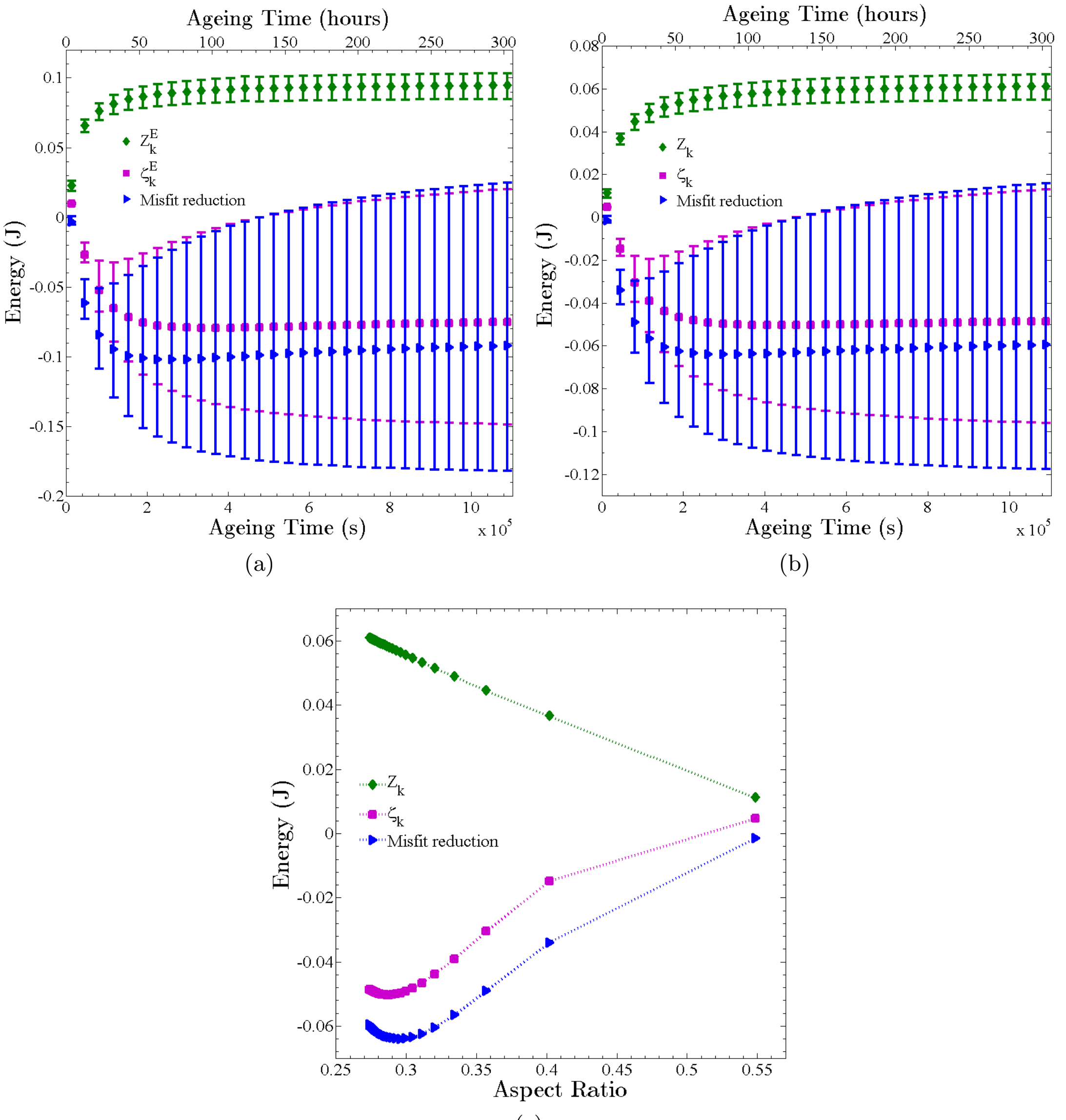

(a)

(b)

(c)

Figure 6.43: Time evolution of a) ζ_k^E, Z_k^E and $8\rho_k\Lambda_k^E[3\xi_k^2]^{-1}$ and b) ζ_k, Z_k and $8\rho_k\Lambda_k[3\xi_k^2]^{-1}$. Data points correspond to average values and the error bars to the first and third quartiles of the major radius particle size distribution. c) Evolution of the average values ζ_k, Z_k and $8\rho_k\Lambda_k[3\xi_k^2]^{-1}$ with average aspect ratio calculated from their relative distributions.

Chapter 7

Conclusion

§ 7.1 Research Summary

The widely recognised dominance of intermetallic γ'' ($\mathrm{D0}_{22}$) precipitates in dictating many of the mechanical properties of the nickel base superalloy 625 necessitated the generation of a modelling technique to describe their evolution (nucleation, growth and coarsening) in the alloy during high temperature ageing. An appraisal of the available literature descriptions identified the Svoboda-Fischer-Fratzl-Kozeschnik (SFFK) framework as the most suitable on which to base the model owing, primarily, to its ability to handle not only the complicated chemistry of the alloy (12 elements), but also the shape changing behaviour of γ'' precipitates. As a result, an SFFK based model, subject to modifications that allowed for a more complete dependence of factors such as the interfacial energy (ζ) and misfit strain (λ) on the changing precipitate aspect ratio (α), was created in this research to describe homogeneous γ'' precipitation in Alloy 625 during isothermal ageing.

In view of the design of the mathematical framework of the new SFFK model, numerous multiple input descriptions were required from experimental data such as $\alpha(r_{\mathrm{M}})$ and $\alpha(t)$. Consequently, a rigorous experimental investigation into the isothermal precipitation of γ'' (under the conditions of a solution annealed matrix) was undertaken. This research also provided for the generation of experimental results for the purposes of model validation. Considering its previous successful demonstrations in the literature, the specific experimental methodology chosen to analyse the γ'' statistics was that of Transmission-Electron-Microscopy (TEM); however, this posed many challenges with respect to the obtaining of accurate obtaining population variables. To this end a novel methodology was established for quantifying the statistics of γ'' precipitates in TEM foils (under certain conditions) and appropriately validated against theoretical distributions.

In the absence of suitable, derivable descriptions, in its initial construction the SFFK based model designed in the work was executed for the purposes of calibrating values for the precipitate-matrix interfacial energy and also the behaviour of the strain tensor components $\epsilon_{1,1}(\alpha)$ and $\epsilon_{3,3}(\alpha)$. After an extensive and lengthy trial and error exercise eventually the appropriate (*i.e.* best replicating experimental results whilst parametrised by the constraints of lattice parameters) hyperbolic functions defining $\epsilon_{1,1}(\alpha)$ and $\epsilon_{3,3}(\alpha)$ were identified; excellent agreement with the calibration statistics between 100-1000 hours of ageing at 650° C was obtained for the population evolution in terms of aspect ratio, major radius and number density. The result with respect to number density was additionally significant as it provided validation of the aforementioned novel methodology for gathering experimental statistics. Finally at this stage, the apparently unphysical result of a negative interfacial energy was identified as relating to a contribution from decreasing interface coherency/increasing misfit strain. A successful deconvolution of the various contributions to the output misfit strain value was achieved, revealing a "true" interfacial energy (Z_k) and misfit strain behaviour consistent with physical expectations. To the author's knowledge, this study is the first instance of such statistics being calculated for γ'' precipitates and also for the production of a dynamic value of the interfacial energy in a class type computation.

Unfortunately, despite the calibration of the interfacial energy, a sufficiently detailed, separate mathematical description for Z_k could not be achieved, necessitating the continued input of $\alpha(t)$ to the calculation. Nevertheless, under this condition the model successfully replicated the γ'' aspect ratio and number density evolution between at 50 and 3000 hours at 650° C and the major radius evolution between at 50 and 1000 hours. Noticeable disagreement with the precipitate major radius statistics after 3000 hours was attributed to the phenomenon of "encounter" described by Davis *et al.* [1]. Of the remaining experimentally aged material, only the 600° C isothermal set revealed precipitate evolution consistent with the underlying assumptions of the model; at temperatures $\geq$ 700° C the nucleation of γ'' was heterogeneous (because of the smaller undercooling) and subject to significant influence from δ-phase precipitation. In view of this outcome, the validation of the SFFK model with respect to the experimental data acquired in the present research was limited to this single temperature set.

Owing to slower precipitation kinetics at 600° C, only two ageing durations were found to contain measurable γ'' populations; however, their statistics were not sufficient to generate appropriate functions for either $\alpha(r_{\mathrm{M}})$ or $\alpha(t)$. For this reason, the descriptions utilised for the SFFK simulation at 600° C were formed through a transformation of the functions defined at 650° C. Analysis of the results of the simulation found significant disparities with the input $\alpha(t)$ trend, the origin of which was identified as the time step progression mechanism. Regrettably, whilst a procedure to eliminate this problem was identified its implication for the simulation duration meant it was not feasible to implement under the existing calculation conditions. Nonetheless, despite this eventuality, inspection of the statistics produced for the precipitate major radius at 600° C yielded the conclusion that reasonable agreement should be possible if suitable correction to the time step mechanism were to be implemented.

Finally in this research, even though the calibration of the evolution of γ'' precipitates was conducted with respect to Alloy 625, a comparison to the results published by other researchers in the literature for γ'' precipitates in Alloy 718 was made by modifying descriptions for the driving forces and elastic constants. Once again in this instance, the time step mechanism was found to have a detrimental impact on the results of the simulation. However, on this occasion the faster precipitation kinetics facilitated the reasonable application of the correction derived from the results at 600 °C in Alloy 625. The outcome of the modification to the SFFK frame work was the achievement of a reasonable agreement with the results of Han *et al.* [2] for an isothermal ageing at 700 °C. Conversely, at higher temperatures ($\geq 720^\circ$C) the precipitation kinetics proved too fast to be accurately described.

§ 7.2 Recommendations for future work

Under the assumptions outlined in its creation (*q.v.* Chapter 2) it is evident from the results produced in this research that the framework of the constructed γ'' SFFK model is adequately formulated for the description of isothermal ageing of suitable Ni-base alloys between 650-700 °C. This is especially true given the degree of precision desired for the appropriate calculation of mechanical properties such as material hardness for material manufacture and service performance. Nevertheless, however, consideration of the discrepancies at other temperatures as well as phenomena in the actual experimental data obtained yields the conclusion that many advantageous modifications to the framework are desirable. In addition, further analysis of the experimental behaviour of Alloy 625 may allow for the development of new understanding regarding the physical phenomena which take place within it.

7.2.1 SFFK model

Analysing the validation results obtained for the model it is clear that the most obvious future work to the framework could comprise a modification to the time step mechanism to facilitate a speedy but accurate simulation over all relevant ageing temperatures. Although many alternatives may exists to achieve this, the most obvious one is that of a class management function which controls the number of classes in the PSD based on the time step. Specifically, for small time steps the function would be required to reduce the number of classes by merger whereas for large time steps it would be required to separate classes. The successful computational mechanism to achieve such processes would likely be based on that defined by Perez *et al.* [221, 222] (subject to the new distribution density calculation method defined in Section 6.3.2) and implemented at stage 8 in the model Flow-Chart (Figure 3.5). Despite this seeming simplicity, however, far from being a trivial addition, the class management would be necessarily subject to complicated conditions that ensured that 1) parameters such as the aspect ratio and major radius remained compatible, 2) detail was maintained through choosing which classes to merge and split and 3) the simulation results were not affected. In other words, as well maintaining a threshold number of classes, effectively two simultaneous checks pertaining to both the precipitate size distribution and aspect ratio distribution would be necessitated for each new class and correlated to interfacial energy so that its stability is correct.

The second obvious adaptation to the SFFK framework based on the results obtained in this research would be a modification to account for the effect of “encounter”. An assessment of the available literature reveals that the most fruitful approach to this problem would likely comprise a combination and extension of recent works by the present author [344] and Basoalto *et al.* [354]: Specifically, by removing the contribution of so-called "directional" encounter from the measured particle size distributions through the mechanism outlined by Moore *et al.* [344] and extending the modifications of Basoalto *et al.* [354] from solely describing the effect of encounter in SFFK for purely spherical particles to that of ellipsoidal/shape changing particles, an appropriate mathematical description would likely be achieved.

Finally, considering the images acquired from the real Alloy 625 material the last significant modification to the SFFK framework would be the inclusion of heterogeneous γ'' and homogeneous/heterogeneous δ-phase precipitation. In this instance, the mechanism behind the modifications themselves is essentially trivial to explain: They would simply constitute a simultaneous calculation to that presented in this research, computed for each population/phase and linked to each other by the continuity equation *viz.* effectively a set of outputs (PSD, ARD etc.) would be generated by the model. The significant barrier posed to this modification, however, is the fact that identical inputs would also be required for each population thereby necessitating an extensive evaluation of parameters such as the nucleation site density, diffusion constants (enhanced by dislocations), $\alpha(t)$ and $\alpha(r_M)$.

7.2.2 ALLOY 625

Of the features noted within Alloy 625 the two that would likely yield interesting results if subject to further investigation are the effect of δ-phase on material hardening and also the transition from heterogeneous to homogeneous γ'' precipitation when ageing at 700-750°C. In the case of the former, if the key strengthening mechanism of δ-phase can be definitively identified (*i.e.* fibre strengthening or "punched out" dislocations) this could have significant processing applications owing to the high thermodynamic stability of the phase and its current use in processing [82, 83, 84, 85]. Secondly, if a causality between the coincidental appearance of δ-phase and the replacement of a heterogeneous γ'' population with a homogeneous one at 700-750°C could be identified, this would have significant implications for any precipitation model/description. Moreover, if δ-phase was found to nucleate on heterogeneous γ'' this would be the first such instance that the mechanism has occurred without the need for externally applied deformation to sheer the γ'' precipitates.

Appendices

Appendix A: Thermo-Calc

Thermo-Calc is a piece of computer software developed at the Royal Institute of Technologys Department of Materials Science and Engineering in Stockholm, Sweden [24, 25]. It is used by scientists the world over, particularly those interested in materials, with regard to a multitude of different problems in variety of fields. Although it is equipped with many modules, its core function is the prediction of phase behaviour in materials, under specified conditions at equilibrium, by minimisation of the Gibbs energy of the system. It is for this purpose that it was used in the present study.

From thermodynamics it is known that the relative stability of two systems, particularly at constant temperature and pressure, can be calculated from comparison of the total Gibbs free energy they possess. When a system has the lowest possible value of the Gibbs free energy (*i.e.* a transformation leads to $\Delta G > 0$) classical thermodynamics dictates that the system is in equilibrium [19]. Consequently, by finding the phase composition of a system which results in the lowest overall Gibbs energy, one is able to state what phases should be present at equilibrium and in what ratio/abundance.

The process used by Thermo-Calc to find this lowest energy phase composition can be illustrated most simply by the case of a binary metallic solution. In such a regime, the Gibbs free energy can be calculated according to the substitutional-regular-solution model from Equation A.1 where G_i^0 is the molar Gibbs energy of the pure element i with the same crystal structure as the binary phase, n is the number of elements, X_i is the molar Gibbs energy of the element i and G_i^E is the molar excess Gibbs energy [355]; this model assumes that each crystalline phase constitutes a substitutional solution where each of the constituents have the same probability of occupying any site in the unit cell.

$$G_m = \sum_{i=1}^{n} X_i G_i^0 + RT \sum_{i=1}^{n} X_i \ln(X_i) + G_i^E \tag{A.1}$$

The first part in Equation A.1 relates to the Gibbs energies of the unary elements in their reference phase. Assessment of the Gibbs energies of many unary elements was made by Dinsdale in 1991 [356] and has since been expanded upon to include almost the entire periodic table. During a simulation these reference values are provided to Thermo-Calc via a look-up scheme from the installed Scientific Group Thermodata Europe (PURE) database. The second term in Equation A.1 represents the ideal mixing part of the Gibbs energy. It is derived in this regime by: 1) Assuming that the free energy change (equal to the enthalpy at constant temperature and pressure) on mixing two elements is only due to the change in entropy [19]. 2) Substituting in Boltzmanns equation, which allows for the incorporation of a configurational contribution to the entropy by taking account of the number of different way the atoms in solutions can be arranged, and 3) using Stirlings approximation to simplify the expression for the number of distinguishable arrangements.

Taken together, the first and second terms of Equation A.1 define the ideal-substitutional-solution model which is valid for non-interacting constituents mixing randomly with each other (*e.g.* two noble gasses) [355]. In a binary metallic solution the assumption of non-interacting components is not valid and hence a third/correction term is introduced to account for the molar excess Gibbs energy (G_i^E). Typically G_i^E is described by Redlich-Kister polynomials containing interaction parameters for the relevant phase and it is the determination of these parameters by least squares fitting to experimental data which forms the basis of the CALPHAD (CALculation of PHAse Diagrams) approach [355]. Such assessments can be made using the Thermo-Calc software (and in fact constitute one of the primary applications alluded to earlier) but for the calculation of phase stability is it necessary for the software to call these coefficients from a database. Databases containing values established from hundreds of different systems are readily available; the Thermo-Calc Software TCNI7 Ni-based Superalloys database versions 7 and 8 utilised in this work are such databases.

In the case of a binary alloy of the elements A and B with phases α, β, by calculating the values for the first and third terms in Equation A.1 for each phase, during a simulation Thermo-Calc computes the relevant ideal mixing terms and is, therefore, able to produce values of the Gibbs energy of each phase as a function of temperature and elemental concentration. Using these relations, the equilibrium phase composition of the alloy can then be determined by the software through constructing common cotangents between the calculated Gibbs energy curves of the possible phases (α, β and liquid) over the temperature range of interest. As shown graphically in Figure A.1, from these cotangents the stable phases present at a given temperature is defined by the points of contact between the cotangent and the curve. The quantity of each of the stable phases is found through through the "lever rule". The methodology of constructing common cotangents between Gibbs energy curves is utilised by Thermo-Calc as it defines the condition of the elements having the same chemical potential in each phase. In other words, it describes the condition of the phases being in equilibrium.

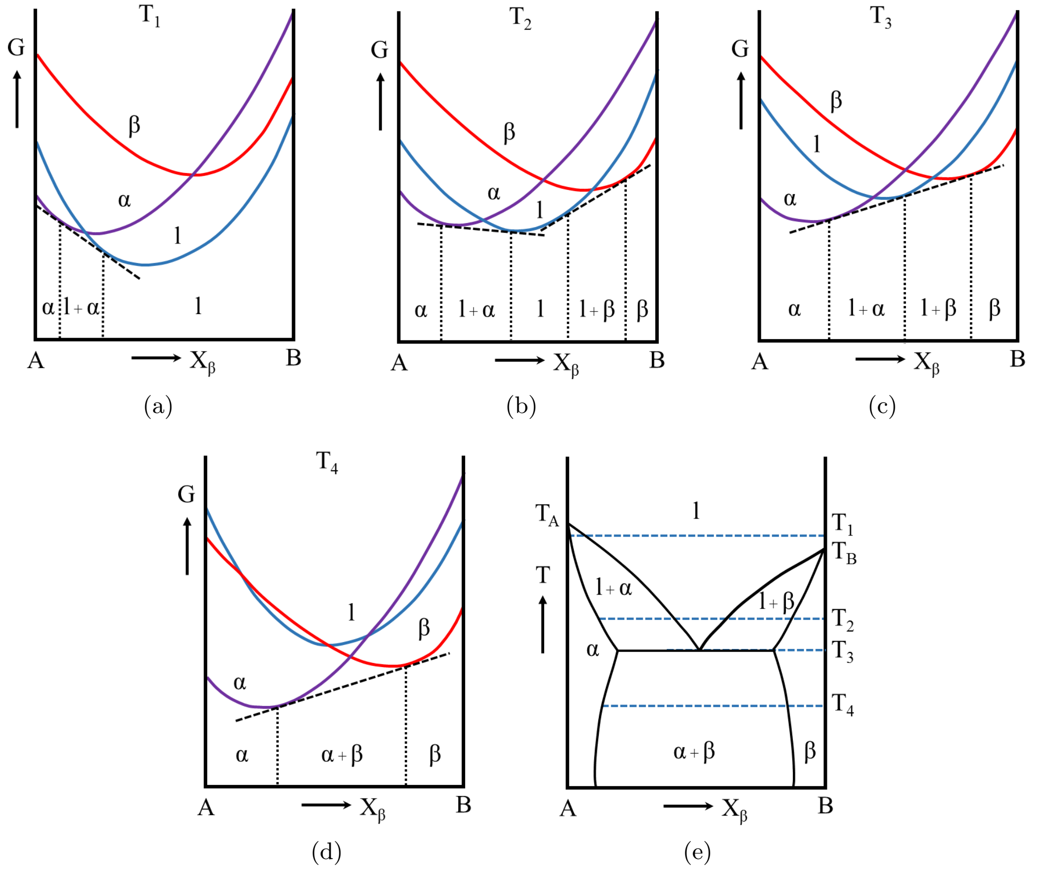

(a) (b) (c)

(d) (e)

Figure A.1: a-d) Calculated Gibbs energy curves for the binary system of elements A and B with structures α, β at four different temperatures. Cotangent lines are drawn and the compositional range over which phases are stable are indicated. e) Binary phase diagram constructed from incremental assessment over the temperature range T$_A$ to 0. Adapted from Porter [19].

Appendix B: Lattice Parameter measurement by XRD

When a beam of X-rays are incident onto a crystalline sample, Bragg famously found that at certain incident angles intense reflected radiation peaks could be detected. This strong angular dependence led him to the conclusion that the crystal lattice of the sample was resulting in either the constructive or destructive interference of the incident radiation as the relative angle of the source to the sample was varied. As a result of this analysis, labelling the spacing between parallel atomic planes in a crystal lattice as d, Bragg developed the relation for the angles at which reflection peaks should be observed shown in Equation A.2 where λ corresponds to the wavelength of the incident radiation and n is an integer.

$$n\lambda = 2d\sin\theta \tag{A.2}$$

Calculation of the lattice parameters a, b and c of the sample from which the peaks in a X-ray diffraction spectrum are produced can be achieved for cubic ($a = b = c$), tetragonal ($a = b \neq c$) and orthorhombic ($a \neq b \neq c$) systems through Equation A.3 where h, k, and l, constitute the standard labels for the Miller indices used to define the crystallographic lattice planes [357].

$$d = \frac{a^2}{\mathrm{h}^2} + \frac{b^2}{\mathrm{k}^2} + \frac{c^2}{\mathrm{l}^2} \tag{A.3}$$

From Equation A.3 it is evident that identification of the correct lattice plane for each of the detected peaks in a spectrum is crucial for the accurate calculation of the lattice parameters of the structure. Typically, identification of the reflection can be made through the use of Equations A.2 and A.3, together with established selection rules for the indices defining those planes which are able to produce reflections. However, it must be noted that such analysis is often dependent upon assumptions in the shape and symmetry of the crystal and, therefore, in real systems it is susceptible to error. Owing to the simplification which is achieved for Equation A.3, calculation of the single lattice parameter in cubic systems is possible through the correct indexing of a single peak whereas for tetragonal and orthorhombic systems the increased number of variables necessitates more peaks are identified.

Appendix B.1: Extraction Residues

The extraction of second phase particles such as γ'' for XRD analysis has been performed in the literature by researchers such as Slama *et al.* [4] through the dissolution of the surrounding material matrix. The liqueur produced by the dissolution is passed through filter papers (although separation using a centrifuge is also possible) with the remaining residue then diluted and re-filtered several times before being dried out to leave only the intermetallic particles behind. The small size and random orientation of the particles means that such a sample constitutes a near ideal specimen for XRD analysis, with any distortion effects in the magnitude of the peaks obtained (resulting from factors such as preferential crystallographic orientation) being minimised [357]. As a result of this methodology, therefore, a high degree of precision should be possible for any results obtained.

In addition to the aforementioned intrinsic advantages presented by acquiring precipitate extraction residues, as discussed in Section 3.1.4, an additional benefit is offered with regard to the statistics desired for γ'' in this research, namely the removal of any distorting strain effects imposed by the surrounding matrix. Consequently, it seems obvious that extraction residue analysis should constitute part of the research programme carried out; however, this was not possible based on the quantity of material required.

Although an indicative size of 8cm^3 is stated for the size of each sample in Section 4.2.1, the significant cut-out presents (which can be interpreted from Figure 4.2) means the actual mass of material was only around 24g. As a result, even with the theoretical maximum limit of 10wt% of the sample consisting of γ'' precipitates, the highest possible yield dissolving all of the sample would only be around 2.4g and this is subject to significant reduction from losses associated with the dissolution and filtering process (not to mention the decrease in the sample size owing to the removal of material for TEM analysis). Given the difficulty of performing precise measurements on such a small quantity of material (*i.e.* producing a continuous and flat powder surface), therefore, it is obvious that the chances of creating a suitable specimen from the aged samples made in this research is remote.

Appendix B.2: Bulk

Collection of a diffraction from a bulk sample is trivial, with just a flat, clean surface (easily obtained obtained from sectioning) required. An example of such a data set for an aged specimen of Alloy 625 is shown in Figure A.2. Unfortunately, however, for a multiphase specimen the reflections corresponding to each of the separate phases can become very difficult to identify as a result of peak overlap. In addition, for systems such as Alloy 625 containing γ'' this problem is exacerbated by the similar crystal structures the large disparity in the quantity of the FCC matrix and precipitate phase present.

A potential resolution to the problem of peak overlap, published Sarkar *et al.* [280, 277], involves the use of peak fitting software to de-convolute the overlapping peaks and thereby enable their separate identification; an example of the peaks produced by this method using the software Peakfit [358] is presented in Figure A.3. At first glance it seems that the peak deconvolution is successful with an r^2 value very close to unity[1] being obtained. In spite of this eventuality though, comparison of the peak positions shows them to deviate significantly from those contained in published spectra (43.6° 2θ for the largest γ'' reflection versus 42.9° 2θ measured by Kaufman *et al.* [275]). In light of the method used in their determination, rather than a significant change in the material properties or instrumental problems, Occam's razor dictates that this change in the peak position compared to the literature data results principally from

---

[1] In statistics r^2 or the coefficient of determination is a number that indicates how well data fit a statistical model with r=1 signifying a prefect fit [359]

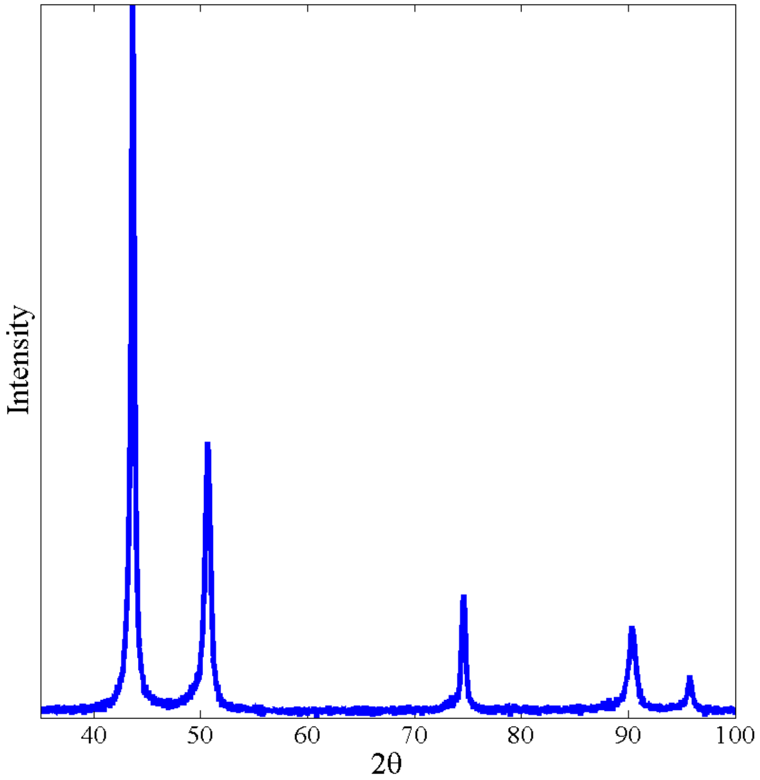

Figure A.2: X-ray diffraction pattern obtained from a bulk sample of Alloy 625 aged for 3000 hours at 650 °C. Data collected using a D2 phaser with a Cu source.

the deconvolution technique and the strains present within the bulk samples which can act to distort the crystal lattice. Even a minor deviation the angle between the various axes away from perpendicular or in the deconvoluted peak position can result in a significant change in the lattice parameters.

As shown by comparison of the work of Sarkar *et al.* [280, 277] with others in the literature (*e.g.* Cozar *et al.* [172] and Kaufman *et al.* [275]) calculation of the lattice parameter of the γ'' phase using the resolved new peak positions for the reflections corresponding to the allowed lattice planes produces significantly different values. More crucially, however, as alluded to in Section 3.1.4, the use of these values in the calculation of the strain tensor as per Equation 3.2 would lead to an insurmountable barrier for precipitation according to the mathematics outlined in Section 2.2 (harnessing the inputs detailed in Chapter 3). Further still, whilst the significant challenge of correcting the misfit strain/lattice distortion contribution to the peak shift seen in the patterns collected from bulk specimens may be achievable, the uncertainty in the peak positions from the peak deconvolution will remain an insurmountable problem unless a better procedure for this process (likely requiring very high resolution data) becomes available in the future.

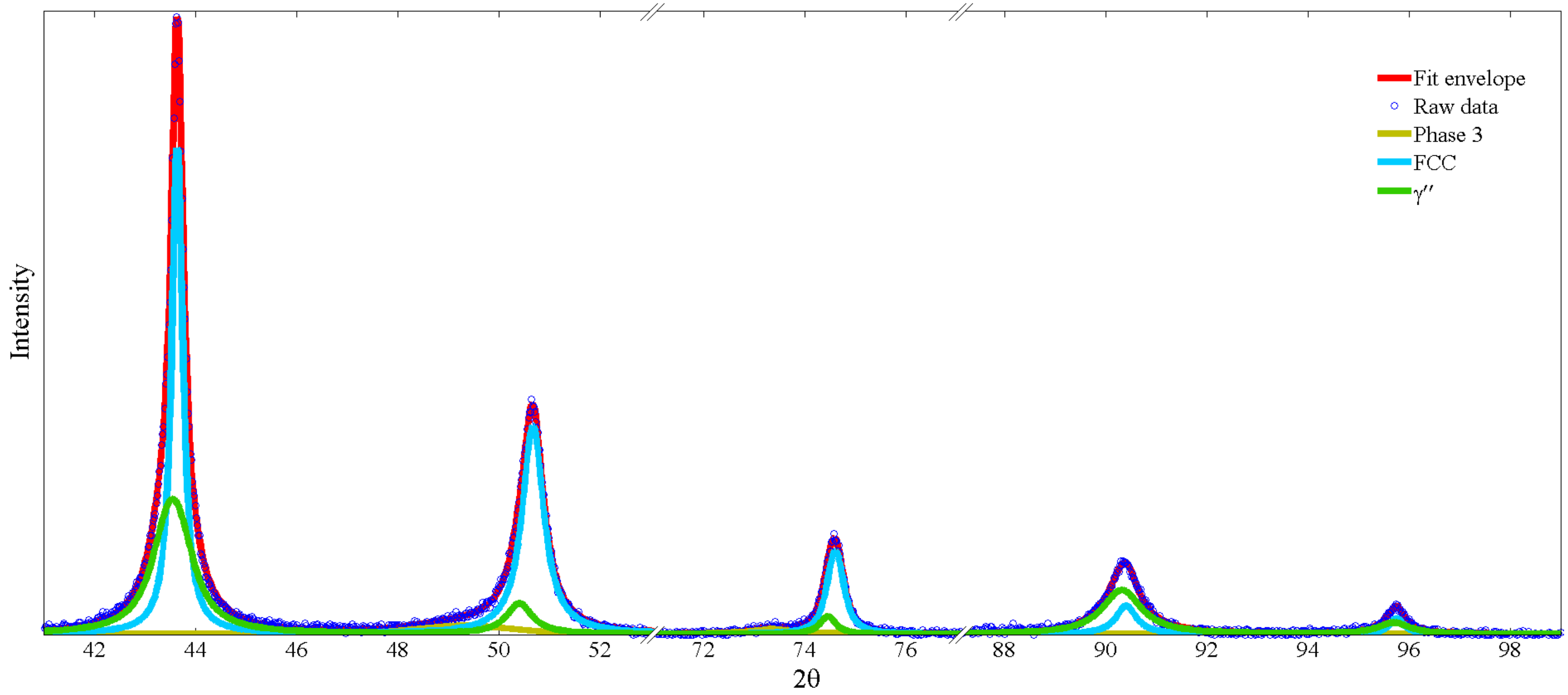

Figure A.3: Example of the peaks resulting from the deconvolution of the signals in A.2 indicating the corresponding phases they are attributed to. The k-α2 signal present in the acquired pattern has been removed prior to deconvolution using the software PowerX [45] and implementing a published method devised by the software developers [46]. Fits were made using Voight line profiles with the coefficient of determination (r^2) calculated for the whole profile as 0.998. Due to the mechanism of deconvolution it must be stressed that peak positions rather than magnitudes are used principally for the identification of phases by comparison to literature.

Appendix C: Amec Summary of HN104 Data

amec

Summary of HN104 Data

A 160 x 500 mm bar of Alloy 625 was obtained from Intamet (original supplier Acciaierie Valbruna, Italy), the material certificate is shown in Figure 1. This material has been assigned the code HN104 by AMEC.

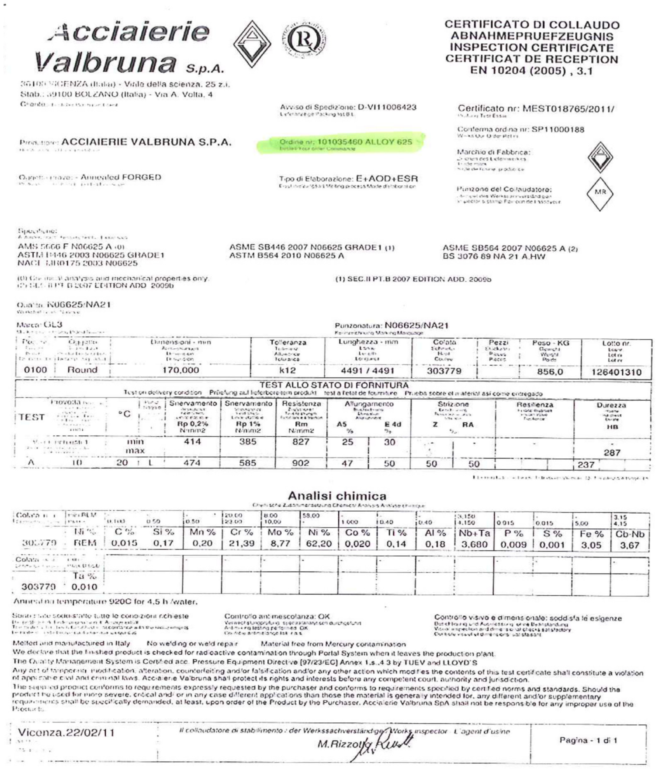

Acciaierie Valbruna S.p.A.
36100 VICENZA (Italia) - Viale della scienza, 25 z.i.
Stab.: 39100 BOLZANO (Italia) - Via A. Volta, 4

CERTIFICATO DI COLLAUDO
ABNAHMEPRUEFZEUGNIS
INSPECTION CERTIFICATE
CERTIFICAT DE RECEPTION
EN 10204 (2005) , 3.1

Avviso di Spedizione: D-VI11006423

Certificato nr: MEST018765/2011/

Conferma ordine nr: SP11000188

Produttore: ACCIAIERIE VALBRUNA S.P.A.

Ordine nr: 101035460 ALLOY 625

Marchio di Fabbrica:

Oggetto: - Annealed FORGED

Tipo di Elaborazione: E+AOD+ESR

Punzone del Collaudatore: MR

Specifiche:
AMS 5666 F N06625 A (0)
ASTM B446 2003 N06625 GRADE1
NACE MR0175 2003 N06625

ASME SB446 2007 N06625 GRADE1 (1)
ASTM B564 2010 N06625 A

ASME SB564 2007 N06625 A (2)
BS 3076 69 NA 21 A.HW

(0) Chemical analysis and mechanical properties only
(2) SEC.II PT.B 2007 EDITION ADD 2009b

(1) SEC.II PT.B 2007 EDITION ADD. 2009b

Qualità: N06625/NA21

Marca: GL3

Punzonatura: N06625/NA21

Pos.	Oggetto	Dimensioni - mm	Tolleranza	Lunghezza - mm	Colata	Pezzi	Peso - KG	Lotto nr.
0100	Round	170,000	k12	4491 / 4491	303779		856,0	126401310

TEST ALLO STATO DI FORNITURA
Test on delivery condition Prüfung auf lieferbereitem produkt test à l'etat de fourniture Prueba sobre el material así come entregado

TEST Provetta		°C		Snervamento Rp 0,2% N/mm2	Snervamento Rp 1% N/mm2	Resistenza Rm N/mm2	Allungamento A5 %	Allungamento E 4d %	Strizione Z %	Strizione RA	Resilienza	Durezza HB
Valori richiesti 1		min		414	385	827	25	30	-	-	-	-
		max										287
A	10	20	L	474	585	902	47	50	50	50		237

Analisi chimica

Colata	min/max														
		- 0,100	- 0.50	- 0.50	20.00 23.00	8.00 10.00	58.00 -	- 1.000	- 0.40	- 0.40	3.150 4.150	- 0.015	- 0.015	- 5.00	3.15 4.15
	Ni %	C %	Si %	Mn %	Cr %	Mo %	Ni %	Co %	Ti %	Al %	Nb+Ta	P %	S %	Fe %	Cb-Nb
303779	REM	0,015	0,17	0,20	21,39	8,77	62,20	0,020	0,14	0,18	3,680	0,009	0,001	3,05	3,67
Colata	min/max														
	Ta %														
303779	0,010														

Annealing temperature 920C for 4,5 h /water.

Sono state soddisfatte tutte le condizioni richieste

Controllo antimescolanza: OK

Controllo visivo e dimensionale: soddisfa le esigenze

Melted and manufactured in Italy No welding or weld repair Material free from Mercury contamination

We declare that the finished product is checked for radioactive contamination through Portal System when it leaves the production plant.

The Quality Management System is Certified acc. Pressure Equipment Directive [97/23/EC] Annex 1,s.,4.3 by TUEV and LLOYD'S

Any act of tampering, modification, alteration, counterfeiting and/or falsification and/or any other action which modifies the contents of this test certificate shall constitute a violation of applicable civil and criminal laws. Acciaierie Valbruna shall protect its rights and interests before any competent court, authority and jurisdiction.

The supplied product conforms to requirements expressly requested by the purchaser and conforms to requirements specified by certified norms and standards. Should the product be used for more severe, critical and/ or in any case different applications than those the material is generally intended for, any different and/or supplementary requirements shall be specifically demanded, at least, upon order of the Product by the Purchaser. Acciaierie Valbruna SpA shall not be responsible for any improper use of the Products.

Vicenza,22/02/11

Il collaudatore di stabilimento : der Werkssachverständiger Works inspector : L'agent d'usine
M.Rizzotto

Pagina - 1 di 1

Figure 1 Materials Certificate for material HN104.

The standard composition for Alloy 625 and the elemental analysis for material HN104 are shown in Table 1.

Table 1 Chemical Composition of Alloy 625 and HN104 bar.

	C %	Si %	Mn %	Cr %	Mo %	Ni %	Ti %	Al %	P %	S %	Fe %	Other %
Alloy 625	0.1 max	0.5 max	0.5 max	20.0-23.0	8.0-10.0	58.0 min	0.4 max	0.4 max	0.015 max	0.015 max	5.0 max	Co 1.0 Nb (+Ta) 3.15-4.15
HN104	0.016	0.20	0.21	21.89	8.80	61.84	0.23	0.13	<0.005	<0.001	3.01	Co 0.08 Cu 0.09 Nb 3.64 W 0.13 N 0.02

A cross-sectional slice was taken from the end of the bar and offcut HN104/2 was examined optically. This revealed banding, running in the longitudinal direction through the length of the bar, Figure 2.

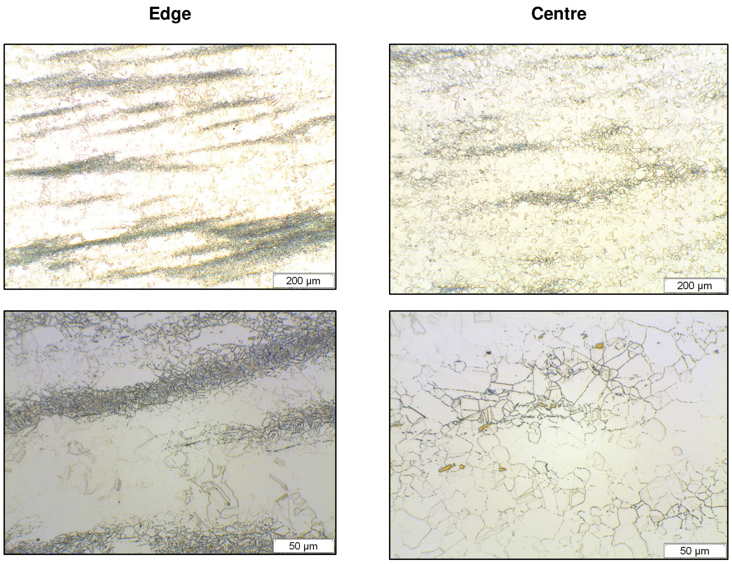

Figure 2 Optical examination of banding observed in HN104 at the edge and centre of the bar.

SEM examination (Figure 3) also showed bands of finer grains as well as the presence of grain boundary carbides. EDS analysis (Table 2) identified the particles present as Ti and Nb particles and Nb(CN) particles.

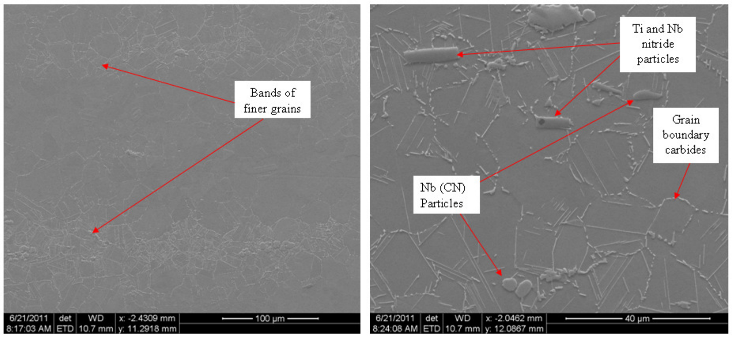

Figure 3 SEM examination of HN104.

Table 2 EDS Analysis of particles shown in Figure 3.

Dark angular particles		Light round Particles	
Element	**Wt %**	**Element**	**Wt %**
NbL	39.2	NbL	92.2
TiK	37.3	TiK	4.8
CrK	7.1	CrK	0.8
NiK	15.2	NiK	2.2
FeK	1.1		
Total	100	Total	100

Appendix D: Buehler Summet Technique For The Preparation of Nickel

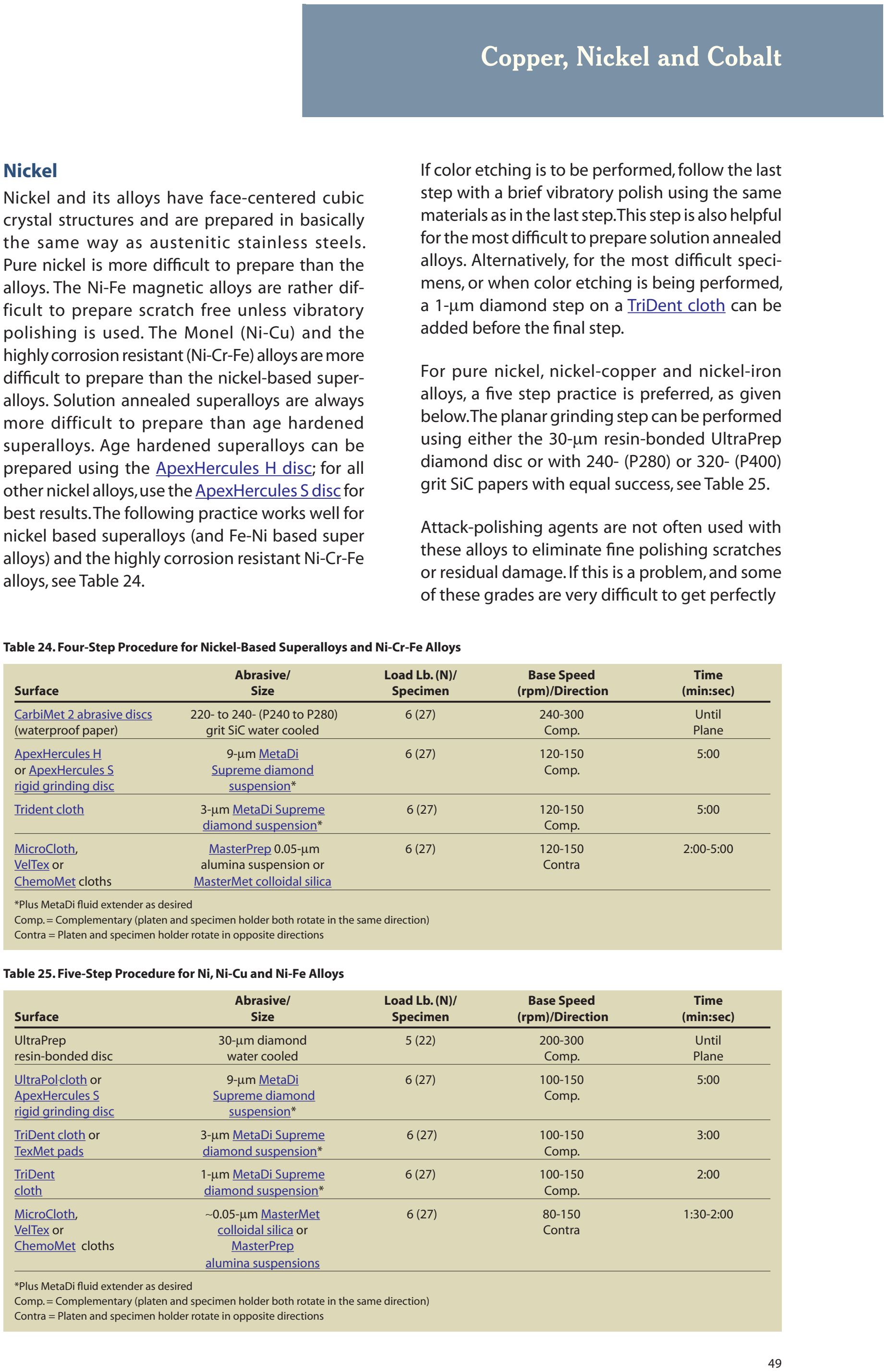

Copper, Nickel and Cobalt

Nickel

Nickel and its alloys have face-centered cubic crystal structures and are prepared in basically the same way as austenitic stainless steels. Pure nickel is more difficult to prepare than the alloys. The Ni-Fe magnetic alloys are rather difficult to prepare scratch free unless vibratory polishing is used. The Monel (Ni-Cu) and the highly corrosion resistant (Ni-Cr-Fe) alloys are more difficult to prepare than the nickel-based superalloys. Solution annealed superalloys are always more difficult to prepare than age hardened superalloys. Age hardened superalloys can be prepared using the ApexHercules H disc; for all other nickel alloys, use the ApexHercules S disc for best results. The following practice works well for nickel based superalloys (and Fe-Ni based super alloys) and the highly corrosion resistant Ni-Cr-Fe alloys, see Table 24.

If color etching is to be performed, follow the last step with a brief vibratory polish using the same materials as in the last step. This step is also helpful for the most difficult to prepare solution annealed alloys. Alternatively, for the most difficult specimens, or when color etching is being performed, a 1-µm diamond step on a TriDent cloth can be added before the final step.

For pure nickel, nickel-copper and nickel-iron alloys, a five step practice is preferred, as given below. The planar grinding step can be performed using either the 30-µm resin-bonded UltraPrep diamond disc or with 240- (P280) or 320- (P400) grit SiC papers with equal success, see Table 25.

Attack-polishing agents are not often used with these alloys to eliminate fine polishing scratches or residual damage. If this is a problem, and some of these grades are very difficult to get perfectly

Table 24. Four-Step Procedure for Nickel-Based Superalloys and Ni-Cr-Fe Alloys

Surface	Abrasive/ Size	Load Lb. (N)/ Specimen	Base Speed (rpm)/Direction	Time (min:sec)
CarbiMet 2 abrasive discs (waterproof paper)	220- to 240- (P240 to P280) grit SiC water cooled	6 (27)	240-300 Comp.	Until Plane
ApexHercules H or ApexHercules S rigid grinding disc	9-µm MetaDi Supreme diamond suspension*	6 (27)	120-150 Comp.	5:00
Trident cloth	3-µm MetaDi Supreme diamond suspension*	6 (27)	120-150 Comp.	5:00
MicroCloth, VelTex or ChemoMet cloths	MasterPrep 0.05-µm alumina suspension or MasterMet colloidal silica	6 (27)	120-150 Contra	2:00-5:00

*Plus MetaDi fluid extender as desired
Comp. = Complementary (platen and specimen holder both rotate in the same direction)
Contra = Platen and specimen holder rotate in opposite directions

Table 25. Five-Step Procedure for Ni, Ni-Cu and Ni-Fe Alloys

Surface	Abrasive/ Size	Load Lb. (N)/ Specimen	Base Speed (rpm)/Direction	Time (min:sec)
UltraPrep resin-bonded disc	30-µm diamond water cooled	5 (22)	200-300 Comp.	Until Plane
UltraPol cloth or ApexHercules S rigid grinding disc	9-µm MetaDi Supreme diamond suspension*	6 (27)	100-150 Comp.	5:00
TriDent cloth or TexMet pads	3-µm MetaDi Supreme diamond suspension*	6 (27)	100-150 Comp.	3:00
TriDent cloth	1-µm MetaDi Supreme diamond suspension*	6 (27)	100-150 Comp.	2:00
MicroCloth, VelTex or ChemoMet cloths	~0.05-µm MasterMet colloidal silica or MasterPrep alumina suspensions	6 (27)	80-150 Contra	1:30-2:00

*Plus MetaDi fluid extender as desired
Comp. = Complementary (platen and specimen holder both rotate in the same direction)
Contra = Platen and specimen holder rotate in opposite directions

Appendix E: Angular Resolution

Classically (*i.e.* neglecting photon statistics [360]), irrespective of the point that resolution is defined (Abbe, Rayleigh, or Sparrow criterion), it is understood that the resolving power of a given microscope is fundamentally limited by two factors: The light wavelength and the size of the lens aperture [361, 362]. Following the criterion outlined by John William Strutt (3rd Baron Rayleigh) typically adhered to in microscopy, these two dependencies can be illustrated from the set-up shown in Figure A.4.

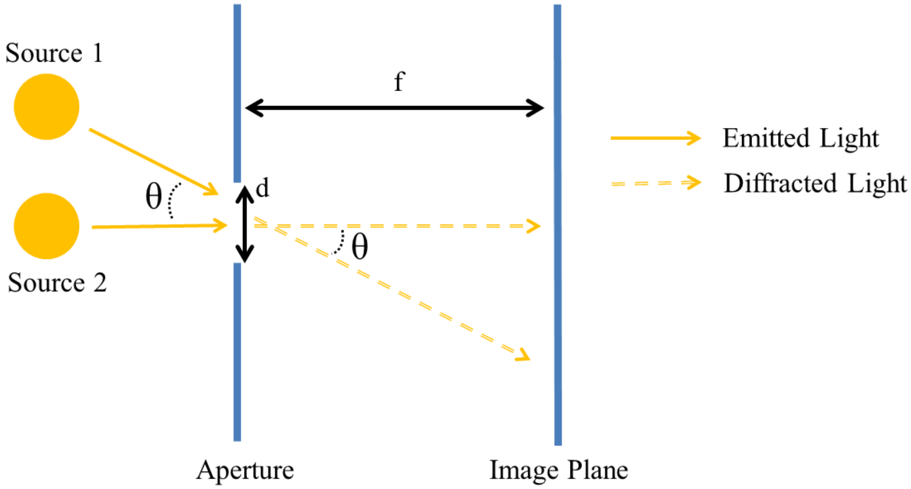

Figure A.4: Two monochromatic light sources, with angular separation θ, incident onto a circular aperture of diameter $= d$ (2D slice shown) sufficiently small to cause the light to diffract. Images of the light sources are produced on an image plane at a distance f behind the aperture.

As light from the two sources passes through the aperture it diffracts, resulting in an Airy disc forming for each of the sources on the image plane (Figure A.5a). If the light sources are close enough, the Airy discs of each will begin to overlap making them hard to distinguish (Figures A.5b and A.5c). The Rayleigh criterion stipulates that in order for these two sources to be classed as "resolved", the smallest separation between them must be such that central diffraction maximum of one disc coincides with the first minimum of the other as shown in Figure A.6 [362, 35]. Working in a vacuum, this limit (*i.e.* the point at which the first minima of the diffraction pattern occurs) can be represented mathematically, according to Equations A.4 and A.5, where Δl corresponds to spatial rather than angular (θ) resolution [361, 362]. From these relationships one is able to infer that for greater resolution to be achieved in this set-up, one must utilise either a larger aperture and/or radiation with a smaller wavelength.

$$\sin\theta \geq \frac{1.22\lambda}{d} \tag{A.4}$$

$$\Delta l \geq \frac{1.22 f \lambda}{d} \tag{A.5}$$

$$\Delta l \geq \frac{1.22\lambda}{n \sin\theta_{\text{condenser}} + n \sin\theta_{\text{aperture}}} \qquad \text{or} \qquad \Delta l \geq \frac{1.22\lambda}{\text{NA}_{\text{condenser}} + \text{NA}_{\text{aperture}}} \tag{A.6}$$

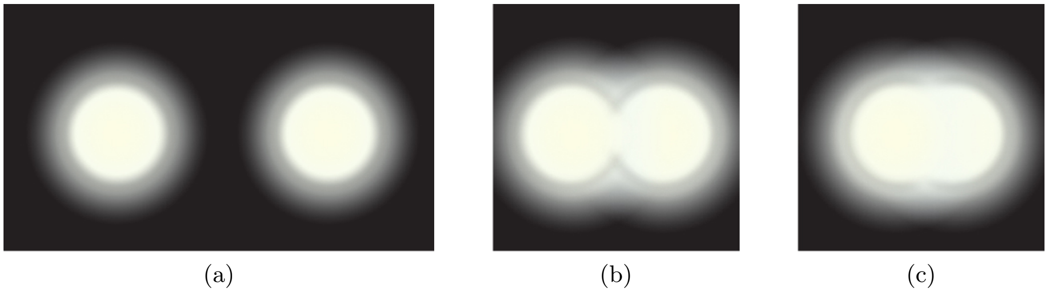
(a) (b) (c)

Figure A.5: Airy discs produced from two light sources by the diffraction of the light as it passes through a small circular aperture as in Figure A.4. Light sources are placed closer together (*i.e.* θ decreases) from a → c.

In a transmitted light microscope, Equation A.5 is modified to Equation A.6, where ν is the refractive index of the medium between the apertures/lenses and the sample (condenser/collimator before sample and objective after) and NA is known as the numerical aperture [361, 362, 36]. Using a violet wavelength of 400nm (*i.e.* on the lower limit of what can be detected by the human eye [363]) and assuming both apertures have an NA value of 1, therefore, one can calculate from this equation a maximum achievable resolution (ignoring aberrations) of 244nm.

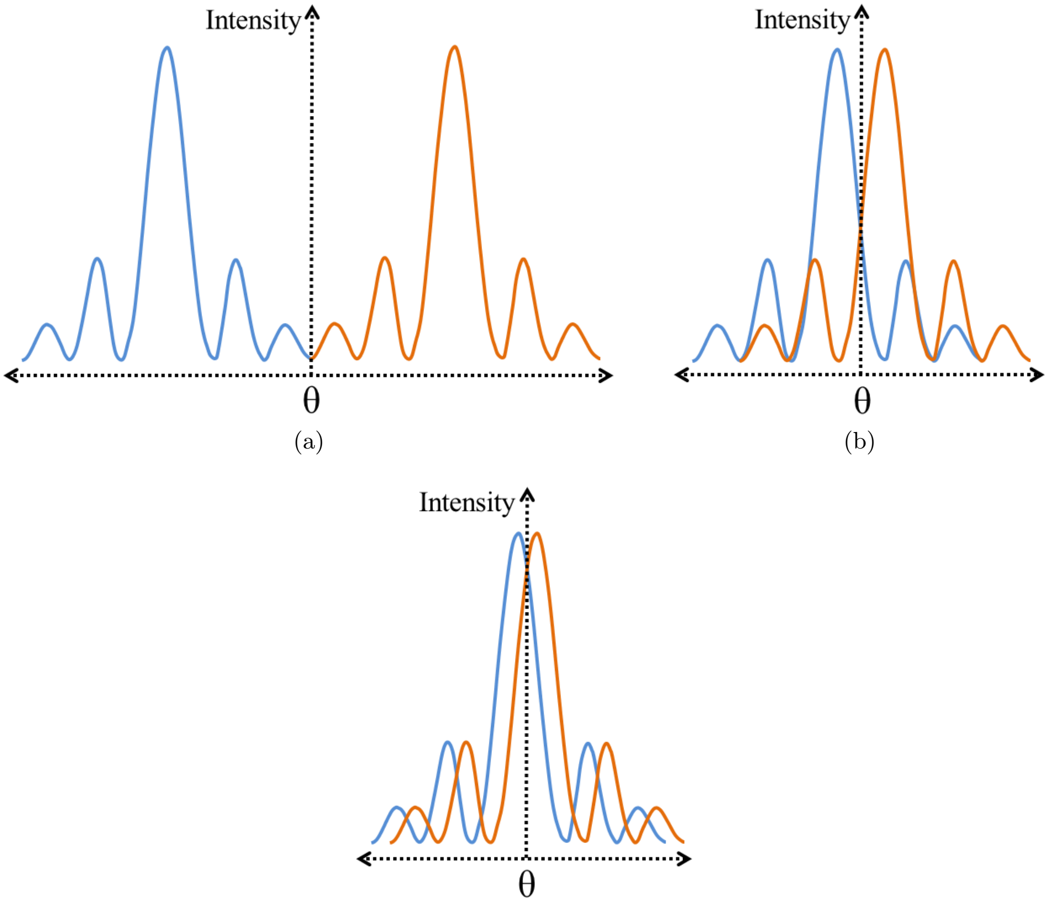

(a) (b) (c)

Figure A.6: 2-Dimensional cross section of the centre of the Airy fringe patters produced by the two light sources shown in Figure A.4. Both lights have the same frequency, colour is just used to help the eye distinguish between the fringes of each. a) Lights are easily resolved. b) Rayleigh criterion *i.e.* lights just resolvable. c) Lights not classed as resolvable in the Rayleigh regime.

Appendix F: Synthetic Particle Distribution Image Generation

In a high-concept manner, the construction of synthetic images can be understood as the creation of a pictorial representation of a mathematical distribution. Consequently, when producing such images, the first step is to define the distribution which is to be illustrated. As described in Section 4.3.3 this is accomplished by defining specific variables such as the distribution mean and/or standard deviation/variance. Unfortunately, given the continuous nature of a mathematical distribution, however, it is clear that a strict representation cannot be realised for any particle image as it would necessarily contain an infinite amount of particles, each corresponding to an infinitesimally small size interval in the distribution. As an alternative, therefore, it becomes necessary to use a coarse, discretised distribution instead.

The process of discretising the desired distribution as performed in this research consists of two stages: Firstly, the distribution is evaluated over a range of (radius) values at fixed intervals creating a series of particle classes. Next the normalised distribution values are scaled to match that of a specified number density (selected so as to create a densely packed foil) before a subsequent threshold procedure is implemented to remove those classes with particle frequencies below a specified limit. The value of the cut-off limit is selected so as to maintain as much as practicable the true shape of the distribution (*i.e.* to retain the shape of the distribution edges whilst precluding excessive numbers of classes with very low probability values). Examples of the distribution histogram produced by this process compared to the original mathematical description is shown in Figure A.7.

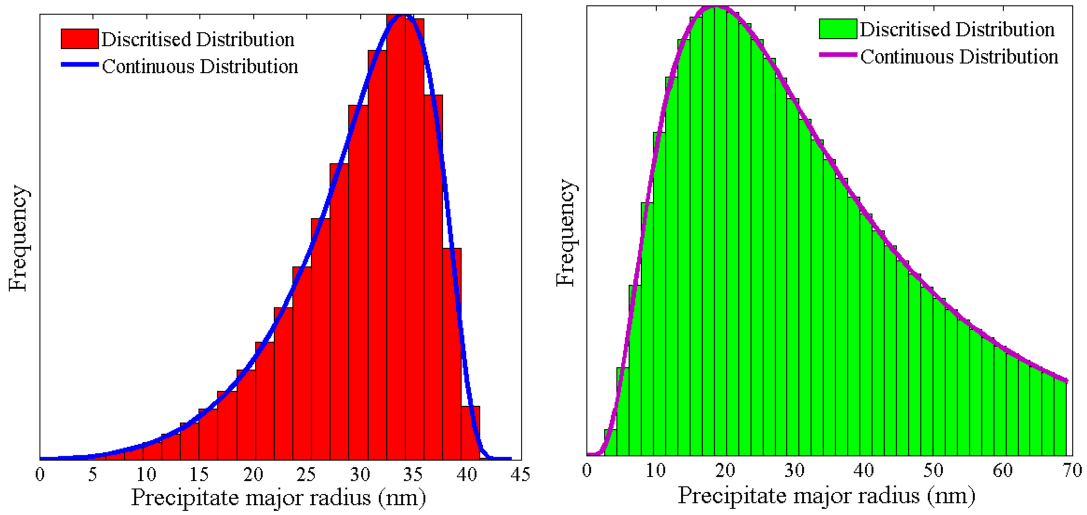

(a) (b)

Figure A.7: Example classified distribution resulting from the discretisation of a continuous a) LSW and b) Log-normal distribution.

Once each of the descritised distributions had been defined, the next procedure carried out towards constructing the synthetic foil is a translation of each of the PSD's into individual particle statistics. The ellispodal nature of the particles comprising the images created here, however, necessitates that this information is further appended with information on their aspect ratio (and concomitantly the minor radius length). To this end, rather than utilising a single value, to be consistent with the shape changing nature of γ'' precipitates, aspect ratios are selected based on a hyperbolic fit made to the data collated by Devaux *et al.* [47] shown in Figure A.8.

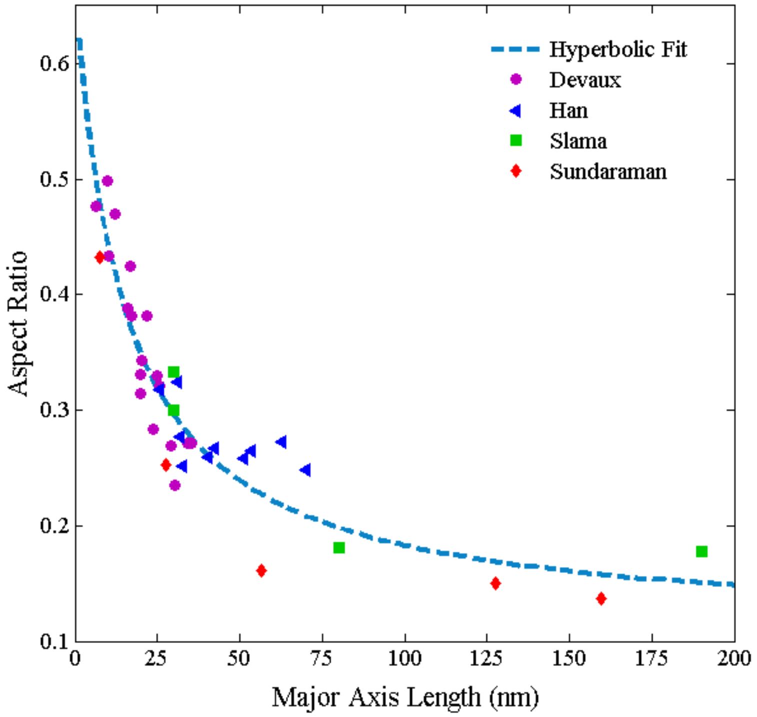

Figure A.8: Plot of γ'' aspect ratio as a function of major axis length constructed by Devaux *et al.* [47] based on measurements made on their own samples and literature data (Han [2], Slama [4], Sundararaman [39]). Hyperbolic fit made to the data for calculating aspect ratios here is indicated.

Once dimensions and quantity of each particle have been defined, the foil construction proceeds in a similar manner to that outlined in Section 4.3.2; particles are prohibited from overlapping and the thickness of the foil given by twice the average edge-on particle diameter. The equal probability assumed for each of the three γ'' orientational variants in the real system means that in the synthetic foil each orientational population is constructed to be identical. Dissimilarly, despite utilising the same random location technique within the x-y plane, a stark contrast occurs with respect to the foil reconstruction technique when determining position of the particle centroid along the z-axis synthetic distributions. That is, instead of a purely random location inside the foil thickness, the centroid is positioned along this axis such that the correct volume (determined by integration) remains inside the foil according to the predetermined PSD. Nevertheless, owing to them being arbitrary, the foil plane the partial precipitates intersect, together with the specific position of those which lay completely within the foil, is still determined randomly.

Example images created according to three different distributions are shown in Figure A.9. In accordance with the new technique described in Section 4.3.2 the bottom row of images shows a final transformation whereby the foil projections are altered to make them representative of experimentally obtained Dark-field TEM images *viz.* face-on precipitates (relative to the x-y plane) are removed and the image is transformed to an intensity map.

The specific number density selected for the aforementioned foil construction procedure here was that of 100 particles in the foil volume, with the foil volume itself varying in accordance with the distribution average radius statistics. Under this condition, it was found that a significant fraction of both whole and sectioned particles could be obtained through the use of 40 different size classes to represent the distribution leading to such a discretisation being used for image construction. In addition, however, because of the arbitrary nature of the radius values of the classes and the necessary truncation of the continuous distribution extremes (discussed earlier), a more rigorous representation of the distribution was obtained through the creation of 20 different foils Each foil corresponded to a different classification of the same distribution which could be combined with the other 19 by the image analysis method. The process used to create each of the classifications, effectively leading to 800 different class intervals being implemented to represent the distribution of interest, is depicted in Figure A.10; the start radius radius value is incrementally increased by a magnitude equivalent to 5% of the class width of the first discrete distribution.

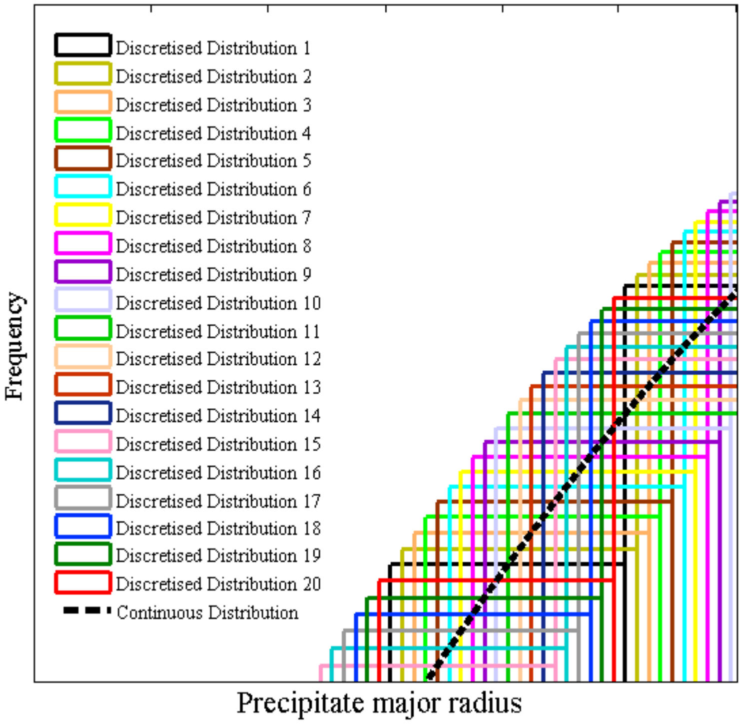

Figure A.10: Incremental discretisation positions shown for a small area of a normal distribution. Histograms bars sets for each of the 20 different discretisations are colour coordinated.

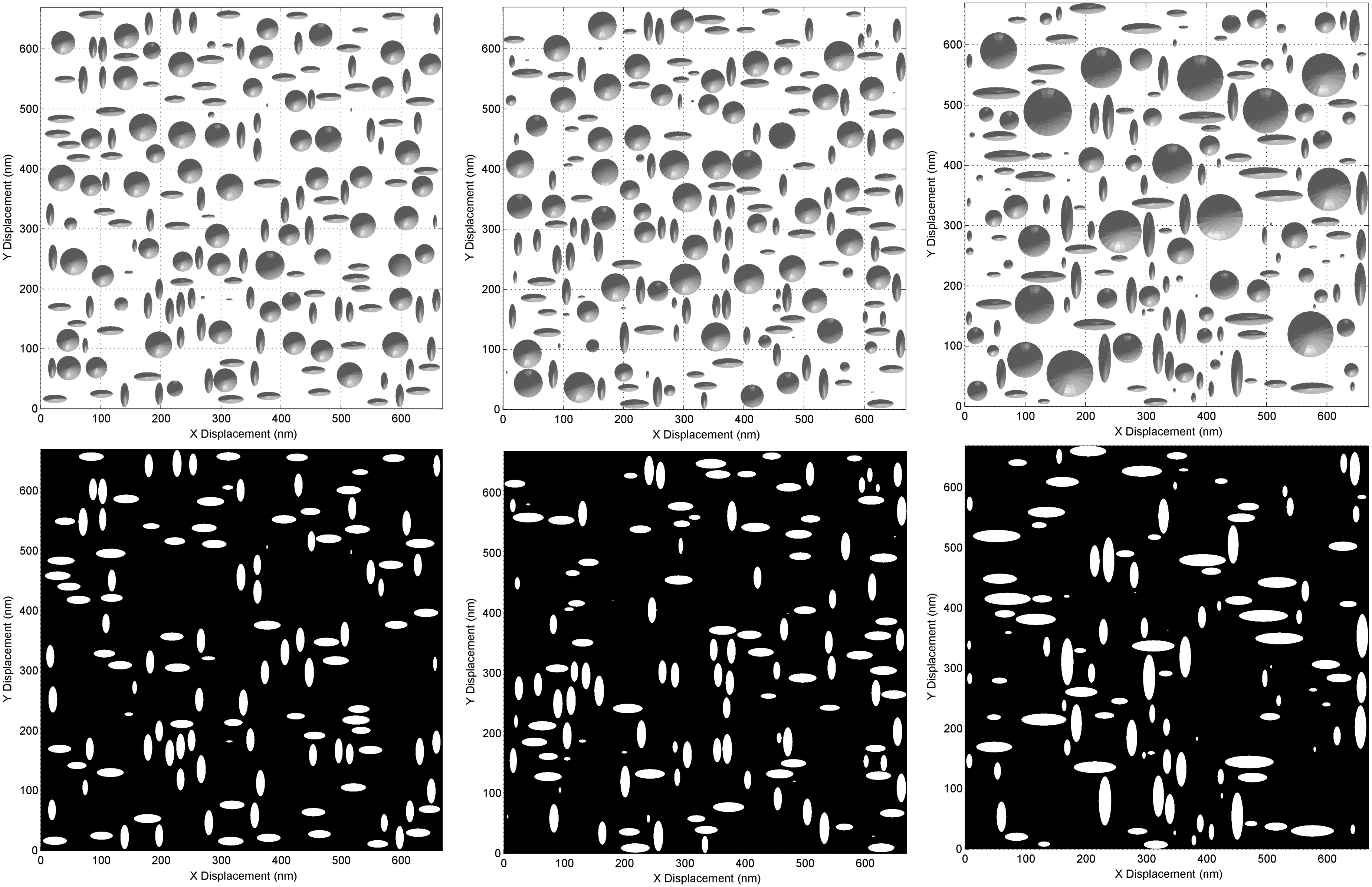

(a)

(b)

(c)

Figure A.9: Synthetic image of ellipsoidal precipitates obeying three different distributions: a) Normal, b) LSW, c) Log-normal. Final images where face-on precipitates have been removed are also shown. Distributions each have the same mean precipitate size of 20 nm and (for images a and c) the same standard deviation of 2. Aspect ratios follow the trend shown in Figure A.8.

Appendix G: Element Materials Technology ICP-OES Analysis Report

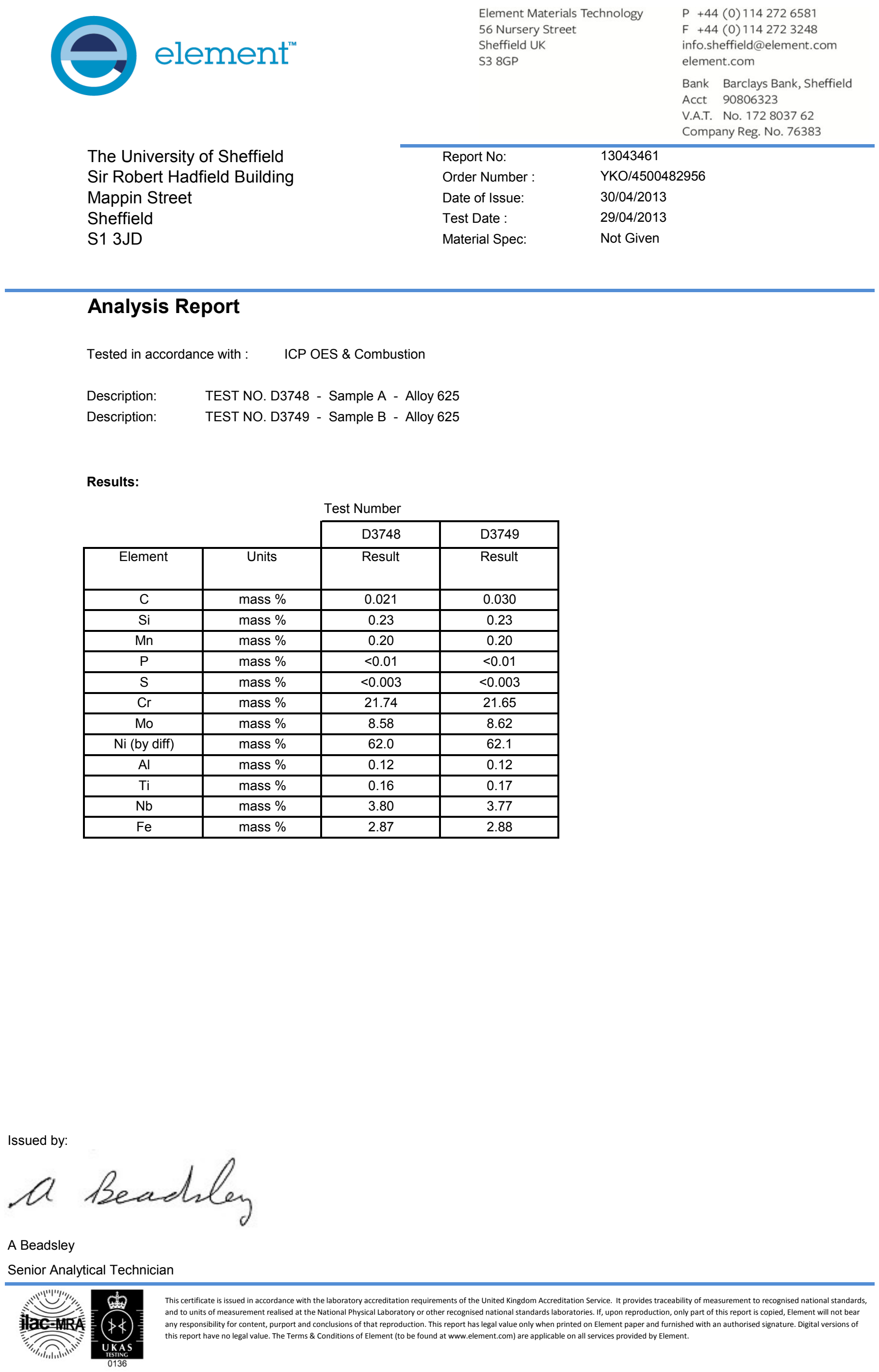

element™

Element Materials Technology
56 Nursery Street
Sheffield UK
S3 8GP

P +44 (0) 114 272 6581
F +44 (0) 114 272 3248
info.sheffield@element.com
element.com

Bank Barclays Bank, Sheffield
Acct 90806323
V.A.T. No. 172 8037 62
Company Reg. No. 76383

The University of Sheffield
Sir Robert Hadfield Building
Mappin Street
Sheffield
S1 3JD

Report No:	13043461
Order Number :	YKO/4500482956
Date of Issue:	30/04/2013
Test Date :	29/04/2013
Material Spec:	Not Given

Analysis Report

Tested in accordance with : ICP OES & Combustion

Description: TEST NO. D3748 - Sample A - Alloy 625
Description: TEST NO. D3749 - Sample B - Alloy 625

Results:

		Test Number	
		D3748	D3749
Element	Units	Result	Result
C	mass %	0.021	0.030
Si	mass %	0.23	0.23
Mn	mass %	0.20	0.20
P	mass %	<0.01	<0.01
S	mass %	<0.003	<0.003
Cr	mass %	21.74	21.65
Mo	mass %	8.58	8.62
Ni (by diff)	mass %	62.0	62.1
Al	mass %	0.12	0.12
Ti	mass %	0.16	0.17
Nb	mass %	3.80	3.77
Fe	mass %	2.87	2.88

Issued by:

A Beadsley

A Beadsley
Senior Analytical Technician

ilac-MRA UKAS TESTING 0136

Appendix H: Calibration Parameter Sensitivity

The sensitivity of the SFFK based model created in this research to the particular inferred trends for the misfit strains on the precipitate mantle (ϵ_{11}) and ends (ϵ_{33}) is best illustrated through the use of extremal fits. Accordingly, following the hyperbolic descriptions in Equation A.7, two of the most contrasting, valid relationships[2] for each of the strains and their corresponding coefficient values are presented in Figure A.11 and Table A.1 respectively.

$$\epsilon_{1,1} = \frac{E\alpha}{F+\alpha} + Y \qquad \epsilon_{3,3} = \frac{EF}{F+\alpha} + Y \tag{A.7}$$

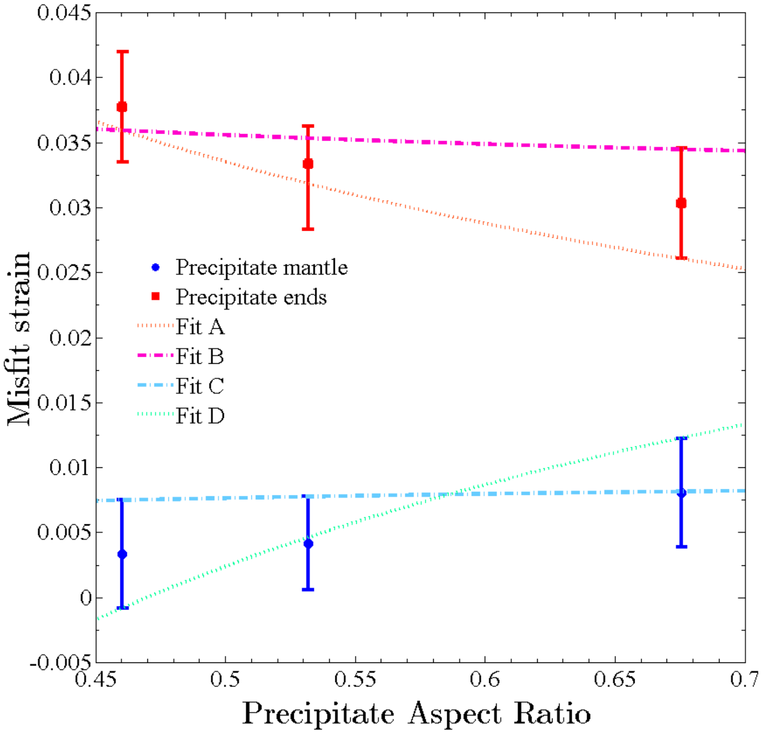

Figure A.11: Example hyperbolic fits to misfit strains on the precipitate mantle and ends complying with the range of possible values indicated by the data points in Figure 6.3.

Ostensibly, the conformity of the four different plots selected for the misfit strains within the range (defined by the error bars) of each of the data points (calculated in Section 6.1.1) should allow for four different calculations of the precipitate evolution. However, it turns out that the use of A and C (*i.e.* pair A-C) actually leads to the creation of an insurmountable energy barrier for nucleation, thereby preventing precipitate formation and evolution taking place. This eventuality is ultimately the result of the intricate

---

[2] Although the absolute extremal and most disparate fits are desirable, the range of possible values means their precise identification itself would be difficult, and for the purposes of this appendix would be largely arbitrary compared to those ultimately selected.

Table A.1: Coefficient values for the correspondingly labelled extremal trends in Figure A.11.

Trend	ϵ component	Coefficients		
		E	F	Y
A	ϵ_{33}	0.3382	0.0504	0.0026
B	ϵ_{33}	0.0375	0.072	0.0309
C	ϵ_{11}	0.0151	0.086	-0.0052
D	ϵ_{11}	0.5133	0.0428	-0.4704

relationship of the fit parameters to the various governing equations of the model detailed in Section 2.2. The use of strains generated from certainly/likely incompatible lattice parameter values as indicated by Figure A.12, whilst having implications for the validity of the result (an arbitrary outcome with reference to this appendix), does not prohibit precipitate formation in any of the other trend parings.

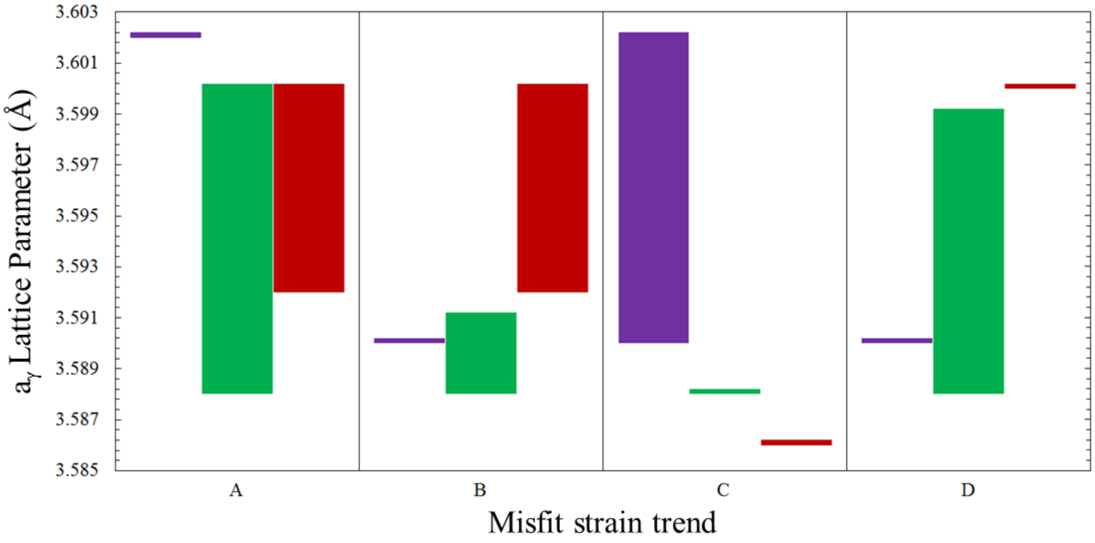

Figure A.12: Floating bar chart indicating the value range for the lattice parameter a_γ calculated separately from the fits A, B, C and D in Figure A.11 and conforming to the experimental measurements of a_{γ}, $a_{\gamma''}$ and $c_{\gamma''}$ by Slama *et al.* [4]. The three colour coordinated bar sets correspond to the three data points in Figure 6.3 such that in the notation: colour(α), Purple(0.676), Green(0.532) and Red(0.460).

Following the same initial assumptions and calculation conditions outlined in Section 6.2, the aspect ratio evolution computed using the permitted ϵ_{11} and ϵ_{33} evolution pairs A-D, B-C and B-D are shown in Figure A.13a with their corresponding values for the system molar volume Ω in Table A.2.

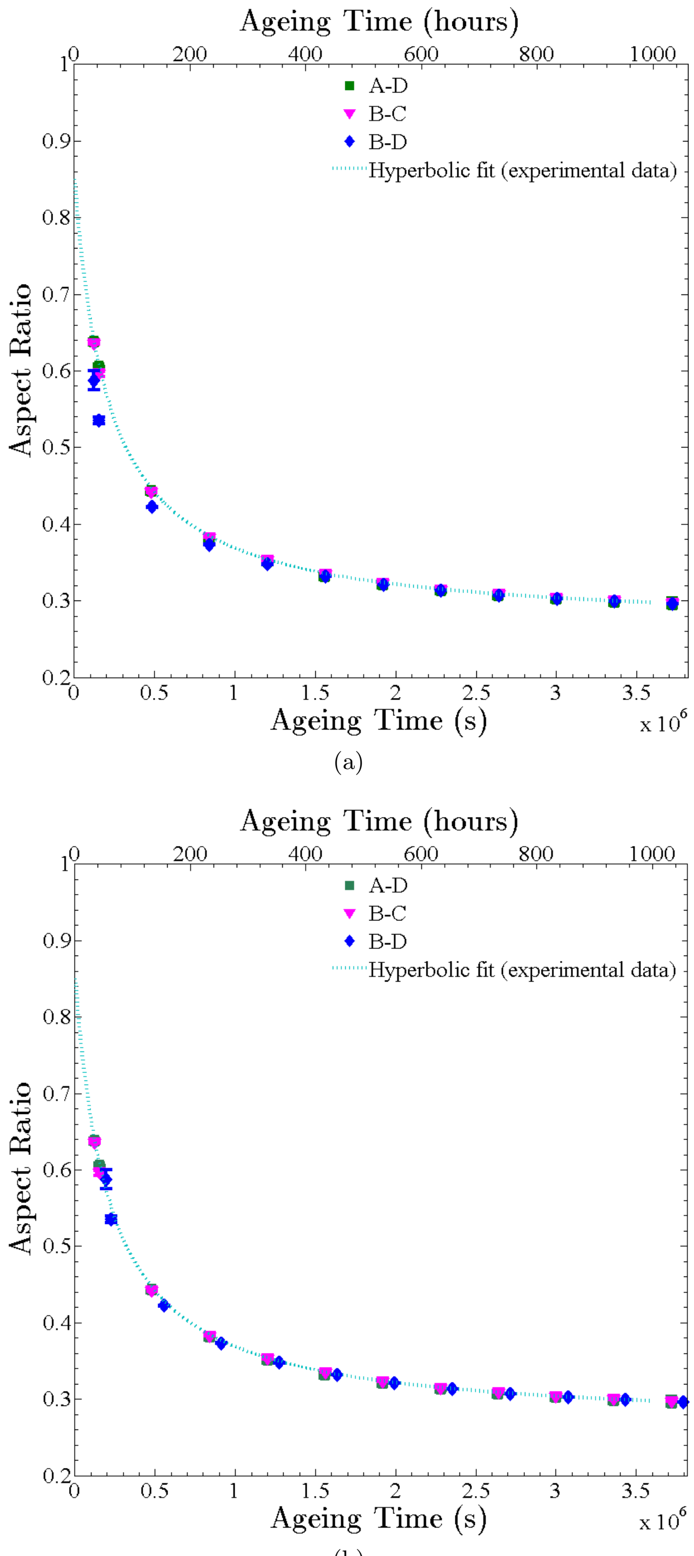

(a)

(b)

Figure A.13: Calculated aspect ratio evolution for γ'' precipitates predicted from the various pairings of the misfit trends presented in Figure A.11. Data points correspond to average values after a time correction has been applied and the error bars to the first and third quartiles of the aspect ratio distribution. a) Data as output from the model. b) Plots subsequent to a shifting operation on B-D. The hyperbolic relationship derived from the experimental observations and input to the model is shown for comparison.

Table A.2: Ω values calculated for the allowed pairs of the misfit strain energy trends defined in Table A.1 in order to comply with the initial conditions of the model calculation.

Misfit strain trend pair	Ω ($\mathrm{m^3mol^{-1}}$)	τ (s)
A-D	4.94866×10^{-5}	1759.5
B-C	3.47398×10^{-5}	1484.5
B-D	2.55288×10^{-5}	285.02

Despite the function defining the change in the aspect ratio being input to the model, examination of Figure A.13a yields the conclusion that the differing misfit strain evolutions produce a notable variation in the behaviour of the aspect ratio. The fact that the contrast is most marked at shorter ageing times indicates the result is most strongly associated with the factors governing the incubation period (τ) calculated for the system (values also shown in Table A.2), with an intrinsically higher/lower resistance to precipitation effectively delaying/hastening γ'' evolution. Confirmation of this effect manifesting only as a time phenomenon, rather than a fundamental change in the specific evolution with respect to the aspect ratio (thereby maintaining consistency with relationship to the calculation in all cases), is provided by the excellent alignment of the plots (both relatively and with the input function) subsequent to a shift along the x-axis as shown in Figure A.13b.

The major radius evolutions predicted by the SFFK model created in this research from the allowed misfit strain pairs are displayed in Figure A.14. In contrast to the relatively small (correctable) discrepancies discussed previously for α, analysis of these corresponding particle size trends immediately identifies the presence of an irreconcilable divergence over the entire ageing range (average precipitate radii differ by as much as 100%). Considering that every other variable is held constant, this significant eventuality can plainly only be interpreted as proof that the trends for ϵ_{11} and ϵ_{33} exert a monumental impact on the calculation of γ'' precipitate evolution and, therefore, that each must be highly non arbitrary. Similarly, considering the relative distribution of the trends[3], although one could reasonably infer that the ϵ_{33} path selection transitioning in a direction from A$\rightarrow$B and/or the ϵ_{11} selection transitioning in a direction from C$\rightarrow$D should always lead to an increase in the average precipitate major radius and distribution width across all ageing times, such a relationship is contradicted by the results shown in Figure 6.8. That is, the fact that larger average precipitate major radii and distribution widths were calculated using strain paths in the A$\leftrightarrow$B and C$\leftrightarrow$D intervals mean a more complicated relationship is present.

---

[3] Owing to their preclusion from precipitation, a constant value of 0nm can be assumed for γ'' precipitates following the theoretical A-C strain paring.

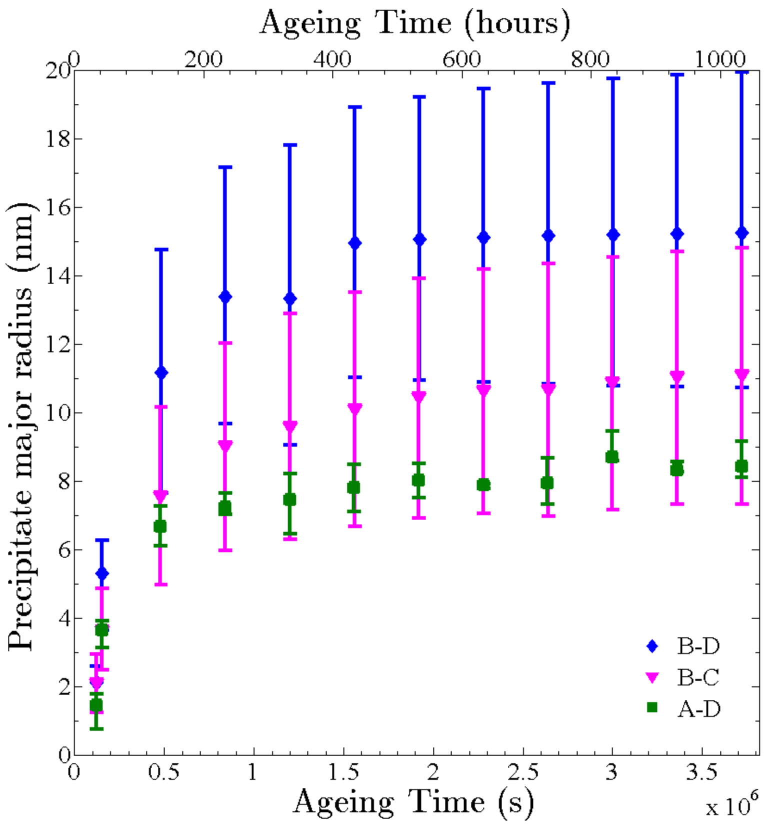

Figure A.14: Calculated major radius evolution for γ'' precipitates predicted from the various pairings of the misfit trends presented in Figure A.11. Data points correspond to average values and the error bars to the first and third quartiles of the aspect ratio distribution.

The final key variable for illustrating the effect of the inferred trends for ϵ_{11} and ϵ_{33} is the precipitate number density. In his regard, the outputs of the model after converting the raw discrete distribution to a continuous one (using the distribution density as described in Section 3.2.8) are presented in Figure A.15. In this instance it is again observed that changing the interpreted evolutions for ϵ_{11} and ϵ_{33} has a marked effect on the model outputs, with precipitate populations observing complementary/inverse behaviour (consistent with an identical equilibrium precipitate volume fraction being used in the calculation of the driving force) to the radius values shown in Figure A.14.

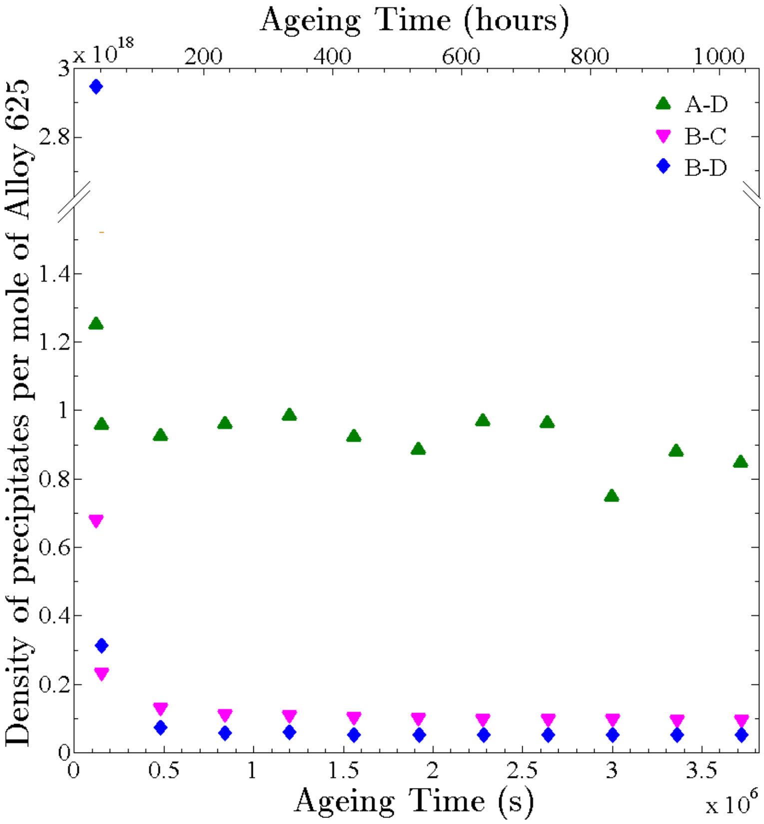

Figure A.15: Calculated number density evolution for γ'' precipitates predicted from the various pairings of the misfit trends presented in Figure A.11. Data points correspond to average values and the error bars to the first and third quartiles of the aspect ratio distribution.

In view of the results presented for the effect of both ϵ_{11} and ϵ_{33} on the evolution of both size and number density of γ'' precipitates, it is evident that the SFFK based model developed in this research can only successfully predict the behaviour of such variables (demonstrated in Figure 6.2.4) if the evolution of the strain experienced by a precipitate particle is defined precisely and correctly. Furthermore, by demonstrating the need for coherent, representative descriptions, these outcomes also support the appropriateness and physicality of the conclusions regarding ϵ_{11} and ϵ_{33} behaviour drawn from the validation calculation in Section 6.2.2.

References

[1] C.K.L. Davies, P. Nash, and R.N. Stevens. The effect of volume fraction of precipitate on Ostwald ripening. *Acta Metallurgica*, 28(2):179–189, 1980.

[2] Y.F. Han, P. Deb, and M.C. Chaturvedi. Coarsening behaviour of γ'' and γ' particles in Inconel alloy 718. *Metal Science*, 16(12):555–562, 1982.

[3] Special Metals Corporation, New York, NY. *Inconel alloy 625*, August 2013. Available from `http://www.specialmetals.com/assets/documents/alloys/inconel/inconel-alloy-625.pdf`.

[4] C. Slama, C. Servant, and G. Cizeron. Aging of the Inconel 718 alloy between 500 and 750°C. *Journal of Materials Research*, 12(9):2298–2316, 1997.

[5] R.A. Ricks, A.J. Porter, and R.C. Ecob. The growth of γ' precipitates in nickel-base superalloys. *Acta Metallurgica*, 31(1):43–53, 1983.

[6] M.P. Jackson and R.C. Reed. Heat treatment of Udimet 720Li: The effect of microstructure on properties. *Materials Science and Engineering A*, 259(1):85–97, 1999.

[7] E.L. Raymond and D.A. Wells. Effects of aluminum content and heat treatment on gamma prime structure and yield strength of Inconel nickel-chromium Alloy 706. In *Superalloys 1972 (Proceedings of the Second International Symposium on Superalloys)*, pages N1–N21. The Minerals, Metals & Materials Society, Warrendale, PA, 1972.

[8] M.G. Burke, W.J. Mills, and R. Bajaj. Microstructure and properties of direct-aged Alloy 625. In E.A. Loria, editor, *Proceedings of the International Symposium on Superalloys 718, 625, 706 and Various Derivatives*, pages 389–398. The Minerals, Metals & Materials Society, Warrendale, PA, 2001.

[9] G. Sjöberg, T. Antonsson, S. Azadian, R. Warren, and H. Fredriksson. Effect of δ-phase on the weldability and the hot ductility of Alloy 718. In E.A. Loria, editor, *Proceedings of the International Symposium on Superalloys and Various Derivatives*, pages 351–362. The Minerals, Metals & Materials Society, Warrendale, PA, 2005.

[10] V. Shankar, K. Bhanu Sankara Rao, and S.L. Mannan. Microstructure and mechanical properties of Inconel 625 superalloy. *Journal of Nuclear Materials*, 288(2-3):222–232, 2001.

[11] A.K. Sinha. *Materials Science: Topologically Close-packed Structures of Transition Metal Alloys.* Progress in Materials Science. Pergamon, Oxford, UK, 1972.

[12] International Union of Pure and Applied Chemistry. Periodic table of the elements, June 2012. Available from `http://old.iupac.org/reports/periodic_table/`.

[13] R.C. Reed, D.C. Cox, and C.M.F. Rae. Damage accumulation during creep deformation of a single crystal superalloy at 1150 °C. *Materials Science and Engineering A*, 448(1-2):88–96, 2007.

[14] D.M. Moon and F.J. Wall. The effect of phase instability on the high trmperature stress-rupture properties of representative nickel-base superalloys. In *Proceedings of the International Symposium on Structural Stability in Superalloys*, pages 115–133. The Minerals, Metals & Materials Society, Warrendale, PA, 1968.

[15] K. Zhao, L.H. Lou, Y.H. Ma, and Z.Q. Hu. Effect of minor niobium addition on microstructure of a nickel-base directionally solidified superalloy. *Materials Science and Engineering A*, 476(1-2):372–377, 2008.

[16] Y.S. Lim, D.J. Kim, S.S. Hwang, H.P. Kim, and S.W. Kim. $M_{23}C_6$ precipitation behavior and grain boundary serration in Ni-based Alloy 690. *Materials Characterization*, 96:28–39, 2014.

[17] Z. Xu, L. Jiang, J. Dong, Z. Li, and X. Zhou. The effect of silicon on precipitation and decomposition behaviors of M_6C carbide in a Ni-Mo-Cr superalloy. *Journal of Alloys and Compounds*, 620:197–203, 2014.

[18] A. Putnis. *An Introduction to Mineral Sciences.* Cambridge University Press, Cambridge, UK, 1992.

[19] D.A. Porter and K.E. Easterling. *Phase Transformations in Metals and Alloys.* CRC Press, Boca Raton, FL, second edition, 1992.

[20] J.W. Martin. *Micromechanisms in Particle-Hardened Alloys.* Cambridge Solid State Science Series. Cambridge University Press, Cambridge, UK, 1980.

[21] K.C. Russell. Nucleation in solids: The induction and steady state effects. *Advances in Colloid and Interface Science*, 13(3-4):205–318, 1980.

[22] J.W. Cahn. Nucleation on dislocations. *Acta Metallurgica*, 5(3):169–172, 1957.

[23] S. Floreen, G.E. Fuchs, and W.J. Yang. The metallurgy of Alloy 625. In E.A. Loria, editor, *Proceedings of the International Symposium on Superalloys 718, 625, 706 and Various Derivatives*, pages 13–37. The Minerals, Metals & Materials Society, Warrendale, PA, 1994.

[24] J.O. Andersson, T. Helander, L. Höglund, P. Shi, and B. Sundman. Thermo-Calc & DICTRA, computational tools for materials science. *Calphad: Computer Coupling of Phase Diagrams and Thermochemistry*, 26(2):273–312, 2002.

[25] Thermo-Calc Software AB, Stockholm, Sweden. *Thermo-Calc*. (`http://www.thermocalc.com/`).

[26] Thermo-Calc Software AB, Stockholm, Sweden. *Thermo-Calc Software TCNI7 Ni-based Superalloys database version 7.*

[27] D. Connétable, M. Mathon, and J. Lacaze. First principle energies of binary and ternary phases of the Fe-Nb-Ni-Cr system. *Calphad: Computer Coupling of Phase Diagrams and Thermochemistry*, 35(4):588–593, 2011.

[28] F. Luo, X.R. Chen, L.C. Cai, and Q. Wu. Thermoelastic properties of nickel from molecular dynamic simulations. *Journal of Atomic and Molecular Sciences*, 2(1):10–19, 2011.

[29] T. Wang. Inductively coupled plasma optical emission spectroscopy. In J. Cazes, editor, *Analytical Instrumentation Handbook*. CRC Press, Boca Raton, FL, third edition, 2004.

[30] H.E. Boyer and American Society for Metals. Committee on Hardness Testing. *Hardness testing*. ASM International, Metals Park, OH, 1995.

[31] P.J. Goodhew. *Thin foil preparation for electron microscopy*, volume 11 of *Practical methods in electron microscopy*. Elsevier, Amsterdam, NL, 1985.

[32] Wikipedia. Transmission electron microscopy - Wikipedia, the free encyclopedia, 2016. `https://en.wikipedia.org/wiki/Transmission_electron_microscopy`.

[33] I.S. Grant and W.R. Phillips. *Electromagnetism*. John Wiley & Sons, Chichester, UK, 2008.

[34] R.F. Egerton. *Physical Principles of Electron Microscopy: An Introduction to TEM, SEM, and AEM*. Springer-Verlag, New York, NY, 2005.

[35] I.M. Watt. *The Principles and Practice of Electron Microscopy*. Cambridge University Press, Cambridge, UK, 1997.

[36] S. Wischnitzer. *Introduction to Electron Microscopy*. Pergamon Press, Oxford, UK, third edition, 1989.

[37] J.R. Crum, M.E. Adkins, and W.G. Lipscomb. Performance of high nickel alloys in refinery and petrochemical environments. *Materials Performance*, 25(7):27–33, 1986.

[38] E. Schnabel, H.J. Schueller, and P. Schwaab. Precipitation and recrystallization behavior of the nickel-base alloy Inconel 625 [Das ausscheidungs und rekristallisationsverhalten der nickelbasislegierung Inconel 625]. *Praktische Metallographie/Practical Metallography*, 8(9):521–527, 1971.

[39] M. Sundararaman, P. Mukhopadhyay, and S. Banerjee. Some aspects of the precipitation of metastable intermetallic phases in Inconel 718. *Metallurgical Transactions A*, 23(7):2015–2028, 1992.

[40] J.M. Oblak, D.F. Paulonis, and D.S. Duvall. Coherency strengthening in Ni base alloys hardened by $D0_{22}$ γ'' precipitates. *Metallurgical Transactions*, 5:143–153, 1974.

[41] L.M. Suave, J. Cormier, P. Villechaise, A. Soula, Z. Hervier, D. Bertheau, and J. Laigo. Microstructural evolutions during thermal aging of Alloy 625: Impact of temperature and forming process. *Metallurgical and Materials Transactions A: Physical Metallurgy and Materials Science*, 45(7):2963–2982, 2014.

[42] M. Perez, C. Sidoroff, A. Vincent, and C. Esnouf. Microstructural evolution of martensitic 100Cr6 bearing steel during tempering: From thermoelectric power measurements to the prediction of dimensional changes. *Acta Materialia*, 57(11):3170–3181, 2009.

[43] Special Metals Corporation, New York, NY. *Inconel alloy 718*, September 2007. Available from `http://www.specialmetals.com/assets/documents/alloys/inconel/inconel-alloy-718.pdf`.

[44] Thermo-Calc Software AB, Stockholm, Sweden. *Thermo-Calc Software TCNI8 Ni-base Superalloys database version 8.*

[45] C. Dong. Powderx: Windows-95-based program for powder X-ray diffraction data processing. *Journal of Applied Crystallography*, 32(4):838, 1999.

[46] C. Dong, H. Chen, and F. Wu. A new Cu Kα2 elimination algorithm. *Journal of Applied Crystallography*, 32(2):168–173, 1999.

[47] A. Devaux, L. Nazé, R. Molins, A. Pineau, A. Organista, J.Y. Guédou, J.F. Uginet, and P. Héritier. Gamma double prime precipitation kinetic in Alloy 718. *Materials Science and Engineering A*, 486(1-2):117–122, 2008.

[48] W.D. Callister. *Materials Science and Engineering: An Introduction.* John Wiley & Sons, New York, NY, seventh edition, 2007.

[49] D.L. Klarstrom. Wrought cobalt-base superalloys. *Journal of Materials Engineering and Performance*, 2(4):523–530, 1993.

[50] F.R. Morral. The metallurgy of cobalt alloys: A 1968 review. *Journal of Metals*, 20(18):52–59, 1968.

[51] W. Betteridge and S.W.K. Shaw. Development of superalloys. *Materials Science and Technology*, 3(9):682–694, 1987.

[52] D.R. Askeland and W.J. Wright. *Essentials of Materials Science and Engineering.* Cengage Learning, Stamford, CT, third edition, 2013.

[53] C.T. Sims, N.S. Stoloff, and W.C. Hagel. *Superalloys II.* John Wiley & Sons, New York, NY, first edition, 1987.

[54] R.C. Reed. *The Superalloys: Fundamentals and Applications.* Cambridge University Press, Cambridge, UK, first edition, 2006.

[55] M.J. Donachie and S.J. Donachie. *Superalloys: A Technical Guide.* ASM International, Materials Park, OH, second edition, 2002.

[56] E.F. Bradley. *Superalloys: A Technical Guide.* ASM International, Materials Park, OH, first edition, 1989.

[57] W.B. Pearson. *A Handbook of lattice spacings and structures of metals and alloys.* Pergamon, Oxford, UK, 1967.

[58] M.V. Nathal, R.A. Mackay, and R.G. Garlick. Temperature dependence of γ-γ' lattice mismatch in Nickel-base superalloys. *Materials Science and Engineering*, 75(1-2):195–205, 1985.

[59] F. Pyczak, B. Devrient, and H. Mughrabi. The effects of different alloying elements on the thermal expansion coefficients, lattice constants and misfit of nickel-based superalloys investigated by X-Ray diffraction. In *Superalloys 2004 (Proceedings of the Tenth International Symposium on Superalloys)*, pages 827–836. The Minerals, Metals & Materials Society, Warrendale, PA, 2004.

[60] H. Gleiter and E. Hornbogen. Theory of the interaction of dislocations with coherent ordered zones (I) [Theorie der wechselwirkung von versetzungen mit kohärenten geordneten zonen (I)]. *Physica Status Solidi (B)*, 12(1):235–250, 1965.

[61] E. Nembach and G. Neite. Precipitation hardening of superalloys by ordered γ' particles. *Progress in Materials Science*, 29(3):177–319, 1985.

[62] M. Chandran and S.K. Sondhi. First-principle calculation of APB energy in Ni-based binary and ternary alloys. *Modelling and Simulation in Materials Science and Engineering*, 19(2):025008, 2011.

[63] A. Kelly and R. Nicholson. *Strengthening methods in crystals.* Halstead Press Division, John Wiley & Sons, New York, NY, 1972.

[64] W. Huther and B. Reppich. Interaction of dislocations with coherent, stress-free, ordered particles. *Zeitschrift fuer Metallkunde/Materials Research and Advanced Techniques*, 69(10):628–634, 1978.

[65] R.W. Cahn, P.A. Siemers, J.E. Geiger, and P. Bardhan. The order-disorder transformation in Ni_3Al and Ni_3(Al,Fe) alloys I. Determination of the transition temperatures and their relation to ductility. *Acta Metallurgica*, 35(11):2737–2751, 1987.

[66] F.J. Bremer, M. Beyss, and H. Wenzl. The order-disorder transition of the intermetallic phase Ni_3Al. *Physica Status Solidi (A)*, 110(1):77–82, 1988.

[67] X. Xie, J. Dong, M. Zhang, G. Wang, and S. Zhao. Embrittling effect of iron and nickel base superalloys in high temperature long time exposures. In G. Fuchs, A. James, T. Gabb, M. McLean, and H. Harada, editors, *Advanced Materials and Processes for Gas Turbines*, pages 207–215. The Minerals, Metals & Materials Society, Warrendale, PA, 2003.

[68] Special Metals Wiggin Ltd, Hereford, UK. *Inconel Alloy 740*, September 2004. Technical Bulletin SMC-090. Available from `http://www.specialmetalswiggin.co.uk/pdfs/products/Inconel%20alloy%20740.pdf`.

[69] D.F. Paulonis, J.M. Oblak, and D.S. Duvall. Precipitation in nickel-base Alloy 718. *ASM-Trans*, 62(3):611–622, 1969.

[70] I. Kirman and D.H. Warrington. The precipitation of Ni_3Nb phases in a Ni-Fe-Cr-Nb alloy. *Metallurgical Transactions*, 1(10):2667–2675, 1970.

[71] J.M. Oblak, D.S. Duvall, and D.F. Paulonis. An estimate of the strengthening arising from coherent, tetragonally-distorted particles. *Materials Science and Engineering*, 13(1):51–56, 1974.

[72] M. Sundararaman, P. Mukhopadhyay, and S. Banerjee. Deformation behaviour of γ'' strengthened Inconel 718. *Acta Metallurgica*, 36(4):847–864, 1988.

[73] J.B. Singh, J.K. Chakravartty, and M. Sundararaman. Work hardening behaviour of service aged Alloy 625. *Materials Science and Engineering A*, 576:239–242, 2013.

[74] M. Sundararaman, P. Mukhopadhyay, and S. Banerjee. Precipitation of the δ Ni_3Nb phase in two nickel base superalloys. *Metallurgical Transactions A*, 19(3):453–465, 1988.

[75] W.D. Cao and R.L. Kennedy. New developments in wrought 718-type superalloys. *Acta Metallurgica Sinica (English Letters)*, 18(1):39–46, 2005.

[76] A. Strondl, M. Palm, J. Gnauk, and G. Frommeyer. Microstructure and mechanical properties of nickel based superalloy IN718 produced by rapid prototyping with electron beam melting (EBM). *Materials Science and Technology*, 27(5):876–883, 2011.

[77] M. Sundararaman, P. Mukhopadhyay, and S. Banerjee. Precipitation and room temperature deformation behaviour of Inconel 718. In E.A. Loria, editor, *Proceedings of the International Symposium on Superalloys 718, 625, 706 and Various Derivatives*, pages 419–440. The Minerals, Metals & Materials Society, Warrendale, PA, 1994.

[78] K. Kusabiraki, T. Tsutsumi, and S. Saji. Effects of cold rolling and annealing on the structure of γ'' precipitates in a Ni-18Cr-16Fe-5Nb-3Mo alloy. *Metallurgical and Materials Transactions A: Physical Metallurgy and Materials Science*, 30(8):1923–1931, 1999.

[79] F.A. Paneth. The discovery and earliest reproductions of the widmanstätten figures. *Geochimica et Cosmochimica Acta*, 18(3-4):176–182, 1960.

[80] J.P. Collier, S.H. Wong, J.K. Tien, J.C. Phillips, and J.K. Tein. Effect of varying Al, Ti, and Nb content on the phase stability of Inconel 718. *Metallurgical Transactions A (Physical Metallurgy and Materials Science)*, 19 A(7):1657–1666, 1988.

[81] B.Z. Hyatt and C.M. Brown. Microstructure and mechanical properties of stress relieved electron beam welded Alloy 625. In E.A. Loria, editor, *Proceedings of the International Symposium on Superalloys 718, 625, 706 and Various Derivatives*, pages 645–656. The Minerals, Metals & Materials Society, Warrendale, PA, 2001.

[82] F.P. Cone. Observations on the development of delta phase in In718 alloy. In E.A. Loria, editor, *Proceedings of the International Symposium on Superalloys 718, 625, 706 and Various Derivatives*, pages 323–332. The Minerals, Metals & Materials Society, Warrendale, PA, 2001.

[83] J. Cardenas, H. Guajardo, C. Harwood, and J.A. Manriquez. Effects of large reductions and heating temperature-times on grain size control of Alloy 718 rolled rings. In E.A. Loria, editor, *Proceedings of the International Symposium on Superalloys 718, 625, 706 and Various Derivatives*, pages 679–686. The Minerals, Metals & Materials Society, Warrendale, PA, 2005.

[84] J.L. Russell, M.L. Lasonde, and L.A. Jackman. Microstructure development and thermal response of delta processed billet and bar for Alloy 718. In E.A. Loria, editor, *Proceedings of the International Symposium on Superalloys 718, 625, 706 and Various Derivatives*, pages 363–372. The Minerals, Metals & Materials Society, Warrendale, PA, 2005.

[85] H.T. Lee and W.H. Hou. Influence of precipitated phase formation on recrystallization behavior of superalloy 718. *Materials Transactions*, 53(7):1334–1342, 2012.

[86] E.O. Hall. The deformation and ageing of mild steel: III Discussion of results. *Proceedings of the Physical Society. Section B*, 64(9):747–753, 1951.

[87] N.J. Petch. The cleavage strength of polycrystals. *Journal of the Iron and Steel Institute*, 174:25–28, 1953.

[88] R.E. Schafrik, D.D. Ward, and J.R. Groh. Application of Alloy 718 in GE aircraft engines: Past, present and next five years. In E.A. Loria, editor, *Proceedings of the International Symposium on Superalloys 718, 625, 706 and Various Derivatives*, pages 1–11. The Minerals, Metals & Materials Society, Warrendale, PA, 2001.

[89] A.W. Dix, J.M. Hyzak, and R.P. Singh. Application of ultra fine grain Alloy 718 forging billet. In S.D. Antolovich, R.W. Stusrud, R.A. MacKay, D.L. Anton, T. Khan, R.D. Kissinger, and D.L. Klarstrom, editors, *Superalloys 1992 (Proceedings of the Seventh International Symposium on Superalloys)*, pages 22–32. The Minerals, Metals & Materials Society, Warrendale, PA, 1992.

[90] D. Gopikrishnra, S.N. Jha, and L.N. Dash. Influence of microstructure on fatigue properties of Alloy 718. In E.A. Loria, editor, *Proceedings of the International Symposium on Superalloys 718, 625, 706 and Various Derivatives*, pages 567–573. The Minerals, Metals & Materials Society, Warrendale, PA, 1997.

[91] E.J. Pickering, H. Mathur, A. Bhowmik, O.M.D.M. Messé, J.S. Barnard, M.C. Hardy, R. Krakow, K. Loehnert, H.J. Stone, and C.M.F. Rae. Grain-boundary precipitation in Allvac 718Plus. *Acta Materialia*, 60(6-7):2757–2769, 2012.

[92] H.J. Penkalla, J. Wosik, H. Fischer, and F. Schubert. Structural isvestigatioivs of candidate materials for turbine disc applications beyond 700 °C. In E.A. Loria, editor, *Proceedings of the International Symposium on Superalloys 718, 625, 706 and Various Derivatives*, pages 279–290. The Minerals, Metals & Materials Society, Warrendale, PA, 2001.

[93] W. Betteridge and J. Heslop. *The Nimonic alloys, and other nickel-base high-temperature alloys.* Edward Arnold, London, UK, second edition, 1974.

[94] R.E. Smallman and R.J. Bishop. *Modern Physical Metallurgy and Materials Engineering: Science, Process, Applications.* Butterworth Heinemann, Oxford, UK, sixth edition, 1999.

[95] R.W. Ross. Rene 100: A sigma free turbine blade alloy. *Journal of Metals*, 19(12):12–14, 1967.

[96] R.A. Hobbs, L. Zhang, C.M.F. Rae, and S. Tin. The effect of ruthenium on the intermediate to high temperature creep response of high refractory content single crystal nickel-base superalloys. *Materials Science and Engineering A*, 489(1-2):65–76, 2008.

[97] A.C. Yeh and S. Tin. Effects of Ru on the high-temperature phase stability of Ni-base single-crystal superalloys. *Metallurgical and Materials Transactions A: Physical Metallurgy and Materials Science*, 37(9):2621–2631, 2006.

[98] M. Simonetti and P. Caron. Role and behaviour of μ phase during deformation of a nickel-based single crystal superalloy. *Materials Science and Engineering A*, 254(1-2):1–12, 1998.

[99] C.M.F. Rae, M.S.A. Karunaratne, C.J. Small, R.W. Broomfield, C.N. Jones, and R.C. Reed. Topologically close packed phases in an experimental rhenium-containing single crystal superalloy. In T.M. Pollock, R.D. Kissinger, K.A. Green, M. McLean, S. Olson, and J.J. Schirra, editors, *Superalloys 2000 (Proceedings of the Ninth International Symposium on Superalloys)*, pages 767–776. The Minerals, Metals & Materials Society, Warrendale, PA, 2000.

[100] A. Mitchell, A.J. Schmalz, C. Schvezov, and S.L. Cockcroft. The precipitation of primary carbides in Alloy 718. In E.A. Loria, editor, *Proceedings of the International Symposium on Superalloys 718, 625, 706 and Various Derivatives*, pages 65–78. The Minerals, Metals & Materials Society, Warrendale, PA, 1994.

[101] A. Mitchell and T. Wang. Solidification and precipitation in IN718. In E.A. Loria, editor, *Proceedings of the International Symposium on Superalloys 718, 625, 706 and Various Derivatives*, pages 81–90. The Minerals, Metals & Materials Society, Warrendale, PA, 2001.

[102] S. Tin, T.M. Pollock, and W.T. King. Carbon additions and grain defect formation in high refractory nickel-base single crystal superalloys. In T.M. Pollock, R.D. Kissinger, K.A. Green, M. McLean, S. Olson, and J.J. Schirra, editors, *Superalloys 2000 (Proceedings of the Ninth International Symposium on Superalloys)*, pages 201–210. The Minerals, Metals & Materials Society, Warrendale, PA, 2000.

[103] R.J. Grice, R.G. Faulkner, and Y. Yin. Novel hafnium containing steels for power generation. *Ironmaking & Steelmaking*, 36(3):170–175, 2009.

[104] Y.F. Yin and R.G. Faulkner. Creep damage and grain boundary precipitation in power plant metals. *Materials Science and Technology*, 21(11):1239–1246, 2005.

[105] H.L. Eiselstein and D.J. Tillack. The invention and definition of Alloy 625. In E.A. Loria, editor, *Proceedings of the International Symposium on Superalloys 718, 625 and Various Derivatives*, pages 1–14. The Minerals, Metals & Materials Society, Warrendale, PA, 1991.

[106] J. Wang, L. Zhou, X. Qin, L. Sheng, J. Hou, and J. Guo. Primary MC decomposition and its effects on the rupture behaviors in hot-corrosion resistant Ni-based superalloy K444. *Materials Science and Engineering A*, 553:14–21, 2012.

[107] G. Lvov, V.I. Levit, and M.J. Kaufman. Mechanism of primary MC carbide decomposition in Ni-base superalloys. *Metallurgical and Materials Transactions A: Physical Metallurgy and Materials Science*, 35A(6):1669–1679, 2004.

[108] T. Garosshen and G. McCarthy. Low temperature carbide precipitation in a nickel base superalloy. *Metallurgical and Materials Transactions A*, 16:1213–1223, 1985.

[109] G. Bai, J. Li, R. Hu, T. Zhang, H. Kou, and H. Fu. Effect of thermal exposure on the stability of carbides in Ni-Cr-W based superalloy. *Materials Science and Engineering A*, 528(6):2339–2344, 2011.

[110] R. Reed, M. Jackson, and Y. Na. Characterization and modeling of the precipitation of the sigma phase in Udimet 720 and Udimet 720Li. *Metallurgical and Materials Transactions A*, 30:521–533, 1999.

[111] Q.Z. Chen, C.N. Jones, and D.M. Knowles. The grain boundary microstructures of the base and modified RR 2072 bicrystal superalloys and their effects on the creep properties. *Materials Science and Engineering A*, 385(1-2):402–418, 2004.

[112] L.Z. He, Q. Zheng, X.F. Sun, H.R. Guan, Z.Q. Hu, A.K. Tieu, C. Lu, and H.T. Zhu. Effect of carbides on the creep properties of a Ni-base superalloy M963. *Materials Science and Engineering A*, 397(1-2):297–304, 2005.

[113] K. Zhao, Y.H. Ma, and L.H. Lou. Improvement of creep rupture strength of a liquid metal cooling directionally solidified nickel-base superalloy by carbides. *Journal of Alloys and Compounds*, 475(1-2):648–651, 2009.

[114] A.K. Koul and R. Castillo. Assessment of service induced microstructural damage and its rejuvenation in turbine blades. *Metallurgical Transactions A*, 19(8):2049–2066, 1988.

[115] Y. Xu, Q. Jin, X. Xiao, X. Cao, G. Jia, Y. Zhu, and H. Yin. Strengthening mechanisms of carbon in modified nickel-based superalloy Nimonic 80A. *Materials Science and Engineering A*, 528(13-14):4600–4607, 2011.

[116] R. Hu, G. Bai, J. Li, J. Zhang, T. Zhang, and H. Fu. Precipitation behavior of grain boundary $M_{23}C_6$ and its effect on tensile properties of Ni-Cr-W based superalloy. *Materials Science and Engineering A*, 548(0):83–88, 2012.

[117] Y. Zheng, S. Li, L. Zheng, and Y. Han. Abnormal phases in high W content nickel base superalloys and phase control. In *Superalloys 2004 (Proceedings of the Tenth International Symposium on Superalloys)*, pages 743–751. The Minerals, Metals & Materials Society, Warrendale, PA, 2004.

[118] J.R. Davis. *Heat-Resistant Materials.* ASM Specialty Handbook. ASM International, Materials Park, OH, 1997.

[119] W.L. Clarke Jr. and C.W. Titus. Long-time stability of Hastelloy X. In *ASM Metal Congress*, Cleveland, OH, 1967. ASM International.

[120] Q. Wu, H. Song, R.W. Swindeman, J.P. Shingledecker, and V.K. Vasudevan. Microstructure of long-term aged IN617 Ni-base superalloy. *Metallurgical and Materials Transactions A*, 39:2569–2585, 2008.

[121] S. Zhang and D. Zhao. *Aerospace Materials Handbook.* Advances in Materials Science and Engineering Series. CRC Press, Boca Raton, FL, 2012.

[122] M. Raghavan, R.R. Mueller, C.F. Klein, and G.A. Vaughn. Carbides in Ni-Cr-Mo system. *Scripta Metallurgica*, 17(10):1189–1194, 1983.

[123] L. Ratke and P.W. Voorhees. *Growth and Coarsening: Ostwald Ripening in Material Processing.* Engineering Materials. Springer-Verlag, Berlin, Germany, 2002.

[124] I.S. Servi and D. Turnbull. Thermodynamics and kinetics of precipitation in the copper-cobalt system. *Acta Metallurgica*, 14:161–169, 1966.

[125] E.A Trillo and L.E Murr. A TEM investigation of $M_{23}C_6$ carbide precipitation behaviour on varying grain boundary misorientations in 304 stainless steels. *Journal of Materials Science*, 33:1263–1271, 1998.

[126] R. Stickler and A. Vinckier. *Memoires Scientifiques Revue de Metallurgie*, 60:489–502, 1963.

[127] M.A. Mangan, M.V. Kral, and G. Spanos. Correlation between the crystallography and morphology of proeutectoid widmansttten cementite precipitates. *Acta Materialia*, 47(17):4263–4274, 1999.

[128] R. Gomez-Ramirez and G. Pound. Nucleation of a second solid phase along dislocations. *Metallurgical and Materials Transactions B*, 4:1563–1570, 1973.

[129] F.R.N. Nabarro. *Dislocations In Solids: The Elastic Theory*. North-Holland Pub. Co., New York, NY, 1979.

[130] C.C. Dollins. Nucleation on dislocations. *Acta Metallurgica*, 18(11):1209–1215, 1970.

[131] M. Hillert. Diffusion and interface control of reactions in alloys. *Metallurgical and Materials Transactions A*, 6:5–19, 1975.

[132] R.W. Cahn and P. Haasen. *Physical Metallurgy*. Elsevier Science, London, UK, 1996.

[133] H.I. Aaronson. Decomposition of austenite by diffusional processes. *Interscience*, pages 387–548, 1962.

[134] H.I. Aaronson, C. Laird, and K Kinsman. *Phase Transformations*. American Society of Metals, Materials Park, OH, 1970.

[135] C. Wagner. Theory of precipitate change by redissolution. *Z. Electrochem*, 65(7-8):581–591, 1961.

[136] I.M. Lifshitz and V.V. Slyozov. The kinetics of precipitation from supersaturated solid solutions. *Journal of Physics and Chemistry of Solids*, 19(1-2):35–50, 1961.

[137] H. Kirchner. Coarsening of grain-boundary precipitates. *Metallurgical and Materials Transactions B*, 2:2861–2864, 1971.

[138] H.A. Calderon, P.W. Voorhees, J.L. Murray, and G. Kostorz. Ostwald ripening in concentrated alloys. *Acta Metallurgica et Materialia*, 42(3):991–1000, 1994.

[139] J. Kolts, J.B.C. Wu, and A.I. Asphahani. Highly alloyed austenitic materials for corrosion service. *Metal progress*, 124(4):25–29, 32, 1983.

[140] J.R. Davis and Asm International Handbook Committee. *Nickel, Cobalt, and Their Alloys*. Asm Specialty Handbook. ASM International, Materials Park, OH, 2000.

[141] W.F. Savage, E.F. Nippes, and G.M. Goodwin. Effect of minor elements on hot-cracking tendencies of Inconel 600. *Welding Journal*, 56(8):245s–253s, 1977.

[142] T.J. Morrison, C.S. Shira, and L.A. Weisenberg. The influence of minor elements on Alloy 718 weld microfissuring. In *Effect of Minor Elements on the Weldability of High Nickel Alloys*, pages 47–67, New York, NY, 1967. Welding Research Council Symposium.

[143] G.D. Smith, S.D. Kiser, J.R. Crum, and C.S. Tassen. Nickel base alloys improve corrosion resistance. *The International Journal of Hydrocarbon Engineering*, 5(2):7, 1999.

[144] J.K. Chakravartty, J.B. Singh, and M. Sundararaman. Microstructural and mechanical properties of service exposed Alloy 625 ammonia cracker tube removed after 100 000h. *Materials Science and Technology*, 28(6):702–710, 2012.

[145] J. Crum, G. Smith, and H. Flower. Resistance of automotive exhaust flexible coupling alloys to hot salt attack, stress corrosion cracking and high temperature embrittlement. *SAE Technical Paper 1999-01-0372*, 1999.

[146] J.M. Rakowski, C.P. Stinner, M. Lipschutz, and J.P. Montague. The use and performance of wrought 625 Alloy in primary surface recuperators for gas turbine engines. In E.A. Loria, editor, *Proceedings of the International Symposium on Superalloys 718, 625, 706 and Various Derivatives*, pages 271–286. The Minerals, Metals & Materials Society, Warrendale, PA, 2005.

[147] F. Curá, A. Mura, and R. Sesana. Aging characterization of metals for exhaust systems. *International Journal of Automotive Technology*, 13(4):629–636, 2012.

[148] M. Kutz. *Handbook of Materials Selection.* John Wiley & Sons, New York, NY, 2002.

[149] Special Metals Corporation, New York, NY. *Corrosion-resistant alloys for oil and gas production*, 2003. Publication Number SMC-013. Available from `http://www.specialmetals.com/documents/CRAs%20for%20Oil%20and%20Gas.pdf`.

[150] D. Capitanescu. Alloy 625 weld overlays for offshore and onshore projects. In E.A. Loria, editor, *Proceedings of the International Symposium on Superalloys 718, 625 and Various Derivatives*, pages 821–835. The Minerals, Metals & Materials Society, Warrendale, PA, 1991.

[151] G.Y. Lai. *High-Temperature Corrosion and Materials Applications.* ASM International, Materials Park, OH, 2007.

[152] G.D. Smith, D.J. Tillack, and S.J. Patel. Alloy 625 - Impressive Past/Significant Presence/Awesome Future. In E.A. Loria, editor, *Proceedings of the International Symposium on Superalloys 718, 625, 706 and Various Derivatives*, pages 35–46. The Minerals, Metals & Materials Society, Warrendale, PA, 2001.

[153] A. Boubault, B. Claudet, O. Faugeroux, G. Olalde, and J.J. Serra. A numerical thermal approach to study the accelerated aging of a solar absorber material. *Solar Energy*, 86(11):3153–3167, 2012.

[154] J.E. Pacheco and Sandia National Laboratories. Final test and evaluation results from the solar two project, 2002. Report SAND2002-0120. Available from `http://www.samsi.info/sites/default/files/Solar.pdf`.

[155] R. Bajaj, W.J. Mills, M.R. Lebo, B.Z. Hyatt, and M.G. Burke. Irradiation-assisted stress corrosion cracking of hth Alloy x-750 and Alloy 625. In *Seventh International symposium on environmental degradation of materials in nuclear power plants: Water reactors*, pages 1093–1107, Breckenridge, CO, 1995. The Minerals, Metals & Materials Society.

[156] United States Nuclear Regulatory Commission. Document ML081980032. Available from `http://pbadupws.nrc.gov/docs/ML0819/ML081980032.pdf`.

[157] United States Nuclear Regulatory Commission. Document ML040260481. Available from `http://pbadupws.nrc.gov/docs/ML0402/ML040260481.pdf`.

[158] United States Nuclear Regulatory Commission. Document ML040300624. Available from `http://pbadupws.nrc.gov/docs/ML0403/ML040300624.pdf`.

[159] H.G. Kim. The design characteristics of advanced power reactor 1400. Available from `http://www-pub.iaea.org/MTCD/publications/PDF/P1500_CD_Web/htm/pdf/topic3/3S09_Hangon%20Kim.pdf`.

[160] United States Nuclear Regulatory Commission. Document ML072830016. Available from `http://pbadupws.nrc.gov/docs/ML0728/ML072830016.pdf`.

[161] United States Nuclear Regulatory Commission. Document ML103410351. Available from `http://pbadupws.nrc.gov/docs/ML1034/ML103410351.pdf`.

[162] Electrical Power Research Institute. Critical issues report and roadmap for the advanced radiation-resistant materials program, 2012. Available from `http://www.epri.com/abstracts/Pages/ProductAbstract.aspx?ProductId=000000000001026482`.

[163] United States Department of Energy. A Technology Roadmap for Generation IV Nuclear Energy Systems, Document GIF-002-00, 2002. Available from `http://nuclear.energy.gov/genIV/documents/gen_iv_roadmap.pdf`.

[164] United States Nuclear Regulatory Commission. Document ML081400680. Available from `http://pbadupws.nrc.gov/docs/ML0814/ML081400680.pdf`.

[165] Oak Ridge National Laboratory W.R. Corwin. Updated Generation IV Reactors Integrated Materials Technology Program Plan Revision 1, Document ORNL/TM-2003/244/R1 , 2004. Available from `http://nuclear.inl.gov/deliverables/docs/intg-matls-plan-rev-1a.pdf`.

[166] M. Kondo, T. Nagasaka, T. Muroga, A. Sagara, N. Noda, Q. Xu, D. Ninomiya, N. Masaru, A. Suzuki, and T. Terai. High performance corrosion resistance of nickel-based alloys in molten salt flibe. *Fusion Science and Technology*, 56(1):190–194, 2009.

[167] M. Köhler. Effect of the elevated-temperature-precipitation in Alloy 625 on properties and microstructure. In E.A. Loria, editor, *Proceedings of the International Symposium on Superalloys 718, 625 and Various Derivatives*, pages 363–374. The Minerals, Metals & Materials Society, Warrendale, PA, 1991.

[168] M. Köhler and U. Heubner. The effect of final heat treatment and chemical composition on sensitiztation, strength and thermal stability of Alloy 625. In E.A. Loria, editor, *Proceedings of the International Symposium on Superalloys 718, 625, 706 and Various Derivatives*, pages 795–803. The Minerals, Metals & Materials Society, Warrendale, PA, 1997.

[169] J. Mittra, S. Banerjee, R. Tewari, and G.K. Dey. Fracture behavior of Alloy 625 with different precipitate microstructures. *Materials Science and Engineering A*, 574:86–93, 2013.

[170] J.M. Corrieu, C. Vemot-Loier, and F. Cortial. Influence of heat treatments on corrosion behaviour of Alloy 625 forged rod. In E.A. Loria, editor, *Proceedings of the International Symposium on Superalloys 718, 625, 706 and Various Derivatives*, pages 795–806. The Minerals, Metals & Materials Society, Warrendale, PA, 1994.

[171] M.A. Shaikh, M. Ahmad, K.A. Shoaib, J.I. Akhter, and M. Iqbal. Precipitation hardening in Inconel* 625. *Materials Science and Technology*, 16(2):129–132, 2000.

[172] R. Cozar and A. Pineau. Influence of coherency strains on precipitate shape in a Fe-Ni-Ta alloy. *Scripta Metallurgica*, 7(8):851–854, 1973.

[173] G.F. Van der Voort, J.W. Bowman, and R.B. Frank. Microstructural characterization of custom age 625 plus alloy. In E.A. Loria, editor, *Proceedings of the International Symposium on Superalloys 718, 625, 706 and Various Derivatives*, pages 489–498. The Minerals, Metals & Materials Society, Warrendale, PA, 1994.

[174] M. Sundararaman, R. Kishore, and P. Mukhopadhyay. Some aspects of the heterogeneous precipitation of the metastable γ'' phase in Alloy 625. In E.A. Loria, editor, *Proceedings of the International Symposium on Superalloys 718, 625, 706 and Various Derivatives*, pages 405–418. The Minerals, Metals & Materials Society, Warrendale, PA, 1994.

[175] H.C. Pai and M. Sundararaman. A comparison of the precipitation kinetics of γ'' particles in virgin and re-solutioned Alloy 625. In E.A. Loria, editor, *Proceedings of the International Symposium on Superalloys 718, 625, 706 and Various Derivatives*, pages 487–495. The Minerals, Metals & Materials Society, Warrendale, PA, 2005.

[176] J.F. Radavich and A. Fort. Effects of long-time exposure in Alloy 625 at 1200 °F 1400 °F and 1600 °F. In E.A. Loria, editor, *Proceedings of the International Symposium on Superalloys 718, 625, 706 and Various Derivatives*, pages 635–647. The Minerals, Metals & Materials Society, Warrendale, PA, 1994.

[177] G. Shen, J. Radavich, X. Xie, and B. Lindsley. The effects of processing on stability of Alloy 718. In T.M. Pollock, R.D. Kissinger, K.A. Green, M. McLean, S. Olson, and J.J. Schirra, editors, *Superalloys 2000 (Proceedings of the Ninth International Symposium on Superalloys)*, pages 445–448. The Minerals, Metals & Materials Society, Warrendale, PA, 2000.

[178] C. Thomas and P. Tait. The performance of Alloy 625 in long-term intermediate temperature applications. *International Journal of Pressure Vessels and Piping*, 59(1-3):41–49, 1994.

[179] M. Sundararaman, L. Kumar, G. Eswara Prasad, P. Mukhopadhyay, and S. Banerjee. Precipitation of an intermetallic phase with Pt_2Mo-type structure in Alloy 625. *Metallurgical and Materials Transactions A: Physical Metallurgy and Materials Science*, 30(1):41–52, 1999.

[180] M. Sundararaman, P. Mukhopadhyay, and S. Banerjee. Influence of intermetallic phase precipitation during prolonged service in Alloy 625 on its properties. In E.A. Loria, editor, *Proceedings of the International Symposium on Superalloys 718, 625, 706 and Various Derivatives*, pages 367–378. The Minerals, Metals & Materials Society, Warrendale, PA, 2001.

[181] M. Sundararaman, P. Mukhopadhyay, and S. Banerjee. Carbide precipitation in nickel base superalloys 718 and 625 and their effect on mechanical properties. In E.A. Loria, editor, *Proceedings of the International Symposium on Superalloys 718, 625, 706 and Various Derivatives*, pages 367–378. The Minerals, Metals & Materials Society, Warrendale, PA, 1997.

[182] H.K. Kohl and K. Peng. Thermal stability of the superalloys Inconel 625 and Nimonic 86. *Journal of Nuclear Materials*, 101(3):243–250, 1981.

[183] C. Vernot-Loier and F. Cortial. Influence of heat treatments on microstructure, mechanical properties and corrosion behaviour of Alloy 625 forged rod. In E.A. Loria, editor, *Proceedings of the International Symposium on Superalloys 718, 625 and Various Derivatives*, pages 409–422. The Minerals, Metals & Materials Society, Warrendale, PA, 1991.

[184] M. Sundararaman, P. Mukhopadhyay, and S. Banerjee. Carbide precipitation in nickel base superalloys 718 and 625 and their effect on mechanical properties. In E.A. Loria, editor, *Proceedings of the International Symposium on Superalloys 718, 625, 706 and Various Derivatives*, pages 367–378. The Minerals, Metals & Materials Society, Warrendale, PA, 1997.

[185] W.D. Cao and R.L. Kennedy. Thermal stability of alloys 718 and Allvac 718ER. In E.A. Loria, editor, *Proceedings of the International Symposium on Superalloys 718, 625, 706 and Various Derivatives*, pages 455–464. The Minerals, Metals & Materials Society, Warrendale, PA, 2001.

[186] X. Liang, Y. Yang, G. Zhang, and L. Jin. The effects of 650°C long exposure on Alloy 718 da disk. In E.A. Loria, editor, *Proceedings of the International Symposium on Superalloys 718, 625, 706 and Various Derivatives*, pages 535–541. The Minerals, Metals & Materials Society, Warrendale, PA, 2001.

[187] D.E. Camus, R.A. Jaramillo, J.A. Plybum, and F.S. Suarez. Evolution of microstructure during hot rolling of Inconel alloys 625 and 718. In E.A. Loria, editor, *Proceedings of the International Symposium on Superalloys 718, 625, 706*

and Various Derivatives, pages 291–302. The Minerals, Metals & Materials Society, Warrendale, PA, 1997.

[188] O.R. Myhr, O. Grong, H.G. Fjær, and C.D. Marioara. Modelling of the microstructure and strength evolution in Al-Mg-Si alloys during multistage thermal processing. *Acta Materialia*, 52(17):4997–5008, 2004.

[189] A. Deschamps and Y. Brechet. Influence of predeformation and ageing of an Al-Zn-Mg Alloy-II. modeling of precipitation kinetics and yield stress. *Acta Materialia*, 47(1):293–305, 1998.

[190] L. Wu and W.G. Ferguson. Modelling of precipitation hardening in casting aluminium alloys. *Materials Science Forum*, 618 619:203–206, 2009.

[191] V. Nagarajan, E.J. Palmiere, and C.M. Sellars. New approach for modelling strain induced precipitation of Nb(C,N) in HSLA steels during multipass hot deformation in austenite. *Materials Science and Technology*, 25(9):1168–1174, 2009.

[192] B. Dutta, E.J. Palmiere, and C.M. Sellars. Modelling the kinetics of strain induced precipitation in Nb microalloyed steels. *Acta Materialia*, 49(5):785–794, 2001.

[193] F. Perrard, A. Deschamps, and P. Maugis. Modelling the precipitation of NbC on dislocations in α-Fe. *Acta Materialia*, 55(4):1255–1266, 2007.

[194] J. Aldazabal, C. Garcia-Mateo, and C. Capdevila. Simulation of V(C,N) precipitation in steels allowing for local concentration fluctuations. *Materials Transactions*, 47(11):2732–2736, 2006.

[195] P. Maugis and M. Gouné. Kinetics of vanadium carbonitride precipitation in steel: A computer model. *Acta Materialia*, 53(12):3359–3367, 2005.

[196] E. Clouet and F. Soisson. Atomic simulations of diffusional phase transformations [Simulations atomiques des transformations de phases contrôlées par la diffusion]. *Comptes Rendus Physique*, 11(3-4):226–235, 2010.

[197] P. Fratzl, O. Penrose, and J.L. Lebowitz. Modeling of phase separation in alloys with coherent elastic misfit. *Journal of Statistical Physics*, 95(5-6):1429–1503, 1999.

[198] W.M. Young and E.W. Elcock. Monte carlo studies of vacancy migration in binary ordered alloys: I. *Proceedings of the Physical Society*, 89(3):735–746, 1966.

[199] T. Garnier, A. Finel, Y. Le Bouar, and M. Nastar. Simulation of Alloy thermodynamics: From an atomic to a mesoscale Hamiltonian. *Physical Review B*, 86:054103, 2012.

[200] A. Deschamps and M. Perez. Mesoscopic modelling of precipitation: A tool for extracting physical parameters of phase transformations in metallic alloys

[Modélisation mésoscopique de la précipitation: Un outil pour extraire les paramétres physiques des transformations de phase dans des alliages métalliques]. *Comptes Rendus Physique*, 11(3-4):236–244, 2010.

[201] J. Ženíšek, J. Svoboda, E. Kozeschnik, and F.D. Fischer. A combined cluster dynamics/kinetic monte carlo model for precipitate nucleation in interstitial/substitutional alloys. *Modelling and Simulation in Materials Science and Engineering*, 16(7), 2008.

[202] P. Guyot, J. Lepinoux, and C. Sigli. Application of cluster dynamics modeling to the precipitation in aluminum alloys. *International Journal of Materials Research*, 100(10):1440–1445, 2009.

[203] E. Clouet, M. Nastar, A. Barbu, C. Sigli, and G. Martin. Precipitation in Al-Zr-Sc alloys: A comparison between kinetic Monte Carlo, cluster dynamics and classical nucleation theory. In J.M. Howe, D.E. Laughlin, J.K. Lee, U. Dahmen, and W.A. Soffa, editors, *Proceedings of an International Conference on Solid-Solid Phase Transformations in Inorganic Materials*, volume 2, pages 683–703. 2005.

[204] A. Barbu and E. Clouet. Cluster dynamics modeling of materials: Advantages and limitations. *Diffusion and Defect Data Pt.B: Solid State Phenomena*, 129:51–58, 2007.

[205] E. Clouet. Modeling of nucleation processes. In D.U. Furrer and S.L. Semiatin, editors, *Fundamentals of Modeling for Metals Processing*, volume 22A, pages 203–219. ASM International, Materials Park, OH, 1997.

[206] G. Martin. Reconciling the classical nucleation theory and atomic scale observations and modeling. *Advanced Engineering Materials*, 8(12):1231–1236, 2006.

[207] H. Zapolsky, J. Boisse, R. Patte, and N. Lecoq. Phase field simulation of coarsening kinetics in Al-Sc and Al-Sc-Zr alloys. In M. Palm, B.P. Bewlay, Y.H. He, M. Takeyama, and J.M.K. Wiezorek, editors, *Materials Research Society Symposium Proceedings*, volume 1128, pages 549–554. Cambridge University Press, Cambridge, UK, 2008.

[208] N. Masquelier, H. Zapolsky, W. Lefebvre, S.G. Fries, R. Patte, and P. Pareige. Precipitation kinetics study of Al-Zr-X (Sc or Ti) alloys by phase field simulations and atom probe tomography. *Diffusion and Defect Data Pt.B: Solid State Phenomena*, 172-174:869–874, 2011.

[209] V. Fallah, J. Stolle, N. Ofori-Opoku, S. Esmaeili, and N. Provatas. Phase-field crystal modeling of early stage clustering and precipitation in metal alloys. *Physical Review B - Condensed Matter and Materials Physics*, 86(13), 2012.

[210] R. Rettig and R.F. Singer. Numerical modelling of precipitation of topologically close-packed phases in nickel-base superalloys. *Acta Materialia*, 59(1):317–327, 2011.

[211] W. Wang, J.L. Murray, S.Y. Hu, L.Q. Chen, and H. Weiland. Modeling of plate-like precipitates in aluminum alloys-comparison between phase field and cellular automaton methods. *Journal of Phase Equilibria and Diffusion*, 28(3):258–264, 2007.

[212] I. Steinbach, F. Pezzolla, B. Nestler, M. Seeßelberg, R. Prieler, G.J. Schmitz, and J.L.L. Rezende. A phase field concept for multiphase systems. *Physica D: Nonlinear Phenomena*, 94(3):135–147, 1996.

[213] Q. Bronchard, Y. Le Bouar, and A. Final. Quantitative phase field modeling of precipitation processes. *Advanced Engineering Materials*, 8(12):1245–1248, 2006.

[214] J.C. Wang, M. Osawa, T. Yokokawa, H. Harada, and M. Enomoto. Modeling the microstructural evolution of Ni-base superalloys by phase field method combined with Calphad and CVM. *Computational Materials Science*, 39(4):871–879, 2007.

[215] J. Svoboda, F.D. Fischer, P. Fratzl, and E. Kozeschnik. Modelling of kinetics in multi-component multi-phase systems with spherical precipitates I: Theory. *Materials Science and Engineering A*, 385(1-2):166–174, 2004.

[216] E. Kozeschnik, J. Svoboda, P. Fratzl, and F.D. Fischer. Modelling of kinetics in multi-component multi-phase systems with spherical precipitates II: Numerical solution and application. *Materials Science and Engineering A*, 385(1-2):157–165, 2004.

[217] E. Kozeschnik, J. Svoboda, and F.D. Fischer. Modified evolution equations for the precipitation kinetics of complex phases in multi-component systems. *Calphad: Computer Coupling of Phase Diagrams and Thermochemistry*, 28(4):379–382, 2004.

[218] J.S. Langer and A.J. Schwartz. Kinetics of nucleation in near-critical fluids. *Physical Review A*, 21:948–958, 1980.

[219] R. Kampmann and R. Wagner. Kinetics of precipitation in metastable binary alloys - theory and application to Cu-1.9at% Ti and Ni-14at% Al. In P. Hassen, editor, *Decomposition of alloys, the early stages: Proceedings of the 2nd Acta-Scripta Metallurgica Conference.*, pages 91–103. Pergamon Press, Oxford, UK, 1984.

[220] O.R. Myhr and O. Grong. Modelling of non-isothermal transformations in alloys containing a particle distribution. *Acta Materialia*, 48(7):1605–1615, 2000.

[221] M. Perez, M. Dumont, and D. Acevedo-Reyes. Implementation of classical nucleation and growth theories for precipitation. *Acta Materialia*, 56(9):2119–2132, 2008.

[222] M. Perez, M. Dumont, and D. Acevedo-Reyes. Corrigendum to "Implementation of classical nucleation and growth theories for precipitation" [Acta Materialia 56 (2008) 2119-2132]. *Acta Materialia*, 57:1318–1318, 2009.

[223] S.N. Samaras. Modelling of microstructure evolution during precipitation processes: A population balance approach of the KWN model. *Modelling and Simulation in Materials Science and Engineering*, 14(8):1271–1292, 2006.

[224] Q. Du, W.J. Poole, and M.A. Wells. A mathematical model coupled to Calphad to predict precipitation kinetics for multicomponent aluminum alloys. *Acta Materialia*, 60(9):3830–3839, 2012.

[225] L. Wu and W.G. Ferguson. Modeling of particle size distribution (PSD) during the ageing process: A modified KWN model. *International Journal of Modern Physics C*, 20(7):1113–1119, 2009.

[226] J.D. Robson. Modelling the evolution of particle size distribution during nucleation, growth and coarsening. *Materials Science and Technology*, 20(4):441–448, 2004.

[227] E. Hersent, J.H. Driver, D. Piot, and C. Desrayaud. Integrated modelling of precipitation during friction stir welding of 2024-T3 aluminium alloy. *Materials Science and Technology*, 26(11):1345–1352, 2010.

[228] A. Katsman, S. Cohen, and M. Bamberger. Modeling of precipitation hardening in Mg-based alloys. *Journal of Materials Science*, 42(16):6996–7003, 2007.

[229] L.M. Cheng, E.B. Hawbolt, and T.R. Meadowcroft. Modeling of AlN precipitation in low carbon steels. *Scripta Materialia*, 41(6):673–678, 1999.

[230] M. Perez and A. Deschamps. Microscopic modelling of simultaneous two-phase precipitation: Application to carbide precipitation in low-carbon steels. *Materials Science and Engineering A*, 360(1-2):214–219, 2003.

[231] M. Perrier, A. Deschamps, O. Bouaziz, Y. Brechet, F. Danoix, F. De Geuser, P. Donnadieu, K. Hoummada, and P. Maugis. Characterization and modeling of precipitation kinetics in a Fe-Si-Ti alloy. *Metallurgical and Materials Transactions A: Physical Metallurgy and Materials Science*, 43(13):4999–5008, 2012.

[232] C. Sommitsch, E. Kozeschnik, G. Wasle, and B. Buchmayr. A precipitation model for multi-component multi-phase systems in nickel-base superalloys. Available from `https://online.unileoben.ac.at/mu_online/voe_main2.getVollText?pDocumentNr=6523&pCurrPk=8234`.

[233] W.A. Johnson and R.F. Mehl. Reaction kinetics in processes of nucleation and growth. *Transactions of the American Institute of Mining and Metallurgical Engineers*, 135:396–415, 1939.

[234] M. Avrami. Kinetics of phase change. I General theory. *The Journal of Chemical Physics*, 7(12):1103–1112, 1939.

[235] A.N. Kolmogorov. On the statistical theory of the crystallization of metals. *Bulletin of the Academy of Sciences of the USSR, Mathematics Series*, 1:355–359, 1937.

[236] M. Fanfoni and M. Tomellini. The Johnson-Mehl-Avrami-Kohnogorov model: A brief review. *Il Nuovo Cimento D*, 20(7-8):1171–1182, 1998.

[237] S. Esmaeili, D.J. Lloyd, and W.J. Poole. A yield strength model for the Al-Mg-Si-Cu Alloy AA6111. *Acta Materialia*, 51(8):2243–2257, 2003.

[238] S. Sarkar and M. Militzer. Microstructure evolution model for hot strip rolling of Nb-Mo microalloyed complex phase steel. *Materials Science and Technology*, 25(9):1134–1146, 2009.

[239] K.G.F. Janssens, D. Raabe, E. Kozeschnik, M.A. Miodownik, and B. Nestler. *Computational Materials Engineering: An Introduction to Microstructure Evolution*. Elsevier Science, London, UK, 2010.

[240] L. Onsager. Reciprocal relations in irreversible processes. I. *Physical Review*, 37(4):405–426, 1931.

[241] L. Onsager. Reciprocal relations in irreversible processes. II. *Physical Review*, 38(12):2265–2279, 1931.

[242] MatCalc Engineering, Vienna, Austria. *MatCalc - The Materials Calculator*. (`http://matcalc.tuwien.ac.at/`).

[243] E. Kozeschnik, J. Svoboda, and F.D. Fischer. Shape factors in modeling of precipitation. *Materials Science and Engineering A*, 441(1-2):68–72, 2006.

[244] J. Svoboda, F.D. Fischer, and P.H. Mayrhofer. A model for evolution of shape changing precipitates in multicomponent systems. *Acta Materialia*, 56(17):4896–4904, 2008.

[245] E. Kozeschnik, J. Svoboda, R. Radis, and F.D. Fischer. Mean-field model for the growth and coarsening of stoichiometric precipitates at grain boundaries. *Modelling and Simulation in Materials Science and Engineering*, 18(1), 2010.

[246] R. Radis and E. Kozeschnik. Kinetics of AlN precipitation in microalloyed steel. *Modelling and Simulation in Materials Science and Engineering*, 18(5), 2010.

[247] L. Whitmore, H. Leitner, E. Povoden-Karadeniz, R. Radis, and M. Stockinger. Transmission electron microscopy of single and double aged 718Plus superalloy. *Materials Science and Engineering A*, 534:413–423, 2012.

[248] G.A. Zickler, R. Radis, R. Schnitzer, E. Kozeschnik, M. Stockinger, and H. Leitner. The precipitation behavior of superalloy ATI Allvac 718Plus. *Advanced Engineering Materials*, 12(3):176–183, 2010.

[249] R. Radis, M. Schaffer, M. Albu, G. Kothleitner, P. Pölt, and E. Kozeschnik. Multimodal size distributions of γ' precipitates during continuous cooling of Udimet 720 Li. *Acta Materialia*, 57(19):5739–5747, 2009.

[250] J. Svoboda and I. Turek. On diffusion-controlled evolution of closed solid-state thermodynamic systems at constant temperature and pressure. *Philosophical Magazine B: Physics of Condensed Matter; Electronic, Optical and Magnetic Properties*, 64(6):749–759, 1991.

[251] J.D. Eshelby. The determination of the elastic field of an ellipsoidal inclusion and related problems. *Proceedings of the Royal Society of London. Series A, Mathematical and Physical Sciences*, 241(1226):376–396, 1957.

[252] F.D. Fischer and H.J. Böhm. On the role of the transformation eigenstrain in the growth or shrinkage of spheroidal isotropic precipitations. *Acta Materialia*, 53(2):367–374, 2005.

[253] F.D. Fischer, H.J. Böhm, E.R. Oberaigner, and T. Waitz. The role of elastic contrast on the strain energy and the stress state of a spheroidal inclusion with a general eigenstrain state. *Acta Materialia*, 54(1):151–156, 2006.

[254] C. Zener. Theory of growth of spherical precipitates from solid solution. *Journal of Applied Physics*, 20(10):950–953, 1949.

[255] K.C. Russell. Phase transformations. In H.I. Aaronson, editor, *Conference proceedings of the American Society for Metals*, pages 219–267. American Society for Metals, Metals Park, OH, USA, 1970.

[256] R. Becker and W. Döring. Kinetische behandlung der keimbildung in übersättigten dämpfen [Kinetic treatment of nucleation in supersaturated vapors]. *Annalen der Physik*, 416(8):719–752, 1935.

[257] J.W. Christian. *The Theory of Transformations in Metals and Alloys Part 1*. Pergamon Press, Oxford, UK, 1975.

[258] J. Lothe. Simplified considerations of the onsager symmetry in the general diffusion equation of nucleation theory. *The Journal of Chemical Physics*, 45(7):2678–2680, 1966.

[259] L. Onsager and S. MacHlup. Fluctuations and irreversible processes. *Physical Review*, 91(6):1505–1512, 1953.

[260] J.B. Zeldovich. Theory of new phase formation: Cavitation. *Acta Physicochimica*, 18:1–22, 1943.

[261] J. Feder, K.C. Russell, J. Lothe, and G.M. Pound. Homogeneous nucleation and growth of droplets in vapours. *Advances in Physics*, 15(57):111–178, 1966.

[262] H.I. Aaronson, editor. *Lectures on the theory of phase transformations*. Metallurgical Society of AIME, New York, NY, 1975.

[263] P. Shewmon. *Diffusion in Solids*. John Wiley & Sons, New York, NY, second edition, 1989.

[264] H. Mehrer. *Diffusion in Solids: Fundamentals, Methods, Materials, Diffusion-controlled Processes.* Springer series in solid-state sciences. Springer-Verlag, Berlin, Germany, 2007.

[265] R. Wagner, R. Kampmann, and P.W. Voorhees. Homogeneous second-phase precipitation. In G. Kostorz, editor, *Phase Transformations in Materials*, pages 309–407. Wiley-VCH, Weinheim, Germany, 2005.

[266] M.S.A. Karunaratne, P. Carter, and R.C. Reed. Interdiffusion in the face-centred cubic phase of the Ni-Re, Ni-Ta and Ni-W systems between 900 and 1300°C. *Materials Science and Engineering A*, 281(1-2):229–233, 2000.

[267] D. Connétable, B. Ter-Ovanessian, and É. Andrieu. Diffusion and segregation of niobium in fcc-nickel. *Journal of Physics Condensed Matter*, 24(9), 2012.

[268] X.J. Liu, H.H. Hu, J.J. Han, Y. Lu, and C.P. Wang. Assessment of the diffusional mobilities in FCC Ni-Nb and FCC Ni-Mo alloys. *Calphad: Computer Coupling of Phase Diagrams and Thermochemistry*, 38:140–145, 2012.

[269] C.Z. Hargather, S.L. Shang, Z.K. Liu, and Y. Du. A first-principles study of self-diffusion coefficients of FCC Ni. *Computational Materials Science*, 86:17–23, 2014.

[270] A.R. Wazzan. Lattice and grain boundary self-diffusion in nickel. *Journal of Applied Physics*, 36(11):3596–3599, 1965.

[271] M.S.A. Karunaratne and R.C. Reed. Interdiffusion of niobium and molybdenum in nickel between 900-1300°C. *Defect and Diffusion Forum*, 237-240(Part 1):420–425, 2005.

[272] M.S.A. Karunaratne, D.C. Cox, and R.C. Reed. Modelling of the microsegregation in CMSX-4 superalloy and its homogenisation during heat treatment. In T.M. Pollock, R.D. Kissinger, K.A. Green, M. McLean, S. Olson, and J.J. Schirra, editors, *Superalloys 2000 (Proceedings of the Ninth International Symposium on Superalloys)*, pages 263–272. The Minerals, Metals & Materials Society, Warrendale, PA, 2000.

[273] S. Dai and W. Liu. First-principles study on the structural, mechanical and electronic properties of δ and γ'' phases in Inconel 718. *Computational Materials Science*, 49(2):414–418, 2010.

[274] Y.C. Lin, S.C. Luo, M.S. Chen, D.G. He, and C.Y. Zhao. Effects of pressure on anisotropic elastic properties and minimum thermal conductivity of $D0_{22}$-Ni_3Nb phase: First-principles calculations. *Journal of Alloys and Compounds*, 688:285–293, 2016.

[275] A. Kaufman, N.J. Hoffman, and H. Lipson. Intensity anomalies in the X-ray diffraction pattern of Ni_3Nb and their relationship to those for martensite. *Scripta Metallurgica*, 3(10):715–719, 1969.

[276] J.P. Collier, A.O. Selius, and J.K. Tien. On developing a microstructurally and thermally stable iron-nickel base superalloy. In S. Reichman, D.N. Duhl, G. Maurer, S. Antolovich, and C. Lund, editors, *Superalloys 1988 (Proceedings of the Sixth International Symposium on Superalloys)*, pages 43–52. The Minerals, Metals & Materials Society, Warrendale, PA, 1988.

[277] D. Mukherji, R. Gilles, B. Barbier, D.Del. Genovese, B. Hasse, P. Strunz, T. Wroblewski, H. Fuess, and J. Rösler. Lattice misfit measurement in Inconel 706 containing coherent γ' and γ'' precipitates. *Scripta Materialia*, 48(4):333–339, 2003.

[278] W.C. Liu, F.R. Xiao, M. Yao, Z.L. Chen, Z.Q. Jiang, and S.G. Wang. Relationship between the lattice constant of Υ phase and the content of δ phase, γ'' and γ' phases in Inconel 718. *Scripta Materialia*, 37(1):59–64, 1997.

[279] H.J. Wagner and A.M. Hall. *Physical Metallurgy of Alloy 718.* DMIC Report 217. Battelle Memorial Institute, Columbus, OH, 1965. Available from `http://www.dtic.mil/dtic/tr/fulltext/u2/466476.pdf`.

[280] A. Sarkar, P. Mukherjee, P. Barat, T. Jayakumar, S. Mahadevan, and S.K. Rai. Lattice misfit measurement in Inconel 625 by X-ray diffraction technique. *International Journal of Modern Physics B*, 22(23):3977–3985, 2008.

[281] C. Slama and M. Abdellaoui. Structural characterization of the aged Inconel 718. *Journal of Alloys and Compounds*, 306(1-2):277–284, 2000.

[282] J.D. Eshelby. The elastic field outside an ellipsoidal inclusion. *Proceedings of the Royal Society of London. Series A, Mathematical and Physical Sciences*, 252(1271):561–569, 1959.

[283] J. Dong, X. Xie, and S. Zhang. Coarsening behavior of γ'' precipitates in modified Inconel 718 superalloy. *Scripta Metallurgica et Materiala*, 33(12):1933–1940, 1995.

[284] M. Fisk, J. Andersson, R. du Rietz, S. Haas, and S. Hall. Precipitate evolution in the early stages of ageing in Inconel 718 investigated using small-angle X-ray scattering. *Materials Science and Engineering A*, 612:202–207, 2014.

[285] Amec Foster Wheeler. London, UK. (`http://www.amecfw.com/`).

[286] H.D. Young, R.A. Freedman, and A.L. Ford. *University Physics.* Pearson Addison Wesley, London, UK, eleventh edition, 2003.

[287] V.E. Lysaght. *Indentation Hardness Testing.* Reinhold Publishing Corporation, New York, NY, 1949.

[288] D. Tabor. *The Hardness of Metals.* Monographs on the physics and chemistry of materials. Oxford University Press, London, UK, 1951.

[289] R.L. Smith and G.E. Sandly. An accurate method of determining the hardness of metals, with particular reference to those of a high degree of hardness. *Proceedings of the Institution of Mechanical Engineers*, 102(1):623–641, 1922.

[290] K.B. Small, D.A. Englehart, and T.A. Christman. Guide to etching specialty alloys. *Advanced Materials & Processes Magazine*, 166(2):32–37, 2008.

[291] J.N. DuPont, J.C. Lippold, and S.D. Kiser. Appendix D: Etching techniques for Ni-base alloys and welds. In *Welding Metallurgy and Weldability of Nickel-Base Alloys*, pages 419–422. John Wiley & Sons, Hoboken, NJ, 2009.

[292] G.F. Van der Voort. Metallography of superalloys. *Industrial Heating Magazine*, pages 40–43, October 2003.

[293] ASTM International, West Conshohocken, PA. *ASTM E112-13, Standard Test Methods for Determining Average Grain Size*, 2013.

[294] G.F. Van der Voort. Examination of some grain size measurment problems. In G.F. Van der Voort, F.J. Warmuth, S.M. Purdy, and A. Szirmae, editors, *Metallography: Past, Present, and Future (75th Anniversary Volume)*, pages 266–294. American Society for Testing and Materials, Philadelphia, PA, 1993.

[295] E.R. Weibel. *Stereological Methods: Theoretical Foundations*, volume 2. Academic Press, London, UK, 1979.

[296] L. de Broglie. *Recherches sur la théorie des quanta [Research on Quantum Theory]*. PhD thesis, Migration-universitéen cours d'affectation, 1924.

[297] R.D. Schoone and E.A. Fischione. Automatic unit for thinning transmission electron microscopy specimens of metals. *Review of Scientific Instruments*, 37(10):1351–1353, 1966.

[298] N. Ünlü. Preparation of high quality al TEM specimens via a double-jet electropolishing technique. *Materials Characterization*, 59(5):547–553, 2008.

[299] E.P. DeGarmo, J.T. Black, and R.A. Kohser. *Materials and Processes in Manufacturing*. John Wiley & Sons, ninth edition, 2003.

[300] D.J. Whitehouse. *Handbook of Surface and Nanometrology*. CRC Press, Boca Raton, FL, second edition, 2011.

[301] PACE Technologies, Tucson, AZ. *Abrasive Grinding Paper*. Available from `http://www.metallographic.com/Brochures/SiCpaper.pdf`.

[302] W.J. McTegart. *The Electrolytic and Chemical Polishing of Metals*. Pergamon Press, London, UK, 1956.

[303] D. Landolt. Fundamental aspects of electropolishing. *Electrochimica Acta*, 32(1):1–11, 1987.

[304] C.C. Irving. Electropolishing stainless steel implants. *ASTM special technical publication*, 859:136–143, 1985.

[305] T.P. Hoar and G.P. Rothwell. The influence of solution flow on anodic polishing. copper in aqueous orthophosphoric acid. *Electrochimica Acta*, 9(2):135–150, 1964.

[306] L. Ponto and D. Landolt. Electropolishing of chromium in phosphoric acid-sulphuric acid electrolytes. *Journal of Applied Electrochemistry*, 17(1):205–214, 1987.

[307] P.E. Fischione. Materials specimen preparation for transmission electron microscopy. Available from `http://www.fischione.com/product_support/PDF/Matpreplo.pdf`.

[308] K.J. Laidler. *Chemical kinetics*. Harper & Row, New York, NY, 1987.

[309] Struers A/S, Copenhagen, Denmark. *TenuPol-5*, November 2013. Document 62180593. Available from `www.struers.com/-/media/Library/Brochures/English/TenuPol-5.pdf`.

[310] S.L. Flegler, J.W. Heckman, and K.L. Klomparens. *Scanning and Transmission Electron Microscopy: An Introduction*. Oxford University Press, New York, NY, 1993.

[311] C. DeVere. *Circuit Concepts: Cathode -Ray Tubes*. Tektronix Inc., Beaverton, OR, 1969.

[312] D.B.A. Williams and C.B. Carter. *Transmission Electron Microscopy: A Textbook for Materials Science. II. Diffraction*. Plenum Press, New York, NY, 1996.

[313] D. Brandon and W.D. Kaplan. *Microstructural Characterization of Materials*. Quantitative Software Engineering Series. John Wiley & Sons, Chichester, UK, 2008.

[314] D.B.A. Williams and C.B. Carter. *Transmission Electron Microscopy: A Textbook for Materials Science. III. Imaging*. Plenum Press, New York, NY, 1996.

[315] D.B.A. Williams and C.B. Carter. *Transmission Electron Microscopy: A Textbook for Materials Science. I. Basics*. Plenum Press, New York, NY, 1996.

[316] L.M. Cruz-Orive. Particle size-shape distributions: The general spheroid problem. I. Mathematical model. *Journal of Microscopy*, 107(3):235–253, 1976.

[317] L.M. Cruz-Orive. Particle size-shape distributions: the general spheroid problem. II. Stochastic model and practical guide. *Journal of Microscopy*, 112(2):153–167, 1978.

[318] J.E. Hilliard. The counting and sizing of particles in transmission microscopy. *Transactions of the Metallurgical Society of America*, 224:906–917, 1962.

[319] J.M.G. Crompton, R.M. Waghorne, and G.B. Brook. The estimation of size distribution and density of precipitates from electron micrographs of thin foils. *British Journal of Applied Physics*, 17(10):1301–1305, 1966.

[320] S.J. Andersen, B. Holme, and C.D. Marioara. Quantification of small, convex particles by TEM. *Ultramicroscopy*, 108(8):750–762, 2008.

[321] D.G. Jensen. Estimation of the size distribution of spherical, disc-like or ellipsoidal particles in thin foils. *Journal of Physics D: Applied Physics*, 28(3):549–558, 1995.

[322] S.A. Saltykov. *Stereometric Metallurgy.* State Publishing House for Metals and Sciences, Moscow, Russia, second edition, 1958.

[323] R.T. DeHoff and F.N. Rhines. *Quantitative microscopy.* McGraw-Hill series in materials science and engineering. McGraw-Hill, New York, NY, 1968.

[324] The MathWorks Inc., Natick, MA. *MATLAB (MATrix LABoratory).* (`http://www.mathworks.com/`).

[325] V.D. Scott and G. Love. Foil thickness measurements in transmission electron microscope. *Materials Science and Technology*, 3(8):600–608, 1987.

[326] M.V. Castro Riglos and A. Tolley. A method for thin foil thickness determination by transmission electron microscopy. *Applied Surface Science*, 254(1 SPEC. ISS.):420–424, 2007.

[327] R. Egerton. *Electron Energy-Loss Spectroscopy in the Electron Microscope.* Springer-Verlag, New York, NY, third edition, 2011.

[328] A. Bardal and K. Lie. Measuring the thickness of aluminum alloy thin foils using electron energy loss spectroscopy. *Materials Characterization*, 44(3):329–343, 2000.

[329] Z. Pan. Contamination line method and comparison of foil thickness measurement methods in transmission electron microscopy. *Acta Metallurgica Sinica Series B, Process Metallurgy & Miscellaneous*, 7(3):175–178, 1994.

[330] G.M. Novotny and A.J. Ardell. Precipitation of Al_3Sc in binary Al−Sc alloys. *Materials Science and Engineering A*, 318(1-2):144–154, 2001.

[331] D. Acevedo-Reyes, M. Perez, C. Verdu, A. Bogner, and T. Epicier. Characterization of precipitates size distribution: Validation of low-voltage STEM. *Journal of Microscopy*, 232(1):112–122, 2008.

[332] M. Kahlweit. Ostwald ripening of precipitates. *Advances in Colloid and Interface Science*, 5(1):1–35, 1975.

[333] L.M. Suave, D. Bertheau, J. Cormier, P. Villechaise, A. Soula, Z. Hervier, F. Hamon, and J. Laigo. Impact of thermomechanical aging on Alloy 625 high temperature mechanical properties. In E. Ott, A. Banik, X. Liu, I. Dempster, K. Heck, J. Andersson, J. Groh, T. Gabb, R. Helmink, and A. Wusatowska-Sarnek, editors, *Proceedings of the 8th International Symposium on Superalloy 718 and Derivatives*, pages 317–331. John Wiley & Sons, Hoboken, NJ, 2014.

[334] N.N. Greenwood and A. Earnshaw. *Chemistry of the Elements.* Pergamon Press, Oxford, UK, 1984.

[335] L. Ferrer, B. Pieraggi, and J.F. Uginet. Microstructural evolution during thermomechanical processing of Alloy 625. In E.A. Loria, editor, *Proceedings of the International Symposium on Superalloys 718, 625 and Various Derivatives*, pages 217–228. The Minerals, Metals & Materials Society, Warrendale, PA, 1991.

[336] D. Zhao, P.K. Chaudhury, R.B. Frank, and L.A. Jackman. Flow behavior of three 625 type alloys during high temperature deformation. In E.A. Loria, editor, *Proceedings of the International Symposium on Superalloys 718, 625, 706 and Various Derivatives*, pages 315–329. The Minerals, Metals & Materials Society, Warrendale, PA, 1994.

[337] S. Guo, D. Li, Q. Guo, Z. Wu, H. Peng, and J. Hu. Investigation on hot workability characteristics of Inconel 625 superalloy using processing maps. *Journal of Materials Science*, 47(15):5867–5878, 2012.

[338] B. López and J.J. Urcola. Hot deformation characteristics of Inconel 625. *Materials Science and Technology*, 12(8):673–678, 1996.

[339] I.J. Moore, J.I. Taylor, M.W. Tracy, M.G. Burke, and E.J. Palmiere. Grain coarsening behaviour of solution annealed Alloy 625 between 600-800°C. *Materials Science and Engineering A*, 682:402–409, 2017.

[340] J.D. Boyd and R.B. Nicholson. The coarsening behaviour of θ'' and θ' precipitates in two Al-Cu alloys. *Acta Metallurgica*, 19(12):1379–1391, 1971.

[341] A.J. Ardell. The effect of volume fraction on particle coarsening: Theoretical considerations. *Acta Metallurgica*, 20(1):61–71, 1972.

[342] F.J. Humphreys and M. Hatherly. *Recrystallization and Related Annealing Phenomena.* Elsevier Science, Oxford, UK, second edition, 2012.

[343] M. Detrois, R.C. Helmink, and S. Tin. Hot deformation characteristics of a polycrystalline γ-γ'-δ ternary eutectic Ni-base superalloy. *Materials Science and Engineering A*, 586:236–244, 2013.

[344] I.J. Moore, M.G. Burke, N.T. Nuhfer, and E.J. Palmiere. Evaluation of classical precipitation descriptions for γ'' ($\mathrm{Ni_3Nb\text{-}D0_{22}}$) in Ni-base superalloys. *Journal of Materials Science*, 52(14):8665–8680, 2017.

[345] Y. Ji, Y. Lou, M. Qu, J.D. Rowatt, F. Zhang, T.W. Simpson, and L.Q. Chen. Predicting coherency loss of γ'' precipitates in IN718 superalloy. *Metallurgical and Materials Transactions A: Physical Metallurgy and Materials Science*, 47(6):3235–3247, 2016.

[346] J.W. Brooks and P.J. Bridges. Metallurgical stability of Inconel alloy 718. In S. Reichman, D.N. Duhl, G. Maurer, S. Antolovich, and C. Lund, editors, *Superalloys 1988 (Proceedings of the Sixth International Symposium on Superalloys)*, pages 33–42. The Minerals, Metals & Materials Society, Warrendale, PA, 1988.

[347] X. Xie, C. Xu, G. Wang, J. Dong, W. Cao, and R. Kennedy. TTT diagram of a newly developed nickel-base superalloy Allvac 718 Plus. In E.A. Loria, editor, *Proceedings of the International Symposium on Superalloys 718, 625, 706 and Various Derivatives*, pages 193–202. The Minerals, Metals & Materials Society, Warrendale, PA, 2005.

[348] A. Oradei-Basile and J.F. Radavich. A current T-T-T diagram for wrought Alloy 718. In E.A. Loria, editor, *Proceedings of the International Symposium on Superalloys 718, 625 and Various Derivatives*, pages 325–335. The Minerals, Metals & Materials Society, Warrendale, PA, 1991.

[349] W.C. Hagel and H.J. Beattie. Cellular and general precipitation during high-temperature aging. In *Precipitation Processes in Steels*, Iron and Steel Institute Special Report No. 64, pages 98–107. Percy Lund Humphries & Co. Ltd, London, UK, 1959.

[350] A.J. Ardell. The growth of gamma prime precipitates in aged Ni-Ti alloys. *Metallurgical and Materials Transactions B*, 1(2):525–534, 1970.

[351] A.J. Ardell. Interfacial free energies and solute diffusivities from data on Ostwald ripening. *Interface Science*, 3(2):119–125, 1995.

[352] A.J. Ardell. A1-L1_2 interfacial free energies from data on coarsening in five binary Ni alloys, informed by thermodynamic phase diagram assessments. *Journal of Materials Science*, 46(14):4832–4849, 2011.

[353] V. Ganesan, V. Seetharaman, and V.S. Raghunathan. Interdiffusion in the nickel-iron system. *Materials Letters*, 2(4 PART A):257–262, 1984.

[354] H. Basoalto and M. Anderson. An extension of mean-field coarsening theory to include particle coalescence using nearest-neighbour functions. *Acta Materialia*, 117:122–134, 2016.

[355] H.L. Lukas, S.G. Fries, and B. Sundman. *Computational thermodynamics: The Calphad method*, volume 131. Cambridge University Press, Cambridge, UK, 2007.

[356] A.T. Dinsdale. SGTE data for pure elements. *Calphad*, 15(4):317–425, 1991.

[357] B.D. Cullity. *Elements of X-ray Diffraction.* Addison-Wesley, Reading, MA, second edition, 1978.

[358] Systat Software Inc., San Jose, CA. *Peakfit.* (`http://www.sigmaplot.com/`).

[359] R.E. Walpole, R.H. Myers, S.L. Myers, and K.E. Ye. *Probability & Statistics for Engineers & Scientists.* Pearson Education, Boston, MA, ninth edition, 2011.

[360] S. Ram, E.S. Ward, and R.J. Ober. Beyond Rayleigh's criterion: A resolution measure with application to single-molecule microscopy. *Proceedings of the National Academy of Sciences of the United States of America*, 103(12):4457–4462, 2006.

[361] A. Lipson, S.G. Lipson, and H. Lipson. *Optical Physics.* Cambridge University Press, Cambridge, UK, 2010.

[362] M. Born and E. Wolf. *Principles of Optics: Electromagnetic Theory of Propagation, Interference and Diffraction of Light.* Cambridge University Press, Cambridge, UK, 1999.

[363] D.A. Atchison and G. Smith. *Optics of The Human Eye.* Butterworth-Heinemann, Edinburgh, UK, 2000.